GEOCHEMISTRY AND TECTONIC SETTING OF THE EARLY PROTEROZOIC YAVAPAI SUPERGROUP, CENTRAL ARIZONA

Robert Kelly Vance

Submitted in Partial Fulfillment of
the Requirements for the Degree of
Doctor of Philosophy

New Mexico Institute of Mining and Technology
Socorro, New Mexico

1989

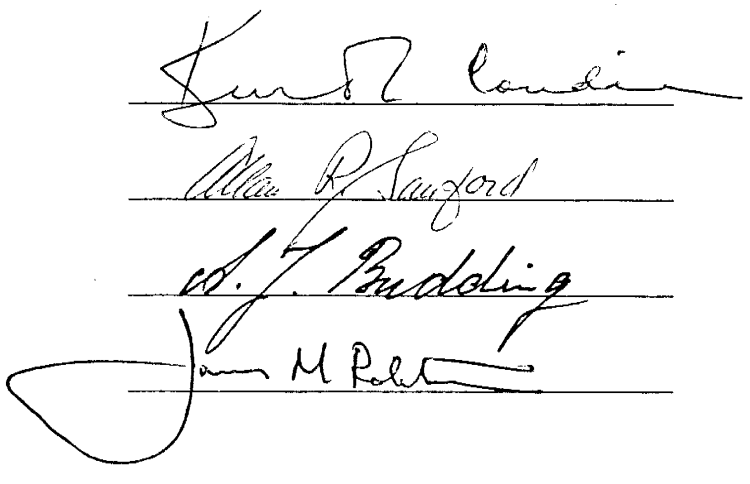

ACKNOWLEDGMENTS

The author gratefully acknowledges the Phelps Dodge Corporation for access to property and preparation of thin sections for this investigation. The cooperation of C. F. Arnold, J. E. DuHamel and Andy Peterson was especially important. The author is especially grateful to Paul A. Lindberg for sharing his insight and experience with the geology of the Jerome District. The author also benefited from the cooperation of D. C. White, P. A. Handverger and R. A. Rivera (Coca Mines) with regard to the Jerome District. Richard Pape is acknowledged for assistance in the Iron King Mine District. The author has also benefited from discussions with Pat O'Hara and Karl Karlstrom. Mike Knoper is acknowledged for use of his MODULUS program and discussions of Proterozoic Geology. The reactor staff of Sandia National Laboratories are acknowledged for irradiation of INAA samples. Research was sponsored by a Sigma Xi grant to the author and a NSF grant EAR-8313735 to K. C. Condie.

The author appreciates the excellent work of C. A. Anderson and co-workers which allowed investigation of volcanic chemistry.

The technical and financial support and general encouragement of my wife, Lisa, was essential to the project. Finally, the thesis director, K. C. Condie is acknowledged for originating and

directing this project. The author gratefully acknowledges the patience of the dissertation committee.

TABLE OF CONTENTS

LIST OF FIGURES

Figure

LIST OF TABLES

ABSTRACT

The Early Proterozoic Yavapai Supergroup of central Arizona includes the fault-bounded Ash Creek, Big Bug and Green Gulch blocks. Each block contains a proximal to vent facies submarine volcanic succession. Submarine diagenesis, hydrothermal alteration, greenschist to amphibolite facies metamorphism and subaerial weathering require rock classification and petrogenetic studies based on immobile elements. Investigation of variably altered felsic volcanics at Jerome confirms the mobility of major elements (except Al and Ti) and the LIL trace elements. REE and HFSE are relatively immobile, even in cases of extreme alteration. Immobile element rock classification indicates 30-50% andesite and dacite in each Yavapai block. Large volumes of andesite indicate an origin in a volcanic arc associated with a convergent plate margin. The association of calc-alkaline volcanics, granitic plutons and greenschist to amphibolite facies metamorphism in each Yavapai block is typical of the magmatic axis and associated low P/T metamorphic belt of Phanerozoic arcs. Geochemical discrimination does not exclude a continental margin arc; however, the submarine nature, the lack of clasts of continental derivation in conglomerates and the metal ratios in proximal massive sulfides favor an island arc setting for each block. The volcanic and plutonic chemical composition and lithologic associations suggest increasing crustal thickness from the Ash Creek to the Green Gulch to the Big Bug block. The composition of Yavapai mafic volcanics is consistent with derivation by 10-30% batch melting of a lherzolite source followed by olivine-clinopyroxene-plagioclase fractionation of parental magma. Yavapai volcanics are similar to those of modern island arcs as both enriched and depleted source regions are tapped. The high-P olivine-clinopyroxene fractionation of Ash Creek and Green Gulch Volcanics is also comparable to modern arc systems. Intermediate to felsic volcanics in each block may be derived by fractional crystallization of mafic parents.

The presence of minor volumes of mafic rock with WPB and MORB affinity, diabase dikes, massive sulfides and preservation of vent facies volcanics is compatible with incipient back-arc extension and associated subsidence. The lack of andesite in other Proterozoic successions with arc-like chemistry reflects a preservational bias toward the mafic-dominated basal succession of arcs which have not been subject to the subsidence associated with incipient extension.

Geochemistry and Tectonic Setting of the Early Proterozoic Yavapai Supergroup, Central Arizona

I. INTRODUCTION

The Problem

In the southwest United States 1800-1600 Ma rocks comprise the basement of large areas of Colorado and Arizona and portions of Utah and northern New Mexico. This early Proterozoic crust is dominated by subaqueous bimodal volcanic successions. The geochemical character and subaqueous nature of the mafic rocks are compatible with an origin in an island arc or associated back-arc basin; however, the lack of intermediate compositions is anomalous with respect to volcanic suites of modern arcs (Condie, 1986; Knoper and Condie, 1988). The paucity of andesite in the arc-like early Proterozoic successions of the southwest United States presents a major problem as andesite is the most diagnostic lithotype of modern volcanic arc successions. Furthermore, investigations of Archean, Proterozoic and Phanerozoic volcanic successions suggest a lack of fundamental change in the plate tectonic system and associated genesis of arc volcanic suites from the Proterozoic through the Phanerozoic (Hoffman, 1980; Condie, 1988).

The Yavapai Supergroup of central Arizona is exceptional among the Early Proterozoic successions as the United States Geological Survey investigations of Anderson and Creasey (1958) and Anderson and Blacet (1972) indicate the presence of large volumes of andesite. These rocks may provide positive identification of the tectonic environment and the key to explain the lack of andesite in other arc-like Early Proterozoic successions. Therefore, investigation of the Yavapai Supergroup is essential with regard to understanding the plate tectonic evolution and crustal growth of a major part of the North American continent.

Objectives of this Investigation

The investigations of Anderson and Creasey (1958) document the presence of andesites in the Proterozoic metavolcanic rocks of central Arizona. Andesitic and dacitic rocks compose > 30% of the exposed Yavapai rocks at Mingus Mountain and the Bradshaw Mountains. Previous identification of andesitic and dacitic protoliths is accomplished by major element analysis and optical petrography (Anderson and Creasey, 1958; Anderson and Blacet, 1972). However, major element composition may be altered by a variety of processes and is therefore unreliable for protolith determination of ancient rocks.

The Yavapai Supergroup was deposited largely in subaqueous conditions as indicated by pillow lavas and breccias,

hyaloclastites, turbidites and ferruginous chert beds (Anderson and Creasey, 1958; Anderson and Blacet, 1972; Lindberg, 1986). Consequently, these rocks were subject to possible submarine alteration. Greenschist to amphibolite-grade metamorphism constitutes an additional episode of alteration (O'Hara, 1980; Vance and Condie, 1986). Finally, the rocks have been subaerially exposed prior to deposition of Paleozoic sediments (Lindberg and Jacobson, 1974) and during Tertiary and Quaternary erosion (Anderson and Creasey, 1958). Collectively, these events provide ample opportunity for alteration of primary rock compositions. Studies documenting the effects of various forms of alteration on major and trace elements are listed in Section IV on alteration at the United Verde mine.

The dubious nature of rock classification by major elements and the tectonic significance of andesites indicate the need for a geochemical classification of the Yavapai Supergroup based on relatively immobile elements such as the scheme of Winchester and Floyd (1977). Furthermore, a data base of relatively immobile trace elements provides a dependable basis for petrogenetic modelling and tectonic discrimination (Vance and Condie, 1987).

The objectives of this investigation are summarized as follows:

(1) Acquire a geochemical data base including immobile trace element contents for a representative suite of the major volcanic units of the Yavapai Supergroup.

(2) Quantify the immobile element approach by testing element mobility in variably altered rocks.

(3) Use this data base for rock classification.

(4) Constrain the tectonic setting of the volcanics and associated sulfide deposits by use of immobile trace element distributions and lithologic associations.

(5) Evaluate magma origin of volcanic rocks of the Yavapai Supergroup.

Geologic Setting

Rocks of the Early Proterozoic Yavapai Supergroup are exposed from Mingus Mountain southwest to the Bradshaw Mountains in Yavapai County, central Arizona (Figs. 1-2). The Yapavai Supergroup consists of the Ash Creek and the Big Bug Groups (Anderson and Creasey, 1958; Anderson et al., 1971). The Ash Creek Group is limited to the Mingus Mountain area where it is in fault contact with the Big Bug Group along the Shylock Fault (Anderson and Creasey, 1958). The Big Bug Group is exposed from the vicinity of Prescott southward through the Bradshaw Mountains to Crown King. Both the Ash Creek and Big Bug Groups are dominated by a metamorphosed suite of volcanics, hypabyssal intrusives and volcaniclastic rocks with lesser amounts of volcaniclastic pelite.

The Texas Gulch Formation consists of pelitic rocks and local conglomerate in fault contact with the Ash Creek Group in the

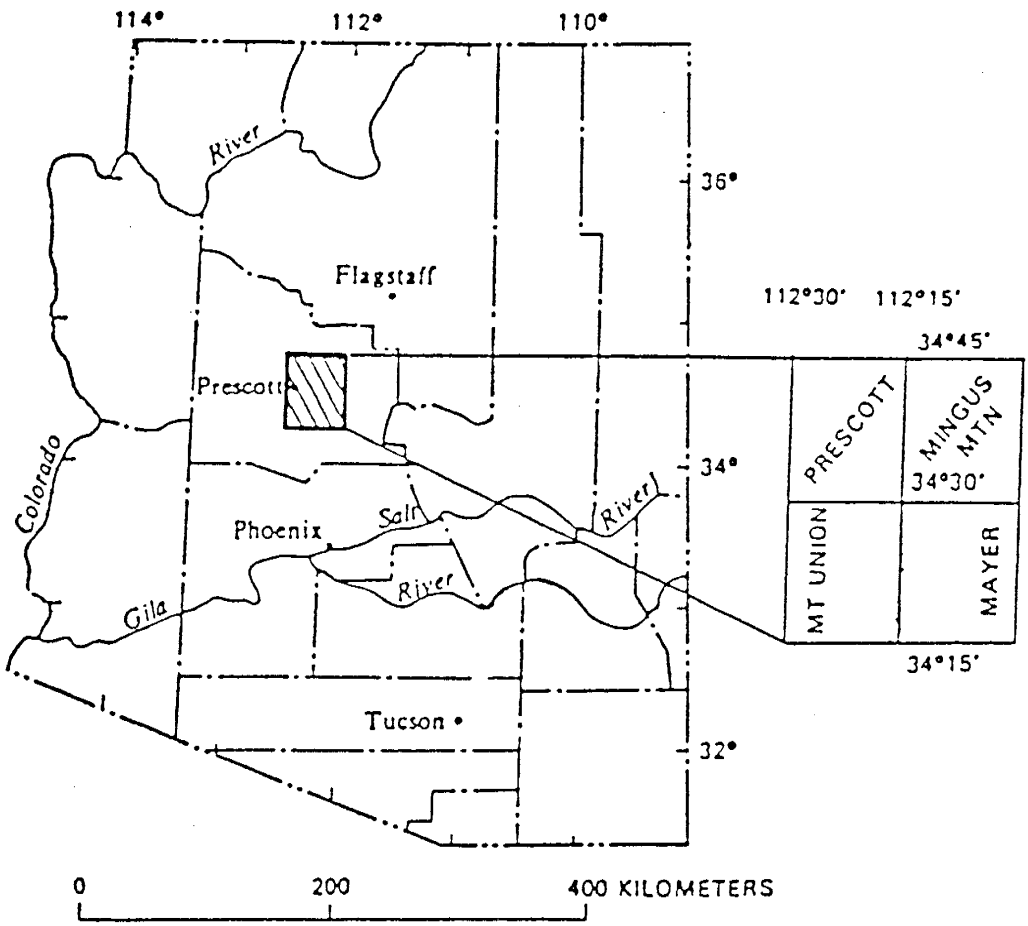

Fig. 1. Index for location and quadrangle base.

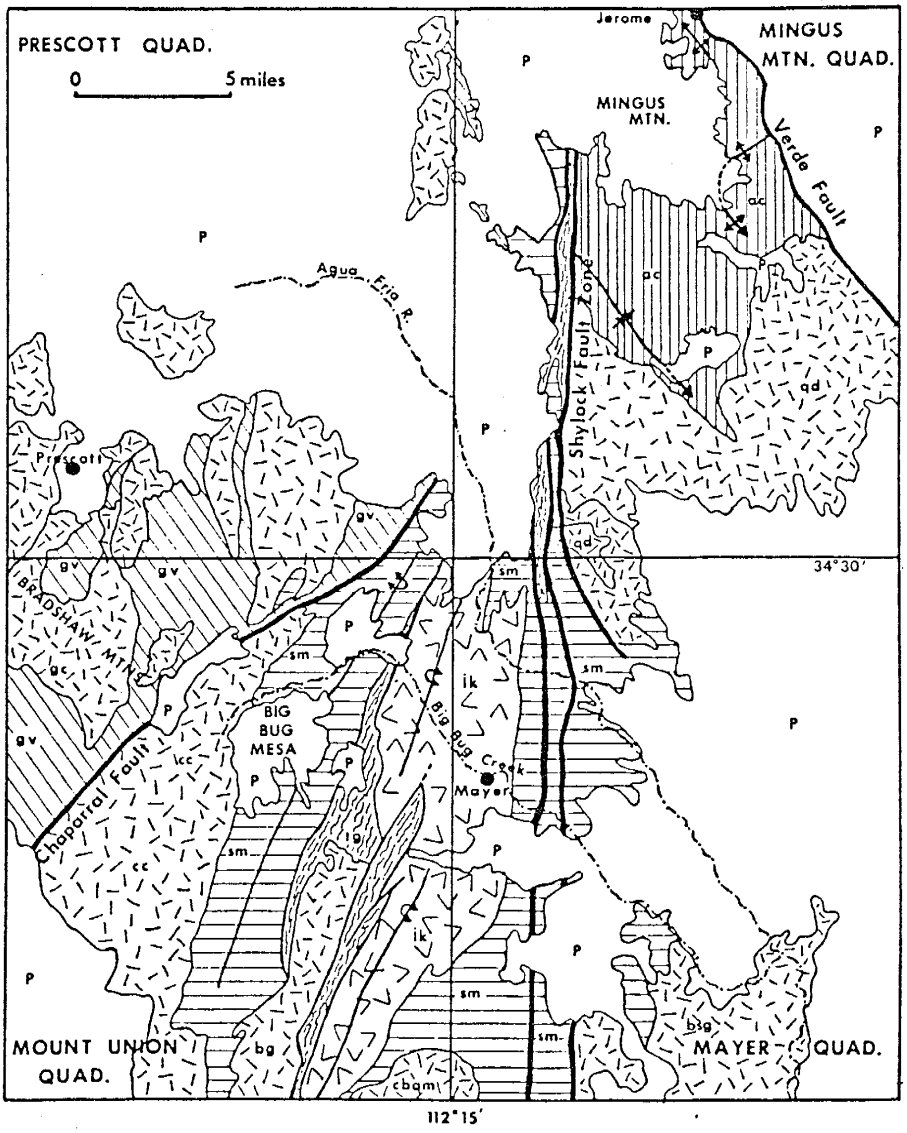

Fig. 2a. Geology of the Yavapai Supergroup (after Anderson et al., 1971)

Phanerozoic undifferentiated

PROTEROZOIC ROCKS

Texas Gulch Formation (1720-1710 Ma)

Granitoid plutons (minor gabbro): gc = Government Canyon Granodiorite (~ 1740 Ma), cc = Crooks Canyon Granodiorite, bg = Brady Butte Granodiorite (~ 1750 Ma), qd = quartz diorite of Cherry Creek (~ 1740 Ma), cbqm = Crazy Basin Quartz Monzonite (~ 1700 Ma), bsg = Badger Springs (~ 1740 Ma) and Bumblebee Granodiorite (~ 1750 Ma)

YAVAPAI SUPERGROUP

Iron King Volcanics

Spud Mountain Volcanics (rhyolite ~ 1750 Ma)

Green Gulch Volcanics

Ash Creek Group (Deception Rhyolite ~ 1790 Ma)

Fig. 2b. Geology of the Yavapai Supergroup (key). (Anderson et al., 1971; Karlstrom et al., 1987)

southwest portion of Mingus Mountain and in depositional contact with the Big Bug Group in the Bradshaw Mountains (Anderson and Creasey, 1958; Blacet, 1966; Anderson et al., 1971). The Precambrian rocks of Mingus Mountain are unconformably overlain by Paleozoic sedimentary rocks, Tertiary volcanic and sedimentary rocks and Quarternary sediments (Anderson and Creasey, 1958). In the Mayer-Prescott region most of the Paleozoic strata have been removed and the Precambrian rocks are overlain by Tertiary volcanic rocks and Quaternary gravels (Lindberg, 1986).

Mingus Mountain and the Bradshaw Mountains lie within the transition zone between the Colorado Plateau and the Basin and Range Province. Consequently, the region has experienced effects of Basin and Range extension as well as Laramide compression. The rocks of the Jerome District have been subject to Laramide high-angle reverse faulting and later normal extensional faulting related to formation of the Verde Graben (Lindberg, 1986). The Prescott-Mayer region to the south has also been affected by Laramide faulting as well as later extensional faulting (Anderson and Blacet, 1972; Lindberg, 1986).

U-Pb dating of zircons indicates an age of 1800 $\pm$ 10 Ma for the Deception Rhyolite of the Ash Creek Group in the Jerome area (Anderson et al., 1971). A date of 1755 $\pm$ 10 Ma has been obtained for a rhyolite in the Big Bug Group using similar methods (Anderson et al., 1971). Consequently, at least a portion of the Ash Creek Group is older than the Big Bug Group. Most of the late to post-kinematic plutons which intrude the Ash Creek and

Big Bug Group have dates of 1740 - 1750 (± 15 Ma) placing a minimum age limit on the Yavapai Supergroup. The Texas Gulch formation unconformably overlies portions of the Yavapai Supergroup yielding a maximum age of 1710 Ma for tuffaceous rocks (Conway and Silver, 1985). All dates are U-Pb zircon dates unless otherwise noted and dates reported before 1977 have been adjusted (Karlstrom et al., 1987) according to decay constants of Steiger and Jager (1971).

Previous Investigations

Geologic investigations of the Yavapai Supergroup have resulted chiefly from the economic significance of mineral deposits in the vicinity of Mingus Mountain and in the Bradshaw Mountains. The investigations of Anderson and Creasey (1958) are among the most significant and provide a foundation for future investigations. The geologic maps of Anderson and Creasey (1958) serve as a sampling guide for the Ash Creek Group in the Mingus Mountain area during this investigation. Recent detailed mapping in the Jerome area and along the east flank of Mingus Mountain (Lindberg, 1986; Lindberg, 1986) has resulted in a better understanding of the volcanic stratigraphy and effects of polyphase deformation.

Important contributions to the geology of the Yavapai Supergroup in the Bradshaw Mountains include the maps and professional papers of Anderson and Blacet (1972), Blacet (1966),

Blacet (1985), Anderson (1972). The USGS 15' Geologic Maps of the Mayer and Mount Union Quadrangles served as sampling guides for the Prescott-Mayer area (Anderson and Blacet, 1972).

An understanding of the structural complexities of the Yavapai Supergroup in the Prescott-Mayer area evolves through the investigations of DeWitt (1979), O'Hara (1980), Karlstrom and O'Hara (1984), Karlstrom (1986), Argenbright and Karlstrom (1986), O'Hara (1986). The present geochronological framework has been established by Anderson et al. (1971) and refined by Bowring et al. (1986). A regional tectonic framework is presented by Karlstrom and Bowring (1988).

Important contributions to the economic geology of the Yavapai Supergroup include the recognition of massive sulfides and related deposits as volcanogenic in origin. Gilmour and Still (1968) are early advocates of this model. Additional contributions include those of Anderson and Nash (1972), Lindberg and Jacobson (1974), Anderson and Guilbert (1979) and Lindberg (1986).

Tectonic Framework of the Yavapai Supergroup

Synthesis of geochronologic and structural data for central Arizona and the Yavapai Supergroup are presented by Karlstrom and Conway (1986) and Karlstrom et al., (1987). Karlstrom and Bowring (1988) describe the Proterozoic rocks of central Arizona in terms of blocks, terranes, and provinces. A block is an area of

Proterozoic basement bounded by major Proterozoic faults or shear zones. A terrane is composed of a block or group of blocks that represent a segment of Proterozoic lithosphere that evolved separately from other terranes. A province is a large tract of an orogen that was assembled during a single, major, convergent pulse. The Yavapai Supergroup may be divided into five blocks: the Big Bug, Ash Creek, Green Gulch, Hulapai-Bagdad and Mojave blocks. These blocks compose the Yavapai Province. This investigation examines three blocks separated by the Shylock and Chaparral Faults (Fig. 2). The eastern block, the Ash Creek block, is bounded on the west by the Shylock Fault zone, covered to the southeast by Tertiary volcanics and bordered by the Verde Graben to the northeast. The northern portion of this block is composed of the Ash Creek Group with a U-Pb zircon date of approximately 1800 Ma (Anderson et al., 1971). The plutons of the late to post-kinematic quartz diorite of Cherry Creek are dated at 1740 - 1720 Ma and separate the Ash Creek Group from the Big Bug Group within this block. The late-kinematic Bumblebee Granodiorite and Badger Springs Granodiorite intrude the Big Bug Group and are dated at 1750 and 1740 $\pm$ 10 Ma respectively (Anderson et al., 1971, Karlstrom et al., 1987).

The area west of the Chaparral Fault (Green Gulch block) consists of the Green Gulch Volcanics of the Big Bug Group and is intruded by the late to post-kinematic Government Canyon Granodiorite (1740 $\pm$ 15 Ma) (Anderson et al., 1971; Anderson and Blacet, 1972) (Fig. 2). The similar style, timing and intensity

of deformation and metamorphism of the Ash Creek and Green Gulch blocks suggest that these blocks are part of the same terrane folded into a crustal-scale antiform cored by the Big Bug block (Karlstrom and Bowring, 1988).

Although the Ash Creek and Green Gulch blocks appear to be essentially contemporaneous with respect to the timing of volcanism and subsequent deformation, the central Big Bug block, is significantly different. This block consists of Spud Mountain and Iron King Volcanics with a date of 1755 $\pm$ 10 Ma on a rhyolite flow from the upper part of the Spud Mountain Volcanics (Anderson et al., 1971). Additional constraints are imposed by the folded nature of the unconformity between the Texas Gulch Formation and the Big Bug Group (Blacet, 1985) and a 1750 $\pm$ 10 Ma date on the pre-kinematic Brady Butte Granodiorite (Anderson et al., 1971). A date of 1699 $\pm$ 5 Ma (Karlstrom and Bowring, 1988) for the Crazy Basin Quartz Monzonite (Fig. 2), which post dates F_2 folding and may be coeval with F_3 movement along the Shylock Fault, constrains the timing of deformation to approximately 1700 Ma (Karlstrom et al., 1987). Consequently, the timing of volcanism in the Spud Mountain Volcanics of the Big Bug block may overlap with the volcanics of the Ash Creek and Green Gulch blocks, however, the age of major deformation lagged behind that of the other blocks by 30 to 50 Ma after a period of erosion and redeposition. This suggests the Shylock Fault zone represents a suture between separate tectonic blocks of the Yavapai Supergroup (K. Karlstrom, 1987 personal communication).

The Ash Creek and Green Gulch blocks experienced ductile deformation prior to 1740 Ma. The Big Bug block is characterized by a 1700 Ma deformation absent in the Ash Creek and Green Gulch blocks, but present in the remainder of the Yavapai Province. The Hulapai-Bagdad and Mojave Blocks were close enough to undergo identical deformational events at 1700 Ma. Karlstrom and Bowring (1988) suggest the Ash Creek-Green Gulch terrane may have been thrust over the Big Bug block during this event, escaping the penetrative 1700 Ma deformation which characterizes the Big Bug block. The constraints imposed by the chronology of volcanism, plutonism and deformation are summarized in Table 1.

Table 1. Tectonic Framework of the Yavapai Supergroup

	Ash Creek Block	Green Gulch Block	Big Bug Block
Volcanics:	Ash Creek Group Spud Mountain Volcanics (~ 1790 Ma)	Green Gulch Volcanics (~ 1790 Ma?)	Iron King Volcanics Spud Mountain Volcanics (~ 1755)
Plutons:	Cherry Creek late to post-kinematic (1740-1720 Ma) Bumblebee (1750 Ma) Badger Springs (1740 Ma) late-kinematic	Govt. Canyon late to post-kinematic (1740 Ma)	Brady Butte pre-kinematic (1750 Ma) CBQM late-kinematic (~ 1700 Ma)

II. GEOLOGY OF THE YAVAPAI SUPERGROUP

Lithology and Stratigraphy

The Ash Creek Block

Early investigations of the Ash Creek Group which focus on the Jerome District were concerned largely with the United Verde and UVX deposits and host rocks. Anderson and Creasey (1958) provide a bibliography of these investigations and others related to the geology of the Jerome District. At the time Anderson and Creasey (1958) produced the first regional scale investigation of the Yavapai Supergroup, the rocks were referred to as the Yavapai Series, which includes the Ash Creek and the Alder Groups. The term "Alder Group" was subsequently dropped and "Big Bug Group" substituted (Anderson et al., 1971). The lithostratigraphic term Yavapai Supergroup is substituted for Yavapai "Series" in accordance with amendments to the U.S. Code of Stratigraphic Nomenclature (Henderson et al., 1980). Anderson and Creasey (1958) recognized seven formations in the Ash Creek Group (Fig. 3). The oldest unit is the Gaddes Basalt and is overlain by the Buzzard Rhyolite. The Shea Basalt, Dacite of Burnt Canyon and Brindle Pup Andesite are interpreted as contemporaneous units that

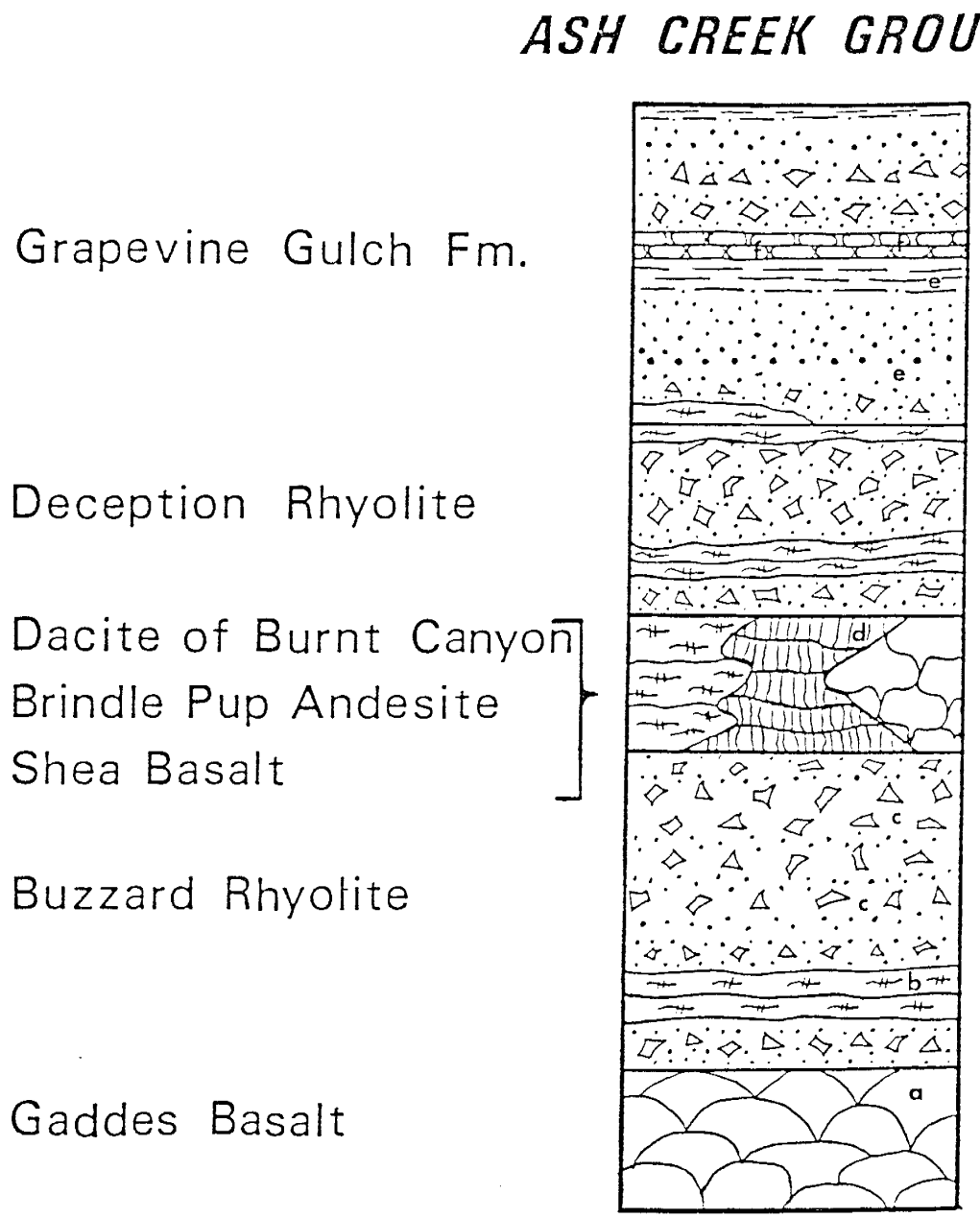

Fig. 3. Generalized stratigraphic column for the Ash Creek Group (after Anderson et al., 1971).

Lithologic key: a, pillow lava; b, rhyolitic lava; c, rhyolite tuff; d, andesite lava; e, bedded coarse to fine-grained volcaniclastic rocks; f, bedded chert and ironstone.

separate the Buzzard Rhyolite from the younger Deception Rhyolite. The Grapevine Gulch formation overlies the Deception Rhyolite.

The Gaddes Basalt forms the basal portion of the exposed volcanic pile and is locally intercalated with rhyolite (Anderson and Creasey, 1958). Anderson and Creasey (1958) recognize pillows and amydules in outcrops along Gaddes and Black Canyon and possible agglutinates on the east flank of Mingus Mountain (Map 1, App. A). The author has observed well preserved pillow lava, pillow breccia and hyaloclastite in Gaddes Canyon. Locally, the rocks are amygdaloidal with chlorite and quartz as the most common fillings. Some pillowed basalts are strongly epidotized in Gaddes Canyon. Anderson and Creasey (1958) note the Gaddes Basalt has compositions intermediate between basalt and andesite. They were also aware of alteration problems but concluded the rock was basaltic based on the high percentage of mafic minerals.

The Buzzard Rhyolite overlies the Gaddes Basalt and is overlain by the Shea Basalt in Black Canyon (Anderson and Creasey, 1958). Anderson and Creasey (1958) note preservation of flow banding, vesicles and amygdules in the Buzzard Rhyolite and the local presence of tuffaceous units and intercalated basaltic agglomerate. In the vicinity of Burnt Canyon, the western outcrops of Buzzard Rhyolite consist of dense dark grey, aphyric rock which interfingers with a green-grey unit characterized by a fragmental texture and possible relict pumice fragments. The 'fragmental' variety contains chlorite and probably represents a pyroclastic rock.

The basaltic agglomerate mapped by Anderson and Creasey (1958) is in contact with a dense, dark grey vesicular flow. The agglomerate consists of amygdaloidal fragments ranging from 1 to 15 cm in size surrounded by an epidote-rich matrix. Some fragments which appear to have chilled borders are probably pillow-breccias.

In Burnt Canyon, several variations are observed in the Buzzard Rhyolite (Map 2, App. A). Much of the Buzzard Rhyolite is a dark grey to black aphanitic rock with fine plagioclase phenocrysts comprising $\leq$ 15% of the rock. Relict eutaxitic texture, flow banding, and amygdules are observed in some outcrops. Fragmental zones bear lithic fragments of volcanic or hypabyssal origin in an aphanitic matrix. These fragments vary in length from < 1 cm to > 5 cm and the extremely vuggy nature of the rock suggests that it originally contained pumice fragments or vesicles. The variation in texture and clast size indicates pyroclastic rocks ranging from volcanic breccia to lapilli tuff and tuff. In Burnt Canyon, a sharp contact exists between a dark aphyric unit characterized by stretched amygdules or pumice fragments and a unit characterized by approximately 10% fine plagioclase phenocrysts in a green aphanitic groundmass. The green unit locally preserves flow banding and contains abundant amygdules filled with chlorite, quartz, calcite, and sulfides. Near the contact, this unit contains inclusions of the dark aphyric rock and jasper, indicating that it was extruded over the dark unit.

The Shea Basalt overlies the Buzzard Rhyolite in Black Canyon and is considered coeval with the Brindle Pup Andesite and the Dacite of Burnt Canyon (Anderson and Creasey, 1958). Detailed mapping by Lindberg (1986) on the east flank of Mingus Mountain indicates the presence of two suites of mafic rocks separated by felsic volcanics. The Shea Basalt, exposed at lower elevations, (Map 3, App. A) consists of both massive and pillowed flows. Massive sulfide deposits are associated with the felsic rocks which overly the Shea Basalt. The mafic rocks overlying the felsic horizon consist of basaltic tuffs and flows (Lindberg, 1986).

The Dacite of Burnt Canyon is a plagioclase-phyric extrusive to shallow-intrusive suite with an aphanitic to fine grained groundmass. Much of this unit consists of thick amygdaloidal lavas or domes with minor pyroclastic deposits or sedimentary beds between flows. Flow surfaces are vesicular and sometimes include fragments of ferruginous chert in basal breccia.

On the southern flank of Mingus Mountain, the Brindle Pup Andesite separates the Buzzard Rhyolite from the younger Deception Rhyolite (Anderson and Creasey, 1958). The Brindle Pup Andesite is a series of lava flows and is very uniform with respect to mineral composition and texture. Most of the rock contains about 20% plagioclase phenocrysts in an aphanitic groundmass. Near flow contacts, the percentage of phenocrysts decreases and amygdules increase. Autobrecciation is common and ferruginous chert fragments are incorporated in the basal breccias of some flows.

Pillow-like structures are observed at one locality, and columnar jointing is preserved locally in both the Deception Rhyolite and the Brindle Pup Andesite along their contact.

The Deception Rhyolite is defined by Anderson and Creasey (1958) to include all rhyolitic rocks older than the Grapevine Gulch Formation and younger than the Shea Basalt-Dacite of Burnt Canyon-Brindle Pup Andesite coeval suite. Detailed mapping by Lindberg (1986) suggests the lower portions of the Deception Rhyolite are contemporaneous with the Shea Basalt. The Deception Rhyolite in the Ash Creek drainage resembles the Buzzard Rhyolite, however, the Deception Rhyolite exposed in Hull Canyon and Mescal Gulch near Jerome weathers red due to hydrothermal alteration associated with the United Verde massive sulfide deposit. The United Verde massive sulfide deposit is situated near the top of the Deception Rhyolite.

The Deception Rhyolite is a suite of lavas, domes, tuffs and breccias. Anderson and Nash (1972) subdivided the Deception Rhyolite near Jerome into a lower unit, the Cleopatra Member and an upper unit (Fig. 4). Lindberg (1986) subdivides the Deception Rhyolite into the Lower Deception Rhyolite and the Upper Deception Rhyolite composed of flows and breccias, the Cleopatra Crystal Tuff and an Upper Succession of flows breccias and tuffs. Lindberg's (1986) Upper Deception and Upper Succession are equivalent to the lower and upper unit respectively, of Anderson and Nash (1972). This investigation suggests that tuffs are also present within the Upper Deception Rhyolite of Lindberg (1986).

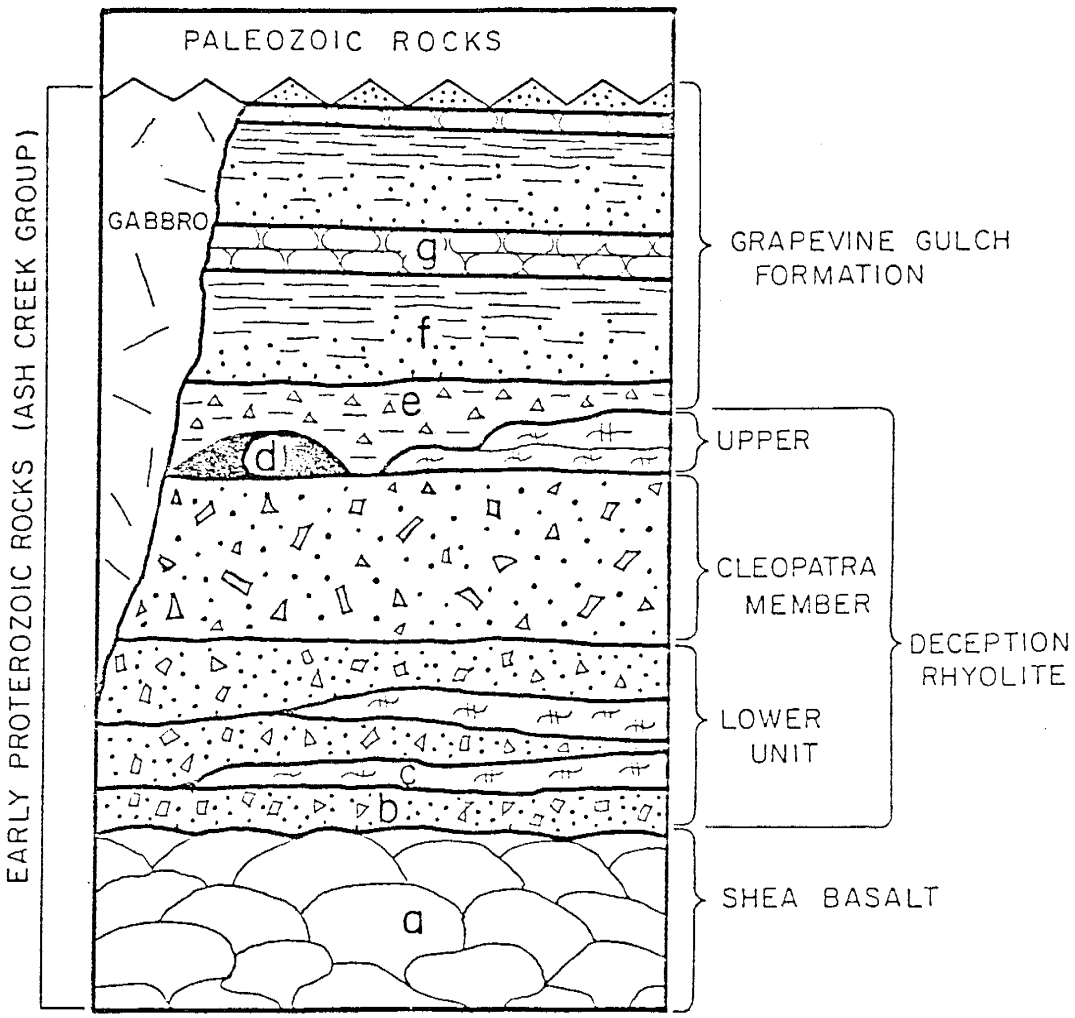

Fig. 4. Generalized stratigraphic section of early Proterozoic rocks in the Jerome area after Anderson and Nash (1972) and Lindberg and Jacobson (1974). Lithologic key: a, pillow basalt; b, rhyodacite tuffs and breccias; c, rhyodacite lava; d, massive sulfides; e, volcaniclastic rocks; f, turbidites; g, bedded ferruginous chert.

The Deception Rhyolite is dated by the U-Pb zircon method as approximately 1800 Ma (Anderson et al., 1971).

The Grapevine Gulch Formation overlies the Deception Rhyolite, specifically the Upper Succession Rhyolite of Lindberg (1986), in the Jerome area. South of Jerome, the Grapevine Gulch Formation consists largely of fine grained sedimentary and volcaniclastic rocks, cherty beds and variable amounts of bedded ferruginous cherts (ironstone), volcanic breccia, and dacitic flows, domes and intrusions (Anderson and Creasey, 1958).

Along Highway 89A, just south of the road crest on Mingus Mountain, fragmental rocks composed chiefly of angular clasts (most < 1 cm) of mafic rock are exposed in the road cuts (Map 4, App. A). Petrographic investigation indicates these clasts were originally glassy and vesicular hyaloclastite and scoria of basaltic composition. These rocks are part of the "lithic tuffaceous beds" of Anderson and Creasey (1958) and may be roughly correlative with some of the hyaloclastite mapped by Lindberg (1986) in the Grapevine Gulch Formation north of Jerome.

In Hull Canyon near Jerome (Map 5, App. A), the Grapevine Gulch Formation consists of volcaniclastic turbidites, bedded sedimentary rocks, minor tuffs and bedded ferruginous chert. These rocks yield to an increasing percentage of andesitic volcanics to the northeast (Lindberg, 1986). The Deception Rhyolite-Grapevine Gulch boundary in Hull Canyon near Jerome locally exhibits chaotic rocks composed of angular rhyolitic blocks mixed with slabs of volcaniclastic turbidite. These probably originated when viscous

rhyolitic magma domed the turbidite covered sea floor. As the rhyolite chilled and spalled, both fragmental rhyolite and turbidites slumped off this local high to produce the chaotic rocks. This process has been used to explain similar rocks in the Ordovician marginal basin of southwest Wales (Kokelaar et al., 1985). Southeastern exposures of the Grapevine Gulch formation also exhibit evidence of coeval felsic volcanism and epiclastic sedimentation. Dacite flows are interlayered with Grapevine Gulch sedimentary rocks and intrusive dacite grades into flows interlayered with tuffaceous sedimentary rocks (Anderson and Creasey, 1958).

Thin sedimentary beds are reported in the Deception Rhyolite, the Buzzard Rhyolite, the Shea Basalt and other mafic units and were observed at the Dacite of Burnt Canyon-Quartz Porphyry contact during this investigation (Anderson and Creasey, 1958; Guston, 1986; Lindberg, 1986; Johnson, 1986). These volumetrically insignificant beds are largely epiclastic rocks and chemical precipitates, consequently, the Grapevine Gulch Formation is the only exposed unit of the Ash Creek Group containing a significant sedimentary component. However, much of this is of volcaniclastic origin (Anderson and Creasey, 1958).

Anderson and Creasey (1958) mapped many quartz-bearing rhyolitic rocks as intrusive "Quartz Porphyry". Consequently, these rocks were considered to be younger than most of the Ash Creek Group. Subsequent mapping by Lindberg (1986) on the east flank of Mingus Mountain indicates that much of the Quartz

Porphyry is extrusive. Field and optical petrographic investigations of Quartz Porphyry in Burnt Canyon and Gaddes Canyon suggest that these rocks are also extrusive. The thick lenticular nature of the outcrops are typical cross sections of short, thick rhyolitic flows or domes and compliment the proximal to vent facies character of the other volcanic rocks. The lack of cross-cutting relationships or obvious xenoliths is consistent with an extrusive origin. Some Quartz Porphyry interlayered with Buzzard Rhyolite contains relict flow banding, amygdules and rudimentary columnar jointing. Relict vesicles are also present in the Gaddes Canyon Quartz Porphyry. Quartz Porphyry interlayered with the Dacite of Burnt Canyon also appears extrusive as indicated by a lack of cross-cutting relationships. The presence of thin volcaniclastic beds indicates a break or change in volcanic activity at the Quartz Porphyry-Dacite of Burnt Canyon contact. The lenticular nature of the outcrop is an aid in distinguishing the felsic lavas from ash flows which cover a much greater area. Although some of the prophyries may be intrusive, most are a local part of the extrusive volcanic stratigraphy.

Gabbro is one of the younger rocks of the Ash Creek Group. These hypabyssal intrusives are subject to the same metamorphic events as their host rocks (Anderson and Creasey, 1958). Lindberg (1986) interprets the gabbro sill at the United Verde Mine as part of a feeder for pillow basalts in the overlying Grapevine Gulch formation. Consequently, much of the gabbro in the Ash Creek

Group could be the hypabyssal equivalent of extrusive mafic rocks in the district.

Spud Mountain Volcanics are exposed in the Ash Creek block south of the Cherry Batholith. Outcrops are largely discontinuous due to Quarternary cover, disruption by plutons and faulting. However, a small area exposed along Yarber Wash reveals plagioclase-phyric mafic dikes and lavas. The high percentage of dikes in the area suggests a proximal or vent volcanic facies.

The final Precambrian igneous event in the Jerome area is represented by the Cherry Batholith (quartz diorite) and associated granodiorite porphyry dikes. The dikes intrude both the batholith and surrounding Ash Creek Group. The Cherry Batholith appears to be in part late kinematic (P. Lindberg, 1984 personal communication) and the dikes are post-kinematic. The batholith is composed of multiple plutons with U-Pb zircon dates that range from 1740 to 1720 Ma (Anderson et al., 1971; Karlstrom and Bowring, 1988.

The Green Gulch Block

The Green Gulch Volcanics, which crop out northwest of Big Bug Mesa (Fig. 2), are interpreted as the oldest rocks of the Big Bug Group by Anderson and Blacet (1972). The investigations of Karlstrom and Bowring (1988) suggest the Green Gulch Volcanics are more likely to be coeval with the Ash Creek Group if these volcanics are related to those in other tectonic blocks. These

rocks are bounded on the east by the northeast-trending Chaparral Fault contact with the Crooks Canyon Granodiorite and intruded on the west by the Government Canyon Granodiorite, defining the Green Gulch Block of Karlstrom and Bowring (1988). The type section is exposed along Green Gulch in the southeast corner of the Prescott Quadrangle.

The lower portion of the Green Gulch Volcanics (Fig. 5) consists of slate with minor ferruginous chert and pebble conglomerate. The basal slate is overlain by pillow basalts with subordinate rhyolitic flows and tuffs interlayered with thin beds of chert and slate. South of Lynx Lake, the Green Gulch Volcanics consist of massive amygdaloidal flows, pillow lavas and breccias. Some of these mafic rocks are porphyritic, bearing plagioclase and blocky pseudomorphs of amphibole after pyroxene. Mafic dikes and sills are also common and have been subject to the same metamorphic effects as their host. Lesser volumes of volcaniclastic rocks characterized by clasts of felsic volcanics in dark matrix are also present. Locally, clasts of ferruginous chert are observed in thin beds between flows or in basal breccias. Thin units of quartz-bearing felsic tuffs are also present. Near Hassayampa Lake, approximately 2.6 km northwest of Mount Union, autobrecciated lavas and possible pillows are observed. Anderson and Blacet (1972) report pillow lava downstream from this site.

BIG BUG GROUP

IRON KING VOLCANICS

SPUD MOUNTAIN VOLCANICS

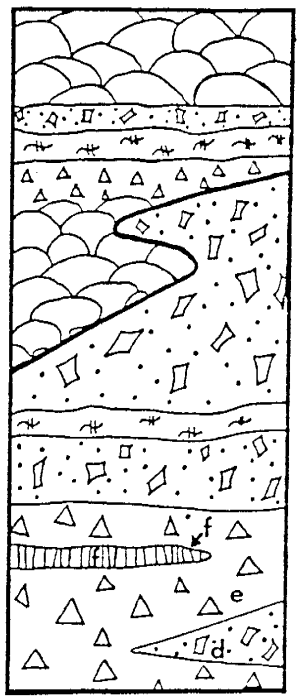

GREEN GULCH VOLCANICS

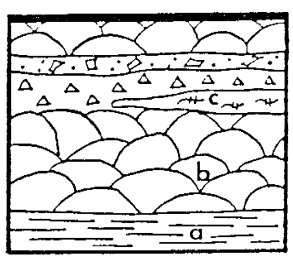

Fig. 5. Generalized stratigraphic columns for the Iron King and Spud Mountain Volcanics (Big Bug block) and the Green Gulch Volcanics (Green Gulch block) (after Anderson and Blacet, 1972). Lithologic key: a, fine-grained tuffaceous sediments; b, pillow lava; c, rhyolite lava; d, andesite to rhyolite tuffs; e, andesite to rhyolite breccia; f, andesite lava.

The Big Bug Block

The stratigraphy of the Big Bug Group depends on structural interpretation of these rocks. The evolution of structural and subsequent stratigraphic interpretation is summarized by O'Hara (1986). The complex interfingering nature of the original volcanic stratigraphy enhances the difficulties of interpretation. An initial stratigraphy for the Big Bug Group developed through the investigations of Anderson and Creasey (1958) and Anderson and Blacet (1972), results in subdivision into the Green Gulch Volcanics, the Spud Mountain Volcanics and the Iron King Volcanics (Fig. 5). The Green Gulch Volcanics are largely confined to the area west of the Chapparal Fault (Green Gulch Block) and consequently, are not discussed here. Each volcanic suite of the Big Bug Block contains numerous subdivisions which are shown on Fig. 2 after Anderson and Blacet (1972). The following descriptions of the Big Bug Group are summarized after Anderson and Creasey (1958) and Anderson and Blacet (1972) with additional observations from this investigation.

The Spud Mountain Volcanics are exposed within the Big Bug and Ash Creek blocks of Karlstrom and Bowring (1988) and are divided into two major units. The Lower Unit is dominated by volcanic breccia bearing variable proportions of rhyolite and porphyritic andesitic clasts interbedded with crystal tuff and graded tuffaceous sediments. The Upper Unit is dominated by andesitic tuffaceous rocks. Anderson and Blacet (1972) recognize

beds 3 to 9 m thick with basal breccias grading upwards into crystal tuffs and siltstones as turbidity current deposits that originated as submarine pyroclastic flows.

South of Big Bug Mesa, exposures of breccia thin and intertongue with a massive crystal tuff bearing plagioclase and quartz phenocrysts. Along Wolf Creek (Map 6, App. A) the breccia contains abundant fragments (> 5 cm) of vuggy rhyolitic rock in a dark matrix. Some of the surrounding tuff in this area exhibits a possible relict eutaxitic texture. North and east of Big Bug Mesa (Fig. 2) amygdaloidal andesitic flows intertongue with tuffaceous rocks of the Upper Unit and breccia of the Lower Unit. Rhyolitic rocks and epiclastic turburdites occur between some of the amygdaloidal andesite flows and the tuffs. Amygdules in the andesitic flows are composed of actinolite, chlorite, quartz, calcite and sulfides.

Although primary textures are well preserved along portions of Big Bug Creek; the intensity of deformation increases to the west approaching the Crooks Canyon Granodiorite, obliterating primary textures in that area. Many of the rocks near the granodiorite are altered. Some of this alteration is late to post-kinematic as actinolite and quartz veins cut the foliation. These veins may be related to Precambrian faulting or younger intrusive activity. The Spud Mountain Volcanics are less foliated in the eastern outcrops along Big Bug Creek where porphyritic flows and breccias bearing up to 25% plagioclase are prominent. In the Mayer Quadrangle, north of Big Bug Creek and west of the

Shylock Fault Zone, andesitic tuffs, ferruginous cherts and pelite dominate the Upper Unit of the Spud Mountain Volcanics. South of Big Bug Creek and west of the Shylock Fault Zone, pelite dominates in the Upper Unit (Anderson and Blacet, 1972). Alternative structural interpretations suggest the pelites in the southeast portion of the Mayer Quadrangle are younger than the Spud Mountain and Iron King Volcanics and may correlate with the Texas Gulch Formation (De Witt, 1979; Argenbright and Karlstrom, 1986).

Quartz Porphyry is mapped within the Big Bug Block and within the Shylock Fault Zone itself. The extensive Quartz Porphyry outcrop within the Shylock Fault Zone is probably a tuff. Other small outcrops may be domes or flows. The Spud Mountain Volcanics host the Quartz porphyry; consequently, the Quartz Porphyry is considered a unit of the Spud Mountain Volcanics in the Big Bug block.

The Iron King Volcanics are also part of the Big Bug block (Fig. 2). These rocks have been interpreted as the youngest of the volcanic suites and are named after exposures in Iron King Gulch (Anderson and Creasey, 1958). The Iron King Volcanics include a lower sequence of pillowed and massive amygdaloidal basaltic to andesitic flows with some interbedded rhyolite and sedimentary rocks and an upper suite of mixed mafic and felsic tuffaceous rock. The Iron King Volcanics are situated between exposures of the Texas Gulch Formation and Spud Mountain Volcanics on the west and the Skylock Fault Zone and Spud Mountain Volcanics on the east. Anderson and Blacet (1972) describe interfingering

contacts between the Iron King and Spud Mountain volcanics and subsequent investigations suggest portions are coeval. Massive sulfides occur near the Iron King - Spud Mountain contact north of Mayer and were exploited by the Iron King mine.

Preservation of primary textures in the Iron King Volcanics is variable. In the area northeast of Poland Junction (Mount Union Quadrangle), metamorphic foliation is well developed, relict textures are rare and contacts are masked by the metamorphic fabric. However, local preservation of porphyritic texture reveals up to 25% plagioclase phenocrysts. Most feldspar is crushed and recrystallized and the groundmass contains abundant fine-grained chlorite and sericite. Horizons bearing about 15% clasts (< 5 cm) of volcanic rock and resemble lithic rich zones of pyroclastic deposits, but have a matrix identical to other Iron King volcanics in the area. In some outcrops fine lithic fragments and wispy streaks resembling flattened pumice occur together supporting an origin as a pyroclastic rock. These outcrops are plagioclase-phyric like most of the Iron King Volcanics in the area. The abundant feldspar fragments suggest a pyroclastic origin; however, cataclasis of a porphyritic lava yields similar textures and the lithic rich zones may represent volcaniclastic beds between flows. The basaltic composition of rocks from this area supports the latter interpretation.

South of Mayer, along Cedar Creek (Mayer Quadrangle) the Iron King Volcanics consist of well preserved aphyric mafic flows with amygdules composed of quartz and calcite. In the vicinity of the

Bluebell Mine (Map 7, App. A) farther to the south, biotite and amphibole appear in the rocks and grain size increases. However, amygdaloidal textures are still recognizable locally. South of the Bluebell Mine the rocks consist of mafic flows and pillow breccias with quartz-calcite amygdules and fillings between clasts. Volcaniclastic beds dominated by mafic to intermediate clasts with subordinate volumes of chert and limestone are abundant. Mafic clasts with relict subophitic textures are also present locally. Thin beds of limestone and pelite are interbedded with tuffaceous rocks in some areas (Anderson and Blacet, 1972; O'Hara, 1980). Rhyolitic rocks at the Bluebell Mine contain abundant sericite and locally fine needles of tourmaline. Quartz phenocrysts are the only definitive relict texture in the intensely foliated felsic rocks.

Structural Geology and Regional Metamorphism

The Ash Creek Block

Major folds in the Jerome and Mingus Mountain area trend north-northwest. These trends are recognized through the investigations of Anderson and Creasey (1958), Anderson and Nash (1972) and Lindberg (1986). Polyphase deformation is also recognized by Anderson and Creasey (1958) noting a northeast trend of secondary fold axes. Detailed mapping by Lindberg (1986) along the northwest flank of Mingus Mountain from Jerome to the Copper

Chief Mine defines north-northwest trending primary folds with east-northeast trending secondary folds. Lindberg (1986) suggests amplitudes of 1800 m for primary folds based on subsurface data and indicates smaller amplitudes for secondary folds, but emphasizes their importance in determining regional outcrop pattern. The outcrop pattern on Lindberg's (1986) detailed maps is typical of the central parts of orogenic belts or regions of reactivated basement rocks and resembles the Type 1 interference pattern of Ramsay (1967).

The dominant foliation appears to parallel the axial plane of the primary folds (Anderson and Creasey, 1958; Anderson and Nash, 1972). This foliation is most prominent near Jerome and thin sections reveal a secondary foliation produced by advanced crenulation of the primary foliation. Although foliation is locally well developed south of Jerome, many of the rocks display only the most rudimentary development of foliation, and consequent preservation of many primary textures.

The timing of faulting has been the subject of considerable debate in the Jerome district. The United Verde Extension (UVX) orebody was explained as the downfaulted apex of the United Verde ore body by Ransome (1932) and by Norman et al. (1958). Subsequent investigations by Lindberg and Jacobson (1974), Handverger (1975), and Lindberg (1986) dispute that theory, indicating that Precambrian fault movement is not required and the UVX ore bodies may be interpreted as independent massive sulfide bodies. The Pine Fault south of Jerome appears to have had Proterozoic

movement, however, interpretations on the nature of the fault differ (Anderson and Creasey, 1958; Anderson and Nash, 1972). Lindberg (1986) interprets the Pine Fault as part of a cauldron subsidence fault system related to the eruption of the Deception Rhyolite.

Anderson and Creasey (1958) suggest Precambrian movement on the Hull, Shea and Cu-Chief Faults but indicate these are post deformation faults. A Precambrian origin for the Hull Fault is not confirmed by subsequent investigations, however, Lindberg (1986) indicates the Shea Fault and Vein and the Cu-Chief Fault are part of the same low angle, post-folding fault system and may be late Precambrian. The late, low angle Shea Fault may be related to thrusting of the Ash Creek-Green Gulch terrane over the Big Bug block, however, this is speculation and requires further investigation to confirm or dismiss this possibility.

The Shylock Fault zone and the Cherry Creek Batholith separate the Ash Creek Group from the Big Bug Group. The significance of the Shylock Fault Zone is controversial. Lindberg (1986) notes lithologies on either side of the zone are not significantly different. P. Anderson (1986) interprets the fault as a zone of extreme strain produced by the buttressing effects of large masses of plutonic rock in the region and suggests the Grapevine Gulch Formation may be traced across the fault zone without offset. The Shylock Fault is interpreted by O'Hara (1980) as a zone of extreme transposition produced during F_1 deformation. Anderson (1967) suggests approximately 8 km of dextral strike slip

has taken place along the fault, based on offset of quartz diorite. Subsequent structural investigations by Argenbright and Karlstrom (1986) suggest sinistral strike slip movement related to F_3 folds along the zone. Recent evaluation of the Shylock Fault by Karlstrom et al. (1987) and Karlstrom and Bowring (1988) suggest it is a major tectonic boundary.

Within the Ash Creek Group, the Gaddes Basalt bears the assemblage actinolite-chlorite-epidote in coexistence with albite and quartz. The Dacite of Burnt Canyon and Buzzard Rhyolite contain biotite which coexists with chlorite, albite and quartz. These assemblages are characteristic of low-grade or greenschist facies metamorphism (Winkler, 1979).

At Jerome, the altered rhyolites are characterized by a quartz-oligoclase-chlorite-sericite assemblage. In pelitic rocks, the assemblage quartz-chlorite-muscovite is considered typical of greenschist facies; however, the transition from albite to oligoclase-andesine compositions may be interpreted as the beginning of the amphibolite facies (Winkler, 1979). The exact T-P conditions of such reactions vary with bulk chemical composition, and consequently, the change in plagioclase composition may vary with lithotype. Although the rocks at Jerome are not pelites, alteration has shifted the bulk chemical composition in that direction.

Moreover, the Shea Basalt contains the assemblage oligoclase-hornblende-chlorite which is typical of low-grade amphibolites (Winkler, 1979). Metagabbro in the Jerome area

contains the assemblage actinolite-chlorite-epidote-calcite-quartz-albite. The collective assemblages from felsic and mafic rocks suggest upper greenschist facies conditions.

Some Spud Mountain Volcanics are exposed east of the Shylock Fault Zone within the Ash Creek block. Limited sampling of these mafic rocks reveals an actinolite-oligoclase-quartz-epidote assemblage which suggests upper greenschist facies. Development of foliation is rudimentary in this area. These characteristics are consistent with the metamorphic grade and texture of the Ash Creek Group north of the Cherry Batholith.

The petrography of the Ash Creek Block indicates greenschist facies metamorphic conditions prevailed but were locally elevated to the greenschist-amphibolite boundary. It is also emphasized that much of the Ash Creek Group generally does not possess a well developed foliation except in areas near major fold hinges.

The Green Gulch Block

In the Green Gulch Volcanics west of the Chaparral Fault, the mafic rocks contain actinolite, biotite, chlorite, albite, calcite and quartz, and locally hornblende and oligoclase are recognized indicating a range from greenschist to lower amphibolite facies. The structural style of the Green Gulch Volcanics is similar to that of the Ash Creek Group with a northwest trend of foliation (Krieger, 1965; Karlstrom and Bowring, 1988). The minimal development of foliation in much of the Green Gulch terrane is

also similar to the Ash Creek block. Consequently, primary textures are preserved in many of the Green Gulch rocks.

The Big Bug Block

Interpretation of the structural geology of the Big Bug Group is crucial to development of a stratigraphy and consequent volcanic history. Structural models have evolved continuously from the foundations lain by Anderson and Creasey (1958), Anderson (1972) and Anderson and Blacet (1972). These and subsequent models proposed by DeWitt (1976) and O'Hara (1980) are summarized and reviewed in O'Hara (1986) and Karlstrom and Conway (1986). Structural investigations concentrate on the Big Bug block of Karlstrom and Bowring (1988). Recent models emphasize complex polyphase deformation (O'Hara and Karlstrom, 1984; Argenbright and Karlstrom, 1986; O'Hara, 1986) beginning with early isoclinal recumbent folds (F_1) which are overprinted and transposed by upright folds (F_2) which form the dominant north-northeast structural grain of the region (Karlstrom et al., 1987). Recent work along a mylonite zone of the Shylock Fault recognizes an F_3 fold generation associated with sinistral strike-slip faulting (Argenbright and Karlstrom, 1986). The presence of thrusts, nappes and potential allochthonous rock associated with the recumbent F_1 folding is indicated by O'Hara (1986) and further complicates stratigraphic reconstruction. Current synthesis of available structural, metamorphic, and geochronological data

suggest the Big Bug block is characterized by northwest verging recumbent folds (F_1) and thrusts overprinted by tight to isoclinal upright folds (F_2). This interpretation correlates sinistral strike-slip reactivation of the Shylock Fault zone with progressive F_2 shortening (Karlstrom and Bowring, 1988).

The metamorphic grade of the Big Bug Group ranges from lower greenschist facies to middle amphibolite facies. Anderson and Creasey (1958) indicate greenschist assemblages in Big Bug rocks southwest of Mingus Mountain, but locally higher grade assemblages in rhyolitic tuffs east of the Iron King Mine.

In the Spud Mountain and Iron King Volcanics of the Big Bug block, most of the rocks contain greenschist-facies assemblages. The Iron King Volcanics between the Iron King Mine and Mayer typically contain albite, actinolite, quartz, calcite, biotite, chlorite and epidote indicating greenschist facies. The optical determination of An content in plagioclase in this area is difficult due to crushing and recrystallization. Along Big Bug Creek, the amygdaloidal andesitic flows of the Spud Mountain Volcanics contain actinolite, quartz, biotite, epidote and oligoclase, another greenschist assemblage.

South of Big Bug Mesa, large volumes of crystal tuff are exposed. These rocks contain the assemblage albite-biotite-quartz-epidote-calcite typical of the greenschist facies. However, metamorphic grade increases to the southeast and south toward the Crazy Basin Quartz Monzonite, and the southern end of the Brady Butte Granodiorite (Anderson, 1972; DeWitt, 1979; Blacet, 1985).

Staurolite and andalusite schists are present in the vicinity of Crazy Basin and middle-amphibolite assemblages are reported near Crown King indicating metamorphic temperatures of 500-600°C and pressures < 2.5 kb (Anderson, 1972; O'Hara, 1980 and Blacet, 1985). Karlstrom and Bowring (1988) indicate metamorphism at temperatures of 550°C and pressures of 3.7 kb which post-date major F_2 deformation in the Crazy Basin area. The Big Bug block is intruded by a multitude of plutons (Anderson and Blacet, 1972) and these affect local metamorphic grade according to the timing of intrusion and the thermal peak of regional metamorphism. Metamorphic assemblages may also be affected by local chemical gradients as described in the Bluebell area south of Mayer (O'Hara, 1980). The mafic rocks in this Bluebell Mine area contain abundant hornblende and oligoclase-andesine typical of amphibolite facies. Altered felsic rocks associated with massive sulfides near the Bluebell Mine contain minor amounts of tourmaline (schorl).

III. PETROGRAPHY OF THE YAVAPAI SUPERGROUP

Volcanics of the Ash Creek Block

The Gaddes Basalt

The Ash Creek Group is described according to the chronology and stratigraphic interpretation of Anderson et al. (1971). Each 'formation' contains multiple volcanic units, therefore considerable mineralogical and textural variation is present. The Gaddes Basalt generally contains 2-10% plagioclase phenocrysts (1-3 mm) in a groundmass dominated by plagioclase microlites (< 0.2 mm). Plagioclase displays Carlsbad and combined Carlsbad-Albite twinning with common glomeroporphyritic texture. Epidote and calcite comprise over 1% of the groundmass. Chlorite and actinolite also occur in the groundmass and amygdules, and locally compose up to 5% of the rock. Large amygdules exhibit crenulated actinolite. Amygdules also contain quartz and may account for 3% of the rock. Fine quartz 'eyes' probably originated as tiny vesicles.

The Buzzard Rhyolite

The Buzzard Rhyolite is characterized by < 5% plagioclase phenocrysts ($\leq$ 2 mm). Some units contain 3-5% plagioclase microlites (< 0.2 mm) as well as larger phenocrysts (> 1 mm). Glomeroporphyritic texture is common in some units. Quartz phenocrysts (0.2-1 mm) characterize some units of the Buzzard Rhyolite and range from 1-3%. The presence of fine anhedral quartz phenocrysts with rounded margins suggest magmatic resorption. The groundmass consists largely of very fine grained quartz and feldspar with small amounts of biotite and chlorite (1-2%), up to 3% calcite and sericite plus accessory epidote, opaque minerals, apatite and zircon. Amygdules are present in some units and consist of quartz and calcite, and spherulitic texture is also preserved in some samples.

Lithic inclusions, fragmented crystals and wispy concentrations of sericite and chlorite resembling flattened pumice suggest that much of the Buzzard Rhyolite originated as ash flows supporting field observations indicative of pyroclastic rocks. Other units in the Buzzard Rhyolite probably originated as lava flows and alignment of amygdules and plagioclase laths in these rocks may define a primary flow foliation.

The basaltic agglomerate mapped within the Buzzard Rhyolite by Anderson and Creasey (1958) is a vesicular to scoriaceous mafic pyroclastic unit. Amygdules composing over 30% of each clast are mainly quartz and epidote. Vesicle walls contain skeletal opaque

needles, epidote, chlorite, actinolite, calcite and plagioclase microlites.

The Shea Basalt

The Shea Basalt consists of approximately 67% plagioclase and 30% hornblende. Some blocky hornblende suggests pseudomorphs after pyroxene. The remainder of the rock consists of opaque minerals, epidote, chlorite, apatite and calcite. Apatite needles are extremely long and prominent in these high P_2O_5 rocks. Metamorphic foliation is rudimentary and a relict diabasic texture is common. Alteration is minimal in these rocks, consisting of minor amounts of epidote and small quartz-calcite veinlets related to brittle deformation.

The Dacite of Burnt Canyon

The Dacite of Burnt Canyon is a porphyritic rock with a microgranular to felty groundmass composed of fine-grained plagioclase and minor quartz. Vermiform intergrowths in some groundmass feldspar suggest the presence of K-feldspar. Biotite and chlorite (1-2%) mixtures are scattered through the groundmass. Epidote and calcite account for 1-2% of the rock and are accompanied by accessories including opaque minerals, sphene-leucoxene and zircon. Phenocrysts in the Dacite of Burnt Canyon are mostly plagioclase (1-6 mm) varying from 2 to 15%, and

minor quartz (< 0.4 mm) which is often rounded suggesting resorption. Plagioclase phenocrysts are subhedral to euhedral, display Albite, Carlsbad and combined twinning, zoning and glomeroporphyritic texture. Optical determination of An content indicates an albite composition. Amygdules consisting of quartz, calcite, epidote, biotite and chlorite are scattered through most units. The presence of spherulitic texture suggests some of the units were vitrophyric. Although some pyroclastic beds occur between flows, the absence of shattered phenocrysts in these rocks supports an origin as lava flows or domes.

The Brindle Pup Andesite

The Brindle Pup Andesite exhibits minor mineralogical-textural variation and is characterized by 20-25% plagioclase phenocrysts (1-5 mm) in an aphanitic groundmass. Most of the groundmass is too fine-grained for accurate mineral identification, however, some coarser samples have a groundmass dominated by plagioclase microlites and up to 10% interstitial biotite and chlorite. Fine-grained calcite and epidote may comprise 1% of the rock. Accessories include opaque minerals, zircon, apatite and sphene-leucoxene.

Plagioclase phenocrysts are subhedral to euhedral and display a variety of twinning. Some laths are rounded suggesting abrasion or resorption. Relict zoning is prominent and marked by an increase in calcite and epidote alteration toward cores.

Glomeroporphyritic texture is prevalent and clots may exceed 5 mm. Inclusions are also common and resemble the host rock, albeit, the plagioclase size is intermediate between that of the groundmass microlites and the phenocrysts. Thin sections reveal concentrations of chlorite with curved margins suggesting initial replacement of autobrecciated glass. Relict textures include a primary flow foliation defined by alignment of amygdules, inclusions and phenocrysts.

The Deception Rhyolite

The Deception Rhyolite is a volcanic suite which exhibits considerable variety in texture and mineralogy. The Deception Rhyolite samples were obtained mostly in the Jerome area (Fig. 6). In Hull Canyon, the lower unit of the Deception Rhyolite contains abundant breccia with dark chlorite-rich rock fragments. The curved outlines of the fragments suggest the rocks were originally glassy. Breccia samples from the lower unit contain 2 to 3% subhedral to euhedral phenocrysts of quartz (0.5-5 mm) in diameter. Embayments are common in quartz phenocrysts and are interpreted as primary textures developed by resorption prior to eruption. Plagioclase is not ubiquitous as a phenocryst phase in the lower unit, but locally comprises up to 4% of the rock, and laths range in length from 0.4 to 1.2 mm. Fine-grained angular fragments of quartz and/or plagioclase phenocrysts are abundant and scattered throughout the groundmass, which consists chiefly of

quartz, feldspar, sericite, and chlorite. Carbonate and opaque minerals occur as accessories. The abundance of shattered phenocrysts indicates an ash flow origin for at least part of the lower unit. Rhyolite flows typically contain 2 to 3% of euhedral to subhedral quartz phenocrysts less than 2 mm in diameter. Embayments are also common in these phenocrysts, but the lack of fragmented phenocrysts supports an origin for these rocks as flows.

The Cleopatra Member is generally more phenocryst rich than the lower unit and locally contains > 25% phenocrysts. These phenocrysts are chiefly quartz with smaller amounts of sodic plagioclase. Sericite, chlorite, and carbonate collectively comprise 4 to 6% of these rocks; apatite, opaque minerals, zircon, and/or allanite occur as accessories. Primary embayments are common in quartz phenocrysts and the abundance of angular phenocryst fragments suggests an ash-flow origin for the Cleopatra Member. Although flattened pumice fragments are not recognized, wispy concentrations of sericite are suggestive of collapsed pumice (Anderson and Nash, 1972). The Cleopatra Member is characterized by brecciation and purple hematitic staining along the contact with the upper unit (Lindberg, 1986). This portion of the Cleopatra contains 7% plagioclase and 3% quartz phenocrysts in a groundmass of quartz, plagioclase and sericite with accessory carbonate, epidote, apatite, zircon and opaque minerals. Quartz phenocrysts display embayments and plagioclase laths have rounded or abraded corners.

A typical upper unit dome or thick flow from Hull Canyon contains 5% plagioclase phenocrysts in a groundmass of fine quartz, plagioclase and sericite. Accessories include epidote, apatite and opaque minerals. Plagioclase laths display albite, Carlsbad and combined twinning and rounded corners. Some replacement of plagioclase by epidote is common. Fine lithic fragments or inclusions are present and appear to be cognate. An upper unit sample from the UVX mine contains < 1% plagioclase ($\leq$ 1 mm) phenocrysts. Optical determination of An content indicates an albite-oligoclase composition. Some plagioclase is partially replaced by carbonate. The groundmass is extremely fine quartz and feldspar with 2-3% sericite. A few elongate clots of chlorite, quartz and carbonate suggest relict amygdules.

Quartz Prophyry

These porphyritic rocks have a microgranular to spherulitic groundmass. The groundmass probably contains a significant amount of K-feldspar as various exsolution textures ranging from micrographic to plumose to vermiform are observed. Spherulites are morphologically identical to orthoclase-cristobalite spherulites which occur in young volcanic rocks. Radiating quartz-feldspar overgrowths also surround some phenocrysts. As metamorphic recrystallization is minimal in these rocks, the textures are probably relict and indicate the original rock was vitrophyric. The Quartz Porphyry contains of 2-4% plagioclase

(< 3 mm) and 2-3% quartz (0.3-4 mm) phenocrysts. Quartz exhibits beta morphology and prominent embayments. Some plagioclase also appears to have been subject to magmatic corrosion as many phenocrysts are rounded or possess irregular margins. Some plagioclase is zoned and albite and Carlsbad twinning are present in many laths. Alteration is minimal with minor replacement of plagioclase by calcite and sericite.

Some Quartz Porphyry from the east flank of Mingus Mountain (Cu Chief Area) exhibits cataclastic features such as crushed quartz and feldspar phenocrysts. Some of the cracked feldspar is healed with quartz. The rocks in this area are exposed along the eroded fault scarp of the youthful Verde Graben. Consequently, these rocks have been subjected to an additional recent period of brittle deformation and alteration as well as initial Precambrian alteration and metamorphism. The Quartz Feldspar Porphyry (QFP) of Lindberg (1986) is also exposed in this area and contains 15% plagioclase with 5% as phenocrysts (1-3 mm) and 10% as fine (< 1 mm) fragments. Larger crystals exhibit albite, Carlsbad and combined twinning. Quartz composes 6% of the sample with 3% as subhedral, embayed, beta-form crystals (> 1 mm) and 3% as fragments (< 1 mm). The abundance of shattered phenocrysts and lithic fragments indicate this rock is an ash flow and distinguish it from other quartz porphyries which originated as lavas. The groundmass is spherulitic to microgranular and dominated by quartz and feldspar. Epidote, opaques and sericite plus chlorite each comprise < 1% of the rock. Carbonate is abundant (> 3%) and

occurs as fracture fillings in phenocrysts, local concentrations and disseminated in the groundmass. Fine-grained sericite and chlorite occur with the intergranular carbonate and may be coeval. The pervasive 'rusty' appearance of the rocks suggests the carbonate may be ferroan calcite or dolomite.

Grapevine Gulch Formation

The Grapevine Gulch Formation exhibits significant lithologic variation, however, a high percentage of the rocks are volcaniclastic. The possibilities of mixing of diverse volcanic rock types makes most of these rocks undesirable for geochemical sampling. Consequently, only a few of the most homogeneous rocks were sampled. The 'lithic tuffaceous beds' of Anderson and Creasey (1958) appear to have originated from a relatively homogenous mafic source as revealed in thin section. These rocks are pyroclastic and consist of vesicular to scoriaceous ash and lapilli plus 2-10% crystals and crystal fragments of plagioclase (< 2mm). Coarser plagioclase phenocrysts exhibit albite twinning; however, much of the feldspar has altered to a mixture of epidote, calcite and chlorite. Some of the coarsest ash and lapilli contain 10% plagioclase microlites in vesicle walls. Many are skeletal and extremely fine, resembling quench texture plagioclase observed in young volcanic rocks. Some clasts exhibit pilotaxitic texture. In some lapilli, the amygdules decrease from 1 mm near the center to < 0.1 mm at the margin. Amygdules consist of

chlorite, quartz, epidote, calcite and opaque dust. Calcite also occurs as fillings between pyroclasts and may constitute 3-5% of some samples. Vesicle walls also contain abundant chlorite, epidote, calcite and pervasive opaque dust. Some of the ash and lapilli exhibit slight flattening of vesicles.

These rocks are part of a uniform pyroclastic deposit of coarse ash to lapilli. The lack of quartz phenocrysts and consistent petrography and chemistry indicate a lack of mixing with other volcanic rocks. The near-opaque character of the groundmass may result in part from alteration of basaltic glass to palagonite. Diagenesis and regional metamorphism result in conversion of the original Fe-rich glass to a low grade metamorphic assemblage with disseminated hematitic dust. The homogenous composition and texture of this unit and submarine nature of the enclosing rocks suggest this rock originated as a pyroclastic apron around a submarine or shoaling mafic vent.

In Hull Canyon, near Jerome, the lower portion of the Grapevine Gulch Formation contains volcaniclastic turbidite deposits (Figs. 4 & 6). Some of these deposits are very rich in plagioclase and resemble subaerial ash flows except for well developed graded bedding. Examination of this lithotype reveals 30% chalky white plagioclase phenocrysts (2-4 mm) and fragments plus 5-10% quartz phenocrysts. Although plagioclase appears fresh in some outcrops, it is almost totally altered to epidote and opaque minerals. This appears to have been a two stage process with initial replacement by epidote and calcite and subsequent

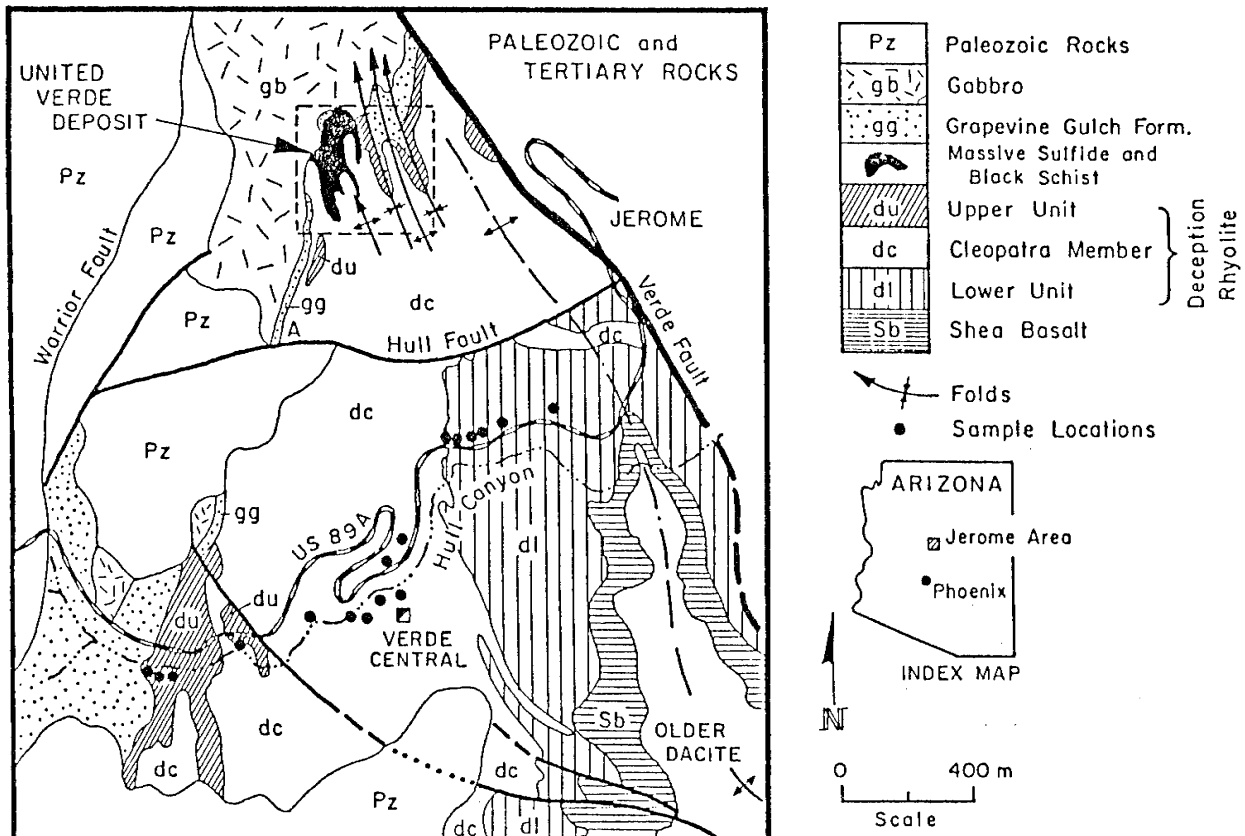

Fig. 6. Simplified geologic map of early Proterozoic rocks from the Jerome area, west-central Arizona. Modified after Anderson and Nash (1972) and Lindberg and Jacobson (1974). Area of the United Verde deposit (Fig. 7) is outlined.

replacement by opaque minerals. Lithic fragments include ferruginous chert (< 2 mm) and clasts of chlorite-rich rock (> 3 mm). The chloritic clasts may be chloritized rhyolite associated with the United Verde massive sulfide deposit (Anderson and Nash, 1972). Alternatively these clasts may represent original clasts of pumice which have been replaced by chlorite. Some local concentrations of wispy sericite also resemble pumice fragments. Groundmass minerals are difficult to identify but probably include quartz, feldspar, chlorite and variable amounts of calcite, epidote, sericite and accessory apatite and opaque minerals.

Gabbro from the United Verde Mine and exposures to the southwest along the roadcuts of highway 89A exhibits relict igneous textures in hand specimen, but thin sections reveal substantial alteration. Pseudomorphs suggest an original composition of 25-30% pyroxene (2 mm) and 70-75% plagioclase (3-4 mm). Some relict augite or pigeonite remains; however, most has been replaced by actinolite, chlorite, and epidote. Replacement of plagioclase by epidote, calcite, quartz, chlorite and opaque dust is near total. The few remaining grains of plagioclase are albite.

There appears to be two generations of chlorite in the gabbro; a green chlorite and a blue chlorite which may represent Mg and Fe-rich species respectively. Investigations of two generations of chlorite in the altered rocks of the Copper Queen area of the Big Bug Group, indicate an early Mg-chlorite

associated with hydrothermal alteration and a second generation of Fe-chlorite produced by metamorphic fluids (O'Hara et al., 1987). The chlorites in the Ash Creek Group gabbros may originate in a similar manner. The gabbro at the United Verde Mine is interpreted as a shallow sill by Lindberg (1986) and the gabbros in road cuts also appear concordant. Consequently, the magma was probably injected at a shallow level allowing interaction with seawater saturated volcaniclastic sediment. This event may have produced much of the pervasive alteration of original igneous minerals and generation of the Mg-chlorite.

Spud Mountain Volcanics

Rocks in Yarber Wash, east of the Shylock Fault, are commonly plagioclase-phyric and include dikes as well as lavas. A typical sample contains up to 20% plagioclase phenocrysts (4-5 mm) which are extensively saussuritized. Subordinate proportions of amphibole pseudomorphs after pyroxene phenocrysts are also present. The rocks are approximately 70% plagioclase and 20% amphibole, 4% secondary quartz and the remainder consists of opaques, carbonate, epidote and sericite.

Volcanics of the Green Gulch Block

Basaltic rocks from the Green Gulch Volcanics in the northwestern portion of the Mount Union quadrangle include

pyroxene and plagioclase-phyric lavas and hypabyssal intensive rocks. Some pyroxene-phyric rocks contain two generations of amphibole including blocky pseudomorphs after pyroxene phenocrysts (3-4 mm) and a second generation of elongate (6-7 mm) amphibole needles. This rock consists of approximately 65% amphibole (hornblende or actinolite), 25% saussuritized plagioclase with minor quartz, 5% chlorite, 4% carbonate and traces of apatite and opaque minerals, an assemblage characteristic of both the pyroxene and plagioclase-phyric lavas.

Some plagioclase-phyric basalts display a bimodal plagioclase distribution bearing 2-5% phenocrysts (3-6 mm) and microlites (< 2 mm). Relict trachytic and amygdaloidal texture are locally preserved, and amygdules consist of carbonate, quartz and chlorite. Basaltic andesite flows contain 65-70% plagioclase with traces of secondary quartz. Amphibole composes 35-30% of the rock with accessory apatite, epidote and opaque minerals. Samples from the Hassayampa Lake area exhibit autobrecciation which is not apparent at outcrop scale. Numerous amygdules are filled with quartz and amphibole. Relict intersertal to intergranular texture is preserved in some rocks.

Andesitic rocks contain up to 30% plagioclase phenocrysts and fragments in a groundmass dominated by fine-grained feldspar and minor quartz with 4-5% fine-grained chlorite and biotite, up to 4% carbonate and 1-2% opaque minerals. An abundance of crystal fragments suggests that a portion of the andesites are tuffs. One

of the more siliceous andesites (13grb20) contains some beta-form quartz phenocryst fragments.

Felsic rocks are also porphyritic with one sample bearing 3% plagioclase and 1% quartz phenocrysts in a groundmass of fine-grained feldspar and quartz with 2% chlorite-biotite, 2% carbonate and accessory opaque minerals plus sericite. Relict spherulitic texture is observed in one sample. The development of foliation is variable and marked by alignment of amphiboles, micaceous minerals and sometimes alignment of plagioclase. Stretched spherulites and amygdules provide strain indicators in some rocks.

Volcanics of the Big Bug Block

The Spud Mountain Volcanics

The Big Bug Group map units of Anderson and Creasey (1958) and Anderson and Blacet (1972) include multiple lithotypes within each unit. Consequently, map unit abbreviations are included in discussions of the Big Bug Group to indicate the unit affiliation samples. These abbreviations are explained in Appendix B. The Spud Mountain andesitic flows (sma) exposed north of Big Bug Mesa exhibit weak to strong foliation and amygdules are one of the few relict textures. In some areas amygdules comprise 10-20% of the rock and are composed of quartz and fibrous actinolite. These rocks consist of fine-grained plagioclase, biotite and quartz with

minor amounts of actinolite, carbonate, epidote, chlorite and opaque minerals. Alignment of biotite and stretched amygdules define the foliation.

The crystal tuffs (smct and smt) exposed south of Big Bug Mesa contain 5-30% plagioclase phenocrysts and abundant fine-grained fragments of plagioclase. Most of the quartz 'eyes' in these rocks appear to be polygonized amygdules, however, a few grains in each sample are phenocrysts that display embayments. Biotite defines the foliation composing 2 to 6% of these rocks along with some fine-grained chlorite. Carbonate composes up to 3% of the rocks disseminated and in clots which resemble vesicles. Other constituents include fine-grained actinolite and skeletal opaque crystals. The abundance of crystal fragments and local lithic fragments is typical of a tuff. Much of the plagioclase is poikilitic with inclusions of sericite, biotite and quartz. Optical determination of anorthite content indicates compositions of An_{7-13}.

The fine tuffs (smt) north of Big Bug Mesa contain an assemblage of very fine-grained plagioclase, quartz, biotite, actinolite, apatite and opaque minerals. Biotite imparts a strong metamorphic fabric to these rocks and a crenulation cleavage is apparent in thin section. Recognizable phenocrysts are not abundant. The Spud Mountain rhyolite (smr) north of Big Bug Mesa is also extremely fine grained, dominated by quartz and feldspar. Extremely fine laths of albite-twinned plagioclase are recognized

along with scattered fine grains of chlorite, carbonate, sericite and epidote.

Optical identification of the Spud Mountain breccia (smb) mineral composition is difficult. Plagioclase is abundant in matrix and lithic fragments, but is totally saussuritized. The groundmass is a mixture of alteration products and the contacts between lithic fragments and matrix are masked by pervasive alteration. Hand specimen studies are more useful with respect to identification of lithics. The breccia unit (smb) also includes numerous coherent flows. A typical lava consists of 70% subhedral plagioclase, 28% actinolite, 2% carbonate with minor chlorite, quartz, accessory opaque minerals and apatite. The alignment of amphibole and plagioclase imparts a metamorphic foliation. The rocks include crystal clots which may be cognate inclusions or glomeroporphyritic texture.

The development of metamorphic fabric is variable in the Spud Mountain Volcanics, consequently, so is the preservation of relict textures. A dike exposed along Big Bug Creek preserves original diabasic to subophitic texture. This rock consists of 60% plagioclase, 20-30% poikilitic actinolite with abundant opaque inclusions, 10-20% biotite and 2-4% skeletal opaques with the morphology of ilmenite or hematite. The rock also contains 2% interstitial quartz with abundant apatite needles. Apatite is also observed in the plagioclase which has andesine compositions. The texture and the high percentage of opaques and apatite strongly resemble the Shea Basalt of the Ash Creek Group.

The Iron King Volcanics

The Iron King volcanics (ika) exposed northeast of Big Bug Mesa contain 25-30% relict phenocrysts (3-4 mm) of variably altered or poikilitic albitic plagioclase. The groundmass is dominated by fine-grained plagioclase and quartz, 5-15% biotite and chlorite, 2-5% carbonate and sericite, 1-2% epidote and accessory opaque minerals. Some stretched quartz-carbonate blebs may be relict amygdules. Metamorphic fabric is well developed and biotite defines the foliation. Granulation of feldspar and development of pressure shadows are pervasive features.

Rocks from the Bluebell area south of Mayer are amphibolites. The Iron King Volcanics (ika and ikab) in this area are characterized by variable proportions of hornblende, plagioclase, biotite, quartz, carbonate and opaque minerals. Development of foliation is often weak with well developed granoblastic polygonal textures. Most carbonate is concentrated in relict amygdules. The Iron King rhyolites (ikr) in this area contain 2-3% quartz polygonized phenocrysts, in a matrix of feldspar and quartz characterized by granoblastic polygonal texture. Some rocks contain 1-2% fine plagioclase phenocrysts. Several percent of fine-grained sericite and chlorite are scattered through the groundmass along with traces of opaque minerals and locally tourmaline.

IV. MAJOR AND TRACE ELEMENT MOBILITY IN VARIABLY ALTERED ROCKS

Introduction

Numerous studies have focused on element mobility during alteration, metamorphism, and subaerial and submarine weathering (Condie et al., 1977; Bland, 1978; Campbell et al., 1984). Elements that remain relatively immobile during such secondary processes may be utilized for rock classification and constraining tectonic setting. Trace elements such as high field strength elements and rare earth elements show the most promise in terms of relative immobility. Consequently these elements are commonly used in rock classification schemes (Winchester and Floyd, 1977) and tectonic discrimination diagrams (Pearce and Cann, 1973).

The Deception Rhyolite at Jerome, provides an opportunity to test geochemical mobility in rocks subjected to various degrees of hydrothermal alteration as well as greenschist facies metamorphism. Massive sulfide deposits at the top (Fig. 4) of the Deception Rhyolite were exploited at the United Verde Mine (Lindberg, 1986). In the vicinity of the United Verde mine (Figs. 6 & 7), the upper unit of the Deception Rhyolite is absent (Lindberg and Jacobson, 1974) and the Cleopatra Member and associated massive sulfides are overlain by the Grapevine Gulch

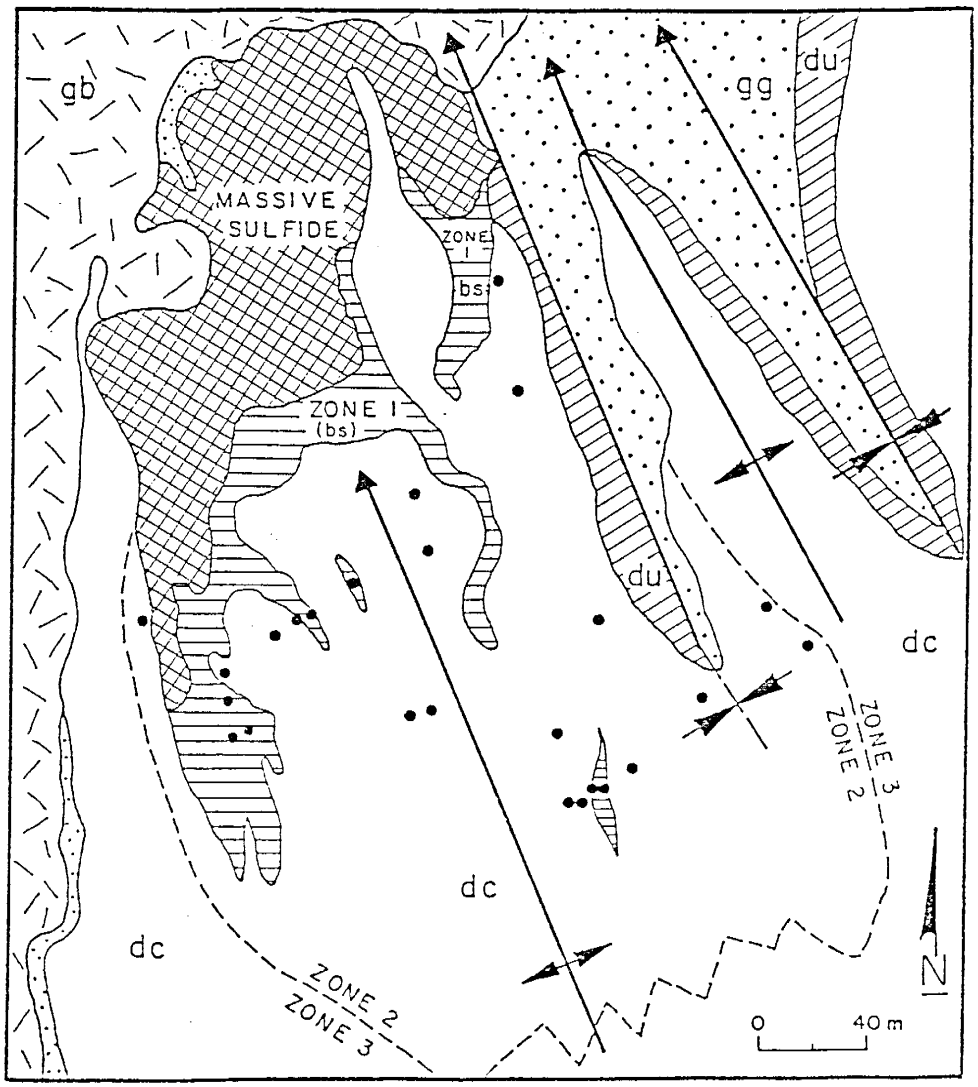

Fig. 7. Geologic map of the United Verde massive sulfide deposit with approximate limits of alteration zones. Geology is modified after Anderson and Creasey (1958). Zones 1 and 2 are somewhat expanded versions of the "black schist" and "chloritized quartz porphyry" units of Anderson and Creasey (1958). Key for units: dc - Cleopatra Member, bs - black schist, gg - Grapevine Gulch Formation, gb - gabbro, ● -sample locations.

Formation. The United Verde massive sulfide deposit lies along the folded contact of the Cleopatra Member and the Grapevine Gulch Formation. Due to original localization along faults and subsequent deformation, the massive sulfide deposit is a rod-shaped body with a lensoid cross section and occupies the hinge area of steeply plunging folds. Mining operations have exposed sulfides in the northwest wall of the open pit and altered footwall rocks are exposed in the southeast wall. The massive sulfides, the Cleopatra Member, and the Grapevine Gulch Formation are intruded by gabbro along the west side of the pit (Fig. 7).

The Cleopatra Member, which hosts the massive sulfide deposits, was originally interpreted as an intrusive quartz porphyry and the massive sulfides as metasomatic replacement deposits (Reber, 1938; Fearing and Benedict, 1925; Lindgren, 1926; Anderson and Creasey, 1958). It is now recognized as a submarine crystal tuff or series of tuffs with local breccia facies (Lindberg, 1986). The massive sulfides are interpreted as volcanogenic deposits by most investigators (Lindberg and Jacobson, 1974; Anderson and Nash, 1972). Although some prefer alternative origins (Bain, 1973; Norman, 1977), the lithologic associations, morphology of the orebodies, and associated alteration are most easily reconciled with a volcanogenic model.

Estimates of the original mass at the United Verde deposit exceed 100 x 10^6 short tons of sulfide ore and production includes about 33 x 10^6 tons of ore with 4.8% Cu, 1.6 oz/metric ton Ag, and 0.04 oz/metric ton Au (Armstrong and Handverger, 1986; Lindberg,

1986). The United Verde deposit shares common features with the Noranda deposits of Quebec and the Kuroko deposits of Japan (Anderson and Nash, 1972; Anderson and Guilbert, 1979). The spatial association with felsic volcanic rocks and a well-developed footwall alteration halo are common to many of the Noranda and Kuroko deposits. The United Verde deposit has an alteration zone consisting of a chlorite core, referred to as chlorite phyllite or black schist, surrounded by a more extensive zone characterized by chlorite, minor sericite, and variable amounts of quartz. The general characteristics of the United Verde deposit indicate a proximal setting (Plimer, 1978; Anderson and Guilbert, 1979).

In this investigation a suite of felsic volcanic rocks that range from intensely to only slightly altered is chemically analyzed (Table 1, App. A; Table 2e, App. B) in order to understand element mobility associated with hydrothermal alteration accompanying massive sulfide deposition and determine the relative mobility or immobility of major and trace elements.

Sample Base

The geologic maps of Anderson and Creasey (1958) and Lindberg and Jacobson (1974) served as sampling guides for the Deception Rhyolite in the United Verde deposit and at localities 1 to 1.5 km to the south in Hull Canyon (Fig. 6). Samples were also obtained

from the lower and upper units of the Deception Rhyolite in Hull Canyon.

In the footwall rocks of the United Verde mine (i.e., the south wall of the open pit), samples were collected along traverses both crossing and parallel to the strike of the foliation. The deteriorated condition of benches in the south wall of the open pit limited the traverses in this area. From the suite of samples collected, a smaller group was selected for petrographic and geochemical studies. Samples near zone of obvious surface weathering were avoided in order to evaluate the effects of hydrothermal alteration or metamorphism. Samples were also obtained from the deeper parts of Hull Canyon to increase the distance from the surface of the Precambrian-Paleozoic unconformity.

Structure and Metamorphism

Regional structural features and structural history are described on pages 28 and 32 and the metamorphic grade on page 35. Development of foliation in the Jerome area varies and the major foliation generally strikes northwest with steep to vertical inclination. Foliation on a microscopic scale is defined largely by alignment of sericite. In some outcrops, two foliations are observed and intersect at 30° to 40°, with the second foliation developed by advanced crenulation and microshearing of the first foliation. This dual foliation is especially evident in samples

from the western part of Hull Canyon and in the vicinity of the United Verde deposit. The United Verde mine is located along a fold hinge (Anderson and Nash, 1972) and intense granulation of quartz in the Cleopatra host rock may be due in part to folding. The response of units of differing competence (rhyolite, phyllite, massive sulfide) to local deformation is probably a contributing factor of the intensity of shearing.

Hydrothermal Alteration

Because deformation followed alteration, hydrothermal alteration halos are folded. The upper unit overlies the ore horizon at Jerome and appears to be relatively unaltered, thus providing some control for the composition of unaltered rock. Other felsic volcanic samples from the Jerome area also provide control on prealteration rock composition (Table 2d, App. B). The use of an alteration index such as Na2O content or the alteration index (See App. B) proposed by Ishikawa et al. (1976) provides a major element gauge of relative degress of alteration. Consequently, chemical changes through different degrees of alteration can be evaluated by comparison with the compositional range of the least altered rocks of the Deception Rhyolite. Three generalized alteration zones are recognized in the Jerome area (Fig. 7). These zones, however, are not precisely defined with respect to the United Verde massive sulfide deposit but may be

equated with some of the units mapped by Anderson and Creasey (1958).

Zone 1 is the "black schist" of Anderson and Creasey (1958) (Fig. 7). The mineralogy of this rock, which is a chlorite phyllite, is dominated by Mg chlorite with rare quartz eyes. Zircon is an accessory phase and was cited by Anderson and Nash (1972) as evidence for a protolith of Cleopatra Rhyolite. The black schist of zone 1 is the most highly altered part of the Cleopatra Member. Although it is located below the massive sulfide, it does not possess the morphology of a single pipe or core. The black schist in the footwall rocks of the United Verde open pit consists of several narrow zones within the altered Cleopatra Member. P. Lindberg (pers. commun., 1984) suggests that these zones mark the site of faults or fractures which served as conduits for the hydrothermal solutions that deposited the sulfides. The rapid transition from chloritized quartz porphyry to chlorite phyllite along these zones support this interpretation.

Zone 2 corresponds roughly with the chloritized quartz porphyry of Anderson and Creasey (1958) and it grades rapidly into zone 1 over a few centimeters. Recent interpretations indicate that this unit is the Cleopatra Member (Anderson and Nash, 1972; Lindberg and Jacobson, 1974). Zone 2 is dominated by quartz and chlorite with minor amounts of sericite. Relict phenocrysts of quartz are preserved within this zone; feldspar, however, is not preserved. Sheared and deformed quartz veinlets are common.

Zone 3 consists of approximately equal amounts of sericite and chlorite which generally comprise less than 7% of the total rock. Primary textures are preserved and unlike zone 2, feldspar is present. Phenocrysts of quartz and plagioclase reside in a groundmass of fine-grained quartz and feldspar. Most of the Cleopatra Member and rocks in the lower unit along Hull Canyon belong to zone 3. Except for the contact with the upper unit in Hull Canyon, the limits of zone 3 are not observed. Locally in Hull Canyon, the extent of chemical alteration is nearly as severe as that of zone 2. This may reflect differences in primary porosity and permeability of pyroclastic rocks and/or proximity to the hydrothermal system associated with the Verde Central deposit (Lindberg, 1986).

Nature and Timing of Alteration and Metamorphism

Three possible secondary processes must be considered at Jerome. These include: syngenetic alteration produced by interaction of submarine extrusive rocks with seawater and hydrothermal alteration associated with massive sulfide deposition, regional metamorphism to upper greenschist facies, and subaerial weathering.

Distinguishing these processes requires interpretation of micro- and macrotextures with respect to mineralogy, bulk composition, and geologic setting. Most of the chloritic alteration responsible for zones 1, 2, and 3 is recognized as

hydrothermal by the spatial relationship with the United Verde deposit and by similarities to alteration zones described in other proximal volcanogenic sulfide deposits (Plimer, 1978; Franklin et al., 1981; Urabe et al., 1983; Larson, 1984). Evidence for a hydrothermal origin for the United Verde deposit is reviewed by Anderson and Nash (1972), Lindberg and Jacobson (1974), and Anderson and Guilbert (1979); field and petrographic investigations conducted during this study support the syngenetic interpretation. The presence of clasts of chloritized rock in the Grapevine Gulch Formation provides strong evidence for a hydrothermal origin of the chloritic alteration. The Grapevine Gulch Formation overlies the altered Cleopatra rocks, indicating that alteration took place prior to or perhaps concurrent with deposition of the Grapevine Gulch volcaniclastic rocks.

Petrographic examination of the Deception Rhyolite also provides evidence for timing of the alteration. Thin sections obtained from the lower unit and the Cleopatra Member in Hull Canyon and the more altered Cleopatra rocks at the United Verde mine (zones 3 and 2, respectively) contain quartz phenocrysts with extremely irregular margins which appear to be corroded. Along these irregular surfaces, quartz is replaced by or intergrown with chlorite. In turn, the corroded phenocrysts and chlorite replacements are enveloped by a corona or overgrowth of quartz. Strain shadows penetrate both the inner quartz grain and the secondary overgrowth. In zone 3, fractured phenocrysts of plagioclase or quartz are often filled with carbonate and/or

chlorite. This filling does not extend beyond broken crystals into the groundmass. However, the groundmass does contain a fine-grained mixture of chlorite, sericite, quartz, and minor carbonate.

These features suggest an early period of submarine diagenetic or hydrothermal alteration in which quartz was unstable and subject to corrosion and replacement by chlorite. Such corrosion and replacement have been described in alteration zones of other massive sulfide deposits (MacGeehan and MacLean, 1980). The carbonate-chlorite fracture filling of phenocrysts may also have occurred at this time. Later, the chemical environment changed and quartz appears to have been deposited as overgrowths on corroded grains and some sericite was produced. Corrosion of quartz is not evident in every phenocryst and some phenocrysts display euhedral beta-form morphology with no evidence of corrosion. The nonuniform nature of corrosion may reflect the pyroclastic nature of the original rock. The corroded phenocrysts were probably surrounded by a matrix of ash or fine-grained rock fragments, whereas pristine phenocrysts are incorporated within lithic fragments. Consequently, hydrothermal fluids or seawater have direct access to phenocrysts in the matrix, but the phenocrysts incorporated in lithic fragments are protected.

Some sericite was generated or recrystallized during regional metamorphism as the unaltered upper unit contains minor sericite and foliation is defined largely by sericite. This is observed for rocks both above and below the ore horizon. However, the

rocks below the ore horizon contain a greater abundance of sericite and the intergrowth of sericite with quartz coronas around phenocrysts suggests some hydrothermal production of sericite. Anderson and Nash (1972) indicate that chlorite and sericite crystallized and recrystallized through a series of events ranging from hydrothermal alteration to regional metamorphism.

Hydrothermal silicification is suggested by the presence of the quartz overgrowths and continuity of strain shadows through phenocryst and overgrowth. The presence of folded and sheared quartz veinlets in rocks of zones 1 and 2 also suggests premetamorphic silicification. Some silicification could have taken place during the early stages of regional metamorphism as well. Anderson and Nash (1972) associate some quartz-carbonate veining with the last recognizable deformation. However, the folded and extremely sheared nature of many veinlets requires either formation early in the deformational history or during hydrothermal alteration. Slightly high SiO_2 values in the upper unit may result in part from the metamorphic silicification described by Anderson and Nash (1972), however, investigations in the United Verde Extension mine indicate some hydrothermal activity persisted after eruption of upper unit rhyolitic rocks (Don White, pers. commun., 1987). The possible chemical effects of waning hydrothermal activity are minimal in rocks from Hull Canyon and include minor silicification and alkali mobility in samples which appear to have had an original glassy groundmass.

The high SiO2 values observed in zones 2 and 3 (Table 2e, App. A) are probably products of the hydrothermal event.

Geochemical Results

Evaluation of Alteration

Compositional changes in the Deception Rhyolite with increasing alteration are evaluated by: (1) comparing the composition of rocks from each of the alteration zones with the compositional range of a suite of relatively unaltered samples including samples from the upper unit that lie above the ore horizon (Table 2e, App. B), and (2) comparing element ratios of relatively unaltered and altered rocks (Table 2). Comparison is made in terms of range of values because the Deception Rhyolite is not a single eruptive unit but a succession of units. These units are, however, confined to the dacite-rhyodacite composition field using the relatively immobile element classification of Winchester and Floyd (1977). Element ratios are particularly valuable in seeing through apparent element losses caused by a dilution effect due to silicification or concentration effects due to SiO_2 losses. For example, Table 2e, App. B reveals an apparent loss of Al_2O_3 in zone 2. However, the mean and range of Al_2O_3 ratios (Table 2) do not indicate Al_2O_3 losses in zone 2. Therefore, the apparent Al_2O_3 loss is probably due to the addition of up to 6% SiO_2, which also dilutes trace element concentrations but does not affect

Table 2. Major and Trace Element Ratios for Unaltered and Altered Deception Rhyolite from the Jerome Area

	Unaltered Suite		Zone 3	
	Mean	Range	Mean	Range
Al_2O_3/TiO_2	58	(37-84)	79	(68-92)
P_2O_5/TiO_2	0.25	(0.14-0.29)	0.27	(0.24-0.33)
Ti/Zr	8.6	(5.3-12.6)	5.1	(4.6-6.0)
Zr/Nb	27.3	(23.3-25.9)	24.1	(20.7-27.6)
Zr/Y	4.2	(3.3-6.0)	3.6	(2.7-5.0)
Ta/Hf	0.11	(0.10-0.12)	0.10	(0.08-0.13)
Hf/Th	1.1	(1.1-1.3)	1.3	(1.2-1.5)
Sc/Hf	1.6	(1.1-2.0)	1.4	(1.1-2.0)
La/Yb	5.2	(4.6-5.6)	4.0	(2.4-5.1)
Ta/Yb	0.13	(0.09-0.15)	0.09	(0.07-0.12)
Th/Yb	1.1	(0.7-1.3)	0.7	(0.6-0.9)
U/Th	0.40	(0.38-0.41)	0.52	(0.33-0.62)

	Zone 2		Zone 1	
	Mean	Range	Mean	Range
Al_2O_3/TiO_2	75	(51-88)	102	(45-199)
P_2O_5/TiO_2	0.19	(0.07-0.33)	0.20	(0.07-0.55)
Ti/Zr	5.9	(4.8-9.5)	6.3	(4.9-9.7)
Zr/Nb	22.1	(17.8-27.5)	17.6	(14.1-22.5)
Zr/Y	3.9	(2.8-6.2)	3.5	(1.5-8.3)
Ta/Hf	0.10	(0.08-0.13)	0.09	(0.07-0.10)
Hf/Th	1.2	(1.1-1.3)	1.3	(1.1-1.5)
Sc/Hf	1.3	(0.8-2.7)	1.5	(0.9-2.5)
La/Yb	4.5	(3.1-5.7)	7.3(8.4)	(0.4-19.9)
Ta/Yb	0.11	(0.07-0.16)	0.09	(0.06-0.12)
Th/Yb	0.9	(0.6-1.2)	0.8	(0.5-1.1)
U/Th	0.59	(0.24-1.24)	0.52	(0.41-0.64)

their ratios. The use of element ratios in characterizing elemental mobility in alteration studies has been successfully applied in other studies (Finlow-Bates and Stumpfl, 1981; Campbell et al., 1984).

Major Elements

Significant major element changes are summarized for each zone in Table 3. Losses and gains are apparent in terms of changes of both element concentrations and element ratios, where major elements are related to the relatively immobile oxide, TiO_2 (Table 2). The addition of MgO, Fe_2O_{3total}, and loss on ignition (chiefly H_2O) and the corresponding losses of Na_2O and CaO are apparent for all zones. Zones 2 and 3 are somewhat enriched in SiO2, with SiO2 values reaching 85% in zone 2 where silicification is most intense. Zone 1 differs from the less altered zones in that it is characterized by extreme depletion in SiO_2 and K_2O and enrichment in Al_2O_3, which is generally considered relatively immobile. The major element composition of zone 1 is approximately that of Mg-rich chlorite which is also observed to be the dominant mineral in this zone. K_2O which is almost totally lost from zone 1, may have been addeed to zones 2 and 3 in comparison to relatively unaltered samples.

The Na_2O and CaO depletion is the most striking aspect of the alteration at Jerome (Figs. 8 and 9, Table 2e, App. B). Loss of these elements increases toward zone 1 concurrent with increases

Table 3. Mineralogy and Composition of Alteration Zones Associated with the United Verde Massive Sulfide Deposit

Zone	Mineralogy	Compositions Gains	Losses
1	Chlorite	MgO Fe_2O_{3total} Al_2O_3 L.O.I.	SiO_2 Na_2O CaO K_2O
2	Quartz Chlorite Sericite	MgO Fe_2O_{3total} SiO_2 L.O.I. K_2O(local)	Na_2O CaO
3	Quartz Sericite Chlorite	MgO Fe_2O_{3total} SiO_2 L.O.I. K_2O(local)	Na_2O CaO

Fe_2O_{3total} = total Fe calculated as Fe_2O ; L.O.I. = loss on ignition

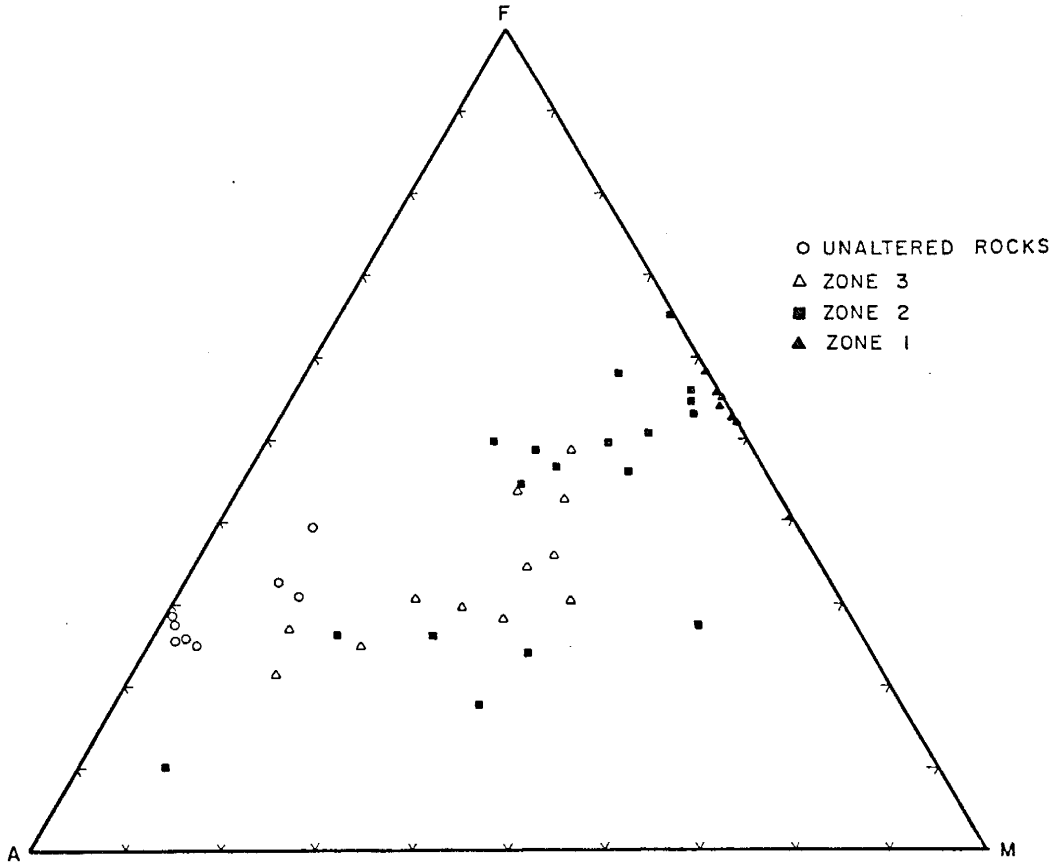

Fig. 8. AFM diagram for the Deception Rhyolite. Zone 3 samples from the Lower Unit and Cleopatra Member, Zone 2 samples from the Cleopatra Member, and Zone 1 samples (black schist) from the Cleopatra Member. The diagram illustrates depletion of Na_2O and K_2O concurrent with enrichment of Fe_2O_3T and MgO during progressive alteration. A = Na_2O + K_2O, M = MgO, F = total Fe as Fe_2O_3.

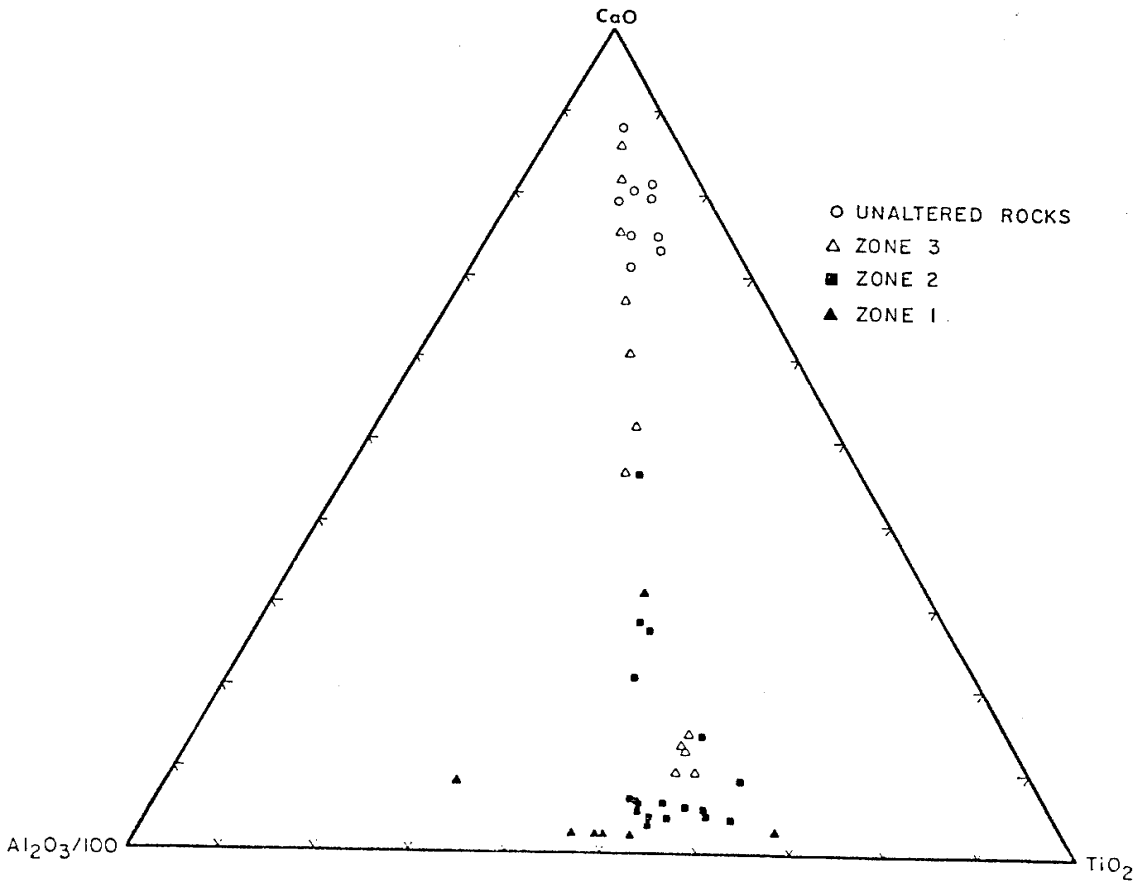

Fig. 9. Al_2O_3-CaO-TiO_2 diagram for the Deception Rhyolite. Sample locations given in Figs. 6 & 7. Progressive depletion of CaO characterizes alteration. Note the extreme CaO depletion in zones 1 and 2. Al_2O_3 and TiO_2 are relatively immobile except in rocks of Zone 1 where addition of Al_2O_3 has occurred. A similar distribution of points is obtained if Na_2O is plotted in place of CaO.

in MgO and Fe_2O_{3total}. Depletion of Na_2O and CaO characterizes many proximal massive sulfide deposits of varied ages (Riverin and Hodgson, 1980; Franklin et al., 1981; Date et al., 1983; Hashiguchi et al., 1983; Urabe et al., 1983; Larsen, 1984) and has been successfully employed as an exploration tool. The increases in MgO and Fe_2O_{3total} with intensity of alteration are also accompanied by increasing chlorite content, and the increasing loss on ignition values (chiefly H_2O) reflect increasing amounts of both chlorite and sericite. Some depletion in MnO and P_2O_5 may have occurred in zone 2.

The major element alteration index (AI) of Ishikawa et al. (1976) is greater than 95 for most samples from zones 1 and 2 (Table 2e, App. B). Samples from zone 3 range from 48 to 99 and the relatively unaltered samples have values $\leq$ 50, averaging 29. Extremely low AI values are associated with K_2O loss (See D22, Table 2e, App. B) and may reflect losses from devitrification and/or waning hydrothermal activity. However, this sample does not display the strong Na_2O depletion characteristic of hydrothermal systems and therefore remains in the unaltered suite.

Trace Elements

The mobility of major elements and some light intermediate lithophile trace elements during hydrothermal alteration or metamorhism has been documented and renders these elements unfavorable as a data base for petrogenetic modeling, rock

classification, or tectonic discrimination (Condie et al, 1977; MacGeehan and MacLean, 1980; Gelinas et al., 1982; Ludden et al., 1982). Although trace elements such as high field strength elements and rare earth elements show very limited mobility during alteration, even these elements may be mobilized by processes such as carbonate alteration or extreme hydrothermal alteratiion such as that associated with proximal massive sulfide deposits (Graf, 1977; Davies and Whitehead, 1980; Hynes, 1980; Finlow-Bates and Stumpfl, 1981; Ludden et al., 1982; Campbell et al., 1984).

The contents of light intermediate lithophile elements, including K, Rb, Sr, Ba, Cs, U, and Th, are quite variable both within the relatively unaltered terrane and within each alteration zone (Table 2e, App. B). The most dramatic changes occur in zone 1 where K, Rb, Sr, and Ba show major losses and Cs, U, Th, and rare earth elements show significant enrichments. The decoupling of light intermediate lithophile elements, and especially of Cs and U, from K and Rb is puzzling. Cs and U, which are the most mobile of these elements in a aqueous phase, appear to have been added to zone 1 yet remain relatively unchanged in the other zones. U and Th behaved in a similar manner during alteration since the U/Th ratio is relatively constant in all alteration zones and only slightly elevated relative to unaltered rocks (Table 2). The apparent increases of U and Th in zone 1 could reflect their concentration in resistant phases such as zircon that may have been relatively enriched in the rock during alteration.

Together with Fe_2O_{3total} and MgO, the transition metals Sc, Co, Mn, Cu, Zn, and Pb are relatively enriched in the altered rocks (Table 2e, App. A). Sc, Co, and Mn exhibit an abrupt enrichment in zone 1, whereas the chalcophile elements also show some enrichment in zones 2 and 3. V is variable and does not show a consistent pattern.

As a group, the high field strength elements (Zr, Th, Ti, Nb, Y, Ta, Hf) exhibit very limited mobility in zones 2 and 3, whereas they show a notable increase in zone 1 (Table 2e, App. B). Rock classifications based on immobile element ratios (Winchester and Floyd, 1977) indicate compositions of dacite or rhyodacite for the Deception Rhyolite. Even most of the samples from zone 1 fall in these classification fields. Ta, Hf, and Th exhibit a small range of values and when plotted on a triangular diagram define a remarkably tight cluster in which unaltered and altered samples cannot be distinguished (Fig. 10). Ratios of high field strength elements are also relatively constant in most altered rocks (Table 2) and provide an important means of identifying the protolith of rocks that have been highly altered by hydrothermal waters. On a Ti-Y-Zr plot, sample distribution suggests relative enrichment of Y and the presence of two populations in the unaltered suite: one with chemical affinities of the upper unit and the other with affinities to the Cleopatra Member and lower unit (Fig. 11). As some of the samples from zone 1 and 2 plot near the upper unit population, upper unit rocks may be involved in the alteration at the United Verde deposit. The somewhat low Zr/Nb ratios

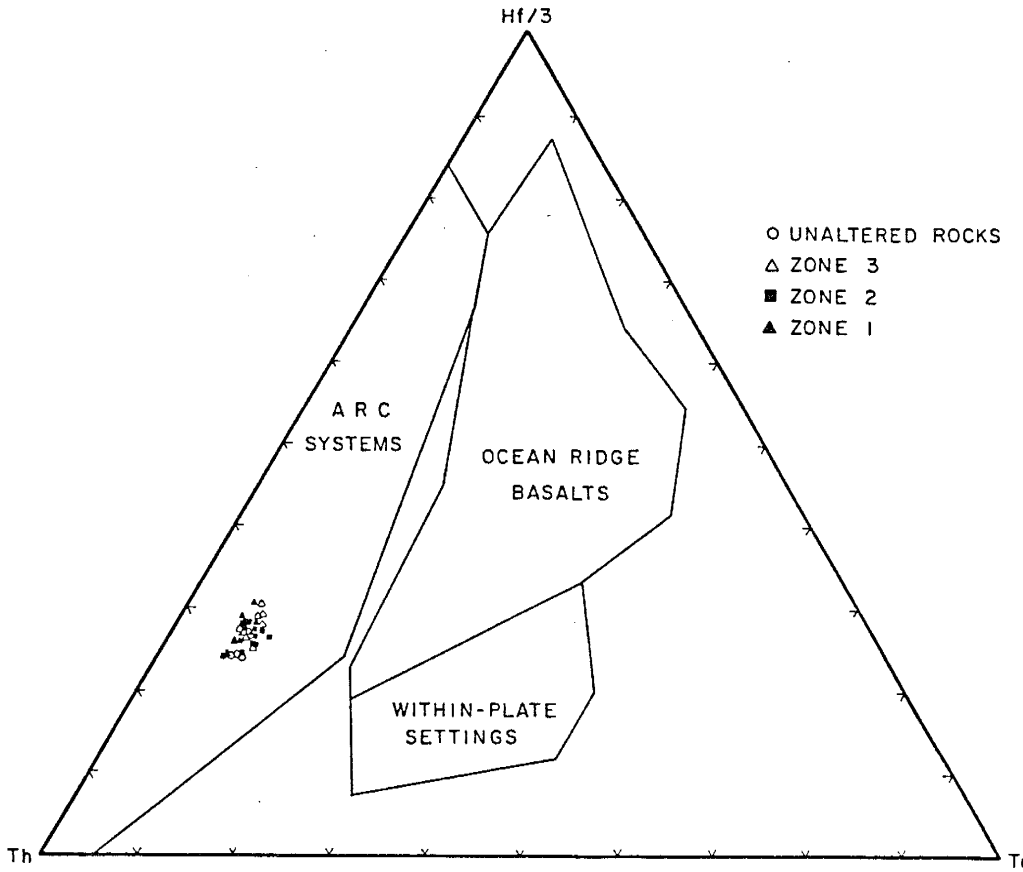

Fig. 10. Th-Hf-Ta diagram for the Deception Rhyolite. Sample locations given in Figs. 6 & 7. The tight grouping illustrates the relative immobility of these elements during alteration. The samples plot in the field for destructive plate margins indicating an affinity with volcanics from arc systems. Fields after Wood (1980).

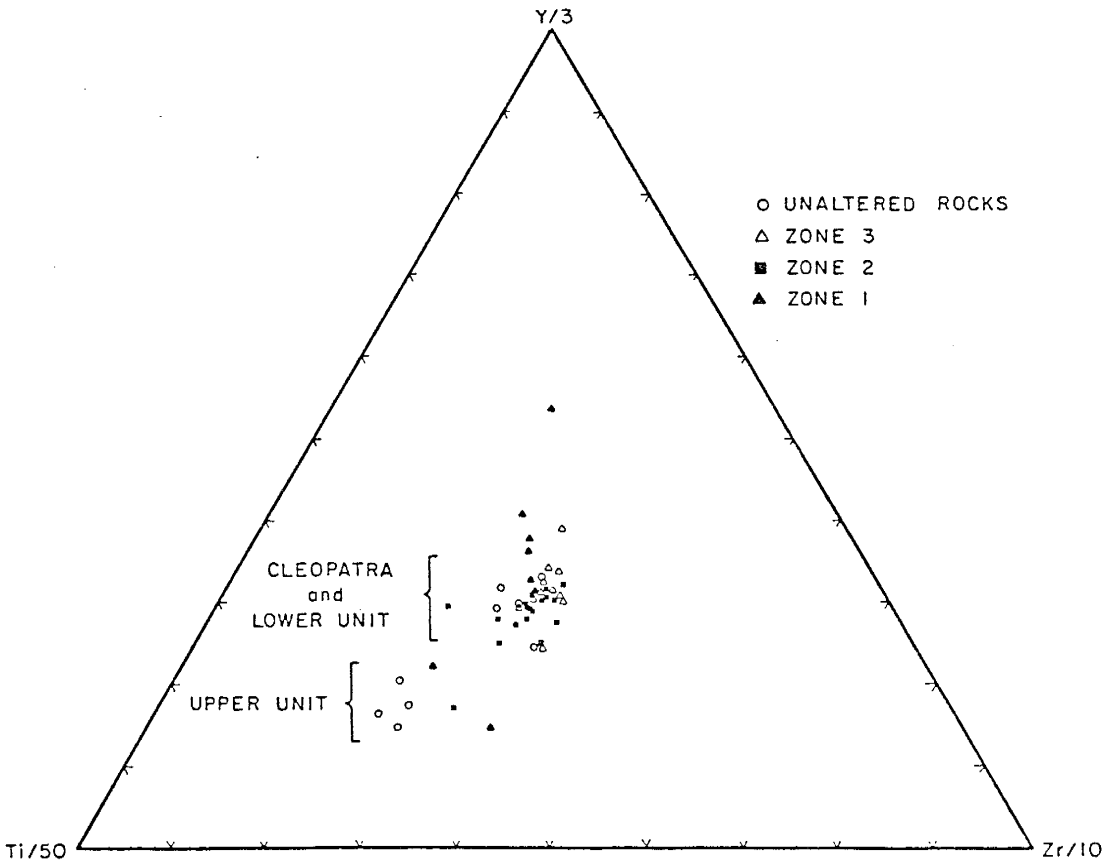

Fig. 11. Ti-Y-Zr diagram for the Deception Rhyolite. Sample locations given in Figs. 6 & 7.

characteristic of zone 1 may reflect minor addition of Nb during intense alteration.

Chondrite-normalized rare earth element plots of samples from the unaltered upper unit and altered samples from the lower unit and Cleopatra Member are remarkably similar and are characterized by flat heavy rare earth element distributions, negative Eu anomalies, and light rare earth element enrichment (Fig. 12a). Samples from zone 2 are diluted with quartz by silicification and rocks with > 79% SiO_2 exhibit lower total rare earth element contents, yet preserve the relative rare earth element pattern observed in the unaltered and less silicified rocks (Fig. 12b). Zone 2 rocks with < 79% SiO_2 also preserve the same relative rare earth element pattern but are higher in total rare earth elements than the silicified rocks. Most rocks from zone 1 exhibit similar rare earth element patterns but have higher total rare earth element contents (Fig. 12c). The apparent rare earth element enrichment may reflect losses of silica, since zone 1 rocks contain less than 30% SiO_2. However, three samples from zone 1 exhibit significant light rare earth element enrichment and one sample from the Verde Central mine shows light rare earth element depletion (Fig. 13). The average La/Yb ratio from zone 1 is somewhat higher than that from other zones (Table 2) and the size of the Eu anomaly increases with light rare earth element enrichment (Fig. 12c).

A Ta-Hf-La plot is used to gauge the mobility of La against the relatively immobile elements Ta and Hf (Fig. 14a). Most

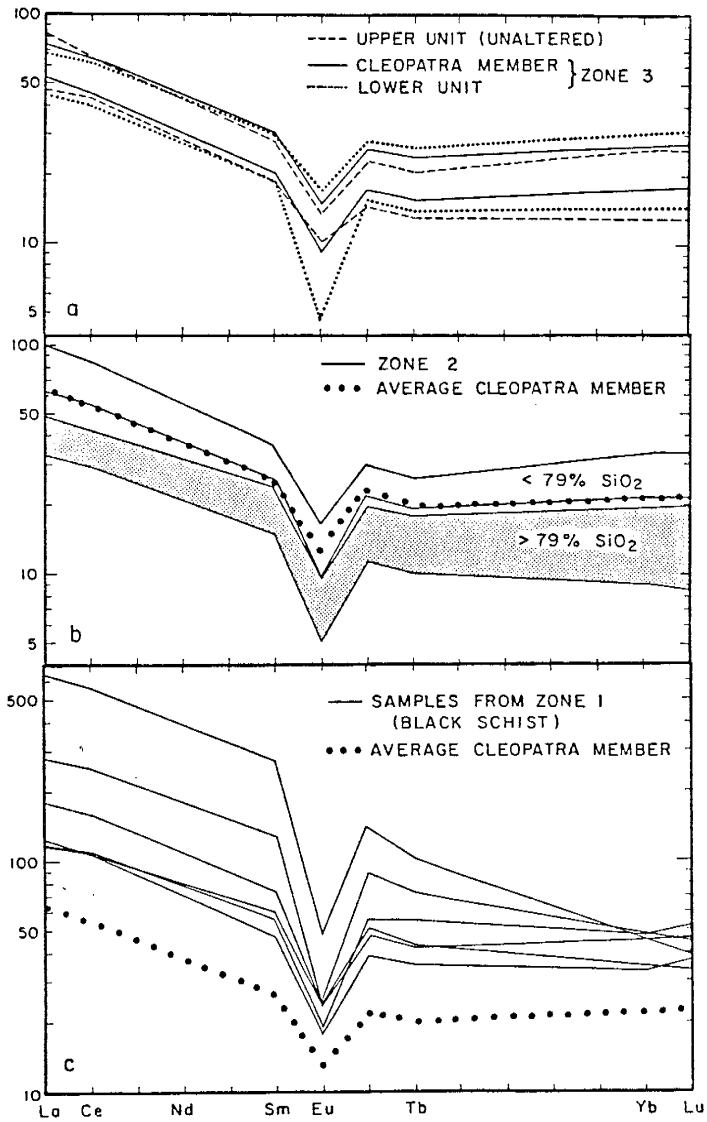

Fig. 12a. Chondrite-normalized REE envelopes for samples from the unaltered Upper Unit and from the altered Cleopatra Member and Lower Unit from Zone 3.

Fig. 12b. Chondrite-normalized REE distributions for samples from the Cleopatra Member from Zone 2. For Zone 2, envelopes of variation for samples with < 79% and >79% SiO_2 are shown. The similarity of the average Cleopatra pattern to Zone 2 rocks indicates preservation of relative REE patterns during alteration.

Fig. 12c. Chondrite-normalized REE patterns for samples from Zone 1 (black schist) compared to an average from the Cleopatra Member.

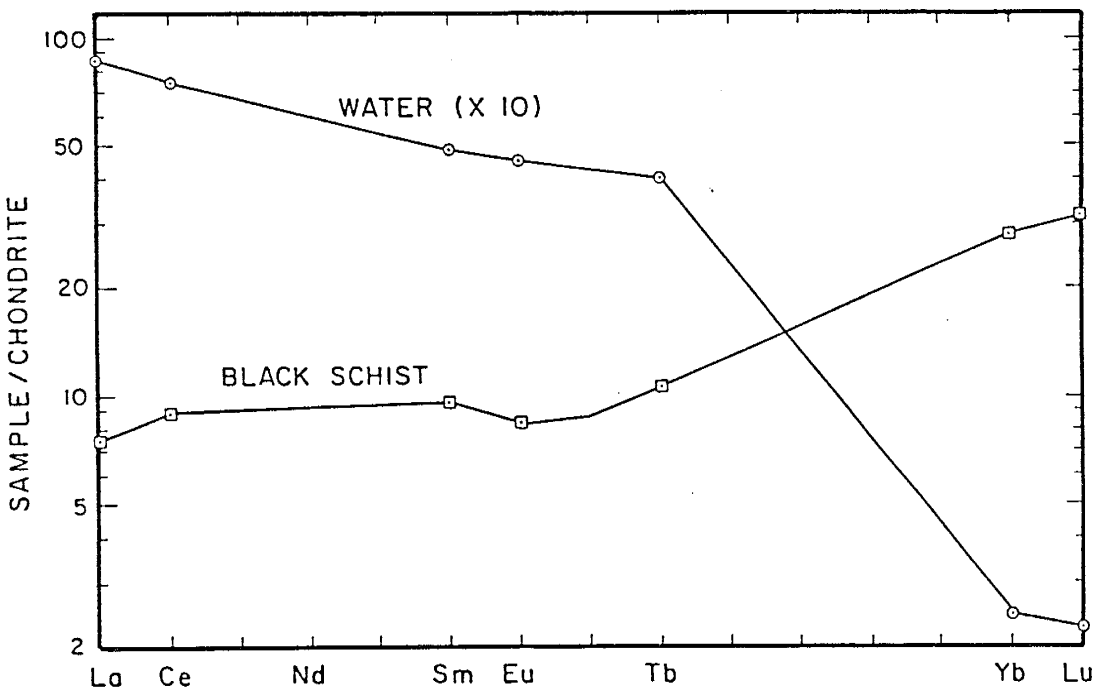

Fig. 13. Chondrite normalized REE pattern for a Zone 1 black schist sample from the Verde Central mine. Also shown is the REE distribution in H_2O after 50% alteration of volcanic glass to produce mica (from Graf, 1977).

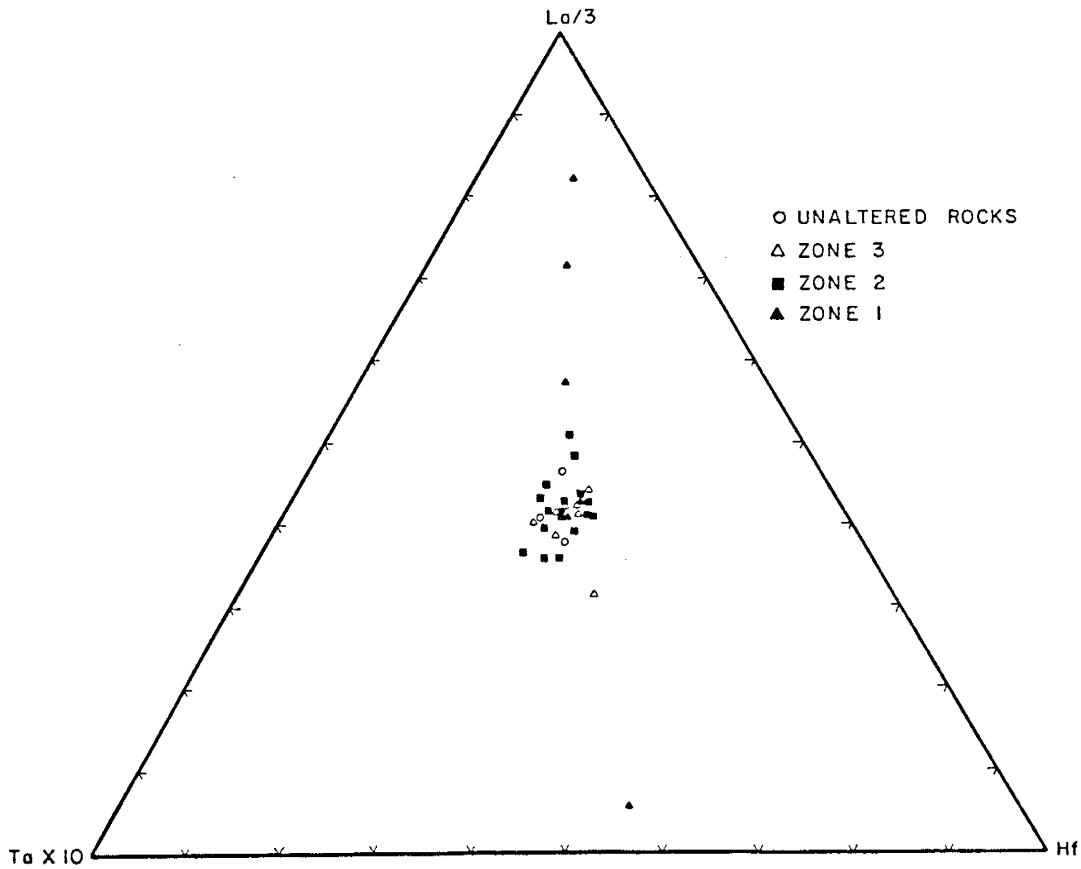

Fig. 14a. Ta-La-Hf diagram for the Deception Rhyolite. Sample locations given in Figs. 6 & 7. Ta and Hf are relatively immobile and the samples trending toward the La apex indicate relative enrichment of La in Zones 1 and 2. A Zone 1 sample from the Verde Central mine has suffered extreme light REE depletion.

samples from zones 2 and 3 cluster near samples from the unaltered suite. However, three samples from zone 1 are relatively enriched in La and the one sample of black schist from the Verde Central mine again shows extreme depletion in La. The heavy rare earth elements are less affected by alteration even under the extreme conditions of zone 1 (Table 2e, App. B and Fig. 12). Compared to Ta and Hf, samples which exhibit extreme depletion or enrichment of light rare earth elements have similar heavy rare earth elements levels as illustrated by Yb relative to Ta and Hf (Fig. 14b). Hence, although light rare earth elements may be mobilized relative to Ta and Hf during hydrothermal alteration, heavy rare earth elements are relatively stable.

Discussion

Characteristics of Hydrothermal Systems

Hydrothermal alteration associated wtih the United Verde massive sulfide deposit was probably controlled by the same parameters that regulate alteration in young geothermal systems. Studies of active geothermal systems in Iceland indicate that system composition, temperature, and kinetic factors determine the alteration mineralogy (Arnorsson et al., 1983). System composition is, in turn, controlled largely by the water/rock ratio. Consequently, the primary porosity and permeability of the host-rocks are major factors. Although host-rock composition

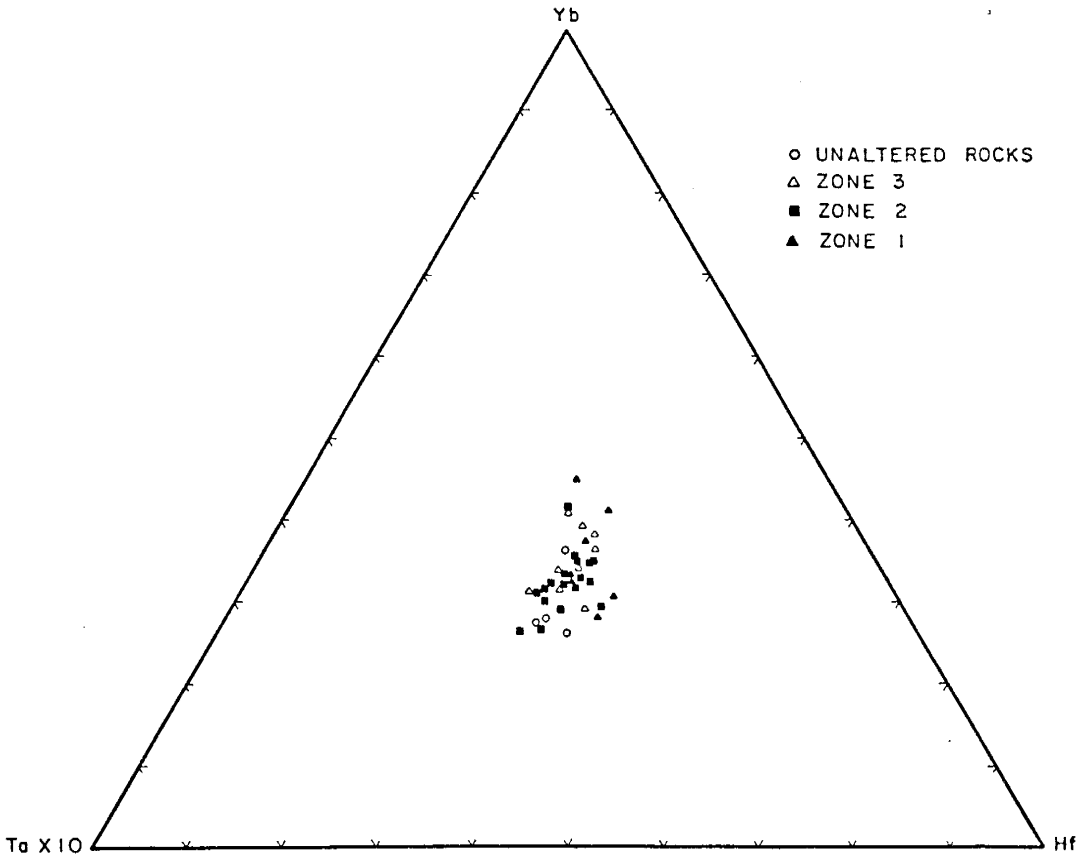

Fig. 14b. Ta-Yb-Hf diagram for the Deception Rhyolite. Sample locations given in Figs. 6 & 7.

influences secondary mineralogy, fluid composition and permeability of the host rocks appear to be most important (Elders et al., 1981; Arnorsson et al., 1983; Henley and Ellis, 1983). Permeability determines the local extent of hydrothermal alteration (Elders et al., 1981; Yashida et al., 1981) and changes in permeability may be vital to deposition of massive sulfides (Cathles, 1983).

The control of temperature and fluid flow in geothermal systems is emphasized by the similarity of the alteration products produced in a variety of host rocks. At elevated temperatures, little variation is observed in the alteration minerals of hosts ranging in composition from basalt, andesite, and rhyolite to quartz sandstone (Brown, 1978; Elders et al., 1981; Anorsson et al., 1983; Larson, 1984). Massive sulfide deposits exhibit similarities in alteration zones for deposits of varied ages and a common pattern consists of an inner zone or zones of chlorite-sericite-quartz with a decrease in chlorite outward. Plagioclase may be preserved in outer zones but is usually absent in the inner zones. In young deposits, additional outer zones may be defined on the basis of clay or zeolite mineralogy. Core zones dominated by chlorite are more common in Precambrian deposits whereas sericite-chlorite mixtures are prevalent in the cores of Kuroko deposits (Urabe et al., 1983).

At Jerome, some of the alteration observed in zone 3 may have occurred during initial interaction of hot pyroclastic rock with seawater. Submarine pyroclastic eruption resulted in deposition

of dacitic to rhyodacitic tuffs, hyaloclastites, and breccias mixed with seawater. Since normal seawater is undersaturated with respect to quartz (Berner, 1971), the rock-water system was initially out of equilibrium and some quartz dissolution may have occurred.

Experimental data from rhyolite-seawater, rhyolite-brine, and basalt-seawater systems at elevated temperatures indicate rapid initial increase of SiO2 in solution accompanied by a drop in pH (Dickson et al., 1978; Liou and Dickson, 1978; Rytuba et al., 1978; Sakai et al., 1978). Experimental work and examination of natural geothermal systems indicate that at temperatures above 180° C, mineral assemblages form from solutions that are saturated with respect to quartz (Henley and Ellis, 1983). Cathles (1983) indicates that chemical kinetics affects alteration rates in cooler near-surface zones of geothermal systems, but that alteration rates of deeper portions of these systems are controlled by the rate of fluid flow and by temperature. Consequently, some of the corrosion and replacement of quartz observed in zone 3 at Jerome may have been produced during initial diagenetic reactions with seawater. The interaction of seawater with volcanic glass probably results in rapid saturation of seawater with SiO_2 and halted dissolution of quartz. Experimental studies also record an initial drop in the Mg content for rhyolite-seawater and rhyolite-brine systems (Hirano and Oki,1978; Sakai et al., 1978). This observation agrees with the presence of chlorite replacement rims on quartz as observed at Jerome.

Initial diagenetic events should include rapid alteration of volcanic glass to an assemblage of zeolites and smectites (Henley and Ellis, 1983; Pisutha-Arnond and Ohmoto, 1983). The chlorite which replaces quartz in the Jerome rocks may have originated as an Mg-Na or Mg-Ca smectite. Although low-grade hydrothermal and diagnentic alteration are masked by metamorphism in ancient deposits, zeolite and montmorillonite zones are well established in Kuroko deposits (Yoshida et al., 1981; Kusakabe, 1982) and the higher Mg content of such rocks indicates early fixing of Mg (Iijima, 1974).

Early diagenetic stages are characterized by cation exchange resulting in addition of Mg accompanied by possible losses of K and Na to seawater (Pisutha-Arnond and Ohmoto, 1983). As a geothermal system develops, temperatures are gradually elevated and assemblages of zeolites and Mg-Na smectites are altered to Mg-Ca smectite. These transformations are reported for temperature ranges of 100° to 120°C (Henley and Ellis, 1983) and probably are completed by 200°C. Such reactions release Na into solution and result in Na depletion of the host rock. In the Cerro Prieto geothermal field, diagenetic kaolinite-montmorillonite-dolomite-FeOH-pyrite assemblages change to illite-chlorite with quartz overgrowths plus calcite and sulfides at temperatures of 140° to 160°C (Henley and Ellis, 1983). This observation compares favorably with the quartz overgrowths associated with sericite at Jerome.

The fixing of Mg in chlorite or phyllosilicate chlorite precursors is an important control of fluid pH (Bischoff and Dickson, 1975; Seyfried and Bischoff, 1977; Saki et al., 1978; Larson, 1984). This process lowers the pH resulting in a shift to the sericite stability field. As temperatures rise to 250°C in areas near major hydrothermal conduits, albite breaks down, reacting with K and H_2O to form sericite and quartz and releasing Na into solution (Pisutha-Arnond and Ohmoto, 1983). The net result is further depletion of Na and possible addition of SiO_2 in the host rock. This agrees with the mineralogy of zone 2 at Jerome where feldspar is absent, SiO_2 is high, and local enrichment of K is observed. The presence of calcite in zone 3 and absence in zone 2 suggests temperatures in excess of 250°C for zone 2. An upper limit of approximately 300°C is recognized for calcite in a variety of geothermal systems (Henley and Ellis, 1983; Pisutha-Arnond and Ohmoto, 1983). The zone 1 Mg-rich chlorites at the United Verde deposit were formed at the highest temperatures and highest water/rock ratios of any rocks at Jerome. Larson (1984) explains the chlorite alteration core at the Proterozoic Bruce deposit in Arizona as a product of a high water/rock ratio and the dependence of sericite stability on production of clinochlore. Production of clinochlore lowers pH allowing solutions to reach the sericite stability field. Once the pipe is totally altered to clinochlore, the fluid composition no longer permits sericite stability. Consequently, no new sericite is formed and the pipe remains chloritic. This

explanation may also apply to the zone 1 massive chlorite at Jerome.

Alteration of host rocks reduces interaction between fluid and rock and this probably contributes to the production of a chlorite core. Observations at the Cerro Prieto geothermal field (Elders et al., 1981) and modeling of Kuroko systems (Cathles, 1983) indicate that porosity is significantly reduced by progressive alteration. At Jerome, this explains the rapid transition from zone 1 chlorite to the silicified rocks of zone 2 and agrees with the interpretation of P. Lindberg (pers. commun., 1984) that the black schist (zone 1) formed along faults or fractures which served as the main conduits for hydrothermal discharge. The rocks of zone 2 may reflect near-surface interaction between cooler seawater and rising hydrothermal solutions. Cathles (1983) indicates that silicification results from mixing with cooler near-surface waters in the upper portions of hydrothermal systems. This silicification may be vital to massive sulfide deposition as it isolates deep solutions from contamination with cooler water and focuses discharge. Locally, the black schist (zone 1) at Jerome contains quartz veinlets which have been subject to folding and shearing. If these veinlets are hydrothermal, they may have been deposited during a temperature drop after maximum geothermal alteration formed the black schist at a temperature $\geq$ 300°C.

Rare Earth and High Field Strength Elements Mobility

As rare earth elements and some high field strength elements partition strongly into accessory minerals such as zircon, allanite, or apatite (Haskin and Paster, 1979), these minerals may carry a major portion of the rare earth elements or high field strength elements in a rock. Zircon is extremely resistant to alteration and is a accessory mineral present in the Deception Rhyolite. It is also found in the black schist of zone 1 and probably carried a major portion of the heavy rare earth elements in these rocks. The limited mobility of some high field strength elements may also reflect the resistance of zircon since Hf, Th, Nb, and Ta also may be concentrated in the zircon (or in inclusions in zircon). The increase in concentration of both high field strength elements and rare earth elements in zone 1 may be the result of significant losses of SiO2 resulting in an overall increase in the abundance of resistant minor phases such as zircon.

The enrichment and depletion observed in the light rare earth elements suggests that these elements are incorporated in phases other than zircon. Some light rare earth elements may have been incorporated in original volcanic glass. Computer modeling of rare earth element behavior based on chloride complexing in hydrothermal systems (Graf, 1977) suggests that alteration of volcanic glass to mica imparts a light rare earth element-enriched pattern to a hydrothermal fluid. If chlorite discriminates

against light rare earth elements or if the hydrothermal fluid is strongly light rare earth element depleted, the altered rock should have a light rare earth element-depleted pattern. Such a pattern may also develop if large volumes of water pass through the system. The rare earth element pattern of the black schist from the Verde Central deposit is a near-perfect inverse to the pattern predicted for the model hydrothermal fluid (Fig. 13), suggesting that this sample may represent residue from such alteration provided one or more of the above conditions are met. This indicates that the original glass content may be an important factor in degree of mobilization of light rare earth elements (i.e., an obsidian may suffer extreme light rare earth element loss, but a crystal-rich tuff may be less affected).

Changes in fluid composition or temperature in different portions of a hydrothermal system may also regulate rare earth element mobility. Investigation of the Kidd Creek massive sulfide deposit suggests dissolution of a light rare earth element-enriched phase in deeper portions of the system and precipitation in shallow portions (Campbell et al., 1984). This situation may also be applicable to the Jerome area. The Verde Central site may actually be a deeper portion of the alteration pipe associated with the United Verde deposit. Investigations by Reber (1938) indicate the presence of black schist and Cu ore, which could be interpreted as zone 1 alteration. The black schist sample from the Verde Central mine exhibits light rare earth element depletion and one of the lower unit samples (zone 3) also

may have undergone light rare earth element depletion. Several of the lower unit samples from zone 3 exhibit intense depletion of Na and Ca like zone 2 rocks. If structural interpretations permit, the area in the vicinity of the Verde Central mine in Hull Canyon could be interpreted as the deeper portion of the hydrothermal system which produced the United Verde massive sulfide deposit. This hypothesis is supported by the distribution of fluorine in rocks of the Jerome area (Lavery, 1985).

The rocks in which substantial changes in rare earth element and high field strength element distribution are recorded are those probably subjected to the highest fluid/rock ratios and most extreme temperatures during alteration. Even under these conditions, many of these rocks maintained rare earth element distributions and high field strength element ratios similar to probably protoliths of Deception Rhyolite. With a reasonable sample base, these elements may be used in areas of extreme alteration for correlation of local rock units. This investigation indicates that rare earth element patterns (especially heavy rare earth elements) and high field strength element ratios provide the most dependable indices for rock classification, tectonic discrimination, and petrogenetic modeling of altered volcanics.

V. GEOCHEMISTRY

Classification of the Yavapai Supergroup

Volcanics of the Ash Creek Block

Reliable classification of the volcanic rocks of the Yavapai Supergroup is one goal of this investigation. The Zr/TiO_2 - Nb/Y scheme of Winchester and Floyd (1977) is employed in this study (Fig. 15). The classification utilizes Zr/TiO_2 as a differentiation index and Nb/Y as an alkalinity index. The relative immobility of these high field strength elements (HFSE) and the use of ratios allows dependable rock classification even for cases of extreme alteration (Vance and Condie, 1987).

The sample suite for the Ash Creek block (Fig. 15) is from the Ash Creek Group and the Spud Mountain Volcanics exposed in Yarber Wash near the Yarbo Mine. Collectively, these volcanics exhibit a continuous compositional spectrum from basalt to rhyodacite. The units of the Ash Creek Group are described according to the chronologic order of Anderson et al. (1971). The Gaddes Basalt is one of the least desirable units with respect to sample quality as epidotization and vug filling by secondary assemblages are common. Of the five samples selected for

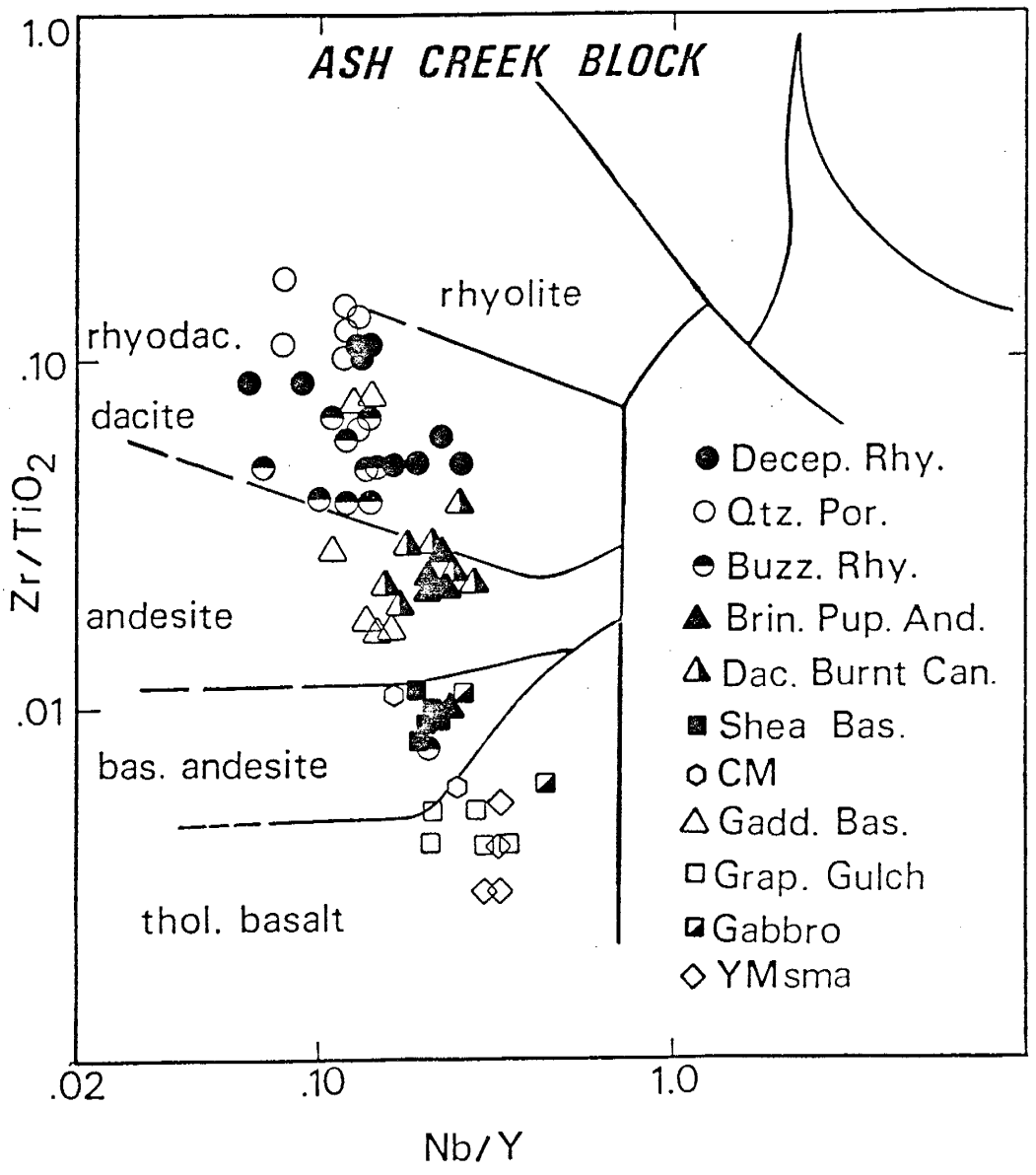

Fig. 15. Classification of volcanic rocks from the Ash Creek block (after Winchester and Floyd, 1977).

analysis, four are andesites and one is dacite or rhyodacite. Anderson and Creasey (1958) tenatively labeled these rocks as basalts, but acknowledged the intermediate character of the SiO_2, Al_2O_3 and MgO contents and the altered condition of much of this unit. Consequently, the Zr/TiO_2 - Nb/Y classification confirms the doubts of Anderson and Creasey (1958) and indicates the presence of more andesites than previously suspected.

Nine samples of Buzzard Rhyolite are analyzed and plot in the lower portion of the dacite-rhyodacite field suggesting dacitic compositions. A sample of the "basaltic agglomerate" interlayered with the Buzzard Rhyolite sequence plots as basaltic andesite. The Dacite of Burnt Canyon also exhibits compositional variation with four samples plotting as andesite, two on or near the andesite-dacite boundary and two within the dacite-rhyodacite field. Consequently, most of the Dacite of Burnt Canyon is actually andesite but ranges to rhyodacitic compositions.

The Brindle Pup Andesite is one of the most uniform units of the Ash Creek volcanics with respect to texture and composition. Of the five samples selected for analysis, four classify as andesite, chemically overlapping the Dacite of Burnt Canyon. A fifth sample is basaltic andesite. The andesites of the Brindle Pup and Dacite of Burnt Canyon are more felsic than those of the Gaddes Basalt as indicated by Zr/TiO_2 ratios. Five samples of Shea Basalt are analyzed, and plot as basaltic andesite on the immobile element plot and most samples also qualify as basaltic andesite in terms of major element contents.

The Deception Rhyolite is a felsic volcanic suite of dacitic to rhyodacitic composition. These rocks are relatively unaltered compared to those examined in the alteration study (Sec. IV). However, both altered and unaltered samples plot in the dacite-rhyodacite field. In general, the Cleopatra and lower unit (Anderson and Nash, 1972) are more differentiated than the upper unit as exposed in Hull Canyon near Jerome. The Deception sample from the southern flank of Mingus Mountain is similar to the upper unit as it is dacitic, plotting in the lower half of the dacite-rhyodacite field. Subsurface samples of domes exposed in the UVX Mine have attained a similar degree of differentiation as the upper unit and occupy the same stratigraphic position. Most of the Quartz Porphyry samples are rhyodacites which have Zr/TiO_2 ratios equal or exceeding those of the lower Deception rhyolite. These units are shallow intrusions or thick flows. The QFP unit of Lindberg (1986) is lumped with the Quartz Porphyry suite but is a tuff and plots with the most differentiated rocks of the Buzzard Rhyolite.

Other samples of mafic units in the Ash Creek group include mafic lithic tuffs from the Grapevine Gulch Formation, two gabbros and two core samples. The Grapevine Gulch lithic tuffs are some of the least differentiated rocks in the Ash Creek suite and plot as tholeiitic basalt. The two core samples (CM) are obtained from drill holes east of Jerome and one is tholeiitic basalt like the Grapevine Gulch rocks; however, the other is basaltic andesite and may be correlative with the Shea Basalt. Plutonic rocks present

problems on the Winchester and Floyd plots due to the possible effects of cumulus phases. One gabbro plots with basalts and the other the basaltic andesites, yet the spatial and temporal relations, as well as the petrogenetic modelling suggests identical parentage. Their separation may reflect differences in ratios of cumulus phases such as pryoxene, plagioclase and magnetite-ilmenite. Samples of lavas and dikes from the Spud Mountain Volcanics (YMsma) plot as tholeiitic basalts, overlapping lithic tuffs of the Grapevine Gulch formation. These are the least differentiated rocks of the Ash Creek block, and they are chemically quite similar to the Grapevine Gulch mafic rocks.

Volcanics of the Green Gulch Block

A lithologic classification of 34 samples of the Green Gulch Volcanics is presented in Figure 16. Among these samples are 10 basalts, 13 basaltic andesites, 8 andesites and 3 dacites or rhyodacites. Many of the basalts and basaltic andesites have similar Zr/TiO_2 ratios but different Nb/Y ratios. The basaltic flows (grb) of Anderson and Blacet (1972) contain a greater proportion of more differentiated lavas than previously recognized with basaltic andesite and andesite prevailing in the northwest corner of the Mount Union Quadrangle. Samples from the Hassayampa Lake area to the south are basaltic andesite. Consequently, these rocks are characterized by a greater proportion of intermediate

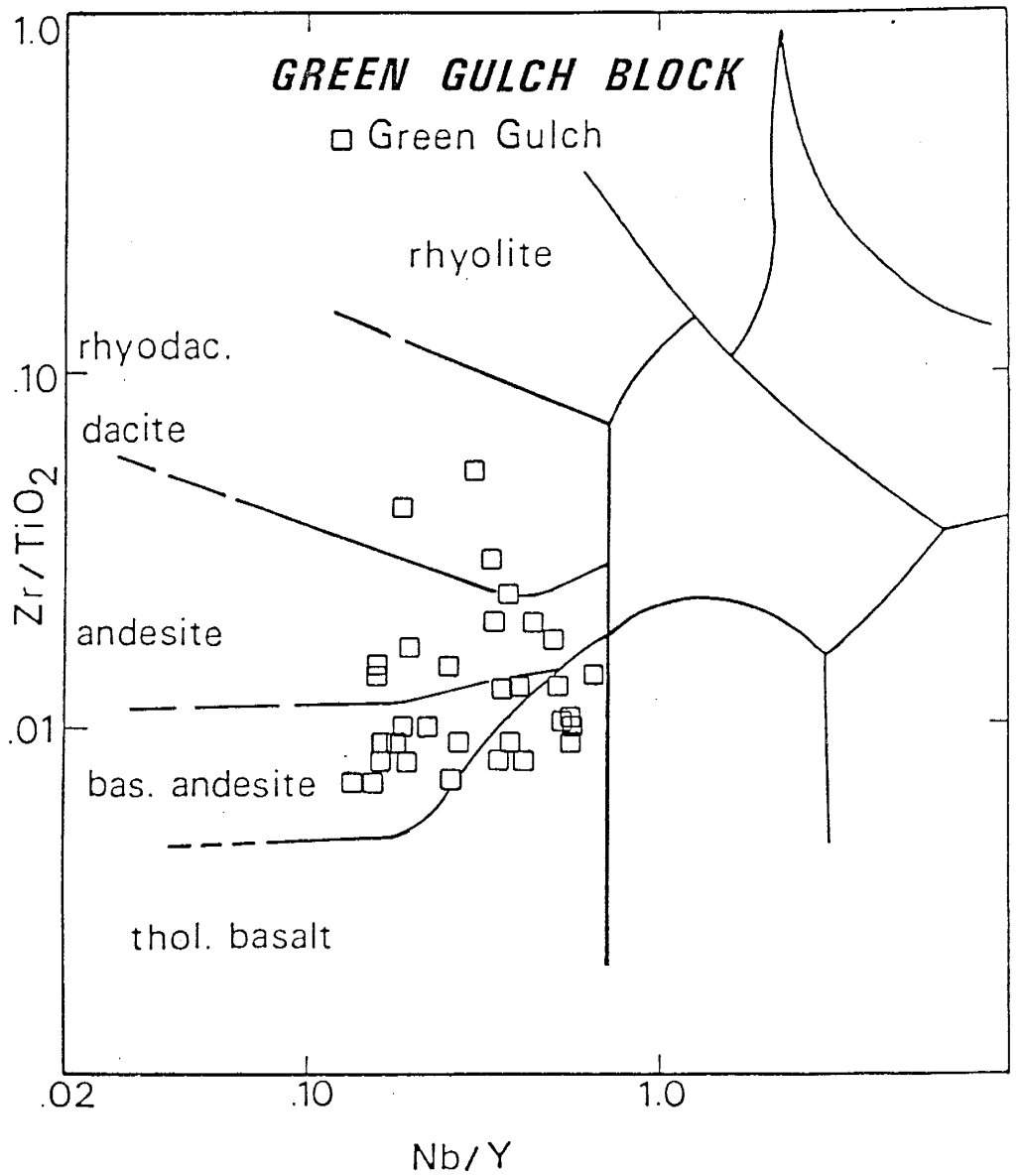

Fig. 16. Classification of volcanic rocks from the Green Gulch block (after Winchester and Floyd, 1977).

composition lavas, rather than the bimodal distribution suggested on the Mount Union GQ of Anderson and Blacet (1972).

Volcanics of the Big Bug Block

The Big Bug block includes outcrops of both the Spud Mountain and Iron King Volcanics. Forty-four samples of the Spud Mountain and 14 samples of Iron King Volcanics include representatives from each of the major map units of Anderson and Blacet (1972). A classification is presented in Figure 17. The andesitic Lower Unit of the Spud Mountain breccia (smb) contains both mafic and felsic lithic fragments. However, much of the breccia is characterized by porphyritic lithic fragments of mafic to intermediate composition. Analysis of breccia indicates the lithic fragments are andesite and the matrix has the composition of basaltic andesite. The matrix probably represents a mixture of andesite and basaltic debris. The remainder of the smb samples are from lava flows interlayered with the breccia. Six of these samples are basaltic andesite and one is basalt.

Anderson and Blacet (1972) indicate andesite compositions for several units of the Spud Mountain Volcanics including andesitic flows (sma) and tuffs (smct and smt). Analysis of 11 samples of andesitic flows (sma) identifies eight true andesites and three basalts. The andesitic tuffs (smct and smt) south of Big Bug Mesa appear to be a continuous pyroclastic eruptive sequence and most plot in a cluster in the andesite field. A couple of samples lie

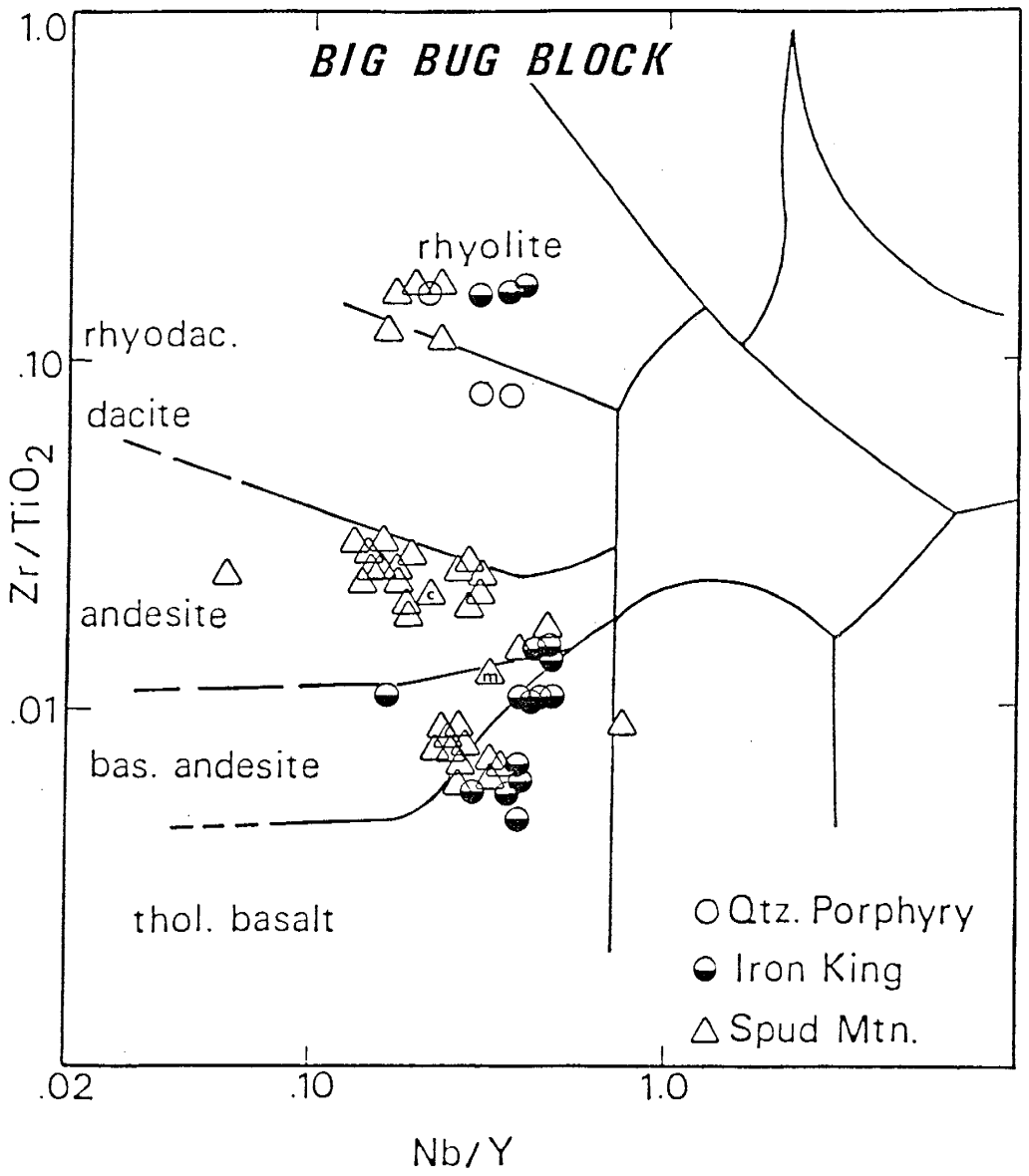

Fig. 17. Classification of volcanic rocks from the Big Bug block (after Winchester and Floyd, 1977). The 'c' and 'm' identify a clast-matrix pair from the Spud Mountain breccia.

along the andesite-dacite border indicating compositional variation. One sample from the same area is isolated from the others by its low Nb/Y ratio; however, the Zr/TiO_2 ratio is equivalent to the other samples. The andesitic tuffs (smt) exposed along Big Bug Creek exhibit greater compositional diversity. Three massive flows interlayered with the tuffs plot as andesite and may be correlative with other andesitic flows (sma) as suggested by Anderson and Blacet (1972). One sample of tuff plots as rhyodacite and three as andesite. An additional three samples (smIK) of Spud Mountain tuff obtained from the Iron King Mine dumps include two basalts and one basaltic andesite. This suggests that a large portion of the smt 'tuff' in the Iron King Mine area may have originated as plagioclase-phyric basaltic lavas. However, the cataclastic effects of extreme deformation have crushed and granulated plagioclase phenocrysts and resemble true tuffs.

Felsic units of the Spud Mountain Volcanics include flows, domes and tuffs (smr and QP). Five samples of the rhyolitic flows and tuffs unit (smr) include one andesite and four rhyolites obtained along Big Bug Creek. Metamorphism has destroyed most relict textures, however, the extensive and stratiform nature of the outcrop suggests these rocks are tuffs or epiclastic deposits. The samples of Quartz Prophyry include two rhyodacites from a tuff within the Shylock Fault zone and a rhyolite from a dome or flow near Cleator.

The Spud Mountain Volcanics include samples from two mafic dikes. One dike (9sm11, Table 4a, App. B) contains a high percentage of blocky amphibole pseudomorphs after pyroxene and plots in the alkalic basalt field near the border with tholeiitic (subalkalic) basalts. The other dike (9sm46, Table 4a, App. B) plots as basaltic andesite and has a distinctive composition and relict diabasic texture very similar to the Shea Basalt of the Ash Creek block.

The Iron King Volcanics are dominated by samples from the andesitic and basaltic flows unit (ika) with a few samples from the Iron King Rhyolite (ikr). Samples obtained from the ika unit exposed in ravines between Big Bug Creek and the Iron King Mine include six basalts and one basaltic andesite. Samples obtained from the Bluebell Mine area south of Mayer include four basalts, one basaltic andesite and two andesites from the ika and ikab units. Three samples of felsic rocks (ikr) were also obtained from the Bluebell area. These samples are variably altered rhyolites. Studies of the altered felsic rocks at Jerome (Sec. IV), however, indicate the Zr/TiO_2 - Nb/Y classification is relatively unaffected by such alteration. Although sample collection is concentrated in units thought to contain andesite, the Iron King Volcanics are bimodal, composed dominantly of basalts and rhyolites. The two samples which plot as andesites (11ika8 and 9) have major element compositions, Mg Numbers, Cr and Ni contents which are more typical of basalts and basaltic andesites.

The Spud Mountain samples are chiefly andesites as originally suggested by Anderson and Blacet (1972). However, basalts, rhyodacites and rhyolites are recognized and indicate a greater compositional variety than the Iron King Volcanics. The paucity of dacite partially reflects a sampling bias toward the mafic rocks. Many of the felsic rocks are silicified and contain abundant veins. The potential epiclastic component in the fine tuffaceous rocks renders them unfavorable for analysis. The borderline andesite-dacite composition of some tuffs and the rhyodacitic composition of the Quartz Porphyries suggests an expanded felsic sample base may encounter dacites.

Major Element Geochemistry

Introduction

Sample acquisition, preparation and analytical methods are described in Appendix B and sample locations are indicated in Appendix A. Major and trace element chemical analysis for representative samples of volcanic rocks of the Yavapai Supergroup are presented in Tables 2, 3, 4 of Appendix B. Samples are organized with respect to lithologic classification, the map units of Anderson and Creasey (1958); Anderson and Blacet (1972) and tectonic blocks of Karlstrom and Bowring (1988). It is emphasized that the lithotype name used by Anderson and Creasey (1958) or Anderson and Blacet (1972) for the map unit name may differ from

the true rock type(s) as identified during this investigation. CIPW norms are presented in Tables 1-3, App. C.

Mafic Rocks

The mafic rocks of the Yavapai Supergroup exhibit considerable chemical variation within single tectonic blocks and map units and between different blocks (Tables 2-4, App. B). Mean values for map units within blocks are presented to facilitate comparison with other blocks in Table 5-7, App. B. Some units are further subdivided according to Mg number (100 MgO/MgO + FeO), mole ratio) to allow comparison of lavas resulting from similar degrees of fractionation. Collectively, the Yavapai basalts exhibit a range of Mg numbers of 33-74 and the basaltic andesites a range of 30-58. The Green Gulch basalts contain the most magnesian lavas of the Yavapai volcanics including a primitive suite with Mg numbers in the range of 60-74 and an evolved suite with Mg numbers of 33-52. 'Primitive' and 'evolved', as used here, refer to the relative state of fractionation with respect to a parental magma. Primitive lavas are characterized by a high-Mg number and high Ni and Cr contents. Evolved lavas are characterized by lower Mg numbers, Ni and Cr contents. The basaltic andesites of the Green Gulch Volcanics are also more magnesian than other Yavapai basaltic andesites.

Lavas and dikes from the Spud Mountain Volcanics in the Ash Creek block rank second with respect to Mg numbers. Gabbro in the

Grapevine Gulch Formation is also quite magnesian but may contain cumulate pyroxene and olivine. The mafic pyroclastic rocks of the Grapevine Gulch Formation have much lower Mg contents representing more fractionated volcanics. Basaltic andesites of the Ash Creek block have lower Mg numbers than those of the Green Gulch block, but are comparable to the values observed in the Big Bug block basaltic andesites. Most basalts of the Big Bug block possess lower Mg numbers than other Yavapai volcanics, with the exception of lavas from the Iron King Volcanics in the Bluebell area south of Mayer. These Bluebell lavas and one pyroxene-phyric dike from the Spud Mountain Volcanics are the only Big Bug rocks with Mg numbers in excess of 50. Two 'andesites' from the Bluebell area have Mg numbers of 55 and 58. The major element composition of these 'andesites' suggests basalt to basaltic andesite composition and presents no indication of significant alteration. These rocks are enriched in high field strength elements (HFSE), consequently, such rocks present problems for HFSE based classifications such as the Winchester and Floyd (1977) scheme employed in this investigation. The HFSE-rich mafic rocks occur in both the Ash Creek and Big Bug blocks. The high contents of TiO_2 and P_2O_5 are the only major elements that are distinctive in this suite. These rocks include the Shea basaltic andesite, sample CM-9 of the Ash Creek block and basaltic andesites 9sm46, Qika5 and 10ika3 of the Spud Mountain, and Iron King Volcanics from the Big Bug block. The high TiO_2 and P_2O_5 contents of these rocks probably reflect original igneous composition as the alteration index and local

preservation of diabasic texture indicates a lack of substantial alteration. Furthermore, the suite includes a dike, as well as pillowed and massive flows. Metamorphic grade ranges from greenschist to amphibolite facies. The distinctive TiO_2 and P_2O_5 contents cannot be regarded simply as products of fractional crystallization. Although some igneous series reach peak TiO_2 contents at this stage of evolution, other basaltic andesites in the Yavapai Supergoup do not achieve such values (Carmichael et al., 1974). This suggests either a distinctive parental magma or an unique fractionation history with respect to the other mafic rocks.

With respect to CIPW norms (Tables 1-3, App. C) most basalts of the Green Gulch block are olivine and hypersthene normative with quartz appearing in the norms of the more fractionated basalts and basaltic andesites. The Spud Mountain basalts (YMsma) and Grapevine Gulch gabbro of the Ash Creek block are also olivine and hypersthene normative, whereas, the basaltic tuffs of the Grapevine Gulch Formation and Shea basaltic andesites are quartz normative. The bulk of the basalts and basaltic andesites of the Spud Mountain and Iron King Volcanics are quartz normative. The basalts from the Bluebell area are the only olivine normative suite in the Big Bug block. Most of these basalts are nepheline normative with compositions similar to olivine basalts of mixed tholeiite-alkali basalt provinces (Carmichael et al., 1974). The basaltic andesites and andesites from the Bluebell area are, however, quartz normative.

The bulk of the Yavapai mafic rocks have a normative mineralogy typical of tholeiites and olivine tholeiites (Williams, Turner and Gilbert, 1982). The dominantly tholeiitic character of the mafic rocks is also demonstrated (Figs. 18-20) on the FeO_T/MgO vs SiO_2 and AFM diagrams (Miyashiro, 1974; Irvine and Barager, 1971). On AFM plots, each block exhibits moderate Fe enrichment; however, the total compositional range of mafic rocks within the Big Bug block is rather restricted when compared to that of the Ash Creek and Green Gulch blocks. The Green Gulch Volcanics also exhibit a greater percentage (27%) of mafic samples with calc alkaline affinities than the Big Bug or Ash Creek volcanic suites.

Although less dependable in ancient rocks, major element composition provides important information with regard to the fractionation history of mafic lavas. Screening the samples for obvious silicification and for alkali mobility by using the AI enhances the utility of major element plots. Construction of isomolar pseudo-liquidus phase diagrams following the method of Elthon (1983) provides a means of examining the liquidus phases significant to the compositional evolution of basaltic rocks. The basalts and basaltic andesites of the Green Gulch and Ash Creek blocks are presented together, as structural and geochronologic characteristics suggest a possible correlation (Karlstrom and Bowring, 1988). Pseudo-liquidus phase diagrams for the olivine-clinopyroxene-plagioclase-silica tetrahedron are projected on the clinopyroxene-olivine-silica and plagioclase-olivine-silica planes (Figs. 21-24). In each tectonic block, most samples plot

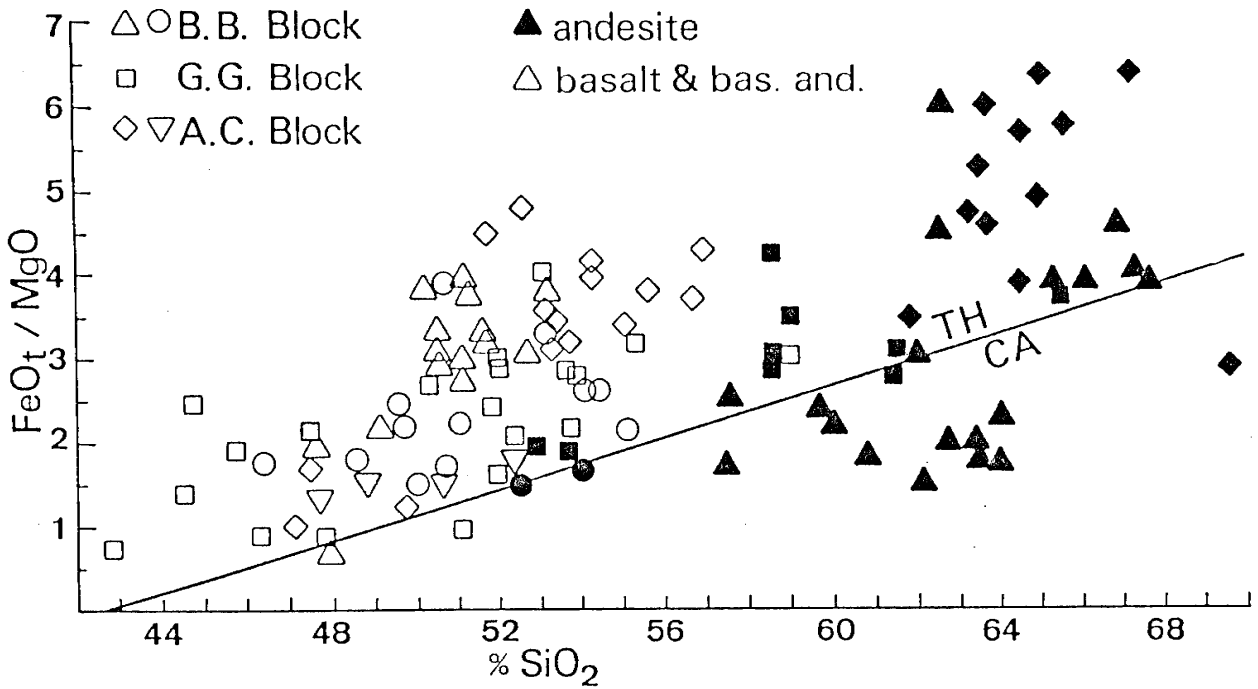

Fig. 18. The FeO_T/MgO vs SiO_2 plot (after Miyashiro, 1974). Explanation: BB = Big Bug, Triangles = Spud Mountain Volcanics, Circles = Iron King Volcanics, GG = Green Gulch, AC = Ash Creek, diamonds = Ash Creek Group, inverted triangle = Spud Mountain basalts from Yarber Wash; open symbols = basalt and basaltic andesite, solid symbols = andesite, TH = tholeiitic, CA = calc-alkaline.

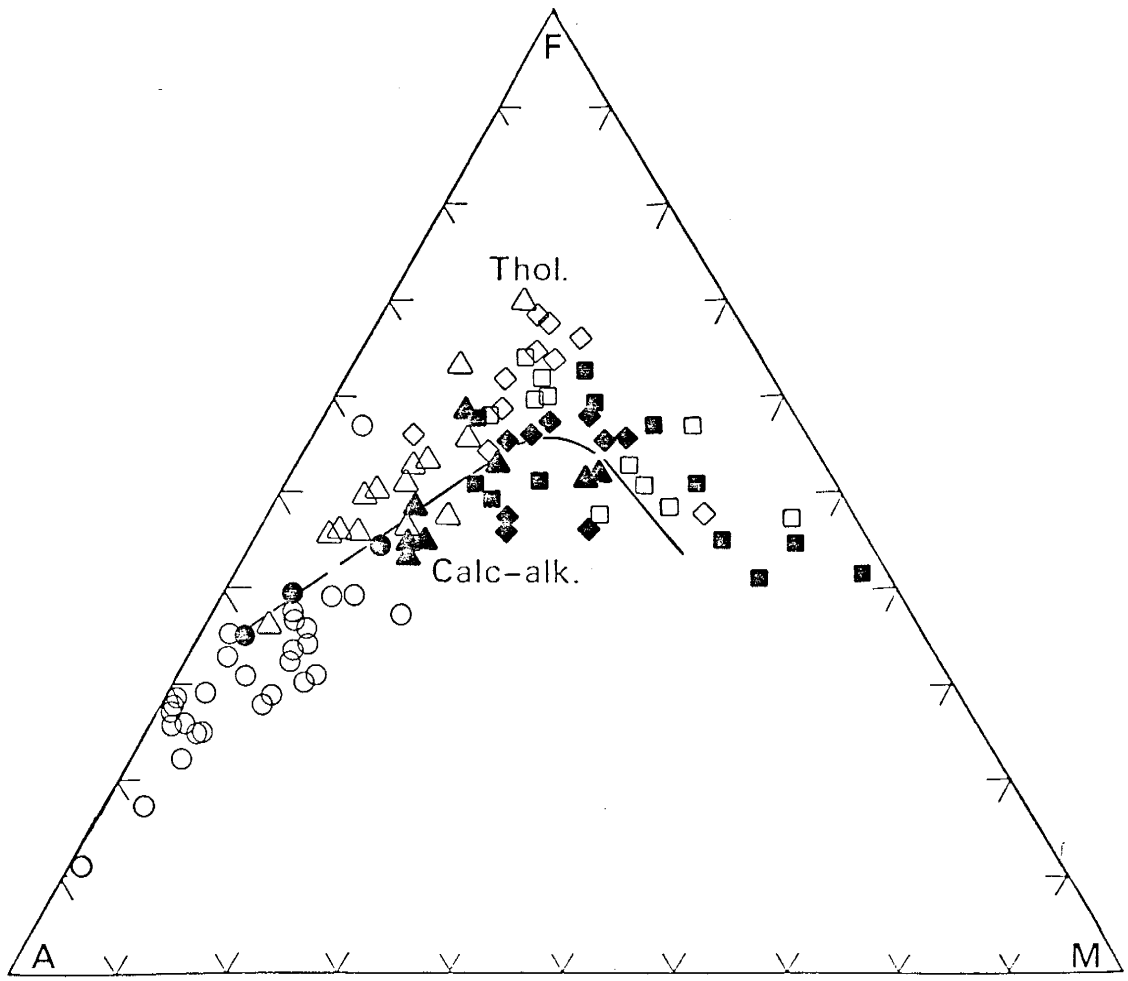

Fig. 19. AFM diagram for volcanics from the Green Gulch (solid symbols) and Ash Creek blocks (open symbols). Key: squares = basalt, diamonds - basaltic andesite, triangles = andesite, circles = dacite-rhyodacite. Tholeiitic-calc-alkaline boundary after Irvine and Barager (1971).

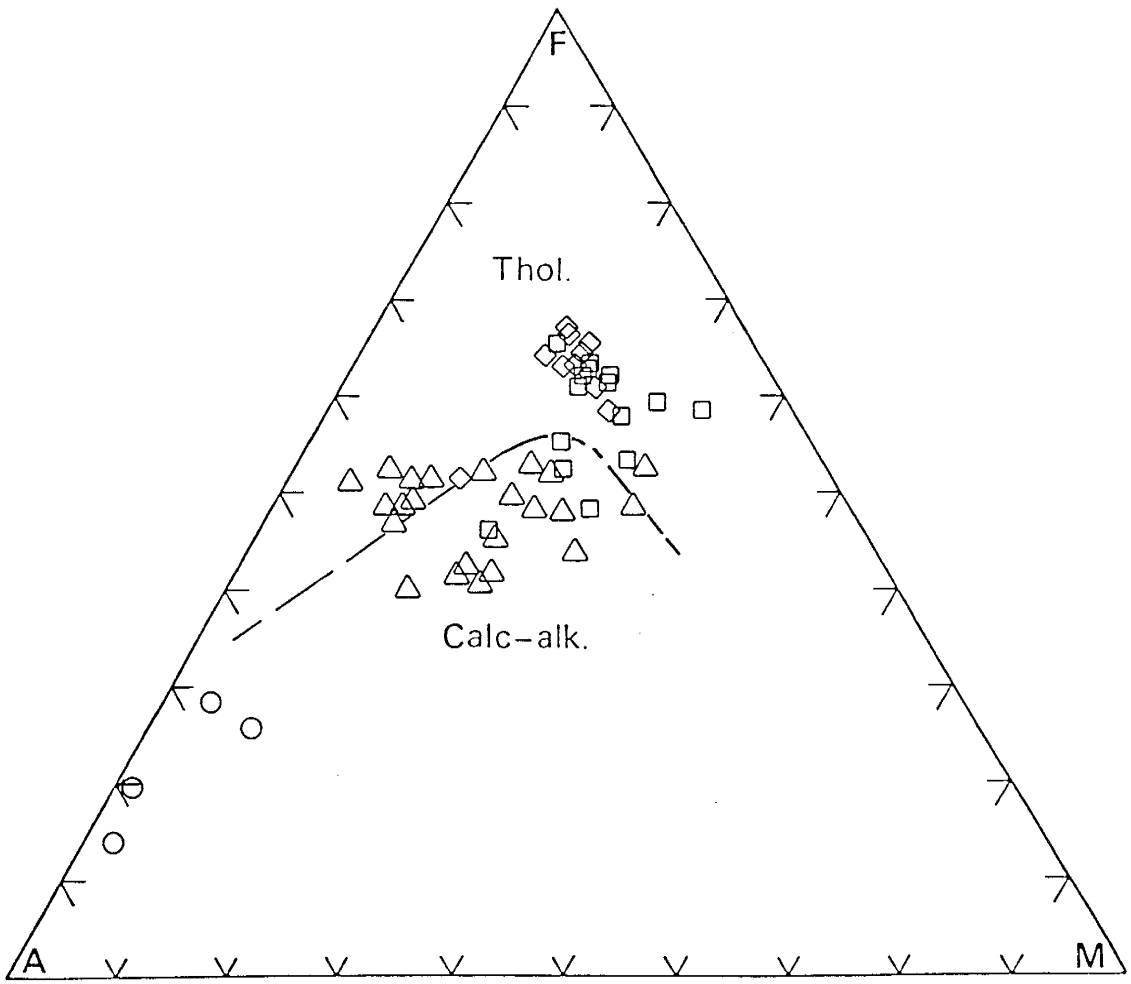

Fig. 20. AFM diagram for volcanics from the Big Bug block. Lithologic key as in Fig. 19. Tholeiitic-calc-alkaline boundary after Irvine and Barager (1971).

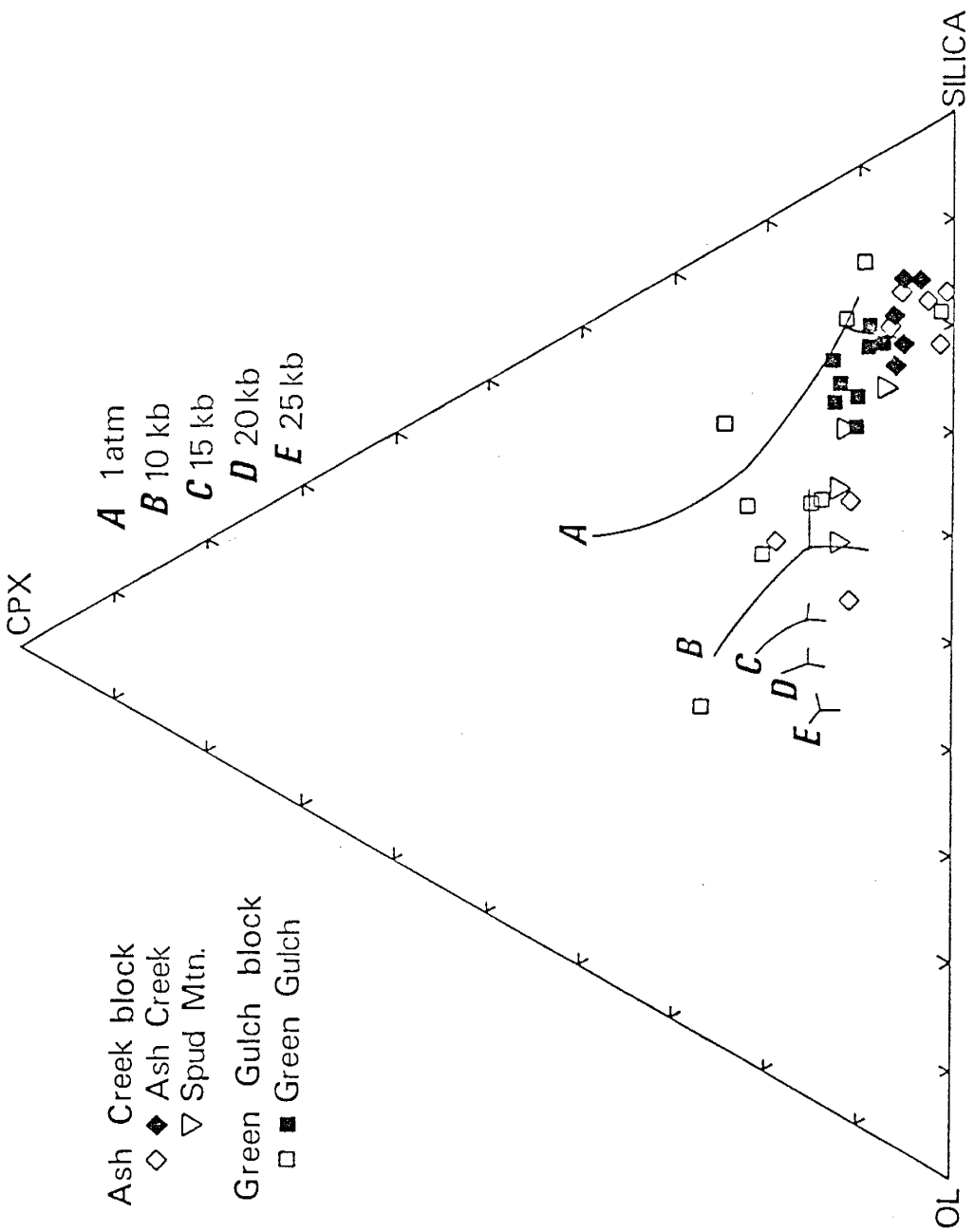

Fig. 21. Olivine-clinopyroxene-plagioclase-silica tetrahedron projected from the plagioclase apex. Cotectics and method after Elthon (1983) and Elthon and Scarfe (1984). Open symbols = basalt, solid symbols = basaltic andesite.

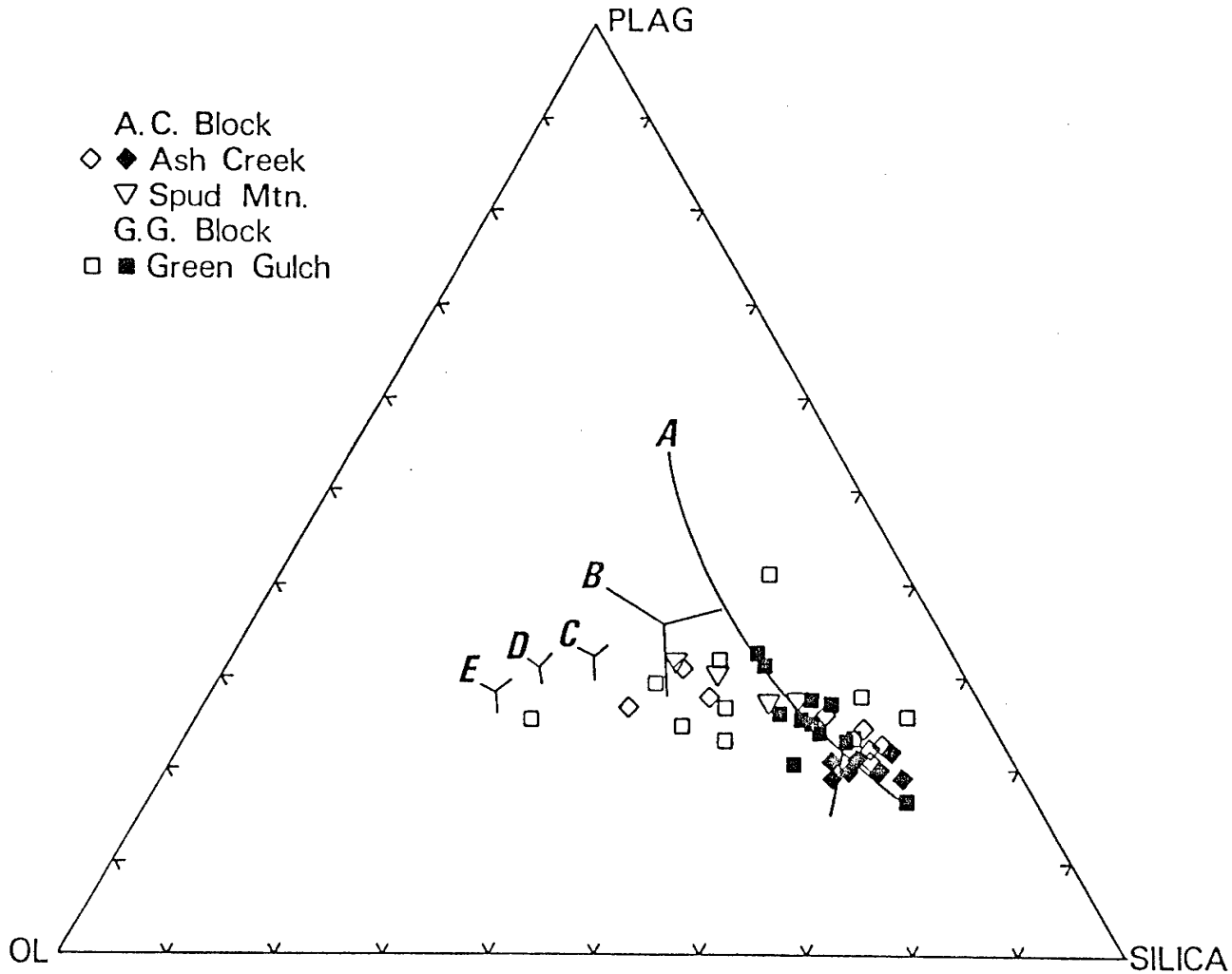

Fig. 22. Olivine-clinopyroxene-plagioclase-silica tetrahedron projected from clinopyroxene apex. Cotectics and method after Elthon (1983) and Elthon and Scarfe (1984). Pressure and lithologic key as in Fig. 21.

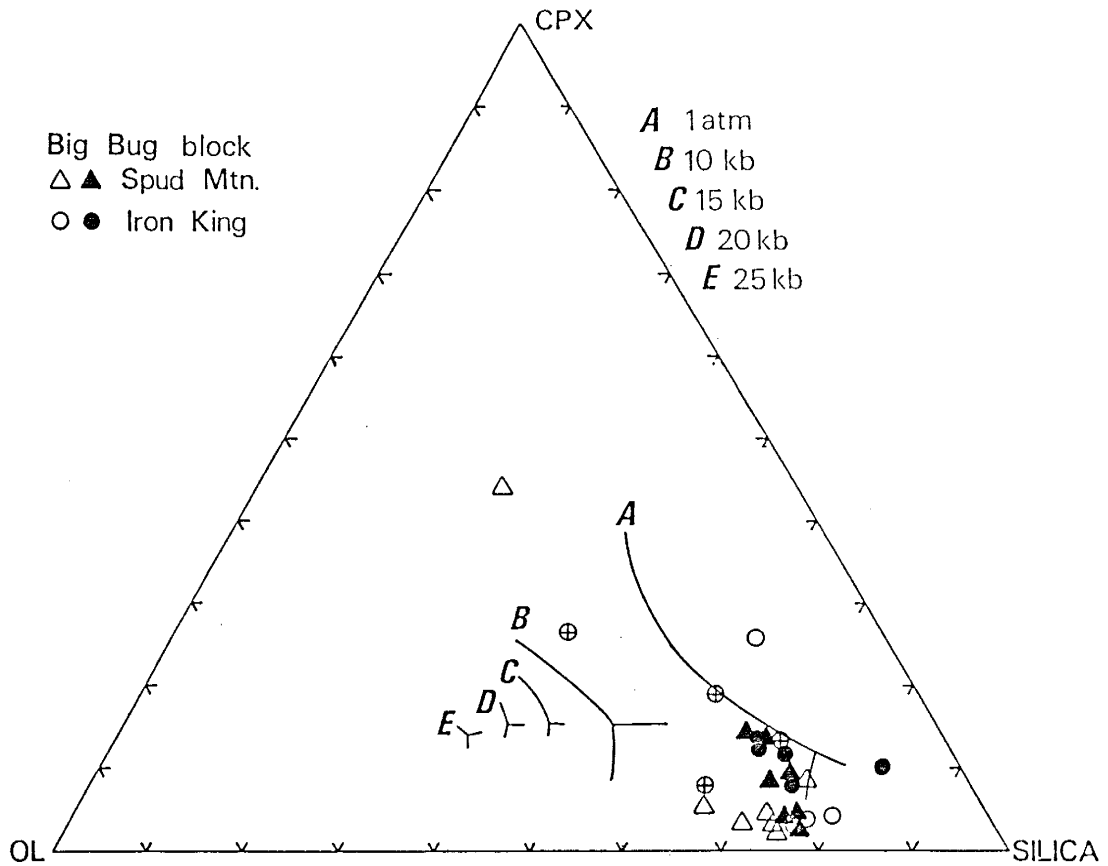

Fig. 23. Olivine-clinopyroxene-plagioclase-silica tetrahedron projected from the plagioclase apex. Cotectics and method after Elthon (1983) and Elthon and Scarfe (1984). Open symbols = basalt, solid symbols = basaltic andesite. Circles with crosses = Bluebell basalts of the Iron King Volcanics.

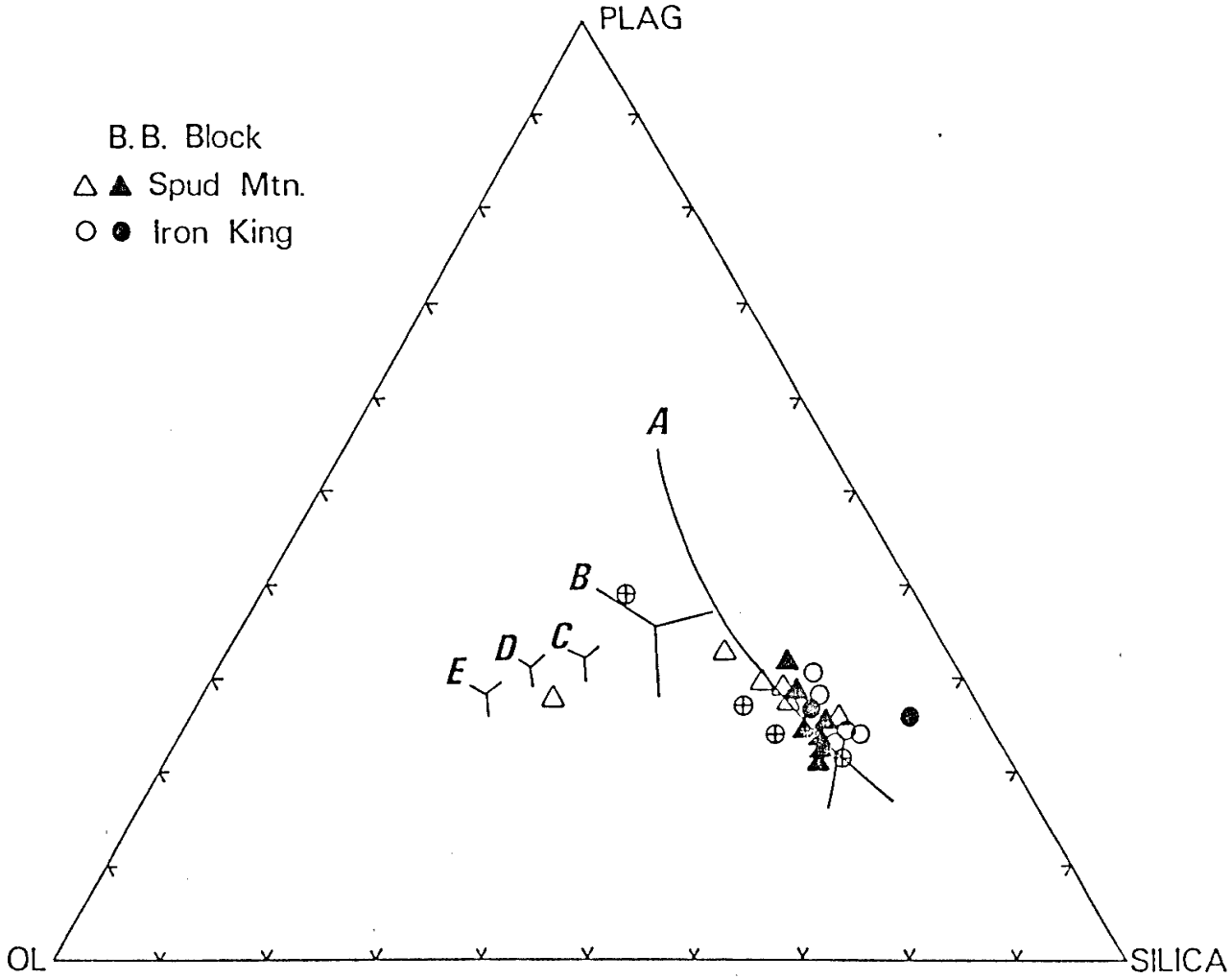

Fig. 24. Olivine-clinopyroxene-plagioclase-silica tetrahedron projected from the clinopyroxene apex. Cotectics and method after Elthon (1983) and Elthon and Scarfe (1984). Pressure and lithologic key as in Fig. 23.

near the one atmosphere cotectic or the invariant point and basaltic andesites plot closer to the invariant point than basalts. Collectively these data suggest low pressure equilibration of most basaltic magmas.

Basalts of the Ash Creek and Green Gulch blocks, however, exhibit significant differences from those of the Big Bug block (Fig. 24) on the Elthon projections. The olivine-clinopyroxene-silica projection (Fig. 21) suggests an olivine-clinopyroxene controlled fractionation trend which originates from a point between the 10 and 15 Kb invariant points. A smaller suite of four samples lie along olivine control lines which may also be extended toward higher pressure invariant points. The olivine-plagioclase-silica projection (Fig. 22) also exhibits a trend which may be extended toward the 10-15 Kb invariant points along olivine-plagioclase control lines suggesting the presence of plagioclase as a significant liquidus phase. Although olivine is not observed as relict grains or pseudomorphs in these lavas, pyroxene pseudomorphs and plagioclase-phyric flows and dikes are present. The CaO vs MgO plot (Fig. 25) reinforces the olivine-clinopyroxene-plagioclase fractionation suggested by the isomolar plots. The initial fractionation trend is characterized by a rapid drop in MgO relative to CaO followed by a rapid drop in CaO relative to MgO. This variation is interpreted as the product of initial olivine with minor clinopyroxene fractionation followed by clinopyroxene-plagioclase fractionation at lower pressures. The sequence agrees with experimental data indicating olivine and

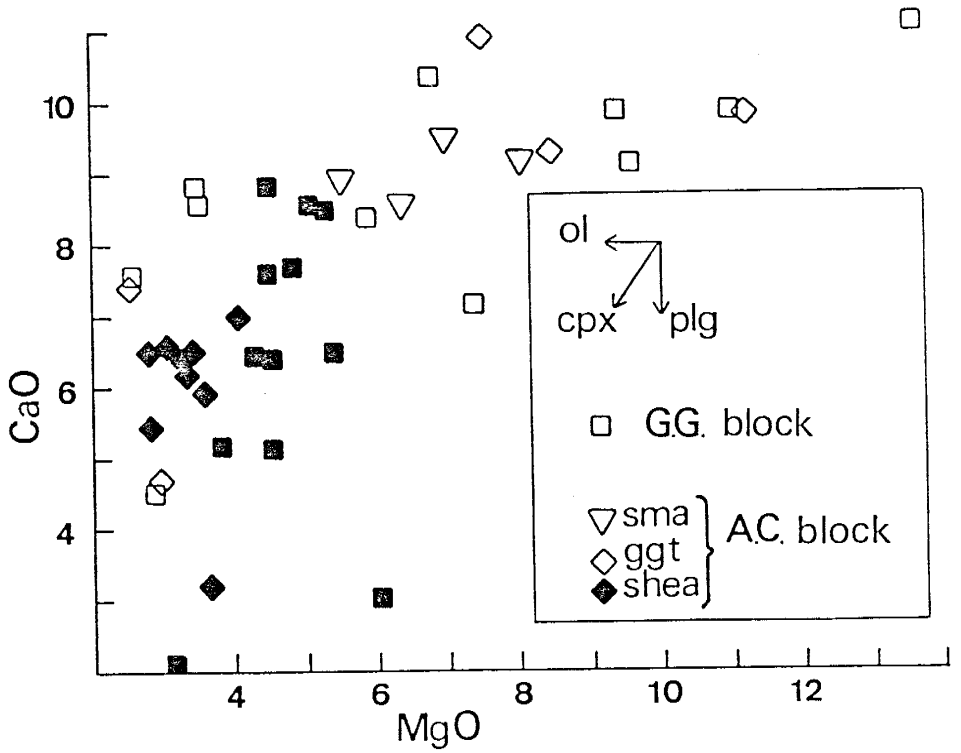

Fig. 25. CaO vs MgO plot for basalts (open symbols) and basaltic andesites (solid symbols) of the Green Gulch and Ash Creek blocks. Units in the Ash Creek block as follows: sma = Yarber Wash basalts, ggt = Grapevine Gulch tuff, and Shea Basalt. Vectors indicate the trends produced by crystallization of olivine (ol), clinopyroxene (cpx) and plagioclase (plg).

clinopyroxene as major liquidus phases between 10 and 20 Kb and plagioclase prevailing over clinopyroxene at less than 10 Kb (Elthon and Scarfe, 1984). Investigation of cumulus assemblages at the base of a dissected island arc indicates pressures of 9.5 to 11.5 kb (pyroxene thermobarometry) for olivine-clinopyroxene fractionation (De Bari, 1989), supporting the pseudoliquidus phase diagram interpretations.

The Big Bug Group lacks obvious evidence of high pressure olivine-clinopyroxene fractionation on isomolar plots (Fig. 23 & 24). This does not eliminate olivine-clinopyroxene fractionation as an evolutionary mechanism in production of Big Bug basalts; however, no intermediate products between possible parental liquids and the final fractionated basalts were erupted. The olivine-normative Bluebell basalts lack an obvious trend on the olivine-clinopyroxene-silica projection (Fig. 23). However, these basalts form a linear trend across the 10 Kb invariant point on the olivine-plagioclase-silica projection suggesting an olivine-plagioclase dominated evolution. The CaO vs MgO plot (Fig. 26) for the Big Bug block indicates plagioclase dominated fractionation for the Bluebell basalts and plagioclase $\pm$ clinopyroxene for other Big Bug volcanics. These features agree with the abundance of plagioclase phyric mafic rocks in the Big Bug Group. Olivine control lines to the most magnesian Bluebell basalt nearly intersect the 20 and 25 Kb invariant points. Consequently, the Bluebell basalts may be derived from primary magmas generated at 20-25 Kb. The postulated depth of generation

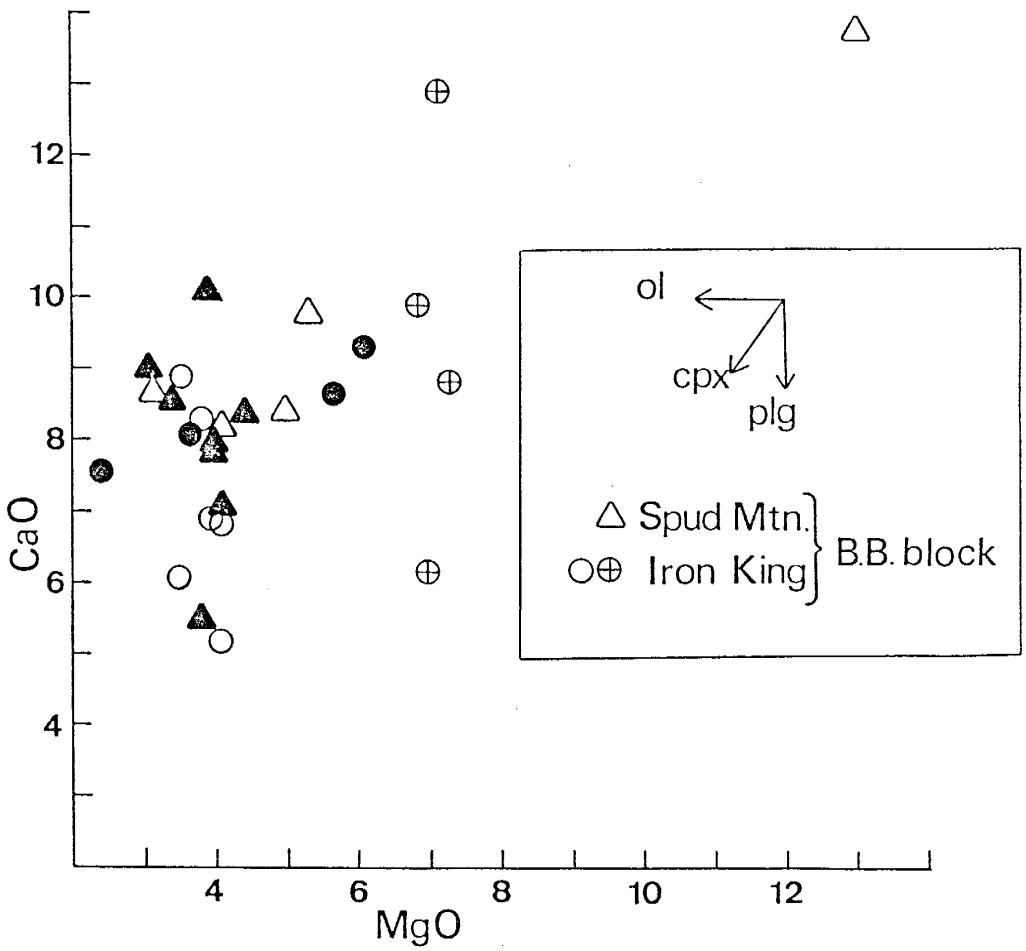

Fig. 26. CaO vs MgO plot for basalts (open symbols) and basaltic andesites (solid symbols) of the Big Bug block. The Bluebell basalts are identified by a cross within the circle. Vectors indicate the trends produced by crystallization of olivine (ol), clinopyroxene (cpx) and plagioclase (plg).

and olivine-plagioclase dominated fractionation trends are similar to those of modern MORB (Elthon and Scarfe, 1984). Two of these nepheline normative basalts lie near the 9 Kb cotectic for Plateau-type basalts from the British Tertiary volcanic province on normative nepheline-diopside-olivine-hypersthene-quartz plots (Thompson, 1982; Thompson et al., 1983). The other two basalts lie within or near the near the field of analysis for Plateau basalts.

The majority of basaltic rocks from the Green Gulch and Ash Creek Blocks lie between the MORB and deep crustal cotectics (Fig. 27). Basaltic rocks of the Big Bug Block plot from the MORB-arc cotectic across the deep crustal cotectic. This plot suggests high-pressure fractionation may also have been significant in evolution of other Big Bug Group volcanics although only the more evolved products were erupted.

Consequently, basalts from the Green Gulch and Ash Creek blocks exhibit the greatest evidence for significant high pressure olivine-clinopyroxene fractionation. This fractionation also offers a possible explanation for differences in the timing of the appearance of normative corundum in the Yavapai Supergroup. Over 50% of the Green Gulch basaltic andesites contain corundum in the norms (Table 2b, App. C), but corundum does not appear until andesitic compositions are attained in the Big Bug volcanics. The crystallization of subaluminous minerals such as olivine and clinopyroxene increase the ASI (Aluminum Saturation Index) index of a magma (Zen, 1986). This feature is demonstrated by an

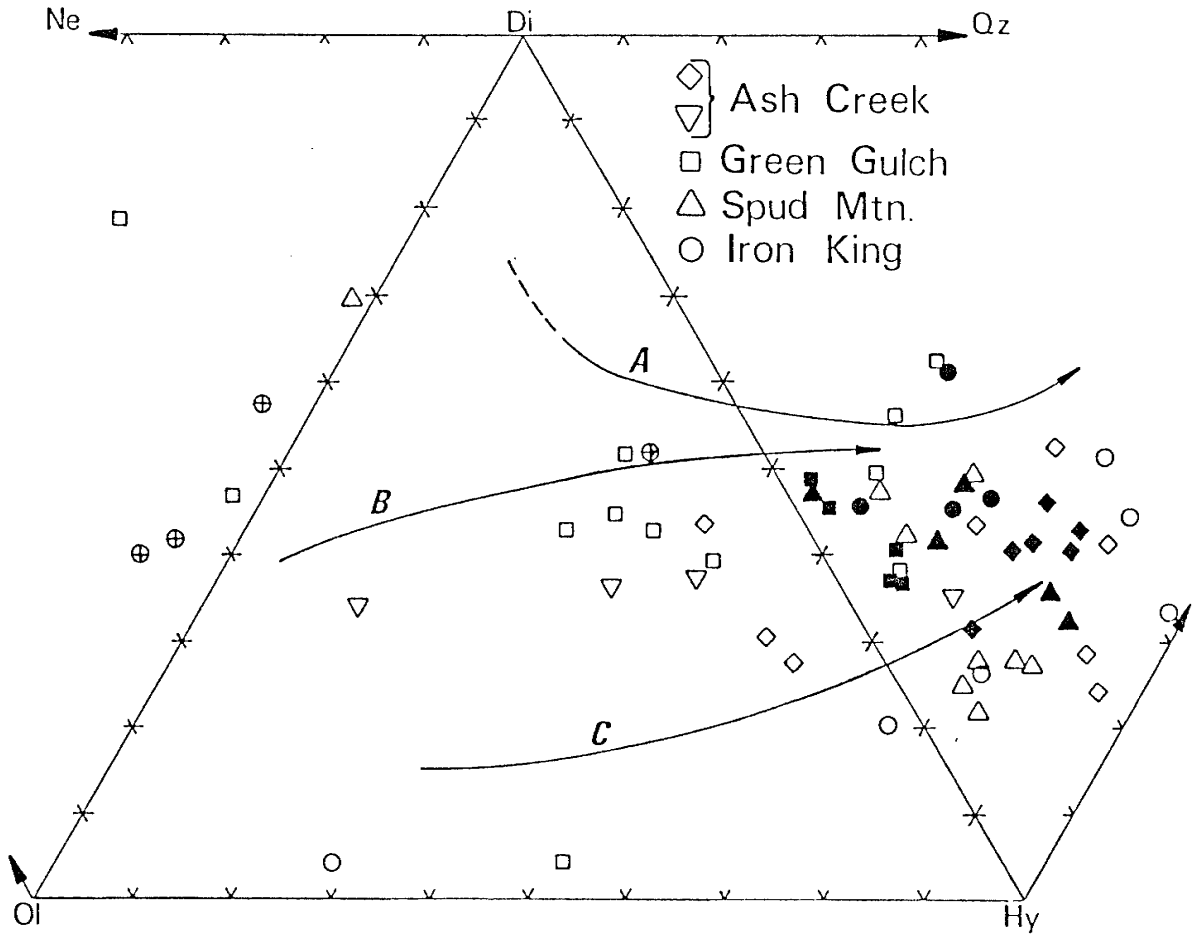

Fig. 27. Normative nepheline-diopside-olivine-hypersthene-quartz plot for Yavapai volcanics (after Thompson, 1982, 1983). Cotectics are: A = 1 atmosphere, B = MORB-arc, C = deep crustal. Lithologic symbols as in Figs. 21-24.

increase in Al_2O_3 with decreasing Mg number for lavas with a Mg number $\geq$ 55 (Uto, 1986). High pressure fractionation delays plagioclase crystallization allowing the ASI to increase enough to produce corundum in the norms of Green Gulch basaltic andesites. The Big Bug Group was not subject to such early fractionation of subaluminous phases consequently the ASI did not reach sufficient levels to produce normative corundum until andesitic compositions (Table 3, App. C).

Uto (1986) ties the origin of high-aluminum basalt to the delay of plagioclase fractionation. The isomolar plots indicate low-P fraction for most Big Bug basalts. Four basaltic andesites of the Spud Mountain Volcanics (Big Bug block) have Al_2O_3 contents comparable to high-Al basalts. These rocks contain a high percentage of plagioclase phenocrysts which probably accounts for part of the high Al contents, but even with Al_2O_3 contents of 18% these rocks do not contain normative corundum. This indicates the importance of subaluminous mineral fractionation in production of corundum normative rock. The extensive fractionation of subaluminous minerals also enriches magmas in silica and the fractionated Green Gulch and Ash Creek lavas plot closer to the silica apex than Big Bug lavas on the isomolar plots (Figs. 21-24).

Andesites

Andesites comprise a significant portion of the volcanic rocks in each tectonic block of the Yavapai Supergroup. However, only two 'andesites' were identified within the Iron King Volcanics and their major element composition is closer to basaltic andesite. The Spud Mountain Volcanics, in the same tectonic block (Big Bug), contain abundant andesite lavas and tuffs. The Mg number of the collective Yavapai andesites range from 23 to 58. In the Ash Creek block, andesites from the Dacite of Burnt Canyon and Gaddes Basalt have the lowest mean Mg numbers at 26 (Tables 5-7, App. B) and the Brindle Pup Andesite the highest at 36. Andesites of the Green Gulch Volcanics have a mean Mg number of 42, are higher in TiO_2, CaO and lower in SiO_2 than Ash Creek Group andesites. The collective andesites of the possibly coeval Ash Crek and Green Gulch blocks span a range of 26 to 53. The Big Bug block contains two major andesite populations with respect to Mg number, the andesite flows (sma) and the massive crystal tuff (smct-smt) with means of 33 and 51, respectively. The massive crystal tuff also has the highest LOI, a feature due in large part to a submarine pyroclastic origin.

With respect to tholeiitic versus calc-alkaline affinity, both characterize Yavapai andesites. The AFM classification (Fig. 19) after Irvine and Barager (1971) indicates a calc-alkaline affinity for most Green Gulch andesites and a tholeiitic affinity for Ash Creek andesites. The Green Gulch andesites actually form

a near continuous trend with calc-alkaline dacites of the Ash Creek Group. On the FeO_T/MgO vs SiO_2 plot both Green Gulch and Ash Creek andesites are tholeiitic, however, most Ash Creek andesites display greater Fe enrichment. The massive crystal tuff (smct-smt) of the Big Bug Group is calc-alkaline on both the FeO_T/MgO vs SiO_2 and the AFM classification (Figs. 18-20). The andesitic flows (sma) of the Big Bug Group are tholeiitic on both plots.

Many Green Gulch andesites lie close enough to the tholeiitic/calc-alkaline boundary that loss of silica or addition or subtraction of Fe or Mg could shift sample points across the boundary. Silica and MgO gains could also shift the classification of the Spud Mountain massive crystal tuff, however, the ratios of relatively immobile trace elements indicate this unit (smct-smt) is compositionally distinct. Consequently, the calc-alkaline character of the tuff is probably real. The Green Gulch andesites are a borderline case and given the mobility of major elements their affinity remains uncertain.

Normative mineralogy also differs among the Yavapai andesites. The high magnesium in the Green Gulch andesites and massive crystal tuff of the Spud Mountain Volcanics is reflected as diopside in norms (Table 2 & 3, App. C), a constituent absent in the other andesites. Normative corundum is prevalent in Ash Creek andesites and the andesitic flows (sma) of the Big Bug block, but the Green Gulch andesites and massive crystal tuff

(smct) of the Big Bug block contain normative corundum in less than half the samples.

In summary, the Green Gulch andesites are less fractionated than Ash Creek andesites but exhibit a greater calc-alkaline affinity relative to the tholeiitic andesites of the Ash Creek block. In a similar fashion the less fractionated andesitic tuffs are calc-alkaline relative to the tholeiitic andesite lavas of the Big Bug block. However, the mobility of major elements in the submarine environment (Sec. IV) indicate this classification is not infallible.

Felsic Rocks

The bulk of the Yavapai felsic volcanic samples were obtained from the Ash Creek block where they comprise a major portion of the volcanic pile. These rocks are calc-alkaline according to AFM criteria. (Fig. 19) but most plot in tholeiitic fields on the Jensen cation plot (Jensen, 1976). Although the Jensen cation plot eliminates the use of mobile alkali components, it is subject to the effects of Fe and Mg mobility. Felsic rocks have initial low Fe and Mg contents, consequently addition or subtraction of these mobile components has a large effect on FeO/MgO ratios. The FeO_T/MgO plot is not suitable beyond andesite compositions for this reason. A test plot of dacitic and rhyodacitic samples produced contrasting indications for closely spaced samples from

single eruptive units. Consequently, the dependability of FeO_T/MgO ratios decreases as SiO_2 increases.

The submarine pyroclastic nature of many of the felsic volcanic rocks increases the initial surface area which may have been in contact with sea water and consequently, the possibility of alteration of original rock composition. Comparisons of compositions of major felsic volcanic units are therefore checked against the relatively immobile Zr/TiO_2 differentiation index employed in the classification scheme (Figs. 15 -17). Among the major felsic units of the Ash Creek Group, the Buzzard Rhyolite contains the lowest mean contents of SiO_2, K_2O and highest Fe_2O_{3T} and MgO contents appearing to be the least fractionated unit. Several Buzzard Rhyolite samples plot near the andesite boundary on Figure 15 suggesting the mean composition is fairly accurate. The major element composition of the remaining units does not allow further distinction with respect to relative degree of fractionation; however, the Zr/TiO_2 ratios (Fig. 15) indicate the Quartz Porphyry is in general more fractionated than the Deception Rhyolite. The mean composition of the small felsic suite from the Green Gulch block is characterized by lower SiO_2 and higher TiO_2, Fe_2O_{3T} and MgO than the Buzzard Rhyolite. Like the mafic and intermediate rocks, the felsic rocks of the Green Gulch Volcanics are more magnesian than those of the Ash Creek and Big Bug blocks.

Alteration

A comparison with published means of felsic volcanics (Le Maitre, 1976) suggests most Yavapai felsic rocks have lost some K_2O, and have lost or gained other alkali components. In some cases the alteration is associated with submarine hydrothermal activity. The Iron King Rhyolite in the vicinity of the Bluebell massive sulfide deposit exhibits the extreme alkali depletion which characterizes the Deception Rhyolite at Jerome. Addition of Fe is also common in many felsic rocks. High LOI in the felsic volcanic rocks is most typical of pyroclastic origin. Sample QFP1 of the Ash Creek Group (Table 2d, App. B) is an example at 6% LOI. The rock is high in Fe, Mg and Ca which are incorporated in chlorite an carbonate. High sericite contents account for the LOI of some of the tuffs of the Spud Mountain Volcanics.

The lower contents of Al_2O_3 and other components relative to younger volcanics, is in part due to dilution by silicification. Over 5% SiO_2 has been added to much of the suite. Silicification is prevalent in the intermediate to felsic sequences where more total SiO2 is available. The basaltic agglomerate (bag) from the Ash Creek Group is an extreme example (Table 2b, App. B). This scoriaceous mafic rock is interbedded with rhyolitic rocks. Vesicle filling by quartz has added 16-18% SiO_2 to a rock of original basaltic andesite composition. In the Big Bug block most of the Spud Mountain andesitic flows (sma) qualify as dacites by

SiO_2 content, therefore classification schemes using SiO_2 as a differentiation index are misleading. Mafic dominated sequences are generally not subject to such extreme silicification, although these rocks may be vesicular or brecciated.

Trace Element Geochemistry

Introduction

The incompatible nature of K, Rb and Ba increases the concentration of these large ion lithophile elements (LILE) in residual liquids during igneous fractionation until crystallization of K-feldspar. The abundance of Sr is tied to plagioclase fractionation. Th is incompatible until crystallization of accessories such as zircon. Consequently, LILE in unaltered igneous suites generally increase toward felsic compositions, except for Sr. Trace element investigations indicate that with exception of Th, the LILE are quite mobile and concentrations in ancient rocks must be interpreted with caution.

The relatively immobile HFSE (Sec. IV) are also generally incompatible, increasing in felsic compositions. However, with the initiation of magnetite-ilmenite and apatite fractionation, Ti and P contents decrease. Crystallization of zircon may affect Zr concentrations in a similar manner but is most common in felsic compositions. Individual HFSE such as Zr are useful indices of relative degrees of fractionation. The incompatible nature and

relative immobility of HFSE such as Ti, Zr, Y, Nb, Ta, Hf and Th allows use of their ratios as indicators of source composition. The REE are also relatively incompatible and generally increase in felsic rocks. Mineral phases with large partition coefficients for REE include clinopyroxene, zircon and garnet for heavy REE, amphibole and plagioclase for Eu, and allanite for light REE (Henderson, 1984). Consequently, crystallization of these phases may alter the original REE pattern inherited from the source, but indicate mineral phases involved in the evolution of the magma.

The transition metals Cu, Pb and Zn are extremely mobile and therefore unsuitable for investigation of original compositional variation. The compatible transition elements V, Cr, Ni and Co display limited mobility and are useful indicators of fractionation. Cr and Ni partition strongly into olivine, pyroxenes, chromite and magnetite. Co and V also have high partition coefficients for magnetite (Duke, 1976; Takahashi, 1978). Consequently, the concentrations of the transition metals generally decrease as fractionation proceeds toward felsic compositions.

Basalts and Basaltic Andesites

The Green Gulch basalts have the highest LILE levels of the Yavapai Supergroup basaltic suite. These rocks also have the highest total HFSE contents, a surprising feature as Mg numbers and high Ni and Cr contents indicate they are the least

fractionated (Tables 5-7, App. B) Yavapai rocks. The Ash Creek block basalts exhibit the lowest Th and HFSE contents of the Yavapai Supergroup. The low Ni and Cr contents indicate the Grapevine Gulch basaltic tuffs are the most fractionated Ash Creek basalts.

The basalts of the Big Bug block are more diverse than other blocks. The Bluebell basalts (ika-ikab) of the Iron King Volcanics exhibit moderate HFSE contents and the lowest LILE concentrations of the block. The high Ni and Cr contents indicate these are the least fractionated. The Iron King (ika) and Spud Mountain basalts (sma-smb) share similar HFSE levels and very low Ni and Cr contents. The Iron King basalts have distinctly higher Th contents, relative to other basalts from the Big Bug block.

Basaltic andesites of the Shea Basalt have slightly lower Th contents but higher total HFSE contents than Green Gulch basaltic andesites at comparable Mg numbers (Tables 5-7, App. B). The high-Ti Iron King basaltic andesites of the Big Bug block display similar concentrations of Th and HFSE at comparable Mg numbers. A dike (9sm46) from the Spud Mountain Volcanics is also a member of this HFSE enriched subset of basaltic andesites. The two 'andesites' from the Iron King Volcanics may be the least fractionated representatives of this suite. These rocks do not exhibit the high Ti concentrations characteristic of the other basaltic andesites; however, Ti levels do not peak until a Mg number range of 45-30. These 'andesites' have Mg numbers of 55

and 58 and higher Ni and Cr contents than other basaltic andesites, indicating less fractionation.

The Spud Mountain basaltic andesites include high-Ti and high-Al suites (Table 7, App. B). This high-Ti group does not attain the HFSE levels of the suite previously described, but approximates those of the Green Gulch basaltic andesites. The high-Al group contains the lowest LILE and HFSE contents of all Yavapai basaltic andesites, although Ni and Cr contents suggest comparable levels of fractionation.

Predicted enrichment trends of LILE and HFSE are recognized in the transition from basalt to basaltic andesite for Yavapai volcanics. However, systematic increases are not apparent within the basalt compositional range despite a Mg number range of 70 to 33 in the Green Gulch basalts. For the LILE, except Th, this problem may result from mobilization of these components. For the HFSE, the problem may be explained by the difficulty of detecting concentration changes which are within or near the limits of analytical error. Concentration and dilution effects from major element alteration (Sec. IV) may also mask small variations.

The Ni and Cr contents of Yavapai basalts generally decrease with decreasing Mg numbers. The Green Gulch basalts exhibit the greatest compositional range and mean Ni contents decrease from 271 to 67 to 25 ppm during the evolution from primitive to evolved basalt to basaltic andesite, respectively. The transition metals V, Sc and Co peak with TiO_2 in the 45-30 Mg number range. This suggests magnetite-ilmenite fractionation is a major control on

these transition metals in this compositional range and conforms with data on experimental and natural systems (Duke, 1976; Mahood and Hildreth, 1983).

The REE variation of the Yavapai volcanics is illustrated by comparison of chondrite-normalized variation diagrams (Figs. 28-41) and La/Yb ratios (Tables 8-10, App. B). Basalts of the Ash Creek block exhibit slightly light REE enriched patterns with flat to gently sloping heavy REE patterns (Fig. 28). Small negative Eu anomalies are observed in one gabbro and a basalt from the Spud Mountain suite (YMsma). The two gabbros may be in part cumulate, consequently, the concentration differences between them may reflect differences in proportions of plagioclase and pyroxene. The Ash Creek basalts are characterized by a La/Yb ratio range of 2.5-4.4 and the lowest total REE contents of the Yavapai volcanics.

The Big Bug block basalts exhibit greater diversity with respect to REE. Spud Mountain basalts (sma-smb) are slightly light REE enriched with some negative Eu anomalies and flat heavy REE patterns (Fig. 29). The two basalts from the Iron King mine area (smIK) have REE concentrations within the range of the other Spud Mountain basalts; however, La/Yb ratios (3.1-3.6) exceed those of the Spud Mountain basalts (2.7-3.3). The Iron King basalts (ika) are characterized by the greatest light REE enrichment (La/Yb = 4.2-5.5) of the Big Bug block basalts, a lack of Eu anomalies, and flat heavy REE patterns (Fig. 29). The Bluebell basalts (ika-ikab) of the Iron King volcanics exhibit the

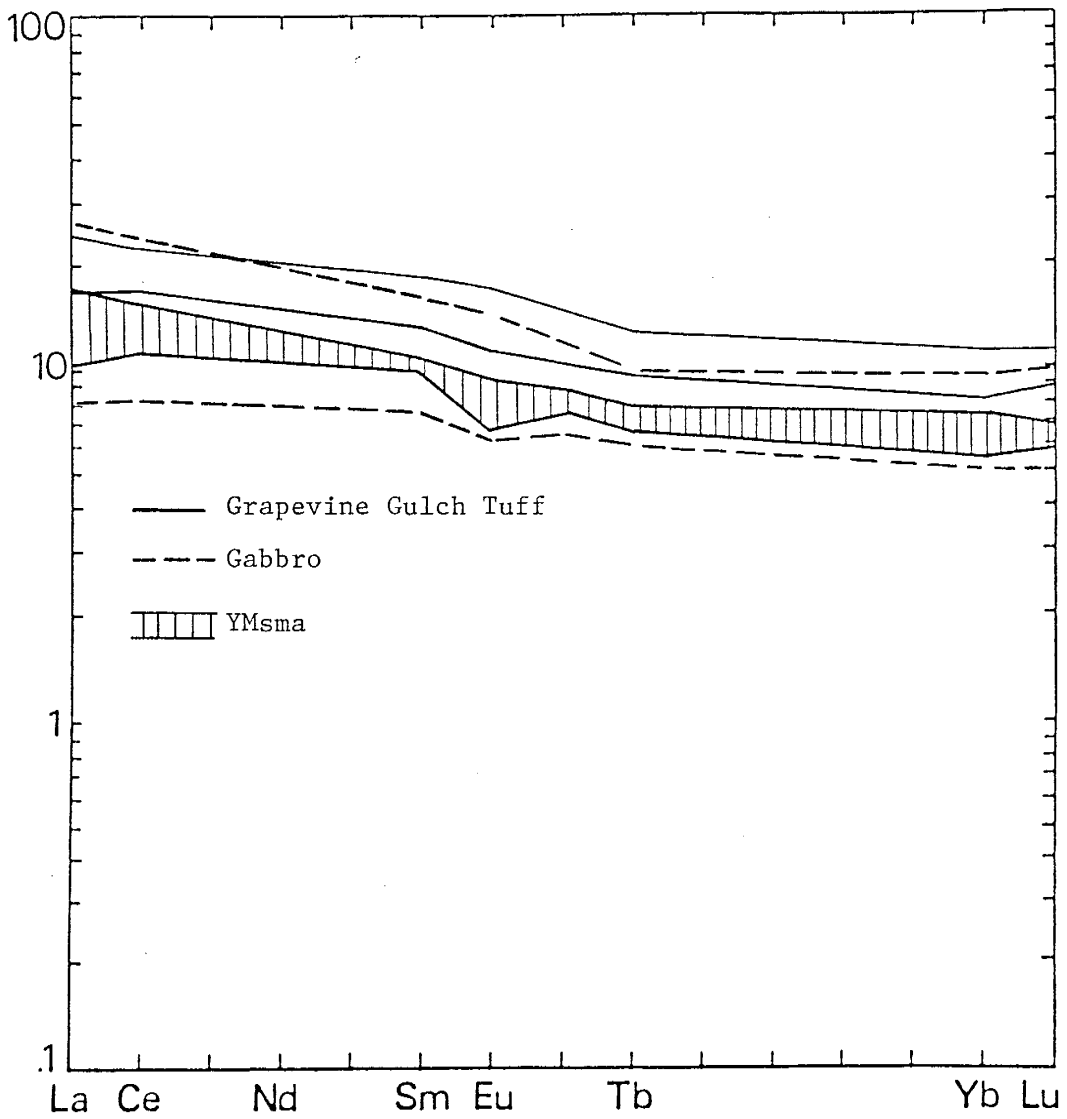

Fig. 28. Chondrite-normalized REE variation envelope (n=3) for Spud Mountain basalts (YMsma) from Yarber Wash. REE variation for individual samples of gabbro and Grapevine Gulch basaltic tuff.

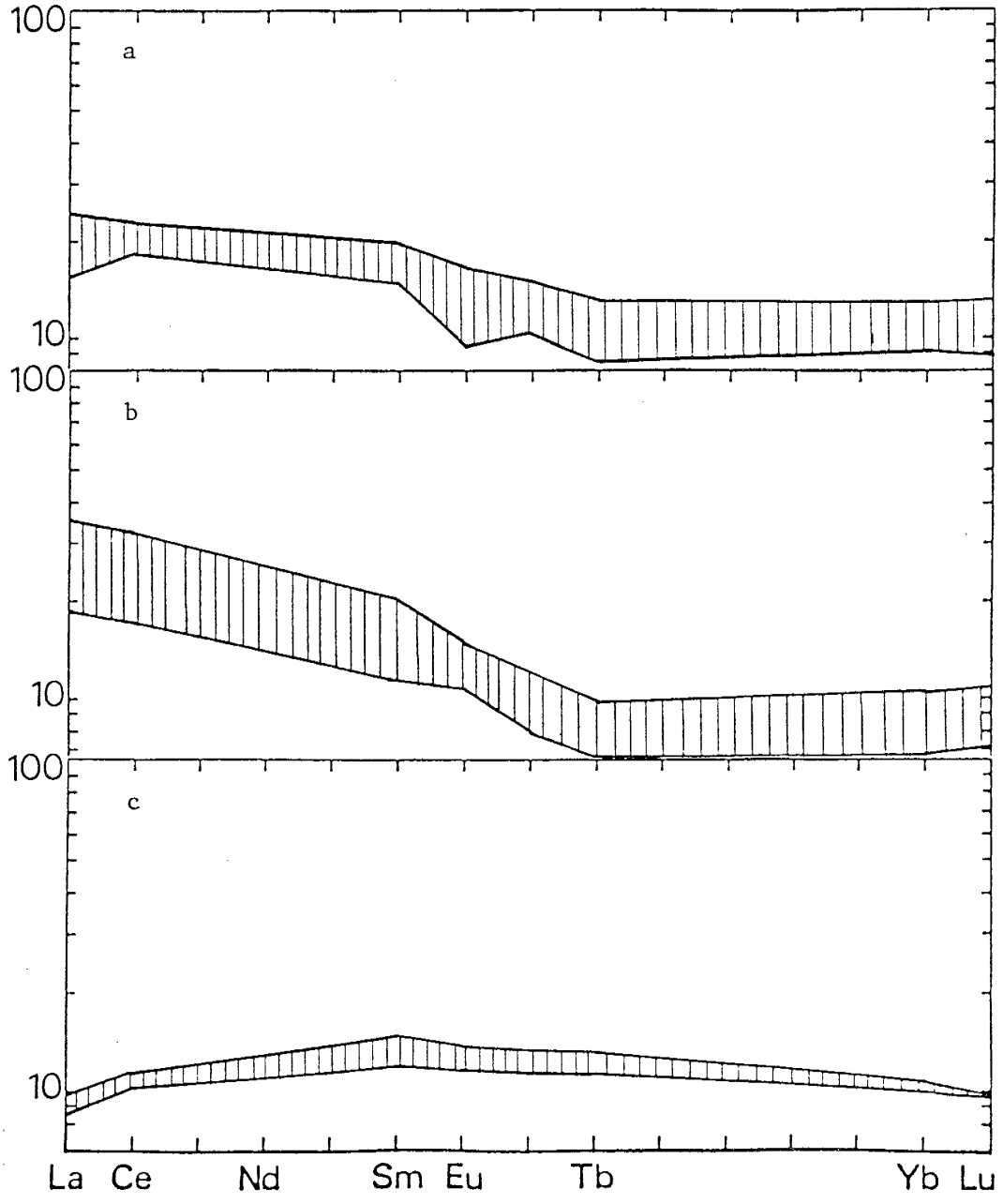

Fig. 29. Chondrite-normalized REE variation envelopes for: (a) the Spud Mountain basalts (sma, smb, n=3), (b) the Iron King basalts (ika, n=5), and (c) the Bluebell basalts (ika, ikab, n=3).

most distinctive REE patterns (Fig. 29) of the Yavapai basalts. These rocks are characterized by flat to slightly convex patterns with a La/Yb ratio range of 1.4-1.7.

The primitive and evolved basalts of the Green Gulch Block exhibit similar light REE enriched patterns, small negative Eu anomalies and sloping heavy REE patterns (Fig. 30). The two suites differ most by their heavy REE concentrations. These rocks exhibit the greatest light REE enrichment of the Yavapai basalts with a La/Yb ratio range of 4.1-10.4 for the primitive suite and 1.7-9.0 for the evoled suite.

The basaltic andesites of the Ash Creek block are dominated by the HFSE enriched Shea Basalt. These rocks are characterized by light REE enrichment (La/Yb = 3.3-3.6), some small negative Eu anomalies and flat to gently sloping heavy REE patterns (Fig. 31a). The single Brindle Pup sample exhibits similar light REE enrichment (La/Yb = 3.7) but lower total concentrations. The total REE concentrations of the Shea Basalt exceed those of andesites and many felsic rocks of the Ash Creek Block.

The basaltic andesites of the Big Bug Block include the high-Al and high-Ti lavas interlayered with the Spud Mountain breccia (Fig. 31b). Both suites are characterized by light REE enrichment and small negative Eu anomalies. The high-Al basaltic andesite REE pattern is a higher concentration mimic of the Spud Mountain basalt (sma-smb) pattern suggesting a potential genetic link. The high-Al basaltic andesites have flat heavy REE patterns, lower total REE concentrations and lower La/Yb ratios

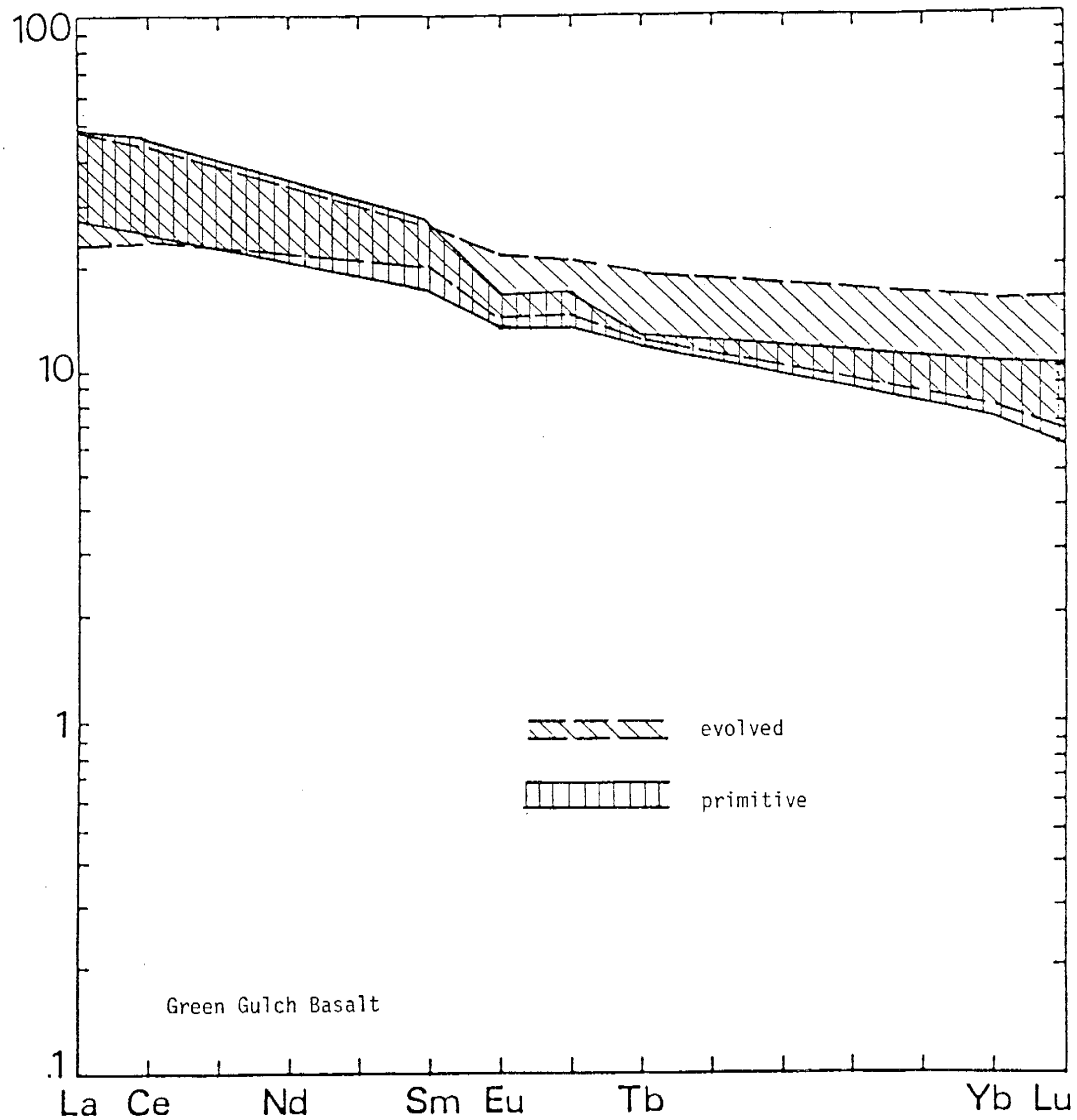

Fig. 30. Chondrite-normalized REE variation envelopes for primitive (n=3) and evolved (n=5) Green Gulch basalts.

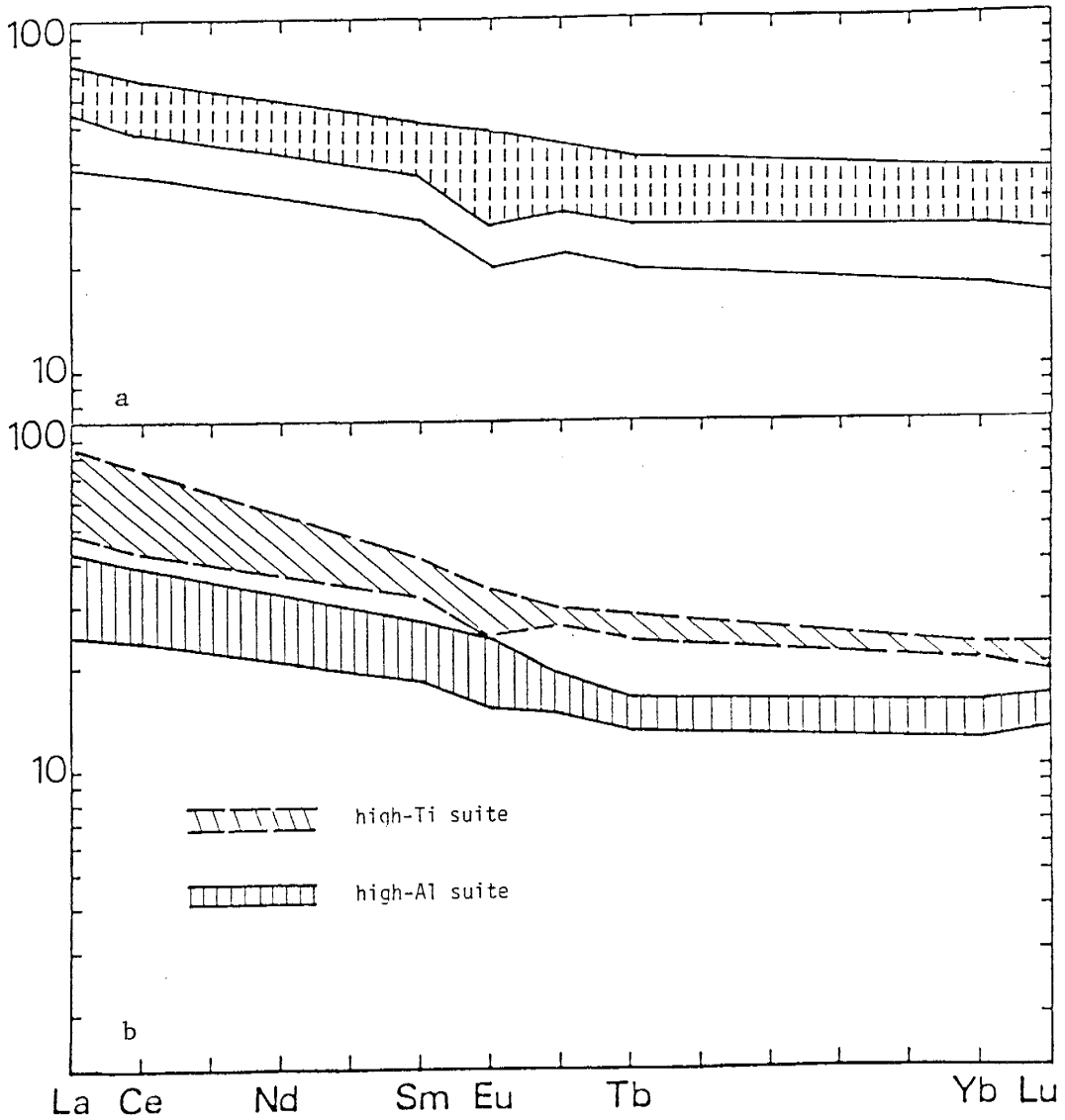

Fig. 31a. Chondrite-normalized REE variation envelope (shaded) for Shea basaltic andesite (n=5) and a single plot of Brindle Pup basaltic andesite.

Fig. 31b. Chondrite-normalized REE variation envelopes for high-Ti (n=3) and high-Al (n=3) Spud Mountain basaltic andesites.

(3.4-4.6) compared to the high-Ti suite (La/Yb = 4.1-5.3). An andesitic lithic fragment (10smb16) from the interlayered breccias has an REE pattern which falls within the envelope for the high-Al basaltic andesite lavas. The Iron King Volcanics include two high-Ti basaltic andesites with La/Yb ratios of 4.1 and 5.3 (Fig. 32). One sample exhibits a negative Eu anomaly and a sloping heavy REE pattern, the other a flat heavy REE pattern and no Eu anomaly. The two Iron King 'andesites' exhibit the most pronounced light REE enrichment (La/Yb = 6.1 and 7.1) of the basalts and basaltic andesites in the Big Bug Block. The HFSE enriched 'andesites' and basaltic andesites of the Iron King Volcanics (Big Bug Block) and the Shea basaltic andesite of the Ash Creek Block display the highest total REE contents of the Yavapai basaltic andesites.

The REE variation envelope of the Green Gulch basaltic andesites is a higher concentration extension of the Green Gulch basalt envelopes (Fig. 33). The La/Yb ratios (2.2-8.3) are nearly identical to those of the evolved basalts. The greatest difference is enhancement of the negative Eu anomaly in the basaltic andesite pattern. This indicates the importance of plagioclase fractionation in the magmatic evolution from basalt to basaltic andesite and is consistent with the interpretation of the isomolar and CaO vs MgO plots (Figs. 22 & 25).

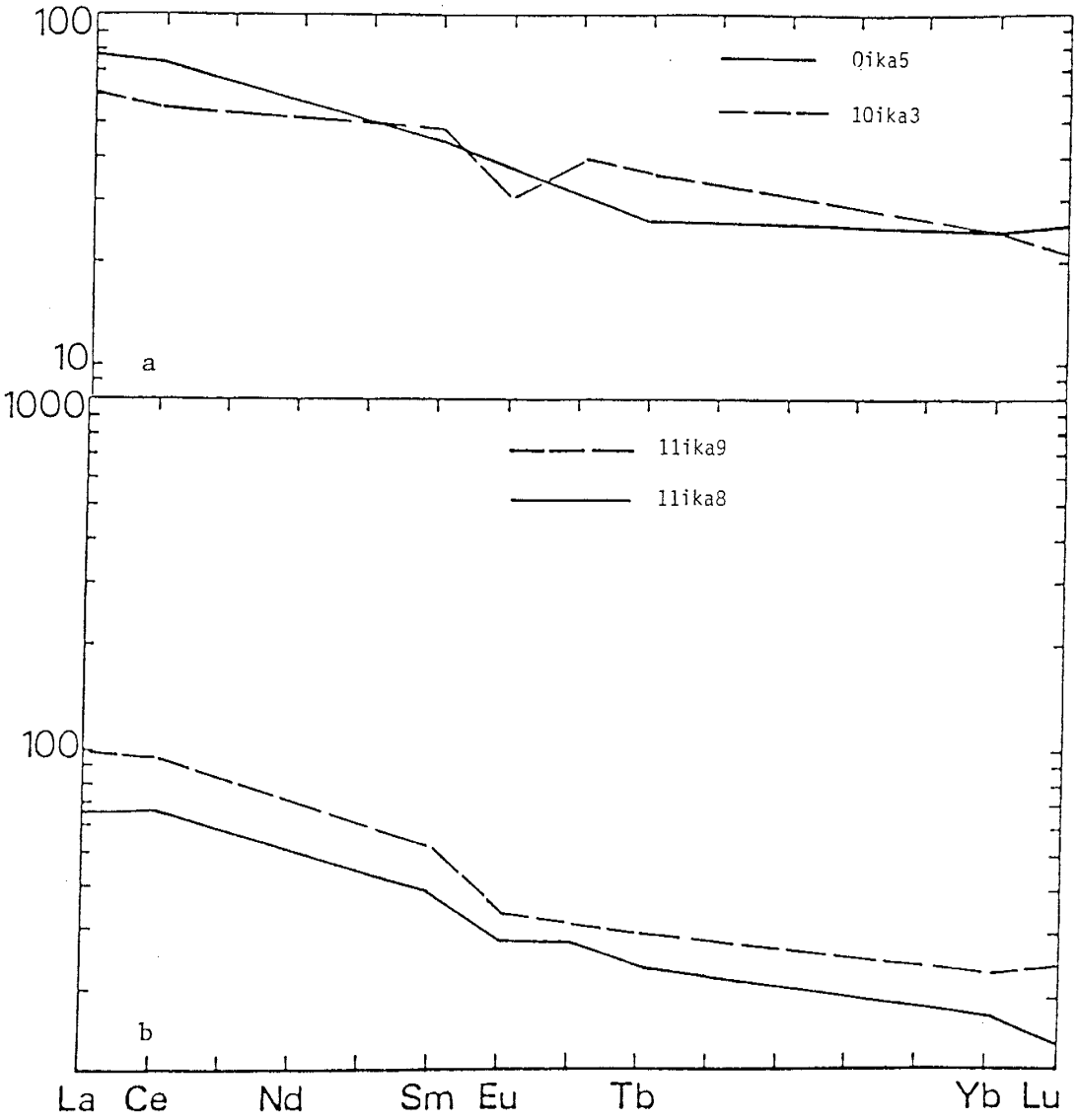

Fig. 32. Chondrite-normalized REE variation of (a) Iron King basaltic andesite and (b) Iron King 'andesite'.

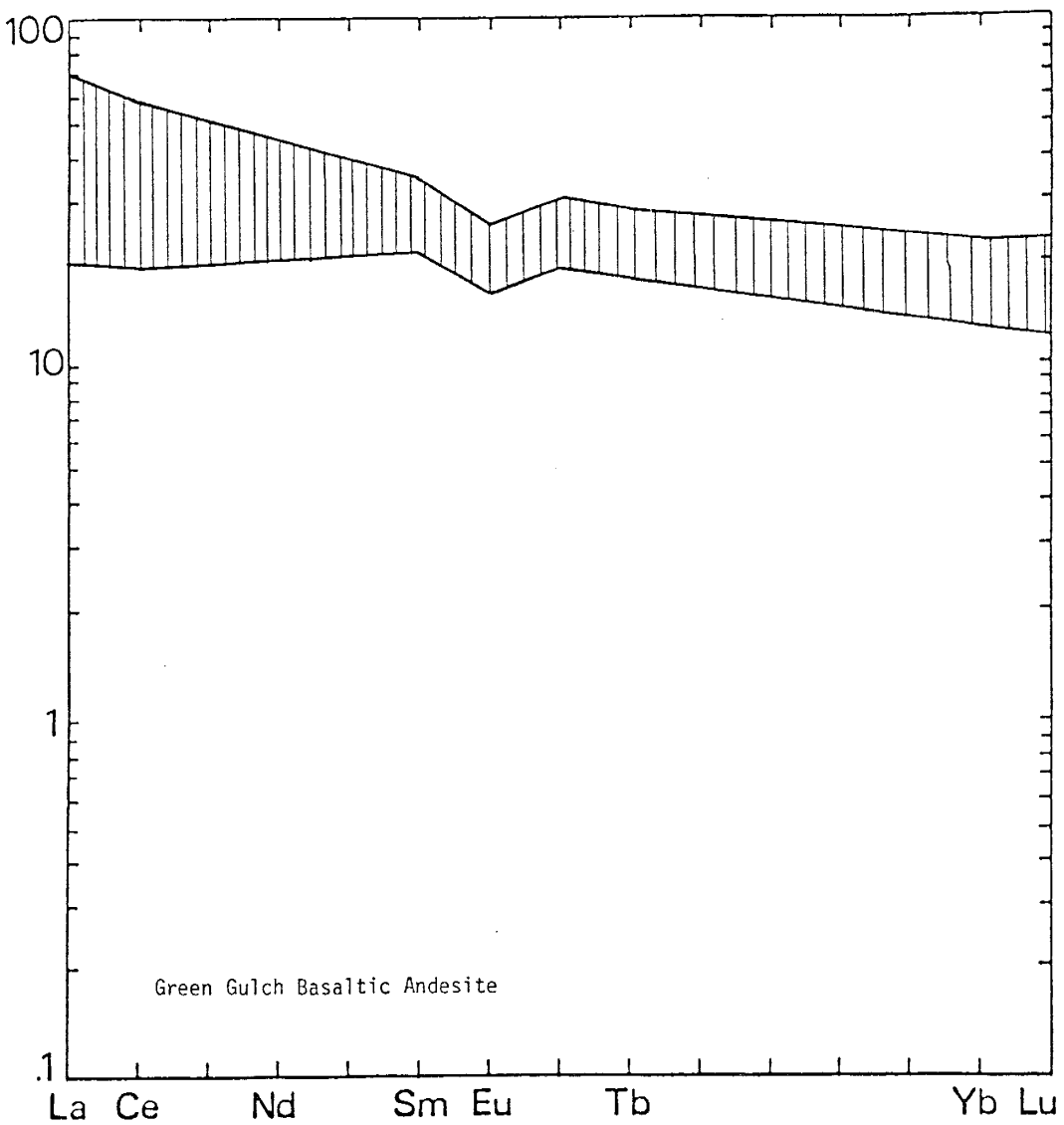

Fig. 33. Chondrite-normalized REE variation envelope (n=6) for Green Gulch basaltic andesite.

Andesites

The andesite units of the Big Bug block exhibit a general increase in mean contents of Rb, Ba, Cs and Th from the andesitic tuff (smct) to lavas (smt and sma) with decreasing Mg number. Such trends are not recognized among the Ash Creek or Green Gulch andesites with respect to Mg number. The Ash Creek andesites appear to be the most fractionated with respect to Mg number, but have the lowest Th concentrations. With respect to comparable levels of fractionation, Green Gulch andesites have the highest Th concentrations.

The HFSE concentrations of the Green Gulch andesites and Spud Mountain andesites (sma) of the Big Bug Block are nearly equal at comparable Mg numbers. These units contain the highest HFSE concentrations of the entire Yavapai andesite suite, and the Ash Creek andesites have the lowest HFSE concentrations. Among the andesite units of the Big Bug Block, little difference in HFSE concentration is apparent between the smt lavas and smct-smt tuffs.

The transtion metal concentrations are highest in the least fractionated Big Bug and Green Gulch andesites (Tables 6 & 7, App. B). Among the Big Bug andesites the Spud Mountain lavas contain the lowest transition metal concentrations. In the Ash Creek andesites, Cr and Ni contents are at or below detection limits in the Gaddes Basalt and Dacite of Burnt Canyon. The Brindle Pup

Andesite exhibits the highest total transition metal contents in accord with the highest Mg numbers of the Ash Creek andesites.

Andesites of the Ash Creek Block are characterized by light REE enriched patterns, negative Eu anomalies and flat to gently sloping heavy REE patterns (Fig. 34). The La/Yb ratio increases from the Gaddes Basalt (2.6-2.9) to the Dacite of Burnt Canyon (3.2-4.9) to the Brindle Pup Andesite (3.7-6.4). The basaltic andesite of the Brindle Pup unit differs from the Brindle Pup andesite only by slightly lower light REE contents.

The Green Gulch andesites have REE patterns (Fig. 35) characterized by light REE enrichment, sloping heavy REE patterns and small negative Eu anomalies. The mean concentrations of basaltic andesites and andesites of the Green Gulch Block differ in light REE. The La/Yb ratios increase from 2.2-8.3 in basaltic andesites to 2.7-11.2 in the andesites.

The Spud Mountain andesite suite from the Big Bug Block is characterized by variable light REE enrichment, flat to gently sloping heavy REE patterns and negative Eu anomalies (Figs. 36 & 37). The mean REE concentrations among the smct-smt, smt and sma units increase concurrently with decreasing Mg number. The La/Yb ratios are highest in the smt lavas and smct-smt tuffs (Table 10, App. B). The tuffs (smct-smt) and lavas (sma) display a very narrow REE concentration range (Fig. 36). The smt lavas contrast sharply with extreme variation in heavy REE concentrations (Fig. 37). The very restricted range of La concentrations suggests

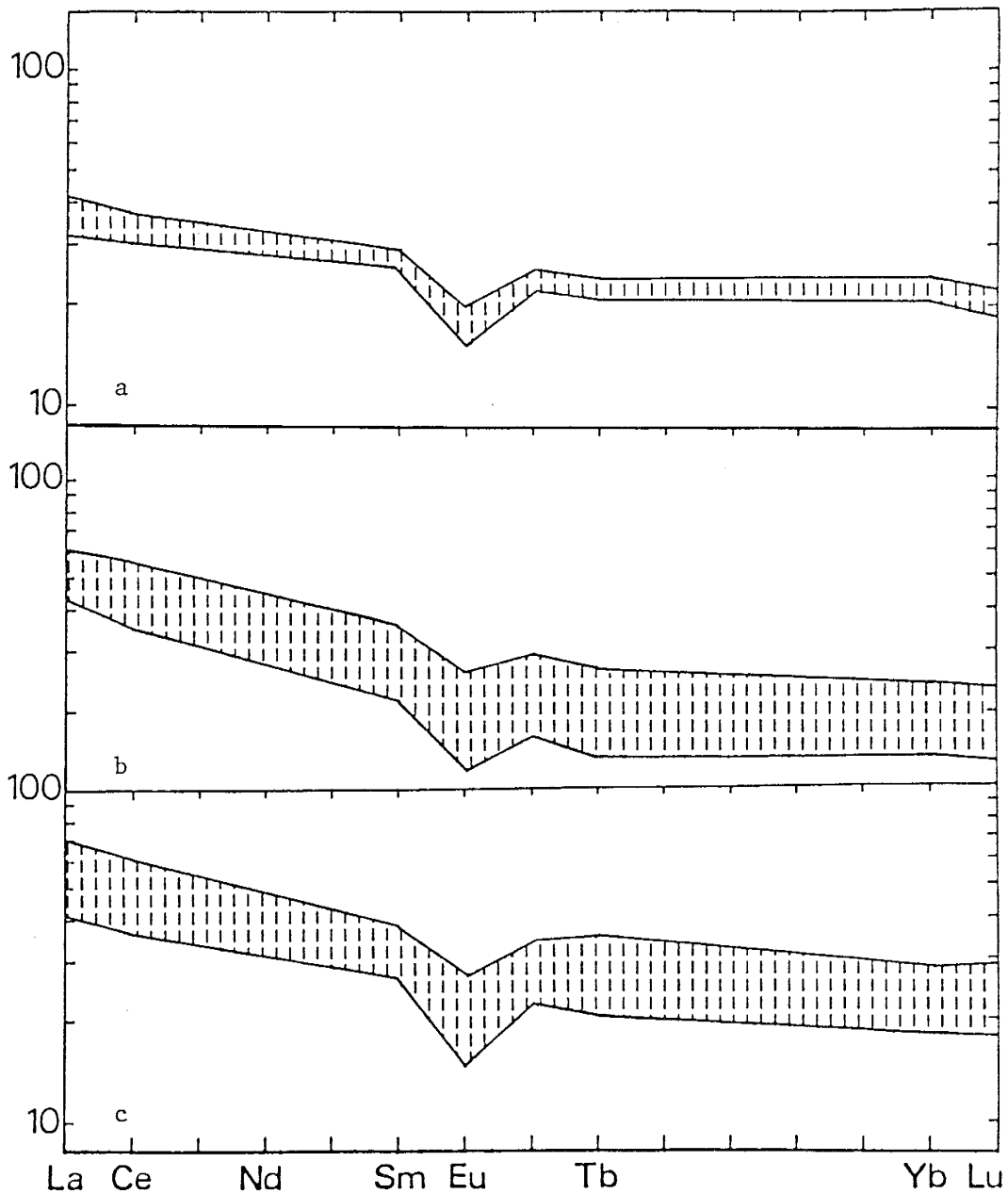

Fig. 34. Chondrite-normalized REE envelopes of variation for andesites from the (a) Gaddes Basalt (n=4), (b) the Brindle Pup Andesite (n=5), and (c) the Dacite of Burnt Canyon (n=5).

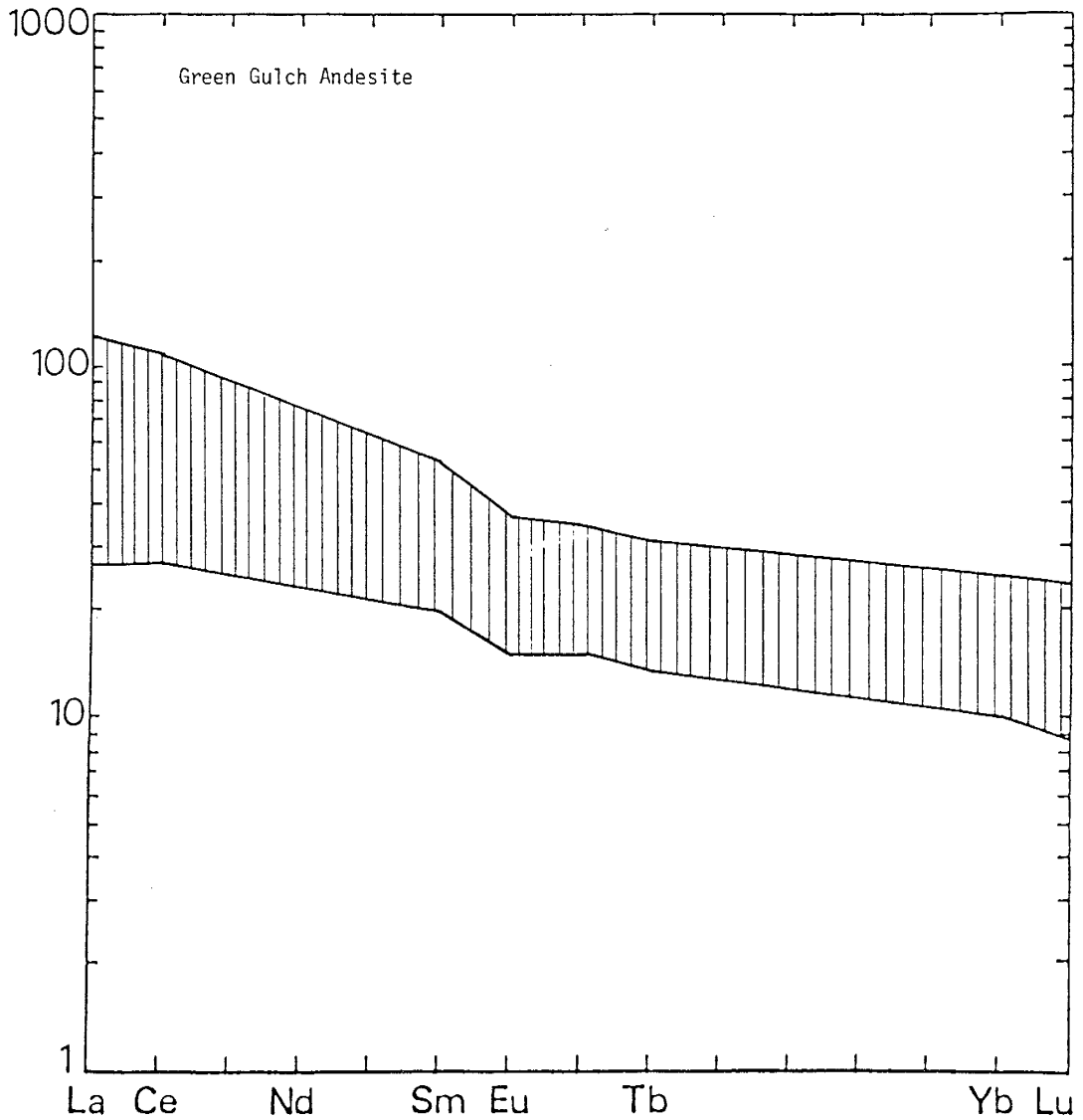

Fig. 35. Chondrite-normalized REE variation envelope (n=5) for Green Gulch andesites.

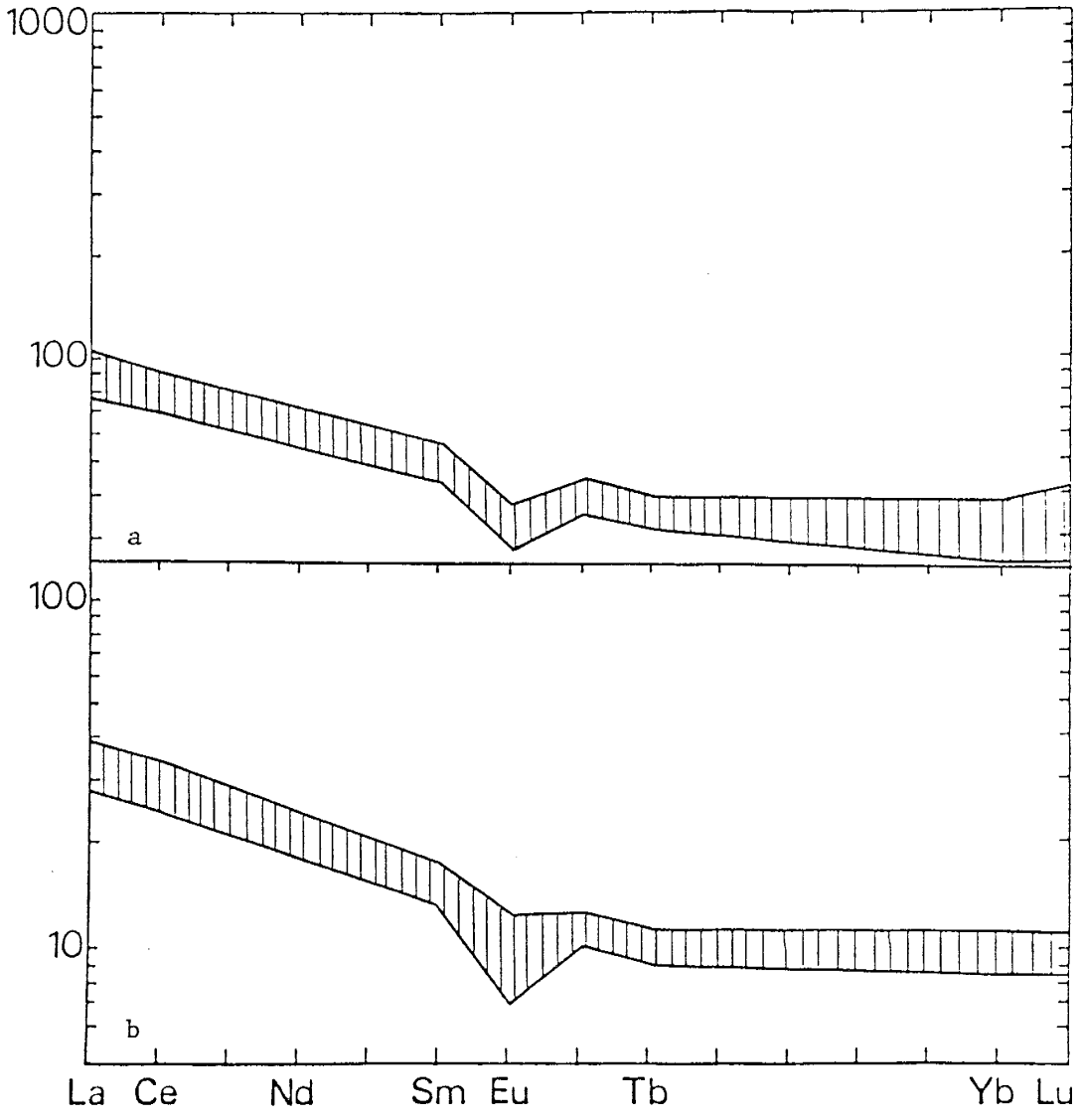

Fig. 36. Chondrite-normalized REE envelopes of variation for: (a) Spud Mountain andesite (sma, n=8) and (b) Spud Mountain andesitic tuff and massive crystal tuff (smt & smct, n=7).

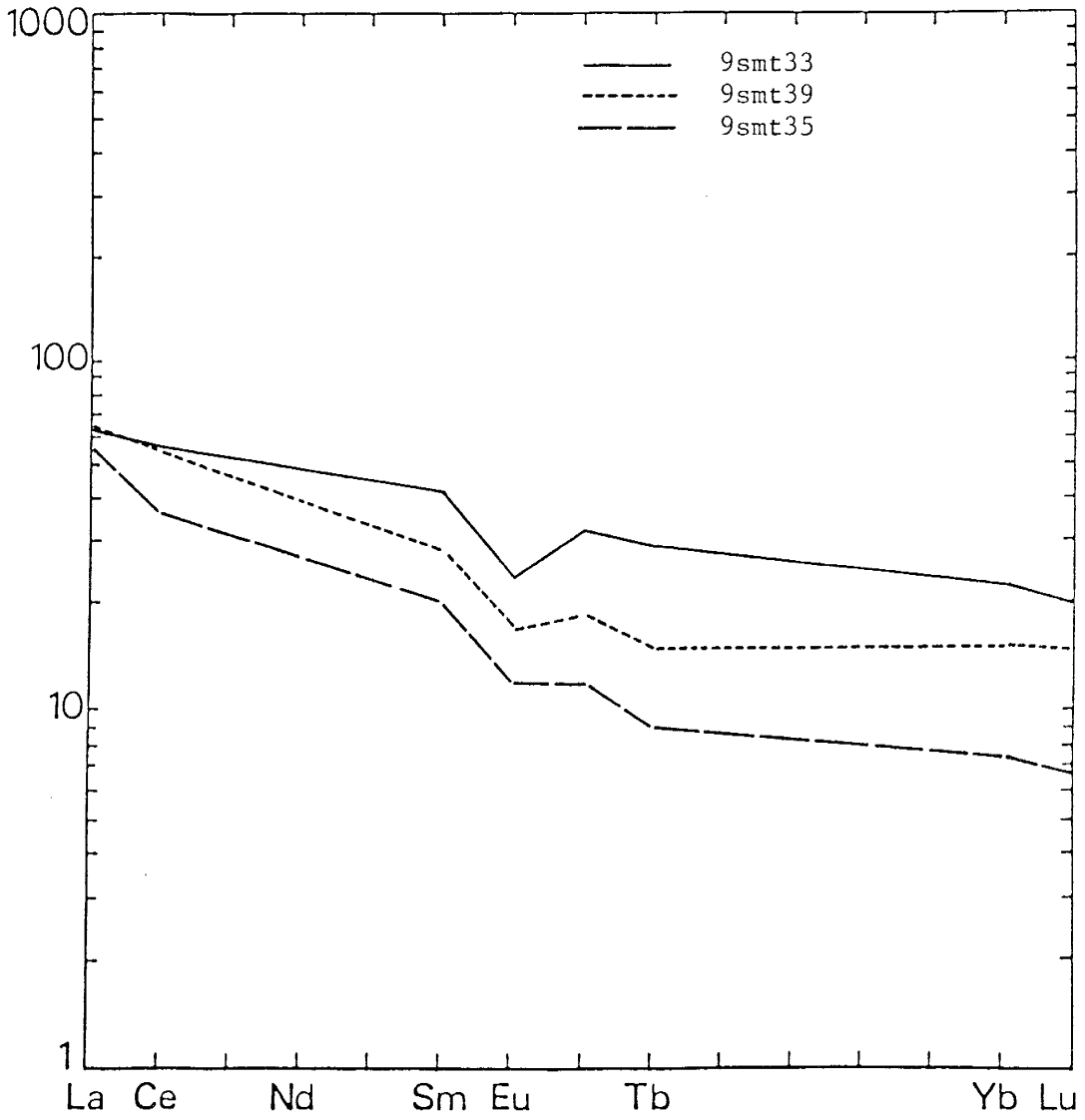

Fig. 37. Chondrite-normalized REE variation for Spud Mountain andesite lavas interlayered with tuff (smt).

either some homogenization of light REE by alteration or near uniform contents of major light REE bearing phases.

At comparable levels of fractionation, the Spud Mountain andesite lavas (sma) from the Big Bug Block exhibit total REE concentrations similar to those of the Green Gulch Block, albeit with slightly higher heavy REE. The Ash Creek and Green Gulch andesites have similar heavy REE concentrations but differ in light REE concentrations. The andesite tuffs (smct-smt) and the lavas from the smt unit of the Big Bug Block contain the lowest REE concentrations of the Yavapai andesites.

Felsic Volcanics

The mean SiO_2 contents and DI (sum of normative salic components) indicate that the Green Gulch dacitic to rhyodacitic rocks are the least fractionated members of the Yavapai felsic suite (Table 6, App. B). These are the only felsic rocks with detectable concentrations of Cr and Ni. However, these rocks have higher Th and HFSE concentrations than most of the more fractionated Yavapai rhyodacites. Although Rb, Cs and Ba concentrations parallel K_2O concentrations, it is very doubtful that they represent original values. Consequently, Th is the only reliable indicator of original LILE concentrations.

The Big Bug Block contains the only rhyolite recognized in the Yavapai Supergroup. The Spud Mountain rhyolites (smr) contain the highest mean concentration of Th and HFSE in the Yavapai

Supergroup. Concentrations of Th and HFSE are similar among the other rhyodacites and rhyolites from the Spud Mountain quartz porphyry and Iron King rhyolite but difficult to evaluate because of the concentration-dilution effects caused by variable silicification and alkali leaching.

The Ash Creek felsic sample base is larger and of higher quality. The Th contents increase progressively from the dacitic Buzzard Rhyolite to the Quartz Porphyries to the rhyodacitic Deception Rhyolite (Table 5, App. B). This trend is not recognized for the other LILE. The Th and HFSE contents of Ash Creek rhyodacites are greater than or equal to Big Bug Block rhyodacites. Comparison of HFSE concentrations among the Ash Creek felsic volcanics indicate the Quartz Feldspar Porphyry tuff is nearly identical to other Quartz Porphyries. In the Deception Rhyolite from the Jerome area, (Table 2d, App. B), HFSE concentrations are higher in the tuff-dominated lower unit and Cleopatra Member than in the overlying domes and flows of the upper unit.

The Ash Creek felsic suite exhibits variable degrees of light REE enrichment with flat heavy REE patterns and pronounced negative Eu anomalies (Figs. 38 & 39). The Buzzard Rhyolite and Quartz Porphyries have La/Yb ratios ranging from 2.3-3.9 (Table 8d, App. B) but the Deception Rhyolite is higher with a La/Yb ratio range from 4.6-5.6. The Quartz Porphyry (Fig. 38) samples exhibit pronounced negative Eu anomalies indicating these rocks originated from magmas subjected to extensive plagioclase

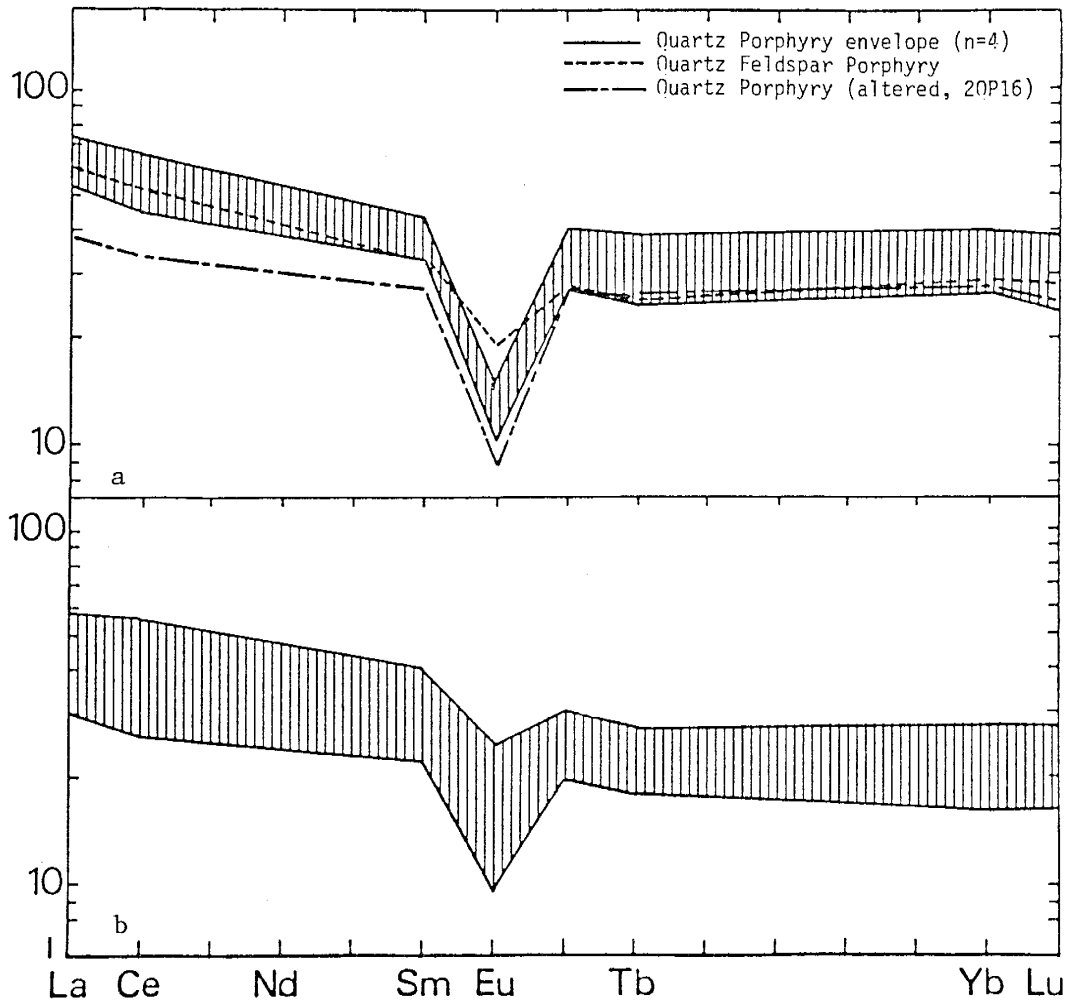

Fig. 38a. Chondrite-normalized REE variation for Quartz Porphyry (n=4) and Quartz Feldspar Porphyry (dacite-rhyodacite).

Fig. 38b. Chondrite-normalized REE variation envelope for the Buzzard Rhyolite (dacite-rhyodacite, n=5).

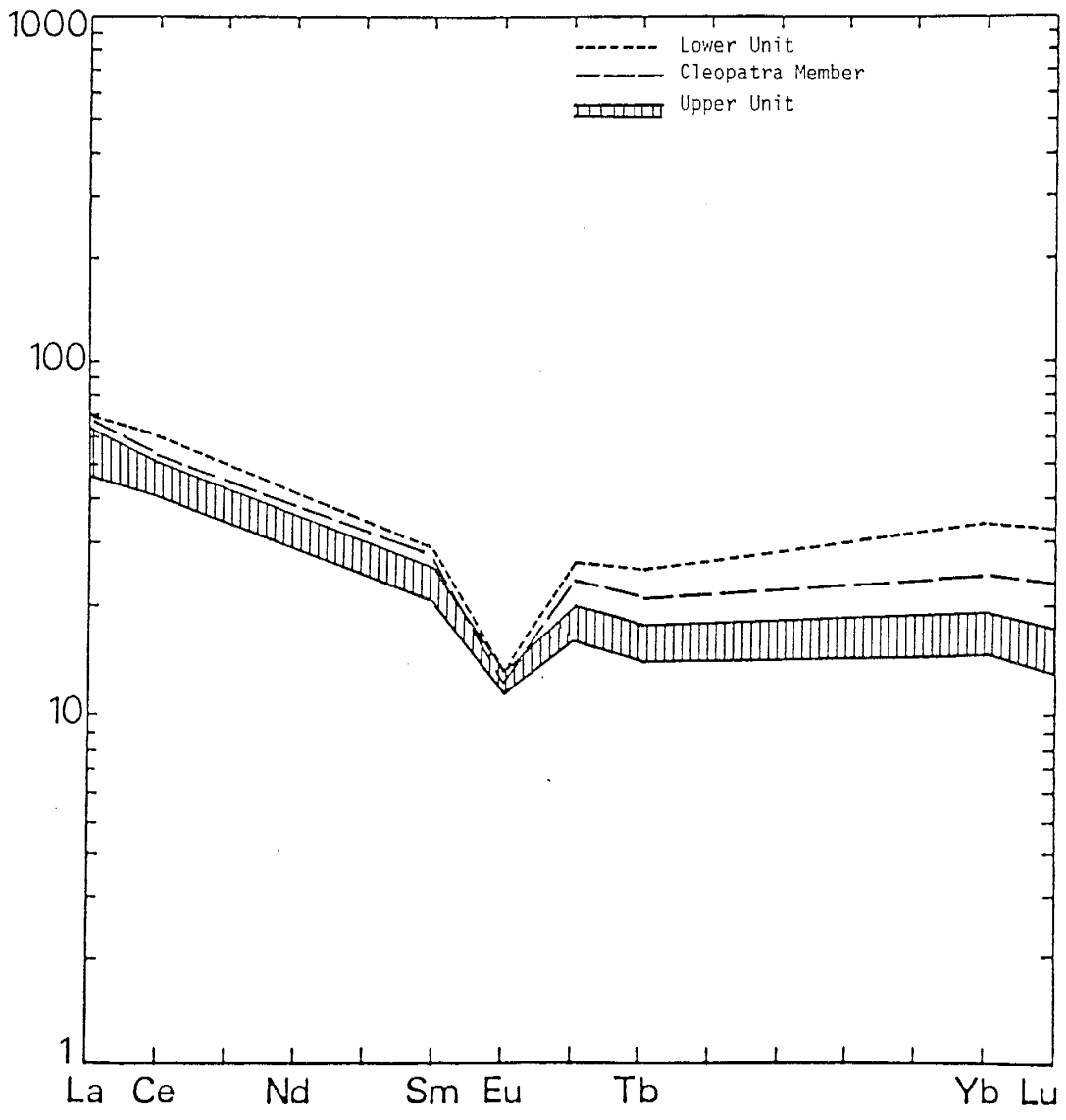

Fig. 39. Chondrite-normalized REE variation among the least altered Lower Unit sample, the mean Cleopatra Member and envelope for the Upper Unit (n=3) of the Deception Rhyolite (rhyodacite).

fractionation. The REE pattern of the Quartz Feldspar Porphyry from the Copper-Chief area along the east scarp of Mingus Mountain resembles that of the Buzzard Rhyolite (Fig. 38). One sample (4bcd28) of dacitic rock from the Dacite of Burnt Canyon was collected near the contact with the overlying Grapevine Gulch Formation. This unit differs from the other felsic rocks by its low total REE contents, small Eu anomaly and high La/Yb ratio (6.7). The HFSE contents are the lowest of the Ash Creek Block felsic rocks (Table 2d, App. B).

As previously discussed, the Deception Rhyolite suite includes an upper unit, the Cleopatra Member and a lower unit (Anderson and Nash, 1972) which are equivalent to the Upper Succession Rhyolite, Cleopatra Crystal Tuff and Upper Deception Rhyolite of Lindberg (1986). The Deception Rhyolite suite reveals decreasing REE contents from the lower unit and Cleopatra member to the upper unit in the local evolution of the volcanic pile (Fig. 39). This feature has implications for magmatic evolution and is addressed in the section on petrogenesis.

Green Gulch dacites (Fig. 40) exhibit differences in total REE concentrations but nearly parallel patterns characterized by strong light REE enrichment (La/Yb = 7.1-9.0) and sloping heavy REE patterns. The negative Eu anomalies vary in magnitude indicating varied degrees of plagioclase fractionation during the magmatic evolution of these rocks. The REE distribution in the Green Gulch dacites is nearly identical to that of the Green Gulch andesites.

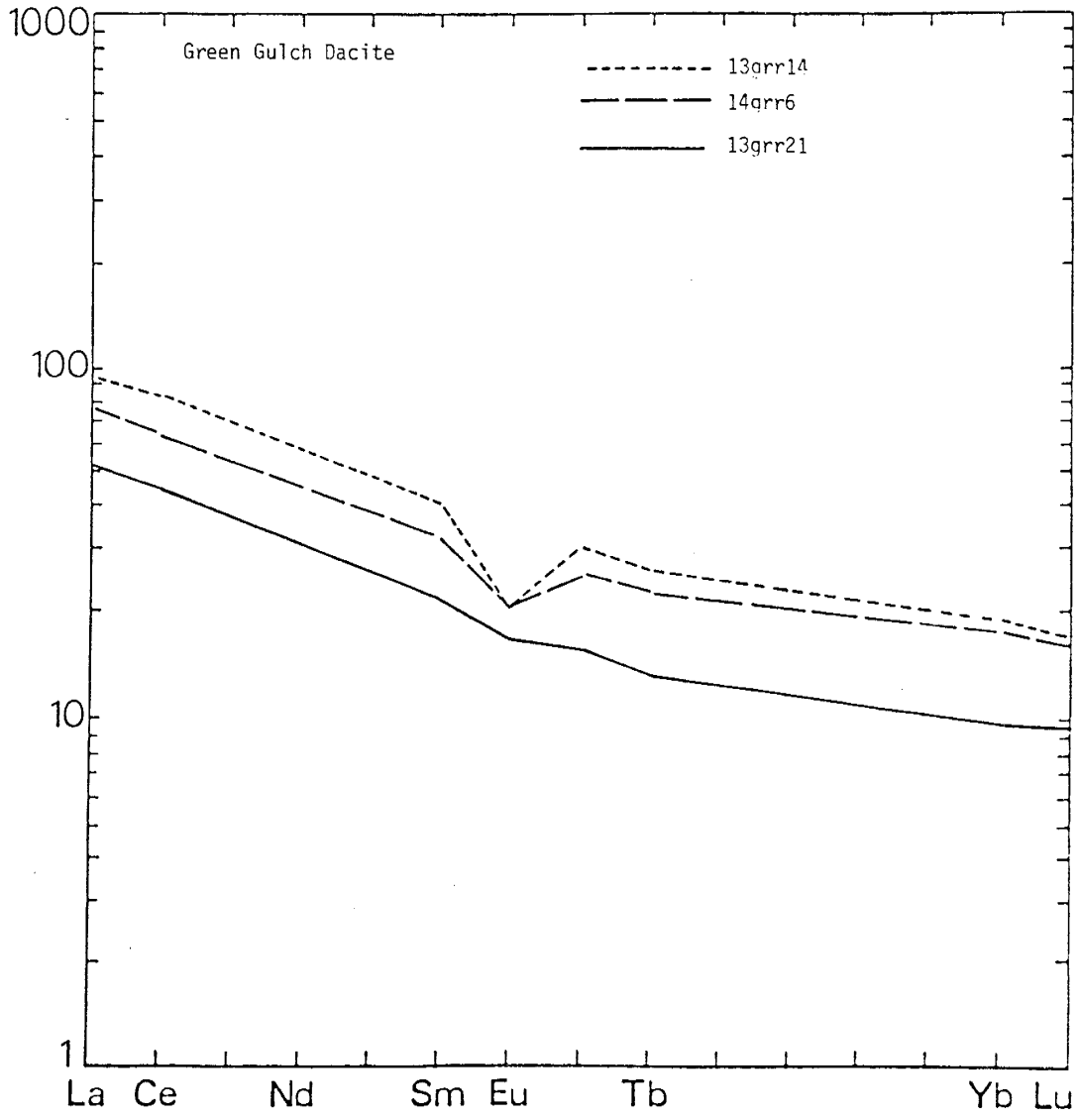

Fig. 40. Chondrite-normalized REE distribution in Green Gulch dacites.

The REE patterns of the Big Bug felsic suite are distinctive for Quartz Porphyries, Spud Mountain rhyolites and Iron King rhyolite (Fig. 41). Both the Quartz Porphyries and rhyolites (smr) are characterized by light REE enriched patterns with nearly flat heavy REE patterns. The rhyolites (smr) exhibit higher concentrations and larger negative Eu anomalies than the Quartz Porphyries. There is little difference in REE concentrations between the rhyodacitic and rhyolitic Quartz Porphyries except for the greater magnitude of the negative Eu anomaly in the rhyolite. The La/Yb ratios (Table 10d, App. B) indicate little difference in the degree of light REE enrichment between the Spud Mountain rhyolite (smr) and Quartz Porphyry (qp). The Iron King rhyolite exhibits an enriched, steep REE pattern with heavy REE concentrations exceeding those of the Quartz Porphyries and light REE concentrations within the smr range. The magnitude of the Iron King negative Eu anomaly is comparable to that of the Quartz Porphyries.

With respect to differences in REE patterns among Blocks, the Green Gulch and Big Bug Block volcanics exhibit greater light REE enrichment than the Ash Creek Block. Heavy REE concentrations are higher in the Ash Creek rhyodacite than the rhyodacites of the Big Bug Block. The Spud Mountain rhyolite (smr) has the highest total REE concentrations of the Yavapai felsic suite followed by the Green Gulch dacites. The Green Gulch dacites have the highest La/Yb ratios.

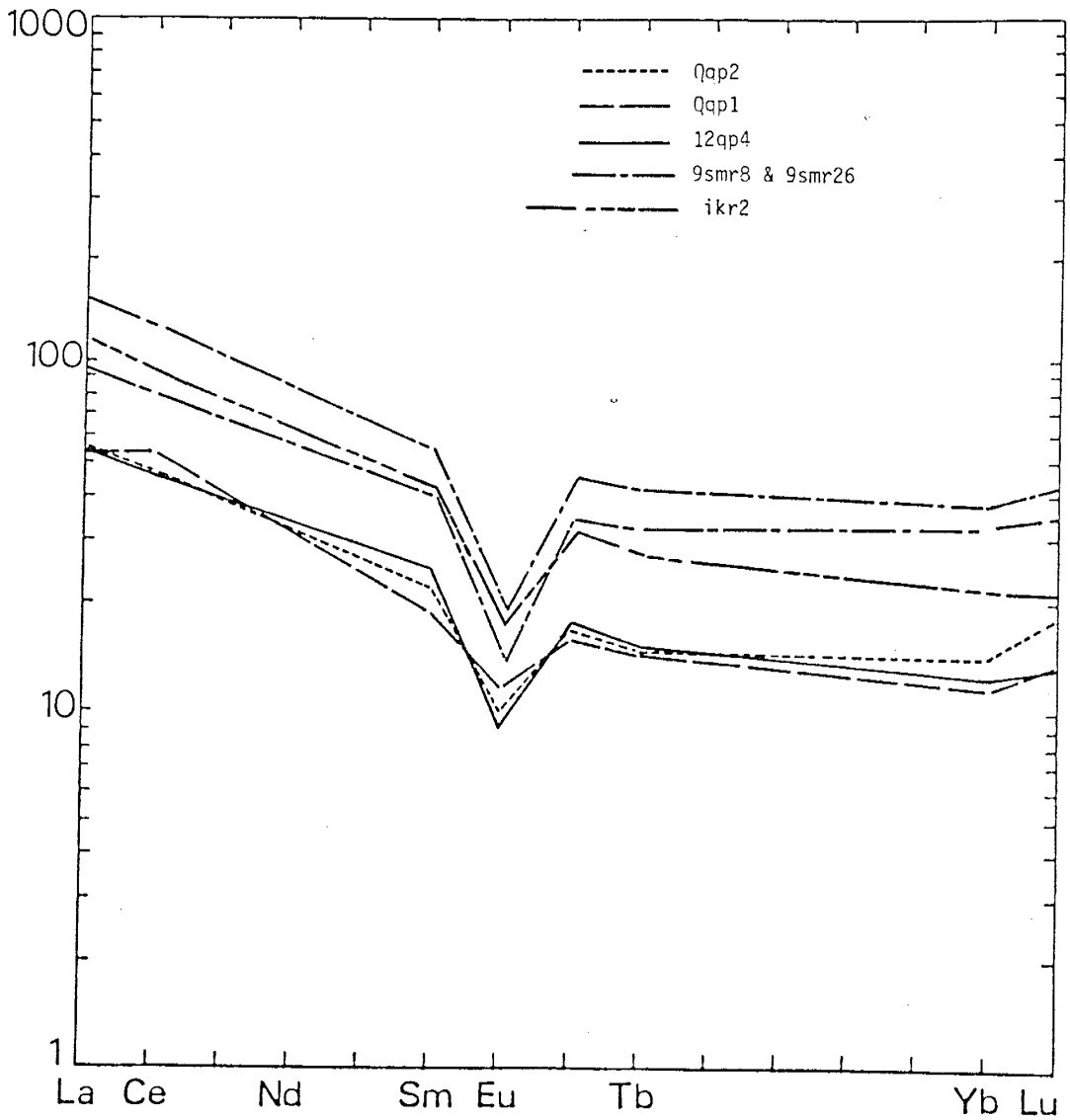

Fig. 41. Chondrite-normalized REE variation for rhyolite and rhyodacite of the Spud Mountain and Iron King Volcanics.

Tectonic Discrimination

Introduction

Discrimination of tectonic setting by trace element ratios or ranges represents one approach to identification of tectonic environments of ancient volcanic successions. To optimize positive identification, the trace element approach must be constrained by additional techniques (Sec. VI). The trace element discrimination techniques are based on statistical evaluation of chemical analysis of young volcanic rocks from known tectonic settings (Pearce and Cann, 1973; Wood, 1980; Pearce, 1982). Ratios of incompatible trace elements are a geochemical signature of source composition because they are unchanged by variations in melting or crystal fractionation as long as liquid fractions exceed 10% (Allegre and Minster, 1978; Gill, 1981). Therefore, the differences in incompatible element ratios for basalts from different tectonic settings indicate a close link between mantle source composition and tectonic setting. Evaluation of Phanerozoic, Proterozoic and Archean successions suggests modern tectonic systems and associated mechanisms of magma generation were operative in the Early Proterozoic (Hoffman, 1980; Condie, 1985; Condie, 1988).

Volcanic Arcs

Basalts erupted in modern volcanic arc systems are typically subdivided into island arc tholeiites, calc-alkaline basalts, and shoshonites characterized by an increase in LILE from tholeiites to shoshonites (Jakes and White, 1972; Peccerillo and Taylor, 1976). Investigations of young volcanic arcs indicate these lava series do not necessarily appear in a systematic progression across arcs or temporally within arcs, emphasizing the individual character of each arc or tectonic segment of the arcs (Arculus and Johnson, 1977;Scott, 1983; Davidson, 1986; Gill, 1987; Hildreth and Moorbath, 1988). With respect to general abundance of magma series, some generalizations are useful. Youthful island arcs are characterized by greater proportions of low-K tholeiitic basalt (LKT) and basaltic andesite (Carmichael et al., 1974; Davidson, 1986; Ewart and Hawkesworth, 1987). Proportions of calc-alkaline basalts (CAB), andesites and felsic rocks increase with crustal thickness and consequently, are generally more abundant in mature island arcs or continental margin arcs (Miyashiro, 1974; Saunders et al., 1980; Takahashi, 1986).

Volcanic arc basalts can usually be distinguished from basalts of other tectonic settings by selective enrichment of the LILE Sr, K, Rb, Ba and Th relative to the HFSE Ta, Nb, Ce, P, Zr, Hf, Sm, Ti, Y and Yb (Gill, 1981; Pearce, 1983). The low abundance of HFSE in LKT of island arcs relative to mid-ocean ridge tholeiites (MORB) also distinguishes between arc and MORB

settings (Pearce, 1982; Ewart and Hawkesworth, 1987). The LILE have low ionic potential and are easily mobilized by aqueous fluids. Consequently, their enrichment in arc basalts is interpreted as a product of devolatization of the subducted slab with consequent LILE enrichment of the arc source region (Saunders and Tarney, 1979; Gill, 1981). This selective enrichment is referred to as the subduction zone component.

Calc-alkaline and shoshonitic basalts are characterized by additional LILE enrichment plus variable enrichment of light REE and P. The other HFSE maintain low abundances (Pearce, 1983). These additional enrichments have been interpreted in terms of mantle source variation, contamination of magmas during ascent through crust and subduction of continent-derived sediments (Gill, 1974; Hickey et al., 1980; Davidson, 1986; Hildreth and Moorbath, 1988).

At comparable stages of magmatic evolution volcanic rocks of continental margin arcs exhibit a greater abundance of K, Rb, Cs, Sr, Ba, Pb, U, Th, light REE and HFSE than island arcs. The thicker crust of continental margin arcs is especially effective at increasing La/Yb ratios of magmas through partial melting and assimilation along the mantle-crust transition. Hildreth and Moorbath (1988) describe this as a melting, assimilation, storage and homogenization (MASH) process. Arc geochemical evolution may begin with an early stage when the trace element characteristics of arc volcanics are produced by a mantle wedge source contribution depleted in LILE, LREE and HFSE and overprinted with

the subduction zone LILE component from the devolatization of the descending slab. The mature arc geochemical signature may be influenced by the MASH process in the pluton-rich base of the thicker arc crust yielding significant contributions of HFSE, Th and LREE to arc magmas (Gill, 1981; Pearce, 1983; Davidson et al., 1987; Hildreth and Moorbath, 1988).

Rifting is recognized in modern island arc systems such as the Mariana, Tonga and South Sandwich Islands (Karig, 1971; Gill, 1976; Saunders and Tarney, 1979) and continental margin arc systems such as the South Shetland Islands, Japanese Islands, New Zealand and the continental margin of South America (Dalzeil et al., 1974; Weaver et al., 1979; Saunders et al., 1982; Ohmoto, 1983; Cathles et al., 1983; Cole, 1984). The process may be aborted resulting in development of grabens within the arc (Ohmoto, 1983), or continued to produce an active arc and inactive remnant arc separated by a youthful ocean basin (Carey and Sigurdsson, 1984). Arcs subjected to back-arc extension erupt basalts with both MORB and arc geochemical signatures and complicate the expected progression to greater proportions of calc-alkaline basalts with increasing arc maturity. Rifted arcs may erupt MORB, LKT basalts, CAB, alkali olivine basalts and transitional varieties within a very limited time interval (Pearce, 1982; Kokelear et al., 1984; Saunders and Tarney, 1984; Gill, 1984; Gill, 1987). Consequently, back-arc extension may produce conflicting geochemical signatures within an arc succession and lead to misidentification with a limited sample

base, or if unconstrained by additional criteria such as lithologic associations.

Divergent and WPB Settings

Basalts which originate at divergent and within plate settings (WPB) display higher HFSE contents relative to arc basalts, providing a basis for geochemical discrimination. Some of the WPB trace element enrichment is attributed to an enriched mantle source (Wood, 1979; Stern et al., 1986). The trace element enrichment depends on the incompatibility of the element relative to garnet lherzolite (Wood et al., 1979; Pearce, 1983). Consequently, Th, Ba, Ta and Nb are enriched relative to elements such as P, Zr, Hf and Sm (Pearce, 1982; 1983). WPB erupted through continental crust may be subject to contamination by assimilation of crustal rocks (Thirlwall and Jones, 1983; Thompson et al., 1983; Alibert et al., 1986). This results in addition of a LILE, light REE and HFSE crustal component to the WPB (Wood, 1979; Cox, 1983). The net result may be WPB with geochemical signatures similar to arc volcanics. Basalts with subduction zone components have been recognized within the Karoo, Columbia River and Deccan continental flood basalt sequences and emphasize the need for additional constraints for interpretation of tectonic setting (Thompson, 1983; Marsh, 1987; Duncan, 1987). Continental rifts, like back-arc rifts, display compositional diversity. Basalts include both alkali basalt with chemical compositions much

like oceanic alkali basalts, and olivine tholeiites which are compositionally distinct from their MORB counterparts (Depaolo and Wasserburg, 1976; Perry et al., 1987).

Basalts and Basaltic Andesite

The lower abundance of HFSE in arc lavas relative to MORB or WPB settings provides the basis for many discrimination diagrams (Pearce and Cann, 1973; Pearce and Norry, 1979; Wood, 1979). The Ti-Zr plot discriminates between arc and within-plate lavas because the early crystallization of magnetite typical of arc volcanism, prevents lavas from achieving the high Ti contents characteristic of within plate settings. The Zr contents provide a differentiation index. Volcanic rocks of the Yavapai Supergroup are presented with regard to lithotype and tectonic block (Figs. 42 & 43) with fields after Pearce et al. (1981) and a mafic-evolved fractionation boundary after Pharoah and Pearce (1984). The fractionation boundary identifies rocks subjected to magnetite-ilmenite fractionation. Fields are based on fractionation trends of arc and within-plate volcanics.

Most Green Gulch and Ash Creek volcanics plot within the arc field (Fig. 42). However, a large group of mafic rocks also plot within the MORB-Arc overlap zone and require further discrimination to define their tectonic setting. One suite of Ash Creek rocks plots in the within-plate field. These are the Shea basaltic andesite and correlative CM-9 core sample. A few Green

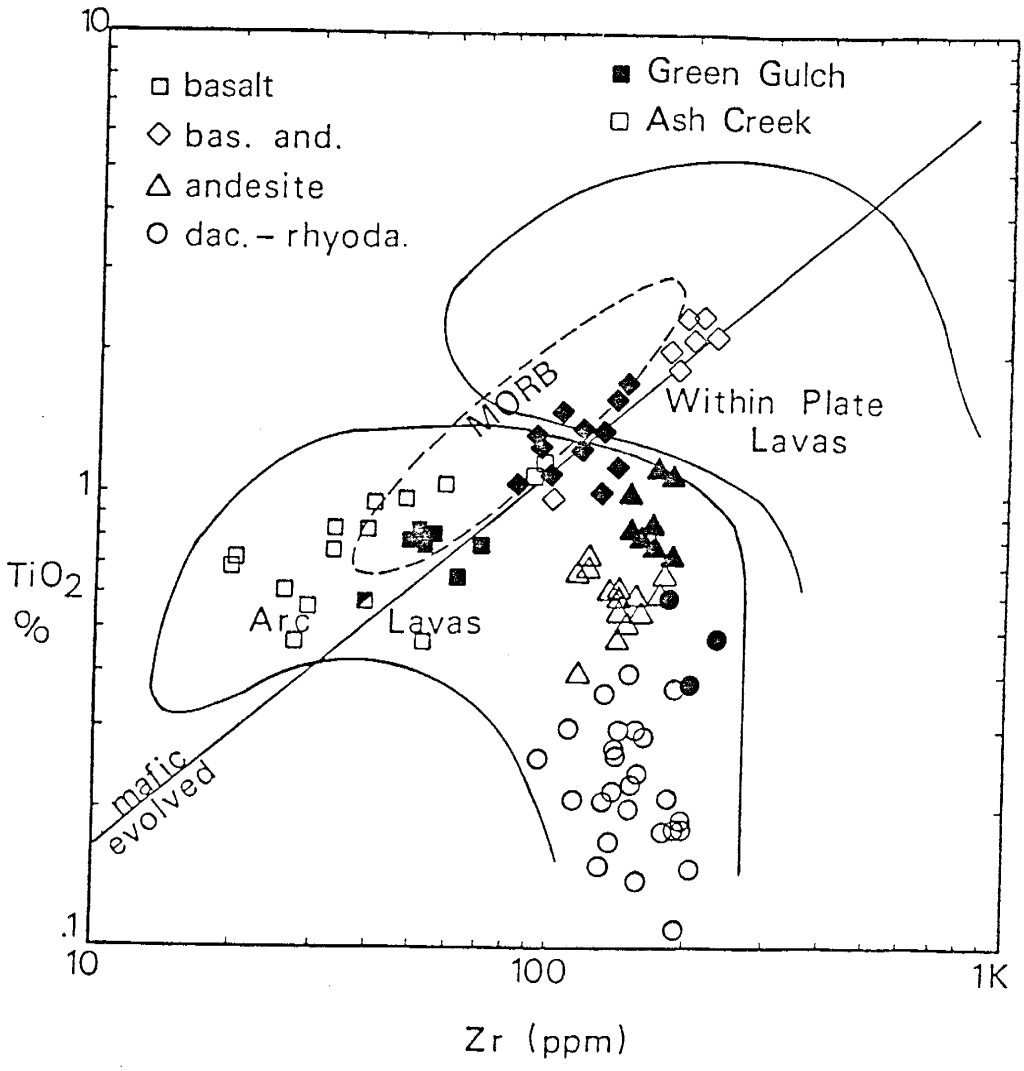

Fig. 42. TiO_2-Zr discriminant for volcanics of the Green Gulch and Ash Creek blocks (fields after Pearce et al., 1981 and Pharoah and Pearce, 1984).

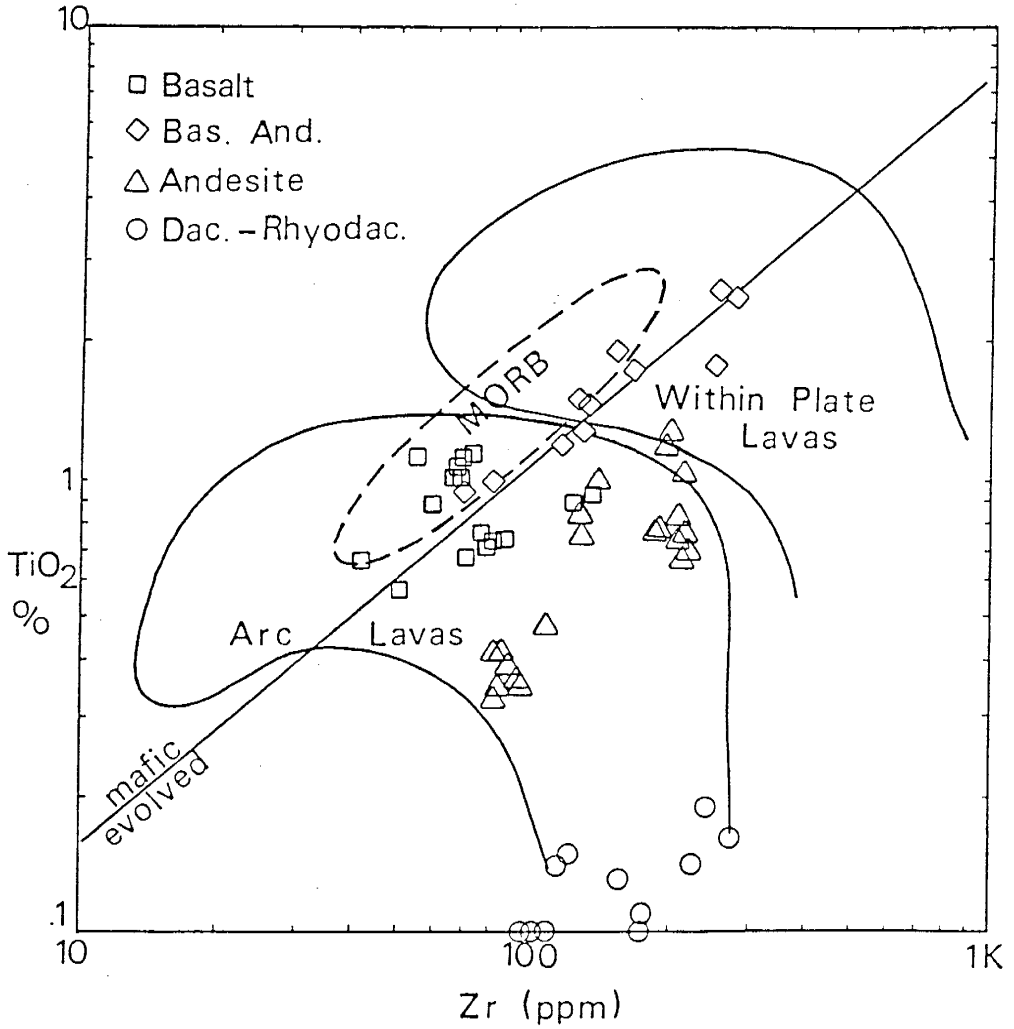

Fig. 43. TiO_2-Zr discriminant for volcanics of the Big Bug block (fields after Pearce et al., 1981 and Pharoah and Pearce, 1984).

Gulch samples plot in the within-plate field but do not attain the HFSE levels of the Shea Basalt. The combined Ash Creek and Green Gulch Volcanics define a compositional continuum from basalt to rhyodacite. Viewing the volcanics independently, the Green Gulch volcanics exhibit a continuous compositional range from basalt to rhyodacite and elevated Ti-Zr contents relative to most of the Ash Creek Volcanics. The Ash Creek volcanics exhibit a small compositional gap in the arc field as there is a single sample of basaltic andesite from the Brindle Pup Andesite. The within-plate Shea basaltic andesite does not appear to be part of the main Ash Creek or Green Gulch fractionation trends as this would require a decrease in Zr from basaltic andesite to rhyodacite, a trend atypical of arc fractionation (Pearce, 1982). However, the high-Ti Green Gulch basaltic andesite cannot be eliminated from the observed Green Gulch trend.

The Big Bug Block (Fig. 43) is dominated by basaltic andesite and andesite. The obvious dacite gap may be due in part to a limited felsic sample base. Basalts are evolved and most plot within or near the MORB-Arc overlap zone and require additional discriminants. The within-plate sample suite includes the high-Ti, HFSE enriched basaltic andesite lavas and dikes from the Iron King and Spud Mountain Volcanics. Any attempt to relate these HFSE enriched basaltic andesites to other Big Bug volcanics presents the same problems described for the Shea basaltic andesite of the Ash Creek Block. The other within-plate rocks cannot be eliminated in such a manner. The two unusual Iron King

'andesites' are indicated by half-shaded andesite symbols and have distinctive Ti-Zr concentrations for rocks which are of basaltic composition, according to Mg number and transition metal contents. The calc-alkaline andesite tuffs (smct) of the Spud Mountain Volcanics are distinctive with the lowest Ti and Zr contents of any Yavapai andesite. The number of basalts below the mafic-evolved fractionation boundary indicates early magnetite crystallization characteristic of calc-alkaline trends, in contrast to the tholeiitic pattern of the Ash Creek and Green Gulch basalts.

The Ti-V diagram of Shervais (1982) discriminates among arc basalts, MORB and alkalic WPB (Fig. 44). The crystal/melt partitioning of polyvalent V depends on oxygen fugacity, with higher oxygen fugacity promoting incompatible behavior at higher valence states and allowing compatible behavior at lower valence states promoted by lower oxygen fugacity (Lindstrom, 1976). Consequently, the low oxygen fugacity conditions which characterize the source regions for generation of MORB and alkali basalts result in low V and high Ti values in derivative basalts. The Ti crystal/melt partition coefficients are less affected by oxygen fugacity in the source and remain < 1. Fractionation of hornblende and magnetite lowers concentrations of both V and Ti with the potential for shifts across the Arc-MORB field boundary (Fig. 44) in andesites. Restriction of these plots to basalt and basaltic andesite compositions avoids this problem. Shervais (1982) emphasizes the trend defined by suites of related samples

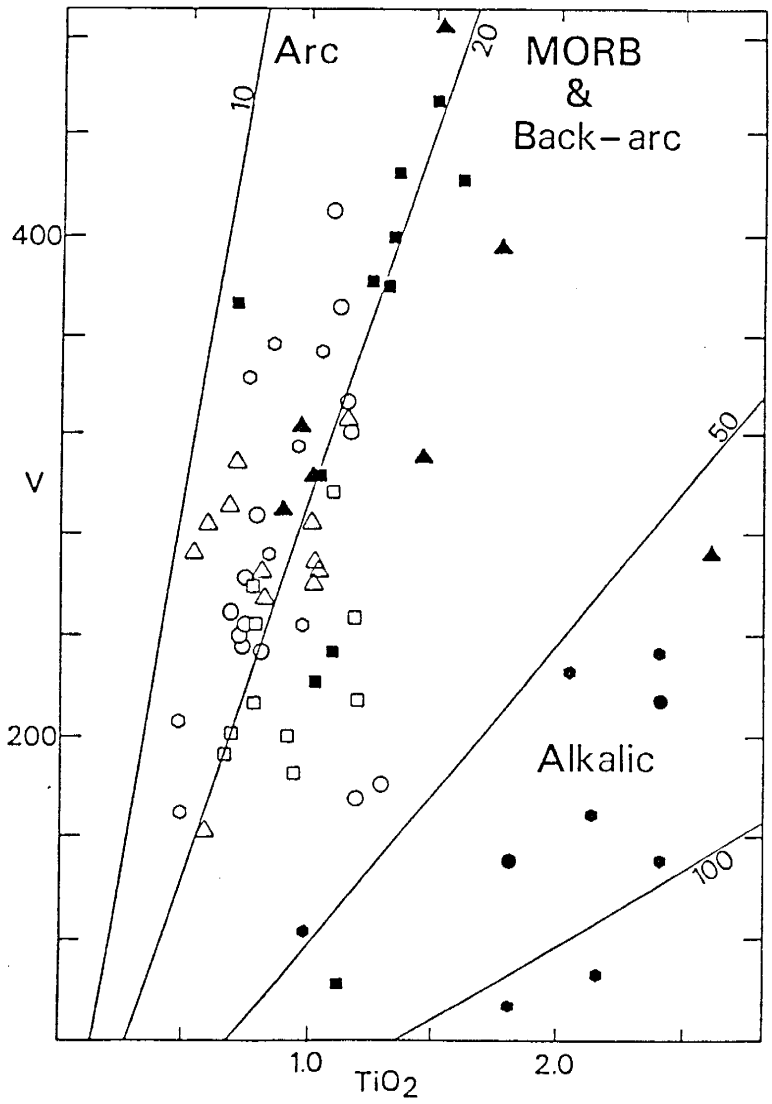

Fig. 44. Ti-V discriminant for the Yavapai volcanics (after Shervais, 1982). Diagonal lines indicate Ti/V ratios. (Open symbols = basalt, solid symbols = basaltic andesite, hexagons = Ash Creek block, squares = Green Gulch block, triangles and circles = Spud Mountain and Iron King Volcanics of the Big Bug block.)

rather than individual plots for interpretation of tectonic setting. This approach minimizes the potential for misinterpretation caused by overlap of arc, MORB and WPB sample distribution and potential V mobilization.

Basalts and basaltic andesites of the Yavapai Supergroup are presented in Figure 44. The Ash Creek basalts have the lowest Ti/V ratios and plot within the arc field. Both the Green Gulch and Big Bug suites exhibit Ti/V ratios near 20. Most Green Gulch basalts plot in the MORB and Back-arc field, but cross into the Arc field at basaltic andesite compositions. The distribution of the Big Bug and Green Gulch samples is similar to that of basaltic rocks from the South Sandwich and Marianas tholeiitic suite (Shervais, 1982). The high-Ti, HFSE enriched suite, including the Shea Basalt and samples from the Iron King and Spud Mountain volcanics, plot within or near the Alkalic field. This field includes within-plate tholeiitic and alkali basalts and alkali variants of MORB. The Ash Creek and Green Gulch basaltic andesites, which lie astride the Ti/V = 50 line at 1% TiO_2, do not exhibit the extreme HFSE enrichment that characterizes the other samples in the Alkalic field. These are probably products of magnetite and/or amphibole fractionation. The distribution of most of the Yavapai suite is more typical of arc tholeiite suites. The sharp contrast with the Ti/V ratios of the subordinate group of HFSE enriched samples suggests a distinctive source for the high-Ti suite.

The Yb-normalized covariation of Th and Ta (Fig. 45) discriminates between island arcs and continental margin arcs and between arc and MORB settings (Pearce, 1982; 1983). The potential effects of subduction (s), crustal contamination (c), within-plate enrichment (w) and fractional crystallization (f) are indicated by vectors. Most Yavapai basalts and basaltic andesites lie within the CAB arc field. The Ash Creek mafic rocks exhibit the lowest Ta/Yb ratios and straddle the LKT/CAB border. The Ta/Yb ratios of most Green Gulch and Iron King basalts and basaltic andesites are indicative of either continental margin arcs or island arcs such as Grenada and parts of the Aleutians where basalts appear to have trace element enriched source regions similar to those of alkalic MORB (Shimizu and Arculus, 1975; Pearce, 1982; 1983). The Bluebell basalts of the Iron King volcanics plot within the field of MORB and WPB with Th/Yb and Ta/Yb ratios approaching those of primordial mantle. Three of the HFSE enriched Iron King rocks also plot in or near the nonsubduction field. However, the HFSE-enriched Shea basaltic andesite plots within the CAB field.

The Th-Ta-Hf discriminant of Wood (1979) also records source heterogeneities as extremely high or low degrees of fractional crystallization or partial melting, respectively are required to change ratios of these incompatible elements. Consequently, this plot may be applied to the full compositional spectrum of volcanic rocks for discrimination between arc and MORB-WPB settings (Figs. 46 & 47). Most of the Yavapai volcanics plot within the calc-alkaline end of the arc field. The Bluebell basalts and

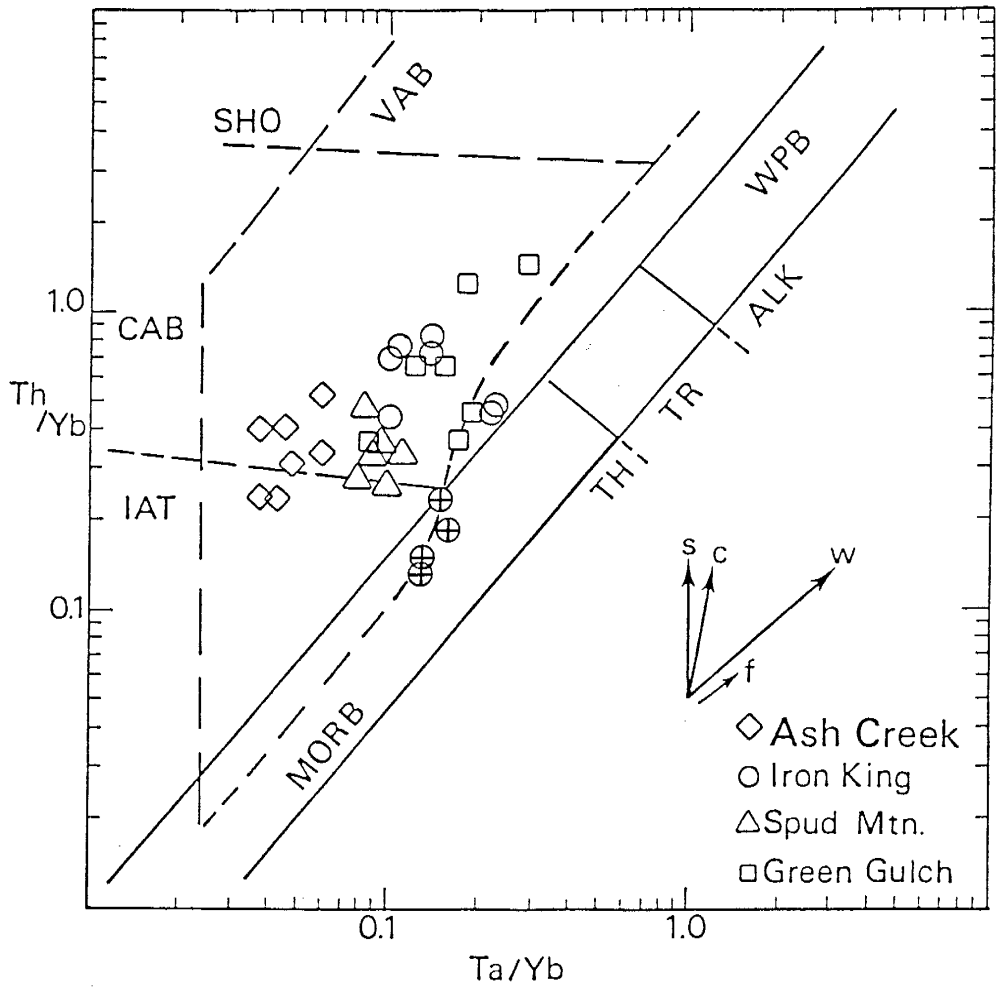

Fig. 45. Yb-normalized Th-Ta covariation plot (Pearce, 1982) for Yavapai basalts. Volcanic arc basalt field (VAB) is subdivided into island arc tholeiites (IAT), calc-alkaline basalt (CAB) and shoshonite (SHO). MORB and within plate basalt field (WPB) is subdivided into tholeiitic (TH), transitional (TR) and alkalic (ALK). Vectors indicate the effects of the subduction component (s), crustal contamination (c), within plate enrichment (w) and fractional crystallization on a MORB-type source. Bluebell basalts = circles with crosses.

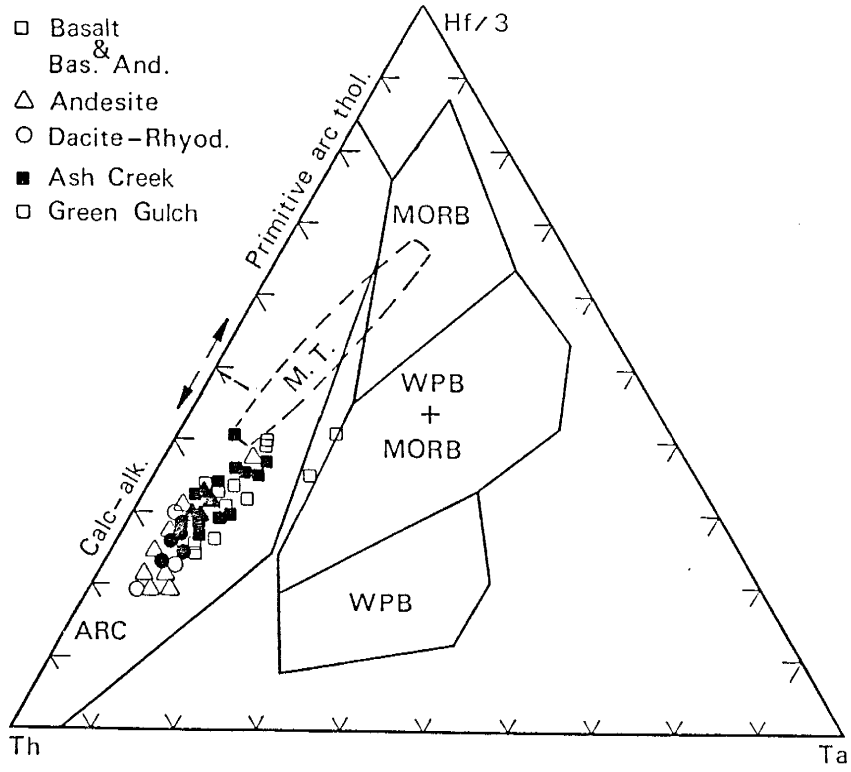

Fig. 46. Th-Ta-Hf discriminant for volcanics from the Ash Creek (solid symbols) and Green Gulch blocks (open symbols) after Wood (1979).

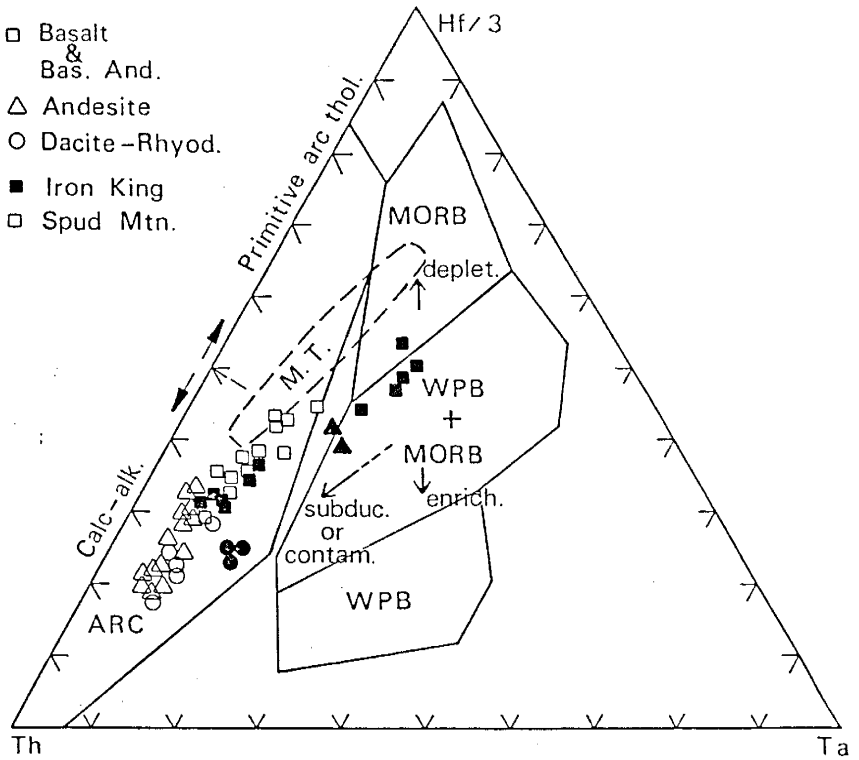

Fig. 47. Th-Ta-Hf discriminant for the Iron King (solid symbols) and Spud Mountain (open symbols) Volcanics in the Big Bug block (after Wood, 1979). Vectors indicate the effect of the subduction component or crustal contamination, within plate enrichment, and within plate depletion on a MORB source (Pearce, 1983).

HFSE-enriched basaltic andesites and 'andesite' of the Iron King Volcanics plot within or near the MORB-WPB field. The other Iron King basalts plot in the arc field with the Spud Mountain basalts. Two of the Green Gulch Block basalts also plot near the MORB-WPB field. The M.T. field is defined by mafic rocks from the Mariana Trough back-arc basin. The trend of this field across ARC-MORB boundaries indicates conflicting or transitional geochemical signatures may arise from lavas erupted in arcs subjected to back-arc extension.

The distribution of the Yavapai volcanics suggests a mature arc system for all volcanics, but slightly thinner crust for the Ash Creek Block as indicated by Th contents. The Iron King sample distribution could result from within-plate enrichment, crustal contamination, addition of the subduction component to a MORB-type source or a combination of these processes. Within-plate enrichment should affect Ta and Th equally but crustal contamination or the addition of the subduction component will affect Th more than Ta (Pearce, 1983). The compositional vectors and the sample distribution of other Yavapai volcanics suggests both within plate enrichment and the subduction component as important controls on HFSE distribution.

Andesites

Ratios of relatively immobile incompatible elements are also useful for examining source variations of andesites. Figures

48 & 49 also provide an indication of the original K_2O contents of Yavapai andesites by comparison with the K_2O contents and trace element ratios of modern andesites (Gill, 1981). Since K_2O is extremely mobile the La/Th and La/Nb ratios may provide a better approximation of K_2O contents in these ancient rocks. The original K_2O content is significant with respect to the crustal thickness of the arc (Hildreth and Moorbath, 1988). Low-K andesites are typical of primitive island arcs whereas medium and high-K andesites are more abundant in mature island arcs or continental margin arcs (Miyashiro, 1974; Bailey, 1981; Ewart, 1982). The La vs Th plot (Fig. 48) for Yavapai andesites and basaltic andesites suggests affinities to modern medium and high-K andesites. The La/Yb vs Sc/Ni and Th plots (Fig. 49) indicate a composition transitional between medium and low-K types (Bailey, 1981).

Most andesites and basaltic andesites have La/Th ratios near 7 plotting near the E MORB-Orogenic andesite boundary (Fig. 48). The sample distribution for the Big Bug Block illustrates significant differences between Spud Mountain andesitic flows (sma) and tuffs (smct). The possibility of some La loss from the submarine tuffs (smct) cannot be excluded. The scatter observed in the distribution of Ash Creek and Green Gulch andesites suggests slight source variation and/or Th additions.

Application of the incompatible element ratio classification screens of Condie (1988) suggests a mature island arc or continental margin setting for andesites of the Green Gulch block.

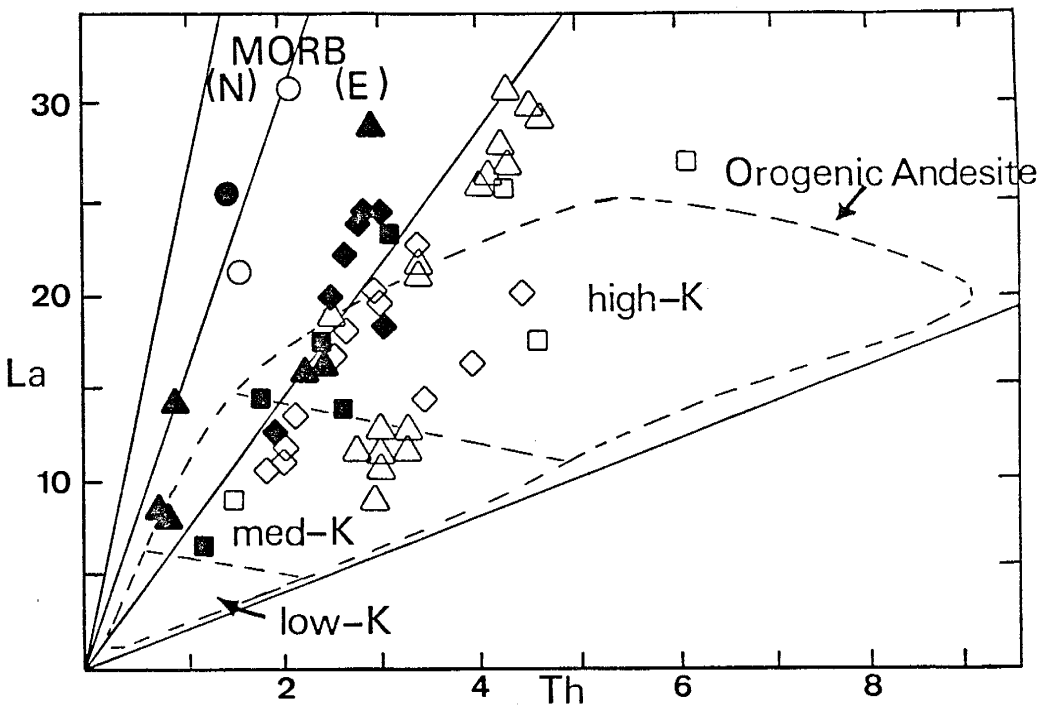

Fig. 48. La-Th plot (Gill, 1981) for andesite (open symbols) and basaltic andesite (solid symbols) of the Yavapai Supergroup. N and E represent fields of normal and enriched MORB. Diamonds = Ash Creek Group, circles = Iron King Volcanics, triangles = Spud Mountain Volcanics and squares = Green Gulch Volcanics.

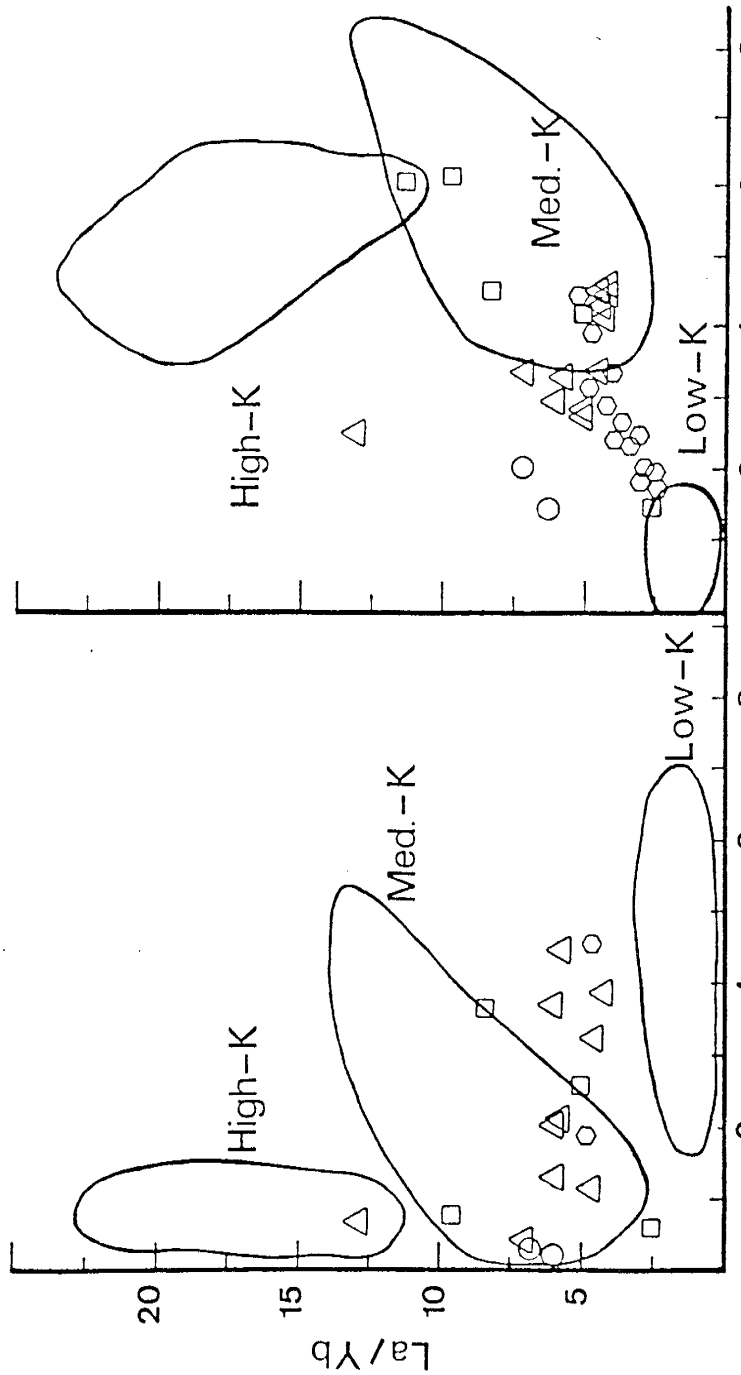

Fig. 49. La/Yb vs. Sc/Ni and Th plots (Bailey, 1981) for andesite of the Yavapai Supergroup. Fields represent ranges for modern arc andesites of low, medium and high-K character. Open symbols = basalt, solid symbols = basaltic andesite, hexagons = Ash Creek block, squares = Green Gulch block, triangles and circles = Spud Mountain and Iron King Volcanics of the Big Bug block.

Classification of andesites from the Ash Creek block vary with unit from island arc to island arc-continental margin to continental margin for the andesites of the Gaddes Basalt, Brindle Pup Andesite and Dacite of Burnt Canyon, respectively. The classification screens for andesite from the Big Bug block indicate an island-arc and Andean arc for the Spud Mountain tuffs (smct) and lavas (sma), respectively.

Spidergrams - Implications for tectonic setting and genesis

The MORB-normalized plot (Fig. 50) or 'spidergram' provides a means of illustrating LILE and HFSE distribution on a single graph. The low ionic potential LILE, on the left side of the graph, are mobile in aqueous phases. The HFSE, on the right side of the graph, are relatively immobile. Both LILE and HFSE are ordered according to their degree of incompatibility relative to garnet lherzolite, with increasing incompatibility from the outside toward the center of the pattern (Pearce, 1983). Because these elements are incompatible, the shape of the spidergram is dictated by source region composition, modifications from enrichment processes affecting the source region, and/or contamination of the magma during ascent. Partial melting and closed system fractional crystallization will change only the level of the pattern as long as the liquid fraction exceeds 10% (Gill, 1981; Pearce, 1982). However compatible behavior with regard to specific phases may alter the shape of the pattern. For

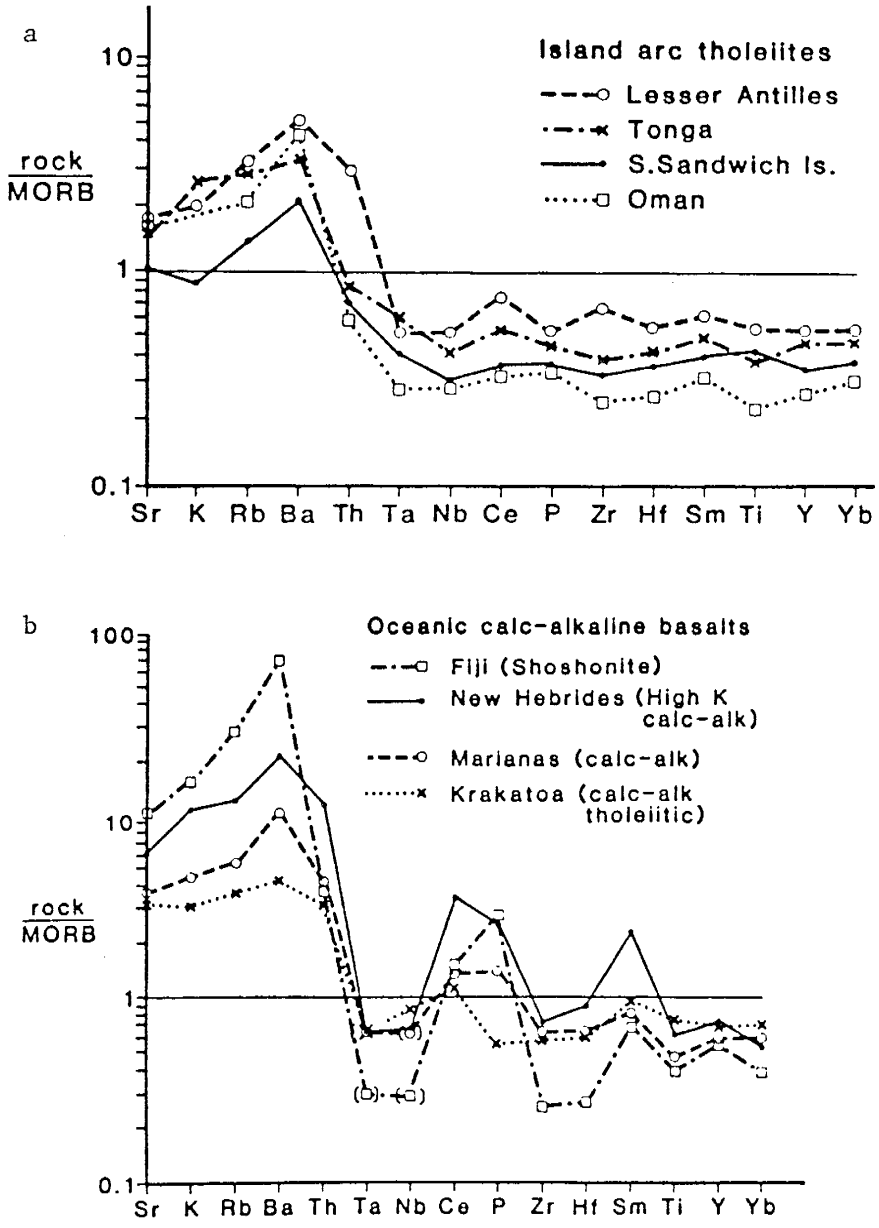

Fig 50. MORB-normalized 'spidergrams' for: (a) island arc tholeiitic basalts, (b) island arc calc-alkaline and shoshonitic basalts (from Pearce, 1983).

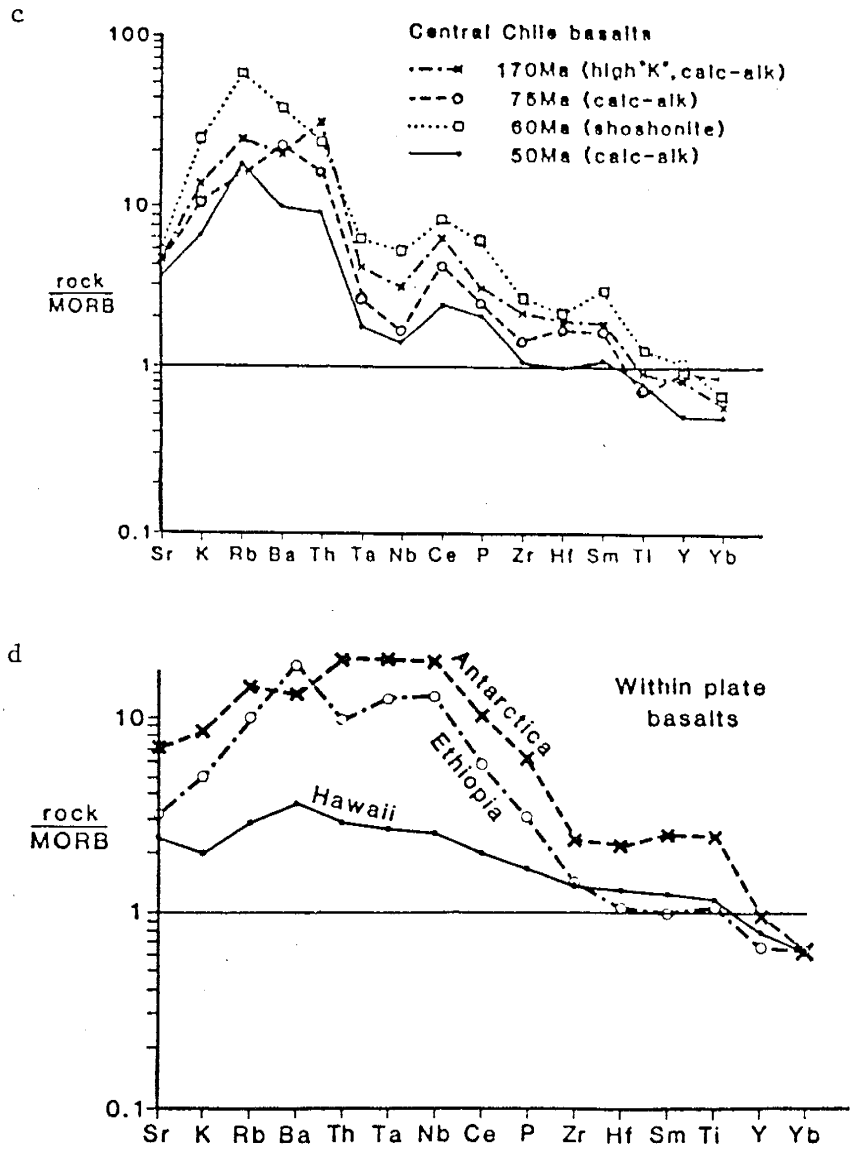

Fig. 50. MORB-normalized 'spidergrams' for: (c) continental margin calc-alkaline and shoshonitic arc basalts, (d) continental and oceanic within plate basalts (from Pearce, 1983).

example, the crystallization of plagioclase, apatite, magnetite-ilmenite and garnet will affect Sr, P, Ti, Y and Yb, respectively.

Geochemical investigations of LILE and HFSE in lavas from varied tectonic settings indicate Ta, Nb, Hf, Zr, Ti, Y and Yb are mantle derived. The LILE and to a lesser extent Ce, P and Sm are in part derived from the subduction zone (Saunders and Tarney, 1979; Pearce, 1982). Enriched source regions such as those producing WPB, yield a greater incompatible element contribution to the spidergram. Crustal contamination during ascent of magma contributes to both LILE and HFSE (Pearce, 1983; Hildreth and Moorbath, 1988). Consequently, the spidergram provides information on source region, subsequent modifications and tectonic setting. Spidergrams of typical island arc LKT, island arc CAB, continental CAB and WPB volcanics (Figs. 50a-d) provide a reference for comparison.

The tuffs (ggt), gabbro and lavas (YMsma) of the Ash Creek block exhibit nearly identical MORB-normalized patterns (Fig. 51). The low LILE contents of the Grapevine Gulch rocks (ggt) probably result from LILE leaching enhanced by the original pyroclastic nature of the rock. The patterns differ slightly with respect to concentration suggesting small variations in source partial melting or fractionation of a common parental magma for these basalts. Comparison with modern basalts (Fig. 50) reveals a strong resemblance to island arc CAB and high-K suites characterized by prominent negative Ta-Nb and positive Ce-P anomalies.

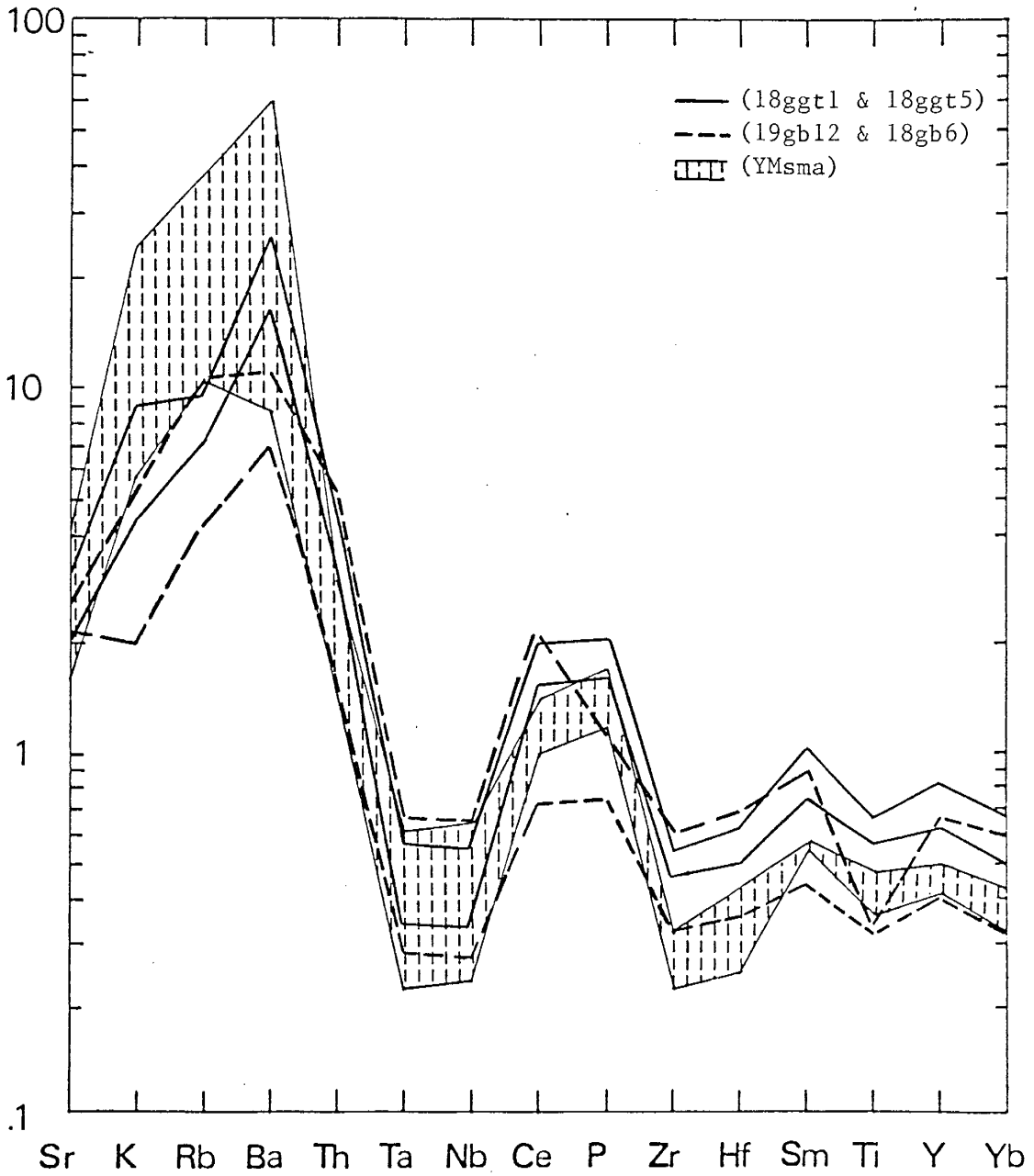

Fig. 51. MORB-normalized Grapevine Gulch basaltic tuff (ggt) and gabbro (gb) and envelope of variation for Yarber Wash basalts (YMsma, n=3).

The spidergrams (Fig. 52) of the primitive and evolved Green Gulch basalts exhibit slight differences in levels of HFSE, but nearly identical patterns. The small negative Ta-Nb and Zr-Hf anomalies and higher total HFSE levels differ markedly from the pronounced anomalies and low concentrations of the Ash Creek basalts. The Green Gulch pattern is observed in modern CAB of continental margins (Fig. 50c) and some southwest Pacific island arcs (Fig. 53). The Th contents are more typical of continental margin arcs; however, similar patterns occur in island arc basalts where major faults intersect the subduction zone or back-arc extension is present (Pearce, 1982). Such transitional patterns reflect source enrichment superimposed on the subduction component (Weaver et al., 1979; Pearce, 1982).

The Big Bug block exhibits greater diversity in basalt spidergrams. The Iron King basalts (Fig. 54) have patterns similar to those of the evolved Green Gulch basalts. Compared to Spud Mountain basalts (Fig. 55), the Iron King basalts exhibit lower P, Y and Ti relative to adjacent HFSE suggesting a greater degree of apatite and magnetite-ilmenite fractionation. The broad LILE envelope of the Iron King basalt is probably a result of alteration during diagenesis, metamorphism or subaerial weathering. The Spud Mountain basalts (sma-smb) have greater LILE/HFSE ratios and a pattern intermediate between island arc LKT and CAB (Figs. 50a & b). The Bluebell basalts (ika-ikab) have a distinctive pattern (Fig. 56) which is nearly flat from P to Yb, has a very slight positive LILE anomaly and higher Ta, Nb and Ce

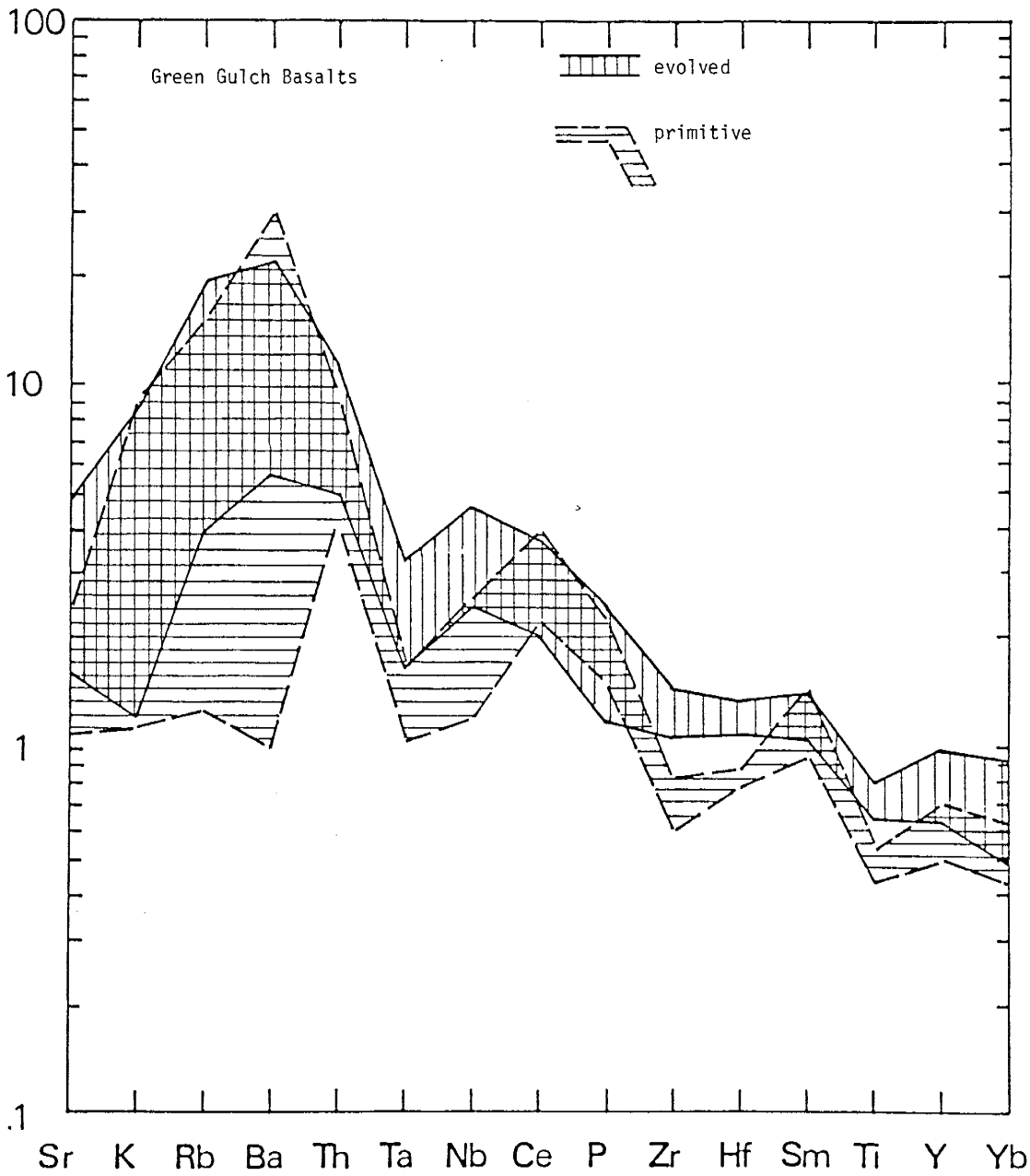

Fig. 52. MORB-normalized envelopes of variation for evolved (n=5) and primitive (n=3) Green Gulch basalts.

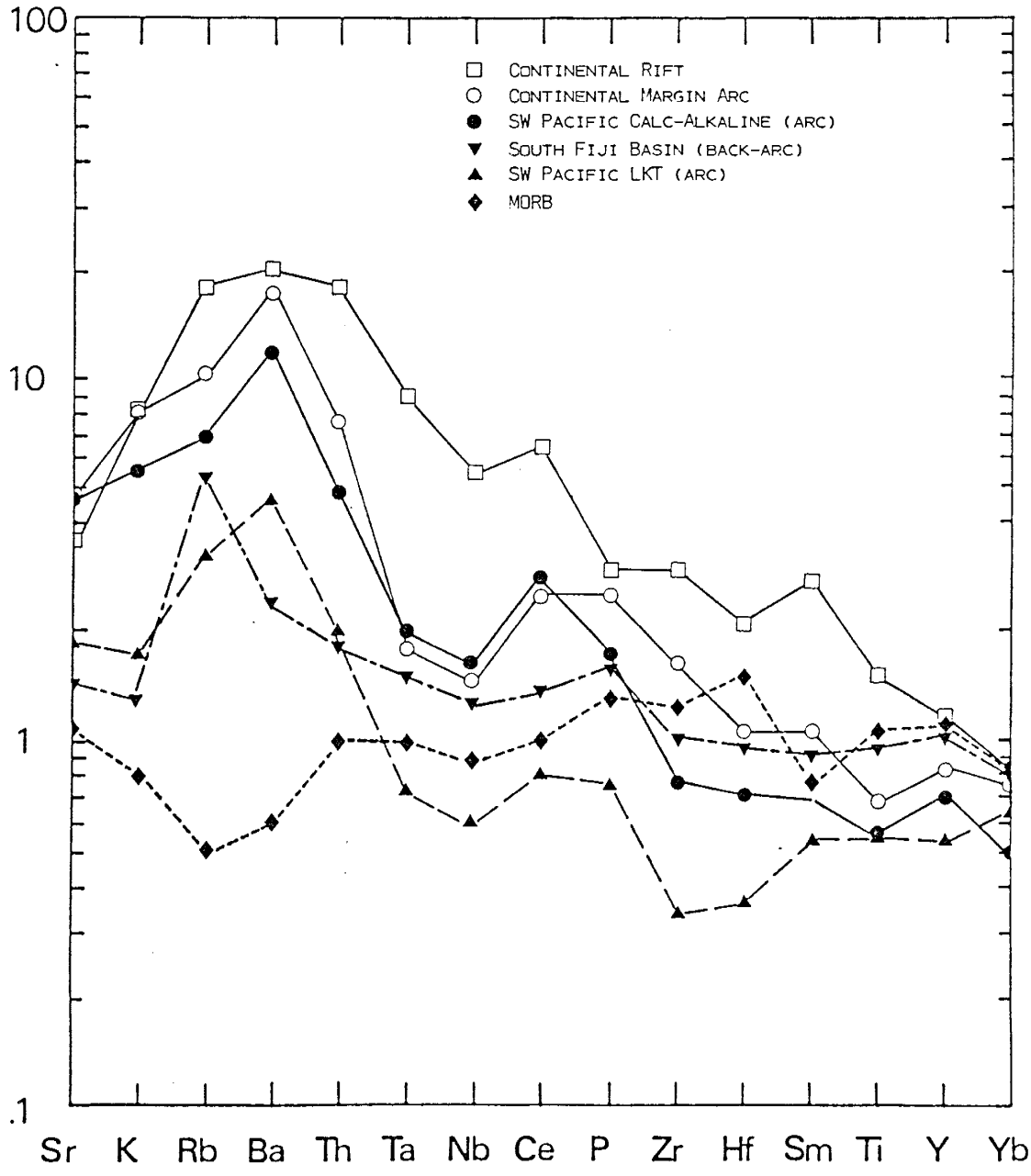

Fig. 53. MORB-normalized basalt (mean compositions, n=10-30 for each setting). Data sources: NMIMT Precambrian Research Group Geochemical Data Base; Ewart, 1982; Gill, 1987.

Fig. 54. Envelope of variation (n=4) for MORB-normalized Iron King basalts (ika).

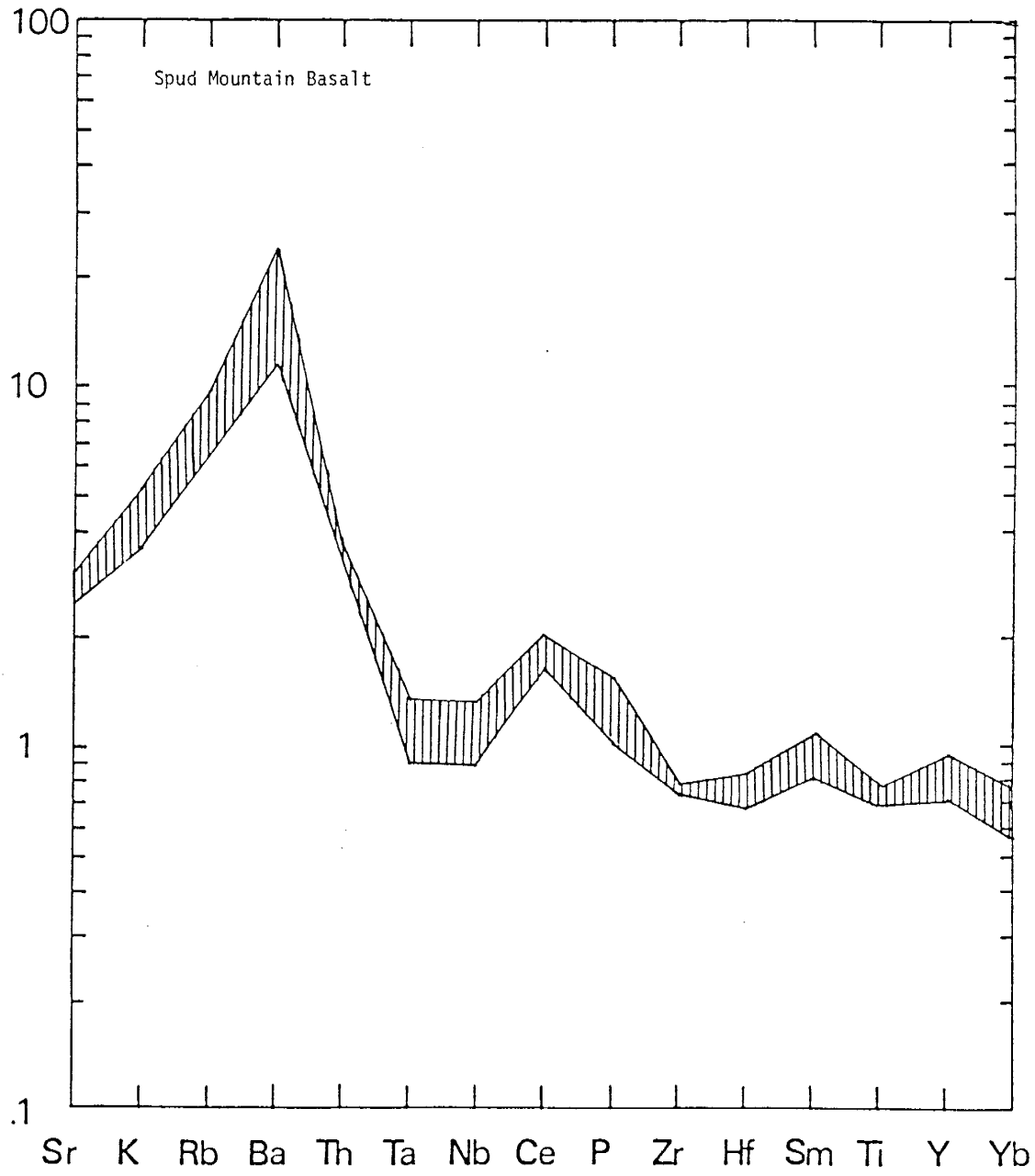

Fig. 55. MORB-normalized envelope of variation for Spud Mountain basalts (sma=smb, n=4).

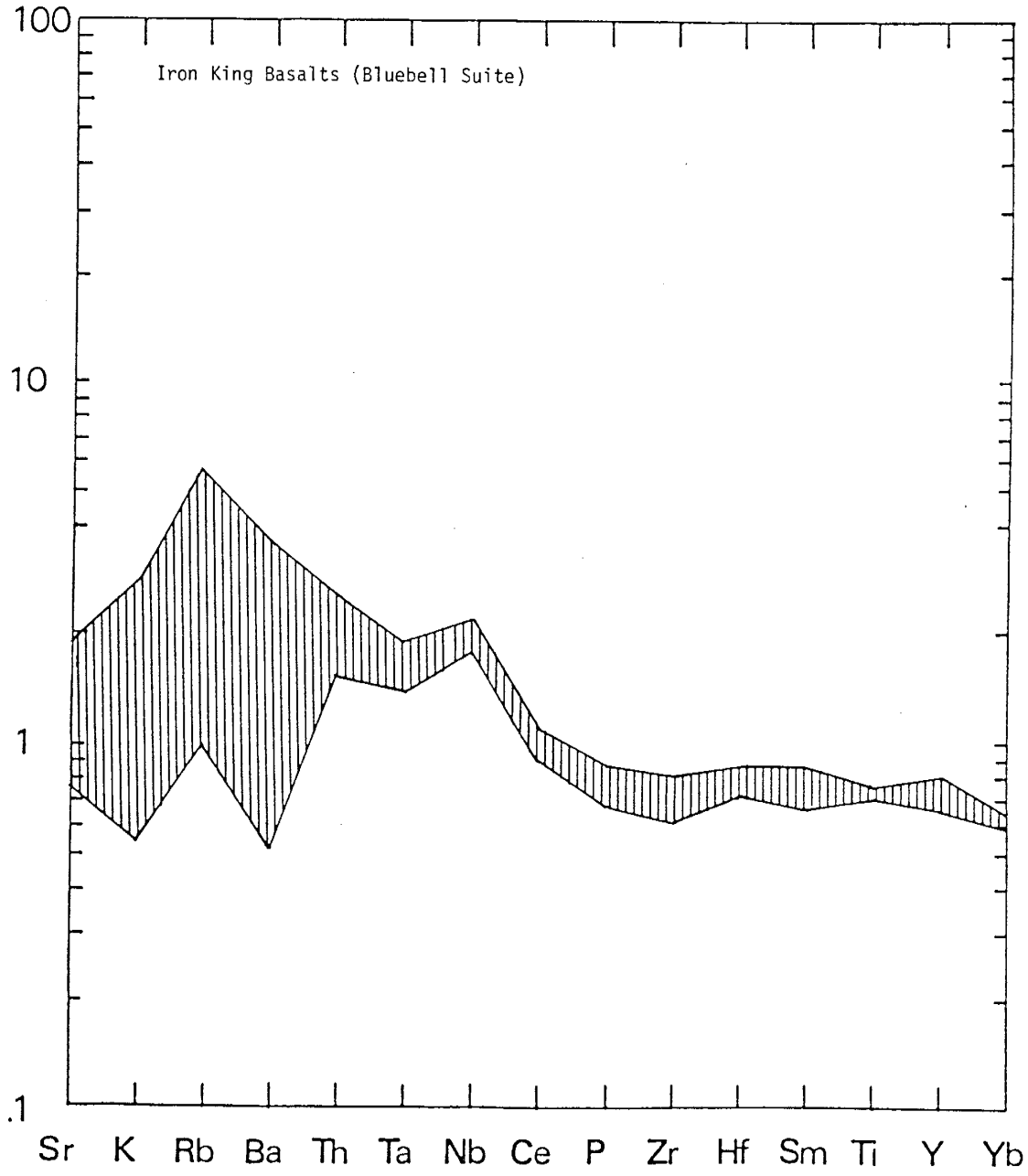

Fig. 56. Envelope of variation for MORB-normalized Iron King basalts (Bluebell suite, ika and ikab, n=4).

relative to other HFSE. The spidergram suggests a MORB or arc LKT pattern with a superimposed within plate enrichment (Pearce, 1983). The levels of P through Yb are similar to arc LKT, but the pattern form resembles MORB and WPB. The low Th and Ba contents preclude a major contribution from crustal contamination.

Basaltic andesites of the Ash Creek Block are dominated by the Shea Basalt (Fig. 57). The pattern of the single Brindle Pup sample differs, with more prominent negative Ta-Nb and Zr-Hf anomalies and lower total concentration. The minor pattern differences and major concentration differences at similar Mg numbers indicate different parental magmas for the Shea and Brindle Pup basaltic andesites. The Brindle Pup pattern appears somewhat intermediate between calc-alkaline volcanic patterns of continental margins and island arcs (Fig. 58).

The HFSE enriched basaltic andesite and 'andesite' of the Iron King volcanics (Fig. 59) have spidergrams similar to those of the Shea basaltic andesite. These patterns are characterized by lack of a prominent subduction component as expressed by magnitude of the LILE/HFSE ratios and positive Ce, P or Sm anomalies. This pattern could be produced by superimposing the subduction component on a within plate enrichment signature. The Shea pattern resembles continental margin calc-alkaline patterns such as those from the Aleutians and Cascades, however, the higher concentrations of Zr-Yb are closer to those of the Bransfield Strait back-arc or anorogenic suites such as those from Queensland (Fig. 58). The depleted LILE contents of these basaltic andesites

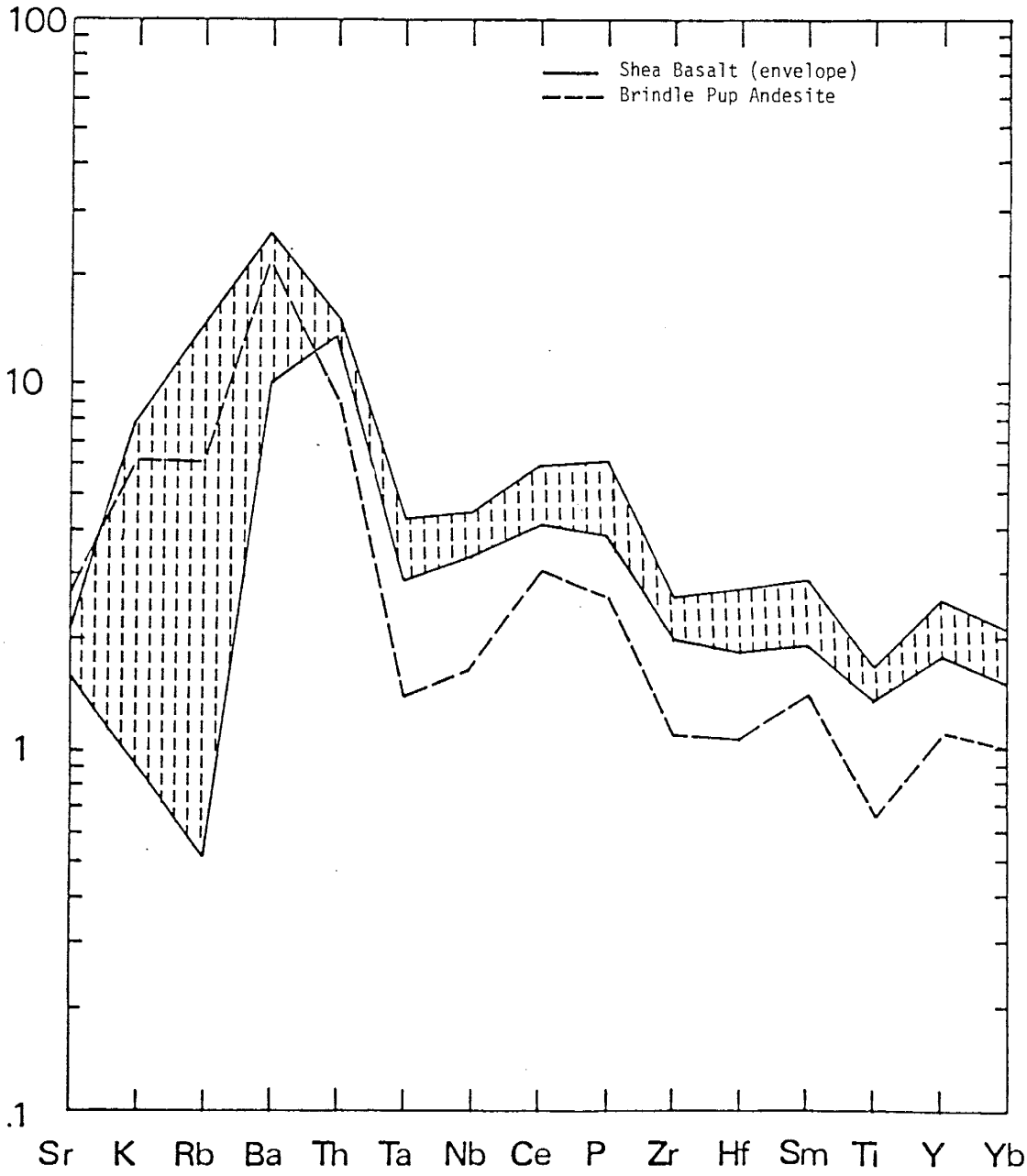

Fig. 57. MORB-normalizaed basaltic andesite of the Shea Basalt (n=5) and the Brindle Pup Andesite.

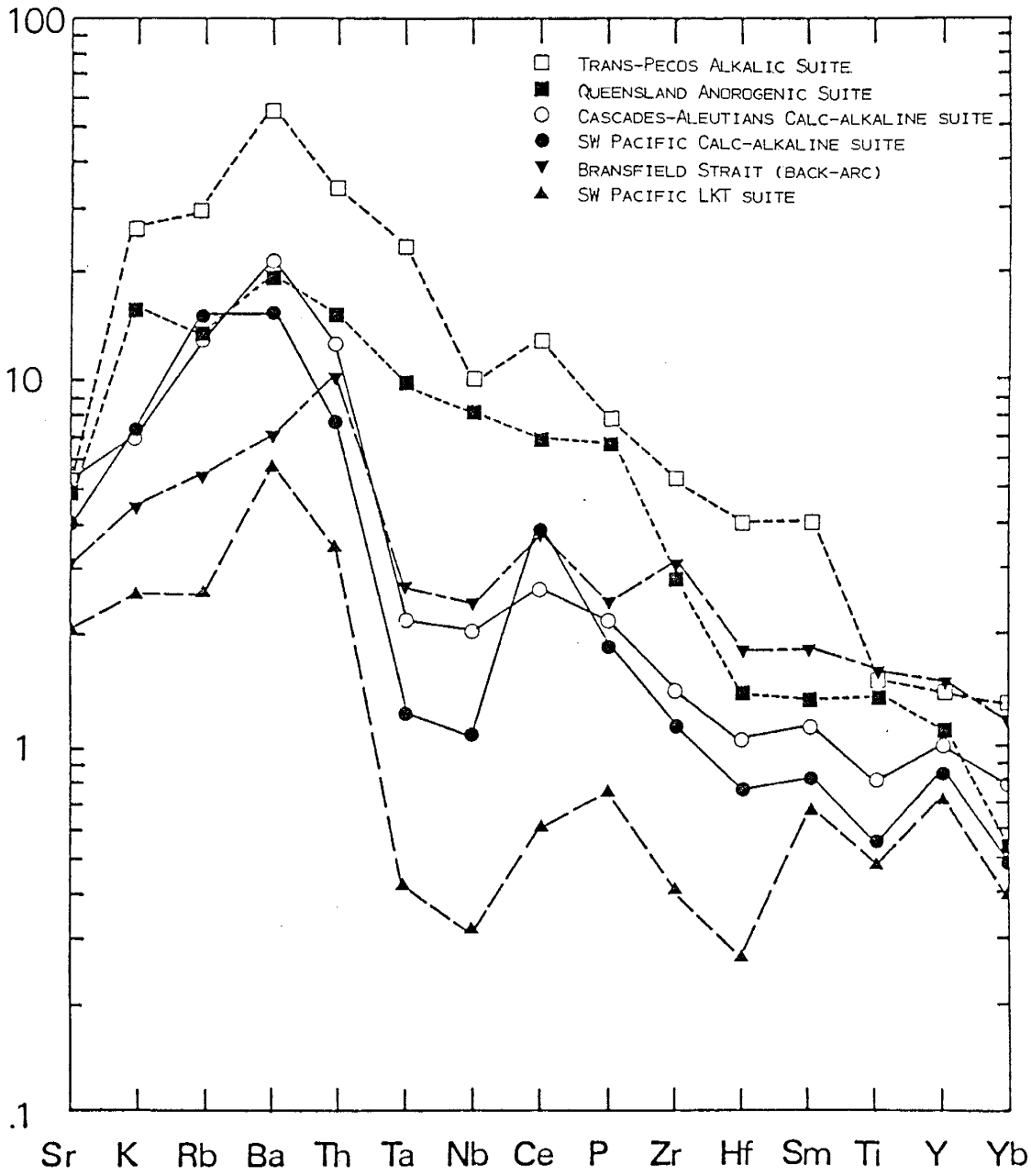

Fig. 58. MORB-normalized basaltic andesite (mean compositions, n=3-30 samples for each suite). Data sources: Weaver et al., 1979; Ewart, 1982; Gill, 1987; Nelson et al., 1987; Ewart et al., 1985.

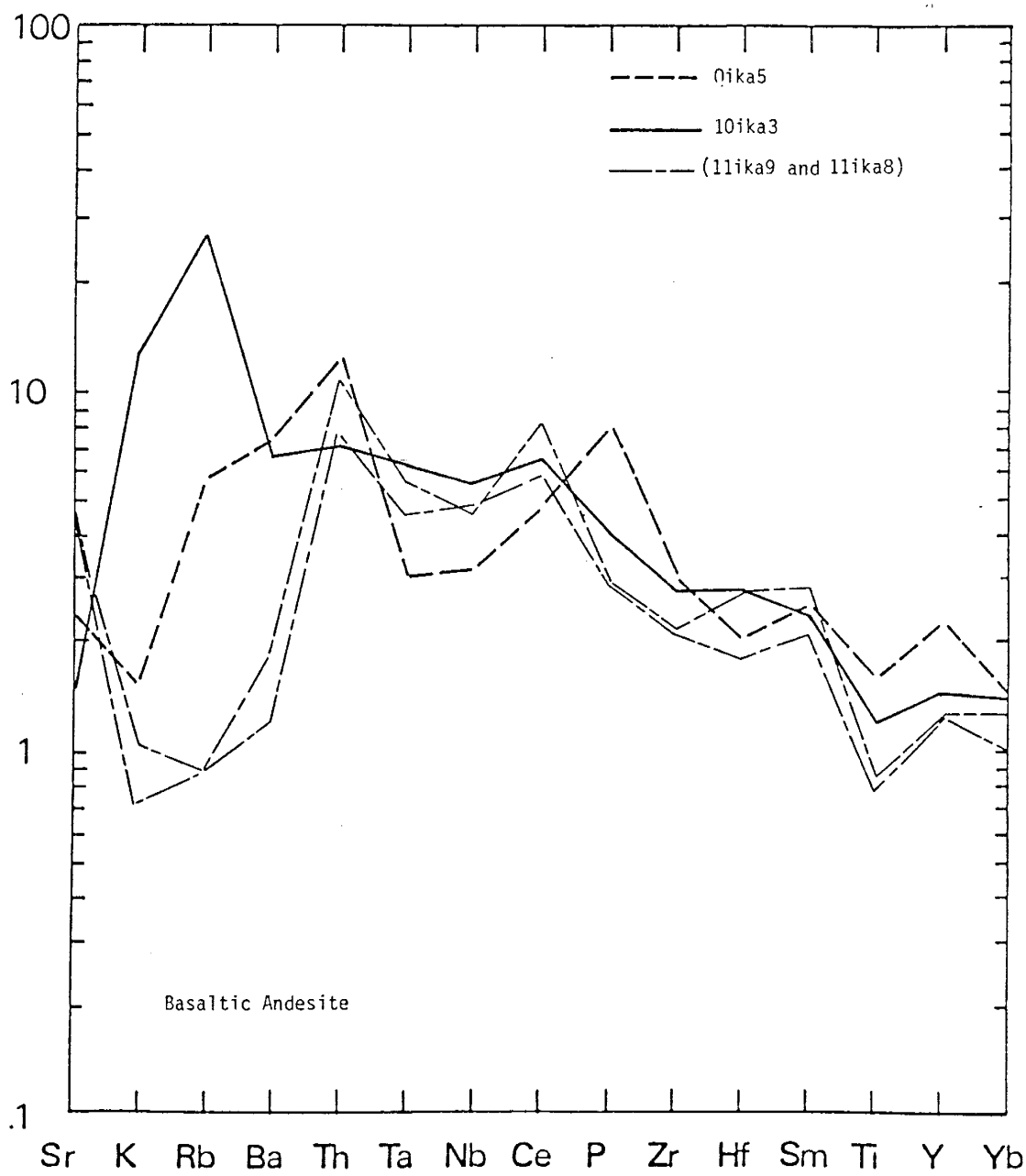

Fig. 59. MORB-normalized Iron King basaltic andesite (Qika5, 10ika3) and 'andesite' (11ika9, 11ika8).

probably results from inital low values in the lavas followed by leaching during submarine diagnesis and metamorphism.

The other basaltic andesites (Fig. 60) of the Big Bug block exhibit more prominent negative Ta-Nb and Zr-Hf anomalies than the HFSE enriched suite. The high-Ti Spud Mountain basaltic andesite has patterns similar to continental margin andesites and back-arc basaltic andesites (Fig. 58). The Spud Mountain high-Al basaltic andesites have patterns like those of calc-alkaline suites of the southwest Pacific and the Cascades-Aleutians continental margin suite. The Spud Mountain high-Al and high-Ti basaltic andesite patterns resemble those of the Spud Mountain basalt (sma-smb), and the Iron King basalt (ika), respectively.

The Green Gulch basaltic andesites have spidergrams (Fig. 61) nearly identical to those of the evolved Green Gulch basalt. The envelopes overlap and the slightly higher LILE and HFSE levels of the basaltic andesite suggest fractionation of a common parental magma. The Green Gulch basaltic andesite pattern is comparable to modern continental margin calc-alkaline suites such as the Cascades-Aleutian suite (Fig. 58). The spidergram envelope for andesites of the Green Gulch Block (Fig. 62) overlaps that of the basaltic andesites from the same area. Although concentrations are shifted higher in the andesites, the only significant difference in form is the greater magnitude of the negative Ti anomaly in the andesite pattern. This indicates the role of magnetite fractionation during the magmatic evolution from basaltic andesite to andesite. The form of the spidergram is most

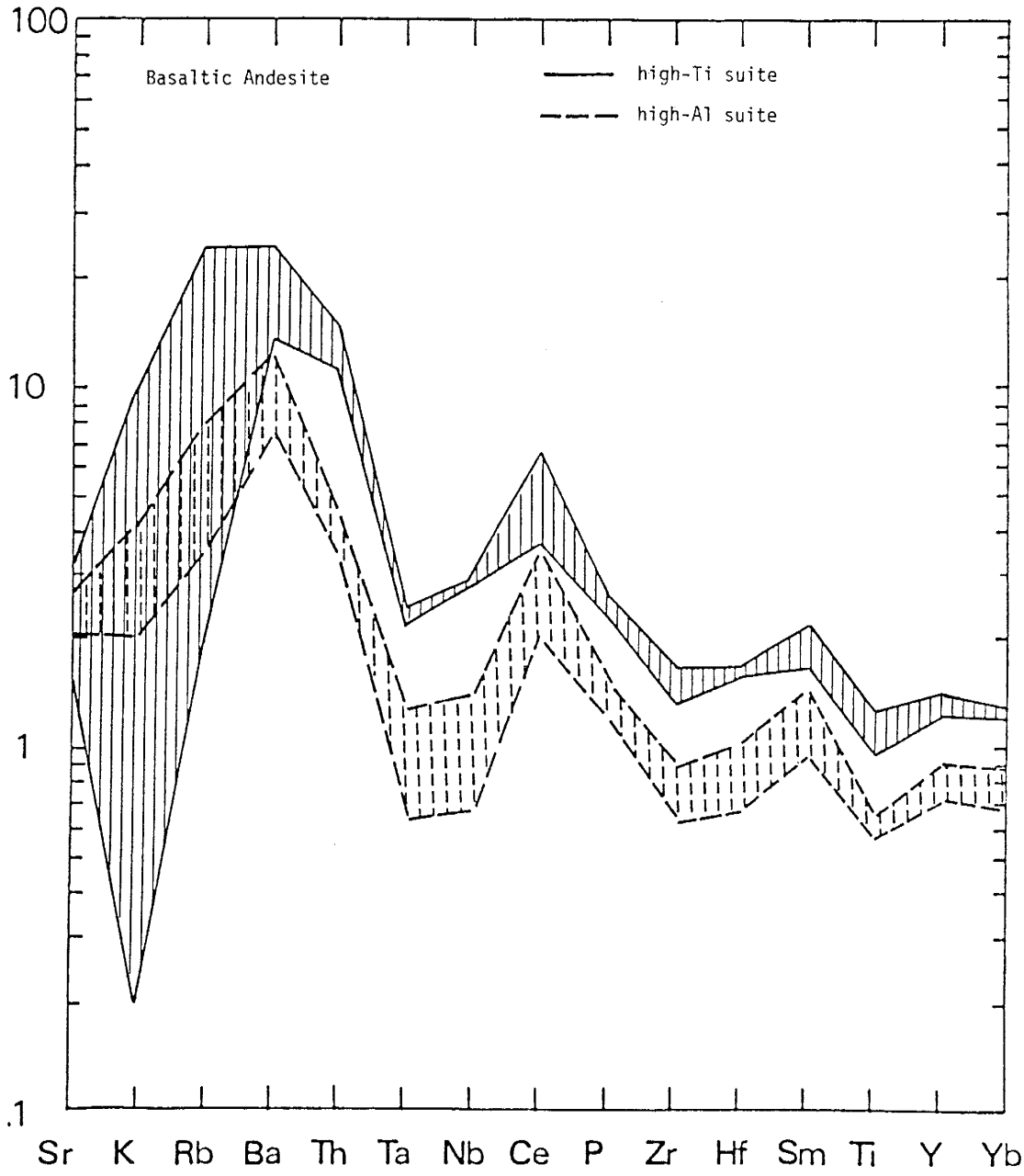

Fig. 60. MORB-normalized envelopes of variation for high-Ti (n=3) and high-Al (n=3) basaltic andesite of the Spud Mountain Volcanics.

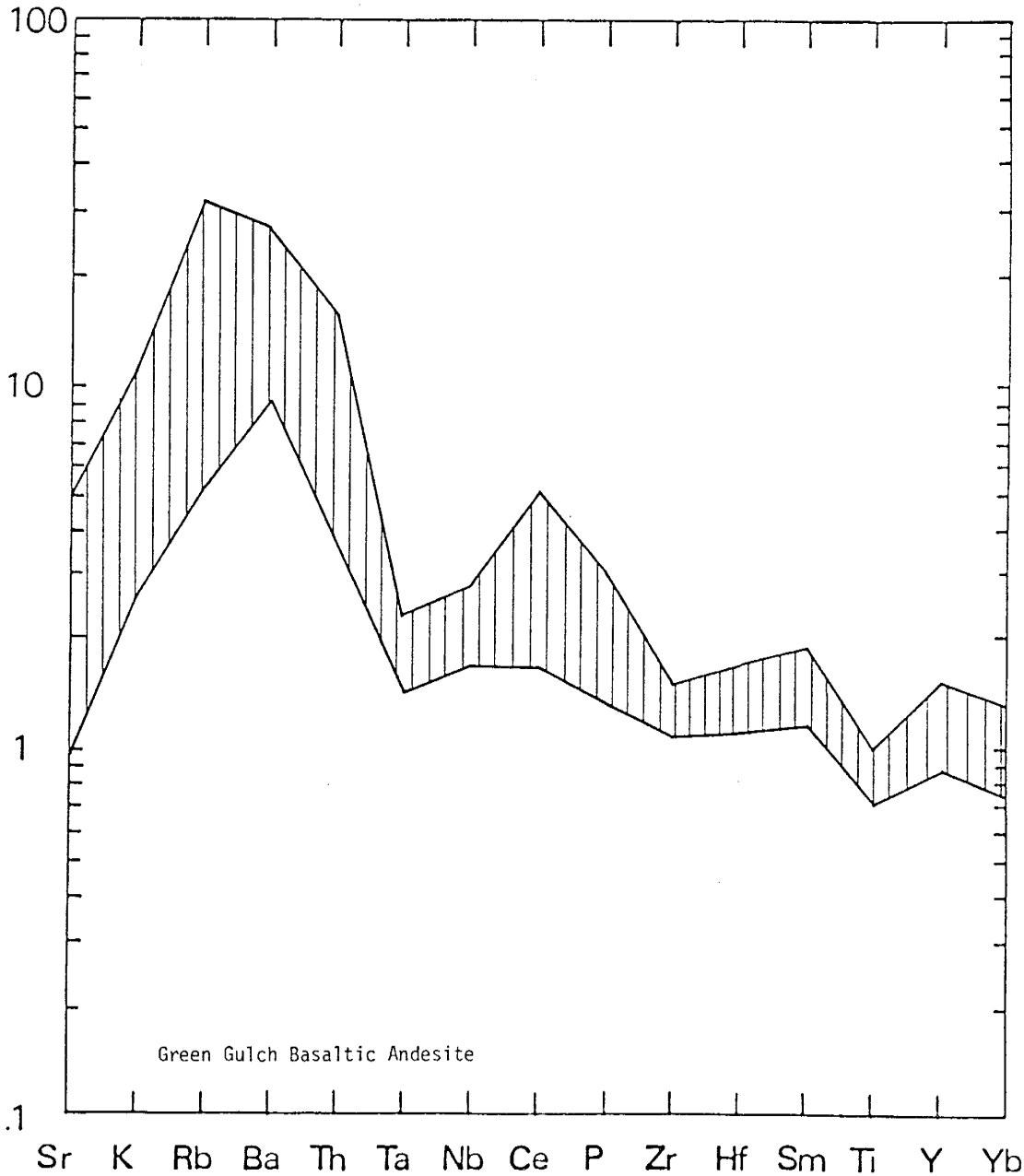

Fig. 61. Variation envelope for MORB-normalized Green Gulch basaltic andesite (n=6).

Fig. 62. Variation envelope for MORB-normalized Green Gulch andesites (n=5).

like calc-alkaline andesites of the southwest Pacific or Cascades-Aleutians suite, albiet with higher HFSE concentrations (Fig. 63).

Among the Ash Creek andesites, the form of the spidergrams is nearly identical (Figs. 64-66). Concentrations increase slightly from the Gaddes Basalt to the Dacite of Burnt Canyon. The wide LILE envelope of the Gaddes andesite is probably due to greater alteration promoted by the hyaloclastic origin of this rock. The patterns are much like those of the Green Gulch andesite; however, the Ash Creek concentration range is more restricted and the HFSE slope from Ce to Yb is steeper in the Green Gulch andesites. The larger negative Ti anomaly in the Ash Creek andesite indicates greater magnetite fractionation.

Andesites of the Big Bug block (Fig. 67 & 68) are variable. The Spud Mountain andesite lavas (sma) have patterns similar to those of the Green Gulch and Ash Creek andesites, but with higher concentrations of Zr-Yb. The magnitude of the negative Ta-Nb and positive Ce and LILE anomalies resembles those which characterize calc-alkaline andesites of the southwest Pacific and the Cascades-Aleutian continental margin suite. The Spud Mountain andesite tuffs (smct-smt) have a greater slope from Ta to Yb and a smaller negative Ta-Nb anomaly than the lavas. The pattern for the tuffs resembles that of the southwest Pacific calc-alkaline andesites, albeit with greater negative P and Ti anomalies (Fig. 63). The broad LILE envelope and implied LILE loss appears to be characteristic of pryoclastic rocks.

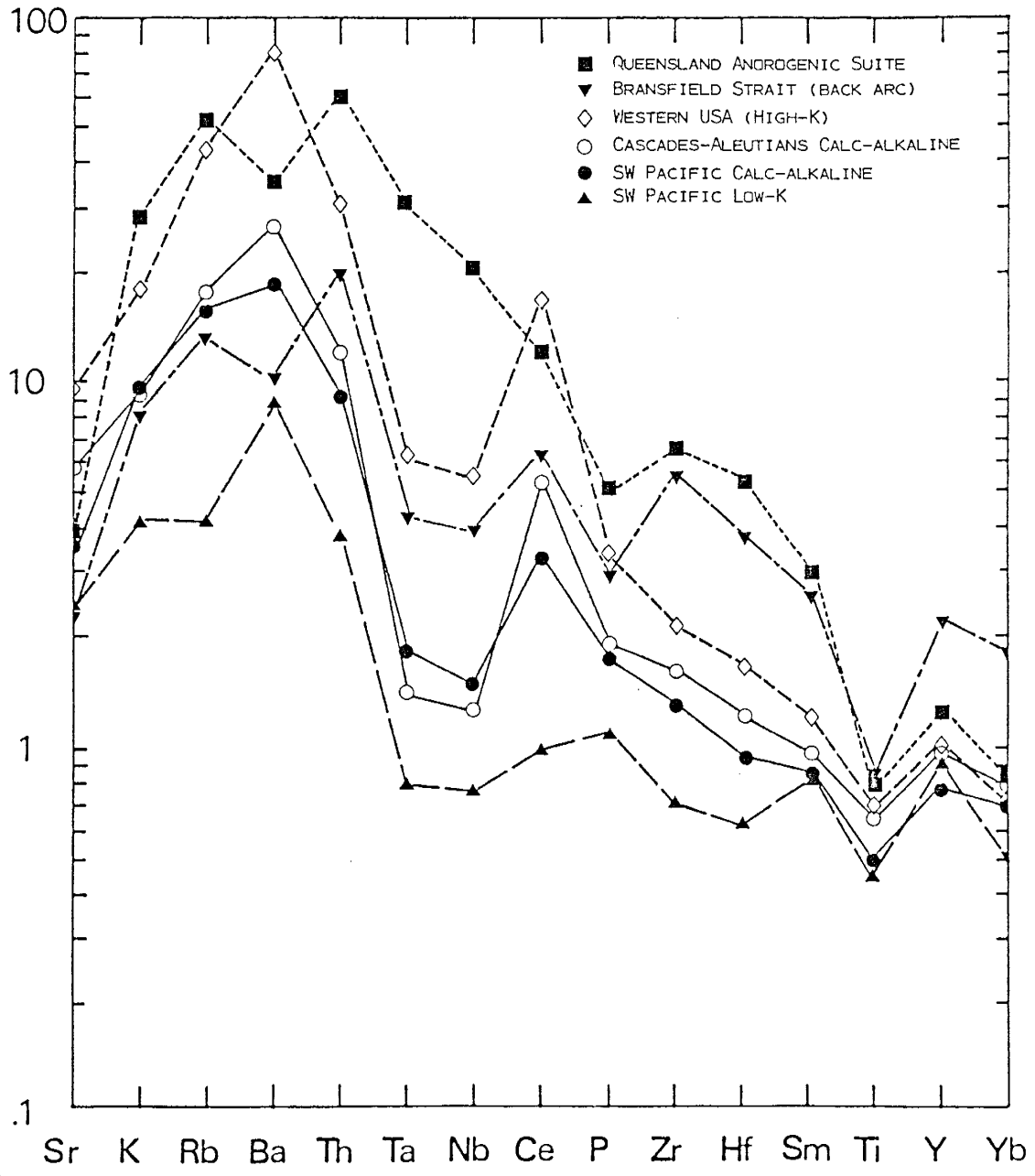

Fig. 63. MORB-normalized andesite (mean compositions, n=5-30 samples for each suite). Data sources: Ewart, 1982; Gill, 1987; Ewart, 1985; Weaver et al., 1979.

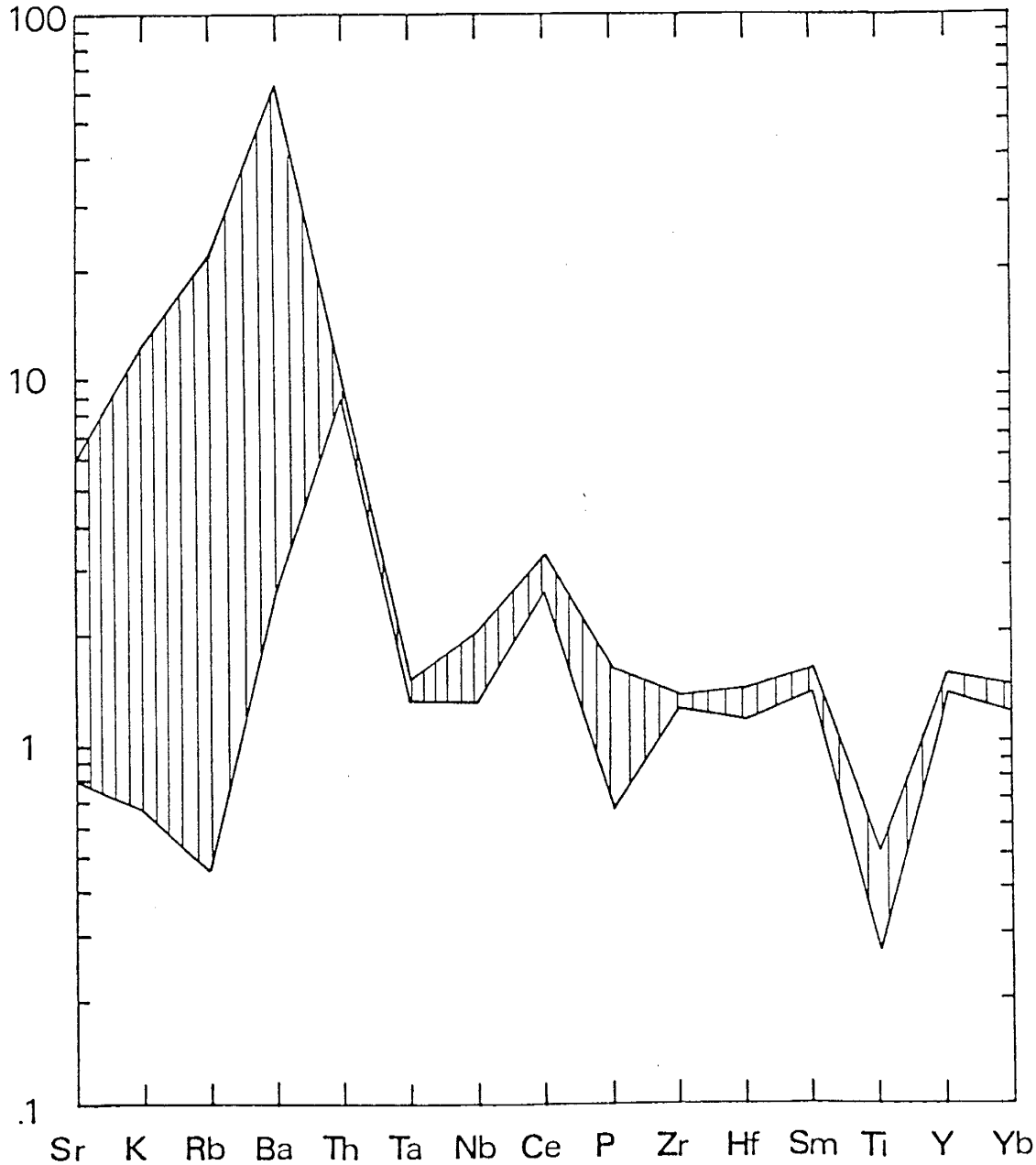

Fig. 64. Variation envelope for MORB-normalized Gaddes Basalt (andesite, n=4).

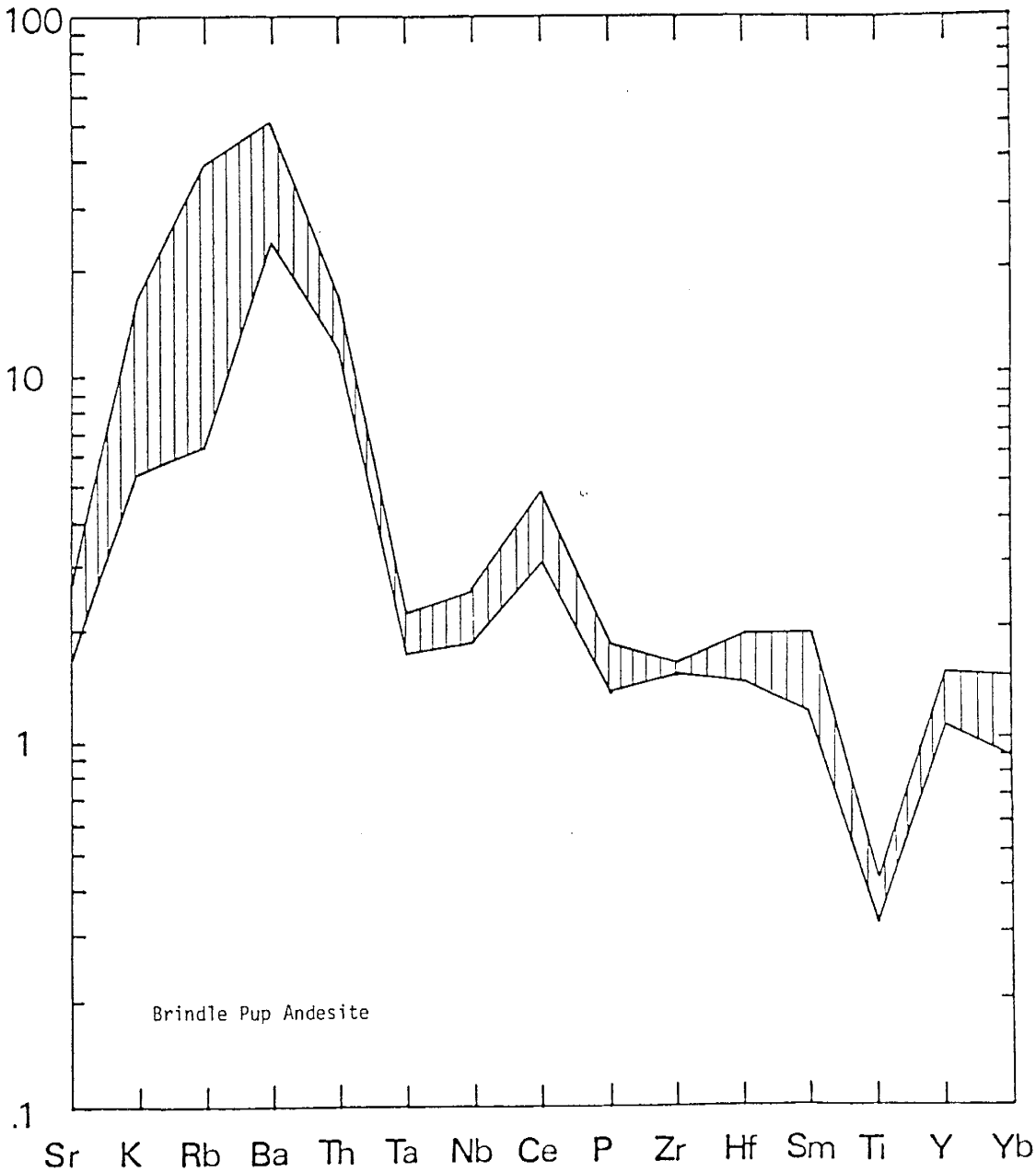

Fig. 65. Variation envelope for MORB-normalized Brindle Pup Andesite (n=4).

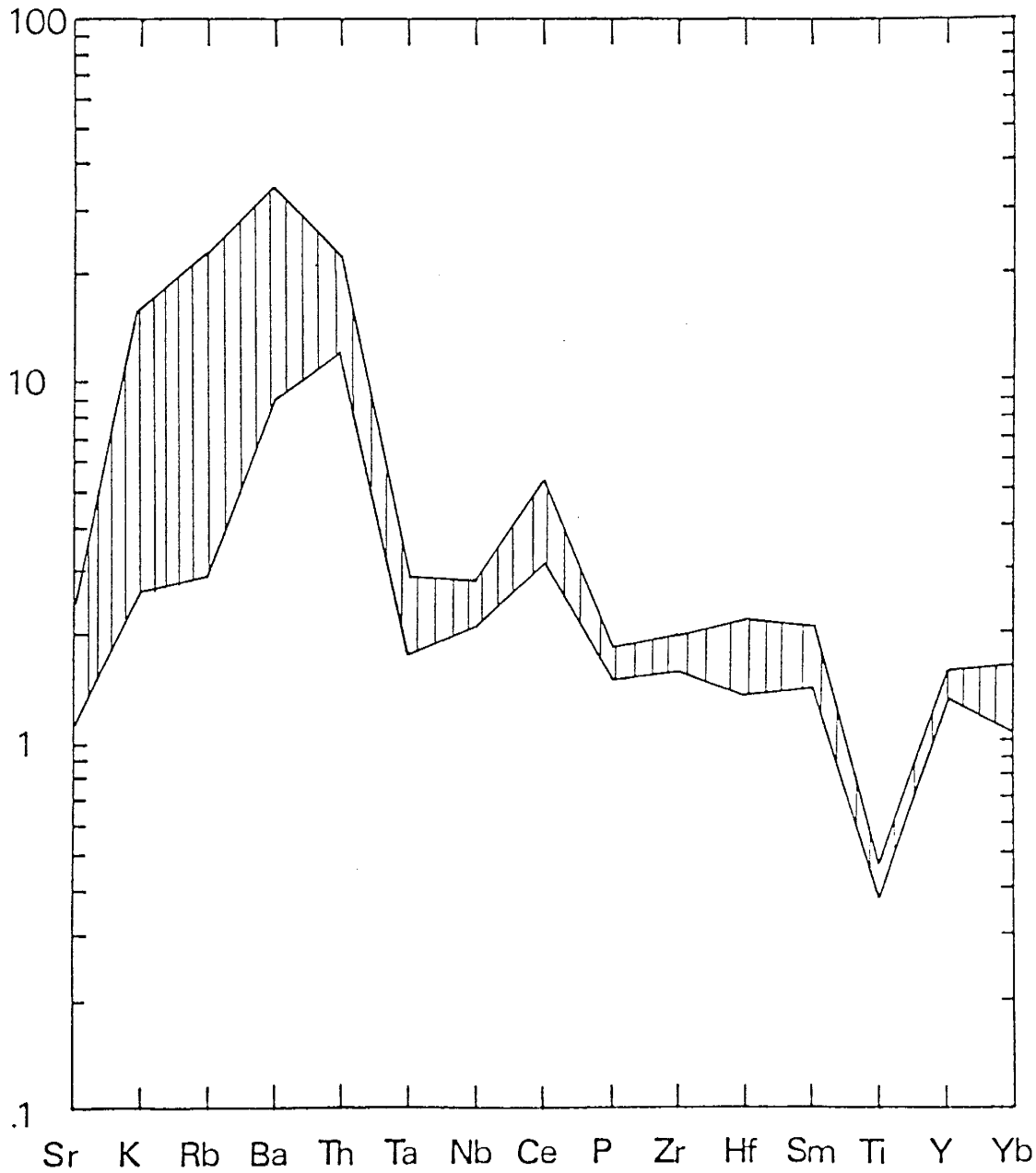

Fig. 66. Variation envelope for MORB-normalized Dacite of Burnt Canyon (andesite, n=5).

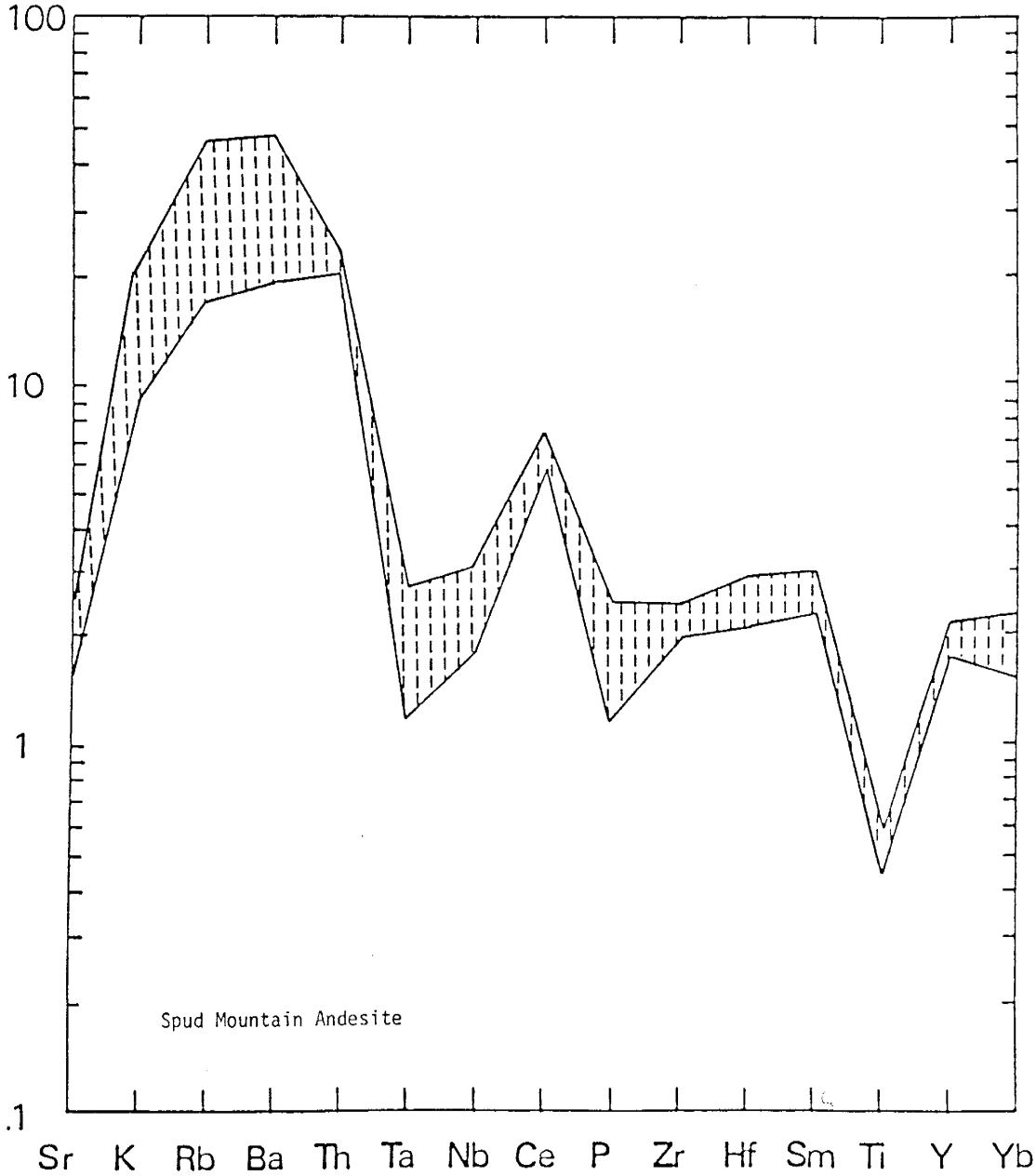

Fig. 67. MORB-normalized envelope of variation for Spud Mountain andesite (sma, n=8).

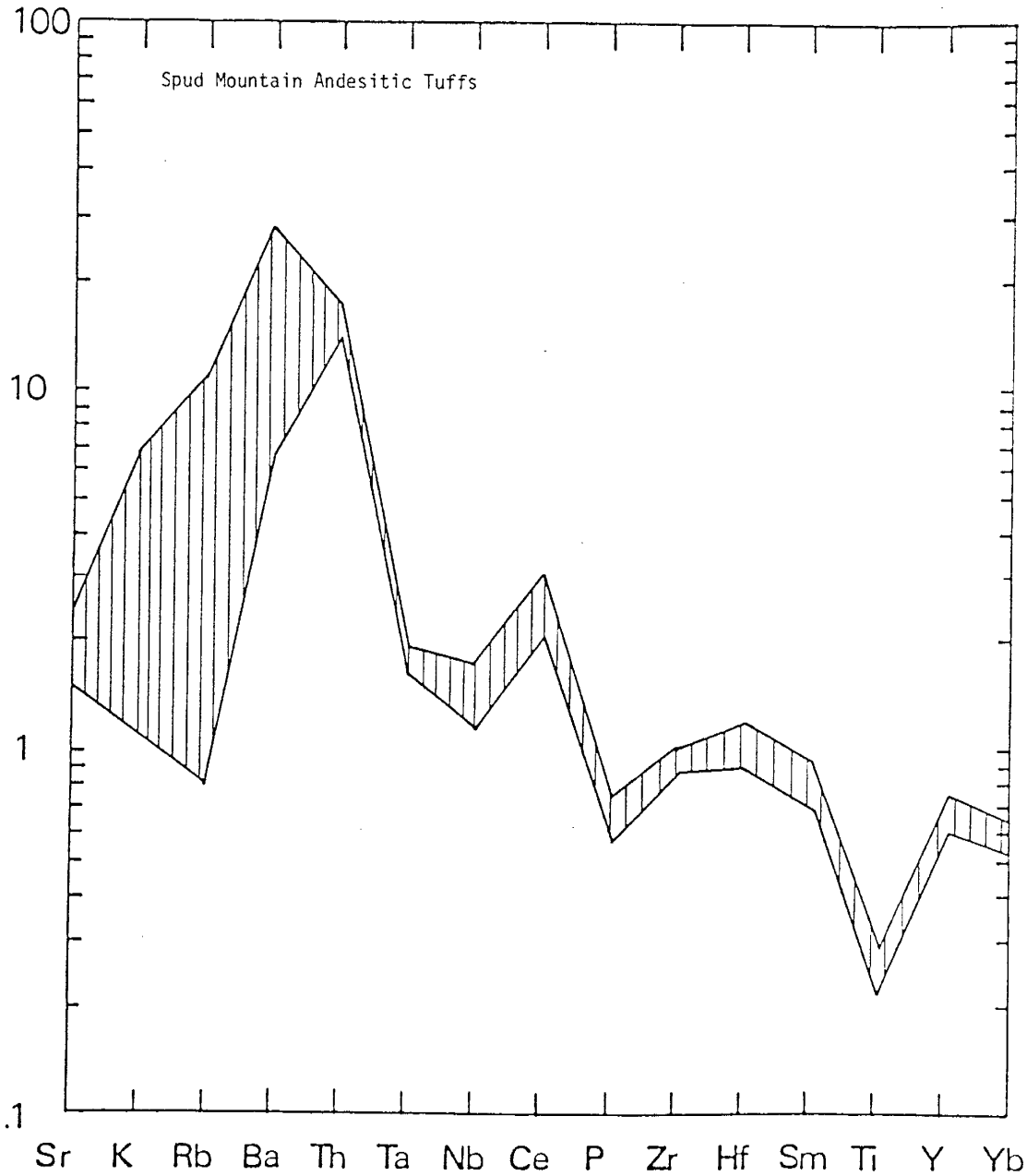

Fig. 68. MORB-normalized envelope of variation (n=7) for Spud Mountain andesitic tuff (smt) and massive crystal tuff (smct).

The spidergrams (Fig. 69) of Green Gulch dacites and andesites have nearly identical forms. The slightly higher concentrations of Th, Zr and Hf and enhanced negative P and Ti anomalies in the dacite are the only significant differences. The Green Gulch dacite spidergrams resemble those from modern continental arcs (Fig. 70).

The Ash Creek felsic units have nearly identical spidergram forms (Figs. 71-73). Concentrations of Th and most HFSE shift upwards from the Buzzard Rhyolite to the Deception Rhyolite and Quartz Porphyry. The magnitude of the negative P and Ti anomalies also increase from Buzzard Rhyolite to Quartz Porphyry indicating the relative degrees of apatite and magnetite fractionation, respectively. The progressive effect of apatite-magnetite fractionation is also recognized within the Deception Rhyolite suite from Hull Canyon (Fig. 72). The Ti and P anomalies, as well as Yb contents indicate the Lower Unit and Cleopatra Member were produced by greater fractionation relative to the Upper Unit. The Ash Creek felsic patterns differ from Ash Creek andesite patterns only by enhanced Ti and P anomalies and elevated concentrations.

Comparison with reference patterns (Figs. 70 & 74) indicates the Ash Creek felsic rocks have a pattern intermediate between those of island arcs and continental margins. The magntiude of the negative Ta-Nb, P and Ti anomalies resemble those of continental margin felsic rocks; however, the Ash Creek rhyolitic rocks do not display the steep HFSE slope from Ce to Yb which

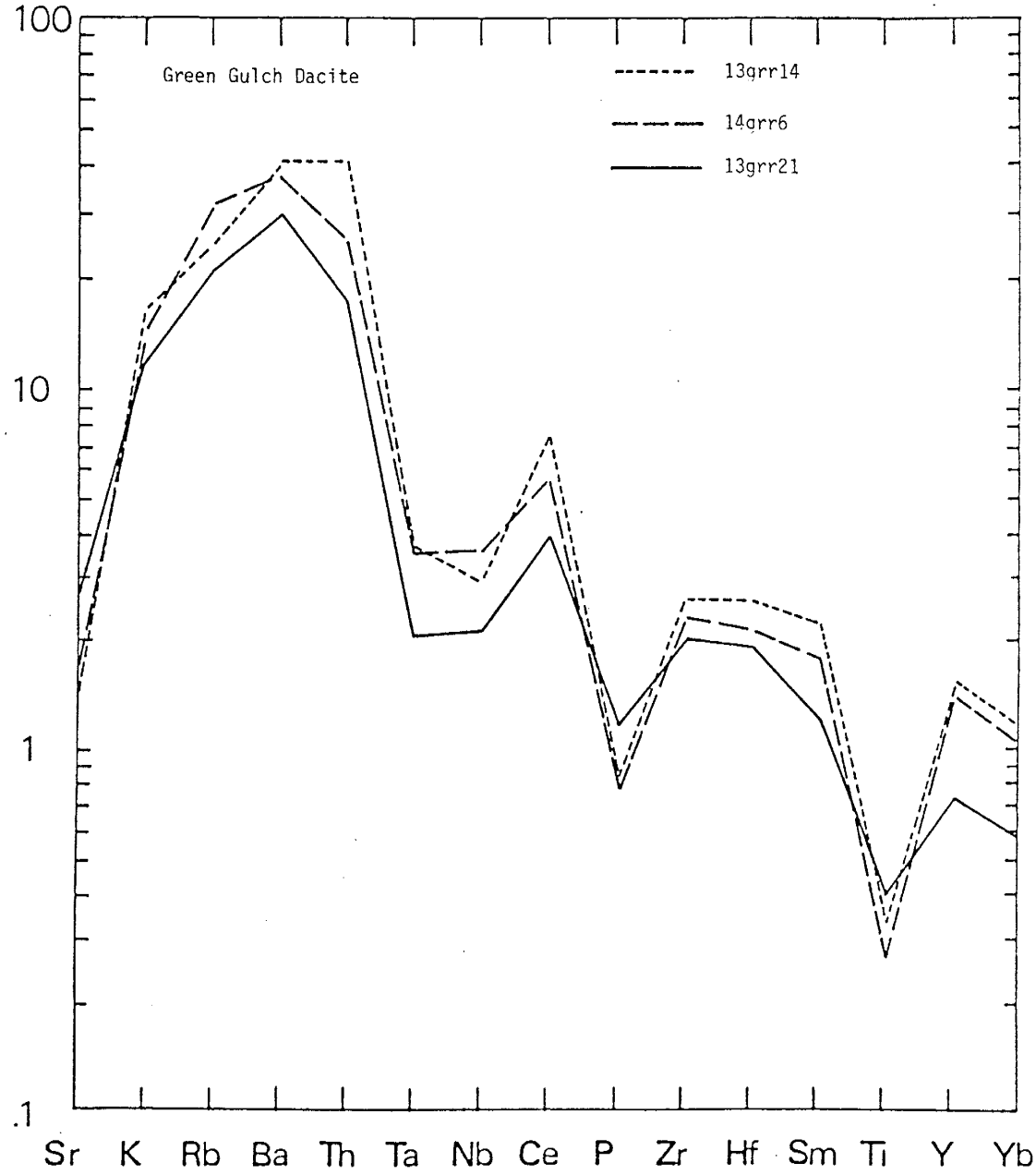

Fig. 69. MORB-normalized Green Gulch dacite.

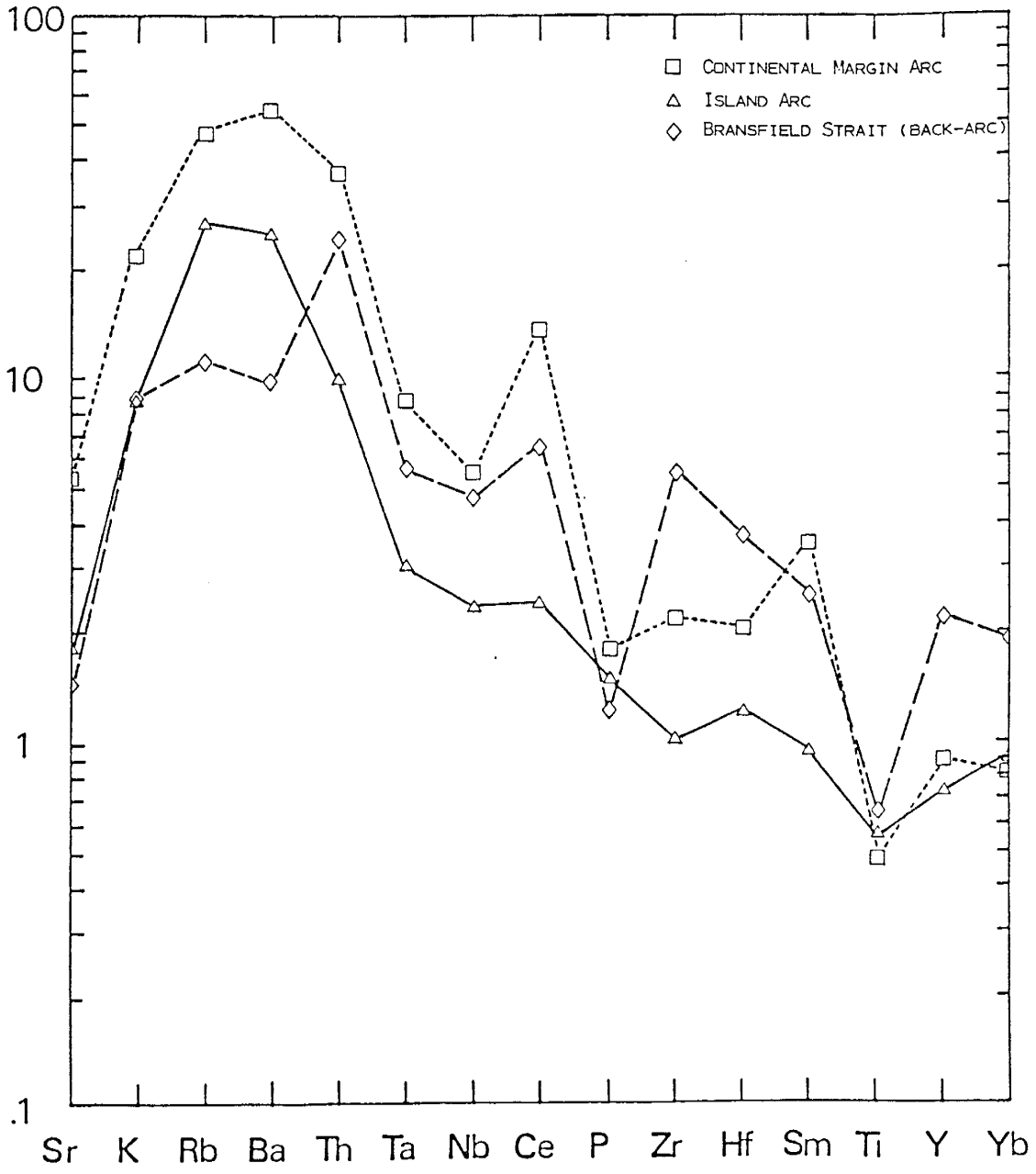

Fig. 70. MORB-normalized dacite (mean compositions, n=3-25). Data source: NMIMT Precambrian Research Group Geochemical Data Base.

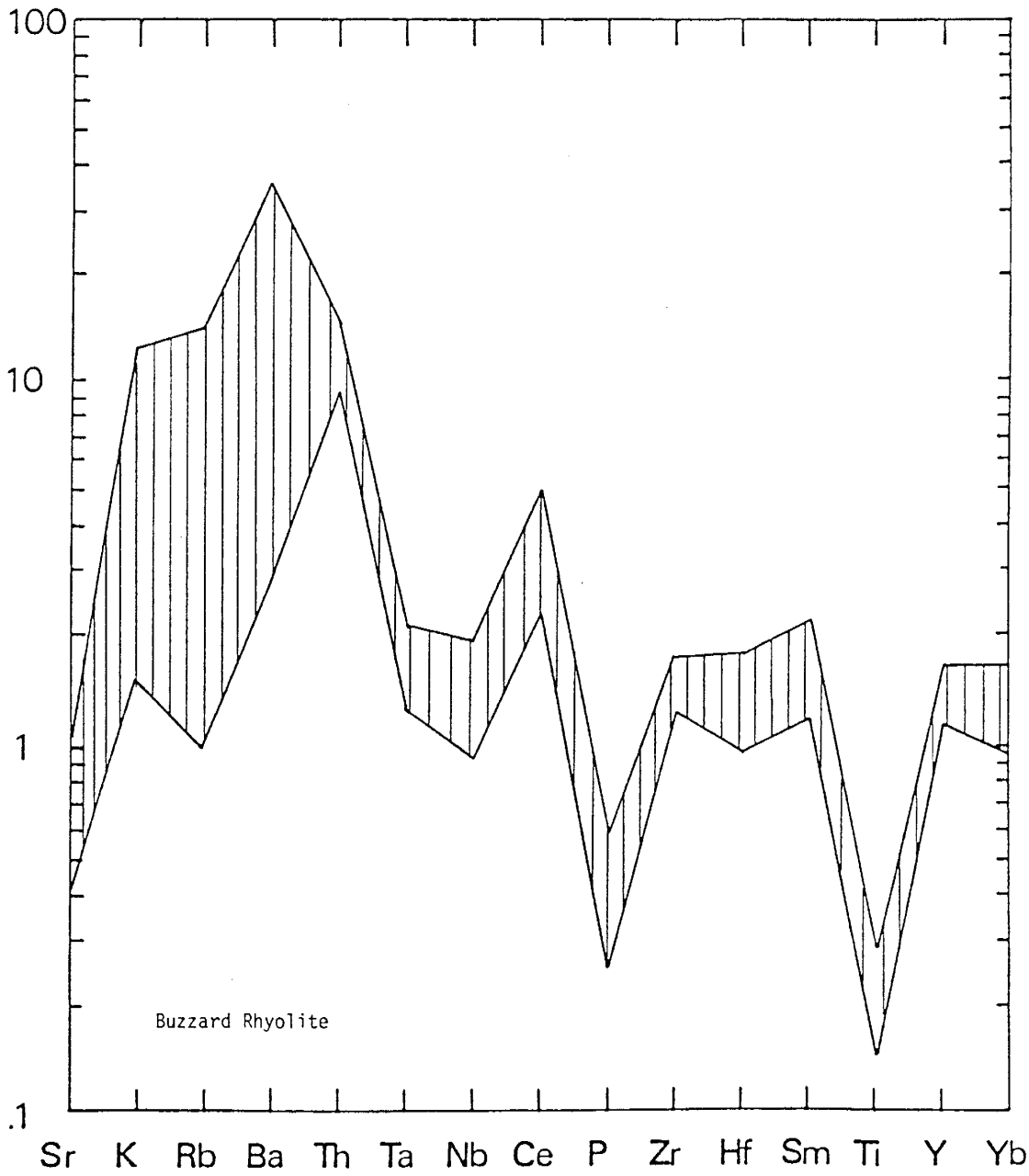

Fig. 71. Variation envelope for MORB-normalized Buzzard Rhyolite (dacite-rhyodacite, n=5).

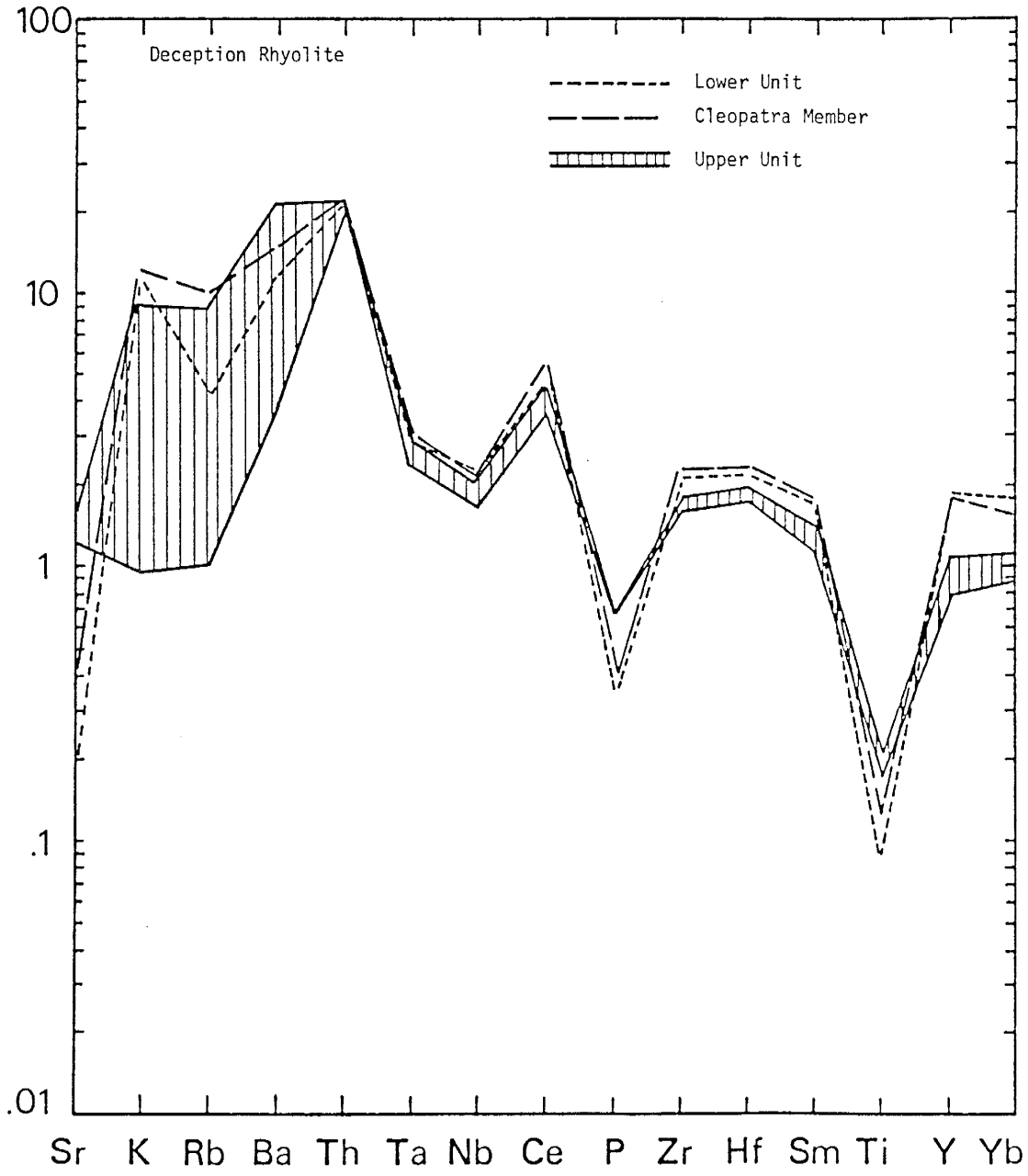

Fig. 72. MORB-normalized Lower Unit (least altered), Cleopatra Member (least altered) and unaltered Upper Unit (n=3) of the Deception Rhyolite (rhyodacite).

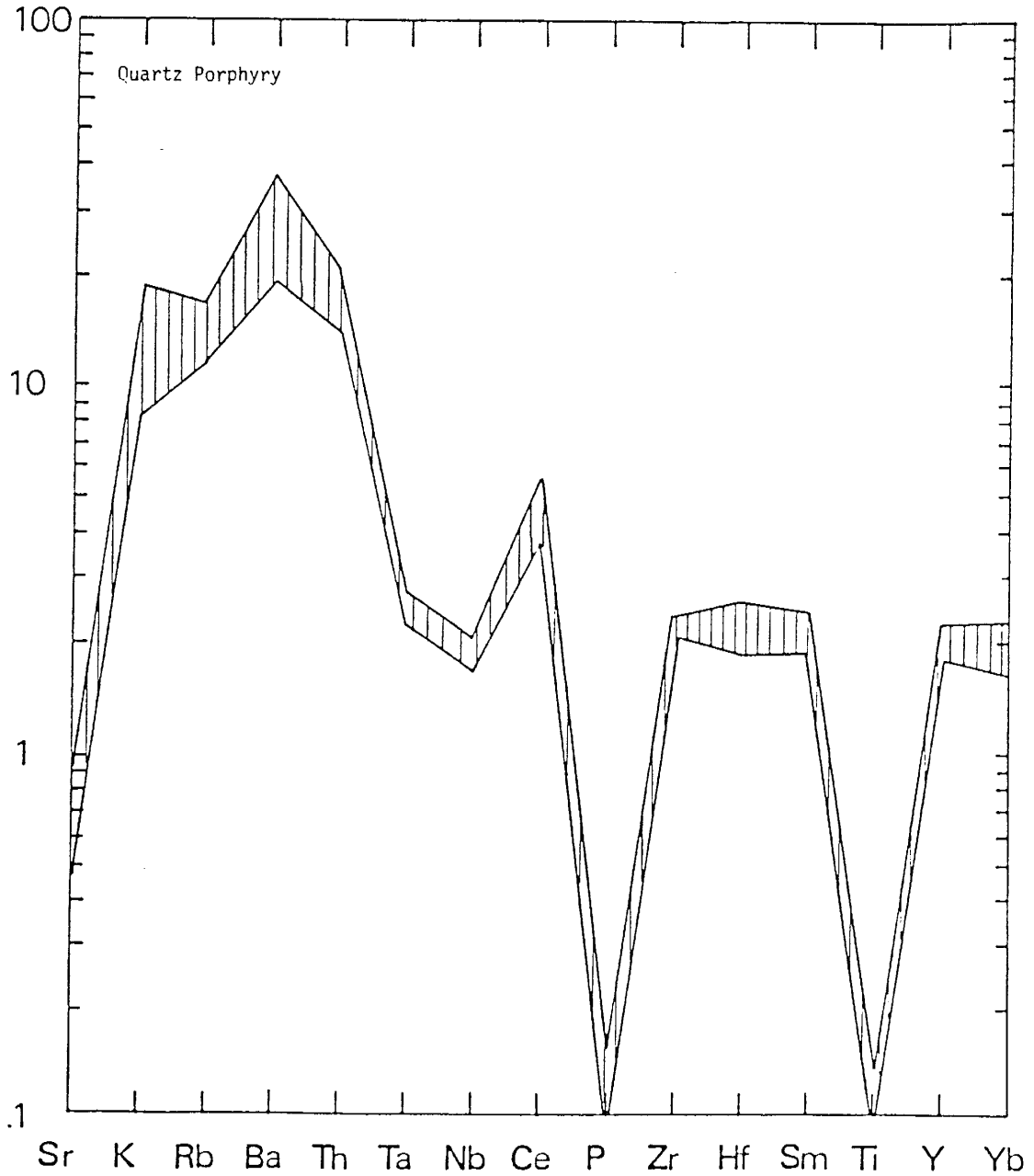

Fig. 73. Variation envelope for Quartz Porphyry (rhyodacite, n=4).

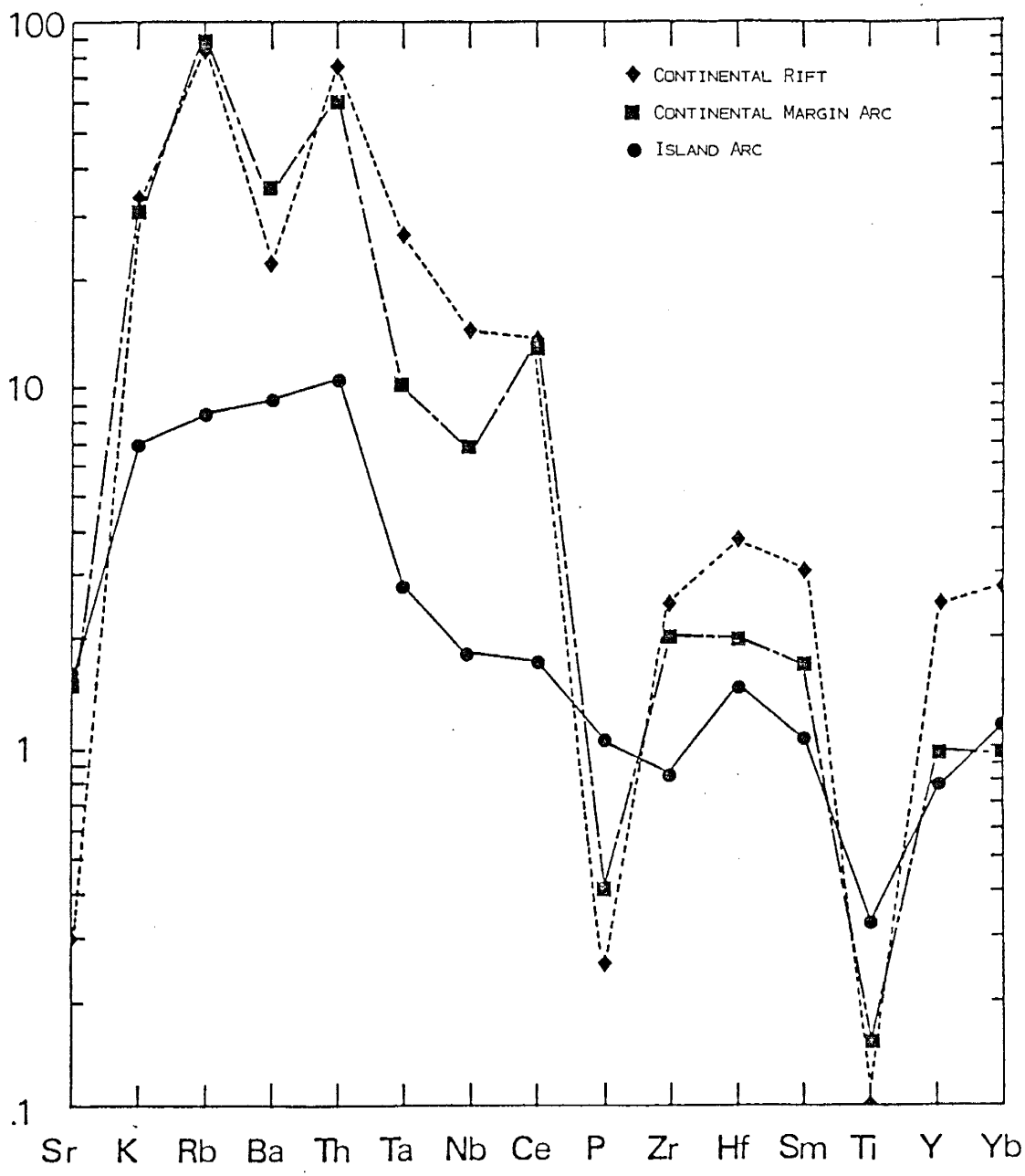

Fig. 74. MORB-normalized rhyolites (mean compositions, n=10-30). Data sources: NMIMT Precambrian Research Group Geochemical Data Base.

characterizes continental settings. In this respect the Ash Creek felsic suite also differs from the Green Gulch felsic rocks.

The Big Bug block felsic suite is limited, but similar patterns are observed among the Iron King rhyolite, Spud Mountain rhyolite and Spud Mountain rhyodacites (Figs. 75 & 76). Concentrations shift upwards from the Spud Mountain rhyolite and all patterns display profound negative P and Ti anomalies and variable LILE depletion. Alteration is responsible for the LILE depletion and may be partially responsible for the magnitude of the negative Ti and P anomalies in the Iron King rhyolite. The HFSE slope of the Big Bug felsic suite is similar to that of the Green Gulch dacite, but the magnitude of the P and Ti anomalies exceeds that of Ash Creek rhyodacites. The Big Bug patterns resemble those of rhyolitic rocks from modern continental margin arcs (Fig. 74).

Petrogenesis

Procedure

The origin and evolution of the Yavapai magmas is evaluated using well-established geochemical modelling techniques (Allegre and Minster, 1978). The rocks are modelled (App. D) using mean compositions (Tables 5-7, App. B) of the major volcanic units of Anderson and Creasey (1958) and Anderson and Blacet (1972) with respect to geochemical subdivisions of units and the blocks

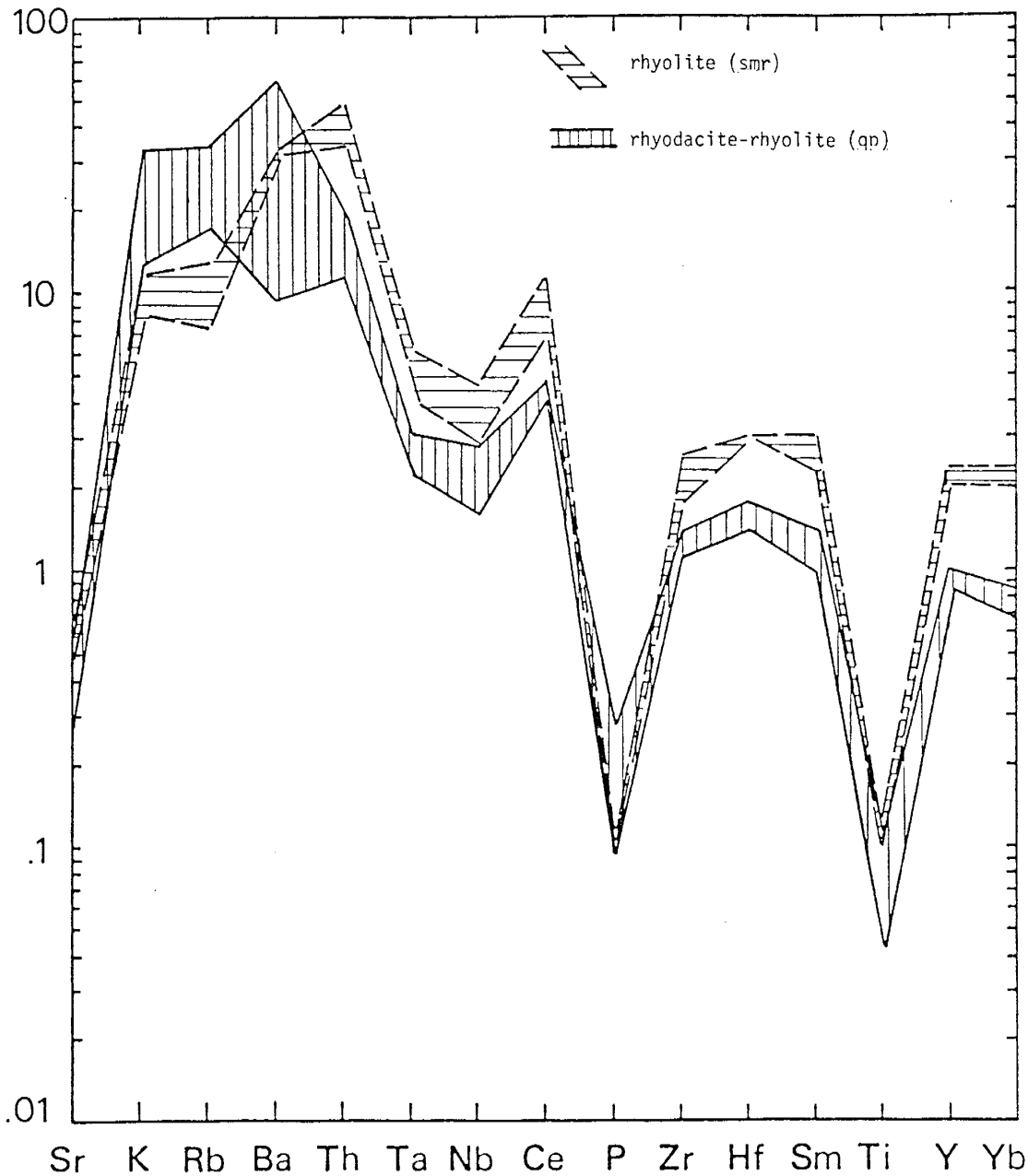

Fig. 75. MORB-normalized envelopes of variation for rhyolite and rhyodacite of the Spud Mountain Volcanics (n=2smr), (n=3qp).

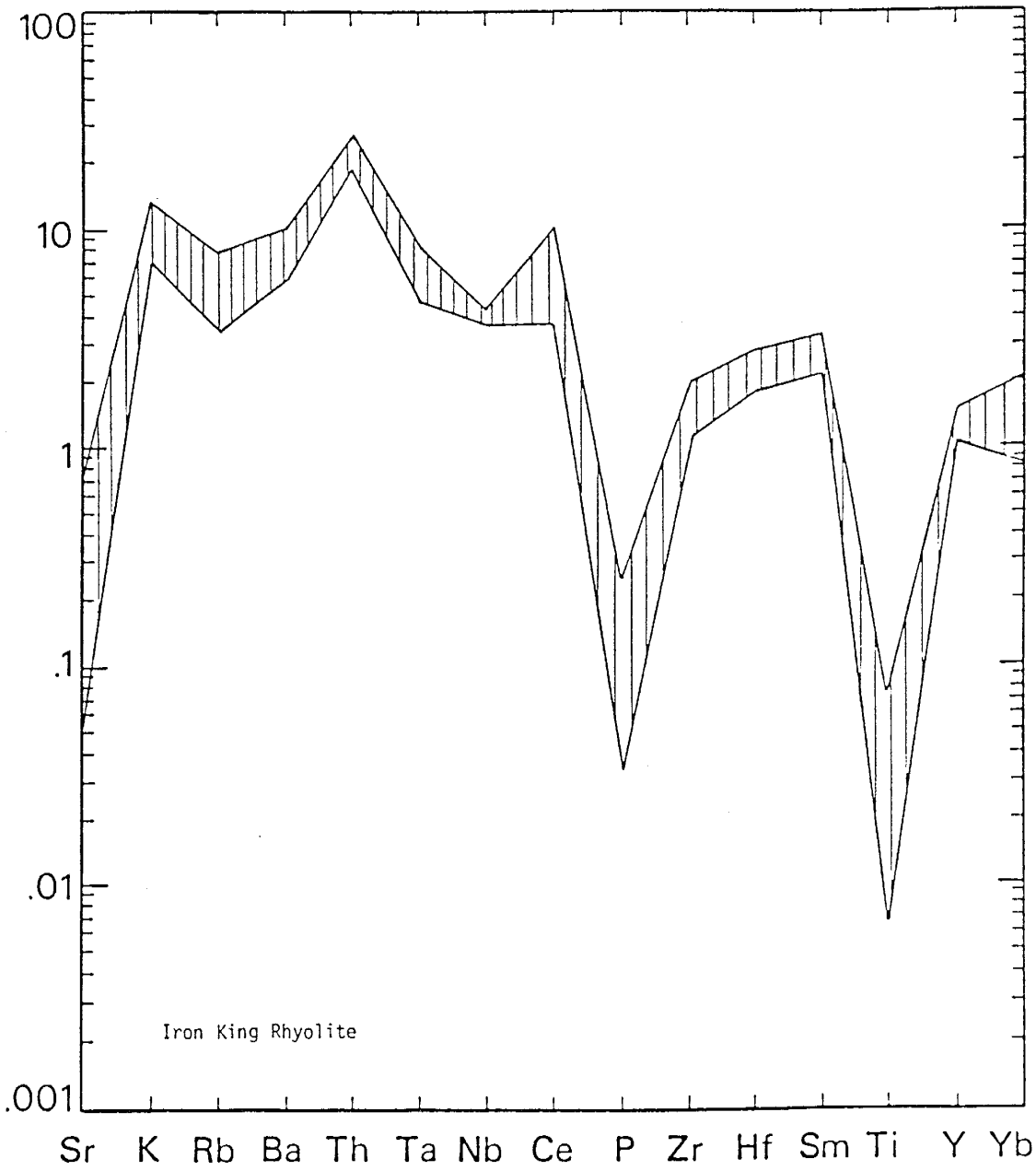

Fig. 76. MORB-normalized envelope of variation for variably altered Iron King rhyolite (ikr, n=3).

defined by Karlstrom and Bowring (1988). The initial modelling step is testing for genetic links within volcanic groups by closed system Rayleigh fractional crystallization, in which an isolated magma chamber is subject to continuous crystal fractionation. The melt behaves as a uniform reservoir and crystals are removed as soon as they form so the total residue achieves equilibrium with the melt only at the initiation of crystallization. The degree of enrichment or depletion of incompatible and compatible elements respectively, in the melt fraction, depends on the bulk distribution coefficient and degree of crystallization. Equations used to explore these relations are presented in Appendix D.

For units which cannot be related by closed system fractionation but exhibit compositional similarities, open system fractional crystallization is tested. The open system fractionation model is based on continuous crystal fractionation of a high level magma chamber which is periodically injected with a new batch of parental magma that displaces a certain volume of residual liquid as a lava flow (O'Hara, 1977). Open system fractionation explains rapid increases in incompatible element concentrations with little change in major elements (O'Hara, 1977; Robson and Cann, 1982; Kay et al., 1982). The concentration of an element in the residual liquid of such a system varies with the bulk distribution coefficient, cumulate proportion, and the number of cycles of injection and effusion. The equations expressing these relationships are presented in Appendix D. Both open and

closed system fractional crystallization models were performed using the MODULUS Program (Knoper, 1988).

Attempts to relate units by crystal fractionation are guided by progressive decrease in Mg number and increasing incompatible element contents. The slight upward concentration shifts between units with nearly identical chondrite-normalized REE and MORB-normalized patterns suggest potential fractionation links. Major element trends are also considered, but are not relied on because of major element mobility. The mineral phases used in models are constrained by relict phenocrysts, phenocrysts of modern arc volcanics, and minerals required to account for the enrichment or depletion of the various chemical species in the proposed fractionation link. The isomolar plots (Figs. 21-24) also constrain the choice of phases.

Phenocrysts in young arc volcanics include plagioclase, clinopyroxene, olivine and magnetite for mafic rocks as well as orthopyroxene in some mafic to felsic suites (Weaver et al., 1979; Gill, 1981; Ewart, 1982; Ewart and Hawkesworth, 1987; Gill, 1987). Andesitic to dacitic rocks contain phenocrysts of plagioclase, clinopyroxene, orthopyroxene, hornblende, minor biotite, magnetite and quartz (Bryan, 1979; Tomblin, 1979; Gill, 1981; Ewart, 1982). Within the Proterozoic Yavapai volcanics, relict phenocrysts of plagioclase and clinopyroxene are preserved in mafic rocks and plagioclase, magnetite-ilmentite, quartz and possible biotite in intermediate to felsic rocks. The relict phenocryst mineralogy of the Yavapai volcanics is summarized in Table 4. Pearce (1982)

Table 4. Relict Phenocryst Proportions in the Yavapai Volcanics

Tectonic Block	Composition	Phenocryst	%
Ash Creek	basalt	plagioclase	2-20
		clinopyroxene (?)	$\leq$ 20
	basaltic andesite	plagioclase	20-25
	andesite	plagioclase	2-25
	dacite-rhyodacite	quartz	$\leq$ 15
		plagioclase	2-25
Green Gulch	basalt	plagioclase	$\leq$ 25
		clinopyroxene	$\leq$ 20
	basaltic andesite	plagioclase	$\leq$ 25
	andesite	plagioclase	$\leq$ 30
		quartz	< 1
	dacite-rhyodacite	plagioclase	3
		quartz	1
Big Bug	basalt	plagioclase	$\leq$ 30
	basaltic andesite	plagioclase	20-30
	andesite	plagioclase	$\leq$ 30
		quartz	< 2
	rhyodacite-rhyolite	plagioclase	< 2
		quartz	$\leq$ 15

provides an excellent summary of the effects of crystallization of these minerals on magma evolution for differing igneous series. The partition coefficients for the mineral phases employed in the models are listed in Table 1b-d, Appendix D. The data sources for the partition coefficients are given in MODULUS files of Knoper (1988) and in the geochemical data base of the Precambrian Research Group of the New Mexico Institute of Mining and Technology.

Temperature dependent partition coefficients for Ni and Cr are used in modelling the mafic to intermediate compositions (Duke, 1976; Irving, 1978; Hart and Davis, 1978). The 1150°C to 990°C temperature range is constrained by considering subvolcanic magma chambers, phase relations and physical measurements of active lava flows (Thompson and Tilley, 1969; Carmichael et al., 1974).

The Green Gulch basalts include the only primitive samples of the Yavapai volcanics as identified by a Mg number > 70, Ni > 400 ppm and Cr between 800 and 900 ppm. Consequently, these are the only basalts that are considered as possible parental compositions. The remaining basalts are products of olivine-clinopyroxene-plagioclase fractionation as indicated by relict phenocrysts and isomolar projections. The approximate degree of fractionation from parental compositions is constrained by Zr-Ni and Cr-Y systematics (Rajamani et al., 1985; Pearce, 1982). The incompatible element vs compatible element plots distinguish fractional crystallization and batch melting trajectories. The

mantle source is characterized by comparing incompatible element ratios to those of modern basalts and primordial mantle (Wood, 1979; Pearce, 1982; Knoper and Condie, 1988).

It is emphasized that the models serve to constrain the magmatic evolution of these rocks and do not necessarily represent the actual mechanisms which produced a volcanic rock. Throughout modelling, the greatest emphasis is placed on HFSE and the low mobility transition elements. These are the components which are least effected by submarine diagenesis, hydrothermal alteration and subaerial weathering. All models are presented in Tables 2-4, Appendix D.

Volcanics of the Ash Creek Block

The Cr vs Y plot (Fig. 77) illustrates both fractional crystallization trends and partial melting trends (Pearce, 1982; 1984). The compatible component Cr partitions into, olivine and clinopyroxene, decreasing continually in residual liquids during fractionation of a parental magma. The incompatible element Y has initial concentrations dependent on the degree of partial melting of the source. Fractional crystallization produces a continual increase of Y in residual liquids. Consequently the initial Cr-Y trend is steep and reflects olivine-clinopyroxene dominated fractionation. As plagioclase begins to crystallize the trend slope becomes less steep.

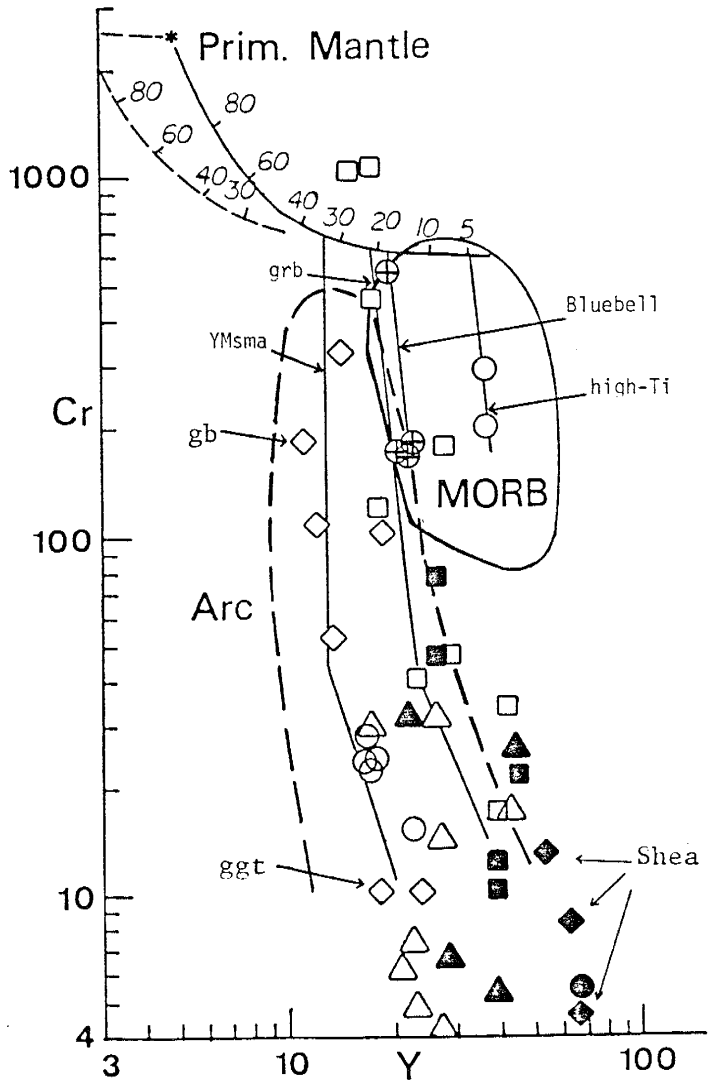

Fig. 77. Cr-Y plot for Yavapai basalts (open symbols) and basaltic andesites (solid symbol) with batch melt curves for primordial mantle (solid) and depleted mantle (dashed) after Pearce (1982). Diamonds = volcanics of the Ash Creek block. Triangles and circles = Spud Mountain and Iron King Volcanics of the Big Bug block. Circles with crosses = Bluebell basalts, squares = Green Gulch Volcanics. Units associated with ol-cpx-plag fractionation trends (solid, near-vertical lines) are indicated.

The distribution of the gabbros (gb), Yarber Mine basalts (YMsma) and Grapevine Gulch mafic tuff (ggt) samples suggest a common parental magma for the Ash Creek basalts. This observation is also supported by incompatible element ratios such as Th/Yb and Zr/Y (Table 8, App. B). The fractionation trend illustrated in Fig. 77, indicates olivine-clinopyroxene fractional crystallization may be responsible for compositional variation among the Yarber basalts, and that plagioclase fractionation was important in producing the Grapevine Gulch mafic tuff. Isomolar plots (Figs. 21-24) and relict phenocrysts (Table 4) suggest a fractionation history of olivine $\pm$ clinopyroxene crystallization followed by clinopyroxene-plagioclase dominated fractionation at lower pressures.

Ash Creek gabbro may be related to mean Yarber Mine basalt (ggt) composition by 20% crystallization of a plagioclase-clinopyroxene-olivine magnetite assemblage (Table 2a, App. D). The model is quite feasible (low squared residuals) with respect to REE and most HFSE but the Cr, Co and Ni contents require cumulate olivine and pyroxene. TiO_2-normalized Al_2O_3-CaO covariation plots (Ewart and Hawkesworth, 1978) also indicate cumulate plagioclase. Although the Grapevine Gulch basalts are pyroclastic, optical petrography and chemical composition indicate a uniform pyroclast composition. Therefore, the Yarber Mine basalt - Grapevine Gulch link is modelled to test the terrane proposals of Karlstrom and Bowring (1988). The Grapevine Gulch mafic tuffs can be produced by 40% crystallization of a plagioclase-clinopyroxene-olivine-

magnetite assemblage from a Yarber Mine basalt (YMsma) parent (Table 2b, App. D).

The Cr-Y systematics, MORB-normalized plots (Figs. 64-66), and incompatible element ratios (Table 8, App. B) suggest the Gaddes, Brindle Pup and Dacite of Burnt Canyon andesites originated from nearly identical parent magmas. The Gaddes andesite differs slightly from the others with respect to incompatible element ratios, but ratios such as Zr/Nb and Hf/Th overlap the range of the other andesites. Attempts to relate the Brindle Pup Andesite (bpa) to a parent magma of Yarber basalt (YMsma) composition cannot produce the required enrichment of Nb, Hf, Zr and middle REE. The Cr-Y systematics suggest a potential fractionation link between the Green Gulch basaltic rocks and the Ash Creek andesites and the interpretation of Karlstrom and Bowring (1988) suggests these volcanics come from correlative terranes. The Brindle Pup Andesite can be derived from an evolved Green Gulch basalt by 28% crystallization of olivine-clinopyroxene-plagioclase (Table 2c, App. D). Ta and Nb present problems for this model, and Nb has been difficult to model in most cases. This may result from a higher analytical error associated with Nb, or a lack of accurate partition coefficients.

The andesitic Dacite of Burnt Canyon (bcd) is a slightly more fractionated version of the Brindle Pup Andesite (bpa). The Burnt Canyon andesite (bcd) may originate by 10% fractional crystallization of plagioclase-clinopyroxene-magnetite-biotite from a Brindle Pup melt (Table 2d, App. D). Relict plagioclase

phenocrysts are abundant in both the proposed parent and daughter. Although clinopyroxene is not recognized, fine-grained chlorite and biotite may be alteration products of this phase.

Relating the Buzzard Rhyolite (br) to the Burnt Canyon (bcd) or Brindle Pup (bpa) andesite by fractional crystallization requires excessive biotite fractionation and manipulation of accessory minerals to satisfy a drop in light REE and HFSE. The less fractionated Gaddes andesite may yield a Buzzard rhyodacite daughter magma by 20% fractional crystallization of a plagioclase-clinopyroxene- magnetite with trace apatite assemblage. This simple model (Table 2e, App. D) is probably the most realistic and agrees with the proposed stratigraphy of Anderson and Creasey (1958) and the presence of a dacite (7gb8), with a composition like Buzzard Rhyolite, interlayered with the Gaddes Andesite.

The dacitic Buzzard Rhyolite may be a parent for the rhyodacitic Cleopatra member of the Deception Rhyolite. This link requires 35-45% fractional crystallization of a plagioclase-amphibole-biotite-quartz-magnetite assemblage with traces of zircon and apatite. Both major and trace elements support this model (Table 2f, App. D). The Buzzard Rhyolite may also be parental to the Quartz Porphyries. The model requires 40-43% fractional crystallization of a plagioclase dominated (77%) assemblage which includes amphibole-biotite-magnetite-quartz and accessory apatite (Table 2g, App. D). The required magnetite-apatite fractionation in the genesis of the Deception Rhyolite and

Quartz Porphyry is illustrated by the magnitude of the negative P and Ti anomalies of the MORB spidergrams (Figs. 71-73).

The Deception Rhyolite in Hull Canyon (Fig. 4) is characterized by a decrease in REE (Fig. 39) and HFSE (Fig. 72) from the lower unit and Cleopatra Member to the upper unit. Similar chemical variation is observed within modern pyroclastic rocks and has been interpreted as originating through the tapping of a graded magma chamber from the roof downward into more mafic rocks (Smith and Bailey, 1966; Lipman, 1967). Sampling and available structural detail do not permit recognition of this inverse zoning within a single eruptive unit such as the Cleopatra Member; however, it is apparent within a limited eruptive sequence from lower unit and Cleopatra to the upper unit. The magnitude of the negative P and Ti anomalies (Fig. 72) in the spidergrams appears to be a sensitive fractionation indicator for rhyodacite compositions and supports the conclusions drawn from the REE data, that the upper unit is the least fractionated. The lower unit and Cleopatra Member are mostly tuffs, but the upper unit includes thick flows or domes. This sequence of pyroclastic eruptions followed by extrusion of viscous domes is typical of modern stratovolcanoes of island arcs and continental margins such as Mount Pelee or Mount St. Helens as well as continental caldera complexes such as the San Juan field.

The Shea basaltic andesite cannot be derived from Ash Creek basalts by closed or open-system fractional crystallization. It is also impossible to relate the Shea Basalt to more fractionated

compositions by fractional crystallization. The incompatible element ratios (Table 8, App. B), MORB spidergrams and compatible vs incompatible element plots (Figs. 77-79) indicate the Shea Basalt is derived from a distinctive source more like that of the Green Gulch basalts than the Ash Creek basalts.

Volcanics of the Green Gulch Block

The mafic rocks of the Green Gulch Volcanics include high-Mg primitive and evolved basalts. The Cr vs Y and Ni vs Zr plots (Fig. 77-79) suggest these rocks evolved from parental magmas produced by 12-23% partial melting of a lherzolite source. The Cr vs Y plot suggests initial olivine dominated fractionation followed with increasing proportions of clinopyroxene and plagioclase at shallower levels. This interpretation agrees with the sample distribution on the isomolar plots (Figs. 21 & 22) and observed relict phenocrysts (Table 4).

Primitive basalt, evolved basalt, basaltic andesite and andesite are interlayered in the Green Gulch succession. Ranges of incompatible element ratios (Table 9, App. B) vary but overlap among the different compositions. This feature is consistent with an open-system fractional crystallization model (O'Hara, 1977). The evolved basalts may be derived from a primitive basalt melt (Table 3a, App. D) by clinopyroxene-plagioclase-olivine crystallization. Magnetite and apatite are also required to satisfy Ti and P variation. By increasing the percentage of

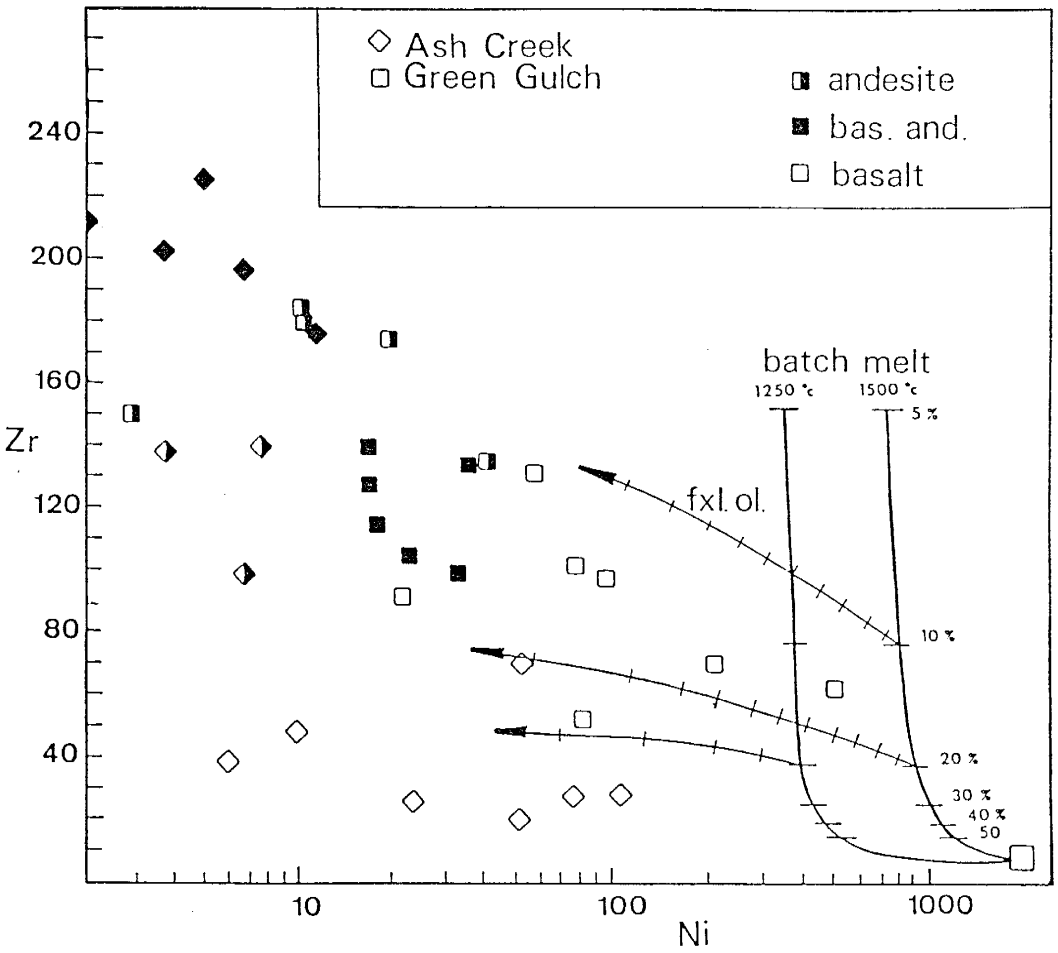

Fig. 78. Zr-Ni fractionation for batch melting of a lherzolite source and olivine-dominated crystallization (ticks = 5% increments) of the parental magma (after Rajamani et al., 1985 and Condie, 1986). Symbols: open = basalt, solid = basaltic andesite, half-solid = andesite-dacite.

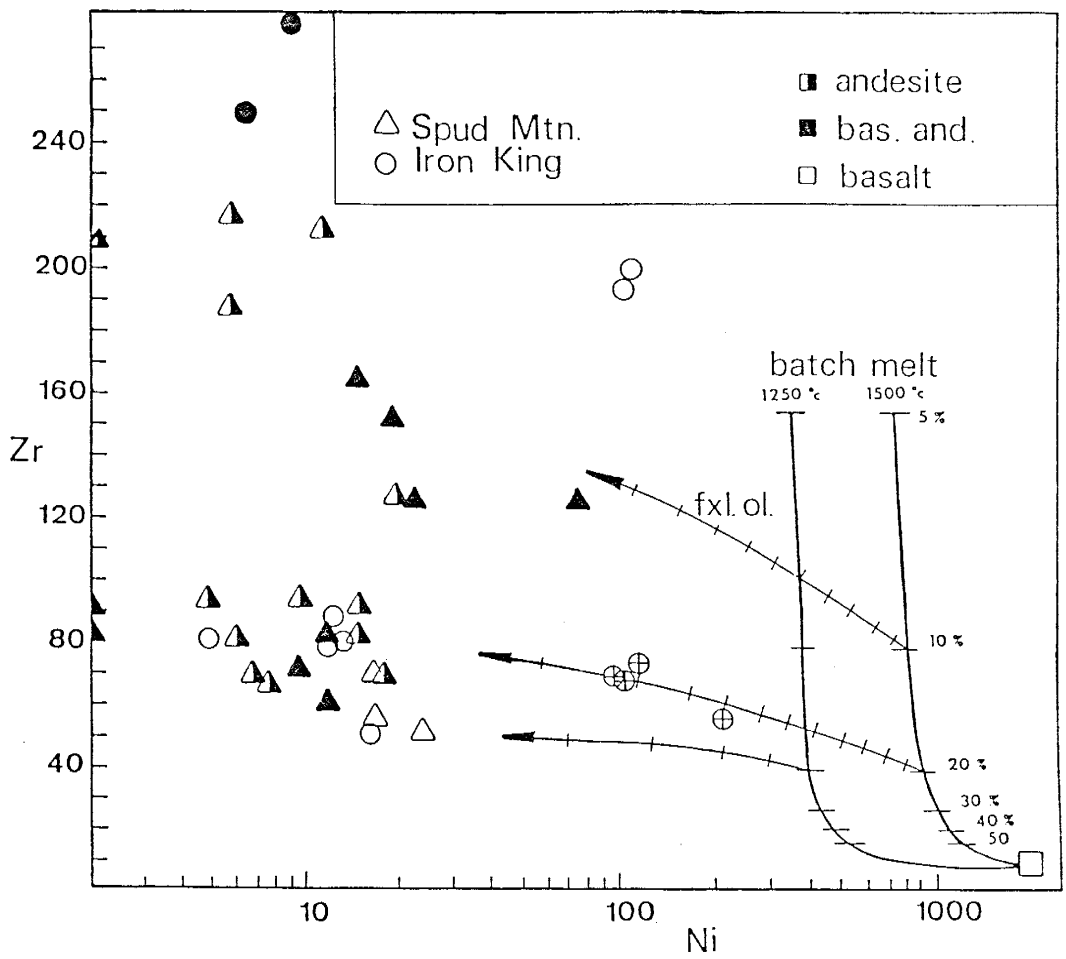

Fig. 79. Zr-Ni fractionation for batch melting of a lherzolite source and olivine-dominated crystallization (ticks = 5% increments) of the parental magma (after Rajamani et al., 1985 and Condie, 1986). Symbols: open = basalt, solid = basaltic andesite, half-solid = andesite-dacite, circles with crosses = Bluebell basalts.

plagioclase and decreasing magnetite in the crystallizing assemblage, the Green Gulch primitive basalt may yield the basaltic andesite (Table 3b, App. D). The primitive to evolved basalt fractionation link requires the percentage of leakage to exceed cumulate, but the primitive basalt to basaltic andesite link requires the cumulate fraction to exceed leakage from the magma chamber. Although Cr presents problems for the latter model, the squared residuals for Ni, Sc and V are low suggesting the model is possible.

The Green Gulch basaltic andesite melt may yield the Green Gulch andesite (Table 3c, App. D) by open-system fractionation of a plagioclase-clinopyroxene dominated assemblage with magnetite and minor amphibole. This system requires leakage to slightly exceed residue accumulation. The Green Gulch dacite is modelled from andesite by closed system crystal fractionation of a plagioclase-amphibole-clinopyroxene-magnetite assemblage with traces of apatite and allanite to satisfy variation in P and light REE contents (Table 3d, App. D).

Volcanics of the Big Bug Block

The Bluebell basalts are the least fractionated mafic rocks of the Big Bug block. The Cr-Y and Ni-Zr plots suggest these basalts originate by 16-20% partial melting of a lherzolite source and subsequent olivine-clinopyroxene fractionation (Figs 77-79). Isomolar projections (Figs. 23 & 24) suggest an olivine-

plagioclase dominated fractionation. The Th/Yb ratios (Table 10, App. B) and MORB spidergrams suggest the Bluebell basalts are unrelated to any basaltic andesites or andesites of the Big Bug block.

The remaining Iron King and Spud Mountain basalts are quite fractionated. The Cr-Y and Ni-Zr plots (Figs 77-79) suggest extensive olivine-clinopyroxene fractionation of a parental magma produced by 20-30% partial melting. These basalts plot near the one atmosphere cotectic on the isomolar plots suggesting low pressure equilibration following fractionation from parental liquids. The Iron King basalts are plagioclase-phyric and the Spud Mountain basalts are aphyric.

Although fractional crystallization links were tested for most mafic to intermediate to felsic links, only a few models are viable. The Spud Mountain basalts cannot be linked to the voluminous Spud Mountain andesite flows by cloased or open-system crystal fractionation. The andesites are modelled successfully by closed system fractional crystallization of a plagioclase-clinopyroxene assemblage with minor amphibole, magnetite and apatite (Table 4a, App. D) from the high-Ti Spud Mountain basaltic andesite (smb). The same genetic link can be accomplished by open system fractionation using a plagioclase-amphibole-magnetite and trace apatite assemblage. This model (Table 4b, App. D) requires leakage to exceed crystal accumulation.

The high-Ti, HFSE enriched basaltic andesite and 'andesite' of the Iron King Volcanics cannot serve as a parent to the more

fractionated Big Bug volcanics. The Cr-Y and Zr-Ni plots (Figs. 77-79) require extremely low degrees of partial melting for a lherzolite source to produce parental magmas for this suite. The Yb normalized Ce-Ta covariation plot suggests these rocks evolved from parental magmas generated from an enriched source (Fig. 80) not unlike that which produced the Green Gulch basalts.

The Spud Mountain andesites may be capable of generating the Spud Mountain rhyolites by fractional crystallization of plagioclase, minor amphibole-clinopyroxene-biotite-magnetite. Traces of apatite, zircon and allanite are required to reduce the modelled increase in Y, Zr and light REE. The link however, is still quite dubious as modelled increases of Th, Eu, Y, Zr and Ta do not match those of the rhyolite (Table 4c, App. D). Because of the altered condition of much of the rhyolite and possible tuffaceous origin, a possible genetic link should not be dismissed.

The Iron King basalts and the andesitic Spud Mountain crystal tuff sample distribution suggests potential links on the Ni-Zr plot (Fig. 79). The best model (Table 4d, App. D) requires 10% crystallization of an amphibole-plagioclase-magnetite assemblage from an Iron King melt. However, the model does not reproduce the Th, Eu, Cr, Sc and V concentrations. It is probable, however, that these rocks evolved from similar parental magmas.

The Spud Mountain crystal tuff composition is capable of generating the Quartz Porphyry by crystallization of a simple, plagioclase-clinopyroxene-ilmenite assemblage with traces of

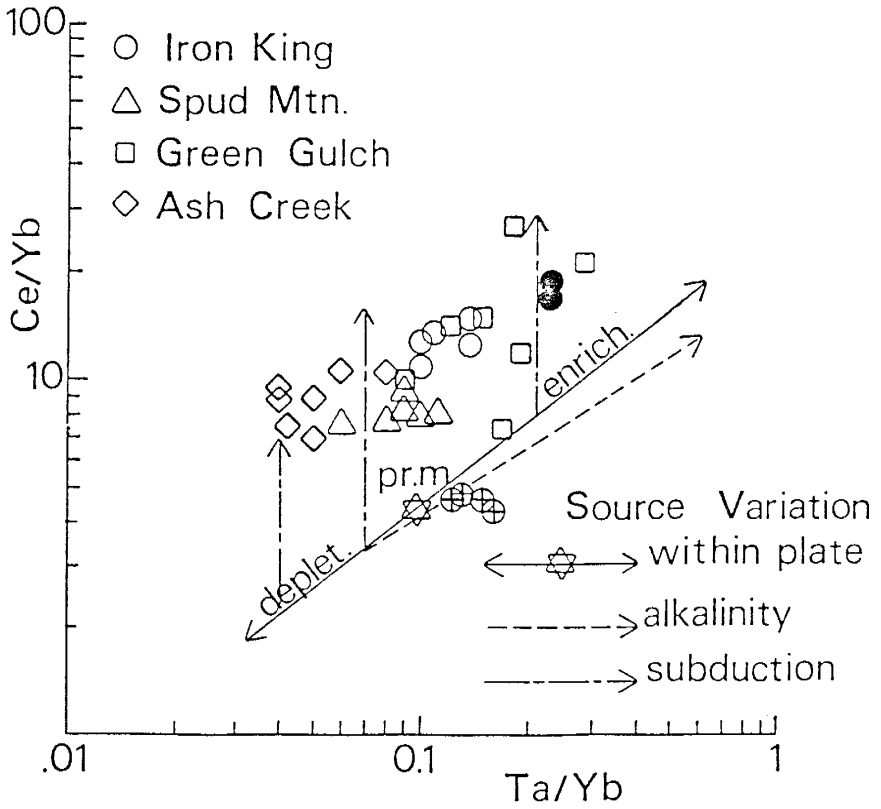

Fig. 80. Yb-normalized Ce-Ta covariation diagram (after Pearce, 1982) for Yavapai basalts. Solid symbols represent HFSE-rich Iron King mafic rocks. Bluebell basalts are circles with crosses. The star represents primordial mantle. Vectors indicate effects of within plate enrichment and depletion, subduction, and alkalinity source variations.

zircon and apatite to reduce Y and heavy REE increases. The modelled HFSE and REE concentrations suggest this is a vaiable model (Table 4e, App. D).

It is not possible to link all units within a given block by fraction crystallization. However, a number of successful links in each block provides a framework for evolution of the volcanic pile. The Green Gulch Volcanics display a nearly continuous compositional spectrum from primitive basalts to dacites which may be linked by fractional crystallization. The mafic parent for andesites of the Ash Creek is not present, but modelling suggests it is similar (but less enriched) to evolved basalts of the Green Gulch Block. The andesites of the Ash Creek Block may be related to associated dacites and rhyodacites by fractional crystallization. The successful fractionation model links Big Bug Volcanics suggest that andesites are derived from fractional crystalization of basaltic andesites or basalt and felsic rocks may be derived from the andesitic volcanics by fractional crystallization.

Mantle Source

The mantle source of Yavapai magmas is characterized using incompatible element ratios. Ratios of the least fractionated (Mg number > 45) mafic volcanics are presented on a primodial mantle-normalized graph (Fig. 81) with reference plots for modern basalts (Knoper and Condie, 1988). The patterns for the Green Gulch and

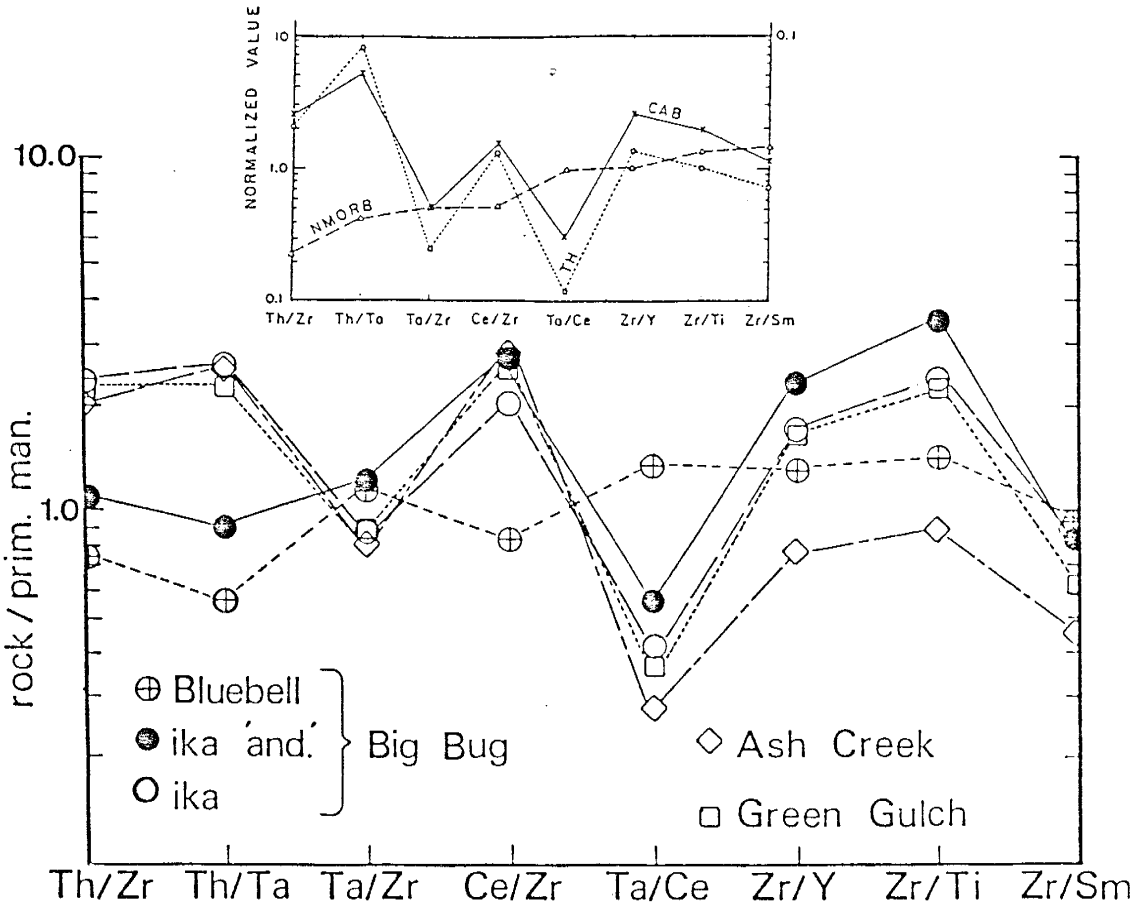

Fig. 81. Primordial mantle-normalized incompatible element ratios for mean compositions of Yavapai mafic volcanics (Mg No. >45) after Knoper and Condie (1988). Normalized values from Wood (1979). Reference plot key: CAB = calc-alkaline basalt, TH = tholeiitic basalt.

Iron King basalts indicate nearly identical sources. The Ash Creek basalt pattern, on the other hand, indicates a source depleted in Y, Ti and Sm relative to Zr. The HFSE-rich Shea basaltic andesite is not shown (Mg number < 40) but has a pattern like that of the Green Gulch basalts. Consequently, the Ash Creek volcanics tapped both enriched and depleted mantle sources. The Bluebell basalts resemble N-MORB whereas the other Iron King basalts match CAB patterns. Consequently, Big Bug basalts also carry multiple source signatures. The HFSE-rich Iron King suite appears transitional between CAB and MORB.

The Yb-normalized Ce-Ta covariation diagram (Fig. 80) is also an indicator of source variation (Pearce, 1982). Vectors are indicated for effects of within plate enrichment, depletion, and the subduction component relative to primordial mantle. The Bluebell basalts plot near the primordial mantle ratio. The position of the HFSE-rich Iron King suite suggests an original MORB-like source modified by within plate and/or subduction zone enrichment or possible crustal contamination. The Green Gulch Volcanics may also reflect some within plate enrichment or the effects of open-system fractionation. The distribution of the Ash Creek basalts is compatible with derivation from a depleted source overprinted by a subduction component.

Although the Shea basaltic andesite has incompatible element ratios comparable to CAB, it also has trace element characteristics similar to WPB (Figs. 42 & 44). This suggests a possible origin from a WPB-type enriched source, to which the

subduction component is added later. The Th-Ta covariation plot (Fig. 45) and Th-Hf-Ta (Figs. 46 & 47) suggest a similar origin for the HFSE rich suite from the Big Bug Block. The Th-Hf-Ta plot suggests some continuity between the MORB-like Bluebell lavas and HFSE rich suite. Vectors suggest mantle enrichment plus Th addition via the subduction component or crustal contamination may produce the HFSE rich suites.

In summary, the Ash Creek, Green Gulch and Big Bug blocks all contain basalts derived from an enriched mantle source much like the source of modern CAB. The Ash Creek and Big Bug basalts also reflect mantle source variations. A depleted source produced basalts with LKT affinities and extremely low HFSE and REE contents in the Ash Creek block. The Big Bug block contains basalts with nearly primordial ratios plus HFSE enriched basalts. The incompatible element plots suggest within-plate enrichment plus subduction zone enrichment and/or contamination may account for an apparent transition from MORB-WPB type basalts to CAB.

VI. TECTONIC SETTING OF THE YAVAPAI SUPERGROUP

Introduction

Identification of tectonic setting to this point, is based on geochemical discriminants. This technique requires additional constraints as misidentification of tectonic setting is possible. For example, basalts with MORB geochemical characteristics may be erupted during initial island arc formation, back-arc rifting, and in continental rifts and WIP settings (Pearce, 1982; Saunders and Tarney, 1984; Colley and Hindle, 1984; Gill, 1987; Crow and Condie, 1988). Lavas with arc geochemical signatures may be produced in within-plate continental settings by crustal contamination, within-plate enrichment processes or tapping subcontinental lithosphere that was involved in an earlier subduction event (Cox, 1983; Thirlwall and Jones, 1983; Alibert et al., 1986; Gust and Arculus, 1986).

Additional constraints for interpretation of ancient tectonic settings include lithologic associations, inferred sedimentary environments and sediment provenance, the igneous compositional range and series (continuous or bimodal, tholeiitic or calc-alkaline), experimental constraints on magma genesis, composition and structural character of plutons and the style of

deformation and metamorphism (Miyashiro, 1974; Dickinson and Suczek, 1979; Condie, 1982; Dickinson et al., 1983; Brown et al., 1984). Identification of the tectonic setting of the Yavapai Supergroup is therefore based on a diverse group of constraints.

Metamorphic and Plutonic Constraints

The Ash Creek and Green Gulch blocks contain mineral assemblages characteristic of greenschist to lower amphibolite facies metamorphism. The Big Bug block contains greenschist to middle amphibolite assemblages formed at temperatures of 500-600°C and pressures of 2 to 4 kb (Anderson, 1972; O'Hara, 1980; Blacet, 1985; Karlstrom and Bowring, 1988). The metamorphic facies which characterize the Yavapai Supergroup form at temperatures of 300-600°C and pressures of 1.5 to 4.5 kb at depths of 5-16 km in volcanic arcs (Ernst, 1976). The greenschist to amphibolite facies which characterize each block, and the presence of staurolite and andalusite within the Big Bug block are typical of the low-pressure, high heat flow conditions of regional metamorphism along the volcanic-plutonic axis of modern arc systems (Dewey, 1970; Miyashiro, 1973; Ernst, 1976). The association of greenschist to amphibolite facies metavolcanic rocks with large volumes of granitic rock suggests relatively deep portions of volcanic arc(s) are represented by the Yavapai Supergroup and associated plutonic rocks (Miyashiro, 1973). The depths suggested by the metamorphic-plutonic association and

metamorphic facies are compatible with the presence of metamorphic rocks at depths between 3 and 10 km in the Lesser Antilles, a Mesozoic-Cenozoic mature, island arc system developed on oceanic crust (Tomblin, 1974). Consequently, the metamorphic facies which characterize the tectonic blocks of the Yavapai Supergroup do not require collisions of arcs, microplates or continents or the presence of underlying continental crust.

Granitoid plutons constitute a major portion of the Ash Creek, Big Bug and Green Gulch blocks. The plutons of the Ash Creek block consist of low-K quartz diorite, tonalite and granodiorite; the Green Gulch block plutons are medium-K tonalite, granodiorite and quartz monzanite (Anderson and Blacet, 1972; DeWitt, 1986). Plutons of the Big Bug block include medium-K granodiorite and quartz monzanite and the distinctive two-mica, microcline-rich Crazy Basin Quartz Monzanite (CBQM) (Anderson and Blacet, 1972; Karlstrom and Conway, 1986). The compositional range and calc-alkaline, metaluminous character of most plutonic rocks is comparable to that of granitoid plutons exposed in Mesozoic-Cenozoic calc-alkaline arcs of ocean islands or continental margins; however, the strongly peraluminous CBQM is more typical of continental margins than island arcs (Brown, 1982; Brown et al., 1984; Pearce et al., 1984). The mineral composition of the CBQM resembles that of granites that are interpreted as originating through the partial melting of metasediments (Karlstrom and Conway, 1986). Initial investigations suggest that for comparable values of SiO_2, the plutons of the Big Bug block

contain greater concentrations of K and Rb than those of the Ash Creek and Green Gulch blocks (Anderson and Blacet, 1972; Anderson, 1972; Blacet, 1985). Subsequent investigations indicate the plutons of the Green Gulch block are higher in Rb, Ba, Zr and Y than the Ash Creek block plutons (DeWitt, 1986). It is emphasized that these chemical data are of a reconnaissance nature and seven plutonic units are mapped within the Ash Creek block alone (Anderson and Blacet, 1972). The higher K and Rb of the Big Bug block plutons may result from greater degrees of crustal contamination, subduction zone enrichment or source variation relative to other blocks (Saunders et al., 1979; Brown et al., 1984; Takahashi, 1986; Hildreth and Moorbath, 1988). Without a detailed trace element and/or isotopic investigation of the granitoid plutons, it is not possible to narrow the origin of the variation. If reconaissance chemical analyses of the collective plutonic suite are representative, these data are compatible with an increase in crustal thickness from the Ash Creek to the Green Gulch to the Big Bug block. The general calc-alkaline character and compositional range is a compatible with continental margin or island arcs.

The plutons are important with regard to constraints on chronology of volcanism, plutonism and metamorphism. The plutons of the Ash Creek and Green Gulch blocks are 1740 to 1720 Ma and late kinematic, the CBQM of the Big Bug block is synkinematic at 1700 Ma (Krieger, 1965, Anderson et al., 1971; Karlstrom and Bowring, 1988). The Brady Butte Granodiorite is a prekinematic

1750 Ma pluton truncated by an unconformable surface which is also folded (Anderson et al., 1971; Blacet, 1985; Karlstrom and Bowring, 1988). The dating of these plutons and their relation to metamorphism indicates the volcanics of the Big Bug block were deformed 40 Ma later than volcanics of the Ash Creek and Green Gulch blocks. The general metamorphic style also varies among the Yavapai blocks. The development of foliation and transposition of units is much greater in most of the Big Bug block relative to other blocks (O'Hara, 1986). The only 1700 Ma deformation affecting the Ash Creek and Green Gulch blocks is a nonpenetrative deformation along the bounding faults.

Karlstrom and Bowring (1988) interpret the Ash Creek and Green Gulch blocks as correlative sequences thrust over the Big Bug block to produce a crustal scale anticline. The CBQM may have formed in response to crustal thickening during thrusting (Karlstrom and Conway, 1986). Consequently, Karlstrom and Bowring (1988) interpret the evolution of the Proterozoic rocks of the Southwest in terms of a complicated assembly of various terranes rather than a continual arc accretion from north to south (Reed et al., 1987). Although volcanic and associated plutonic activity of the Ash Creek, Green Gulch and Big Bug blocks may overlap with regard to age, and metamorphic conditions were similar; the difference in timing of deformation indicates these regions may have been separated. Therefore, tectonic evaluation of lithologic association and geochemistry should proceed on a block by block basis.

Lithologic Association

Lithologic proportions within the Ash Creek, Green Gulch and Big Bug blocks have been estimated using the Winchester and Floyd (1977) rock classification applied to the areal distribution of the map units of Anderson and Creasey (1958) and Anderson and Blacet (1972). Results are presented in Table 5. The Ash Creek block contains the highest percentage of felsic rocks including domes, lavas and tuffs. Andesites include thick flows or domes and pillow breccias. The abundance of felsic domes and lavas and mafic dikes and sills suggests that the Ash Creek Block preserves a vent to proximal volcanic facies (Williams and McBirney, 1979; Roobol and Hacket, 1986; Cas and Wright, 1987). Furthermore, Lindberg (1986) interprets the sequence at Jerome as a submarine caldera. Massive sulfide deposits occur at the top of felsic eruptive sequences at Jerome and along the east flank of Mingus Mountain (Lindberg, 1986). The proximal to vent facies succession is buried by volcaniclastic turbidite deposits, pelite, banded ironstone, cherts and mafic scoria and hyaloclastite. The upper volcaniclastic succession also includes some lavas and gabbro with LKT affinities. The Mingus Mountain succession records a transition from a proximal volcanic succession dominated by andesitic to felsic volcanics to a succession of volcaniclastic deposits and tholeiitic volcanics.

The Green Gulch block contains the highest percentage (Table 5b) of basaltic andesite and andesite and like the Ash Creek

LITHOLOGIC PROPORTIONS:

Table 5a. The Ash Creek Block

Dacite & Rhyodacite	40%
Volcaniclastic Sediment	28%
Andesite & Basaltic Andesite	20%
Basalt & Gabbro	10%
Banded Ironstone & Chert	2%

Table 5b. The Green Gulch Block

Basaltic Andesite & Andesite	42%
Basalt & Gabbro	38%
Dacite & Rhyodacite	14%
Volcaniclastic Sediment	5%
Banded Ironstone & Chert	1%

Table 5c. The Big Bug Block

Basalt & Gabbro	45%
Basaltic Andesite & Andesite	30%
Rhyodacite & Rhyolite	15%
Volcaniclastic Sediment	8%
Banded Ironstone & Chert	2%

block, exhibits a compositional range from basalt to rhyodacite. The mafic to intermediate compositions are mostly lavas and dikes. Some of the andesites and dacites are tuffs. The abundance of lavas suggests a proximal volcanic facies. The sedimentary portion includes volcaniclastic breccias and conglomerates, tuffaceous sediment and pelite.

The Big Bug block (Table 5c) includes the greatest proportion of basalts but also contains a high percentage of andesites. This terrane also exhibits the full compositional spectrum including rhyolites. Abundance estimates for the Big Bug block sediments exclude the Spud Mountain sediments (sms) as Argenbright and Karlstrom (1986) interpret these as part of the Texas Gulch Formation. The sediments included are volcaniclastic breccias and conglomerates and tuffaceous sediments interlayered with the volcanics. Massive sulfide deposits occur in the Big Bug block and larger deposits are near felsic units (Anderson and Guilbert, 1979). The upper succession of the Big Bug block is composed of the bimodal Iron King Volcanics. Although much of the succession is mapped as an andesitic unit, true andesites were not recognized by the chemical analyses. Consequently, if the Iron King Volcanics are indeed the stratigraphic upper portion of Big Bug block, there is an evolution from the full compositional range typical of calc-alkaline successions to a late bimodal suite.

The full compositional range and abundance of andesites in the Yavapai Supergroup is unusual among Proterozoic suites of the Southwestern United States (Condie, 1987). Large volumes of

andesite occur only in convergent plate tectonic settings (Carmichael et al., 1974; Condie, 1976). Consequently, the confirmation of andesites in each block of the Yavapai Supergroup indicates a convergent plate margin tectonic setting for each block. The full compositional spectrum (Figs. 15-17) which characterizes each block is also indicative of volcanic arcs. Divergent plate margins in continental crust are characterized by bimodal volcanism and large volumes of clastic sediment. Divergent plate margins in oceanic crust are characterized by the typical ophiolite suite containing a thin layer of pelitic sediment and chert, tholeiitic pillow lavas, a sheeted diabase dike complex and an ultramafic base (Condie, 1976; Burke and Kidd, 1980; Hoffman, 1980; Dickinson, 1980). Clearly, sediments of the Yavapai Supergroup are volcaniclastic-dominated and they are subordinate to volcanic rocks. The coarse terrestrial clastic deposits of young continental rifts are missing, as are the carbonate and sandstone shelf sequences of passive continental margins (Hoffman, 1980; Dietz, 1972). The absence of such lithologic associations negates any serious consideration of either a MORB or continental rift setting.

Consequently, the choice of tectonic setting is that of an island arc or continental margin arc. Investigation of modern volcanic arcs indicates that the proportion of CAB, andesite and felsic rocks increase with crustal thickness and are therefore more abundant in mature island arcs or continental margin arcs (Miyashiro, 1974; Saunders et al., 1980). Youthful arcs contain

greater proportions of LKT and basaltic andesite. Although major element criteria indicate most Yavapai basalts are tholeiitic, trace element characteristics are more like those of CAB. Each block of the Yavapai Supergroup contains andesite and felsic volcanics equal to or exceeding basalt in abundance. This feature does not favor an immature or primitive island arc.

Tectonic discrimination by sediment provenance studies is not without complication (Dickinson, 1982; Underwood, 1986). However, investigation of sediments from forearc and back-arc basins associated with continental arcs and island arcs suggests basins associated with continental arcs are characterized by sediments with high percentages of quartz, feldspar and sedimentary and metamorphic lithic fragments (Dickson et al., 1986; Packer and Ingersoll, 1986). These criteria are difficult to apply to the Yavapai Supergroup as much of it represents proximal volcanic facies. However, clasts of underlying continental basement have been recognized in Miocene volcanic-dominated intra-arc basin successions of Japan (Tanimura et al., 1983). The Grapevine Gulch Formation of the Ash Creek block is more typical of a distal facies, containing a large portion of coarse to fine volcaniclastic sediment. The investigation of Anderson and Creasey (1958) indicates that all clasts are volcanic. Furthermore, the conglomeratic horizons in the Green Gulch and Big Bug Blocks are dominated by volcanic or chert clasts. The limestone clasts which are locally common in the volcaniclastic beds of the Iron King Volcanics are probably derived from

contemporaneous limestones as indicated by the local presence of thin limestones interbedded with tuffaceous rocks. The inclusion of small volumes of carbonate clasts within the volcaniclastic beds and the presence of limestone beds suggests an island arc setting by analogy to Miocene successions exposed in the New Hebrides. Carbonate clasts are derived from limestone reefs which fringe the volcanoes and are incorporated in deep water volcaniclastic successions through turbidite deposition (Warden and Mitchell, 1972). The presence of limestone suggests that portions of the volcanic arc achieved shoal or subaerial status. Consequently, the clastic sequences of the Yavapai Supergroup lack any evidence for reworking of older plutonic, sedimentary or metamorphic rocks and do not support a continental margin origin.

Ironstone and chert are common to each block and provide additional constraints on the sedimentary depositional environment. Thin banded ironstones in the Yavapai Supergroup occur within both volcanic and volcaniclastic sequences (Anderson and Creasey, 1958; DeWitt, 1979). A survey of ironstones by Kimberley (1978) allows some interpretation of sedimentary environments by characteristics of the ironstone. The characteristics of the Yavapai ironstone (especially in the Ash Creek block) fit the criteria for deep water iron formation (DWAT-IF). These ironstones are observed in the upper part of the ideal turbidite sequence of Bouma (1962), are generally thin (<30 cm) and associated with volcaniclastic sediments and pelite. Kimberly (1978) interprets the environment as a deep-water slope

near a submarine volcano. Much of the ironstone in the Yavapai Supergroup consists of interlaminated fine clastic sediment and layers of ferruginous chert. These cherts are often spatially related to thicker layers of sulfide-bearing chert and sometimes to massive sulfide deposits. These characteristics are those of the tetsusekiei of Japan. The tetsusekiei are thin beds of cryptocrystalline chert and hematite associated with the Kuroko deposits of Japan (Lambert and Sato, 1974). Collectively, such rocks are referred to as exhalites in massive sulfide districts and suggest an origin by submarine hydrothermal activity for much of the Yavapai ironstone (Ridler, 1971; Kalogeropoulos and Scott, 1983; Johnson, 1986).

The Yavapai volcaniclastic turbidites and subaqueous pyroclastic flows are consistent with deposition on the flanks of a marine volcano. The turbidite deposits are dominated by volcanic clasts, and locally by plagioclase crystals indicating a volcanic source area. The turbidite sequence at Jerome (Ash Creek block) presents a problem. The high concentration of domes and thick rhyolitic flows in the Ash Creek block suggest a vent facies and the Deception Rhyolite sequence at Jerome a caldera (Lindberg, 1986). This type of volcanic association is typical of the apex of stratovolcanoes, yet the thick sequence of volcaniclastic deposits above it suggests a topographic depression or the lower flanks of a volcano. Furthermore, dome intrusion and extrusion continued during initial turbidite deposition as indicated by domes within the lower Grapevine Gulch Formation and chaotic

mixtures of rhyodacitic blocks and bedded slabs of turbidite. The only way to reconcile this relationship is by active subsidence. This provides a mechanism for preserving the apex of a volcanic center. Even if the entire Mingus Mountain area is considered as a cauldron filling sequence, it would stand little chance of preservation and incorporation in the stratigraphic record without regional subsidence. This is a problem for the entire Yavapai Supergroup as the volcanic association of each block is typical of the upper tier of stratovolcanoes. Rapid subsidence is the only method of preserving the vent to proximal facies of stratovolcanoes which are generally prominent topographic highs.

This solution may explain the apparently bimodal character of much of the Proterozoic volcanics of the Southwestern United States. The apex of an arc system is subject to rapid erosion and will be deposited in adjacent basins and along the lower flanks of the arc as volcaniclastic sediment. Consequently, the portion of the arc preserved in the geologic record will be the basalt-dominated basal sequence and associated extensional basin volcanics and sediments. Extensional basins are common features of modern arc systems and are recognized in arcs underlain by continental or oceanic crust such as Japan, New Zealand, Chile, and the South Sandwich and Mariana Islands respectively (Saunders and Tarney, 1984). These basins form by rifting of arc systems and the nature of the volcanic-sedimentary sequences preserved in such basins depends on the stage of basin development. Incipient or aborted rifts such as the Green Tuff Belt of Japan preserve

felsic volcanic centers overlain by sequences of mudstone, volcaniclastic sediments, and mafic lavas and tuffs (Cathles et al., 1983). Successful rifts develop into back-arc basins underlain by oceanic crust such as the Bransfield Strait or Lau Basin (Karig, 1971; Saunders and Tarney, 1979; Cathles et al., 1983). Mature back-arc basins have an ophiolite base but may be overlain by tuffaceous sediment and volcaniclastic deposits from an active arc and to a lesser extent from the remmant arc (Carey and Sigurdsson, 1984). Consequently, the character of the back-arc basin sequence depends on the stage of development. An incipient rift may preserve the end of the arc volcanic cycle characterized by felsic eruptives and followed by the LKT or MORB basaltic volcanism which characterizes initial rifting (Ohmoto, 1983; Kokelaar et al., 1984). An evolved back-arc basin is characterized by arc LKT to MORB basalts and felsic tuffaceous rocks from the adjacent arc (Condie, 1987). In this regard, the Yavapai successions show the greatest affinity to the incipient rift setting, especially the aborted Tertiary rifts of Japan.

The submarine volcanic succession in the Big Bug and Ash Creek blocks is much like that of the Oligocene to Pliocene succession of the Green Tuff region of Japan. The Green Tuff region is host to the Kuroko volcanogenic massive sulfide deposits (Anderson and Guilbert, 1979; Ohmoto, 1983). Massive sulfide deposition is coeval with the waning stages of a major andesite to dacite eruptive cycle. The spatial association of proximal massive sulfide deposits with dacite to rhyolite domes emphasizes

the timing of massive sulfide deposition with the end of an eruptive cycle as dome construction typically follows major pyroclastic eruptions (Williams and McBirney, 1979; Franklin et al., 1981; Lindberg, 1986). The inception of mafic volcanism overlaps waning felsic volcanic activity to produce a bimodal volcanic association along the massive sulfide horizons in both the Green Tuff and Yavapai successions (Ohmoto, 1983; Lindberg, 1986). In the Ash Creek block this sequence is represented by the eruption of the Gaddes and Brindle Pup andesites, the Buzzard and Burnt Canyon dacites, followed by the Deception rhyodacite tuffs and rhyodacite dome construction associated with massive sulfide deposition. The extrusion of Shea basaltic andesite prior to the Deception rhyodacite and the extrusion of mafic lavas and tuffs following the Deception rhyodacite produce the bimodal suite which characterizes the ore horizon (Lindberg, 1986). In the Big Bug block a similar sequence is represented by andesite flows and andesite to dacite tuffs of the Spud Mountain Volcanics followed by basalts, rhyolite and massive sulfides (Bluebell area) of the Iron King Volcanics. In the Green Tuff region volcaniclastic rocks, tuffs, mudstones and mafic lavas overly the massive sulfide horizon and are intruded by diabase (Ohmoto and Takahashi, 1983; Tanimura et al., 1983). In the Ash Creek block volcaniclastic turbidites, fine-grained epiclastic rocks, mafic tuffs and lavas of the Grapevine Gulch formation overly the massive sulfides. The Bluebell massive sulfide deposit of the Big Bug block is overlain by mafic volcanics, greywacke, volcaniclastics and pelite. Both

the Ash Creek and Big Bug successions are intruded by gabbro sills and mafic dikes with some relict diabasic texture (Anderson and Blacet, 1972; DeWitt, 1979; O'Hara, 1980; Lindberg, 1986). Diabase dikes are recognized as an indication of incipient rifting and the common occurrence of dikes and sills in the vicinity of massive sulfide deposits suggest both are localized by the same crustal flaws (Scott, 1980; Ratcliffe, 1987; Cathles et al., 1983).

The presence of Kuroko-type proximal massive sulfide deposits in the Yavapai terranes (Anderson and Guilbert, 1979; Lindberg, 1986; Vance and Condie, 1987) is consistent with the incipient rift interpretation. Regions of continental or oceanic crustal extension are often sites of major active and fossil hydrothermal systems. Numerous examples include the massive sulfide deposits and vents of modern mid-ocean ridge systems, the massive sulfide deposits of Tasmania, the Taupo-Rotorua geothermal fields of New Zealand and the Kupferschiefer Cu-Ag sulfide deposits of Europe (Corbett, 1981; Bischoff et al., 1983; Cole, 1984; Hannington et al., 1986; Krupp and Seward, 1987). The rifting of volcanic arcs is employed to explain the massive sulfide deposits and lithologic associations which characterize the Devonian West Shasta District of California, the Archean Abitibi greenstone belt of Canada and the Proterozoic massive sulfide district of Gunnison, Colorado (Lindberg, 1985; Ludden et al., 1986; Condie and Nuter, 1981; Knoper and Condie, 1986). The Early Proterozoic massive sulfide deposits and volcanic rocks of the Bagdad District are part of the Yavapai Province of Arizona (Anderson et al., 1955; Karlstrom and

Bowring, 1988) and are also interpreted as a possible back-arc basin succession (Conway, 1986). The presence of massive sulfides does not demand a back-arc setting as massive sulfides are also recognized in fore-arcs, trenches and mid-ocean ridges (Ripley and Ohmoto, 1977; Ohmoto and Takahashi, 1983; Bischoff et al., 1983). However, the extensive faulting and high heat flow which characterize back-arc extension provide the optimum environment for genesis of massive sulfide deposits (Cathles, 1983).

The proportion of metals in the Yavapai massive sulfide deposits also constrains the tectonic setting. The major factors which determine the size and proportions of metals of volcanogenic sulfides are the regional and local thermal history, the composition of seawater and the dominant rock type in the region (Franklin et al., 1981; Ohmoto and Skinner, 1983). Metal proportions vary with respect to the proximal or distal nature of the deposit (Plimer, 1978). If comparisons are restricted to the proximal type, the variations due to thermal history are reduced. The Iron King deposit of the Big Bug block is eliminated from comparison because of features suggesting distal deposits (Gilmour and Still, 1968; Lindberg, 1986). Although the geologic setting of the proximal Kuroko and Yavapai volcanogenic sulfides is quite similar, the metal proportions differ. The Yavapai deposits are Cu-Zn types; the Kuroko deposits are Zn-Pb-Cu types (Anderson and Guilbert, 1979; Franklin et al., 1981). The Zn-Pb-Cu types are most common in districts characterized by large proportions of sedimentary rocks and felsic volcanics or underlying continental

crust. Examples include the Green Tuff region of Japan, the Bathurst district of New Brunswick and the Tasmanian deposits. In districts where the underlying succession is dominated by mafic to intermediate volcanics or oceanic crust, the deposits are Cu-Zn types. Examples include the greenstone-hosted Archean deposits of Canada, the Cyprus deposits and the West Shasta District of California (Franklin et al., 1981; Reed, 1984). The deep (5-7 km) nature of hydrothermal circulation in extensional environments (Gregory and Taylor, 1981; Cathles, 1983) suggests some of the rock responsible for the metal ratios of massive sulfide deposits may not be exposed. Consequently, the ratios of ore metals may constrain the nature of the underlying crust. These ratios suggest the unexposed base of the Ash Creek and Big Bug blocks is dominated by mafic rock and favor a volcanic arc developed on oceanic crust. The investigations of Titley (1987) suggest the metal ratios of Laramide and younger ores are also controlled by the composition of this Proterozoic crust. Changes in ore metal ratios of Arizona coincide with the approximate boundary between Proterozoic successions with affinities to island arc settings and those of continental margin settings (Condie, 1987; Titley, 1987).

In summary, the preservation of vent and proximal volcanic facies in the Yavapai Supergroup is favored by the rapid and deep subsidence which characterizes initial arc extension (Guber and Merril, 1983; Ohmoto, 1983). The volcanic succession of each block appears to be mostly submarine as indicated by pillow lavas and breccias, hyaloclastite, turbidite deposits, massive sulfide

deposits and ironstone. Ratios of metals in proximal volcanogenic massive sulfides suggest the Yavapai volcanic arc developed over oceanic crust. The lack of older plutonic, metamorphic or sedimentary clasts in the sedimentary suites also favors an island arc over a continental arc but is biased by the proximal character of most of the volcanic suite.

Geochemical Constraints - Discussion

Geochemical discriminants (Table 6) for the Ash Creek block volcanics favor an origin in a mature island arc. The basalts have LKT-CAB chemical affinities; however, the Shea basaltic andesite exhibits chemical affinities to both CAB and WPB. The andesitic to felsic volcanics have geochemical signatures transitional between those of island and continental margin arcs. The Green Gulch volcanics also have compositions intermediate between island and continental margin arcs. The Big Bug basalts and basaltic andesites mostly have chemical signatures which range from island arc LKT and CAB to continental margin CAB. The subordinate Bluebell basalts resemble MORB and the HFSE-enriched basaltic andesites have compositions transitional between MORB-WPB and CAB.

A mature island arc is the tectonic setting which best accounts for both the chemical affinities and lithologic association of each block. However, an origin as a continental margin arc cannot be dismissed solely on the basis of the

Table 6. Summary of Geochemical Discrimination Plots for the Yavapai Supergroup

Discriminant	Block	Composition- Unit	Tectonic Setting
Ti-Zr (Pearce et al., 1981)	Ash Creek	basalt (Ymsma,ggt)	arc or MORB
		basaltic andesite (Shea)	WPB
		andesite-rhyodacite	arc
	Green Gulch	basalt	arc or MORB
		basaltic andesite	arc, MORB, WPB
		andesite-rhyodacite	arc
	Big Bug	basalt (sma-smb,ika)	arc or MORB
		basaltic andesite (smb)	arc, MORB
		basaltic andesite (ika)	WPB
		andesite-rhyodacite	arc
Ti-Zr-Y (Pearce and Cann, 1973)	Ash Creek	basalt	arc, LKT
		basaltic andesite (Shea)	arc-MORB
	Green Gulch	basalt	arc-MORB
		basaltic andesite	arc-MORB
	Big Bug	basalt	arc-MORB
Ti-Zr-Sr (Pearce and Cann, (1973)	Ash Creek	basalt	LKT
		basaltic andesite (Shea)	MORB
	Green Gulch	basalt and andesite	CA
	Big Bug	basalt (sma-smb & ika)	LKT, CA
		basalt (Bluebell)	MORB
		basaltic andesite (smb)	CA
		basaltic andesite (HFSE-rich, sm & ika)	MORB
Ti-Mn-P (Mullen, 1983)	Ash Creek	basalt	LKT-CA
		basaltic andesite (Shea)	WPB, A
	Green Gulch	basalt-basaltic andesite	LKT, CA
	Big Bug	basalt (Bluebell)	LKT
		basalt-basaltic andesite	LKT-CA
		basaltic andesite (HFSE-rich, sm & ika)	WPB, A
Th-Hf-Ta (Wood, 1979)	Ash Creek	basalt-rhyodacite	arc, CA
		basaltic andesite (Shea)	arc, CA
	Green Gulch	basalt-rhyodacite	arc, CA
	Big Bug	basalt-rhyolite	arc, CA
		Bluebell basalt	WPB-MORB
		basaltic andesite (HFSE-rich)	WPB-MORB to arc, CA

Table 6. - Continued

Discriminant	Block	Composition- Unit	Tectonic Setting
Ti-V (Shervais, 1982)	Ash Creek	basalt	arc
		basaltic andesite (Shea)	WPB, A
	Green Gulch	basalt-basaltic andesite	arc-MORB
	Big Bug	basalt-basaltic andesite	arc-MORB
		basaltic andesite (HFSE-rich)	MORB-WPB
Ti-Cr (Pearce, 1975)	Ash Creek	basalt	arc
	Green Gulch	basalt	arc-MORB
	Big Bug	basalt (ika, sma-smb)	arc
		basalt (Bluebell)	MORB
Cr-Y Pearce, 1982)	Ash Creek	basalt	arc
		basaltic andesite (Shea)	arc-MORB
	Green Gulch	basalt-basaltic andesite	arc to arc-MORB
	Big Bug	basalt and basaltic andesite	arc
		basalt-basaltic andesite (Bluebell & HFSE-rich suite)	MORB
Th/Yb-Ta/Yb (Pearce, 1982)	Ash Creek	basalt	IA, LKT-CA
		basaltic andesite	IA, CA
	Green Gulch	basalt-basaltic andesite	CM, CA (or IA,A)
	Big Bug	basalt-basaltic andesite	IA, CA-CM, CA (or IA,A)
		basalt (Bluebell)	MORB
Cr-Ce/Sr (Pearce, 1982)	Ash Creek	basalt	arc
		basaltic andesite (Shea)	MORB-arc
	Green Gulch	basalt-basaltic andesite	arc
	Big Bug	basalt-basaltic andesite	arc
		basalt-basaltic andesite (Bluebell & HFSE-rich suite)	MORB

Table 6. - Continued

Discriminant	Block	Composition- Unit	Tectonic Setting
Ce/Yb-Ta/Yb (Pearce, 1982)	Ash Creek	basalt-bas. andesite	arc, CA
	Green Gulch	basalt-bas. andesite	arc, CA
	Big Bug	basalt-bas. andesite	arc, CA
		basalt (Bluebell)	MORB-arc
Ba/Ta (Gill, 1981)	Ash Creek	basalt-andesite	arc
		basaltic andesite	MORB-WPB-CR
	Green Gulch	basalt-andesite	arc
	Big Bug	basalt-andesite	arc
		basalt-basaltic andesite (Bluebell & HFSE-rich suite)	MORB-WPB-CR
La/Th (Gill, 1981)	Ash Creek	andesite	arc
		basaltic andesite (Shea)	E MORB
	Green Gulch	basaltic andesite	E MORB-arc
		andesite	arc
	Big Bug	andesite	arc
		basaltic andesite	E MORB-arc
		basaltic andesite (HFSE-rich)	N MORB-E MORB
Spidergram (Pearce, 1982; 1983)	Ash Creek	basalt	IA, CA
		basaltic andesite (Shea)	CM or BA, CA
		andesite	IA-CM, CA
	Green Gulch	basalt	IA-CM, CA
		basaltic andesite	CM, CA
		andesite	IA-CM, Ca
	Big Bug	basalt (ika)	IA-CM, CA
		(sma-smb)	IA, LKT-CA
		(Bluebell)	MORB-WPB, LKT
		basaltic andesite (hi-Ti)	CM, CA
		(hi-Al)	IA, LKT-CA
		(HFSE-rich)	CM or BA, CA
		andesite (sma)	IA-CM, CA
		(smct)	IA, CA

Table 6. - Continued

Discriminant	Block	Composition- Unit	Tectonic Setting
Ratio Screens (Condie, 1988)	Ash Creek	basalt	IA, LKT
		basaltic andesite (Shea)	WPB-MORB
		andesite	IA-CM
	Green Gulch	basalt-basaltic andesite	CM, CA
		andesite	IA-CM
	Big Bug	basalt (sma-smb)	IA, LKT-CA
		(ika)	IA-CM, CA
		(Bluebell)	WPB-MORB
		basaltic andesite (hi-Ti)	IA-CM, CA
		(hi-Al)	IA, LKT-CA
		(HFSE-rich)	WPB-MORB
		andesite (sma)	CM
		(smct-smt)	IA

Key: IA = island arc
CM = cont. margin arc
MORB = mid-ocean ridge basalt
WPB = within-plate basalt
CR = cont. rift
LKT = low-K tholeiite
CA = calc-alkaline
A = alkalic

geochemistry of the volcanics. For example, the Green Tuff region of Japan has a basement of continental crust (Tanimura et al., 1983). The Green Tuff mafic and felsic volcanics exhibit Hf/Th ratios of 1.1-3.8 and .60-1.4 respectively (Dudas et al., 1983). The Ash Creek block has a Hf/Th ratio range of 1.5-2.6 and 1.0-1.6 for mafic and felsic volcanics, respectively (Table 8, App. B). Much overlap is also observed for ratios of Th/Yb and Ce/Yb in mafic rocks. The overlap between ranges does not permit unequivocal rejection of a continental basement below the Yavapai volcanics or require the presence of continental crust in the Yavapai blocks. Isotopic studies indicate that some of the felsic rocks of the Green Tuff region are fractionation products of mafic magmas derived from mantle sources without contamination from continental crust (Dudas et al., 1983). Some of the similarities in chemical composition and chemical variance between the Yavapai and Green Tuff successions may be due to incipient rifting. The presence of Yavapai mafic to intermediate lavas with WPB to MORB compositions, or compositions that are transitional between WPB and arc lavas, is compatible with the initiation of back-arc extension in the Big Bug and Ash Creek blocks (Weaver et al., 1979; Pearce, 1982; Saunders and Tarney, 1984). The arc volcanic geochemical signatures and lithologic proportions indicate rifting was aborted prior to development of oceanic crust. The MORB-WPB and transitional basaltic andesites are exposed near prominent massive sulfide horizons in both the Ash Creek and Green Gulch successions. This association suggests that these rocks are

geochemical indicators of incipient arc rifting and consequently, the extensive faulting and high heat flow which optimize major hydrothermal activity. The Green Gulch block does not feature such rocks, nor does it contain a major massive sulfide deposit. If the Green Gulch block is correlative with the Ash Creek block, it may represent a lower or higher part of the succession or a separate volcanic center.

Incompatible element ratios and discriminant diagrams indicate similar mantle source regions for calc-alkaline lavas of the Green Gulch and Big Bug blocks. Element ratios also indicate that the tholeiitic Ash Creek basalts are derived from a relatively depleted mantle source. The HFSE-enriched Shea basaltic andesite is stratigraphically below the tholeiites and is derived from an enriched source more like that of the Green Gulch calc-alkaline basalts. The MORB-like Bluebell basalts of the Big Bug block lack a significant subduction component of LILE. The transitional basaltic andesites reflect source enrichment processes and perhaps minor addition of a subduction component or crustal contamination.

Such variation of magma sources is a trademark of modern volcanic arcs. Investigation of the Fiji island arc and back-arc system indicates initial eruption of LKT and andesite followed by eruption of volcanics with highly variable HFSE contents, some enriched and some depleted (Gill, 1987). The mature arc is dominated by medium-K tholeiitic and calc-alkaline andesites. Eruption of basalts characterized by strong HFSE and REE depletion

is temporally associated with back-arc extension (Gill, 1987). These depleted basalts are also recognized in the Tonga-Kermadee islands, Papua New Guinea, and Japan (Dudas et al., 1983; Johnson et al., 1985; Ewart and Hawkesworth, 1987). Saunders and Tarney (1984) suggest the character of the back-arc basalts depends on maturity of the associated subduction zone; N-MORB are associated with extension of youthful arcs and both N-MORB and CAB with mature arc extension. The Big Bug block displays the characteristics of extension of a mature arc system with MORB, CAB and transitional basalts. The compositional variety is explained by mantle source variation through wedge enrichment via devolatization of a descending slab and repeated melt extraction during basalt genesis (Crawford et al., 1981; Saunders and Tarney, 1984; Ewart and Hawkesworth, 1987; Hildreth and Moorbath, 1988).

The Ash Creek Volcanics include HFSE-REE-depleted basalts similar to those described by Gill (1987). These basalts were erupted following a major andesitic to rhyodacitic volcanic cycle. Although the HFSE and REE contents are markedly lower than other Yavapai basalts, the LILE and Ce-P subduction component is prominent suggesting parental magma genesis in a mantle wedge region subjected to previous melt extraction, but still receiving the subduction component from the descending slab. The high LIL/HFSE ratios of these rocks are characteristic of narrow back-arc basins associated with mature subduction zones (Saunders and Tarney, 1984).

VII. CONCLUSIONS

The geochemical data base, including trace elements, for the Yavapai Supergroup provides the foundation for achievement of project goals which include: (1) testing the mobility of trace elements in variably altered rocks, (2) arriving at a dependable rock classification, (3) identification of the tectonic setting of the volcanics and associated massive sulfide deposits, and (4) evaluation of magma origin for Yavapai volcanic rocks.

Investigation of variably altered dacite to rhyodacite of the Deception Rhyolite at Jerome, confirms the mobility of most major elements. The spectacular CaO and Na_2O depletion and local MgO and Fe_2O_3 enrichment associated with the fossil hydrothermal system is typical of the footwall zones of both Precambrian and Phanerozoic massive sulfide deposits. Al_2O_3 and TiO_2 are the least mobile major elements. Abundance of HFSE and REE in the altered rocks is diluted or concentrated by addition and subtraction, respectively, of major element components. However, ratios of these elements are relatively uneffected, except locally in zones subjected to the highest fluid/rock ratios. However, with a sufficient sample base ratios of HFSE allow recognition of protolith and correlation of volcanic units in the most altered rocks. The investigations at Jerome indicate HFSE and REE provide

a reliable data base for tectonic discrimination, lithologic classification and petrogenetic evaluation of ancient successions. Major elements and LILE elements, with the exception of Th, must be regarded with great caution due to their proven mobility.

Ratios of the relatively immobile HFSE are employed in lithologic classification of the Yavapai Supergroup. This classification confirms the presence of andesite in each tectonic block. The new classification also requires revision of some units. In the Ash Creek block, large portions of the Gaddes Basalt and Dacite of Burnt Canyon are andesites. The composition of the Brindle Pup Andesite is confirmed, but includes some basaltic andesite. The Shea Basalt is high-Ti basaltic andesite. Lithic tuff and gabbro from the Grapevine Gulch formation have basalt compositions which are nearly identical to dikes and lavas from the Spud Mountain Volcanics south of the Cherry Batholith. The felsic rocks of the Ash Creek block have dacite to rhyodacite compositions and constitutes the dominant lithotype of the block.

Volcanic nomenclature of the Big Bug block also requires revision. Unequivocal andesites are not recognized in the andesitic map units of the Iron King Volcanics. The Iron King Volcanics are dominated by basalt to basaltic andesite and rhyolite, composing a bimodal suite. The andesite composition of the Spud Mountain Volcanics is confirmed for both the andesitic lavas and the tuffs. The massive crystal tuff exposed south of Big Bug Mesa shows some variance from andesite to dacite. The identity of andesite clasts in the Spud Mountain breccia is also

confirmed, but the matrix suggests local mixtures of andesite and basalt. Numerous flows of basaltic andesite and lesser basalt are interlayered with the breccias. Andesites comprise a third of the Big Bug block.

The Green Gulch block includes a greater volume of basaltic andesite and andesite than indicated by previous work. The felsic samples are dacitic and a compositional continuum from basalt to dacite is preserved.

The tectonic setting of the Yavapai Supergroup is constrained by the structural, metamorphic and plutonic style and history, the lithologic and metallogenic associations and the geochemistry of the volcanics. The plutonic-volcanic association and greenschist to amphibolite facies metamorphism which characterize each block are typical of the low P/T metamorphic belts associated with the volcanic-plutonic axis of island arcs or continental margin arcs. These conditions do not require collisions between microplates or between arcs and cotinents. However, the 40 Ma difference in the timing of deformation and some plutonism between the Big Bug block and the Ash Creek and Green Gulch block suggest the tectonic environment should be interpreted with regard to individual blocks (Karlstrom and Bowring, 1988).

Plutonic rocks which intrude the Yavapai Supergroup range from quartz diorite to quartz monzanite and most are comparable to calc-alkaline plutons which characterize modern island and continental margin arc settings. The distinctive Crazy Basin Quartz Monzanite in the Big Bug block is more typical of

continental margin settings (Karlstrom and Conway, 1986). The Big Bug Volcanics include the only rhyolites recognized in the Yavapai Supergroup, another feature which suggests a thicker crust in the Big Bug block. The high proportion of felsic rocks in the Ash Creek block reflects the vent to proximal facies nature of the exposed succession, and does not require a continental margin setting. A similar succession is observed in the vent facies of St. Lucia, a mature island arc in the Lesser Antilles (Tomblin, 1979). All blocks lack clasts of continental derivation in the sedimentary beds and the characteristics of the ironstones indicate deep water basins proximal to marine volcanoes. The Cu-Zn character of the proximal volcanogenic massive sulfides in the Big Bug and Ash Creek blocks is more typical of a substrate dominated by mafic rock. Consequently, the lithologic and metallogenic association favors a mature volcanic arc with a base of oceanic crust.

Most of the Yavapai basalts are tholeiitic with regard to major elements but exhibit the trace element characteristics of modern calc-alkaline basalts. Affinities of the more fractionated volcanics vary among blocks. The Ash Creek andesites are tholeiitic and the felsic rocks are calc-alkaline by major element standards. The Green Gulch andesites and dacites are both calc-alkaline using major element criteria. Big Bug andesite lavas are tholeiitic, the tuffs and felsic volcanics calc-alkaline. The trace element composition of the Yavapai

andesites is similar to modern medium-K andesites from mature island arcs or continental margin arcs.

The confirmation of large volumes of andesite within each block is probably the most significant tectonic indicator as andesite is a major lithotype only in subduction zones. Application of numerous geochemical discriminants of tectonic environment confirm an origin as an island or continental margin volcanic arc. Andesitic and felsic volcanics of each block exhibit MORB normalized geochemical patterns intermediate between those of island and continental margin arcs. The majority of Yavapai basalts and basaltic andesites have trace element distributions comparable to mafic rocks from mature island arcs. The Green Gulch basalts trace element ratios and concentrations resemble those of continental margin arcs or alkalic island arcs.

A subordinate volume of the Ash Creek and Big Bug basalts and basaltic andesites exhibit geochemical affinities with MORB and WPB or compositions transitional between WPB and CAB. The presence of non-arc and transitional basalt varieties characterizes modern island and continental margin arcs which have been subjected to back-arc extension. The back-arc rifting suggested by the presence of non-arc and transitional basalts is compatible with the metallogenic character of the region, lithologic associations and preservation of the upper succession of stratovolcanoes. The occurrence of major hydrothermal systems in modern regions of crustal extension, similarities to Japanese Kuroko deposits and hydrothermal modelling indicates incipient

back-arc extension is the most favorable environment for production of the numerous massive sulfide deposits of the Big Bug and Ash Creek blocks. The subsidence which accompanies initial arc extension provides a mechanism for preservation of proximal to vent facies volcanics typical of prominent stratovolcanoes of which the Yavapai Supergroup may be representative. The Ash Creek volcaniclastic turbidite deposits are typical of arc basins, but conformably overly a stratovolcano. This sequence requires rapid subsidence typical of incipient arc rifting.

The origin of magmas which produced the volcanics of the Yavapai Supergroup is interpreted through the use of ratios of incompatible HFSE. These ratios indicate volcanoes of the Green Gulch and Big Bug blocks tapped nearly identical enriched mantle sources to produce basalts with trace element signatures comparable to modern calc-alkaline basalts. The Ash Creek and Big Bug basalts exhibit variations in mantle source. The Ash Creek volcanoes tapped both a depleted mantle source as evidenced by basalts with extremely low HFSE and REE contents, and an enriched mantle source that produced basaltic andesites. The Big Bug volcanoes produced MORB-like basalts from a source with near primordial trace element ratios and basalts which require enriched mantle sources. The MORB-like basalts lack any significant evidence of a subduction component in magma genesis. The incompatible element variation of the non-arc and transitional HFSE-enriched basalts suggests a continuum from MORB to WPB to transitional basalts through within plate source enrichment and

variable addition of the subduction component and/or crustal contamination.

The major and trace element composition of the Green Gulch and Big Bug andesites suggests slightly greater arc maturity than the Ash Creek andesites; however, the three blocks have a similar mantle source for calc-alkaline basalts. The mantle source variations of the Ash Creek and Big Bug volcanics are observed in modern island and continental arc systems subjected to back-arc rifting. The Green Gulch volcanics do not exhibit such source variation nor the consequent presence of basalts with MORB, WPB or transitional affinities. Furthermore, major massive sulfide deposits are unknown in the Green Gulch Volcanics. However, the preservation of a proximal volcanic center with large volumes of andesite presents problems without extension and subsidence. Previous investigations (Anderson and Blacet, 1972) indicate the presence of some high-Ti basaltic rocks, suggesting the presence of non-arc basalts; however, this investigation cannot confirm the existence of such basalts. Consequently, if the Ash Creek and Green Gulch successions are correlative, the Green Gulch Volcanics may represent a separate distinctive volcanic field along the arc or the next phase of arc volcanism following rifting. The pelitic base of the Green Gulch succession may be correlative with the upper part of the Grapevine Gulch volcaniclastic-pelitic sequence in the Ash Creek block. Lithologic associations and chemical composition neither confirm nor preclude correlation of the Green

Gulch and Ash Creek blocks. However, petrogenetic studies indicate a similar fractionation history.

Petrogenetic investigations indicate magmas which produced the Ash Creek and Green Gulch volcanics experienced extensive high pressure olivine-clinopyroxene fractionation with clinopyroxene-plagioclase dominated fractionation at lower pressures. The high pressure fractionation of olivine and clinopyroxene increases the percentage of aluminum in the residual liquid resulting in the appearance of normative corundum in basaltic andesites of the Green Gulch Volcanics. Application of pseudo-liquidus phase diagrams suggests a 30-45 km depth range for olivine-clinopyroxene fractionation, in agreement with the presence of olivine-clinopyroxene cumulates between 28 and 33 km in Phanerozoic island arcs. The eruptives of the Big Bug Block include highly fractionated basalts which experienced clinopyroxene-plagioclase fractionation at relatively low pressures. The Bluebell basalts are similar to MORB with a postulated generation at 20-25 kb and an olivine-plagioclase dominated fractionation trend. Basaltic andesites of all blocks equilibrated at low pressures. Modelling indicates the andesites of each block are products of fractional crystallization of basaltic parents, and in this respect they resemble modern andesites. The felsic volcanics, in turn, may be derived from the intermediate magmas by fractional crystallization.

In summary, the volcanic, sedimentary, metallogenic and plutonic associations, metamorphic conditions, geochemical

discriminants and petrogenesis of the Yavapai Supergroup indicate an origin in a volcanic arc associated with a convergent plate margin by uniformitarian analogy to younger Proterozoic and Phanerozoic plate boundaries.

These lines of evidence suggest an increase in crustal thickness (arc maturity) from the Ash Creek to the Green Gulch to the Big Bug block. The results of this investigation do not eliminate the possibility that these successions were deposited upon continental crust, especially the Big Bug succession. However, evaluation of the total data base favors an origin as a mature island arc (or arcs) constructed upon oceanic crust. Due to the temporal and spatial chemical variation of eruptives within single Phanerozoic arcs, it is extremely difficult to completely resolve the question of whether the individual blocks of the Yavapai Supergroup represent portions of the same arc or portions of different arcs. Petrogenetic data are compatible with the proposed Green Gulch-Ash Creek block correlation of Karlstrom and Bowring (1988). The source variation of mafic volcanics, geochemical discriminants, metallogeny and the preservation of the vent to proximal facies of intermediate to felsic eruptive centers suggest incipient back arc extension and associated subsidence affected each block of the Yavapai Supergroup. The lack of andesites in mafic-dominated Proterozoic successions with arc-like chemical compositions is interpreted as a preservational bias toward the basal portion of arc systems. The few Proterozoic successions which exhibit large volumes of andesites are evidence

or the incipient arc extension and related subsidence required to preserve the upper successions of mature arcs.

APPENDIX A.

SAMPLE LOCATION MAPS

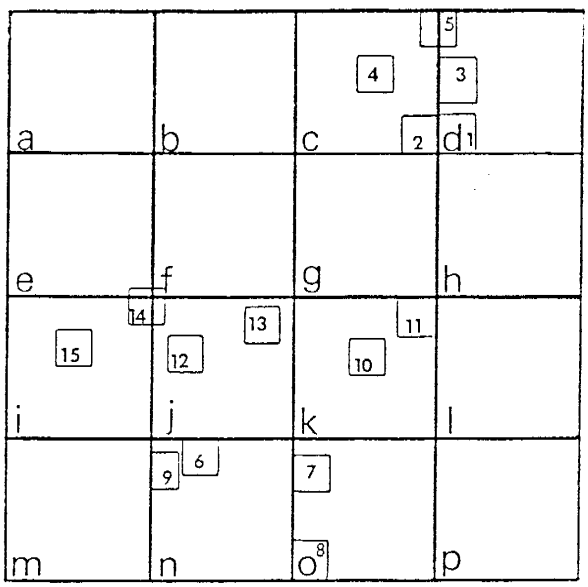

Index for U.S.G.S. 7.5' topographic maps used in this study: a = Chino Valley S; b = Prescott Valley N; c = Hickey Mtn.; d = Cottonwood; e = Prescott; f = Prescott Valley S; g = Humboldt; h = Cherry; i = Groom Creek; j = Poland Jct.; k = Mayer; l = Estler; m = Battleship Butte; n = Battle Flat; o = Cleator; p = Cordes. Approximate loctions of sample maps 1-15 are indicated. Contacts and map unit abbreviations on maps 1-15 after Anderson and Creasey (1958) and Anderson and Blacet (1972).

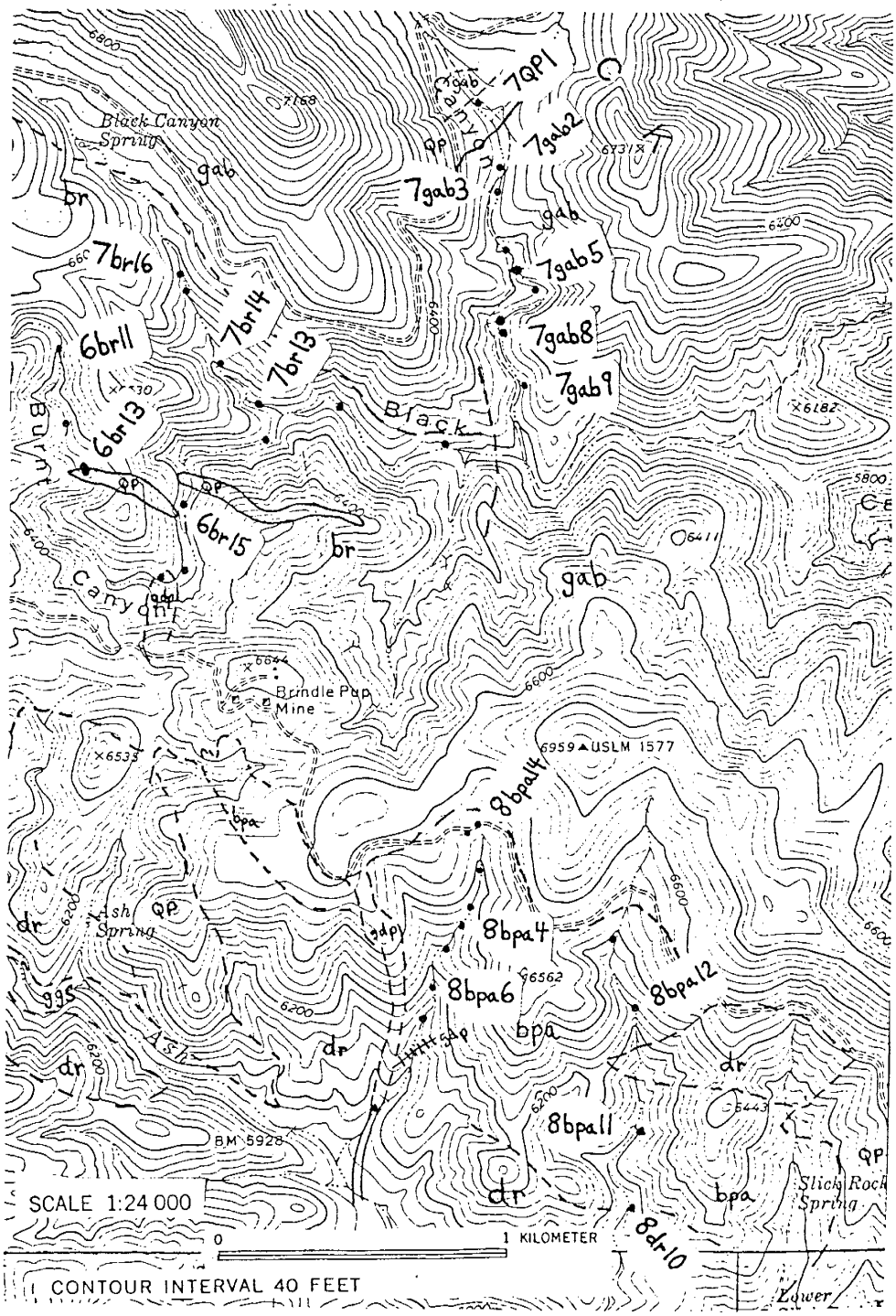

Map 1. SW 1/4 Cottonwood Quad

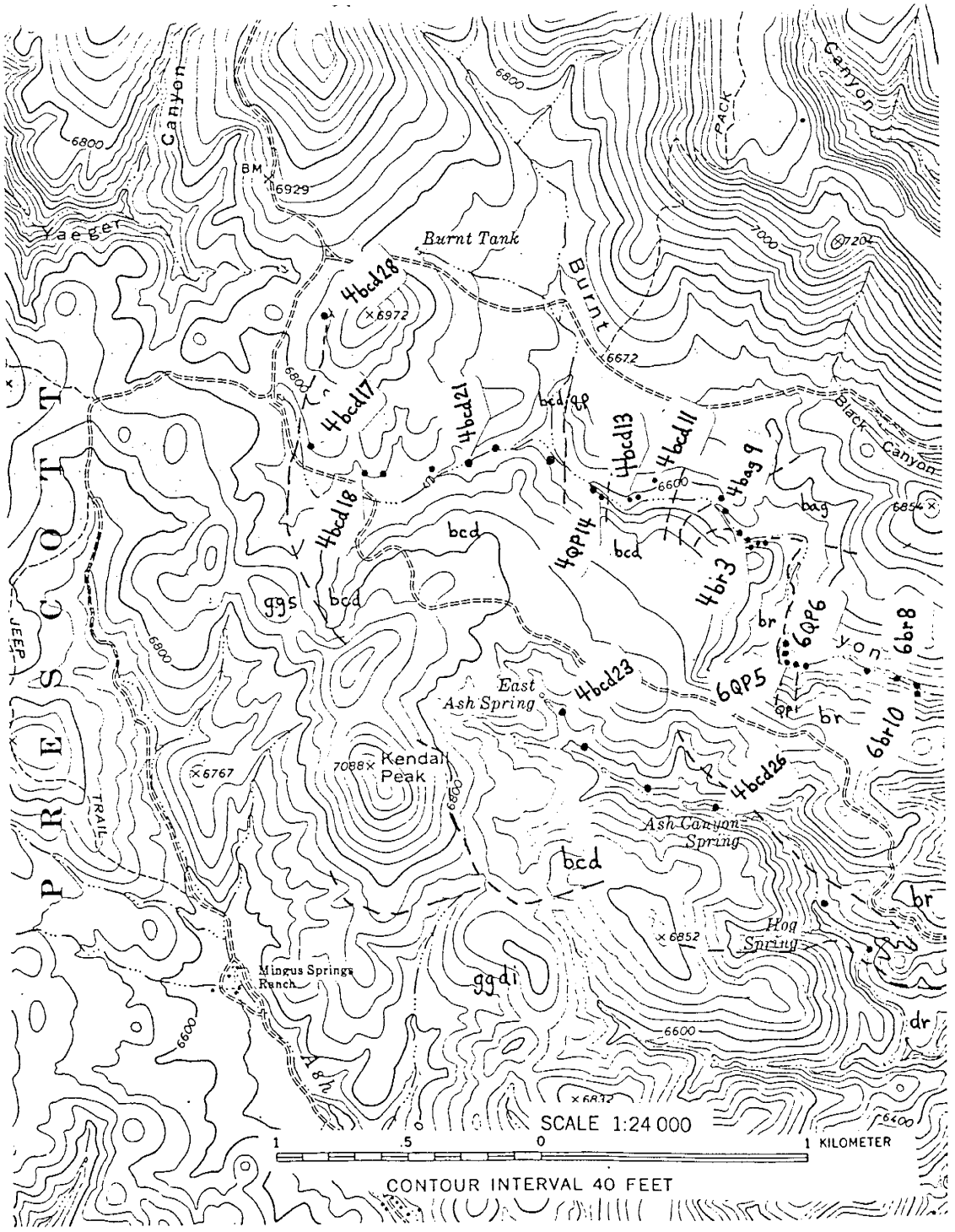

Map 2. SE 1/4 Hickey Mountain Quad

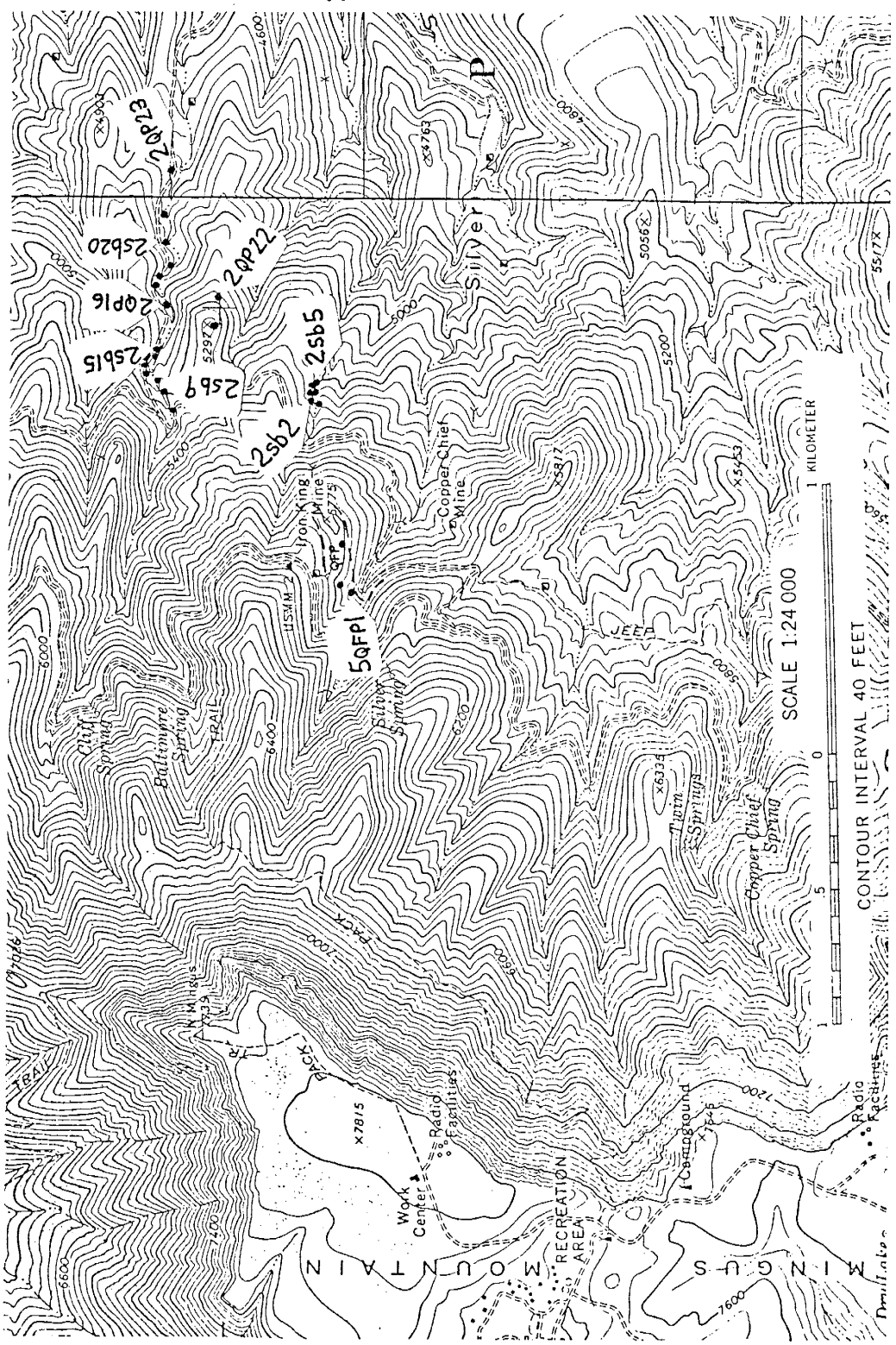

Map 3. Mid-west section Cottonwood Quad

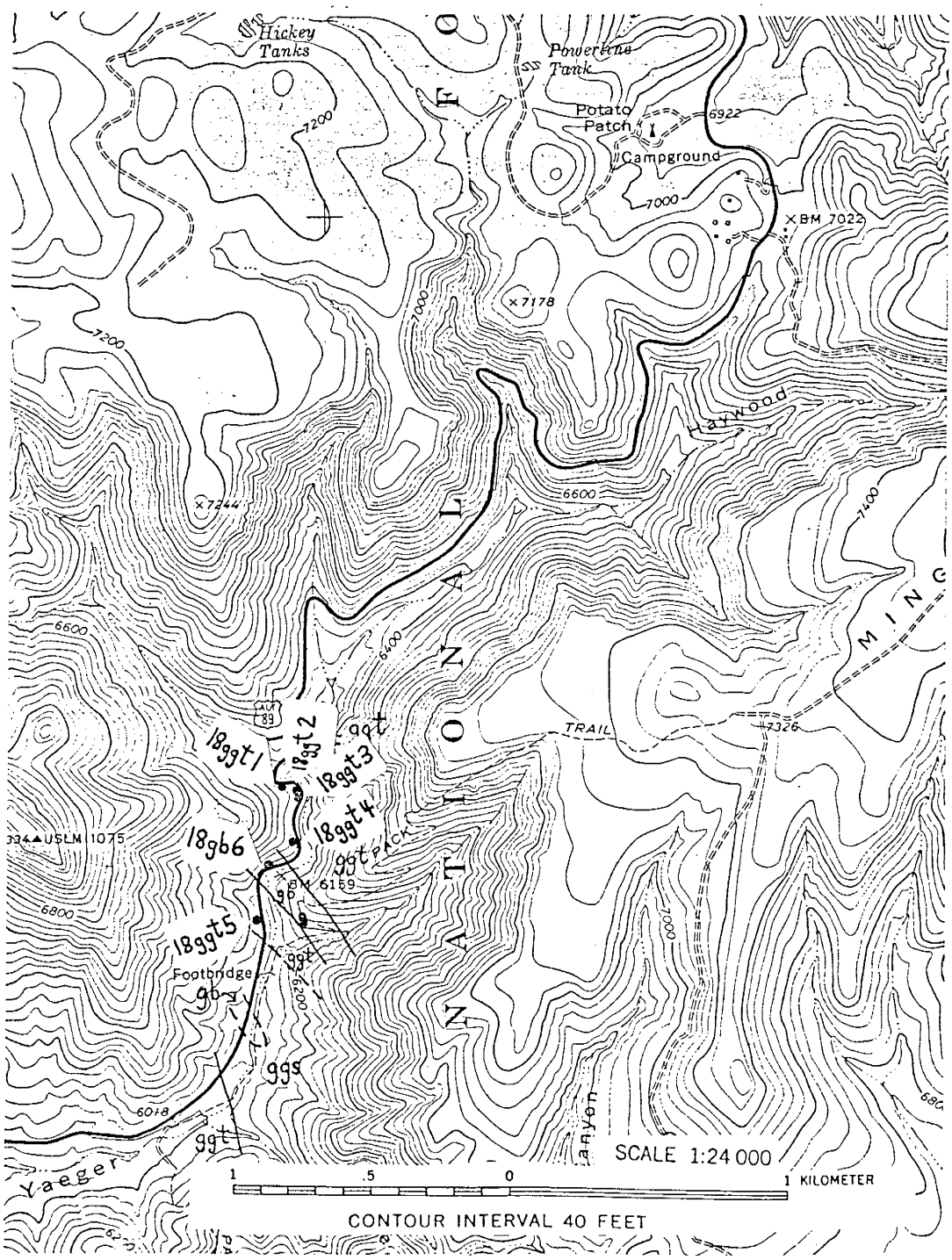

Map 4. Mid-east section of Hickey Mountain Quad.

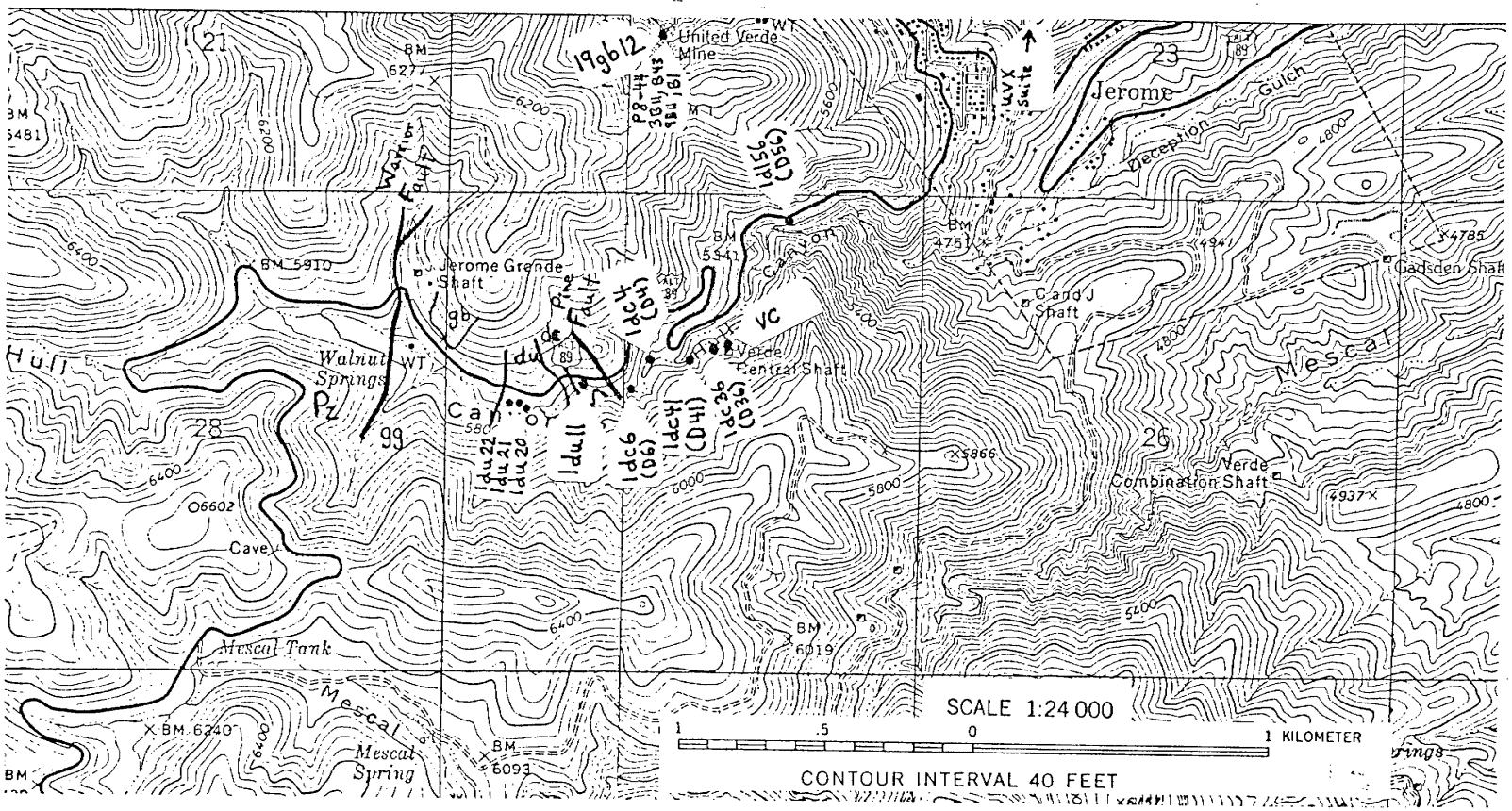

Map 5. NE 1/4 Hickey Mountain, NW 1/4 Cottonwood Quads

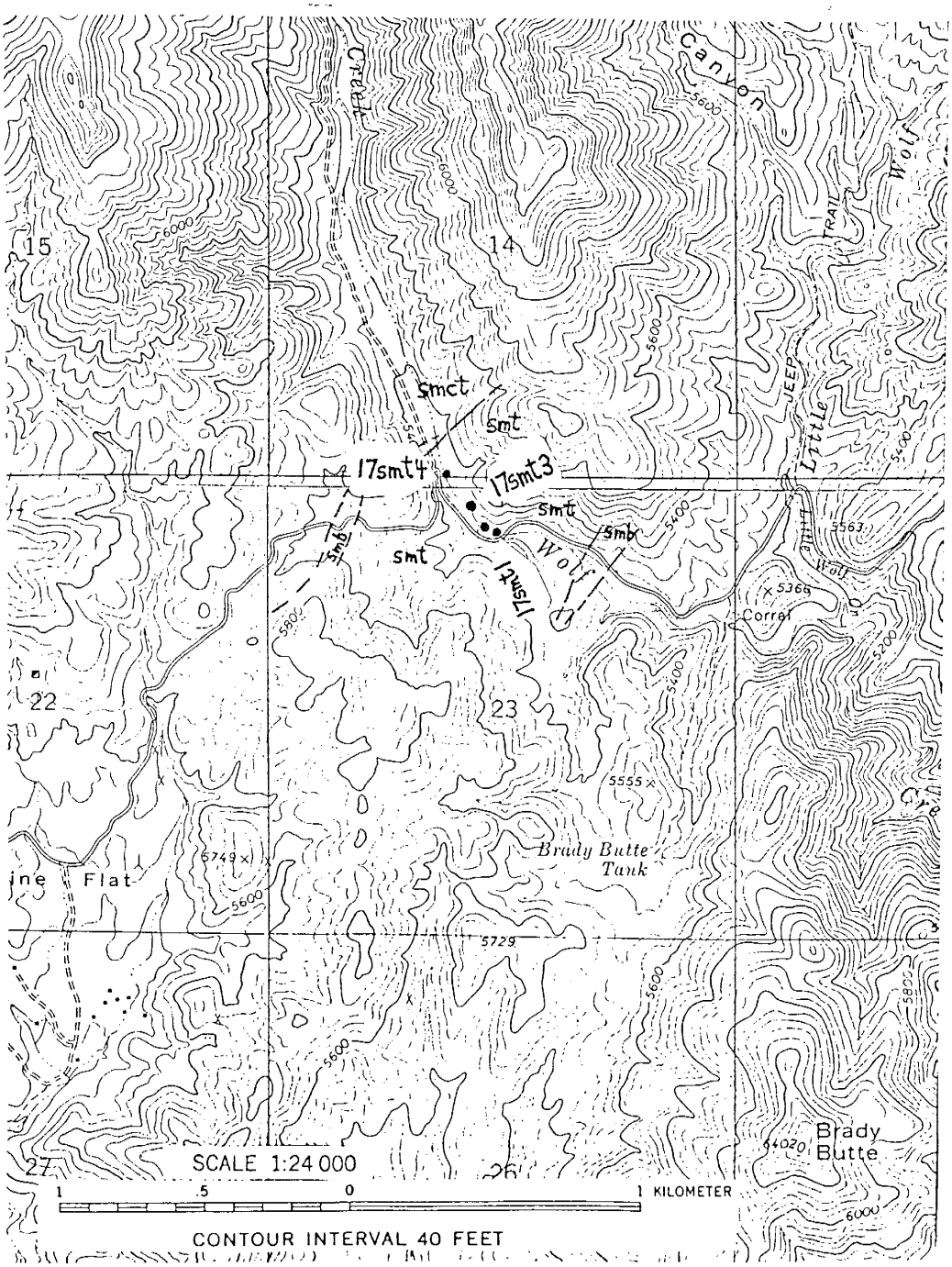

Map 6. Poland Junction and Battle Flat quads (T12N,R1W)

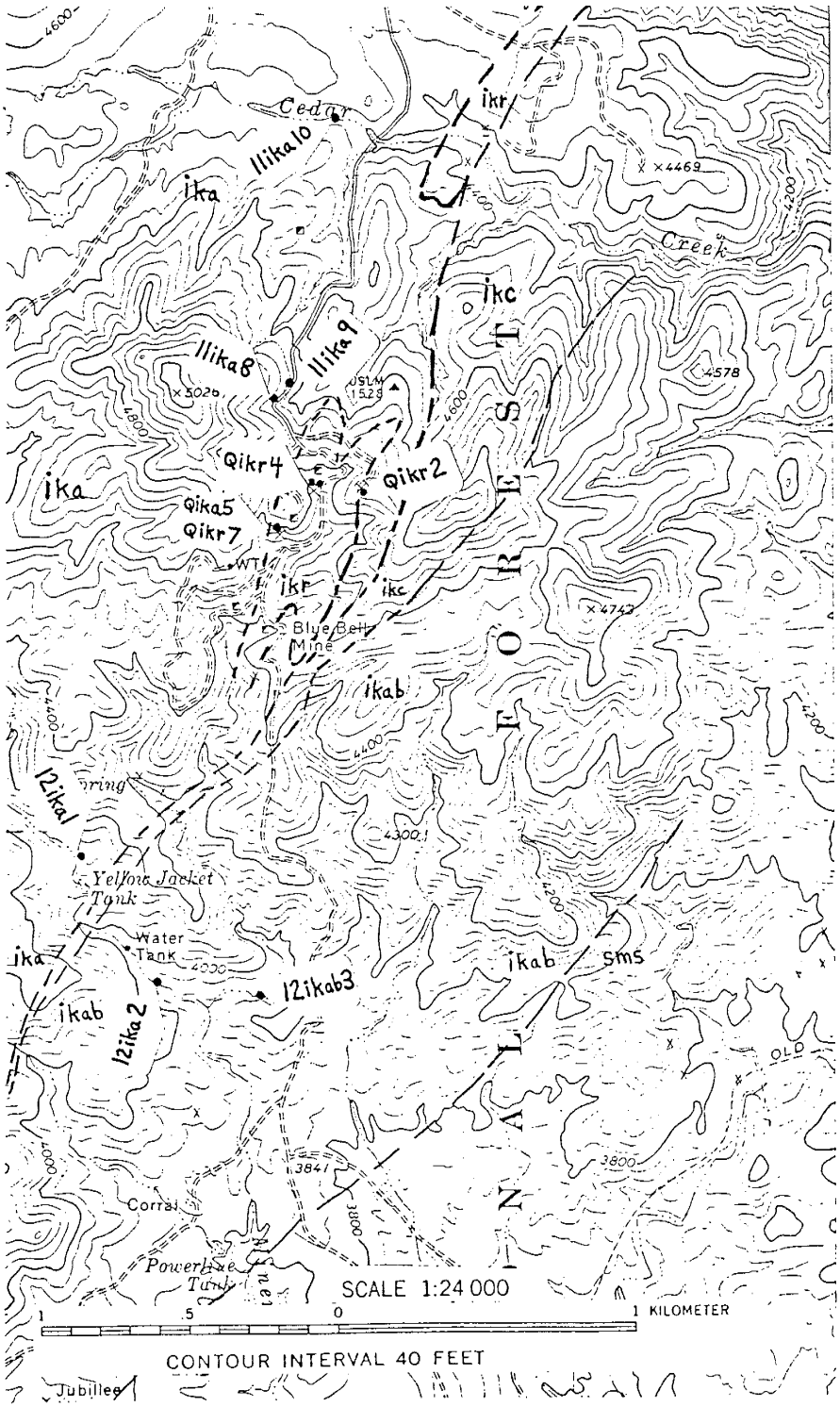

Map 7. NW 1/4 Cleator Quad

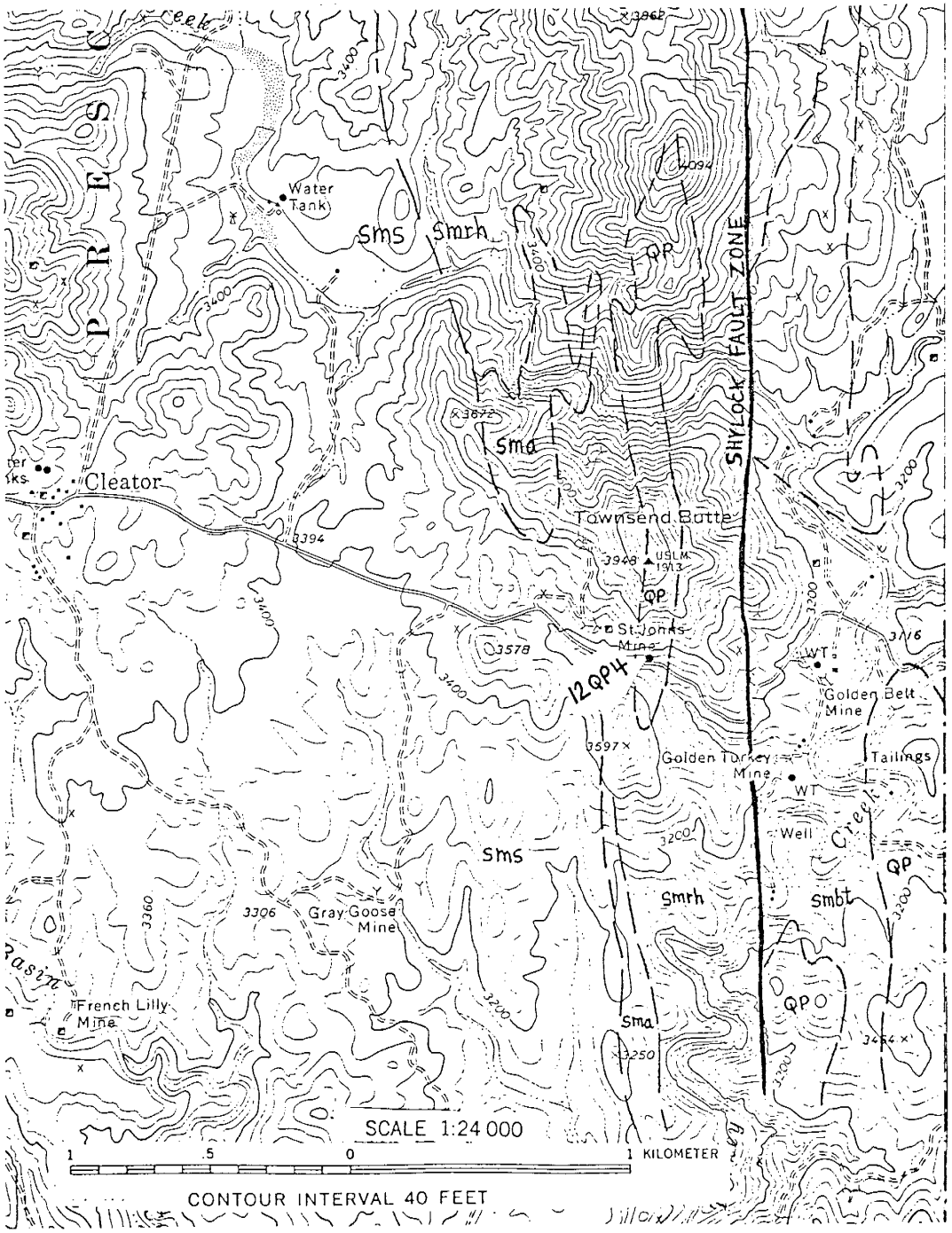

Map 8. SW 1/4 Cleator Quad

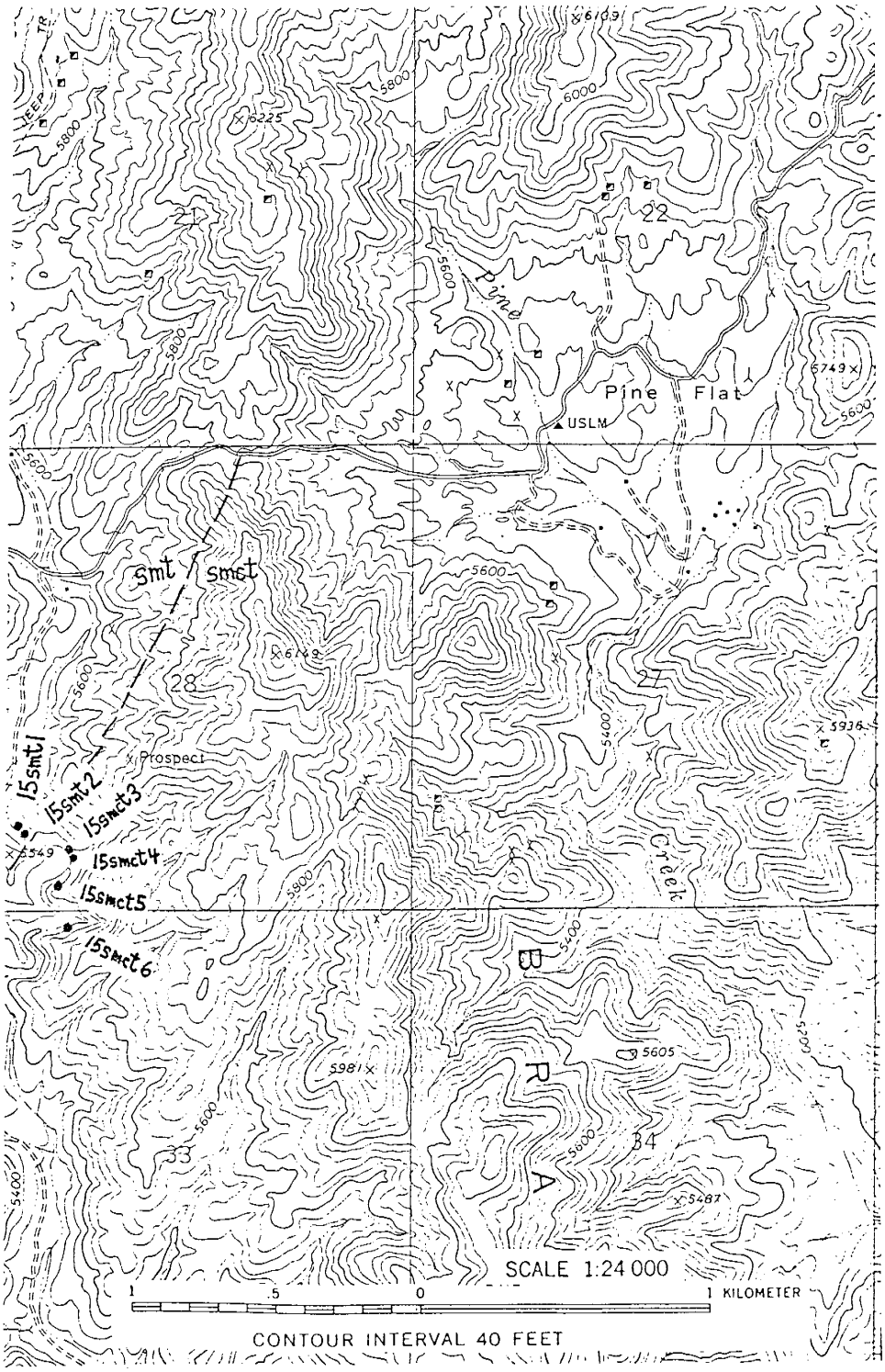

Map. 9. NW 1/4 Battle Flat Quad

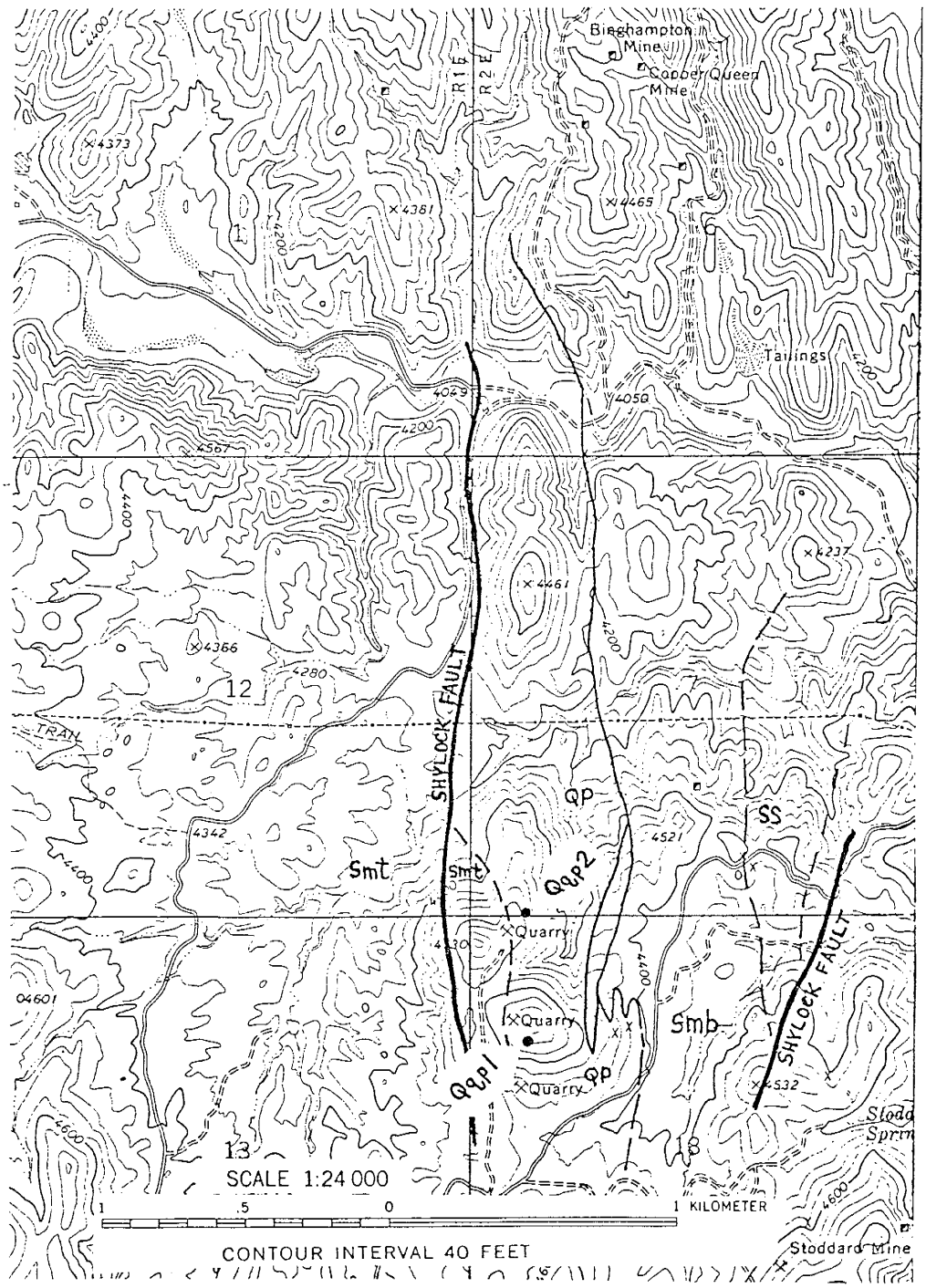

Map 10. Mayer Quad, (T12N,R2E)

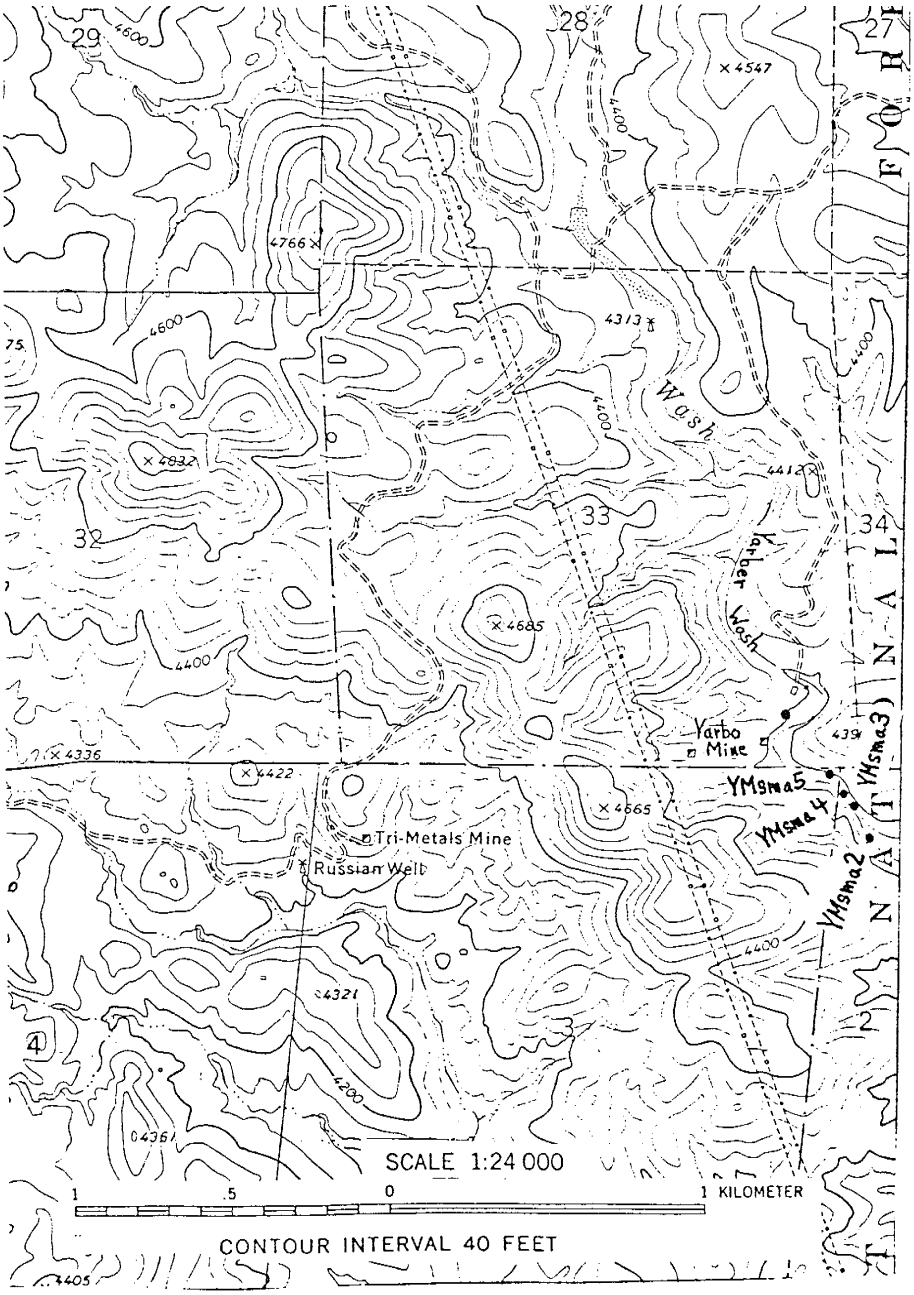

Map 11. NE 1/4 Mayer Quad

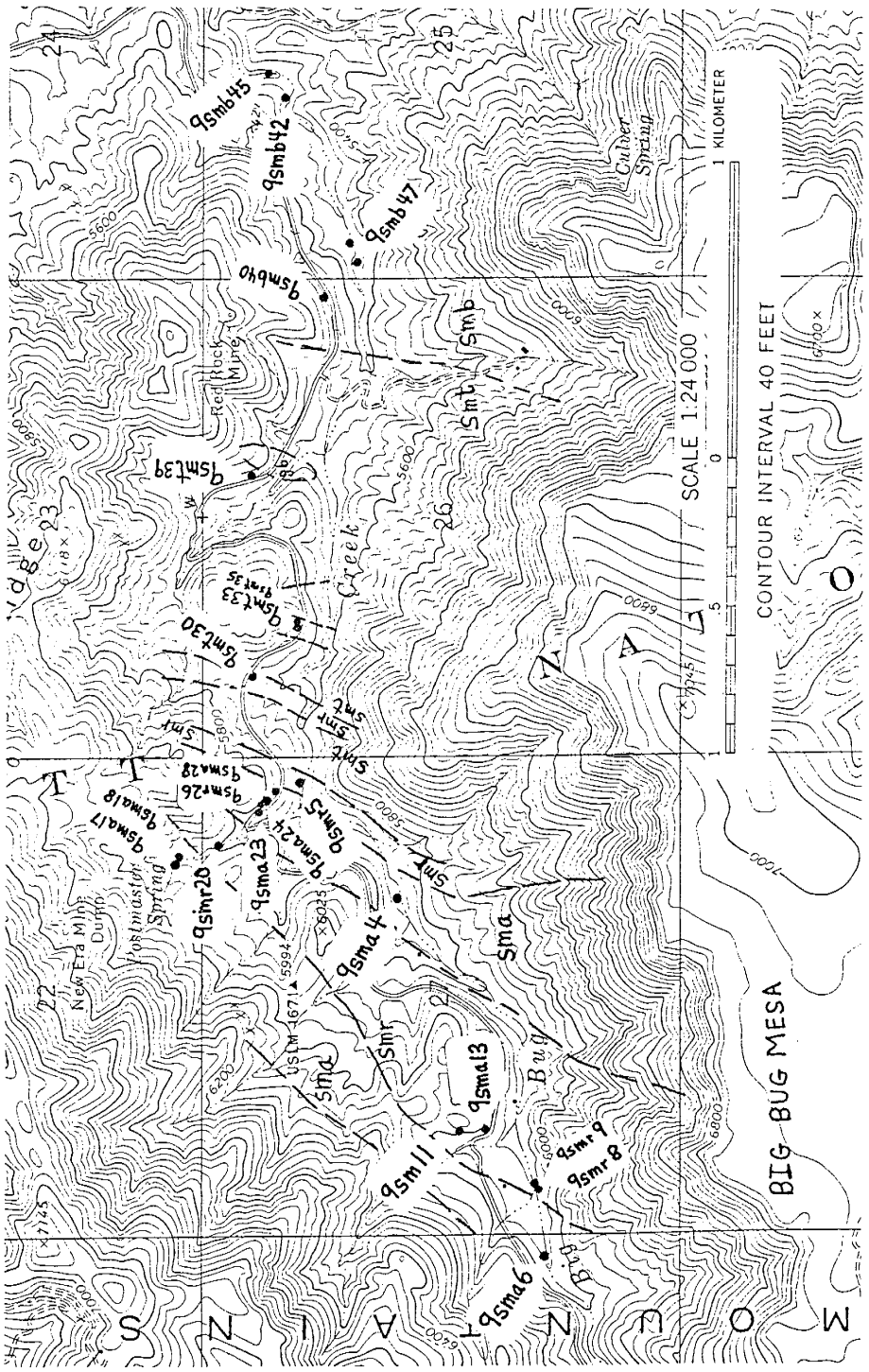

Map 12. Poland Junction Quad (T12½N,R1W)

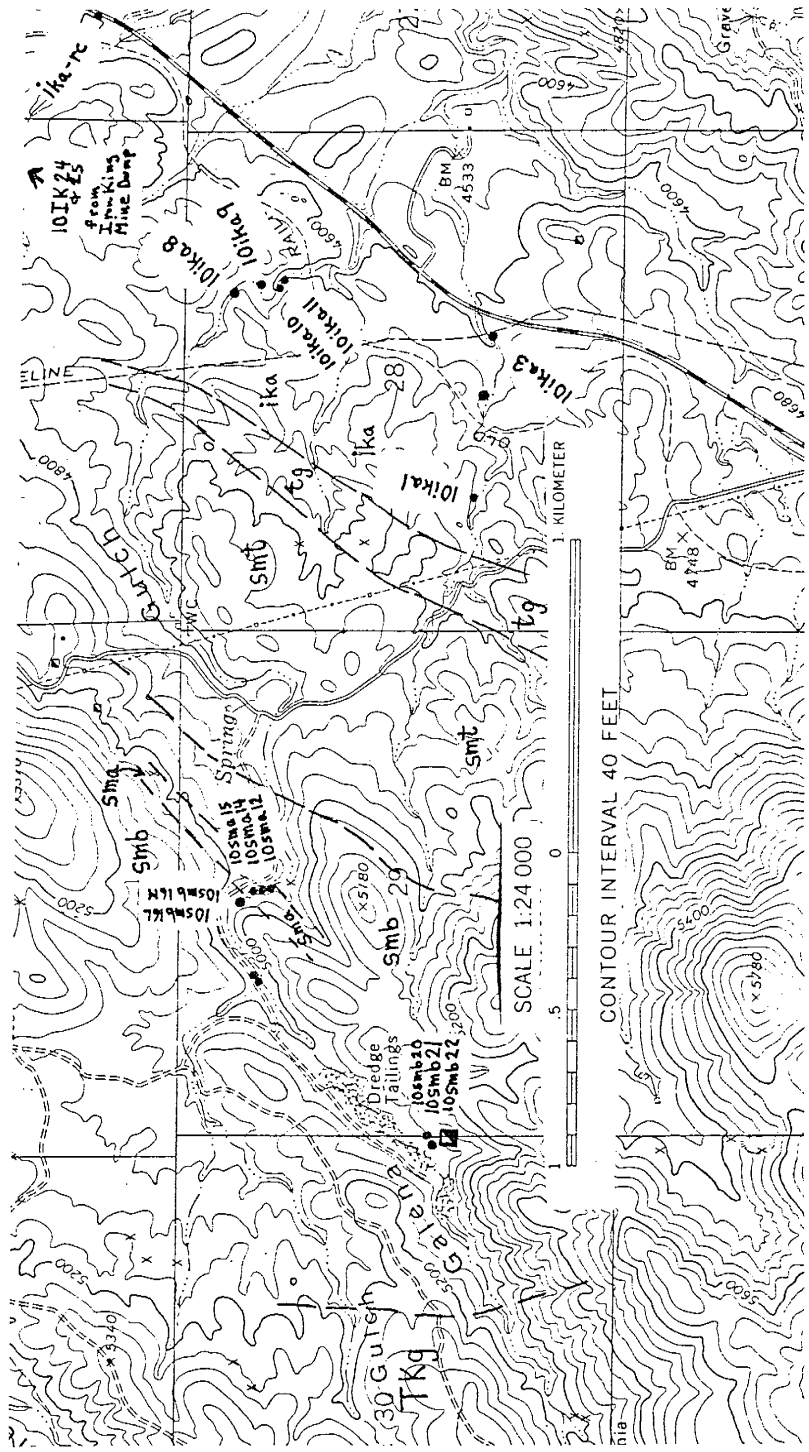

Map 13. NE 1/4 Poland Junction Quad

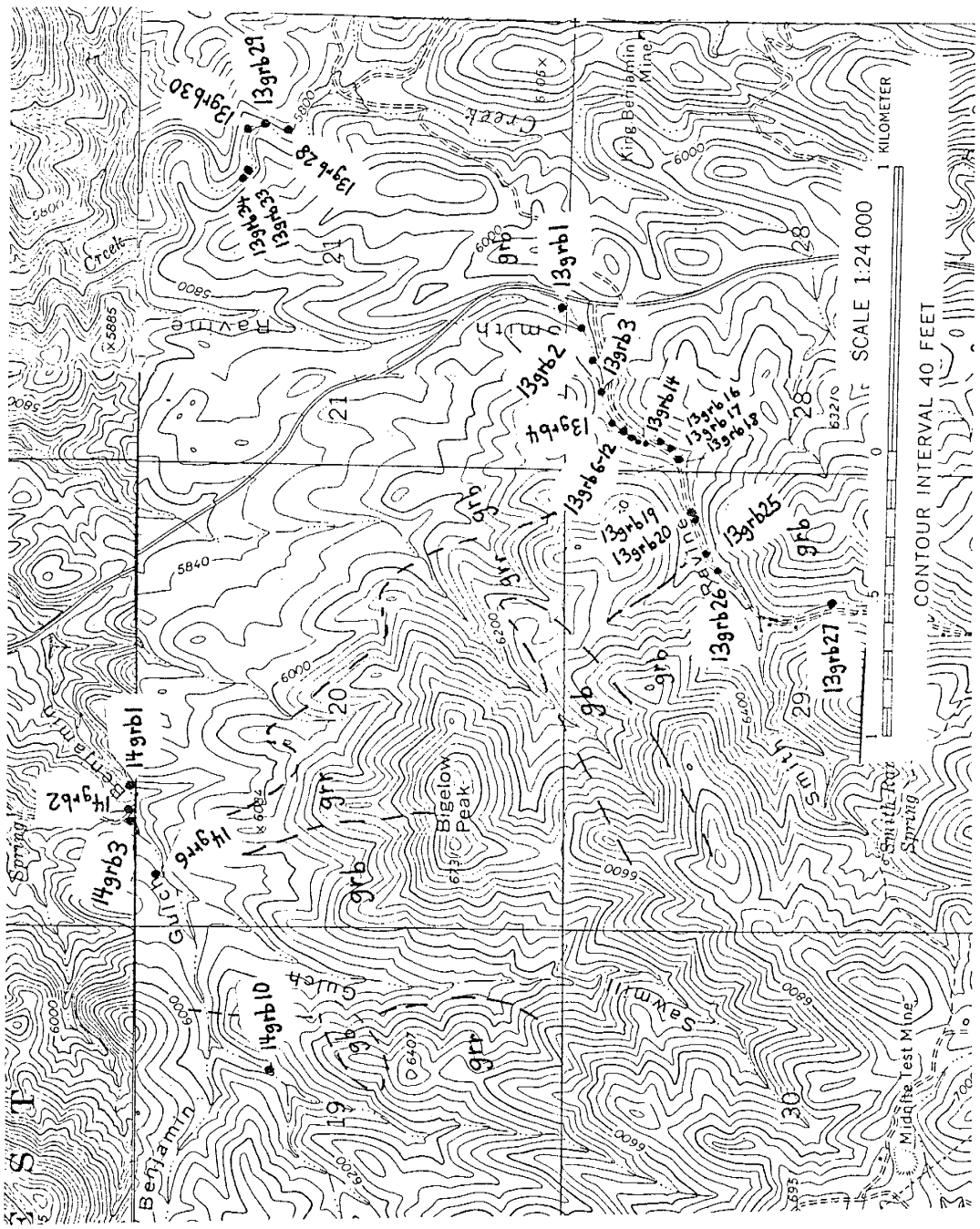

Map 14. Corner of Groom Creek, Poland Jct., Prescott and Prescott Valley South Quads.

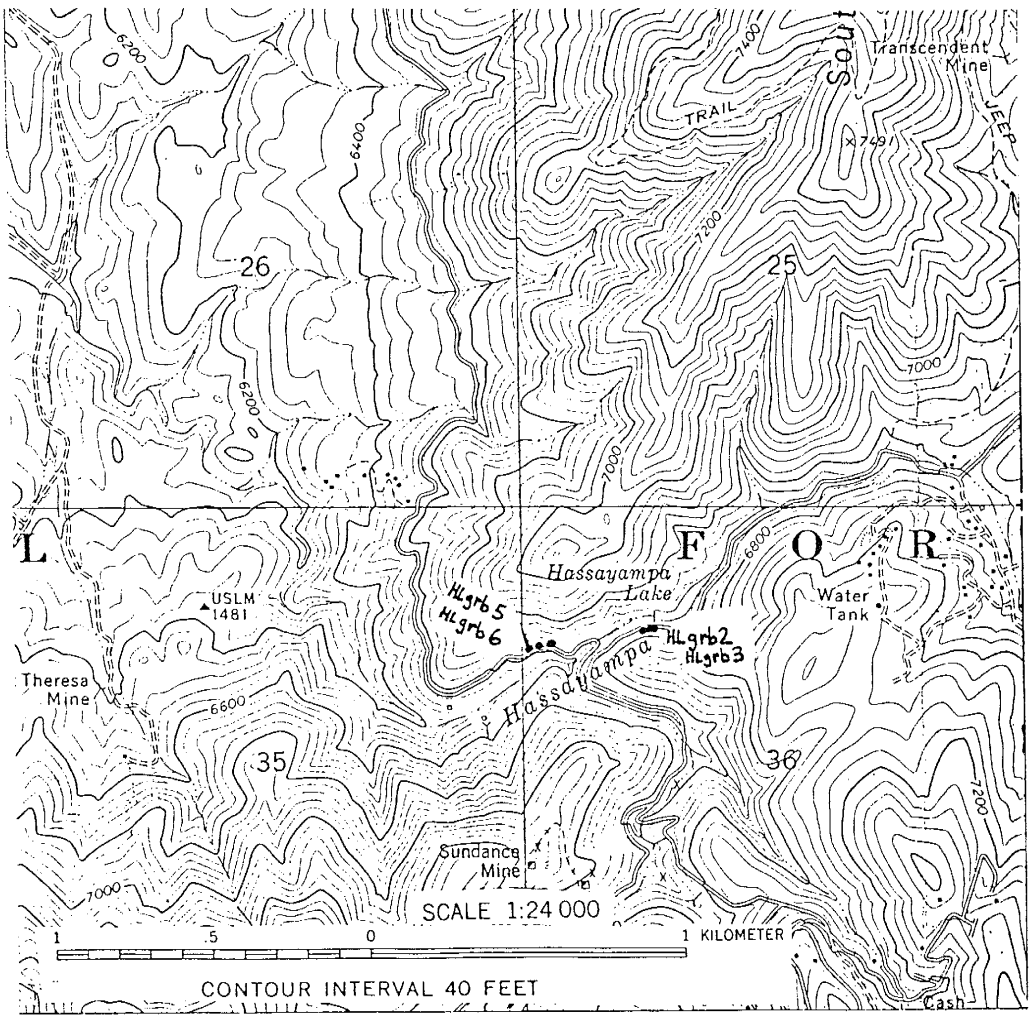

Map 15. Groom Creek Quad (T12½N,R2W)

APPENDIX B

CHEMICAL ANALYSES OF EARLY PROTEROZOIC SUPRACRUSTAL ROCKS FROM THE YAVAPAI SUPERGROUP

* Samples are grouped by their Winchester and Floyd (1977) classification within the Ash Creek, Green Gulch, and Big Bug blocks. The 'unit' description and abbreviations refer to the map nomenclature of Anderson and Creasey (1958) for the Ash Creek Group and Anderson and Blacet (1972) for the Big Bug Group.

Sample Acquisition, Preparation and Analysis

The locations of samples obtained for chemical analysis are given on maps in Appendix A. Sample identification follows this example: 10sma15, 10 = traverse number; sma = map unit abbreviation; 15 = sample number. Unit abbreviations are after map units of Anderson and Creasey (1958) and Anderson and Blacet (1972). Selection of samples for geochemistry is guided by accessibility, degree of weathering, lack of alteration and the need for representative samples. The depth of weathering exceeds 20 meters in regions of vertical foliation (R. Pape, pers. comm., 1984); consequently, most traverses are limited to drainages where severely weathered rock has been removed by erosion and stream polishing enhances recognition of contacts and relict textures.

Each sample was split into three portions for: (a) hand specimen and reference, (b) thin sections and (c) chemical analysis. Samples selected for analysis were cleansed of surficial debris and fed through a large jaw crusher. These coarse fragments were hand-picked to remove weathering rinds, veinlets and fragments with visible contamination by steel from the jaw crusher plates. The fragments selected from this process were pulverized in a rotary grinder with ceramic plates to avoid Ta contamination by tungsten-carbide grinders. Ceramic plates

were thoroughly cleaned by brushes and compressed air between runs and a small aliquot of each sample was pulverized and discarded prior to pulverizing the rest of the sample. This step removes material embedded on the plate surfaces from the previous run. A final grinding step prior to XRF and INAA analysis utilized a motorized agate mortar and pestle or a spex mill with ceramic cylinders and balls.

For XRF trace element analysis (Rb, Sr, Y, Zr, Nb, U, Ba, Cu, Zr and Pb) pellets were pressed using 5-7 g sample with a boric acid backing and several drops of polyvinyl alcohol as a binder under a pressure of 10 tons/in^2. The exact amount of sample powder used in the pellets to ensure adequate thickness is determined by major element analysis. Major element analysis by XRF utilized fused discs prepared from approximately 5 g of sample powder and 2.68 g of lithium tetraborate flux (Spectroflux 105) corrected for flux LOI and fused in Pt-Au alloy crucibles. Sample powders were dried for 2 hours at 110°C and stored in dessicators prior to weighing for fluxing. LOI determination was made by heating at 1000°C for $\geq$ 2 hours. The LOI determinations were required for the major element analysis. Both major and trace XRF analysis were performed using an automated Rigaku 3064 spectrometer with associated PDP-11 computer and in-house software at the XRF-XRD Laboratory of the New Mexico Bureau of Mines and Mineral Resources at the New Mexico Institute of Mining and Technology (NMIMT) following methods described by Norrish and Hutton (1969) and Norrish and Chappell (1977). Calibration curves

were developed using USGS and international standards. Instrumental settings for the XRF spectrometer are presented in Tables 1a and 1b. Representative major and trace element analysis of standards generated from runs and calibrations over a two year period span a compositional range from basalt to rhyolite and are presented in Tables 1c and d, Appendix B. Given values are from the standard evaluations of Abbey (1983). Replicate analyses of standards were used to determine the precision of the analytical procedure. The coefficient of variation (C = S/X x100, where S = standard deviation and X = mean) is less than 5 for most analyses indicating a reliable data base. However, for more siliceous compositions the coefficient increases sharply for very low concentrations of MgO, MnO, P_2O_5 and to a lesser degree TiO_2. Although analyses of MgO, MnO and P_2O_5 cannot be considered very reliable for felsic rocks, these elements do not form the basis for any significant conclusions. Furthermore, low coefficients of variation for replicate analyses of 'in-house' standards (NMR) suggest most felsic data is reliable. The most important conclusions are based on trace element data for mafic rocks, and the coefficient of variation indicates reliable trace element analyses (Table 1d, App. B).

Instrumental Neutron Activation Analysis (INAA) was employed for the trace elements U, Th, Cs, Sc, Hf, Ta, Cr, Ni, Co, and 8 REE. Ba was also analyzed by INAA and values presented are intermediate between those obtained by XRF and INAA. For INAA analyses, approximately 300 mg of rock powder per sample were

sealed in polyethylene vials and irradiated in a thermal neutron flux of 10E12 to 10E13 $n/cm_2/sec$ at a total energy of 3000-5000 megajoules in the Annular Core Research Reactor at the Sandia National Laboratory, Albuquerque, New Mexico. Counts were made at 6-8 and 30-40 days using high purity Ge detectors and a Nuclear Data 6600 multichannel analyzer and LSI-11 computer. Calibrations were performed using the NBS Fly Ash standard 1633a and USGS standard BCR-1. USGS and in-house standards were used as additional checks on accuracy and precision. Evaluation of various standards from runs over a three year period are presented in Table 1e, App. B. Most trace elements with the exception of Ba, Cs, Cr have coefficients of variation less than 5 and are quite reliable despite changes in both instrumentation and data reduction systems during these investigations. Analytical methods are similar to those described by Jacobs et al. (1977), Gibson and Jagam (1980). Data reduction employed the TEABAGS system described by Lindstrom and Korotev (1988) for peak selection and evaluation, peak interference correction, and calculation of concentrations.

Table 1. Instrumental Settings and Standard Analyses

Table 1a. Instrumental Settings for the X-ray Fluorescent Determination of Major Elements

Element	Peak	Source (KV/ma)	Crystal	Counter	Path
Si	K 1,2	Rh (35/75)	PET	FP	vacuum
Ti	K 1,2	Rh (35/75)	LiF3	FP	vacuum
Al	K 1,2	Rh (35/75)	PET	FP	vacuum
Fe	K 1,2	Rh (35/75)	LiF3	FP	vacuum
Mn	K 1,2	Rh (35/75)	LiF3	FP	vacuum
Mg	K 1,2	Rh (35/75)	TAP	FP	vacuum
Ca	K 1,2	Rh (35/75)	LiF3	FP	vacuum
Na	K 1,2	Rh (35/75)	TAP	FP	vacuum
K	K 1,2	Rh (35/75)	LiF3	FP	vacuum
P	K 1,2	Rh (35/75)	GE	FP	vacuum

Table 1b. Instrumental Settings for the X-ray Fluorescent Determination of Trace Elements

Element	Peak	Source (KV/ma)	Crystal	Counter	Path
Y	K 1,2	Rh (60/40)	LiF1	Scint.	vacuum
Zr	K 1,2	Rh (60/40)	LiF2	Scint.	vacuum
Nb	K 1,2	Rh (60/40)	LiF2	Scint.	vacuum
Sr	K 1,2	Rh (60/40)	LiF1	Scint.	vacuum
Rb	K 1,2	Rh (60/40)	LiF2	Scint.	vacuum
Pb	L 1	Rh (60/40)	LiF2	Scint.	vacuum
Cu	K 1,2	Rh (60/45)	LiF1	Scint.	vacuum
Zn	K 1,2	Rh (60/45)	LiF1	Scint.	vacuum
Ba	L 1	Rh (60/40)	LiF3	Scint.	vacuum
V	K 1,2	Rh (60/40)	LiF3	Scint.	vacuum

Table 1c. Representative XRF Major Element Analyses of Standards

BE-N	Abbey	NMIMT	NMIMT	NMIMT	NMIMT
SiO_2	38.39	38.64	38.42	38.44	38.49
TiO_2	2.62	2.69	2.67	2.67	2.67
Al_2O_3	10.12	10.02	10.04	10.02	10.02
Fe_2O_{3T}	12.90	13.00	12.92	12.96	12.99
MgO	13.22	13.09	13.18	13.19	13.17
CaO	13.94	14.20	14.10	14.12	14.24
Na_2O	3.20	3.22	3.20	3.19	3.31
K_2O	1.40	1.37	1.38	1.40	1.39
MnO	.20	.21	.20	.21	.21
P_2O_5	1.06	1.06	1.05	1.05	1.05
LOI	2.39	2.39	2.39	2.39	2.39
Total	99.44	99.89	99.56	99.63	99.94

BE-N	NMIMT	NMIMT	Mean	Std Dev	C
SiO_2	38.26	38.18	38.41	.15	.39
TiO_2	2.60	2.59	2.65	.04	1.51
Al_2O_3	10.09	10.09	10.05	.03	.30
Fe_2O_{3T}	12.30	12.24	12.74	.33	2.59
MgO	13.18	13.21	13.17	.04	.30
CaO	13.85	13.86	14.06	.15	1.07
Na_2O	3.24	3.31	3.25	.05	1.54
K_2O	1.36	1.36	1.38	.01	.72
MnO	.18	.18	.18	.01	5.56
P_2O_5	.99	1.00	1.03	.03	2.91
LOI	2.39	2.39			
Total	98.43	98.40			

Table 1c. - Continued

AGV	Abbey	NMIMT	NMIMT	NMIMT	NMIMT
SiO_2	59.61	59.42	59.43	59.56	59.43
TiO_2	1.06	1.06	1.07	1.08	1.05
Al_2O_3	17.19	16.95	17.29	17.31	17.02
Fe_2O_{3T}	6.80	6.95	6.88	6.91	6.95
MgO	1.52	1.49	1.51	1.41	1.48
CaO	4.94	4.94	4.98	4.98	4.96
Na_2O	4.32	4.32	4.26	4.24	4.17
K_2O	2.92	2.92	2.91	2.92	2.90
MnO	.10	.10	.10	.10	.09
P_2O_5	.51	.49	.49	.49	.48
LOI	.62	.62	.62	.62	.62
Total	99.59	99.22	99.56	99.62	99.16

AGV	NMIMT	NMIMT	Mean	Std Dev	C
SiO_2	59.31	59.51	59.44	.08	.13
TiO_2	1.07	1.00	1.06	.03	2.83
Al_2O_3	17.04	16.94	17.09	.15	.88
Fe_2O_{3T}	6.89	6.63	6.87	.11	1.60
MgO	1.47	1.73	1.53	.14	9.15
CaO	4.96	4.84	4.94	.05	1.01
Na_2O	4.19	4.39	4.26	.08	1.88
K_2O	2.88	2.284	2.90	.03	1.03
MnO	.10	.08	.10	.01	10.00
P_2O_5	.48	.47	.48	.01	2.08
LOI	.62	.62			
Total	99.01	98.43			

Table 1c. - Continued

RGM-1	Abbey	NMIMT	NMIMT	NMIMT	NMIMT
SiO_2	73.47	73.16	73.11	73.32	73.37
TiO_2	.27	.27	.28	.28	.27
Al_2O_3	13.60	13.60	13.64	13.78	13.67
Fe_2O_{3T}	1.88	1.90	1.90	1.93	1.91
MgO	.28	.21	.22	.25	.19
CaO	1.15	1.18	1.18	1.19	1.19
Na_2O	4.12	4.09	4.01	4.10	4.11
K_2O	4.35	4.26	4.28	4.29	4.27
MnO	.04	.04	.04	.04	.03
P_2O_5	.05	.04	.04	.04	.04
LOI	.47	.47	.47	.47	.47
Total	99.88	99.22	99.16	99.67	99.52

RGM-1	Abbey	NMIMT	Mean	Std Dev	C
SiO_2	73.60	73.27	73.31	.16	.22
TiO_2	.25	.22	.26	.02	7.69
Al_2O_3	13.84	13.73	13.71	.08	.58
Fe_2O_{3T}	1.87	1.94	1.91	.02	1.05
MgO	.26	.51	.27	.11	40.74
CaO	1.87	1.94	1.91	.02	1.05
Na_2O	3.83	4.17	4.05	.11	2.72
K_2O	4.35	4.20	4.28	.04	.93
MnO	.03	.02	.03	.01	33.33
P_2O_5	.05	.06	.05	.01	20.00
LOI	.47	.47			
Total	99.74	99.74			

Table 1c. - Continued

NMR	NMR	NMIMT	NMIMT	NMIMT	NMIMT
SiO_2	71.75	71.48	71.32	71.36	71.39
TiO_2	.44	.40	.41	.39	.40
Al_2O_3	14.07	14.04	14.11	14.04	14.07
Fe_2O_{3T}	2.56	2.63	2.62	2.55	2.54
MgO	.39	.66	.66	.64	.65
CaO	1.61	1.59	1.59	1.57	1.57
Na_2O	3.58	3.75	3.75	3.64	3.70
K_2O	4.75	4.60	4.60	4.59	4.59
MnO	.06	.04	.04	.04	.04
P_2O_5	.13	.14	.14	.14	.14
LOI	.51	.51	.51	.51	.51
Total	99.85	99.82	99.74	99.46	99.53

NMR	NMIMT	NMIMT	Mean	Std Dev	C
SiO_2	71.42	71.39	71.38	.06	.08
TiO_2	.39	.40	.40	.007	1.75
Al_2O_3	13.92	14.00	14.03	.594	4.23
Fe_2O_{3T}	2.63	2.63	2.60	.04	1.54
MgO	.63	.64	.65	.012	1.85
CaO	1.58	1.58	1.58	.008	.51
Na_2O	3.70	3.69	3.71	.04	1.11
K_2O	4.64	4.62	4.61	.018	.39
MnO	.04	.04	.04	0	0
P_2O_5	.13	.13	.14	.005	3.57
Total	99.58	99.62			

Table 1d. Representative XRF Trace Element Analyses of Standards

BCR-1	USGS	NMIMT	NMIMT	NMIMT	NMIMT
Rb	47	52	51	51	51
Sr	330	341	341	337	342
Y	39	36	38	37	37
Zr	119	192	192	193	193
Nb	14	16	16	15	15

BCR-1	NMIMT	NMIMT	Mean	Std Dev	C
Rb	51	53	52	.76	1.46
Sr	342	331	339	4.0	1.18
Y	37	38	37	.69	1.86
Zr	192	191	192	.69	.35
Nb	16	14	15	.75	5.00

QLO-1	Abbey	NMIMT	NMIMT	NMIMT	NMIMT
Rb	74	72	72	71	70
Sr	350	341	334	336	335
Y	24	26	25	26	25
Zr	175	187	186	187	185
Nb	11	11	11	11	11

QLO-1	NMIMT	NMIMT	Mean	Std Dev	C
Rb	72	72	72	.76	1.06
Sr	336	335	336	2.3	.68
Y	26	25	26	.50	1.92
Zr	187	186	196	.75	.38
Nb	12	12	11	.47	4.27

Table 1d. - Continued

G-2	Abbey	NIMIT	NMIMT	NMIMT	NMIMT
Rb	170	170	166	165	166
Sr	480	474	478	481	478
Y	11	13	13	12	12
Zr	300	304	299	294	297
Nb	13	11	12	12	12

G-2	NMIMT	NMIMT	Mean	Std Dev	C
Rb	166	166	167	1.6	.96
Sr	476	478	478	2.1	.44
Y	12	13	13	.50	3.85
Zr	298	298	298	3.0	1.01
Nb	12	12	11.8	.37	3.08

Table 1e. Representative INAA Trace Element Analyses of Standards

	NBS1633a	NMIMT	NMIMT	NMIMT
CS	10.4	10.3	10.5	10.8
Ba	1320	1400	1379	1330
Th	24.0	24.1	24.1	24.8
U	10.3	10.5	10.3	10.3
Sc	38.6	38.8	38.7	39.6
Hf	7.29	7.27	7.23	7.24
Ta	1.93	1.97	1.96	1.93
Cr	193	194	192	195
Ni	130	121	128	130
Co	44.1	44.3	44.1	44.8
La	76.7	78.6	79.4	76.9
Ce	168.8	173.1	171.5	171.5
Sm	16.6	17.0	16.6	16.6
Eu	3.5	3.5	3.5	3.6
Tb	2.69	2.73	2.79	2.74
Yb	7.68	7.61	7.48	7.67
Lu	1.15	1.18	1.15	1.20

	NMIMT	X	Std Dev	C
Cs	10.4	10.5	.19	1.81
Ba	1330	1360	30.7	2.26
Th	23.9	24.2	.34	1.40
U	10.3	10.4	.09	.86
Sc	38.6	38.9	.40	1.02
Hf	7.29	7.25	.03	.41
Ta	1.93	1.94	.02	1.03
Cr	193	194	1.12	.58
Ni	130	127	3.70	2.91
Co	44.1	44.3	.29	.65
La	77.2	78.0	1.02	1.30
Ce	171.5	171.9	.65	.38
Sm	16.6	16.7	.17	1.02
Eu	3.5	3.5	.04	1.14
Tb	2.69	2.74	.04	1.46
Yb	7.68	7.61	.08	1.05
Lu	1.13	1.17	.03	2.56

Table 1e. - Continued

	BCR-1	NMIMT	NMIMT	NMIMT
Cs	.90	1.01	1.15	1.16
Ba	670	650	762	780
Th	6.0	6.12	6.51	6.44
U	1.7	1.78	1.83	1.85
Sc	32.4	34.8	38.3	37.8
Hf	5.19	5.35	5.96	5.88
Ta	.78	.82	.89	.86
Cr	15	13.6	15.3	14.3
Ni	10	13	8	11
Co	37.4	40.1	44.0	43.3
La	24.6	27.2	28.8	28.1
Ce	53.7	58.4	63.4	62.9
Sm	6.80	7.6	8.0	7.7
Eu	1.92	2.08	2.28	2.26
Tb	1.10	1.09	1.21	1.19
Yb	3.37	3.62	3.69	4.07
Lu	.53	.55	.62	.56

	X	Std Dev	C
Cs	1.11	.07	6.31
Ba	731	57.5	7.87
Th	6.36	.17	2.67
U	1.82	.03	1.65
Sc	37.0	1.54	4.16
Hf	5.73	.27	4.71
Ta	.86	.03	3.49
Cr	14.4	.70	4.86
Ni	10.7	2.05	19.16
Co	42.5	1.70	4.00
La	28.0	.65	2.32
Ce	61.6	2.25	3.65
Sm	7.7	.21	2.73
Eu	2.21	.09	4.07
Tb	1.16	.05	4.31
Yb	3.79	.20	5.28
Lu	.58	.03	5.17

Table 1e. - Continued

	BLCR	NMIMT	NMIMT	NMIMT
Cs	2.3	2.3	2.4	1.97
Ba	375	371	370	380
Th	4.1	3.90	3.99	3.84
U	1.5	1.49	1.56	1.51
Sc	32	32.4	32.2	30.0
Hf	4.3	4.7	4.7	4.40
Ta	.42	.42	.43	.35
Cr	160	162	167	127
Ni	103	105	99	84
Co	29	29.4	29.4	29.8
La	11.1	12.65	12.30	11.01
Ce	26.7	29.35	28.86	26.4
Sm	3.7	3.97	3.87	3.88
Eu	1.3	1.34	1.34	1.25
Tb	.78	.72	.77	.71
Yb	3.1	2.93	3.19	2.97
Lu	.52	.57	.56	.51

	NMIMT	X	Std Dev	C
Cs	2.03	2.2	.18	8.18
Ba	361	371	6.73	1.8
Th	3.72	3.96	.10	2.59
U	1.49	1.51	.03	1.99
Sc	29.8	31.1	1.20	3.86
Hf	4.4	4.6	.15	3.26
Ta	.37	.39	.03	7.69
Cr	127	146	18.8	12.9
Ni	102	98	8.01	8.17
Co	29.6	29.6	.17	.57
La	11.01	11.8	.73	6.2
Ce	26.5	27.8	1.34	4.82
Sm	3.88	3.90	.04	1.03
Eu	1.30	1.31	.04	3.05
Tb	.74	.74	.02	2.70
Yb	2.91	3.00	.11	3.67
Lu	.51	.54	.03	5.56

TABLE 2. VOLCANICS OF THE ASH CREEK BLOCK

* Unit descriptions and abbreviations after Anderson and Creasey (1958) unless otherwise indicated.

* nd = not detected

* AI = Alteration Index (Ishikawa et al., 1976)
  AI = $[MgO + K_2O/(Na_2O + K_2O + CaO + MgO)] \times 100$

* Mg Number = (100 MgO/MgO + FeO) mole ratio

Table 2a. BASALTS

Units: Grapevine Gulch Fm. (ggt)

Sample	18ggt1	18ggt2	18ggt3
SiO_2	54.27	53.70	53.26
TiO_2	0.83	0.75	0.84
Al_2O_3	15.10	16.67	15.02
Fe_2O_{3-T}	11.90	12.06	12.37
MgO	2.62	3.36	3.56
CaO	7.62	6.52	7.36
Na_2O	2.81	3.44	3.39
K_2O	0.66	0.58	0.54
MnO	0.17	0.17	0.17
P_2O_5	0.19	0.16	0.17
LOI	3.81	2.75	3.79
Total	99.98	100.16	100.47
Mg Number	33	39	39
AI	24	28	28
Rb	14	13	13
Ba	320	241	187
Cs	nd		
Sr	236	243	200
Pb	11	9	12
Th	0.7		
U	0.4		
Sc	34		
V	281	342	352
Cr	10		
Co	24.2		
Ni	6		
Y	18.3	14.6	16.6
Zr	39	33	33
Nb	5.1	4.8	4.9
Hf	1.2		
Ta	0.06		
La	5.5		
Ce	15.1		
Sm	2.41		
Eu	0.78		
Tb	0.45		
Yb	1.64		
Lu	0.30		

Table 2a. - Continued

Units: Grapevine Gulch Fm. (ggt)
& Coca Mines Core (CM)

Sample	18ggt4	18ggt5	CM-8
SiO_2	55.13	55.65	47.50
TiO_2	0.94	0.97	1.04
Al_2O_3	14.93	15.53	14.10
Fe_2O_{3-T}	12.51	12.70	14.13
MgO	3.30	2.98	7.58
CaO	6.42	4.65	10.92
Na_2O	2.86	4.13	1.77
K_2O	0.92	1.31	0.40
MnO	0.18	0.20	0.22
P_2O_5	0.22	0.24	0.13
LOI	2.52	2.03	2.40
Total	99.93	100.39	100.19
Mg Number	37	35	55
AI	31	33	39
Rb	19	19	9
Ba	407	525	119
Cs		0.4	
Sr	232	355	178
Pb	12	12	4
Th		0.9	
U		nd	
Sc		40	
V	315	244	352
Cr		10	
Co		29.3	
Ni		11	
Y	21.4	24.3	25.9
Zr	41	48	58
Nb	4.4	5.1	6.4
Hf		1.5	
Ta		0.10	
La		8.1	
Ce		19.4	
Sm		3.33	
Eu		1.18	
Tb		0.59	
Yb		2.21	
Lu		0.38	

Table 2a. GABBRO

Units: gabbro (gb)

Sample	19gb12	18gb6
SiO_2	49.72	47.14
TiO_2	0.48	0.47
Al_2O_3	15.31	13.70
Fe_2O_3-T	11.54	12.40
MgO	8.55	11.23
CAO	9.32	9.84
Na_2O	2.13	1.08
K2O	0.77	0.30
MnO	0.19	0.19
P_2O_5	0.13	0.09
LOI	2.73	3.77
Total	100.27	100.21
Mg Number	63	67
AI	45	51
Rb	21	8
Ba	210	132
Cs	0.3	0.4
Sr	295	266
Pb	11	8
Th	1.0	0.3
U	0.95	0.17
Sc	37	28
V	172	208
Cr	103	188
Co	56.6	54.6
Ni	71	114
Y	19.6	11.6
Zr	54	28
Nb	5.1	5.1
Hf	1.7	0.8
Ta	0.12	0.05
La	8.7	2.7
Ce	20.9	7.2
Sm	2.94	1.38
Eu	1.01	0.44
Tb	0.47	0.29
Yb	1.97	1.06
Lu	0.35	0.18

Table 2a. BASALTS

Units: andesitic flows (sma), (YM = Yarber Mine - Yarber Wash group)

Sample	YMsma2	YMsma3	YMsma4	YMsma5
SiO_2	50.56	47.75	52.43	48.80
TiO_2	0.53	0.67	0.59	0.70
Al_2O_3	15.51	16.22	16.61	16.03
Fe_2O_{3-T}	10.99	12.12	11.08	12.04
MgO	6.44	8.09	5.57	7.02
CaO	8.58	9.18	8.87	9.52
Na_2O	1.28	2.48	2.43	1.78
K_2O	3.70	1.22	0.87	2.00
MnO	0.26	0.26	0.15	0.22
P_2O_5	0.14	0.19	0.19	0.20
LOI	1.65	1.79	1.33	1.74
TOTAL	99.64	99.97	100.12	100.05
Mg Number	57	60	53	57
AI	51	44	36	44
Rb	75	26	21	32
Ba	1200	267	175	670
Cs	0.8		0.4	0.4
Sr	174	355	345	472
Pb	10	8	8	6
Th	0.6		0.3	0.3
U	0.8		0.2	0.4
Sc	45		29	44
V	273	291	284	308
Cr	334		53	109
Co	42.9		27.5	40.9
Ni	77		24	51
Y	14.9	12.7	13.9	12.5
Zr	28.0	20.0	26.7	20.0
Nb	4.8	3.7	4.5	4.0
Hf	1.0		0.7	0.6
Ta	0.11		0.04	0.06
La	5.6		3.4	4.0
Ce	14.1		10.0	10.6
Sm	1.85		1.78	1.90
Eu	0.65		0.52	0.64
Tb	0.33		0.32	0.36
Yb	1.33		1.07	1.41
Lu	0.22		0.20	0.23

Table 2b. BASALTIC ANDESITE

Units: Shea Basalts (sb)

Sample	2sb2	2sb9	2sb15	2sb5	2sb20
SO_2	51.76	52.61	53.37	56.99	54.34
TiO_2	2.40	2.41	2.13	2.04	2.16
Al_2O_3	12.68	12.95	13.01	13.43	13.08
Fe_2O_3-T	17.93	16.70	15.80	13.87	15.13
MgO	3.60	3.11	4.12	2.91	3.42
CaO	5.94	6.64	6.98	5.39	6.21
Na_2O	4.00	3.38	2.13	4.65	3.75
K_2O	0.15	0.53	1.15	0.23	0.46
MnO	0.242	0.278	0.241	0.14	0.20
P_2O_5	0.624	0.729	0.677	0.46	0.70
LOI	1.21	1.21	1.40	1.05	1.12
TOTAL	100.54	100.55	101.01	101.20	100.60
Mg Number	31	30	37	32	34
AI	27	27	37	24	28
Rb	nd	nd	28	nd	5
Ba	220	386	513	202	266
Cs	0.3	0.4	0.6	nd	0.4
Sr	203	245	226	197	204
Pb	6	3	nd	7	9
Th	2.7	3.0	2.8	3.1	2.9
U	1.2	1.6	1.6	2.0	1.3
Sc	45	47	42	34	38
V	235	152	170	229	107
Cr	8		5	13	
Co	32.9	26.2	26.6	20.1	24.2
Ni	7.0	1.9	3.9	11.8	5.4
Y	63.9	70.6	67.8	53.5	73.5
Zr	197	212	201	178	227
Nb	12.8	15.1	14.4	12.2	14.2
Hf	5.5	6.5	5.9	4.5	6.3
Ta	0.59	0.74	0.66	0.54	0.73
La	22.0	24.4	24.6	18.4	23.44
Ce	50.0	58.6	58.4	41.52	58.59
Sm	8.15	9.10	8.70	6.38	9.43
Eu	2.69	3.28	3.01	1.77	3.24
Tb	1.65	1.87	1.75	1.19	1.87
Yb	6.47	7.23	7.19	5.05	7.16
Lu	1.03	1.22	1.09	0.82	1.07

Table 2b. - Continued

Units: Core samples - Coca Mines (CM); Brindle Pup (bpa); Basaltic Agglomerate (bag)

Sample	CM-9	8bpa12	4bag9*
SiO_2	53.19	56.73	72.11
TiO_2	1.8	0.98	0.72
Al_2O_3	15.38	15.91	10.26
Fe_2O_{3-T}	14.37	11.5	7.13
MgO	3.68	2.78	1.04
CaO	3.19	6.5	3.51
Na_2O	3.48	3.71	2.74
K_2O	0.27	0.91	1.32
MnO	0.25	0.23	0.11
P_2O_5	0.71	0.32	0.42
LOI	4.17	0.73	1.16
TOTAL	100.49	100.28	100.53
Mg Number	36.5	35.2	24.7
AI	37	27	27
Rb	6	12	32
Ba	136	446	275
Cs		0.9	0.3
Sr	100	311	230
Pb	4	4	8
Th		1.9	0.9
U		1	1
Sc		26	16
V	94	124	43
Cr		nd	nd
Co		24.0	6.9
Ni		7	
Y	60.3	33.7	26.4
Zr	188	99	59
Nb	10.0	8.2	5.3
Hf		2.5	1.1
Ta		0.25	0.13
La		12.5	6.4
Ce		31.3	15.2
Sm		4.78	2.95
Eu		1.35	0.89
Tb		0.90	0.58
Yb		3.40	2.26
Lu		0.54	0.32

* silicified scoria

Table 2c. ANDESITES

Units: Brindle Pup Andesite (bpa)

Sample	8bpa4	8bpa6	8bpa11	8bpa14
SiO_2	61.82	69.61	63.73	64.52
TiO_2	0.58	0.48	0.61	0.61
Al_2O_3	15.69	13.14	15.55	14.94
Fe_2O_3-T	7.16	6.04	7.42	8.12
MgO	1.87	1.89	1.44	1.86
CaO	4.57	3.27	4.40	4.29
Na_2O	3.20	2.29	3.76	3.21
K_2O	2.45	1.91	1.28	0.81
MnO	0.12	0.09	0.12	0.15
P_2O_5	0.16	0.17	0.21	0.20
LOI	2.96	1.04	2.36	1.62
TOTAL	100.58	99.93	100.88	100.33
Mg Number	37	41	30	34
AI	36	41	25	26
Rb	77	61	20	13
Ba	1030	550	485	640
Cs	2.0	1.4	0.7	0.4
Sr	271	175	251	315
Pb	14	7	5	7
Th	3.4	3.0	2.9	2.5
U	2.1	1.7	1.8	1.6
Sc	15	17	23	18
V	104	12	45	40
Cr	5	nd	4	2
Co	13.0	7.2	13.0	11.0
Ni	8	nd	nd	4
Y	32.6	32.1	39.0	43.7
Zr	141	140	140	138
Nb	6.9	7.1	8.9	9.0
Hf	3.5	4.6	4.5	3.6
Ta	0.35	0.40	0.39	0.31
La	14.4	19.7	20.2	16.6
Ce	31.2	46.3	47.2	39.4
Sm	3.97	6.17	6.30	5.63
Eu	0.93	1.63	1.76	1.40
Tb	0.70	1.14	1.24	1.13
Yb	3.02	3.10	4.86	4.47
Lu	0.54	0.50	0.80	0.74

Table 2c. - Continued

Units: Dacite of Burnt Canyon (bcd)

Sample	4bcd11	4bcd13	4bcd17
SiO_2	64.49	64.99	65.05
TiO_2	0.57	0.57	0.59
Al_2O_3	14.58	14.62	14.87
Fe_2O_{3-T}	7.91	7.59	6.66
MgO	1.25	1.39	0.94
CaO	2.86	3.74	3.34
Na_2O	4.08	3.54	4.12
K_2O	2.05	1.32	2.31
MnO	0.16	0.13	0.13
P_2O_5	0.18	0.19	0.19
LOI	2.10	1.62	1.27
TOTAL	100.23	99.70	99.47
Mg Number	26	27	23
AI	32	27	30
Rb	37	19	44
Ba	685	435	620
Cs	0.7	0.4	0.2
Sr	227	235	219
Pb	8	8	14
Th	2.7	2.5	3.9
U	1.63	1.43	2.83
Sc	18	15	11
V	22	25	15
Cr	nd	2	3
Co	8.7	6.7	7.5
Ni			
Y	46.9	43.6	39.7
Zr	151	142	172
Nb	9.8	7.4	8.5
Hf	4.1	3.2	3.9
Ta	0.34	0.32	0.47
La	18.0	13.7	16.9
Ce	39.1	31.7	36.5
Sm	5.86	5.10	4.85
Eu	1.44	1.11	0.99
Tb	1.65	1.00	0.95
Yb	4.89	4.24	3.58
Lu	0.77	0.64	0.59

Table 2c. - Continued

Units: Dacite of Burnt Canyon (bcd)

Sample	4bcd21	4bcd23	4bcd26
SiO_2	65.61	63.41	64.34
TiO_2	0.66	0.54	0.58
Al_2O_3	14.57	15.07	14.16
Fe_2O_{3-T}	6.73	7.16	7.96
MgO	1.05	1.37	1.40
CaO	2.97	2.43	3.54
Na_2O	4.25	6.11	4.75
K_2O	2.11	0.40	0.21
MnO	0.14	0.16	0.17
P_2O_5	0.22	0.19	0.19
LOI	1.25	2.98	2.44
TOTAL	99.56	99.82	99.74
Mg Number	24	28	27
AI	30	17	16
Rb	32	6	2
Ba	685	180	300
Cs	0.4	0.3	0.1
Sr	251	132	186
Pb	11	7	12
Th	4.4	3.4	2.5
U	2.76	1.72	1.50
Sc	15	20	18
V	20	13	
Cr	3	nd	nd
Co	9.1	10.0	11.0
Ni			
Y	40.6	45.3	41.4
Zr	176	157	132
Nb	8.6	8.1	8.0
Hf	4.7	5.3	3.5
Ta	0.52	0.46	0.34
La	20.5	22.9	16.5
Ce	46.7	53.4	38.5
Sm	5.60	6.84	5.55
Eu	1.30	1.83	1.40
Tb	1.02	1.30	1.04
Yb	4.22	5.48	4.43
Lu	0.69	0.97	0.74

Table 2c. - Continued

Units: Gaddes Basalt (gab)

Sample	7gab2	7gab3	7gab5	7gab9
SiO_2	73.66	63.74	66.68	63.50
TiO_2	0.40	0.68	0.67	0.72
Al_2O_3	10.91	13.96	12.69	13.56
Fe_2O_{3-T}	5.37	8.75	8.61	9.64
MgO	0.83	1.29	1.21	1.61
CaO	1.64	4.93	4.52	5.83
Na_2O	2.27	5.02	1.60	2.19
K_2O	1.88	0.24	1.75	0.10
MnO	0.09	0.21	0.15	0.22
P_2O_5	0.08	0.19	0.18	0.19
LOI	3.45	1.33	1.67	1.93
TOTAL	100.58	100.34	99.73	99.49
Mg Number	26	25	24	27
AI	41	13	33	18
Rb	43	2	25	nd
Ba	350	84	1300	51
Cs	0.4	0.1	0.5	0.2
Sr	84	115	418	916
Pb	10	8	7	6
Th	2.0	2.1	1.8	2.0
U	1.16	1.12	0.87	1.28
Sc	13	20	16	16
V	16	17	23	19
Cr	2	nd	nd	nd
Co	4.5	9.5	7.7	8.6
Ni				
Y	40.6	45.1	41.8	44.0
Zr	115.8	120.0	114.0	120.0
Nb	4.6	6.5	6.4	7.1
Hf	3.2	3.4	2.8	2.8
Ta	0.25	0.27	0.24	0.27
La	11.9	13.9	10.7	11.2
Ce	29.7	32.5	26.3	26.5
Sm	4.70	5.28	4.69	4.78
Eu	1.05	1.34	1.10	1.07
Tb	0.97	1.09	0.98	1.06
Yb	4.13	4.81	4.15	4.13
Lu	0.65	0.75	0.63	0.63

Table 2d. DACITE-RHYODACITE

Units: Buzzard Rhyolite (br)

Sample	4br3	6br8	6br10
SiO_2	82.65	79.34	72.00
TiO_2	0.21	0.30	0.40
Al_2O_3	9.23	9.54	12.74
Fe_2O_3-T	2.32	3.09	5.23
MgO	0.45	0.23	1.51
CaO	0.23	1.37	0.44
Na_2O	2.76	4.11	5.78
K_2O	1.61	0.91	0.23
MnO	0.04	0.09	0.11
P_2O_5	0.03	0.06	0.07
LOI	0.87	0.98	1.23
TOTAL	100.40	100.02	99.80
Mg Number			
AI	41	17	22
Rb	27	11	2
Ba	585	544	55
Cs	0.3	0.3	nd
Sr	71	88	48
Pb	13	16	12
Th	1.8	2.0	2.8
U	1.11	1.07	1.53
Sc	7	12	17
V	3	2	
Cr	nd		nd
Co	0.6	0.6	1.2
Ni			
Y	45.5	34.6	46.8
Zr	113.0	110.0	149.0
Nb	3.3	4.0	4.9
Hf	2.3	3.0	4.3
Ta	0.23	0.24	0.38
La	10.1	12.7	18.7
Ce	22.7	29.1	48.1
Sm	3.98	4.39	7.28
Eu	0.65	1.10	1.67
Tb	0.88	0.85	1.27
Yb	3.95	3.26	5.66
Lu	0.66	0.56	0.93

Table 2d. - Continued

Units: Buzzard Rhyolite (br)

Sample	6br11	6br13	7br13
SiO_2	69.98	72.83	77.91
TiO_2	0.36	0.30	0.21
Al_2O_3	11.26	12.89	10.85
Fe_2O_{3-T}	6.02	4.79	3.49
MgO	0.41	0.97	0.86
CaO	3.86	0.74	0.65
Na_2O	0.91	4.86	4.51
K_2O	2.90	1.80	0.43
MnO	0.17	0.11	0.08
P_2O_5	0.06	0.07	0.03
LOI	4.36	0.92	1.34
TOTAL	100.29	100.28	100.36
Mg Number			
AI	41	33	20
Rb	60	28	7
Ba	495	690	97
Cs		0.8	
Sr	54	104	38
Pb	9	10	11
Th		2.6	
U		1.53	
Sc		9	
V			
Cr		nd	
Co		1.1	
Ni			
Y	47.7	48.5	44.7
Zr	132.0	155.0	131.0
Nb	6.6	6.8	5.4
Hf		3.4	
Ta		0.35	
La		14.2	
Ce		33.4	
Sm		5.34	
Eu		1.00	
Tb		1.07	
Yb		4.48	
Lu		0.67	

Table 2d. - Continued

Units: Buzzard Rhyolite (br); Dacite of Burnt Canyon (bcd)

Sample	7br14	6br15	7br16	4bcd18	4bcd28
SiO_2	74.34	73.90	74.91	82.03	72.44
TiO_2	0.27	0.24	0.23	0.17	0.26
Al_2O_3	11.52	12.62	11.96	9.7	13.48
Fe_2O_3-T	3.21	4.20	4.33	2.05	3.38
MgO	0.35	1.20	0.83	0.1	0.91
CaO	2.31	0.67	0.80	0.34	2.02
Na_2O	5.01	5.94	5.09	4.5	3.19
K_2O	0.74	0.37	0.87	0.46	2.18
MnO	0.12	0.10	0.10	0.01	0.06
P_2O_5	0.06	0.03	0.03	0.02	0.05
LOI	2.33	1.08	1.27	0.53	1.69
TOTAL	100.26	100.35	100.42	99.8	99.65
Mg Number					
AI	14.0	19.0	22.0	10.4	37.0
Rb	10	3	11	7	37
Ba	385	55	462	138	590
Cs	0.3				1.6
Sr	91	31	80	72	152
Pb	10	8	8	10	10
Th	2.8				2.87
U	1.51				1.9
Sc	12				8
V				2	29
Cr	nd				4
Co	1.2				2.5
Ni					
Y	45.6	55.4	51.0	34.5	17.9
Zr	139.0	157.0	152.0	137.0	95.0
Nb	6.7	6.2	7.1	4.9	4.5
Hf	4.2				2.83
Ta	0.35				0.31
La	17.2				14.8
Ce	39.8				26.0
Sm	5.79				2.74
Eu	1.30				0.81
Tb	1.09				0.47
Yb	5.17				2.21
Lu	0.88				0.36

Table 2d. - Continued

Units: Upper Unit (du) and Cleopatra Member (dc) of the Deception Rhyolite

Sample	1dc11	1du20	1du21	1du22
SiO_2	78.57	77.70	76.27	78.84
TiO_2	0.14	0.30	0.29	0.26
Al_2O_3	11.81	12.10	12.76	11.32
Fe_2O_3-T	2.06	2.24	2.41	2.12
MgO	0.38	0.10	0.05	0.19
CaO	0.97	1.63	1.23	1.01
Na_2O	4.11	4.05	4.36	5.44
K_2O	1.28	1.33	1.22	0.14
MnO	0.01	0.02	0.01	0.01
P_2O_5	0.04	0.08	0.08	0.08
LOI	1.29	1.24	0.81	0.46
TOTAL	100.66	100.79	99.49	99.87
Mg Number				
AI	25	20	19	5
Rb	15	17	15	nd
Ba	564	430	409	77
Cs	0.6	0.4	0.3	0.2
Sr	93	118	157	159
Pb	9	8	11	10
Th	4.0	3.8	4.3	3.9
U	1.5	1.5	1.7	1.6
Sc	6	8	9	6
V	11	18	12	8
Cr	nd	nd	nd	nd
Co	nd	1.7	1.8	2.3
Ni	3	3	3	nd
Y	48.4	29.1	31.9	23.3
Zr	158	142	161	141
Nb	6.5	5.5	6.9	5.8
Hf	5.0	4.1	4.6	4.2
Ta	0.51	0.49	0.52	0.42
La	26.3	18.5	21.1	15.3
Ce	54.5	38.5	43.8	35.3
Sm	5.39	4.06	4.55	3.72
Eu	0.91	0.85	0.90	0.77
Tb	1.03	0.73	0.80	0.66
Yb	5.76	3.39	3.80	2.97
Lu	0.93	0.51	0.55	0.44

Table 2d. - Continued

Units: Coca Mines Core (CM); Deception Rhyolite (southern outcrops) (dr); Deception Rhyolite from the United Verde Extension (uvx)

Sample	CM-6	CM-7	8dr10	uvx-1j5	uvx-5j7
SiO_2	74.64	73.12	70.95	75.51	79.38
TiO_2	0.18	0.18	0.37	0.21	0.15
Al_2O_3	12.64	13.14	13.65	12.57	9.90
Fe_2O_{3-T}	3.19	3.98	4.80	2.21	2.07
MgO	1.23	1.13	1.16	0.42	0.26
CaO	0.91	0.76	2.18	1.38	1.83
Na_2O	3.86	5.22	3.05	4.03	4.30
K_2O	1.56	1.32	2.72	1.77	0.97
MnO	0.03	0.04	0.09	0.06	0.05
P_2O_5	0.05	0.04	0.09	0.05	0.04
LOI	1.8	1.3	1.33	2.03	1.96
TOTAL	100.09	100.23	100.40	100.24	100.91
Mg Number					
AI	37	29	43	29	17
Rb	23	13	41	24	16
Ba	469	507	730	566	327
Cs					
Sr	71	68	132	69	74
Pb	5	4	17	11	13
Th				2.5	3.3
U				2.10	0.56
Sc					
V	13	19	2	nd	nd
Cr					
Co					
Ni	5	4			
Y	50.2	40.3	48.5	60.4	38.5
Zr	178	197	188	183	130
Nb	6.5	5.7	7.5	3.8	3.5
Hf					
Ta					
La					
Ce					
Sm					
Eu					
Tb					
Yb					
Lu					

Table 2d. - Continued

Units: Quartz Porphyry (QP); Quartz Feldspar Porphyry (Lindberg, 1986) (QFP)

Sample	7QP1	6QP5	6QP6	4QP14	5QFP1
SiO_2	76.02	75.92	76.14	81.45	67.84
TiO_2	0.19	0.15	0.18	0.11	0.22
Al_2O_3	12.08	11.54	11.71	9.99	11.43
Fe_2O_{3-T}	2.71	2.91	2.95	1.64	4.66
MgO	0.32	0.93	0.94	0.34	2.02
CaO	1.05	1.12	0.35	0.34	2.52
Na_2O	4.61	3.0	3.71	2.67	3.82
K_2O	1.21	2.74	2.45	2.34	1.48
MnO	0.05	0.07	0.07	0.05	0.1
P_2O_5	0.02	0.01	0.02	0.01	0.04
LOI	1.63	1.74	1.25	1.27	5.97
TOTAL	99.87	100.13	99.76	100.21	100.09
Mg Number					
AI	21	47	46	47	36
Rb	23	31	25	26	18
Ba	380	840	786	730	1010
Cs	0.3	0.5	0.3	0.8	0.6
Sr	101	69	56	72	69
Pb	10	67	9	9	9
Th	3.0	3.8	2.9	4.1	3.3
U	2.02	2.09	2.05	2.00	1.73
Sc	9	8	7	4	11
V			5		4
Cr	nd	nd		nd	nd
Co	0.6	0.7	0.8	0.6	2.3
Ni	nd	nd	nd	nd	nd
Y	56.4	61.4	55.3	68.5	46.8
Zr	196	207	190	192	139
Nb	6.6	7.1	4.4	5.6	6.0
Hf	4.9	5.9	4.4	6.0	4.6
Ta	0.39	0.51	0.42	0.46	0.43
La	19.7	23.9	17.6	22.7	19.5
Ce	44.0	56.8	39.4	54.2	45.0
Sm	6.24	7.56	6.00	7.89	5.88
Eu	0.86	1.01	0.73	0.92	1.30
Tb	1.27	1.56	1.16	1.77	1.20
Yb	5.64	7.14	5.41	7.85	5.71
Lu	0.94	1.11	0.80	1.30	0.95

Table 2d. - Continued

Units: Quartz Porphyry (QP); Gaddes Basalt (gab)

Sample	2QP16	2QP22	2QP23	7gab8
SiO_2	77.61	80.49	75.19	73.86
TiO_2	0.16	0.15	0.19	0.20
Al_2O_3	11.40	11.47	12.27	12.30
Fe_2O_{3-T}	1.45	0.84	3.28	4.13
MgO	0.30	0.10	1.23	0.62
CaO	0.99	0.11	0.42	1.95
Na_2O	5.65	6.06	5.68	4.82
K_2O	0.51	0.29	0.18	1.19
MnO	0.04	0.03	0.06	0.10
P_2O_5	0.02	0.01	0.01	0.05
LOI	1.65	0.43	1.30	1.02
TOTAL	99.76	99.98	99.79	100.24
Mg Number	31.7	21.1	45.7	25.0
AI	11	6	19	21
Rb	6	nd	nd	15
Ba	82	156	68	490
Cs	0.2			
Sr	43	50	49	103
Pb	9	9	8	7
Th	2.9			
U	1.55			
Sc	7			
V	nd			
Cr	nd			
Co	0.6			
Ni	nd			
Y	61.1	59.0	65.2	53.2
Zr	188	192	184	151
Nb	7.6	7.5	7.6	6.6
Hf	4.1			
Ta	0.46			
La	12.6			
Ce	29.8			
Sm	4.89			
Eu	0.59			
Tb	1.22			
Yb	5.50			
Lu	0.85			

Table 2e. Major and Trace Element Concentrations in Representative Samples of the Deception Rhyolite from the Jerome Area, Arizona.

	Unaltered Suite					
Sample No.	D11	D20	D21	D22	J5	Mean
SiO_2	78.57	77.70	76.27	78.84	75.51	76.1
TiO_2	0.14	0.30	0.29	0.26	0.21	0.23
Al_2O_3	11.8	12.10	12.8	11.3	12.6	12.2
Fe_2O_{3total}	2.1	2.2	2.4	2.1	2.2	2.8
MgO	0.38	0.10	0.05	0.19	0.42	0.55
CaO	0.97	1.63	1.23	1.01	1.38	1.32
Na_2O	4.11	4.05	4.36	5.44	4.03	4.27
K_2O	1.28	1.33	1.22	0.14	1.77	1.37
MnO	0.01	0.02	0.01	0.01	0.06	0.04
P_2O_5	0.04	0.08	0.08	0.08	0.05	0.06
L.O.I.	1.29	1.24	0.81	0.46	2.03	1.36
Total	100.7	100.8	99.5	99.9	100.2	100.3
A.I.	24.6	20.1	18.5	4.9	28.8	29.4
Rb	15	17	15	~2	24	19
Cs	0.6	0.4	0.3	0.2	--	0.4
Sr	93	118	157	159	69	104
Ba	564	430	409	77	566	453
Y	48	29	32	23	60	41
Zr	158	142	161	141	183	164
Hf	5.0	4.1	4.6	4.2	--	4.5
Nb	6.5	5.5	6.9	5.8	3.8	5.7
Ta	0.5	0.5	0.5	0.4	--	0.5
Co	--	1.7	1.8	2.3	--	1.9
Sc	5.6	7.7	9.2	5.7	--	7.1
V	10	8	12	8	--	12
Cu	<5	<5	<5	<5	--	<5
Zn	31	34	51	31	--	53
Pb	9	8	11	10	11	10
U	1.5	1.5	1.7	1.6	--	1.6
Th	4.0	3.8	4.3	3.9	--	4.0
La	26	19	21	15	--	20
Ce	55	38	44	35	--	43
Sm	5.4	4.1	4.6	3.7	--	4.4
Eu	0.91	0.85	0.90	0.77	--	0.86
Tb	1.03	0.73	0.80	0.66	--	0.81
Yb	5.8	3.4	3.8	3.0	--	4.0
Lu	0.93	0.51	0.55	0.44	--	0.61
n						4-9

Table 2e. - Continued

Sample No.	Zone 3 D6	D56	D4	D36	D41	Mean
SiO_2	76.73	77.46	77.52	75.68	74.22	77.0
TiO_2	0.15	0.16	0.13	0.17	0.16	0.14
Al_2O_3	11.1	11.2	11.4	13.2	13.0	11.3
Fe_2O_3total	4.1	3.3	2.0	2.3	2.5	3.0
MgO	3.22	3.18	1.35	1.90	1.19	2.54
CaO	0.04	0.03	0.40	0.32	1.30	0.45
Na_2O	0.07	0.03	1.69	2.62	0.59	0.94
K_2O	1.96	2.24	3.79	1.90	4.56	2.52
MnO	0.08	0.08	0.02	0.02	0.02	0.04
P_2O_5	0.04	0.04	0.04	0.04	0.04	0.04
L.O.I.	2.80	2.60	1.59	2.03	2.83	2.52
Total	100.2	100.3	99.92	100.2	100.4	100.49
A.I.	98.7	98.9	73.1	56.4	75.3	80.4
Rb	21	28	32	19	54	25
Cs	0.3	0.4	0.5	0.4	1.2	0.5
Sr	16	10	37	45	30	26
Ba	634	409	921	270	893	489
Y	56	54	43	51	51	48
Zr	189	185	165	185	180	170
Hf	5.2	5.2	4.9	5.2	5.6	4.8
Nb	7.1	7.1	7.2	7.4	8.0	7.1
Ta	0.5	0.5	0.5	0.5	0.5	0.5
Co	1.8	1.3	2.2	2.0	2.1	1.9
Sc	10.1	10.4	5.8	6.0	6.6	7.0
V	3	4.0	7	9.0	10.0	6.1
Cu	<5	31	<5	<5	<5	22
Zn	129	80	29	34	34	115
Pb	6	9	9	7	8	8
U	1.9	2.0	2.0	2.3	2.3	1.9
Th	3.7	3.7	4.0	4.2	4.5	3.7
La	22	22	22	23	23	20
Ce	50	49	47	51	53	44
Sm	6.0	5.8	5.3	5.7	5.6	5.1
Eu	0.87	1.09	0.78	0.95	1.01	0.82
Tb	1.23	1.30	0.93	1.12	1.06	1.0
Yb	6.4	5.8	4.7	5.2	5.6	5.1
Lu	0.98	0.91	0.79	0.87	0.85	0.81
n						12

Table 2e - Continued

	Zone 2					
Sample No.	P8	P20	P22	P39	P44	Mean
SiO_2	75.63	81.26	75.83	81.22	80.28	78.9
TiO_2	0.18	0.10	0.13	0.12	0.15	0.14
Al_2O_3	13.9	6.8	8.2	9.7	9.1	9.2
Fe_2O_3total	2.1	5.4	7.4	3.9	3.9	4.6
MgO	2.22	4.05	5.12	1.72	2.11	3.34
CaO	0.27	0.01	0.01	0.01	0.04	0.04
Na_2O	0.17	0.03	0.12	0.03	0.13	0.19
K_2O	3.24	0.35	0.22	1.90	1.56	1.54
MnO	0.01	0.03	0.04	0.02	0.01	0.02
P_2O_5	0.04	0.02	0.01	0.02	0.01	0.02
L.O.I.	2.71	2.41	3.22	2.07	2.08	2.54
Total	100.5	100.3	100.3	100.7	99.4	100.53
A.I.	92.5	99.1	97.6	98.9	95.6	95.2
Rb	41	2	2	20	18	16
Cs	0.9	0.3	0.8	0.4	0.9	0.5
Sr	28	2	3	15	17	31
Ba	855	295	217	1,068	288	560
Y	51	30	32	38	36	36
Zr	188	107	127	141	131	138
Hf	6.3	3.0	3.3	3.8	3.8	4.0
Nb	8.2	5.3	6.6	6.2	5.5	6.2
Ta	0.6	0.4	0.3	0.4	0.4	0.4
Co	0.20	0.20	6.1	1.4	1.7	1.7
Sc	7.2	2.8	3.3	5.2	4.9	5.3
V	10	7	5	10	5	11
Cu	406	178	37	228	194	169
Zn	346	306	437	261	161	292
Pb	23	20	13	56	31	33
U	2.7	1.3	2.1	2.2	1.6	2.0
Th	4.8	2.6	2.6	3.2	3.1	3.3
La	27	15	12	16	21	18
Ce	62	34	29	33	47	40
Sm	6.4	3.7	3.3	3.9	5.0	4.3
Eu	1.17	0.42	0.44	0.55	0.63	0.66
Tb	1.31	0.76	0.73	0.88	0.89	0.85
Yb	5.7	3.0	3.0	3.83	3.58	4.0
Lu	0.96	0.45	0.54	0.62	0.67	0.63
n						18

Table 2e. - Continued

Sample No.	Zone 1 3B11	B43	9B11	B1	VC	Mean
SiO_2	26.06	28.20	26.23	28.17	26.65	26.9
TiO_2	0.21	0.52	0.23	0.26	0.27	0.26
Al_2O_3	23.8	23.4	23.4	23.0	21.1	22.9
Fe_2O_3total	23.3	16.1	21.7	20.7	23.7	21.8
MgO	17.59	21.92	18.09	17.71	17.83	17.9
CaO	0.01	0.02	0.01	0.01	0.22	0.04
Na_2O	0.03	0.03	0.03	0.03	0.03	0.05
K_2O	0.01	0.01	0.05	0.01	0.01	0.03
MnO	0.12	0.07	0.12	0.10	0.18	0.11
P_2O_5	0.03	0.02	0.05	0.04	0.02	0.04
L.O.I.	9.46	10.58	9.73	9.52	10.03	9.67
Total	100.4	100.6	99.6	99.6	99.9	99.70
A.I.	99.8	99.8	99.8	99.8	98.6	99.5
Rb	1	1	6	6	5	4
Cs	2.0	0.7	1.6	3.4	1.2	1.9
Sr	1	2	1	2	2	3
Ba	120	130	10	20	<10	59
Y	69	80	103	99	28	81
Zr	221	322	225	269	240	243
Hf	7.1	9.4	6.2	8.9	7.7	8.1
Hb	14.3	14.3	15.9	15.4	13.2	13.9
Ta	0.7	0.9	0.6	0.8	0.6	0.7
Co	15.2	10.0	14.2	14.8	29.1	18
Sc	8.9	21.7	7.5	7.9	19.3	12
V	7	9	9	15	1	5.3
Cu	401	1,092	--	--	31	508
Zn	977	700	912	1,033	516	2,272
Pb	82	8	112	31	8	201
U	2.9	4.3	2.6	4.5	2.1	3.4
Th	5.4	8.8	5.3	7.1	5.2	6.5
La	57	39	90	37	2.5	75
Ce	130	87	209	88	7.5	154
Sm	14.3	11.9	25.2	10.7	1.9	18
Eu	1.30	1.72	1.73	1.44	0.62	1.7
Tb	2.14	2.06	3.58	2.76	0.52	2.6
Yb	7.1	9.0	9.8	10.0	6.0	8.4
Lu	1.09	1.53	1.45	1.70	1.03	1.32
n						8

TABLE 3. VOLCANICS OF THE GREEN GULCH BLOCK

* Unit description and abbreviations after Anderson and Blacet (1972)

* nd = not detected

* AI = Alteration Index (Ishikawa et al., 1976)
  AI = $[MgO + K_2O/Na_2O + K_2O + CaO + MgO)] \times 100$

* Mg Number = (100 MgO/MgO + FeO) mole ratio

Table 3a. BASALT (primitive)

Units: basaltic flows (grb)

Sample	13grb1	13grb3	13grb4	13grb8	13grb28
SiO_2	44.47	47.81	46.31	42.84	51.4
TiO_2	0.76	0.77	0.77	0.65	0.68
Al_2O_3	13.36	11.56	11.48	9.49	14.60
Fe_2O_3-T	10.49	10.46	9.76	10.89	9.43
MgO	6.89	11.03	9.74	13.57	9.4
CaO	10.33	9.85	9.13	11.24	9.92
Na_2O	2.37	1.54	1.4	0.38	2.57
K_2O	0.01	1.31	0.03	0.17	0.41
MnO	0.16	0.22	0.24	0.25	0.21
P_2O_5	0.19	0.19	0.29	0.26	0.11
LOI	10.57	2.98	10.46	9.19	1.49
TOTAL	99.70	97.72	99.61	98.93	100.22
Mg Number	60	70	69	74	69
AI	35	52	48	54	44
Rb	2	27	2	3	11
Ba	18	595	63	57	168
Cs	0.2	0.9		0.2	
Sr	294	312	467	131	198
Pb	17	13	17	12	11
Th	0.8	1.1		1.8	
U	0.1	0.4		0.3	
Sc	50	39		27	
V	260	245	214	194	202
Cr	463	1089		1036	
Co	52.0	51.7		64.2	
Ni	84	221		508	
Y	18.5	18.1	17.4	15.5	24.5
Zr	53	71	76	63	70
Nb	6.1	6.8	9.4	8.6	13.4
Hf	1.9	1.9		2.0	
Ta	0.19	0.26		0.26	
La	8.7	10.0		15.3	
Ce	21.3	25.2		39.6	
Sm	3.28	3.12		4.87	
Eu	1.11	0.92		1.09	
Tb	0.55	0.55		0.59	
Yb	2.11	1.69		1.48	
Lu	0.35	0.27		0.21	

Table 3a. BASALT (evolved)

Unit: basaltic flows (grb)

Sample	13grb5	13grb25	13grb26	13grb32	14grb3
SiO_2	53.14	52.03	49.36	45.77	44.69
TiO_2	1.09	0.93	0.90	1.17	1.19
Al_2O_3	15.81	15.36	15.24	16.81	16.61
Fe_2O_3-T	13.14	8.16	8.75	15.25	10.01
MgO	2.92	2.55	3.60	7.38	3.63
CaO	4.48	7.59	8.62	7.23	8.80
Na_2O	5.43	3.34	2.53	2.03	5.63
K_2O	0.43	1.36	1.34	1.24	0.18
MnO	0.12	0.13	0.13	0.23	0.21
P_2O_5	0.29	0.26	0.24	0.14	0.20
LOI	3.84	8.08	9.47	2.60	9.15
TOTAL	100.69	99.79	100.18	99.85	100.30
Mg Number	33	41	48	52	45
AI	25	26	31	48	21
Rb	12	28	25	38	8
Ba	138	440	451	296	113
Cs	0.4	0.7		1.7	0.1
Sr	597	391	321	182	216
Pb	11	16	13	nd	15
Th	1.5	2.3		1.0	1.4
U	0.6	1.3		nd	0.2
Sc	25	18		35	34
V	297	187	201	246	215
Cr	40	121		46	182
Co	32.6	15.3		57.5	50.4
Ni	23	60		100	83
Y	23.7	18.9	19.3	29.5	29.1
Zr	92	133	121	97	103
Nb	8.5	12.3	9.9	12.1	16.2
Hf	2.7	2.9		3.1	3.2
Ta	0.28	0.43		0.48	0.58
La	13.0	14.4		7.6	15.7
Ce	33.0	33.6		20.5	37.2
Sm	4.41	3.59		3.99	4.59
Eu	1.43	0.96		1.21	1.41
Tb	0.73	0.57		0.87	0.83
Yb	2.33	1.60		2.80	3.14
Lu	0.36	0.23		0.45	0.54

Table 3b. BASALTIC ANDESITE

Unit: basaltic flows (grb)

Sample	13grb9	13grb19	13grb27	13grb31	13grb33
SiO_2	51.97	52.38	52.88	51.80	53.76
TiO_2	1.01	1.19	1.03	1.34	0.57
Al_2O_3	17.88	15.38	14.55	13.78	16.40
Fe_2O_3-T	9.30	13.96	12.72	14.10	10.92
MgO	5.37	6.06	5.90	5.25	4.55
CaO	6.47	3.04	8.44	8.48	6.42
Na_2O	3.90	4.07	3.12	3.17	5.54
K_2O	0.31	0.11	0.35	0.74	0.96
MnO	0.16	0.17	0.28	0.24	0.18
P_2O_5	0.32	0.17	0.16	0.12	0.10
LOI	3.33	3.41	0.9	0.97	0.78
TOTAL	100.02	99.94	100.33	99.99	100.18
Mg Number	57	49	51	46	48
AI	36	47	35	34	32
Rb	9	3	8	21	30
Ba	214		149	190	203
Cs					
Sr	761	280	249	173	207
Pb		15	23	8	12
Th					
U					
Sc					
V	223		305	425	372
Cr					
Co					
Ni					
Y	21.6	37.3	34.5	37.5	17.8
Zr	131	96	85	93	40
Nb	8.6	6.0	6.5	5.0	4.5
Hf					
Ta					
La					
Ce					
Sm					
Eu					
Tb					
Yb					
Lu					

Table 3b. - Continued

Unit: basaltic flows (grb); [HL = Hassayampa Lake area]

Sample	HLgrb3	HLgrb6	HLgrb2	HLgrb5
SiO_2	53.95	50.26	55.26	53.71
TiO_2	1.22	1.34	1.24	1.32
Al_2O_3	13.59	14.20	13.93	14.12
Fe_2O_{3-T}	13.54	15.30	13.38	13.30
MgO	4.45	5.13	3.79	4.27
CaO	7.64	8.55	5.19	6.43
Na_2O	4.34	1.98	6.16	3.66
K_2O	0.44	1.56	0.39	1.60
MnO	0.24	0.27	0.21	0.20
P_2O_5	0.20	0.27	0.21	0.27
LOI	0.30	0.84	0.24	0.84
TOTAL	99.91	99.70	100.0	99.72
Mg Number	43	43	39	42
AI	29	39	27	37
Rb	11	49	10	63
Ba	169	1104	181	530
Cs			0.8	5.1
Sr	242	251	108	234
Pb	11	11	9	13
Th			2.4	nd
U			0.7	1.0
Sc			49	44
V	403	462	379	395
Cr			17	22
Co			47.6	47.5
Ni			19	18
Y	45.3	45.7	42.2	45.6
Zr	115	131	116	129
Nb	8.2	9.9	7	8.3
Hf			3.9	4.1
Ta			0.37	0.37
La			17.4	19.4
Ce			42.4	47.7
Sm			5.77	6.23
Eu			1.74	1.59
Tb			1.16	1.29
Yb			4.53	4.39
Lu			0.78	0.78

Table 3b. - Continued

Units: basaltic flows (grb)

Sample	13grb7	13grb10	13grb34	14grb10
SiO_2	48.21	47.49	51.95	58.86
TiO_2	1.11	1.08	1.50	1.60
Al_2O_3	18.33	18.82	13.42	14.97
Fe_2O_{3-T}	12.28	10.85	15.18	10.59
MgO	4.78	4.63	4.61	3.15
CaO	7.72	5.12	8.76	1.93
Na_2O	2.20	5.60	2.60	3.08
K_2O	0.93	1.03	0.81	1.65
MnO	0.17	0.19	0.24	0.14
P_2O_5	0.25	0.36	0.16	0.16
LOI	3.44	5.38	0.64	3.41
TOTAL	99.42	100.55	99.87	99.54
Mg Number	47	49	41	40
AI	37	35	32	49
Rb	26	27	24	44
Ba	498	442	212	876
Cs	0.7	0.7	0.8	1.0
Sr	571	435	165	190
Pb	17	11	12	14
Th	1.7	3.1	1.1	2.6
U	0.6	0.7	0.7	0.92
Sc	35	29	39	40
V	113	234	452	420
Cr	48	79	10	13
Co	41.6	41.7	36.7	33.9
Ni	35	38	24	18
Y	26.6	27.9	39.2	40.4
Zr	100	136	106	141.0
Nb	7.1	9.8	6.0	7.2
Hf	3.1	3.8	2.7	4.1
Ta	0.30	0.42	0.26	0.41
La	14.6	23.1	6.6	14.0
Ce	35.7	51.1	16.9	33.1
Sm	4.74	5.55	3.87	5.14
Eu	1.57	1.73	1.11	1.65
Tb	0.83	0.93	0.85	1.16
Yb	2.56	2.77	2.98	3.60
Lu	0.41	0.43	0.47	0.57

Table 3c. ANDESITE

Unit: basaltic flows (grb)

Sample	13grb16	13grb18	13grb20	13grb30
SiO_2	56.54	58.60	61.42	52.63
TiO_2	0.85	1.08	0.73	1.01
Al_2O_3	15.15	13.09	14.12	15.14
Fe_2O_3-T	9.50	10.42	6.76	11.34
MgO	2.34	2.21	2.19	5.41
CaO	3.76	5.23	4.43	7.80
Na_2O	3.51	3.12	4.47	3.40
K_2O	3.31	1.55	1.10	1.00
MnO	0.14	0.15	0.07	0.20
P_2O_5	0.56	0.32	0.15	0.20
LOI	3.74	3.79	4.54	1.50
TOTAL	99.40	99.56	99.98	99.63
Mg Number	36	32	42	52
AI	44	31	27	36
Rb	53	36	33	28
Ba	1185	705	575	295
Cs	0.9	0.8	0.9	0.5
Sr	384	202	266	265
Pb	25	14	13	11
Th	6.0	4.2	6.1	1.5
U	3.63	2.25	2.71	0.57
Sc	20	28	15	27
V	99	140	103	199
Cr	3	10	33	34
Co	17.8	21.1	15.0	30.8
Ni	nd	11	21	43
Y	36.9	54.5	31.8	43.9
Zr	166	186	176	137
Nb	12.7	10.7	11.9	6.9
Hf	5.0	5.5	5.4	3.2
Ta	0.51	0.53	0.72	0.33
La	40.5	25.9	27.3	9.1
Ce	95.6	62.3	57.0	24.7
Sm	9.60	7.69	5.76	4.52
Eu	2.59	1.98	1.47	1.15
Tb	1.17	1.52	0.98	1.07
Yb	3.62	5.21	2.82	3.35
Lu	0.57	0.85	0.45	0.51

Table 3c. - Continued

Unit: basaltic flows (grb)

Sample	14grb1	13grb17	13grb29	14grb2
SiO_2	58.74	61.49	53.70	58.61
TiO_2	0.83	1.13	1.00	0.81
Al_2O_3	15.41	15.39	15.22	15.42
Fe_2O_{3-T}	7.70	9.50	11.07	7.48
MgO	2.28	2.73	5.44	2.33
CaO	4.00	2.05	8.37	3.84
Na_2O	4.50	1.56	3.18	5.17
K_2O	1.83	2.95	0.79	1.27
MnO	0.09	0.07	0.20	0.11
P_2O_5	0.16	0.16	0.20	0.16
LOI	4.61	2.66	1.00	4.50
TOTAL	100.17	99.69	100.17	99.70
Mg Number	40	39	53	41
AI	33	61	35	29
Rb	54	84	20	28
Ba	646			
Cs	0.4			
Sr	213	203	192	276
Pb	17	17	13	19
Th	4.6			
U	2.24			
Sc	11			
V	116	113	207	116
Cr	11			
Co	15.5			
Ni	3			
Y	25.8	42.0	46.5	25.8
Zr	151	172	150	160
Nb	12.7	10.3	7.3	11.2
Hf	3.8			
Ta	0.64			
La	17.8			
Ce	36.5			
Sm	3.72			
Eu	1.08			
Tb	0.65			
Yb	2.07			
Lu	0.30			

Table 3d. DACITE-RHYODACITE

Unit: rhyolitic rocks (grr)

Sample	14grr6	13grr14	13grr21
SiO_2	70.54	74.02	59.04
TiO_2	0.38	0.48	0.59
Al_2O_3	14.90	11.64	17.40
Fe_2O_3-T	4.36	4.13	7.80
MgO	0.69	0.49	2.01
CaO	2.06	1.14	2.02
Na_2O	3.44	4.23	5.37
K_2O	2.07	2.45	1.73
MnO	0.10	0.06	0.06
P_2O_5	0.09	0.10	0.14
LOI	1.51	1.23	3.17
TOTAL	100.14	99.97	99.33
Mg Number			
AI	33.41	35.38	33.60
Rb	63	48	41
Ba	800	810	600
Cs	1.1	1.8	1.2
Sr	163	133	304
Pb	20	16	16
Th	5.0	8.0	3.4
U	2.5	4.2	1.6
Sc	10	11	16
V	30	10	153
Cr	7	1	60
Co	3.7	3.2	16.1
Ni	nd	nd	12
Y	42.1	46.2	22.0
Zr	206	236	180
Nb	12.4	10.2	7.4
Hf	5.1	6.2	4.6
Ta	0.62	0.67	0.37
La	24.9	31.1	17.4
Ce	55.4	73.0	39.0
Sm	5.91	7.38	3.97
Eu	1.44	1.42	1.16
Tb	1.06	1.24	0.62
Yb	3.51	3.87	1.93
Lu	0.55	0.61	0.32

TABLE 4. VOLCANICS OF THE BIG BUG BLOCK

* Unit descriptions and abbreviations after Anderson and Creasey (1958) unless otherwise indicated.

* nd = not detected

* AI = Alteration Index (Ishikawa et al., 1976)
  AI = $[MgO + K_2O/(Na_2O + K_2O + CaO + MgO)] \times 100$

* Mg Number = (100 MgO/MgO + FeO) mole ratio

Table 4a. BASALTS

Units: andesitic flows (sma);

Sample	10sma12	10sma14	10sma15
SiO_2	50.50	50.51	51.08
TiO_2	1.02	1.03	1.02
Al_2O_3	17.15	17.02	17.35
Fe_2O_3	13.04	13.12	12.94
MgO	4.10	4.02	3.97
CaO	8.21	8.08	8.05
Na_2O	2.63	2.54	2.63
K_2O	0.74	0.57	0.52
MnO	0.23	0.24	0.23
P_2O_5	0.12	0.13	0.13
LOI	2.36	2.43	2.45
TOTAL	100.11	99.68	100.38
Mg Number	41.4	41.0	41.0
AI	31	30	30
Rb	19	13	14
Ba	322	438	256
Cs	0.9	0.4	1.3
Sr	295	287	317
Pb	6	9	9
Th	0.7	0.6	0.7
U	0.4	0.3	0.3
Sc	35	40	25
V	284	267	268
Cr	6	8	5
Co	30.8	34.3	23.6
Ni	8	7	19
Y	21.1	22.6	23.1
Zr	66	68	68
Nb	7.1	7.1	7.3
Hf	1.7	2.0	1.6
Ta	0.22	0.23	0.16
La	6.4	7.9	5.0
Ce	15.9	19.4	15.9
Sm	2.70	3.36	2.67
Eu	0.87	1.08	0.65
Tb	0.40	0.56	0.48
Yb	1.99	2.42	1.85
Lu	0.37	0.45	0.30

Table 4a. - Continued

Units: andesitic flows (smIK = samples from Iron King Mine Dump); andesitic breccia (smb)

Sample	10smb20	10smIK24	10smIK24
SiO2	53.24	49.14	47.61
TiO2	1.14	0.80	0.81
Al2O3	15.64	17.47	18.02
Fe2O3	13.54	11.90	11.91
MgO	3.23	4.98	5.30
CaO	8.70	8.43	9.77
Na2O	2.68	2.63	1.85
K2O	0.62	0.25	0.27
MnO	0.21	0.20	0.20
P2O5	0.18	0.12	0.14
LOI	1.27	4.48	4.02
TOTAL	100.44	100.39	99.90
Mg Number	35.0	49.0	50.0
AI	25	32	32
Rb	13	6	6
Ba	217	188	200
Cs	0.9	0.2	0.1
Sr	349	275	468
Pb	7	11	9
Th	0.7	0.7	0.8
U	0.7	0.4	0.6
Sc	33	37	40
V	325	265	254
Cr	4	30	31
Co	31.9	41.1	49.4
Ni	18	25	17
Y	27.9	17.5	16.9
Zr	69	51	55
Nb	7.2	6.0	6.0
Hf	2.0	1.5	1.7
Ta	0.20	0.13	0.19
La	7.3	6.2	7.9
Ce	19.8	15.5	21.0
Sm	3.51	2.43	2.91
Eu	1.12	0.81	0.95
Tb	0.62	0.35	0.43
Yb	2.57	2.03	2.18
Lu	0.40	0.32	0.38

Table 4a. - Continued

Unit: pyroxene-phyric dike (sm)

Sample	9sm11
SiO_2	47.91
TiO_2	0.58
Al_2O_3	9.20
Fe_2O_3	10.73
MgO	12.98
CaO	13.82
Na_2O	1.77
K_2O	0.68
MnO	0.26
P_2O_5	0.19
LOI	2.20
TOTAL	100.30
Mg Number	73
AI	47
Rb	16
Ba	167
Cs	
Sr	477
Pb	16
Th	0.8
U	1
Sc	
V	163
Cr	
Co	
Ni	
Y	17.3
Zr	51
Nb	12.8
Hf	
Ta	
La	
Ce	
Sm	
Eu	
Tb	
Yb	
Lu	

Table 4a. - Continued

Units: andesitic and basaltic flows (ika)

Sample	10ikal	10ika8	10ika9
SiO_2	49.57	51.25	55.18
TiO_2	0.78	0.75	0.72
Al_2O_3	16.18	17.43	15.08
Fe_2O_3-T	10.73	10.02	9.81
MgO	3.99	4.06	4.11
CaO	6.88	6.82	5.15
Na_2O	3.42	4.56	3.26
K_2O	0.54	0.08	0.83
MnO	0.16	0.17	0.16
P_2O_5	0.13	0.14	0.14
LOI	7.93	4.93	4.96
TOTAL	100.32	100.21	99.39
Mg Number	46	48	49
AI	31	27	37
Rb	15	2	18
Ba	165	65	315
Cs	0.6	0.1	0.5
Sr	112	429	240
Pb	6	12	9
Th	0.6	1.4	1.4
U	0.5	0.8	1.0
Sc	31	33	35
V	287	265	237
Cr	23	24	28
Co	26.8	27.1	29.3
Ni	17	12	13
Y	14.9	17.9	17.1
Zr	49.0	86.5	79.0
Nb	5.3	7.1	6.5
Hf	1.3	2.3	2.4
Ta	0.14	0.24	0.21
La	5.8	9.2	11.4
Ce	15.0	25.6	26.9
Sm	2.05	2.74	3.62
Eu	0.74	0.93	0.99
Tb	0.32	0.44	0.44
Yb	1.39	1.73	2.08
Lu	0.25	0.30	0.38

Table 4a. - Continued

Units: andesitic and basaltic flows (ika)

Sample	10ika10	10ika11	ika-rc
SiO_2	54.25	54.15	49.72
TiO_2	0.72	0.74	0.67
Al_2O_3	16.27	16.74	19.16
Fe_2O_3-T	10.48	10.67	8.38
MgO	3.64	3.75	3.45
CaO	8.76	8.31	6.01
Na_2O	2.01	2.15	4.92
K_2O	0.27	0.28	0.67
MnO	0.19	0.18	0.12
P_2O_5	0.14	0.14	0.11
LOI	3.59	3.48	6.54
TOTAL	100.31	100.55	99.77
Mg Number	44	44	48
AI	27	28	27
Rb	7	7	12
Ba	196	217	725
Cs	0.3	0.3	
Sr	490	415	197
Pb	8	10	11
Th	1.5	1.5	
U	0.9	1.1	
Sc	36	35	
V	260	262	249
Cr	24	25	
Co	31.6	29.7	
Ni	12	5	
Y	18.0	18.2	16.7
Zr	78.0	80.0	41.0
Nb	8.4	7.6	4.7
Hf	2.4	2.3	
Ta	0.22	0.29	
La	10.0	11.4	
Ce	27.4	26.8	
Sm	3.03	3.57	
Eu	1.00	1.03	
Tb	0.46	0.40	
Yb	1.98	2.14	
Lu	0.33	0.37	

Table 4a. - Continued

Units: Bluebell group: andesitic and basaltic flows (ika), mafic flows (ikab)

Sample	11ika10	12ika1	12ika2	12ika3
SiO_2	46.40	50.65	48.57	49.97
TiO_2	1.14	1.15	1.11	1.08
Al_2O_3	15.91	15.65	14.87	14.90
Fe_2O_{3-T}	13.84	12.92	13.61	12.03
MgO	7.19	6.96	6.85	7.30
CaO	12.94	6.21	9.82	8.78
Na_2O	1.56	5.60	3.90	3.39
K_2O	0.18	0.08	0.19	0.42
MnO	0.16	0.17	0.19	0.17
P_2O_5	0.08	0.10	0.10	0.09
LOI	1.20	0.90	0.76	1.47
TOTAL	100.60	100.39	99.97	99.60
Mg Number	54	55	53	58
AI	34	37	34	39
Rb	4	2	4	11
Ba	43	10	34	70
Cs		nd	nd	0.7
Sr	232	92	137	107.0
Pb	5	9	9	9
Th	0.3	0.4	0.3	0.5
U	0.1	nd	nd	nd
Sc	56	49	44	43
V	360	321	370	408
Cr	550	183	170	175
Co	70.0	56.3	48.3	52.4
Ni	222	102	99	109
Y	20.1	24.0	23.2	21.5
Zr	55	73	69	67
Nb	7.6	8.1	7.8	7.1
Hf	1.8	2.1	1.9	1.9
Ta	0.29	0.34	0.25	0.30
La	3.7	3.0	3.1	2.8
Ce	10.6	9.0	9.6	9.0
Sm	2.84	2.52	2.31	2.12
Eu	1.02	0.90	0.79	0.78
Tb	0.35	0.60	0.57	0.52
Yb	2.19	2.10	1.98	1.96
Lu	0.38	0.33	0.33	0.33

Table 4b. BASALTIC ANDESITES

Units: andesitic breccia (smb); (high-TiO2 group)

Sample	10smb21	10smb22	9smb40	10smIK23
SiO_2	52.71	50.54	51.03	51.75
TiO_2	1.45	1.92	1.52	1.76
Al_2O_3	14.55	13.02	13.21	13.42
Fe_2O_{3-T}	14.47	15.98	16.00	14.54
MgO	4.13	4.37	3.77	4.03
CaO	7.12	8.40	5.46	8.01
Na_2O	2.11	2.89	2.92	2.90
K_2O	1.42	1.29	1.42	0.03
MnO	0.25	0.28	0.18	0.23
P_2O_5	0.36	0.28	0.32	0.29
LOI	1.11	0.96	3.95	3.49
TOTAL	99.67	99.93	99.76	100.45
Mg Number	39	38	35	38
AI	38	33	38	27
Rb	33	32	47	4
Ba	530	485	280	112
Cs		1.1	1.8	0.6
Sr	239	264	264	424
Pb	4	8	21	13
Th		2.2	2.9	2.4
U		1.1	1.4	1.2
Sc		46	50	35
V	311	544	483	394
Cr		17	5	26
Co		46.7	59.6	34.0
Ni		21	24	16
Y	43.1	43.7	38.8	44.1
Zr	132	151	125	163
Nb	10.9	10.1	10.3	9.7
Hf		3.9	4.1	4.1
Ta		0.40	0.44	0.45
La		15.9	28.6	16.2
Ce		37.4	64.7	39.2
Sm		5.73	7.43	5.83
Eu		1.98	2.29	1.70
Tb		1.12	1.11	1.31
Yb		4.54	4.22	4.10
Lu		0.77	0.76	0.64

Table 4b. - Continued

Unit: andesitic breccia (smb); (high-Al group)

Sample	9smb42	9smb45	9smb47
SiO_2	51.68	51.35	51.11
TiO_2	0.95	1.01	0.89
Al_2O_3	17.91	18.39	18.16
Fe_2O_{3-T}	12.41	12.83	11.74
MgO	3.41	3.09	3.93
CaO	8.55	9.03	10.09
Na_2O	2.48	2.19	2.45
K_2O	0.31	0.59	0.40
MnO	0.27	0.32	0.22
P_2O_5	0.15	0.18	0.15
LOI	1.96	1.33	1.49
TOTAL	100.08	100.29	100.62
Mg Number	38	35	43
AI	25	25	26
Rb	7	15	9
Ba	153	255	148
Cs	0.6	0.9	0.1
Sr	261	229	304
Pb	13	10	9
Th	0.7	0.9	0.9
U	0.5	0.7	0.6
Sc	37	38	35
V	323	304	290
Cr	7	14	32
Co	37	11.9	36.2
Ni	10	12	12
Y	28.3	26.9	22.7
Zr	70	81	59
Nb	7.2	7.1	5.9
Hf	2.0	2.5	1.7
Ta	0.17	0.23	0.12
La	8.6	14.2	8.1
Ce	21.3	34.3	20.8
Sm	3.81	4.85	3.26
Eu	1.47	1.65	1.04
Tb	0.63	0.75	0.61
Yb	2.84	3.11	2.42
Lu	0.52	0.55	0.45

Table 4b. - Continued

Unit: (sm); (high-Ti group)

Sample	9sm46
SiO_2	50.24
TiO_2	2.61
Al_2O_3	12.29
Fe_2O_{3-T}	16.85
MgO	3.99
CaO	7.94
Na_2O	2.97
K_2O	1.03
MnO	0.30
P_2O_5	1.10
LOI	0.75
TOTAL	100.07
Mg Number	35
AI	32
Rb	28
Ba	432
Cs	
Sr	230
Pb	12
Th	
U	
Sc	
V	273
Cr	
Co	
Ni	
Y	73
Zr	271
Nb	12.3
Hf	
Ta	
La	
Ce	
Sm	
Eu	
Tb	
Yb	
Lu	

Table 4b. - Continued

Unit: andesitic and basaltic flows (ika)

Sample	Qika5	10ika3
SiO_2	53.60	50.67
TiO_2	1.80	2.40
Al_2O_2	15.86	12.84
Fe_2O_{3-T}	8.91	15.84
MgO	2.44	3.65
CaO	7.62	8.10
Na_2O	3.37	3.17
K_2O	1.88	0.23
MnO	0.09	0.27
P_2O_5	0.48	0.98
LOI	3.69	1.85
TOTAL	99.73	100.00
Mg Number	38	34
AI	28	26
Rb	52	11
Ba	130	147
Cs	1.0	0.7
Sr	136	305
Pb		12
Th	1.4	2.5
U	1.6	1.4
Sc	26	27
V	166	215
Cr	nd	6
Co	46.7	19.3
Ni	7	10
Y	43.8	69.3
Zr	249	277
Nb	19.1	11.3
Hf	6.7	4.9
Ta	1.11	0.55
La	25.2	19.9
Ce	64.2	47.6
Sm	7.89	8.54
Eu	2.47	2.07
Tb	1.21	1.65
Yb	4.78	4.85
Lu	0.85	0.71

Table 4c. ANDESITES

Unit: andesitic flows (sma)

Sample	9sma4	9sma6	9sma13	9sma17
SiO_2	67.43	62.52	61.98	66.05
TiO_2	0.73	0.84	0.77	0.75
Al_2O_3	13.43	15.38	14.03	13.57
Fe_2O_{3-T}	7.21	8.07	9.28	7.41
MgO	1.63	1.61	2.75	1.72
CaO	2.58	4.33	3.23	3.43
Na_2O	4.06	3.07	2.01	3.62
K_2O	1.34	2.30	2.99	1.68
MnO	0.11	0.13	0.12	0.11
P_2O_5	0.25	0.30	0.25	0.26
LOI	1.17	1.00	1.81	0.97
TOTAL	99.94	99.54	99.21	99.56
Mg Number	34	31	40	34
AI	31	35	52	33
Rb	33	65	91	37
Ba	370	780	945	650
Cs	2.0	3.2	3.8	1.2
Sr	178	223	144	197
Pb	7	8	8	10
Th	4.2	4.3	4.5	4.3
U	2.1	2.2	2.2	2.1
Sc	21	24	22	20
V	35	29	54	21
Cr	nd	nd	2	nd
Co	10.7	11.4	13.7	9.7
Ni	nd	nd	nd	nd
Y	54.1	62.7	58.1	58.9
Zr	185	206	183	185
Nb	8.3	10.9	10.0	8.8
Hf	5.8	7.0	5.3	5.7
Ta	0.44	0.49	0.43	0.48
La	27.8	30.9	29.8	26.8
Ce	65.4	72.9	67.9	64.5
Sm	8.53	9.60	9.01	8.40
Eu	2.03	2.49	2.17	2.04
Tb	1.67	1.81	1.62	1.69
Yb	6.06	6.80	6.51	6.04
Lu	1.12	1.28	1.14	1.11

Table 4c. - Continued

Unit: andesitic flows (sma)

Sample	9sma24	9sma28	9sma18	9sma23
SiO_2	69.30	66.91	65.27	67.57
TiO_2	0.67	0.77	0.78	0.71
Al_2O_3	12.84	13.74	13.97	13.62
Fe_2O_3-T	6.91	7.09	7.93	7.33
MgO	1.07	1.39	1.81	1.69
CaO	2.94	3.23	4.1	2.56
Na_2O	1.86	3.53	3.32	3.54
K_2O	2.84	1.94	1.7	2.34
MnO	0.11	0.07	0.14	0.08
P_2O_5	0.15	0.19	0.26	0.14
LOI	1.00	0.63	1.01	0.79
TOTAL	99.66	99.49	100.28	100.38
Mg Number	26	31	34	34
AI	45	33	32	40
Rb	60	60	42	69
Ba	1020	485	538	520
Cs	3.0	5.1	1.3	4.3
Sr	141	160	214	189
Pb	10	9	14	13
Th	4.6	4.5	4.0	4.1
U	2.3	2.2	2.3	2.1
Sc	19	23	19	17
V	2	2	31	7
Cr	2	nd	2	nd
Co	8.7	21.3	9.0	12.0
Ni	2	6	6	nd
Y	64.9	61.9	56.2	62.7
Zr	211	215	187	218
Nb	10.2	11.5	7.8	8.3
Hf	6.0	7.2	5.3	5.9
Ta	0.50	0.54	0.47	0.49
La	29.4	33.9	25.9	26.4
Ce	66.9	79.9	61.3	61.8
Sm	9.34	10.13	7.87	8.35
Eu	2.07	2.59	1.93	2.01
Tb	1.83	1.83	1.48	1.59
Yb	7.27	7.69	5.42	5.90
Lu	1.26	1.44	0.93	1.00

Table 4c. - Continued

Units: andesitic tuffs (smt) and rhyolitic flows and tuffs (smr)

Sample	9smr5	9smt33	9smt35	9smt39
SiO_2	69.25	62.63	59.68	57.62
TiO_2	0.74	1.04	0.76	0.85
Al_2O_3	13.60	15.08	17.22	16.15
Fe_2O_3-T	6.93	7.61	7.29	10.20
MgO	0.75	3.30	2.75	3.66
CaO	2.25	3.22	3.38	4.39
Na_2O	4.46	4.16	5.32	2.29
K_2O	0.85	0.88	1.94	2.31
MnO	0.12	0.12	0.09	0.14
P_2O_5	0.17	0.39	0.21	0.18
LOI	1.06	1.91	1.36	2.34
TOTAL	100.19	100.33	99.99	100.13
Mg Number	20	49	46	45
AI	19	36	35	47
Rb	17	24	56	67
Ba	305	231	630	625
Cs		1.8	3.6	2.8
Sr	196	312	343	408
Pb	15	9	11	10
Th		3.4	2.5	3.4
U		2.0	1.7	1.8
Sc		13.0	11.0	26.1
V		68	163	179
Cr		nd	47	174
Co		11	9	27
Ni		12	20	79
Y	61.6	56.1	20.9	26.7
Zr	207	212	126	125
Nb	8.6	10.2	9.4	10.2
Hf		4.6	2.2	3.6
Ta		0.43	0.30	0.47
La		20.9	18.9	21.5
Ce		49.5	32.2	48.3
Sm		7.57	3.68	5.23
Eu		1.64	0.82	1.18
Tb		1.37	0.42	0.71
Yb		4.53	1.45	3.05
Lu		0.68	0.22	0.50

Table 4c. - Continued

Units: andesitic tuff (smt) and massive crystal tuff (smct), (outcrops south of Big Bug Mesa)

Sample	15smt1	15smct3	15smct5	17smt1	17smt3
SiO_2	63.42	60.80	64.00	57.47	63.58
TiO_2	0.37	0.42	0.38	0.35	0.36
Al_2O_3	14.21	15.21	14.42	14.08	14.08
Fe_2O_{3-T}	7.26	8.17	6.38	6.40	6.22
MgO	3.22	4.07	2.81	3.26	3.09
CaO	4.14	4.43	3.47	6.16	3.58
Na_2O	3.22	3.21	4.28	5.16	4.04
K_2O	0.64	0.78	0.86	0.20	0.80
MnO	0.19	0.18	0.12	0.15	0.09
P_2O_5	0.08	0.08	0.09	0.08	0.08
LOI	2.96	2.75	2.81	6.52	3.95
TOTAL	99.71	100.10	99.62	99.83	99.97
Mg Number	50	53	50	53	53
AI	34	39	32	23	34
Rb	11	12	19	2	17
Ba	420	545	300	135	285
Cs	0.3	0.3	0.4	0.1	0.4
Sr	234	164	171	273	305
Pb	18	17	26	27	16
Th	3.0	3.0	3.3	2.8	2.9
U	1.1	1.5	1.7	1.5	2.1
Sc	19	30	21	18	17
V	124	159	128	133	129
Cr	38	57	43	38	33
Co	16.9	22.9	17.3	15.8	12.9
Ni	15	15	10	2	2
Y	18.6	22.4	22.8	20.5	21.1
Zr	91	81	93	83	91
Nb	5.8	4.0	5.5	6.0	5.3
Hf	2.5	2.7	2.8	2.4	2.3
Ta	0.32	0.30	0.34	0.30	0.30
La	10.8	12.9	11.8	9.4	9.2
Ce	25.1	28.4	27.8	21.5	20.9
Sm	2.40	3.12	2.78	2.41	2.37
Eu	0.58	0.86	0.72	0.53	0.48
Tb	0.47	0.52	0.52	0.47	0.43
Yb	1.80	2.16	2.05	1.84	1.72
Lu	0.30	0.37	0.34	0.29	0.30

Table 4c. - Continued

Units: andesitic tuff (smt) and massive crystal tuff (smct), (outcrops south of Big Bug Mesa)

Sample	15smct4	17smt4	15smt2	15smct6
SiO_2	64.0	62.72	62.11	60.00
TiO_2	0.35	0.33	0.42	0.39
Al_2O_3	14.48	13.08	14.36	14.67
Fe_2O_{3-T}	6.75	5.91	7.13	7.85
MgO	2.59	2.65	4.35	3.23
CaO	5.54	4.50	3.94	6.03
Na_2O	2.87	4.08	2.78	2.50
K_2O	0.82	0.94	1.20	0.93
MnO	0.13	0.11	0.18	0.19
P_2O_5	0.08	0.07	0.08	0.08
LOI	2.29	5.30	3.05	3.65
TOTAL	99.90	99.69	99.60	99.52
Mg Number	46	50	58	48
AI	29	30	45	33
Rb	10	20	19	18
Ba	420	310	540	557
Cs	0.3	0.4		
Sr	239	88	131	186
Pb	19	17	13	21
Th	3.3	3.0		5.7
U	1.9	1.4		2.6
Sc	22	22		
V	123	118	145	152
Cr	44	44		
Co	18.2	18.2		
Ni	5	6		
Y	21.5	18.4	19.6	21.6
Zr	93	81	84	87
Nb	5.8	5.9	5.3	6.2
Hf	2.9	2.9		
Ta	0.34	0.31		
La	12.9	11.5		
Ce	29.9	26.5		
Sm	2.92	2.55		
Eu	0.69	0.67		
Tb	0.53	0.53		
Yb	2.21	1.91		
Lu	0.37	0.34		

Table 4c. - Continued

Unit: andesitic and basaltic flows (ika)

Sample	11ika9	11ika8
SiO_2	54.02	52.48
TiO_2	1.28	1.19
Al_2O_3	15.00	15.45
Fe_2O_{3-T}	10.50	9.98
MgO	5.72	6.06
CaO	8.68	9.26
Na_2O	2.85	3.43
K_2O	0.11	0.16
MnO	0.11	0.14
P_2O_5	0.36	0.35
LOI	1.65	1.57
TOTAL	100.27	100.07
Mg Number	55	58
AI	34	33
Rb	2	2
Ba	38	25
Cs	nd	nd
Sr	664	560
Pb	6	7
Th	2.1	1.5
U	1.1	1.2
Sc	32	22
V	182	177
Cr	294	205
Co	49.0	34.4
Ni	129	112
Y	38.5	38.2
Zr	198	193
Nb	15.9	16.9
Hf	6.6	4.4
Ta	1.00	0.80
La	31.2	21.3
Ce	81.1	57.7
Sm	9.35	7.05
Eu	2.52	1.89
Tb	1.34	1.10
Yb	4.37	3.42
Lu	0.81	0.48

Table 4d. DACITE-RHYODACITE

Units: andesitic tuff (smt) and quartz porphyry (qp)

Sample	9smt30	Qqp1	Qqp2
SiO_2	77.87	76.32	77.21
TiO_2	0.19	0.15	0.14
Al_2O_3	12.38	11.62	10.90
Fe_2O_{3-T}	2.15	2.04	1.94
MgO	0.56	0.41	0.29
CaO	0.76	1.07	1.56
Na_2O	1.02	1.12	1.90
K_2O	3.36	4.80	3.58
MnO	0.01	0.02	0.02
P_2O_5	0.02	0.01	0.01
LOI	1.58	2.14	2.37
TOTAL	99.90	99.68	99.93
Mg Number			
AI	69	70	53
Rb	66	68	45
Ba	722	1200	890
Cs		2.4	1.5
Sr	69	49	53
Pb		16	17
Th		4.2	3.8
U		1.6	1.6
Sc		9	8
V	nd	3	8
Cr		nd	nd
Co		1.2	1.3
Ni		nd	nd
Y	59.8	26.0	29.4
Zr	239	120	112
Nb	9.9	9.4	8.7
Hf		4.2	3.5
Ta		0.55	0.54
La		17.3	18.2
Ce		47.1	41.1
Sm		3.39	4.02
Eu		0.78	0.67
Tb		0.67	0.68
Yb		2.28	2.82
Lu		0.46	0.63

Table 4d. RHYOLITE

Unit: rhyolitic flows and tuffs (ikr)

Sample	Qikr2	Qikr4	Qikr7
SiO_2	78.03	89.38	83.83
TiO_2	0.11	0.06	0.01
Al_2O_3	11.79	7.0	7.32
Fe_2O_{3-T}	2.17	0.22	2.72
MgO	2.39	0.2	2.99
CaO	0.26	0.03	0.07
Na_2O	1.74	0.19	0.03
K_2O	1.15	1.9	1.07
MnO	0.01	0	0.02
P_2O_5	0.01	0.01	0.03
LOI	2.21	1.01	1.98
TOTAL	99.86	99.95	100.07
Mg Number			
AI	64	91	98
Rb	13	15	7
Ba	120	200	120
Cs	0.4	0.3	0.1
Sr	88	18	7
Pb	18	23	17
Th	5.3	3.5	3.8
U	2.1	1.4	3.5
Sc	5	1	2
V	nd	nd	nd
Cr	nd	nd	nd
Co	0.6	0.3	5.5
Ni	nd	nd	nd
Y	41.2	32.1	44.1
Zr	173	99	109
Nb	14.8	12.6	12.8
Hf	6.7	4.3	4.5
Ta	1.46	0.84	0.96
La	38.2	29.2	41.3
Ce	80.3	38.0	102.8
Sm	7.94	7.46	10.80
Eu	1.23	1.28	1.96
Tb	1.31	1.17	2.44
Yb	4.41	2.96	6.89
Lu	0.74	0.46	1.05

Table 4e. - Continued

Units: rhyolitic rocks (smr); quartz porphyry (qp)

Sample	9smr8	9smr9	9smr20	9smr26	12qp4
SiO_2	81.33	78.68	77.22	77.99	81.91
TiO_2	0.14	0.16	0.09	0.13	0.06
Al_2O_3	10.22	11.81	12.03	12.13	10.47
Fe_2O_3-T	1.55	2.14	1.28	1.65	1.88
MgO	0.55	0.82	0.25	0.14	0.30
CaO	0.94	0.36	0.79	1.25	0.15
Na_2O	1.97	0.59	4.53	5.0	2.35
K_2O	1.68	3.1	2.63	1.22	1.82
MnO	0.02	0.03	0.03	0.02	0.01
P_2O_5	0.01	0.01	0.01	0.01	0.03
LOI	1.33	2.01	0.83	0.49	1.07
TOTAL	99.75	99.70	99.67	100.03	100.05
Mg Number AI	43	81	35	18	46
Rb	24	44	38	15	34
Ba	605	1520	890	635	185
Cs	0.7			0.5	0.9
Sr	71	18	78	112	29
Pb	14	12	15	15	17
Th	6.7			9.4	2.3
U	2.0			3.2	0.9
Sc	5			5	9
V	nd	4	nd	11	nd
Cr	nd			nd	nd
Co	0.6			2.0	0.3
Ni	nd			nd	nd
Y	59.4	59.8	78.2	67.5	24.9
Zr	223	272	171	153	94
Nb	9.9	11.5	17.8	15.5	5.2
Hf	7.2			6.8	3.2
Ta	0.73			1.10	0.39
La	31.8			49.5	18.0
Ce	70.6			110.6	40.2
Sm	7.32			10.12	4.47
Eu	0.95			1.30	0.61
Tb	1.52			1.98	0.71
Yb	6.57			7.58	2.43
Lu	1.19			1.47	0.44

TABLES 5, 6 AND 7

MEAN VALUES FOR UNITS OF THE YAVAPAI THE SUPERGROUP

Table 5. VOLCANICS OF THE ASH CREEK BLOCK

* Nb value in parenthesis is recommended by MORB-normalized Ta-Nb couplet.
* DI = Differentiation Index of Thornton & Tuttle

Table 5a. BASALT - BASALTIC ANDESITE

Unit	ggt	gabbro	Yarber Wash YMsma	sb
SiO_2	54.40	48.13	48.39	53.81
TiO_2	0.87	0.48	0.62	2.23
Al_2O_3	15.45	14.51	16.09	13.03
Fe_2O_{3T}	12.31	11.97	11.56	15.89
MgO	3.16	9.89	6.78	3.43
CaO	6.51	9.58	9.04	6.23
Na_2O	3.33	1.61	1.99	3.58
K_2O	0.80	0.54	1.95	0.50
MnO	0.18	0.19	0.22	0.22
P_2O_5	0.20	0.11	0.18	0.64
LOI	2.98	3.25	1.63	1.20
Mg Number	33-39	63-67	53-60	30-37
DI	34.50	17 & 23	30.2	42
Rb	15	15	38.0	18
Ba	334	171	578	318
Cs	0.27	0.35	0.53	0.40
Sr	253	280	337	215
Th	0.77	0.68	0.4	2.90
U			0.7	1.53
Sc	37.1	32.5	39.3	41.4
V	307	190	289	179
Cr	10	146	165	9
Co	26.8	55.6	37.1	26.0
Ni	9	93	51	6
Y	19.0	15.6	13.5	65.9
Zr	39	41	24	203
Nb	4.9	5.1	4.3(1.3)	13.7
Hf	1.31	1.24	0.77	5.73
Ta	0.08	0.09	0.07	0.65
La	6.8	5.7	4.3	22.6
Ce	17.3	14.1	11.6	53.4
Sm	2.87	2.16	1.84	8.35
Eu	0.98	0.73	0.60	2.80
Tb	0.52	0.38	0.34	1.67
Yb	1.93	1.52	1.27	6.62
Lu	0.34	0.27	0.22	1.05
N(XRF suite)	5	2	4	5
N(INAA suite)	2	2	3	5

Table 5b. ANDESITE

Unit	gab	bpa	bcd
SiO_2	66.90	63.92	64.65
TiO_2	0.62	0.57	0.59
Al_2O_3	12.78	14.83	14.65
Fe_2O_{3T}	8.09	7.19	7.34
MgO	1.24	1.77	1.23
CaO	4.23	4.13	3.15
Na_2O	2.77	3.12	4.48
K_2O	0.99	1.61	1.40
MnO	0.17	0.12	0.15
P_2O_5	0.16	0.19	0.19
LOI	2.10	2.00	1.94
Mg Number	24-27	30-41	
DI	63.4	62.9	69.8
Rb	18	43	28
Ba	447	678	484
Cs	0.30	1.11	0.40
Sr	383	253	213
Th	1.95	2.93	3.36
U	1.28	1.83	2.07
Sc	16.5	18.4	15.8
V	19	50	2
Cr	2	3	2
Co	7.6	11.0	8.4
Ni	nd	6.0	nd
Y	42.9	36.9	43.2
Zr	117	140	160
Nb	6.2	8.0	8.5
Hf	3.03	4.01	4.24
Ta	0.26	0.36	0.42
La	12.0	17.7	18.4
Ce	28.8	41.1	41.5
Sm	4.86	5.52	5.65
Eu	1.14	1.43	1.33
Tb	1.03	1.05	1.18
Yb	4.31	3.86	4.48
Lu	0.67	0.65	0.73
N (XRF suite)	4	4	6
N (INAA suite)	4	4	6

Table 5c. DACITE-RHYODACITE

Unit	br	QP	du	dl-dc
SiO_2	75.32	77.38	77.609	78.57
TiO_2	0.28	0.16	0.28	0.14
Al_2O_3	11.40	11.33	12.06	11.81
Fe_2O_{3T}	4.08	2.55	2.26	2.06
MgO	0.76	0.63	0.11	0.38
CaO	1.23	0.72	1.29	0.97
Na_2O	4.33	3.50	4.62	4.11
K_2O	1.10	2.19	1.28	1.28
MnO	0.10	0.06	0.01	0.01
P_2O_5	0.05	0.02	0.08	0.04
LOI	1.61	1.47	0.84	1.29
Mg Number				
DI	85.4		89.1	89.5
Rb	18	26	16	15
Ba	385	686	420	564
Cs	0.37	0.46	0.38	0.57
Sr	67	74	145	93
Th	2.41	3.48	3.99	4.01
U	1.35	2.04	1.59	1.52
Sc	11.4	7.0	7.5	5.6
V	nd	nd	nd	nd
Cr	nd	nd	nd	nd
Co	1	8	2	nd
Ni	nd	nd	nd	nd
Y	46.7	60.4	28.1	48.4
Zr	138	196	148	158
Nb	5.7	5.9	6.1	6.5
Hf	3.43	5.28	4.29	5.01
Ta	0.31	0.45	0.48	0.51
La	14.6	21.0	18.3	26.3
Ce	34.6	48.6	39.2	54.5
Sm	5.4	6.92	4.11	5.39
Eu	1.14	0.88	0.84	0.91
Tb	1.03	1.44	0.73	1.03
Yb	4.50	6.51	3.39	5.76
Lu	0.74	1.04	0.50	0.93
N (XRF suite)	9	4	3	1(dc11)
N (INAA suite)	5	4	3	1

TABLE 6. VOLCANICS OF THE GREEN GULCH BLOCK

* Nb value in parenthesis is recommended by MORB-normalized Ta-Nb couplet.
* DI = Differentiation Index of Thornton & Tuttle

Table 6a. BASALTS AND BASALTIC ANDESITE

Unit	grb prim.	grb evolved	grb
SiO_2	46.57	49.0	52.39
TiO_2	0.73	1.06	1.25
Al_2O_3	12.10	15.97	15.25
Fe_2O_{3T}	10.21	11.06	12.88
MgO	10.13	4.02	4.78
CaO	10.09	7.34	6.48
Na_2O	1.65	3.79	3.66
K_2O	0.39	0.91	0.83
MnO	0.22	0.16	0.21
P_2O_5	0.21	0.23	0.22
LOI	6.94	6.63	1.98
Mg Number	60-74	33-52	39-57
DI	18.2	31.4	41.5
Rb	9.0	22.0	25.0
Ba	180.0	288.0	415.0
Cs	0.43	0.73	1.52
Sr	280.0	342.0	305.0
Th	1.23	1.55	2.18
U	0.3	0.5	0.8
Sc	38.9	27.9	39.4
V	263.0	229.0	347.0
Cr	863.0	97.0	32.0
Co	56.0	39.0	41.5
Ni	271.0	67.0	25.0
Y	18.7	24.1	37.0
Zr	67.0	109.0	114.8
Nb	8.9	11.8	7.5
Hf	1.9	3.0	3.6
Ta	0.24	0.44	0.46
La	11.3	12.7	15.9
Ce	28.7	31.1	37.8
Sm	3.76	4.15	5.22
Eu	1.04	1.25	1.57
Tb	0.56	0.75	1.04
Yb	1.76	2.47	3.47
Lu	0.28	0.40	0.57
N(XRF suite)	5	5	12
N(INAA suite)	3	4	6

Table 6b - ANDESITE AND DACITE-RHYOLITE

Unit	grb	grb
SiO_2	57.18	67.87
TiO_2	0.90	0.48
Al_2O_3	14.79	14.65
Fe_2O_{3T}	9.18	5.43
MgO	3.17	1.06
CaO	5.35	1.74
Na_2O	3.91	4.35
K_2O	1.55	2.08
MnO	0.14	0.07
P_2O_5	0.25	0.11
LOI	3.38	1.97
Mg Number	32-53	
DI	54.8	78.7
Rb	36.0	51.0
Ba	681.0	737.0
Cs	0.70	1.37
Sr	257.0	200.0
Th	4.48	5.47
U	2.3	2.8
Sc	20.1	12.4
V	156.0	64.0
Cr	18.0	23.0
Co	20.0	7.7
Ni	16.0	5.0
Y	37.9	36.8
Zr	160.9	207.3
Nb	10.5	10.0
Hf	4.6	5.3
Ta	0.55	0.55
La	24.1	24.5
Ce	55.2	55.8
Sm	6.26	5.75
Eu	1.65	1.34
Tb	1.08	0.97
Yb	3.41	3.10
Lu	0.54	0.49
N(XRF suite)	7	3
N(INAA suite)	5	3

TABLE 7. VOLCANICS OF THE BIG BUG BLOCK

* Nb value in parenthesis is recommended by MORB-normalized Ta-Nb couplet.
* DI = Differentiation Index of Thornton & Tuttle

Table 7a. BASALTS

Unit	Iron King Mine smIK	Bluebell ika-ikab	ika	sma-smb
SIO_2	48.38	48.90	52.36	51.33
TiO_2	0.81	1.12	0.73	1.05
Al_2O_3	17.75	13.62	16.81	16.79
Fe_2O_{3T}	11.91	13.10	11.81	13.16
MgO	5.14	7.08	3.83	3.83
CaO	9.10	9.44	6.99	8.26
Na_2O	2.24	3.61	3.08	2.26
K_2O	0.26	0.22	0.45	0.61
MnO	0.20	0.17	0.16	0.23
P_2O_5	0.13	0.09	0.13	0.14
LOI	4.25	1.08	5.24	2.13
Mg Number	49-50	53-58	44-49	35-41
DI	34.0	30.3	23.8	24.1
Rb	6.0	5.0	10.0	15.0
Ba	194.0	39.0	281.0	308.0
Cs	0.15	0.18	0.36	0.88
Sr	372.0	142.0	314.0	312.0
Th	0.75	0.38	1.28	0.68
U	0.5		0.9	0.4
Sc	38.9	47.6	33.9	33.4
V	260.0	365.0	260.0	286.0
Cr	30.0	270.0	25.0	6.0
Co	45.3	56.8	28.9	30.2
Ni	21.0	133.0	12.0	13.0
Y	17.2	22.2	17.1	23.7
Zr	53.0	65.9	68.7	68.0
Nb	6.0	7.7(6.3)	6.6(5.3)	7.2(4.2)
Hf	1.6	1.9	2.1	1.8
Ta	0.16	0.30	0.22	0.20
La	7.1	3.2	9.6	26.6
Ce	18.3	9.6	24.3	17.8
Sm	2.67	2.45	3.00	3.06
Eu	0.88	0.87	0.94	0.93
Tb	0.39	0.51	0.41	0.52
Yb	2.11	2.06	1.86	2.21
Lu	0.35	0.34	0.33	0.38
N(XRF suite)	2	4	6	4
N(INAA suite)	2	4	5	4

Table 7b. BASALTIC ANDESITE

Unit	smb (high-Ti)	smb (high-Al)	ika (high-Ti)
SiO_2	51.43	51.38	52.14
TiO_2	1.63	0.95	2.10
Al_2O_3	13.59	18.15	14.35
Fe_2O^{3T}	15.48	12.33	12.38
MgO	4.09	3.48	3.05
CaO	6.99	9.22	7.86
Na_2O	2.64	2.37	3.27
K_2O	1.38	0.43	1.06
MnO	0.24	0.27	0.18
P_2O_5	0.32	0.16	0.73
LOI	2.01	1.59	2.77
Mg Number	35-39	35-43	38
DI	36.4	36.8	41.8
Rb	37.0	10.0	32.0
Ba	432.0	185.0	139.0
Cs	1.45	0.53	0.85
Sr	256.0	265.0	221.0
Th	2.55	0.83	1.95
U	1.3	0.6	1.5
Sc	47.8	36.8	26.2
V	346.0	306.0	190.0
Cr	11.0	18.0	6.0
Co	53.2	28.4	33.0
Ni	23.0	11.0	9.0
Y	41.9	26.0	56.6
Zr	135.8	70.1	262.8
Nb	10.4(9.0)	6.7(5.3)	15.2
Hf	4.0	2.1	5.8
Ta	0.42	0.17	0.83
La	22.3	10.3	22.6
Ce	51.1	25.5	55.9
Sm	6.58	3.97	8.22
Eu	2.14	1.39	2.27
Tb	1.12	0.66	1.43
Yb	4.38	2.79	4.82
Lu	0.77	0.51	0.78
N(XRF suite)	3	3	2
N(INNA suite)	2	3	2

Table 7c - ANDESITE

Unit	sma	smct-smt	smt	ika
SiO_2	65.88	62.01	59.98	53.25
TiO_2	0.75	0.37	0.88	1.24
Al_2O_3	13.82	14.29	16.15	15.23
Fe_2O_{3T}	7.65	6.90	8.37	10.24
MgO	1.71	3.25	3.24	5.89
CaO	3.30	4.64	3.66	8.97
Na_2O	3.13	3.57	3.92	3.14
K_2O	2.14	0.80	1.71	0.14
MnO	0.11	0.15	0.12	0.13
P_2O_5	0.23	0.08	0.26	0.36
LOI	1.05	3.70	1.87	1.61
Mg Number	26-40	46-58	46-49	55-58
DI	58.0	57.3	58.8	33.4
Rb	57.0	14.0	49.0	2
Ba	664.0	390.0	495.0	32.0
Cs	2.99	0.31	2.73	nd
Sr	181.0	199.0	354.0	612.0
Th	4.31	3.04	3.10	1.80
U	2.2	1.6	1.8	1.2
Sc	20.5	21.4	16.8	27.2
V	23.0	134.0	137.0	180.0
Cr	1	42.0	110.0	250.0
Co	12.0	17.5	12.5	41.7
Ni	4	8.0	37.0	121.0
Y	59.9	20.7	34.6	38.4
Zr	198.7	87.1	154.3	195.1
Nb	9.5	5.5	9.9	16.4
Hf	6.0	2.6	3.5	5.5
Ta	0.48	0.32	0.40	0.90
La	28.9	11.2	20.4	26.3
Ce	67.6	24.3	43.3	69.4
Sm	8.90	2.65	5.49	8.20
Eu	2.17	0.65	1.21	2.21
Tb	1.69	0.50	0.83	1.22
Yb	6.46	1.96	3.01	3.90
Lu	1.16	0.33	0.37	0.65
N(XRF suite)	8	9	3	2
N(INAA suite)	8	7	3	2

Table 7d. DACITE-RHYODACITE and RHYOLITE

	Dacite-Rhyodacite		Rhyolite (least altered)	
	Spud Mtn. qp(1&2)	Spud Mtn. qp(4)	smr	ikr2
SiO_2	76.77	81.91	78.85	78.03
TiO_2	0.15	0.06	0.12	0.11
Al_2O_3	11.26	10.47	11.46	11.79
Fe_2O_{3T}	1.99	1.88	1.49	2.17
MgO	0.35	0.30	0.31	2.39
CaO	1.32	0.15	0.99	0.26
Na_2O	1.51	2.35	3.83	1.74
K_2O	4.19	1.82	1.84	1.15
MnO	0.02	0.01	0.02	0.01
P_2O_5	0.01	0.03	0.01	0.00
LOI	2.26	1.07	0.88	2.21
Mg Number				
DI	87.7	91.6	90.8	82.2
Rb	57.0	34.0	26.0	34.0
Ba	1045.0	185.0	710.0	190.0
Cs	2.00	0.90	0.60	0.90
Sr	51.0	29.0	87.0	29.0
Th	4.00	2.30	8.10	2.27
U	1.6	0.9	2.6	0.9
Sc	8.2	8.9	4.6	8.9
V	6.0	nd	nd	nd
Cr	nd	nd	nd	nd
Co	0.8	1.3	1.3	0.3
Ni	nd	nd	nd	nd
Y	27.7	24.9	68.4	24.9
Zr	115.7	94.3	182.1	94.3
Nb	9.1	5.2	14.4	5.2
Hf	3.9	3.2	7.0	3.2
Ta	0.55	0.39	0.92	1.46
La	17.8	18.0	40.7	38.2
Ce	44.1	40.2	90.6	80.3
Sm	3.71	4.47	8.72	7.94
Eu	0.73	0.61	1.13	1.23
Tb	0.68	0.71	1.76	1.31
Yb	2.55	2.43	7.08	4.41
Lu	0.55	0.44	1.33	0.74
N(XRF suite)	2	1	3	1
N(INNA suite)	2	1	2	1

TABLES 8 - 10

TRACE AND SELECTED MAJOR ELEMENT RATIOS

FOR UNITS OF THE YAVAPAI SUPERGROUP

TABLE 8. VOLCANICS OF THE ASH CREEK BLOCK

* For units represented by 1 or 2 samples, individual ratios are given. For units represented by 3 or more samples, a range is given.

* The trace element ratios are useful in correlation of units and evaluating potential genetic links as the ratios of relatively immobile elements are uneffected by alteration (See Sec. IV)

Table 8a. BASALT

Grapevine Gulch Fm. (ggt), Coca Mines Core (CM-8), gabbro (gb), Yarber Wash andesitic flow (YMsma)

Unit	ggt	CM-8
Al_2O_3/TiO_2	15.9 - 22.2	13.6
La/Yb	3.4 - 3.6	
Ti/Zr	122.23 - 151.8	107.0
Zr/Nb	6.8 - 9.3	9.1
Nb/Y	.21 - .33	.25
Zr/Y	1.9 - 2.3	2.3
La/Th	8.5 - 9.0	
Th/Yb	.40	
Ta/Yb	.037 - .045	
Hf/Th	1.69 - 1.77	
Ti/V	13.2 - 23.9	17.7
FeO_T/MgO	3.13 - 4.09	1.68

Unit	gb	YMsma
Al_2O_3/TiO_2	31.9 & 29.1	22.9 - 29.3
La/Yb	4.4 & 2.5	2.8 - 4.2
Ti/Zr	53.4 & 100.0	112 - 210
Zr/Nb	10.6 & 5.5	5.0 - 5.9
Nb/Y	.26 & .44	.29 - .32
Zr/Y	2.7 & 2.4	1.6 - 1.9
La/Th	8.5 & 8.3	9.1 - 12.6
Th/Yb	.52 & .30	.24 - .47
Ta/Yb	.061 & .047	.037 - .083
Hf/Th	1.60 & 2.56	1.55 - 2.52
Ti/V	16.7 & 13.6	11.6 - 13.8
FeO_T/MgO	1.21 & .99	1.35 - 1.79

Table 8b. BASALTIC ANDESITE

Shea Basalt (sb), Brindle Pup Andesite (bpa)

Unit	sb	bpa
Al_2O_3/TiO_2	5.3 - 6.6	16.2
La/Yb	3.3 - 3.6	3.7
Ti/Zr	57.0 - 73.1	59.3
Zr/Nb	14.0 - 16.0	12.1
Nb/Y	.19 - .23	.24
Zr/Y	3.0 - 3.3	2.9
La/Th	6.0 - 8.8	6.71
Th/Yb	.39 - .60	.55
Ta/Yb	.091 - .107	.074
Hf/Th	1.48 - 2.16	1.37
Ti/V	53.4 - 121.1	47.4
FeO_T/MgO	3.45 - 4.83	3.72

Table 8c. ANDESITE

Brindle Pup Andesite (bpa), Dacite of Burnt Canyon (bcd) Gaddes Basalt (gab)

Unit	bpa	bcd	gab
Al_2O_3/TiO_2	24.5 - 27.4	22.1 - 27.9	18.8 - 27.3
La/Yb	3.7 - 6.4	3.2 - 4.9	2.6 - 2.9
Ti/Zr	20.6 - 26.5	20.6 - 24.1	20.9 - 36.0
Zr/Nb	15.3 - 20.4	15.4 - 20.5	16.9 - 25.0
Nb/Y	.21 - .23	.17 - .21	.11 - .16
Zr/Y	3.2 - 4.4	3.2 - 4.3	2.7 - 2.8
La/Th	4.2 - 7.0	4.3 - 6.7	5.6 - 6.6
Th/Yb	.56 - 1.13	.55 - 1.09	.43 - .48
Ta/Yb	.069 - .129	.070 - .131	.056 - .065
Hf/Th	1.03 - 1.55	1.00 - 1.56	1.40 - 1.62
Ti/V	33.5 - 240.0	136.8 - 249.2	150.0 -240.0
FeO_T/MgO	2.88 - 4.64	4.70 - 6.38	5.39 - 6.40

Table 8d. DACITE-RHYODACITE

Dacite of Burnt Canyon (bcd), Buzzard Rhyolite (br), Deception Rhyolite (dr)

Unit	bcd	br	dr
Al_2O_3/TiO_2	57.1 & 51.8	31.3 - 52.6	36.9 - 90.8
La/Yb	6.7	2.6 - 3.9	4.6 - 5.6
Ti/Zr	16.5 & 7.4	9.1 - 16.4	5.3 - 12.7
Zr/Nb	18.0 & 21.0	20.0 - 34.2	23.3 - 47.9
Nb/Y	.14 & .25	.07 - .15	.06 - .25
Zr/Y	4.0 & 5.3	2.5 - 3.2	3.0 - 6.1
La/Th	5.2	5.5 - 6.7	3.9 - 6.6
Th/Yb	1.30	.46 - .61	.69 - 1.32
Ta/Yb	.140	.058 - .078	.089 - .145
Hf/Th	.99	1.28 - 1.54	1.06 - 1.25
Ti/V	53.8	420 & 900	58.4 - 1110.0
FeO_T/MgO	3.38	3.12 - 13.22	2.33 - 43.38

Quartz Porphyry (QP), Quartz Feldspar Porphyry (QFP)

Unit	QP	QFP	QP (16,22,23)
Al_2O_3/TiO_2	63.6 - 90.8	52.0	64.6 - 76.5
La/Yb	2.9 - 3.5	3.4	2.3
Ti/Zr	3.4 - 5.8	9.5	4.7 - 6.2
Zr/Nb	29.1 - 43.2	23.2	24.2 - 25.6
Nb/Y	.08 - .12	.13	.12 - .13
Zr/Y	2.8 - 3.5	3.0	2.8 - 3.2
La/Th	5.5 - 6.5	6.0	4.4
Th/Yb	.52 - .54	.57	.52
Ta/Yb	.059 - .078	.075	.084
Hf/Th	1.44 - 1.61	1.41	1.45
Ti/V	216	330	
FeO_T/MgO	2.82 - 7.62	2.08	2.40 - 7.56

TABLE 9. VOLCANICS OF THE GREEN GULCH BLOCK

* For units represented by 1 or 2 samples, individual ratios are given. For units represented by 3 or more samples, a range is given.

* The trace element ratios are useful in correlation of units and evaluating potential genetic links as the ratios of relatively immobile elements are uneffected by alteration (See Sec. IV)

Table 9a. BASALT

basaltic flows (grb)

Ratio	grb (prim)	grb (evolved)
Al_2O_3/TiO_2	14.6 - 21.5	14.0 - 16.9
La/Yb	4.1 - 10.4	2.7 - 9.0
Ti/Zr	58.1 - 85.1	42.0 - 72.3
Zr/Nb	5.2 - 10.4	5.2 - 12.2
Nb/Y	.33 - .55	.36 - .65
Zr/Y	2.9 - 4.4	3.3 - 7.0
La/Th	8.6 - 11.6	6.3 - 11.1
Th/Yb	.36 - 1.20	.36 - 1.42
Ta/Yb	.090 - .176	1.20 - .269
Hf/Th	1.10 - 2.49	1.29 - 3.01
Ti/V	17.5 - 21.6	20.2 - 33.2
FeO_T/MgO	.72 - 1.37	1.86 - 4.05

Table 9b. BASALTIC ANDESITES

basaltic flows (grb)

Unit	grb
Al_2O_3/TiO_2	8.9 - 17.7
La/Yb	2.2 - 8.3
Ti/Zr	46.4 - 86.6
Zr/Nb	8.8 - 19.6
Nb/Y	.13 - .40
Zr/Y	2.2 - 6.1
La/Th	5.4 - 8.5
Th/Yb	.38 - 1.13
Ta/Yb	.082 - .152
Hf/Th	1.22 - 2.39
Ti/V	9.2 - 58.9
FeO_T/MgO	1.56 - 3.18

Table 9c. ANDESITE

basaltic flow (grb)

Unit	grb
Al_2O_3/TiO_2	12.1 - 19.3
La/Yb	2.7 - 11.2
Ti/Zr	24.9 - 44.2
Zr/Nb	11.9 - 20.5
Nb/Y	.16 - .49
Zr/Y	3.1 - 6.2
La/Th	3.9 - 6.8
Th/Yb	.43 - 2.17
Ta/Yb	.099 - .255
Hf/Th	.83 - 2.19
Ti/V	29.0 - 51.5
FeO_T/MgO	1.83 - 4.24

Table 9d. DACITE-RHYODACITE

rhyolitic rocks (grr)

Unit	grr
Al_2O_3/TiO_2	24.3 - 39.2
La/Yb	7.1 - 9.0
Ti/Zr	11.1 - 19.6
Zr/Nb	16.6 - 24.4
Nb/Y	.22 - .34
Zr/Y	4.9 - 8.2
La/Th	3.9 - 5.0
Th/Yb	1.41 - 2.06
Ta/Yb	.173 - .192
Hf/Th	.78 - 1.35
Ti/V	23.1 - 285.1
FeO_T/MgO	3.49 - 7.59

TABLE 10. VOLCANICS OF THE BIG BUG BLOCK

* For units represented by 1 or 2 samples, individual ratios are given. For units represented by 3 or more samples, a range is given.

* The trace element ratios are useful in correlation of units and evaluating potential genetic links as the ratios of relatively immobile elements are uneffected by alteration (See Sec. IV)

Table 10a. BASALTS

andesitic flows (sma), andesitic breccia (smb), andesitic and basaltic flows (ika), Iron King Mine samples (SmIK)

Unit	sma-smb	ika
Al_2O_3/TiO_2	13.7 - 17.0	20.7 - 28.6
La/Yb	2.7 - 3.3	4.2 - 5.5
Ti/Zr	89.9 - 98.7	52.6 - 95.6
Zr/Nb	9.2 - 9.6	9.2 - 12.1
Nb/Y	.26 - .33	.28 - .47
Zr/Y	2.5 - 3.1	2.5 - 4.8
La/Th	7.7 - 12.8	6.5 - 10.6
Th/Yb	.26 - .35	.40 - .82
Ta/Yb	.078 - .111	.101 - .139
Hf/Th	2.52 - 3.21	1.50 - 2.42
Ti/V	21 - 23.1	16.2 - 18.2
FeO_T/MgO	2.86 - 3.77	2.15 - 2.59

Unit	ika (Bluebell)	smIK
Al_2O_3/TiO_2	13.4 - 14.0	22.2 - 21.8
La/Yb	1.4 - 1.7	3.1 - 3.6
Ti/Zr	94.9 - 125.3	87.7 - 93.6
Zr/Nb	7.2 - 9.4	8.6 - 9.2
Nb/Y	.33 - .38	.34 - .36
Zr/Y	2.7 - 3.1	2.9 - 3.3
La/Th	6.0 - 13.3	8.8 - 10.0
Th/Yb	.13 - .23	.35 - .36
Ta/Yb	.126 - .162	.064 - .987
Hf/Th	4.13 - 6.46	2.07 - 2.11
Ti/V	15.9 - 21.5	18.1 - 19.1
FeO_T/MgO	1.48 - 1.79	2.02 - 2.15

Table 10b. BASALTIC ANDESITES

andesitic breccia (smb), andesitic and basaltic flows (ika)

Unit	smb (high-Ti)	smb (high-Al)	ika
Al_2O_3/TiO_2	6.8 - 10.0	18.2 - 20.4	5.4 - 8.8
La/Yb	3.5 - 6.8	3.0 - 4.6	4.1 - 5.3
Ti/Zr	66.2 - 76.4	74.7 - 90.4	43.4 - 52.0
Zr/Nb	12.1 - 14.9	9.7 - 11.4	13.0 - 24.5
Nb/Y	.23 - .27	.25 - .26	.16 - .44
Zr/Y	3.1 - 3.5	2.5 - 3.0	4.0 - 5.7
La/Th	7.4 - 10.0	9.1 - 15.2	8.0 - 17.9
Th/Yb	.47 - .68	.23 - .37	.29 - .51
Ta/Yb	.88 - .104	.050 - .074	.113 - .110
Hf/Th	1.43 - 1.82	1.93 - 3.0	1.97 - 4.75
Ti/V	18.9 - 21.2	17.6 - 19.9	65.1 - 67.1
FeO_T/MgO	3.15 - 3.82	2.69 - 3.74	3.29 - 3.91

Table 10c. ANDESITE

andesitic flows (sma), andesitic tuffs (smt), massive crystal tuff and tuff (smct-smt) from south of Big Bug Mesa, andesitic and basaltic flows (ika)

Unit	sma	smt
Al_2O_3/TiO_2	17.8 - 19.2	14.5 - 22.7
La/Yb	4.0 - 4.8	4.6 - 13.0
Ti/Zr	19.1 - 25.2	29.4 - 40.8
Zr/Nb	18.3 - 25.0	12.3 - 20.8
Nb/Y	.13 - .17	.18 - .45
Zr/Y	3.1 - 3.5	3.8 - 6.0
La/Th	6.2 - 7.6	6.1 - 7.6
Th/Yb	.58 - .74	.76 - 1.72
Ta/Yb	.066 - .087	.095 - .207
Hf/Th	1.19 - 1.61	.86 - 1.34
Ti/V	85.6 - 2310.0	28.0 - 91.5
FeO_T/MgO	3.04 - 5.81	1.08 - 2.51

Table 10c. - Continued

Unit	smct-smt	ika
Al_2O_3/TiO_2	34.2 - 41.4	11.7 & 13.0
La/Yb	5.1 - 6.0	6.2 & 7.1
Ti/Zr	22.6 - 31.0	37.1 & 38.9
Zr/Nb	13.7 - 20.3	11.4 & 12.4
Nb/Y	.18 - 20.3	.41 & .44
Zr/Y	3.5 - 4.9	5.0 & 5.1
La/Th	3.2 - 4.3	13.8 & 15.2
Th/Yb	1.32 - 1.66	.45 & .47
Ta/Yb	.139 - .178	.299 & .234
Hf/Th	.79 - .94	2.88 & 3.22
Ti/V	15.4 - 17.9	40.4 & 42.2
FeO_T/MgO	1.48 - 2.35	1.48 & 1.65

Table 10d. DACITE-RHYODACITE

quartz porphyry (qp)

Unit	qp (1,2)
Al_2O_3/TiO_2	77.5 & 77.9
La/Yb	6.5 & 7.6
Ti/Zr	7.5 & 7.5
Zr/Nb	12.7 & 12.9
Nb/Y	.30 & .36
Zr/Y	3.8 & 4.6
La/Th	4.1 & 4.8
Th/Yb	1.35 & 1.86
Ta/Yb	.191 & .241
Hf/Th	.92 & .98
Ti/V	105.0 & 300.0
FeO_T/MgO	4.48 & 6.02

Table 10e. RHYOLITE

Quartz porphyry (qp), rhyolitic rocks (smr), rhyolite flows and tuffs (ikr)

Unit	qp(4)	smr	ikr
Al_2O_3/TiO_2	174.5	73.0 - 133.7	107.2
La/Yb	7.4	4.8 - 6.5	8.7
Ti/Zr	3.8	3.2 - 5.1	3.8
Zr/Nb	18.2	9.6 - 22.5	11.7
Nb/Y	.21	.17 - .23	.36
Zr/Y	3.8	2.2 - 3.8	4.2
La/Th	7.9	4.7 - 5.3	7.2
Th/Yb	.93	1.02 - 1.24	1.21
Ta/Yb	.160	.73 - 1.07	.331
Hf/Th	1.41	.73 - 1.07	1.26
Ti/V		70.9	
FeO_T/MgO	5.64	2.54 - 10.61	.82

CIPW NORMS

APPENDIX C

* Samples are grouped by their Winchester and Floyd (1977) classification within the Ash Creek, Green Gulch, and Big Bug Blocks. The 'unit' description and abbreviations refer to the map nomenclature of Anderson and Creasey (1958) for the Ash Creek Group and Anderson and Blacet (1972) for the Big Bug Group.

TABLE 1. VOLCANICS OF THE ASH CREEK BLOCK

Table 1a. BASALTS

Grapevine Gulch Fm. (ggt), Coca Mines Core CM

Sample	18ggt1	18ggt2	18ggt3
Quartz	11.53	6.80	6.43
Orthoclase	4.10	3.56	3.39
Albite	25.00	30.21	30.01
Anorthite	28.00	29.41	25.29
Diopside	8.87	2.60	9.91
Hypersthene	18.22	23.41	20.72
Magnetite	2.16	2.15	2.23
Ilmenite	1.66	1.48	1.67
Apatite	0.46	0.39	0.41

Sample	18ggt4	18ggt5	CM-8
Quartz	11.28	6.10	
Orthoclase	5.65	7.96	2.45
Albite	25.13	35.94	15.51
Anorthite	26.15	20.53	30.40
Diopside	4.59	1.34	20.51
Hypersthene	22.59	23.42	21.59
Olivine			4.67
Magnetite	2.23	2.25	2.52
Ilmenite	1.85	1.90	2.05
Apatite	0.53	0.57	0.31

Table 1a. - Continued

Gabbro

Sample	19gb12	18gb6
Orthoclase	4.69	1.86
Albite	18.56	9.59
Anorthite	30.83	33.19
Diopside	13.02	14.15
Hypersthene	25.27	32.93
Olivine	4.36	4.90
Magnetite	2.05	2.23
Ilmenite	0.94	0.94
Apatite	0.31	0.22

Yarber Group

Sample	YMsma2	YMsma3	YMsma4	YMsma5
Quartz			4.11	
Orthoclase	22.53	7.42	5.26	12.15
Albite	11.16	21.61	21.02	15.49
Anorthite	26.43	30.40	32.55	30.69
Diopside	13.60	12.49	9.24	13.63
Hypersthene	17.81	5.71	24.27	15.15
Olivine	5.13	18.46		8.93
Magnetite	1.96	2.15	1.96	2.13
Ilmenite	1.04	1.31	1.15	1.37
Apatite	0.33	0.45	0.45	0.48

Table 1b. - BASALTIC ANDESITE

Shea Basalt (sb)

Sample	2sb2	2sb9	2sb15	2sb5	2sb20
Quartz	4.17	7.60	10.88	9.28	8.48
Orthoclase	0.91	3.20	6.92	1.37	2.77
Albite	34.63	29.22	18.35	39.79	32.34
Anorthite	16.58	19.00	22.95	15.26	17.83
Diopside	8.03	8.34	6.57	7.42	7.55
Hypersthene	26.40	23.28	25.85	19.46	22.54
Magnetite	3.16	2.95	2.78	2.42	2.66
Ilmenite	4.66	4.68	4.12	3.92	4.18
Apatite	1.47	1.73	1.60	1.08	1.65

Coca Mines Core (CM); Brindle Pup Andesite (bpa); basaltic agglomerate (bag)

Sample	CM-9	8bpa12	4bag9
Quartz	14.57	9.38	40.41
Corundum	5.54		
Orthoclase	1.69	5.46	7.90
Albite	30.98	31.85	23.48
Anorthite	11.77	24.42	11.95
Diopside		5.24	2.50
Hypersthene	27.54	19.00	10.14
Magnetite	2.61	2.02	1.25
Ilmenite	3.60	1.89	1.39
Apatite	1.73	0.75	0.99

Table 1c. - ANDESITE

Sample	7gab2	7gab3	7gab5	7gab9
Quartz	47.22	18.73	35.71	31.64
Corundum	2.43		0.39	
Orthoclase	11.49	1.44	10.63	0.61
Albite	19.87	43.24	13.91	19.16
Anorthite	7.88	15.12	21.84	27.79
Diopside		7.33		0.72
Hypersthene	9.17	10.85	14.27	16.50
Magnetite	0.96	1.54	1.52	1.72
Ilmenite	0.79	1.32	1.31	1.41
Apatite	0.19	0.45	0.43	0.46

Brindle Pup Andesite (bpa)

Sample	8bpa4	8bpa6	8bpa11	8bpa14
Quartz	18.25	36.79	22.23	27.20
Corundum		1.80	0.49	1.49
Orthoclase	14.93	11.48	7.73	4.88
Albite	27.92	19.70	32.51	27.71
Anorthite	21.87	15.36	20.90	20.38
Diopside	0.36			
Hypersthene	13.89	12.49	13.15	15.25
Magnetite	1.27	1.06	1.30	1.44
Ilmenite	1.14	0.93	1.18	1.18
Apatite	0.38	0.40	0.50	0.47

Table 1c. - Continued

Dacite of Burnt Canyon (bcd)

Sample	4bcd11	4bcd13	4bcd17	4bcd21	4bcd23
Quartz	21.39	26.10	20.96	22.23	16.08
Corundum	0.90	1.05		0.43	0.65
Orthoclase	12.43	8.01	13.98	12.76	2.46
Albite	35.43	30.75	35.71	36.80	53.73
Anorthite	13.36	17.77	15.63	13.61	11.24
Diopside			0.06		
Hypersthene	13.55	13.42	10.88	11.19	13.04
Magnetite	1.40	1.34	1.17	1.19	1.28
Ilmenite	1.11	1.11	1.15	1.28	1.07
Apatite	0.43	0.45	0.45	0.52	0.46

Table 1d. DACITE-RHYODACITE

Dacite of Burnt Canyon (bcd), Gaddes Basalt (gab)

Sample	4bcd18	4bcd28	7gab8
Quartz	51.03	39.68	34.41
Corundum	4.86	2.37	
Orthoclase	2.64	13.18	7.11
Albite	36.96	27.62	41.25
Anorthite	1.51	9.92	8.51
Diopside			0.82
Hypersthene	1.74	5.05	6.68
Magnetite	0.90	1.56	0.72
Ilmenite	0.31	0.51	0.38
Apatite	0.05	0.12	0.12

Table 1d. - Continued

Buzzard Rhyolite (br)

Sample	7br14	6br15	7br16	4br3	6br8
Quartz	37.67	33.55	37.89	58.92	48.65
Corundum		1.32	1.28	2.62	
Orthoclase	4.48	2.21	5.20	9.57	5.44
Albite	43.38	50.78	43.57	23.50	35.19
Anorthite	6.92	3.16	3.82	0.95	4.95
Diopside	3.78				1.32
Hypersthene	1.62	6.55	5.77	2.92	2.33
Magnetite	1.48	1.91	1.97	1.05	1.41
Ilmenite	0.53	0.46	0.44	0.40	0.58
Apatite	0.14	0.07	0.07	0.07	0.14

Buzzard Rhyolite (br)

Sample	6br10	6br11	6br13	7br13
Quartz	33.22	44.73	33.38	46.70
Corundum	2.39		1.79	1.88
Orthoclase	1.39	17.94	10.74	2.57
Albite	49.83	8.06	41.52	38.63
Anorthite	1.76	18.92	3.25	3.07
Diopside		0.62		
Hypersthene	8.08	6.03	6.41	5.10
Magnetite	2.39	2.84	2.18	1.59
Ilmenite	0.77	0.72	0.58	0.40
Apatite	0.17	0.15	0.16	0.07

Table 1d. - Continued

Deception Rhyolite: Upper Unit (du), Cleopatra member (dc)

Sample	1dc11	1du20	1du21	1du22
Quartz	46.86	45.22	43.64	44.10
Corundum	2.01	1.23	2.26	0.58
Orthoclase	7.62	7.91	7.32	0.83
Albite	35.05	34.47	37.45	46.37
Anorthite	4.59	7.61	5.66	4.52
Diopside				
Hypersthene	2.58	1.78	1.83	1.96
Magnetite	0.94	1.02	1.10	0.96
Ilmenite	0.27	0.57	0.56	0.50
Apatite	0.09	0.19	0.19	0.19

Deception Rhyolite: Coca Mines Core (CM), southern outcrops (dr), United Verde Extension (UVX)

Sample	CM-6	CM-7	8dr10	uvx-1j5	uvx-5j7
Quartz	42.22	33.46	35.48	41.89	47.13
Corundum	3.13	1.86	1.97	1.67	
Orthoclase	9.40	7.91	16.28	10.67	5.80
Albite	33.30	44.77	26.14	34.77	36.83
Anorthite	4.27	3.56	10.36	6.65	4.91
Diopside					3.43
Hypersthene	5.75	6.19	6.77	2.81	0.59
Magnetite	1.46	1.82	2.19	1.02	0.94
Ilmenite	0.35	0.35	0.71	0.41	0.29
Apatite	0.12	0.09	0.21	0.12	0.09

TABLE 2. VOLCANICS OF THE GREEN GULCH BLOCK

Table 2a. BASALTS

Primitive

Sample	13grb8	13grb1	13grb3	13grb28	13grb4
Quartz					3.53
Orthoclase	1.13	0.07	8.25	2.44	0.20
Albite	3.62	22.77	13.89	21.88	13.42
Anorthite	26.67	29.28	22.13	27.25	28.26
Nepheline					
Diopside	27.57	22.56	23.16	17.54	16.93
Hypersthene	26.60	14.87	18.98	22.14	33.35
Olivine	10.22	6.28	9.65	5.28	
Magnetite	2.12	2.04	1.92	1.93	1.91
Ilmenite	1.39	1.64	1.56	1.30	1.66
Apatite	0.68	0.50	0.47	0.26	0.76

Evolved

Sample	13gbrb5	13grb25	13grb26	13grb32	14grb3
Quartz		7.07	5.27		
Orthoclase	21.66	8.83	8.80	7.64	1.18
Albite	48.01	31.06	23.80	17.91	28.61
Anorthite	18.18	25.17	29.21	34.51	21.63
Nepheline					13.10
Diopside	2.52	12.05	13.81	1.61	21.13
Hypersthene	23.25	11.68	14.92	17.67	
Olivine	0.05			15.28	9.42
Magnetite	2.36	1.55	1.68	2.74	1.91
Ilmenite	2.16	1.94	1.90	2.32	2.51
Apatite	0.70	0.66	0.62	0.34	0.51

Table 2b. BASALTIC ANDESITES

Sample	HLgrb3	HLgrb6	13grb9	13grb19
Quartz	1.33	2.27	2.09	5.60
Corundum			0.14	3.62
Orthoclase	2.64	9.45	1.91	0.68
Albite	37.31	17.18	34.42	36.14
Anorthite	16.56	25.90	31.30	14.66
Nepheline				
Diopside	17.30	13.25		
Hypersthene	19.66	26.00	25.70	34.00
Olivine				
Magnetite	2.37	2.71	1.68	2.53
Ilmenite	2.35	2.61	2.00	2.37
Apatite	0.47	0.64	0.77	0.41

Sample	13grb27	13grb31	HLgrb2	HLgrb5	13grb7
Quartz	3.18	1.33		2.33	3.10
Corundum					0.28
Orthoclase	2.10	4.47	2.34	9.68	5.86
Albite	26.85	27.43	52.84	31.70	19.85
Anorthite	25.09	21.67	9.47	17.78	39.09
Nepheline					
Diopside	13.65	17.17	12.85	10.96	
Hypersthene	24.54	22.55	9.80	22.01	26.70
Olivine			7.48		
Magnetite	2.23	2.49	2.34	2.35	2.26
Ilmenite	1.99	2.60	2.39	2.57	2.25
Apatite	0.38	0.28	0.49	0.64	0.62

Table 2b. - Continued

Sample	13grb10	13grb34	14grb10	13grb33
Quartz		4.46	21.84	
Corundum	0.05		5.24	
Orthoclase	6.46	4.89	10.24	5.76
Albite	37.66	22.47	27.37	46.04
Anorthite	24.47	23.04	8.96	17.32
Nepheline	6.85			0.85
Diopside		17.06		11.98
Hypersthene		22.12	20.85	
Olivine	19.48			14.79
Magnetite	1.99	2.68	1.92	1.92
Ilmenite	2.18	2.91	3.20	1.10
Apatite	0.89	0.38	0.39	0.24

Table 2c. ANDESITE

Sample	13grb16	13grb18	13grb20	13grb30
Quartz	16.51	17.52	18.84	1.53
Corundum	0.29			
Orthoclase	18.84	9.66	6.84	6.08
Albite	28.61	27.83	39.82	29.62
Anorthite	14.45	18.07	16.02	23.78
Diopside		6.03	5.02	12.19
Hypersthene	16.93	16.06	8.43	22.34
Magnetite	1.58	1.90	3.21	2.02
Ilmenite	1.56	2.16	1.46	1.98
Apatite	1.25	0.78	0.37	0.48

Table 2c. - Continued

Sample	14grb1	13grb17	13grb29	14grb2
Quartz	10.88	29.15	3.81	9.46
Corundum		6.54		
Orthoclase	11.40	18.12	4.75	7.94
Albite	40.13	13.72	27.40	46.27
Anorthite	17.33	9.49	25.38	15.99
Diopside	2.18		12.89	2.57
Hypersthene	14.64	18.67	21.41	14.39
Magnetite	1.41	1.70	1.95	1.37
Ilmenite	1.66	2.23	1.93	1.63
Apatite	0.39	0.39	0.47	0.39

Table 2d. DACITE-RHYODACITE

Sample	14grr6	13grr14	13grr21
Quartz	36.48	36.37	12.04
Corundum	3.53	0.20	3.51
Orthoclase	12.44	14.71	10.69
Albite	29.61	36.35	47.52
Anorthite	9.80	5.08	9.52
Hypersthene	5.23	4.25	11.54
Magnetite	1.99	1.89	3.67
Ilmenite	0.73	0.93	1.17
Apatite	0.21	0.24	0.34

TABLE 3. VOLCANICS OF THE BIG BUG GROUP

Table 3a. BASALTS

Sample	10sma12	10sma14	10sma15
Quartz	3.17	4.53	4.82
Orthoclase	4.53	3.51	3.18
Albite	23.04	22.36	22.99
Anorthite	33.96	34.71	35.13
Diopside	6.22	5.15	4.42
Hypersthene	24.47	25.05	24.84
Olivine			
Magnetite	2.33	2.35	2.31
Ilmenite	2.01	2.04	2.00
Apatite	0.29	0.31	0.31

Sample	10smIK24	10smIK25	10smb20
Quartz	2.20	2.19	7.64
Orthoclase	1.56	1.68	3.74
Albite	23.45	16.51	23.14
Anorthite	37.02	42.25	29.40
Diopside	5.19	6.56	11.40
Hypersthene	26.51	26.68	19.66
Olivine			
Magnetite	2.17	2.17	2.40
Ilmenite	1.60	1.62	2.21
Apatite	0.29	0.34	0.43

Table 3a. - Continued

Sample	10ika1	10ika8	10ika9
Quartz	2.65		11.48
Orthoclase	3.49	0.50	5.24
Albite	31.65	40.87	29.48
Anorthite	29.75	28.45	25.71
Nephelene			
Diopside	5.56	5.36	0.51
Hypersthene	22.93	20.19	23.96
Olivine		0.96	
Magnetite	2.03	1.83	1.81
Ilmenite	1.62	1.51	1.46
Apatite	0.33	0.34	0.35

Sample	10ika10	10ika11	ika-rc
Quartz	13.93	12.98	
Orthoclase	1.67	1.72	4.28
Albite	17.75	18.92	45.00
Anorthite	36.09	36.60	30.50
Nephelene			
Diopside	6.97	4.45	0.79
Hypersthene	19.94	21.62	4.69
Olivine			11.52
Magnetite	1.89	1.92	1.57
Ilmenite	1.43	1.46	1.38
Apatite	0.34	0.34	0.28

Table 3a. BLUEBELL BASALTS

Sample	12ika1	12ika2	12ikab3	11ika10
Quartz				
Orthoclase	0.48	1.15	2.64	0.93
Albite	42.21	29.63	30.45	4.22
Anorthite	17.62	22.96	17.38	31.46
Nepheline	3.23	2.19		3.99
Diopside	10.76	21.57	23.21	20.81
Hypersthene			16.43	
Olivine	20.98	17.72	5.30	34.61
Magnetite	2.27	2.40	2.20	2.10
Ilmenite	2.22	2.15	2.18	1.90
Apatite	0.24	0.24	0.22	0.16

Table 3a. BASALTIC INTRUSIVE ROCKS

Sample	9sm46	9sm11
Quartz	3.79	
Orthoclase	6.22	4.14
Albite	25.69	12.47
Anorthite	17.54	15.59
Nepheline		1.60
Diopside	13.01	43.30
Olivine		19.42
Hypersthene	23.12	
Magnetite	2.96	1.91
Ilmenite	5.07	1.13
Apatite	2.60	0.45

Table 3b. BASALTIC ANDESITE

(High-Ti Group)

Sample	10smb21	10smb22	9smb40
Quartz	8.26	0.98	4.92
Corundum			
Orthoclase	8.62	7.81	8.89
Albite	18.35	25.06	26.17
Anorthite	26.76	19.21	19.85
Diopside	6.01	18.24	5.62
Hypersthene	25.76	21.47	27.81
Magnetite	2.56	2.82	2.92
Ilmenite	2.83	3.74	3.06
Apatite	0.86	0.67	0.79

(High-Al Group)

Sample	9smb47	10smIK23	9smb42
Quartz	4.11	8.00	7.11
Corundum			
Orthoclase	2.41	0.19	1.89
Albite	21.13	25.65	21.63
Anorthite	38.09	24.57	37.95
Diopside	10.01	12.62	4.02
Hypersthene	20.11	22.17	22.98
Magnetite	2.07	2.62	2.21
Ilmenite	1.72	3.50	1.86
Apatite	0.35	0.70	0.36

Table 3b. - Continued

Sample	Qika5	10ika3
Quartz	6.46	6.25
Orthoclase	11.72	1.41
Albite	30.07	27.72
Anorthite	23.83	20.80
Diopside	10.69	11.95
Hypersthene	10.85	21.99
Magnetite	1.62	2.82
Ilmenite	3.61	4.71
Apatite	1.17	2.35

Table 3c. ANDESITES

Sample	11ika8	11ika9
Quartz	2.45	8.26
Orthoclase	0.97	0.67
Albite	29.73	24.68
Anorthite	26.93	28.46
Diopside	14.60	10.87
Hypersthene	20.41	21.86
Magnetite	1.77	1.86
Ilmenite	2.32	2.49
Apatite	0.83	0.85

Table 3c. - Continued

Sample	9smr5	9smt33	9smt35	9smt39
Quartz	31.23	20.80	6.69	15.81
Corundum	1.68	2.42	0.74	2.41
Orthoclase	5.10	5.32	11.70	14.09
Albite	38.31	36.01	45.93	20.00
Anorthite	10.20	13.73	15.71	21.26
Hypersthene	10.45	17.44	15.98	22.53
Magnetite	1.21	1.35	1.29	1.81
Ilmenite	1.43	2.02	1.47	1.67
Apatite	0.40	0.92	0.50	0.43

Sample	9sma4	9sma6	9sma13	9sma17
Quartz	27.95	21.01	24.09	25.80
Corundum	1.23	0.70	2.29	0.19
Orthoclase	8.07	13.89	18.29	10.14
Albite	35.00	26.55	17.61	31.27
Anorthite	11.38	19.96	14.90	15.64
Diopside				
Hypersthene	13.10	14.13	19.06	13.60
Magnetite	1.27	1.42	1.65	1.30
Ilmenite	1.41	1.63	1.51	1.45
Apatite	0.59	0.71	0.60	0.62

Table 3c. - Continued

Sample	9sma24	9sma28	9sma18	9sma23
Quartz	36.99	28.71	24.72	26.74
Corundum	1.75	0.42		0.95
Orthoclase	17.11	11.65	10.19	13.98
Albite	16.05	30.36	28.50	30.28
Anorthite	13.87	15.03	18.46	11.91
Diopside			0.39	
Hypersthene	11.37	8.55	14.26	13.28
Magneite	1.21	3.35	1.38	1.28
Ilmenite	1.30	1.49	1.50	1.36
Apatite	0.35	0.45	0.61	0.33

Sample	9smr5	9smt33	9smt35	9smt39
Quartz	31.23	20.80	6.69	15.81
Corundum	1.68	2.42	0.74	2.41
Orthoclase	5.10	5.32	11.70	14.09
Albite	38.31	36.01	45.93	20.00
Anorthite	10.20	13.74	15.71	21.26
Hypersthene	10.45	17.44	15.98	22.53
Magnetite	1.21	1.35	1.29	1.81
Ilmenite	1.43	2.02	1.47	1.67
Apatite	0.40	0.92	0.50	0.43

Table 3c. - Continued

Outcrops South of Big Bug Mesa

Sample	15smt1	15smct3	15smct5	17smt1	17smt3
Quartz	25.41	19.59	14.76	9.01	22.36
Corundum	0.92	1.27			0.26
Orthoclase	3.94	4.77	1.19	1.27	4.96
Albite	28.35	28.11	43.84	47.07	35.84
Anorthite	20.83	22.02	15.66	15.81	18.07
Diopside			12.01	13.73	
Hypersthene	18.34	21.60	10.59	11.00	16.47
Magnetite	1.30	1.46	1.11	1.19	1.13
Ilmenite	0.73	0.13	0.67	0.72	0.72
Apatite	0.19		0.19	0.20	0.19

Outcrops South of Big Bug Mesa

Sample	15smct4	17smt4	15smt2	15smct6
Quartz	26.02	21.38	23.36	21.42
Corundum			1.58	
Orthoclase	5.00	5.92	7.39	5.77
Albite	25.03	36.78	24.52	22.22
Anorthite	24.95	15.55	19.83	27.38
Diopside	2.38	6.44		2.92
Hypersthene	14.56	12.02	21.00	17.90
Magnetite	1.20	1.08	1.29	1.42
Ilmenite	0.69	0.67	0.83	0.78
Apatite	0.19	0.17	0.19	0.20

Table 3d. DACITE-RHYODACITE

Sample	9smt30	Qqp1	Qqp2
Quartz	56.99	49.10	49.30
Corundum	5.84	2.73	1.12
Orthoclase	20.23	29.12	21.72
Albite	8.79	9.73	16.50
Anorthite	3.71	5.38	7.88
Hypersthene	3.04	2.69	2.30
Magnetite	0.99	0.94	0.89
Ilmenite	0.37	0.29	0.27
Apatite	0.05	0.02	0.02

Table 3e. RHYOLITE

Sample	9smr8	9smr9	9smr20	9smr26	12qp4
Quartz	61.14	62.18	38.78	41.04	60.57
Corundum	3.54	7.03	0.32	0.34	4.49
Orthoclase	10.10	18.78	15.74	7.25	10.88
Albite	16.96	5.12	38.81	42.55	20.12
Anorthite	4.68	1.76	3.90	6.17	0.56
Hypersthene	2.59	3.82	1.67	1.63	2.36
Magnetite	0.71	0.98	0.59	0.74	0.85
Ilmenite	0.27	0.31	0.17	0.25	0.12
Apatite	0.02	0.02	0.02	0.02	0.07

Table 3e. - Continued

Sample	Qikr2	Qikr4	Qikr7
Quartz	60.11	81.44	75.52
Corundum	7.43	4.65	6.19
Orthoclase	6.97	11.34	6.46
Albite	15.10	1.62	0.26
Anorthite	1.26	0.08	0.16
Hypersthene	7.91	0.62	10.09
Magnetite	1.00	0.10	1.24
Ilmenite	0.21	0.12	0.02
Apatite	0.02	0.02	0.07

APPENDIX D

PETROGENETIC MODELS

Petrogenetic Models

Explanation

The distribution of trace elements in igneous rocks is controlled by the initial concentration of these elements in the parent rock or magma and subsequent redistribution during partial melting or crystallization, respectively. Element partition in mineral/melt systems is influenced by ionic charge, ionic radii and mineral structure (Onuma et al., 1968; Jensen, 1973). The partition of a trace element between mineral and liquid phases can be described in terms of the distribution coefficient K_D: where

$$K_D = \frac{\text{concentration in mineral}}{\text{concentration in liquid}}$$

The distribution coefficient varies with temperature, pressure and composition of the phases (Table 1a, b, c). Selection of distribution coefficients for models is constrained by experimental results on synthetic systems and analyses of phenocryst-matrix pairs from natural systems. The distribution of an element between multiple mineral phases and a liquid phase can be described in terms of the bulk distribution coefficient D, which is the sum of the weight proportion X distribution coefficient for each mineral phase.

Batch Melting

Incompatible vs compatible element plots are based on batch melting of lherzolite sources followed by crystal fractionation of these melts. In batch melting the liquid remains at the site of melting and is in chemical equilibrium with the residual solid until it escapes as a 'batch' of primary magma. The concentration of an element in the liquid (CL) is related to concentration in the original source (Co) by:

$$\frac{CL}{CO} = \frac{1}{F + D - FD} \qquad (D1)$$

where F = weight proportion of melt formed and D = the bulk distribution coefficient for the residual solids at the instant of melt extraction (Wood and Fraser, 1976; Allegre and Minster, 1978).

Closed System Crystal Fractionation

This model involves an isolated magma chamber in which the primary magma undergoes continuous crystal fractionation from an uniform melt (Zielinski, 1975; Allegre et al., 1977). The trace element concentration in the residual liquid (CL) is related to the original melt concentration (CO) by:

$$\frac{CL}{CO} = F^{(D-1)} \qquad (D2)$$

where F = the weight fraction of the melt and D = the bulk distribution coefficient.

In the closed-system fractional crystallization tables (Table 2a-g, 3d, 4a,c,d,e), mean values for less fractionated units are modelled using the previous relationship to test fractionation links to more siliceous compositions. The columns are explained from left to right:

Co = concentration in proposed parent

Cl = concentration in proposed daughter

Cl = modelled concentration of daughter

Squared Residual = Statistical evaluation of model vs real concentration (perfect match = 0)

Cs = concentration in solid residue

D = Bulk distribution coefficient

The mode of crystallizing assemblage and weight proportions of melt and crystals are indicated in the right column.

Open System Fractional Crystallization

The open system models assume a periodically replenished, periodically tapped, continuously fractionated (RTF) magma chamber. This open system is modelled after the work of O'Hara (1977). The concentration of an element in the residual liquid produced in such a magma chamber is given by:

$$ssC_B = Co\ [(x+y)(1-x)^{D-1}/1-(1-x-y)(1-x)^{D-1}] \qquad (D3)$$

where $_{ss}C_B$ = concentration of element in derived steady state liquid, Co = concentration of element in parent, D = bulk distribution coefficient, y = mass fraction liquid escaping in each cycle, x = mass fraction of liquid crystallized in each cycle, f = mass fraction of liquid.

The open system models presented in Tables 3a-c and 4b also utilize mean values of units in attempts to relate more fractionated daughters to parents. The columns are organized from left to right in the same fashion as the closed system model. Nomenclature is the same except for: Cl/Co = ratio of modelled residual liquid to original liquid element concentrations. The right hand column indicates modes of crystallizing minerals, mass fraction (M.F.) of escaping liquid (Y), mass fraction (M.F.) of crystals (X) and mass fraction (M.F.) of injected liquid (Z) to balance the system. Temperatures are indicated for temperature-dependent Kd's and the number of cycles (n) required to achieve steady state conditions. Proposed parent-daughter petrogenetic links (see Table 3a) are evaluated by the similarity between the proposed daughter trace element concentrations (Cl - left column) and the modelled daughter concentration (Cl - right column). A perfect match is indicated by a squared residual of 0. To obtain the closest match between model and proposed daughter concentrations (Cl) both the mode of the crystallizing assemblage and the mass fraction of melt and crystals are adjusted. The number of cycles of injection-leakage required to produce the modelled concentration for a steady state system is calculated.

Both open and closed system models were performed using the MODULUS Program (Knoper, 1988). The program uses a LOTUS spreadsheet and contains separate distribution coefficient files for mafic, intermediate and felsic compositions (Table 1b-d) and includes options for elements with strong temperature dependence. Sources for distribution coefficients are given by Knoper (1988) and are on file with the Precambrian Research Group at NMIMT. A key to modelling abbreviations is presented in Table 1a. The MODULUS working file allows modelling of either parent or daughter compositions. The mineral assemblage and proportions may be adjusted for closed system models. Open system models allow adjustment of leakage and cumulate proportions. These variables are adjusted to obtain the closest match between the proposed parent and daughter composition. Although major elements are included in some models, emphasis is on the relatively immobile REE and HFSE for evaluation of models. If squared residuals for the proposed link approach zero, this indicates genetic relations are feasible through the modelled process, but does not constitute proof that the magmas actually evolved by this process.

Table 1. Nomenclature and Distribution Coefficients for Petrogenetic Models

Table 1a. KEY TO ABBREVIATIONS USED IN DISTRIBTUION COEFFICIENT AND MODELLING TABLES

Mineral Abbreviations

oliv = olivine	qtz = quartz
opx = orthopyroxene	mgnt = magnetite
cpx = clinopyroxene	ilmn = ilmenite
plag = plagioclase	zirc = zircon
amph = amphibole	apat = apatite
garn = garnet	alln = allanite
biot = biotite	sphn = sphene
kspr = potassium feldspar	

Closed-System Model Abbreviations

Co	= concentration in parent
Cl	= concentration in daughter
Cs	= concentration in solid residue
D	= bulk distribution coefficient
Kd	= distribution coefficient
Sqred. Resid.	= Squared Residual
M.F.	= mass fraction
Xtals	= crystals
XL	= crystallization

Open-System Model Abbreviations

same as in closed system plus:

Y	= mass fraction leaked
X	= mass fraction cumulate
Z	= mass fraction injection
n	= number of cycles required for steady state system

Table 1b. MAFIC DISTRIBUTION COEFFICIENTS

DISTRIBUTION COEFFICIENTS					
(primary phases):	oliv	opx	cpx	plag	amph
Na	0.02	0.02	0.27	50	0.75
K	0.007	0.014	0.011	0.17	0.96
Rb	0.01	0.02	0.02	0.13	0.2
Sr	0.015	0.02	0.1	2	0.6
Cs	0.0004	0.02	0.01	0.025	0.1
Ba	0.01	0.013	0.005	0.25	0.7
Th	0.02	0.13	0.02	0.05	0.05
U	0.04	0.007	0.05	0.06	0.15
La	0.00001	0.007	0.07	0.15	0.2
Ce	0.00001	0.008	0.1	0.12	0.26
Nd	0.00007	0.01	0.22	0.08	0.4
Sm	0.0006	0.02	0.4	0.067	0.7
Eu	0.001	0.02	0.4	0.35	0.8
Tb	0.002	0.05	0.5	0.06	0.8
Yb	0.02	0.15	0.6	0.07	0.6
Lu	0.016	0.18	0.6	0.06	0.5
P	0.043	0.014	0.009		
Sc	0.3	1	2	0.04	1.5
Ti	0.02	0.1	0.4	0.04	1.5
Y	0.01	0.2	0.5	0.03	1
Zr	0.01	0.03	0.1	0.01	1.5
Nb	0.01	0.15	0.1	0.01	0.8
Hf	0.04	0.04	0.3	0.01	0.4
Ta	0.03	0.1	0.06	0.04	0.4
V	0.05	0.3	1.2		3.5
Cu	0.37	0.8	2	0.01	0.5
Zn	0.95	0.5	0.41	0.43	0.55
Pb				0.45	
Cr	1	3.9327432	4.5720253	0.001	15
Mg	3.1576409	11.581680	3.9234737	0	10
Mn	0.9242869	2	2.8132769	0	1
Fe	1.0372313	1.4202566	0.4760794	0	10
Co	5.9731926	3	0.3071545	0.001	7
Ni	11.463518	3	26.552749	0.001	7

Mafic Partition Coefficients

(Blanks = "not available" or "not applicable")

Table 1b. - Continued

DISTRIBUTION COEFFICIENTS

	garn	(accessory phases): mgnt	ilmn	zirc
Na	0.01	0		0
K	0.02	0		0
Rb	0.04	0		0
Sr	0.012	0		0
Cs	0.03	0		0
Ba	0.02	0		0
Th	0.001	0		0
U	0.001	0		50
		0		10
La	0.03	0		0.08
Ce	0.03	0		0.1
Nd	0.087	0		0.2
Sm	0.22	0		0.4
Eu	1	0		1.25
Tb	3	0		50
Yb	5	0		138
Lu	5.5	0		170
P	0.15			
Sc	5	2	8	1
Ti	0.3	7.5	50	0
Y	2	0.2		60
Zr	0.3	0.1		800
Nb	0.1	0.7	2.3	0.5
Hf	0.15	0.3		800
Ta	0.1	0.8	2.7	0.6
V	0.27	25		
Cu		4.2		
Zn		12		
Pb				
Cr	17.5	165.3021	4.965312	
Mg		1.268890	15.81849	
Mn		2	1	
Fe		4.309316	24.99241	
Co		10	10	
Ni		10	10	

Mafic Partition Coefficients

(File ID: mafic partition coefficients)

Table 1b. - Continued

DISTRIBUTION COEFFICIENTS	
	apat
Na	0
K	0
Rb	0
Sr	5
Cs	0
Ba	0
Th	1.5
U	0.4
La	7
Ce	15
Nd	12
Sm	14
Eu	13
Tb	11
Yb	7
Lu	5
P	800
Sc	0.04
Ti	0
Y	3
Zr	0
Nb	0
Hf	0.12
Ta	0
V	0
Cu	
Zn	
Pb	
Cr	0
Mg	0
Mn	0
Fe	0
Co	0
Ni	0
Mafic Partition Coefficients	
(Dated: 24nov87)	

Table 1c. INTERMEDIATE DISTRIBUTION COEFFICIENTS

DISTRIBUTION COEFFICIENTS							
(primary phases):	oliv	opx	cpx	plag	amph	biot	kspr
Na	0.02	0.06	0.11	1.5	0.08	0.1	1
K	0.007	0.001	0.01	0.19	0.01	3.5	1.4
Rb	0.01	0.003	0.03	0.05	0.01	3.3	0.35
Sr	0.015	0.01	0.52	3	0.02	0.12	4
Cs	0.0004	0.3	0.01	0.05	0.02	2.4	0.2
Ba	0.01	0.003	0.13	0.4	0.04	10	5
Th	0.02	0.15	0.03	0.05	0.01	0.3	0.01
U	0.04	0.006	0.03	0.006	0.4	0.02	0.005
La	0.00001	0.1	0.2	0.08	0.23	0.03	0.05
Ce	0.00001	0.15	0.4	0.2	0.9	0.04	0.04
Nd	0.00007	0.22	1.1	0.17	2.8	0.04	0.025
Sm	0.0006	0.25	1.67	0.1	4	0.06	0.02
Eu	0.001	0.17	1.5	0.8	3.5	0.15	1.1
Tb	0.002	0.65	2.4	0.085	6	0.16	0.006
Yb	0.02	0.85	2	0.08	5	0.18	0.01
Lu	0.016	0.9	1.5	0.06	4.5	0.2	0.006
P	0.043						
Sc	0.3	7	22	0.1	10	10	0.02
Ti	0.02	0.25	0.4	0.05	3	1.5	0.05
Y	0.01	0.45	1.5	0.06	2.5	0.03	0.1
Zr	0.01	0.08	0.25	0.03	1.4	1.2	0.03
Nb	0.01	0.35	0.3	0.03	1.3	5	0.05
Hf	0.04	0.03	0.25	0.05	1.4	2	0.1
Ta	0.03	0.5	0.4	0.08	1.5	1	0.05
V	0.05	6	1.1	0.01	3?	50	0.01
Cu	0.37						
Zn	0.95	0.9			7	20	
Pb				0.6		0.7	2.5
Cr	1	NA	NA	0.001	15		
Mg	NA	NA	NA	0	10		
Mn	NA	2	NA	0	1		
Fe	NA	NA	NA	0	10		
Co	NA	3	NA	0.001	7		
Ni	NA	3	NA	0.001	7		

Intermediate Partition Coefficients

(Blanks = "not available" or "not applicable")

Table 1c. - Continued

DISTRIBUTION COEFFICIENTS				
	garn	(accessory phases): mgnt	ilmn	zirc
Na				
K				
Rb	0.01	0	0	0
Sr	0.15	0	0	
Cs	0.01	0	0	
Ba	0.015	0	0	
Th	0.02	0.4	0.4	100
U		0.1		
La	0.35	0	0	2
Ce	0.35	0	0	2.5
Nd	0.5	0	0	2.2
Sm	2.6	0	0	3.1
Eu	1.5	0	0	3.5
Tb	35	0.1	0.1	100
Yb	40	0.1	0.1	200
Lu	30	0.1	0.1	200
P				
Sc	11	8	8	60
Ti	0.5	9	50	50
Y	11	0.5	0.1	60
Zr	0.5	0.2	0.6	800
Nb	0.5	0.8	5	50
Hf	0.5	0.5	0.7	500
Ta	0.5	1	7	50
V	8	30	12	
Cu				
Zn				
Pb				
Cr	17.5	NA	NA	
Mg		NA	NA	
Mn		2	1	
Fe		NA	NA	
Co		10	10	
Ni		10	10	

Intermediate Partition Coefficients

File ID: inter partition coefficients)

Table 1c. - Continued

DISTRIBUTION COEFFICIENTS

	alln	apat	sphn
Na			
K			
Rb	0	0	0
Sr			100
Cs			
Ba			1
Th	1500	2	130
U			
La	2500	20	32
Ce	2000	35	60
Nd	1700	57	180
Sm	1300	63	200
Eu	800	30	120
Tb	500	20	210
Yb	100	25	190
Lu	100	25	115
P			
Sc	60	0	40
Ti	50	0.1	
Y	100	20	30
Zr	2	0.1	
Nb	2	0.1	6
Hf	10	0.1	65
Ta	2	0	17
V		0	
Cu			
Zn			
Pb			
Cr		0	
Mg		0	
Mn		0	
Fe		0	
Co		0	
Ni		0	

Intermediate Partition Coefficients

(Dated: 24nov87)

Table 1d. FELSIC DISTRIBUTION COEFFICIENTS

DISTRIBUTION COEFFICIENTS (primary phases):	opx	cpx	plag	amph	biot	kspr
Na	0.06	0.11	1.5	0.08	0.1	1
K	0.001	0.01	0.19	0.01	3.5	1.4
Rb	0.003	0.03	0.04	0.01	2.2	0.35
Sr	0.01	0.52	4	0.02	0.12	4
Cs	0.3	0.01	0.05	0.02	2.4	0.2
Ba	0.003	0.13	0.3	0.04	6	6
Th	0.15	0.03	0.05	0.01	0.5	0.01
U	0.006	0.01	0.006	0.4	0.02	0.005
La	0.1	0.3	0.3	0.33	0.11	0.05
Ce	0.15	0.5	0.25	1.5	0.32	0.04
Nd	0.22	1.1	0.2	4.3	0.3	0.025
Sm	0.25	1.67	0.13	7.8	0.25	0.02
Eu	0.17	1.5	1.5	5	0.25	1.1
Tb	0.65	1.8	0.6	12	0.35	0.006
Yb	0.85	1.5	0.05	8	0.44	0.01
Lu	0.9	1.5	0.05	5.5	0.3	0.006
P						
Sc	7	22	0.04	10	15	0.02
Ti	0.4	0.7	0.05	7	2.5	0.05
Y	1	4	0.1	6	0.03	0.1
Zr	0.2	0.6	0.1	4	2	0.1
Nb	0.8	0.8	0.06	4	5	0.05
Hf	0.1	0.3	0.04	1.4	2	0.1
Ta	0.15	0.4	0.05	1.5	1	0.05
V	6	1.1	0.01	32	50	0.01
Cu						
Zn	0.9			7	20	
Pb			0.6		0.7	2.5
Cr	1.6	90	0.2		19	
Mg						
Mn						
Fe						
Co						
Ni						

Felsic Partition Coefficients

(Blanks = "not available" or "not applicable")

Table 1d. - Continued

DISTRIBUTION COEFFICIENTS	garn	qtz	(accessory phases): mgnt	ilmn	zirc
Na		0.02			
K		0.01			
Rb	0.01	0.01	0	0	0
Sr	0.15		0.15	0	0
Cs	0.01	0.02	0	0	0
Ba	0.015	0.01	0	0	0
Th	0.02	0.01	0.4	0.4	100
U		0.01	0.1	0	
La	0.35	0.015	0	0	2
Ce	0.35	0.014	0	0	2.5
Nd	0.5	0.015	0	0	2.2
Sm	2.6	0.015	0	0	3.1
Eu	1	0.04	0	0	3.5
Tb	35	0.016	0.1	0.1	100
Yb	40	0.015	0.1	0.1	200
Lu	30	0.01	0.1	0.1	200
P					
Sc	20	0.01	8	8	60
Ti	1.2	0.02	12.5	50	50
Y	35	0	2	0.1	60
Zr	1.2	0	0.8	1	1000
Nb	0.5	0	2.5	3	50
Hf	0.5	0.02	0.5	0.7	500
Ta	0.5	0.008	5	30	50
V	8		30	12	
Cu					
Zn					
Pb					
Cr					
Mg					
Mn					
Fe					
Co					
Ni					

Felsic Partition Coefficients

(File ID: felsic partition coefficients)

Table 1d. - Continued

DISTRIBUTION COEFFICIENTS	alln	apat	sphn
Na			
K			
Rb	0	0	0
Sr	100	2	100
Cs			
Ba		2	1
Th	1500		130
U			
La	2500	20	32
Ce	2000	35	60
Nd	1700	57	180
Sm	1300	63	200
Eu	800	30	120
Tb	500	20	210
Yb	100	25	190
Lu	100	25	115
P			
Sc	60	0	40
Ti	50	0.1	
Y	100	40	
Zr	2	0.1	
Nb	2	0.1	
Hf	10	0.1	65
Ta	2	0	800
V		0	
Cu			
Zn			
Pb			
Cr			
Mg			
Mn			
Fe			
Co			
Ni			

Felsic Partition Coefficients

(Dated: 24nov87)

Tables 2 - 4. Petrogenetic Models

Table 2. Petrogenetic Model for the

Ash Creek Block Volcanics

Table 2a. YMSMA BASALT (PARENT) - GABBRO (DAUGHTER)

Closed-System Fractional XL (given Co)
Comment: YM-gabbro

	Co	Cl	Cl	Sqred Resid	Cs	D
Na	14726	11914	149.021	6232.77	73033.9	21.5844
K	16185	4482	19883.9	0.59999	1389.05	0.07759
Rb	38	15	46.8306	0.46198	2.67742	0.0636
Sr	337	280	345.177	0.03565	304.288	0.89255
Cs	0.53	0.35	0.66046	0.22096	0.00815	0.013818
Ba	578	171	704.871	0.57365	70.5142	0.1107
Th	0.73	0.68	0.90622	0.06231	0.02508	0.0309
U	0.69	0.5	0.85338	0.17147	0.03645	0.0476
La	4.3	5.69	5.27342	0.00624	0.40631	0.085501
Ce	11.6	14.05	14.2383	0.00017	1.04655	0.081601
Nd	0	0	NA	NA	NA	0.100411
Sm	1.84	2.16	2.22482	0.00084	0.30068	0.148912
Eu	0.6	0.73	0.70604	0.00115	0.17583	0.27067
Tb	0.34	0.38	0.40861	0.00490	0.06552	0.17614
Yb	1.27	1.52	1.51364	0.00001	0.29542	0.2135
Lu	0.22	0.27	0.26249	0.00081	0.05001	0.20852
P	0	0	NA	NA	NA	0.01001
Sc	39.3	32.5	38.8795	0.02692	40.9817	1.0482
Ti	3720	2880	2868.03	0.00001	7127.85	2.1656
Y	13.5	15.6	16.2156	0.00144	2.63720	0.1786
Zr	23.5	41.1	29.0944	0.17027	1.12204	0.043
Nb	4.3	5.1	5.19343	0.00032	0.72627	0.154
Hf	0.77	1.24	0.93662	0.10490	0.10348	0.1221
Ta	0.07	0.09	0.08410	0.00491	0.01357	0.1773
V	289	190	225.166	0.02439	544.333	2.1185
Cu	0	0	NA	NA	NA	0.9612
Zn	0	0	NA	NA	NA	1.3094
Pb	0	0	NA	NA	NA	0.1935
Cr	165	146	48.2467	4.10512	632.012	6.51043
Mg	0	0	NA	NA	NA	NA
Mn	0	0	NA	NA	NA	NA
Fe	0	0	NA	NA	NA	NA
Co	37.1	55.6	28.3185	0.92809	72.2257	2.21043
Ni	51	93	18.4339	16.3623	181.264	5.56043

Mafic Partition Coefficients

(NA = "not available", ERR = "error")

Kds: Mineral	mafic Mode
oliv	0.1700
opx	0.0000
cpx	0.3000
plag	0.4300
amph	0.0000
	0.0000
	0.0000
garn	0.0000
	0.0000
	0.0000
	0.0000
mgnt	0.0700
ilmn	0.0300
zirc	0.0000
	0.0000
apat	0.0000
	0.0000
	0.0000
	0.0000
	0.0000
	0.0000
Total	1.0000

M. F. Liquid
F = 0.800

M. F. Xtals
(1-F)= 0.200

Dated: 24nov87

Table 2b. YMSMA BASALT (PARENT) - GGT MAFIC TUFF (DAUGHTER)

Closed-System Fractional XL (given Co)
Comment: YM-ggt

	Co	Cl	Cl	Sqred Resid	Cs	D
Na	14726	24642	0.39928	4E+09	36814.4	21.5852
K	16185	6640	25923.0	0.55332	1577.92	0.07787
Rb	38	15	61.2962	0.57045	3.05559	0.064
Sr	337	253	355.905	0.08360	308.642	0.89315
Cs	0.53	0.27	0.87711	0.47910	0.00933	0.013834
Ba	578	334	910.183	0.40074	79.7240	0.1111
Th	0.73	0.77	1.19712	0.12730	0.02931	0.0317
U	0.69	0.36	1.12145	0.46102	0.04281	0.0492
La	4.3	6.79	6.86038	0.00010	0.45941	0.085502
Ce	11.6	17.25	18.5439	0.00486	1.18400	0.081602
Nd	0	0	NA	NA	NA	0.100414
Sm	1.84	2.87	2.84200	0.00009	0.33698	0.148936
Eu	0.6	0.98	0.87084	0.01570	0.19372	0.27071
Tb	0.34	0.52	0.51788	0.00001	0.07317	0.17622
Yb	1.27	1.93	1.89718	0.00029	0.32921	0.2143
Lu	0.22	0.34	0.32951	0.00101	0.05573	0.20916
P	0	0	NA	NA	NA	0.01173
Sc	39.3	37.1	43.5229	0.02177	32.9656	0.8002
Ti	3720	5220	4583.42	0.01928	2424.85	0.5914
Y	13.5	19	20.5548	0.00572	2.91765	0.177
Zr	23.5	38.7	38.3274	0.00009	1.25878	0.0424
Nb	4.3	4.9	6.88532	0.08314	0.42201	0.0784
Hf	0.77	1.31	1.20659	0.00734	0.11510	0.1207
Ta	0.07	0.08	0.11145	0.07964	0.00782	0.0895
V	289	307	185.258	0.43183	444.612	1.8705
Cu	0	0	NA	NA	NA	0.934
Zn	0	0	NA	NA	NA	1.2274
Pb	0	0	NA	NA	NA	0.1935
Cr	165	10	9.29779	0.00570	398.553	6.63043
Mg	0	0	NA	NA	NA	NA
Mn	0	0	NA	NA	NA	NA
Fe	0	0	NA	NA	NA	NA
Co	37.1	26.8	22.1417	0.04426	59.5374	2.01043
Ni	51	9	4.21553	1.28813	121.176	5.88043

Mafic Partition Coefficients

(NA = "not available", ERR = "error")

Kds: Mineral	mafic Mode
oliv	0.2100
opx	0.0000
cpx	0.3000
plag	0.4300
amph	0.0000
	0.0000
	0.0000
garn	0.0000
	0.0000
	0.0000
	0.0000
mgnt	0.0600
ilmn	0.0000
zirc	0.0000
	0.0000
apat	0.0000
	0.0000
	0.0000
	0.0000
	0.0000
	0.0000
Total	1.0000

M. F. Liquid
F = 0.600

M. F. Xtals
(1-F)= 0.400

Dated: 24nov87

Table 2c. EVOLVED GRB BASALT (PARENT) - BRINDLE PUP ANDESITE (DAUGHTER)

Closed-System Fractional XL (given Co)
Comment: GRB Thol - BPA

	Co	Cl	Cl	Sqred Resid	Cs	D
Na	28046	23088	16763.6	0.14233	57057.8	2.5666
K	7553	13363	10438.3	0.07850	133.563	0.01511
Rb	22	43	30.3873	0.17227	0.43243	0.0168
Sr	342	253	454.178	0.19620	53.5408	0.13645
Cs	0.73	1.1	1.01272	0.00742	0.00299	0.003502
Ba	288	678	397.406	0.49852	6.66850	0.0198
Th	1.55	2.93	2.13783	0.13730	0.03841	0.0212
U	0.5	1.83	0.68565	2.78545	0.02259	0.03876
La	12.68	17.73	17.4309	0.00029	0.46334	0.031306
Ce	31.1	41.13	42.5325	0.00108	1.70196	0.047006
Nd	0	0	NA	NA	NA	0.064844
Sm	4.15	5.52	5.57152	0.00008	0.49465	0.103328
Eu	1.25	1.43	1.67101	0.02080	0.16738	0.11633
Tb	0.75	1.05	1.00151	0.00234	0.10324	0.11966
Yb	2.47	3.86	3.27001	0.03255	0.41282	0.1459
Lu	0.4	0.65	0.53056	0.05066	0.06424	0.14008
P	1003	828	955.122	0.01771	1126.11	1.14889
Sc	27.9	18.4	27.2562	0.10557	29.5552	1.071056
Ti	6360	3420	3644.95	0.00380	13341.5	2.6946
Y	24.1	36.9	32.0939	0.02242	3.54414	0.128
Zr	109.2	139.9	149.942	0.00448	4.43306	0.0348
Nb	11.8	8	15.4743	0.23330	2.35177	0.1748
Hf	2.98	4.01	3.99217	0.00001	0.37727	0.109868
Ta	0.44	0.36	0.57133	0.13682	0.10229	0.2049
V	229	56	150.811	0.39523	430.056	2.2715
Cu	0	0	NA	NA	NA	0.9696
Zn	0	0	NA	NA	NA	1.662
Pb	0	0	NA	NA	NA	0.0225
Cr	97.3	3	1.33795	1.54314	344.059	14.04902
Mg	24241	13098	11060.2	0.03394	58134.3	3.388669
Mn	0	0	NA	NA	NA	1.259822
Fe	77309	50258	55624.5	0.00930	133068.	2.002074
Co	39	11	11.0434	0.00001	110.888	4.840820
Ni	66.5	6	1.47098	9.47957	233.717	12.60188

Mafic Partition Coefficients

(NA = "not available", ERR = "error")

Kds: Mineral	mafic Mode
oliv	0.6300
opx	0.0000
cpx	0.2000
plag	0.0500
amph	0.0000
	0.0000
	0.0000
garn	0.0000
	0.0000
	0.0000
	0.0000
mgnt	0.0800
ilmn	0.0400
zirc	0.0000
	0.0000
apat	0.0014
	0.0000
	0.0000
	0.0000
	0.0000
	0.0000
Total	1.0014

M. F. Liquid
F = 0.720

M. F. Xtals
(1-F)= 0.280

Temperature Dependent Kds

Kds: mafic

T(C) = 1110

Dated: 24nov87

Table 2d. BRINDLE PUP ANDESITE (PARENT) - DACITE OF BURNT CANYON (DAUGHTER)

Closed-System Fractional XL (given Co)
Comment:

	Co	Cl	Cl	Sqred Resid	Cs	D
Na	23088	33152	22742.2	0.20951	26199.5	1.1432
K	0	0	NA	NA	NA	0.3187
Rb	42.8	27.6	46.5340	0.16555	9.19375	0.2061
Sr	253	213	220.188	0.00106	548.307	2.3184
Cs	1.1	0.4	1.20195	0.44516	0.18239	0.1587
Ba	678	484	691.301	0.08992	558.288	0.8156
Th	2.93	3.36	3.22411	0.00177	0.28294	0.0921
U	1.83	2.07	2.02967	0.00039	0.03294	0.0171
La	17.73	18.39	19.4412	0.00292	2.32896	0.1255
Ce	41.13	41.48	44.4182	0.00437	11.5355	0.27
Nd	0	0	NA	NA	NA	0.3755
Sm	5.52	5.65	5.87749	0.00149	2.30254	0.4044
Eu	1.43	1.33	1.45316	0.00718	1.22154	0.8475
Tb	1.05	1.18	1.11760	0.00311	0.44153	0.40775
Yb	3.86	4.48	4.12621	0.00735	1.46406	0.367
Lu	0.65	0.73	0.70026	0.00180	0.19759	0.293
P	836	836	928.888	0.01	0	0
Sc	18.4	15.8	13.6200	0.02561	61.4191	3.855
Ti	3420	3540	3463.25	0.00049	3030.66	0.8807
Y	36.9	43.2	39.6971	0.00778	11.7257	0.3065
Zr	139.9	159.8	153.350	0.00176	18.8422	0.1287
Nb	8	8.45	8.54660	0.00012	3.08054	0.3727
Hf	4.01	4.24	4.35911	0.00074	0.86799	0.2077
Ta	0.36	0.42	0.39009	0.00587	0.08915	0.238
V	0	0	NA	NA	NA	5.0395
Cu	0	0	NA	NA	NA	0
Zn	0	0	NA	NA	NA	1
Pb	0	0	NA	NA	NA	0.485
Cr	3	2	NA	NA	NA	NA
Mg	10620	7380	NA	NA	NA	NA
Mn	0	0	NA	NA	NA	NA
Fe	0	0	NA	NA	NA	NA
Co	11	8.4	NA	NA	NA	NA
Ni	0	0	NA	NA	NA	NA

Intermediate Partition Coefficients

(NA = "not available", ERR = "error")

Kds: Mineral	inter Mode
oliv	0.0000
opx	0.0000
cpx	0.1200
plag	0.7500
amph	0.0000
biot	0.0500
kspr	0.0000
garn	0.0000
qtz	0.0000
	0.0000
	0.0000
mgnt	0.0800
ilmn	0.0000
zirc	0.0000
alln	0.0000
apat	0.0020
sphn	0.0000
	0.0000
	0.0000
	0.0000
	0.0000
Total	1.0020

M. F. Liquid
F = 0.900

M. F. Xtals
(1-F)= 0.100

Dated: 24nov87

Table 2e. GADDES ANDESITE (PARENT) - BUZZARD DACITE (DAUGHTER)

Closed-System Fractional XL (given Co)
Comment: Gaddes - Buzzard Rhyolite

	Co	Cl	Cl	Sqred Resid	Cs	D
Na	20500	32042	20488.5	0.31797	20545.7	1.0025
K	8217	9130	9986.48	0.00735	1139.06	0.126
Rb	17.6	18	21.8045	0.03044	0.78197	0.04
Sr	206	67	161.884	0.34354	382.463	2.08
Cs	0.3	0.37	0.37208	0.00003	0.01166	0.035
Ba	447	385	523.445	0.06995	141.218	0.2925
Th	1.95	2.41	2.39223	0.00005	0.18105	0.084
U	1.28	1.35	1.59486	0.02357	0.02053	0.0144
La	11.96	14.59	14.4837	0.00005	1.86513	0.142
Ce	28.75	34.62	33.6104	0.00090	9.30803	0.3
Nd	0	0	NA	NA	NA	0.4995
Sm	4.86	5.36	5.30367	0.00011	3.08531	0.6085
Eu	1.14	1.14	1.15150	0.00009	1.09398	0.955
Tb	1.03	1.03	1.10002	0.00405	0.74991	0.70525
Yb	4.31	4.5	4.69978	0.00180	2.75084	0.612
Lu	0.67	0.74	0.75344	0.00031	0.33623	0.474
P	0	0	NA	NA	NA	0
Sc	16.5	11.4	4.98381	1.65741	62.5647	6.365
Ti	3720	1680	1946.44	0.01873	10814.2	3.9027
Y	42.8	46.65	48.1088	0.00091	21.5647	0.476
Zr	117.4	137.5	142.547	0.00125	16.8089	0.1302
Nb	6.2	5.7	6.98039	0.03364	3.07842	0.4687
Hf	3.03	3.43	3.65531	0.00379	0.52874	0.1592
Ta	0.26	0.31	0.27974	0.01169	0.18102	0.672
V	0	0	NA	NA	NA	2.0215
Cu	0	0	NA	NA	NA	0
Zn	0	0	NA	NA	NA	0
Pb	0	0	NA	NA	NA	0.39
Cr	0	0	NA	NA	NA	NA
Mg	0	0	NA	NA	NA	NA
Mn	0	0	NA	NA	NA	NA
Fe	0	0	NA	NA	NA	NA
Co	0	0	NA	NA	NA	NA
Ni	0	0	NA	NA	NA	NA

Intermediate Partition Coefficients

(NA = "not available", ERR = "error")

Kds: Mineral	inter Mode
oliv	0.0000
opx	0.0000
cpx	0.2500
plag	0.6500
amph	0.0000
biot	0.0000
kspr	0.0000
garn	0.0000
qtz	0.0000
	0.0000
	0.0000
mgnt	0.0300
ilmn	0.0700
zirc	0.0000
alln	0.0000
apat	0.0020
sphn	0.0000
	0.0000
	0.0000
	0.0000
	0.0000
Total	1.0020

M. F. Liquid
F = 0.800

M. F. Xtals
(1-F)= 0.200

Temperature Dependent Kds

Kds: inter

T(C) = 0

Dated: 24nov87

Table 2f. BUZZARD DACITE (PARENT) - DECEPTION RHYODACITE (DAUGHTER)

Closed-System Fractional XL (given Co)
Comment:

	Co	Cl	Cl	Sqred Resid	Cs	D
Na	32042	30414	29557.5	0.00083	35078.5	1.135
K	9130	10624	13721.8	0.05096	3517.70	0.3185
Rb	18	15	30.0816	0.25135	3.23359	0.141
Sr	67	93	19.9728	13.3687	124.477	3.0245
Cs	0.37	0.57	0.61154	0.00461	0.07478	0.1595
Ba	385	564	509.449	0.01146	232.895	0.5315
Th	2.41	4.01	4.06995	0.00021	0.38117	0.1235
U	1.35	1.52	2.40371	0.13516	0.06212	0.035
La	14.59	26.31	22.3294	0.03177	5.13066	0.28815
Ce	34.62	54.51	51.0703	0.00453	14.5139	0.3497
Nd	0	0	NA	NA	NA	0.49519
Sm	5.36	5.39	6.69751	0.03811	3.72526	0.62737
Eu	1.14	0.91	0.87099	0.00200	1.46878	1.4502
Tb	1.03	1.03	0.94826	0.00742	1.12989	1.1383
Yb	4.5	5.76	5.85312	0.00025	2.84617	0.56025
Lu	0.74	0.93	1.04170	0.01149	0.37125	0.428
P	218	179	396.363	0.30073	0	0
Sc	11.4	5.6	5.93268	0.00314	18.0822	2.0925
Ti	1680	840	845.403	0.00004	2700.06	2.1487
Y	46.7	48.4	57.5863	0.02544	33.3944	0.6495
Zr	137.5	157.6	168.774	0.00438	99.2758	0.6572
Nb	5.7	6.5	6.57863	0.00014	4.62611	0.7602
Hf	3.43	5.01	5.04925	0.00006	1.45090	0.3532
Ta	0.31	0.51	0.32462	0.32609	0.29212	0.9229
V	0	0	NA	NA	NA	6.9275
Cu	0	0	NA	NA	NA	0
Zn	0	0	NA	NA	NA	1.35
Pb	0	0	NA	NA	NA	0.485
Cr	0	0	NA	NA	NA	1.1
Mg	0	0	NA	NA	NA	0
Mn	0	0	NA	NA	NA	0
Fe	0	0	NA	NA	NA	0
Co	0	0	NA	NA	NA	0
Ni	0	0	NA	NA	NA	0

Felsic Partition Coefficients

Kds: Mineral	felsic Mode
	0.0000
opx	0.0000
cpx	0.0000
plag	0.7500
amph	0.0500
biot	0.0500
kspr	0.0000
garn	0.0000
qtz	0.0500
	0.0000
	0.0000
mgnt	0.0900
ilmn	0.0100
zirc	0.0002
alln	0.0000
apat	0.0020
sphn	0.0000
	0.0000
	0.0000
	0.0000
	0.0000
Total	1.0022

M. F. Liquid
F = 0.550

M. F. Xtals
(1-F)= 0.450

(NA = "not available", ERR = "error")

Dated: 24nov87

Table 2g. BUZZARD DACITE (PARENT) - QUARTZ PORPHYRY RHYODACITE (DAUGHTER)

Closed-System Fractional XL (given Co)
Comment: br-qp

	Co	Cl	Cl	Sqred Resid	Cs	D
Na	32042	25900	29491.1	0.01482	35868.3	1.1624
K	9130	18177	13140.9	0.14686	3113.57	0.2871
Rb	18	26	28.2220	0.00619	2.66696	0.1196
Sr	67	74	22.8849	4.98884	133.172	3.1029
Cs	0.37	0.46	0.57525	0.04013	0.06212	0.1361
Ba	385	686	502.984	0.13239	208.023	0.4767
Th	2.41	3.48	3.81800	0.00783	0.29799	0.0993
U	1.35	2.04	2.21927	0.00652	0.04609	0.02692
La	14.59	20.98	21.0108	0.00000	4.95868	0.28605
Ce	34.62	48.6	48.9736	0.00005	13.0895	0.321
Nd	0	0	NA	NA	NA	0.40975
Sm	5.36	6.92	7.02353	0.00021	2.86469	0.47085
Eu	1.14	0.88	0.94030	0.00411	1.43954	1.377
Tb	1.03	1.44	1.09131	0.10208	0.93802	0.8868
Yb	4.5	6.51	6.25020	0.00172	1.87468	0.35685
Lu	0.74	1.04	1.07114	0.00084	0.24327	0.276
P	218	87	363.333	0.57843	0	0
Sc	11.4	7	7.84633	0.01163	16.7304	1.7313
Ti	1680	960	1021.11	0.00358	2668.33	1.9747
Y	46.7	60.4	59.7010	0.00013	27.1984	0.5192
Zr	137.5	196.2	190.749	0.00081	57.6257	0.3592
Nb	5.7	5.9	6.91618	0.02158	3.87571	0.6214
Hf	3.43	5.28	5.14567	0.00068	0.85649	0.206
Ta	0.31	0.45	0.33062	0.13036	0.27906	0.8739
V	0	0	NA	NA	NA	5.7877
Cu	0	0	NA	NA	NA	0
Zn	0	0	NA	NA	NA	1.01
Pb	0	0	NA	NA	NA	0.49
Cr	0	0	NA	NA	NA	0.914
Mg					0	0
Mn	0	0	NA	NA	NA	0
Fe					0	0
Co	0	0	NA	NA	NA	0
Ni	0	0	NA	NA	NA	0

Felsic Partition Coefficients

(NA = "not available", ERR = "error")

Kds: Mineral	felsic Mode
	0.0000
opx	0.0000
cpx	0.0000
plag	0.7700
amph	0.0300
biot	0.0400
kspr	0.0000
garn	0.0000
qtz	0.0500
	0.0000
	0.0000
mgnt	0.0900
ilmn	0.0100
zirc	0.0000
alln	0.0000
apat	0.0020
sphn	0.0000
	0.0000
	0.0000
	0.0000
	0.0000
Total	0.9920

M. F. Liquid
F = 0.600

M. F. Xtals
(1-F)= 0.400

Dated: 24nov87

Table 3. Petrogenetic Models for the Green Gulch Block Volcanics

Table 3a. PRIMITIVE GREEN GULCH BASALT (PARENT) - EVOLVED GREEN GULCH BASALT (DAUGHTER)

Open-System RTF (O'Hara)
Comment:

	Co	Cl	Cl	Sqred Resid	Cl/Co	D
Na	12210	28046	1182.60	515.986	0.09685	12.1515
K	3237	7553	5374.33	0.16433	1.66028	0.0479
Rb	9	22	14.9840	0.21923	1.66489	0.0437
Sr	280	342	348.338	0.00033	1.24406	0.54225
Cs	0.43	0.73	0.73141	0.00000	1.70095	0.01156
Ba	180	288	295.661	0.00067	1.64256	0.06425
Th	1.23	1.55	2.06995	0.06309	1.68289	0.0275
U	0.3	0.5	0.49795	0.00001	1.65984	0.0483
La	11.33	12.68	18.4026	0.09670	1.62423	0.081501
Ce	28.7	31.1	46.0989	0.10586	1.60623	0.098801
Nd	0	0	NA	NA	1.55289	0.152210
Sm	3.76	4.15	5.50117	0.06032	1.46307	0.25017
Eu	1.04	1.25	1.46322	0.02123	1.40695	0.31715
Tb	0.56	0.75	0.79540	0.00325	1.42036	0.3007
Yb	1.76	2.47	2.42094	0.00041	1.37553	0.3568
Lu	0.28	0.4	0.38623	0.00126	1.37942	0.3518
P	916	1003	997.798	0.00002	1.08929	0.8114
Sc	38.9	27.9	34.6600	0.03804	0.89100	1.27464
Ti	4380	6360	5075.52	0.06404	1.15879	0.6826
Y	18.7	24.1	26.5916	0.00878	1.42201	0.2987
Zr	66.6	109.2	109.348	0.00000	1.64186	0.0649
Nb	8.9	11.8	14.2762	0.03008	1.60407	0.1009
Hf	1.93	2.98	2.92525	0.00035	1.51567	0.19152
Ta	0.24	0.44	0.38641	0.01923	1.61005	0.0951
V	263	229	170.183	0.11944	0.64708	2.1675
Cu	0	0	NA	NA	0.84467	1.4099
Zn	0	0	NA	NA	0.92183	1.1912
Pb	0	0	NA	NA	1.59681	0.108
Cr	863	97.3	141.486	0.09753	0.16394	8.585925
Mg	61084	24241	46590.3	0.23011	0.76272	1.683418
Mn	0	0	NA	NA	0.94066	1.142599
Fe	71368	77309	89541.6	0.01866	1.25464	0.526031
Co	56	39	45.3726	0.01972	0.81022	1.519079
Ni	271	66.5	40.8693	0.39330	0.15080	9.115149

Mafic Partition Coefficients

(NA = "not available", ERR = "error")

Kds: Mineral	mafic Mode
oliv	0.1500
opx	0.0000
cpx	0.5500
plag	0.2400
amph	0.0000
	0.0000
	0.0000
garn	0.0000
	0.0000
	0.0000
	0.0000
mgnt	0.0600
ilmn	0.0000
zirc	0.0000
	0.0000
apat	0.0010
	0.0000
	0.0000
	0.0000
	0.0000
	0.0000
Total	1.0010

M. F. Leakage
Y = 0.140

M. F. Xtals
X = 0.100

M. F. Injectn
Z = 0.240

Temperature Dependent Kds

Kds: mafic

T(C) = 1150

Number of Cycles

n =1.7E+01

Dated: 24nov87

Table 3b. PRIMITIVE GREEN GULCH BASALT (PARENT) - GREEN GULCH BASALTIC ANDESITE (DAUGHTER)

Open-System RTF (O'Hara)
Comment: GRB Prim - GRB Bas And

	Co	Cl	Cl	Sqred Resid	Cl/Co	D
Na	12210	27084	785.838	1119.91	0.06436	25.0869
K	3237	6889	6191.05	0.01270	1.91258	0.08953
Rb	9	25	17.5053	0.18329	1.94503	0.0728
Sr	280	305	274.447	0.01239	0.98017	1.0384
Cs	0.43	1.5	0.88778	0.47554	2.06461	0.015664
Ba	180.2	415	331.864	0.06275	1.84164	0.12815
Th	1.23	2.18	2.44672	0.01188	1.98920	0.0509
U	0.25	0.78	0.49504	0.33133	1.98017	0.0553
La	11.33	15.9	21.3671	0.06546	1.88588	0.103725
Ce	28.7	37.8	54.0025	0.09001	1.88162	0.106031
Nd	0	0	NA	NA	1.85568	0.120271
Sm	3.76	5.22	6.64633	0.04605	1.76764	0.171716
Eu	1.04	1.57	1.62683	0.00122	1.56426	0.312535
Tb	0.56	1.04	0.95498	0.00792	1.70532	0.21132
Yb	1.76	3.47	2.84602	0.04806	1.61705	0.2726
Lu	0.28	0.57	0.45202	0.06811	1.61438	0.27456
P	916	959	1017.94	0.00335	1.11128	0.80967
Sc	38.9	39.4	45.3841	0.01738	1.16668	0.72834
Ti	4380	7500	6938.48	0.00654	1.58412	0.2972
Y	18.7	37	32.3130	0.02103	1.72796	0.1966
Zr	66.6	109.2	107.062	0.00039	1.60755	0.2796
Nb	8.9	7.5	17.2766	0.32023	1.94120	0.07475
Hf	1.93	3.6	2.92807	0.05266	1.51713	0.35052
Ta	0.24	0.36	0.46037	0.04753	1.91823	0.08658
V	263	347	280.732	0.05572	1.06742	0.88
Cu	0	0	NA	NA	1.13886	0.7682
Zn	0	0	NA	NA	1.16258	0.7341
Pb	0	0	NA	NA	1.68479	0.225
Cr	863	32	209.798	0.71820	0.24310	6.725938
Mg	61084	28823	34191.3	0.02465	0.55974	2.481088
Mn	0	0	NA	NA	0.81102	1.441306
Fe	71368	90031	81894.1	0.00987	1.14749	0.755640
Co	56	41.5	44.3014	0.00399	0.79109	1.499962
Ni	271	25	29.4287	0.02264	0.10859	15.37830

Mafic Partition Coefficients

(NA = "not available", ERR = "error")

Kds: Mineral	mafic Mode
oliv	0.1600
opx	0.0000
cpx	0.3100
plag	0.5000
amph	0.0000
	0.0000
	0.0000
garn	0.0000
	0.0000
	0.0000
	0.0000
mgnt	0.0200
ilmn	0.0100
zirc	0.0003
	0.0000
apat	0.0010
	0.0000
	0.0000
	0.0000
	0.0000
	0.0000
Total	1.0013

M. F. Leakage
Y = 0.010

M. F. Xtals
X = 0.011

M. F. Injectn
Z = 0.021

Temperature Dependent Kds

Kds: mafic

T(C) = 1070

Number of Cycles

n =2.2E+02

Dated: 24nov87

Table 3c. GREEN GULCH BASALTIC ANDESITE (PARENT) - GREEN GULCH ANDESITE (DAUGHTER)

Open-System RTF (O'Hara)
Comment: GRB Bas And - GRB And

	Co	Cl	Cl	Sqred Resid	Cl/Co	D
Na	27084	28934	29217.9	0.00009	1.07879	0.8533
K	6889	12865	12038.2	0.00471	1.74745	0.1067
Rb	25	36	46.2066	0.04879	1.84826	0.0381
Sr	305	257	214.709	0.03879	0.70396	1.8032
Cs	1.52	0.7	2.82450	0.56575	1.85822	0.0317
Ba	415	681	643.765	0.00334	1.55124	0.2639
Th	2.18	4.48	3.89828	0.02226	1.78820	0.0781
U	0.78	2.3	1.43846	0.35871	1.84418	0.04074
La	15.9	24.12	27.3325	0.01381	1.71902	0.1274
Ce	37.8	55.22	57.0478	0.00102	1.50920	0.3025
Nd	0	0	NA	NA	1.21168	0.64524
Sm	5.22	6.26	5.55474	0.01611	1.06412	0.87912
Eu	1.57	1.65	1.44715	0.01964	0.92175	1.1677
Tb	1.04	1.08	0.91398	0.03299	0.87883	1.2709
Yb	3.47	3.41	3.32229	0.00069	0.95743	1.0882
Lu	0.57	0.54	0.60870	0.01274	1.06790	0.8724
P	959	1090	1830.81	0.16373	1.90909	0
Sc	39.4	20.1	5.60385	6.69162	0.14222	8.766
Ti	7500	5400	5659.52	0.00210	0.75460	1.627
Y	37	37.9	42.5499	0.01194	1.14999	0.7364
Zr	114.8	160.9	165.857	0.00089	1.44474	0.3657
Nb	7.5	10.5	11.0793	0.00273	1.47724	0.3332
Hf	3.6	4.6	5.33909	0.01916	1.48308	0.3275
Ta	0.36	0.55	0.49085	0.01451	1.36348	0.4532
V	347	156	144.421	0.00642	0.41619	3.4504
Cu	0	0	NA	NA	1.90909	0
Zn	0	0	NA	NA	1.39330	0.42
Pb	0	0	NA	NA	1.48668	0.324
Cr	32	18	5.57281	4.97275	0.17415	7.559120
Mg	28823	19115	16806.9	0.01885	0.58310	2.327652
Mn	0	0	NA	NA	0.94077	1.124646
Fe	90031	64168	74853.9	0.02037	0.83142	1.395755
Co	41.5	20	40.9233	0.26140	0.98610	1.028044
Ni	25	16	2.83778	21.5129	0.11351	10.21400

Mafic Partition Coefficients

(NA = "not available", ERR = "error")

Kds: Mineral	inter Mode
oliv	0.0000
opx	0.0000
cpx	0.3500
plag	0.5400
amph	0.0600
biot	0.0000
kspr	0.0000
garn	0.0000
	0.0000
	0.0000
	0.0000
mgnt	0.0300
ilmn	0.0200
zirc	0.0002
alln	0.0000
apat	0.0000
sphn	0.0000
	0.0000
	0.0000
	0.0000
	0.0000
Total	1.0002

M. F. Leakage
Y = 0.110

M. F. Xtals
X = 0.100

M. F. Injectn
Z = 0.210

Temperature Dependent Kds

Kds: inter

T(C) = 1100

Number of Cycles

n =2.0E+01

Dated: 24nov87

Table 3d. GREEN GULCH ANDESITE (PARENT) - GREEN GULCH DACITE (DAUGHTER)

Closed-System Fractional XL (given Co)
Comment: GRB And - GRB Dac

	Co	Cl	Cl	Sqred Resid	Cs	D
Na	28934	32190	29563.1	0.00789	26417.4	0.9036
K	12865	17264	15678.0	0.01023	1612.88	0.1138
Rb	36	50.7	44.6419	0.01841	1.43220	0.0358
Sr	257	200	213.682	0.00410	430.269	1.8272
Cs	0.7	1.4	0.86827	0.37503	0.02691	0.0346
Ba	681	737	803.124	0.00677	192.501	0.2608
Th	4.48	5.47	5.33434	0.00064	1.06262	0.2178
U	2.3	2.77	2.81829	0.00029	0.22683	0.08928
La	24.12	24.47	27.2427	0.01035	11.6288	0.4544
Ce	55.22	55.8	59.0431	0.00301	39.9274	0.7
Nd	0	0	NA	NA	NA	1.2326
Sm	6.26	5.75	5.59012	0.00081	8.93949	1.5072
Eu	1.65	1.34	1.44195	0.00499	2.48219	1.604
Tb	1.08	0.97	0.90964	0.00440	1.76142	1.7693
Yb	3.41	3.1	3.06199	0.00015	4.80200	1.4824
Lu	0.54	0.49	0.50607	0.00100	0.67571	1.2908
P	1090	480	667.151	0.07869	2781.39	3.2
Sc	20.1	12.4	6.49297	0.82765	74.5280	6.064
Ti	5400	2880	3240.59	0.01238	14037.6	3.2884
Y	37.9	36.8	38.9737	0.00311	33.6049	0.8748
Zr	160.9	207.3	185.186	0.01425	63.7539	0.37
Nb	10.5	10	11.5213	0.01743	6.41454	0.584
Hf	4.6	5.3	5.27028	0.00003	1.91885	0.3904
Ta	0.55	0.55	0.57888	0.00249	0.43445	0.7706
V	156	64	36.7259	0.55150	633.096	7.4818
Cu	0	0	NA	NA	NA	0
Zn	0	0	NA	NA	NA	1.4
Pb	0	0	NA	NA	NA	0.348
Cr	18	23	1.03779	447.844	85.8488	13.78670
Mg	19115	6392	7724.10	0.02974	64678.5	5.060737
Mn	0	0	NA	NA	NA	1.935432
Fe	64168	37956	29711.4	0.07699	201994.	4.450567
Co	20	7.7	15.9066	0.26617	36.3735	2.026230
Ni	16	5	0.05637	7690.47	79.7745	26.31266

Intermediate Partition Coefficients

(NA = "not available", ERR = "error")

Kds: Mineral	inter Mode
oliv	0.0000
opx	0.0000
cpx	0.1600
plag	0.5800
amph	0.2000
biot	0.0000
kspr	0.0000
garn	0.0000
qtz	0.0000
	0.0000
	0.0000
mgnt	0.0100
ilmn	0.0500
zirc	0.0000
alln	0.0001
apat	0.0040
sphn	0.0000
	0.0000
	0.0000
	0.0000
	0.0000
Total	1.0041

M. F. Liquid
F = 0.800

M. F. Xtals
(1-F)= 0.200

Temperature Dependent Kds

Kds: inter

T(C) = 990

Dated: 24nov87

Table 4. Petrogenetic Models for the

Big Bug Block Volcanics

Table 4a. HIGH-TI SPUD MOUNTAIN BASALTIC ANDESITE (PARENT) - SPUD MOUNTAIN ANDESITE (DAUGHTER)

Closed-System Fractional XL (given Co)
Comment: High Ti SMB - SMA And.

	Co	Cl	Cl	Sqred Resid	Cs	D
Na	19536	23162	0.03694	4E+11	55817.0	31.5915
K	11454	17762	16467.0	0.00618	2144.10	0.1573
Rb	37	57	54.6193	0.00189	4.27829	0.0959
Sr	256	181	223.034	0.03551	317.221	1.32
Cs	1.45	2.99	2.20901	0.12499	0.04040	0.02275
Ba	432	664	611.461	0.00738	98.7143	0.1935
Th	2.55	4.31	3.85439	0.01397	0.12755	0.041
U	1.26	2.17	1.89217	0.02155	0.08595	0.0561
La	22.3	28.9	32.4042	0.01169	3.53488	0.1325
Ce	51.05	67.58	73.9864	0.00749	8.45373	0.1386
Nd	0	0	NA	NA	NA	0.1384
Sm	6.58	8.9	9.34678	0.00228	1.44168	0.18521
Eu	2.14	2.17	2.81146	0.05205	0.89298	0.3665
Tb	1.12	1.69	1.58097	0.00475	0.26390	0.1998
Yb	4.38	6.46	6.16067	0.00236	1.07303	0.2081
Lu	0.77	1.16	1.09020	0.00409	0.17533	0.1928
P	1395	1003	1076.42	0.00465	1986.63	1.6018
Sc	47.8	20.5	48.2077	0.33034	47.0426	0.98028
Ti	9780	4500	4542.41	0.00008	19506.9	2.7802
Y	41.9	59.9	59.3725	0.00007	9.45094	0.1909
Zr	135.8	198.7	199.314	0.00000	17.8453	0.1093
Nb	10.4	9.5	14.5890	0.12168	2.62031	0.2143
Hf	4	6	5.86767	0.00050	0.53146	0.11054
Ta	0.42	0.48	0.58540	0.03241	0.11282	0.2292
V	446	23	242.441	0.81926	824.036	2.415
Cu	0	0	NA	NA	NA	0.7673
Zn	0	0	NA	NA	NA	1.3404
Pb	0	0	NA	NA	NA	0.2835
Cr	11	1	0.00011	7E+07	31.4283	27.53689
Mg	24663	10311	9688.28	0.00413	52473.1	3.169042
Mn	0	0	NA	NA	NA	1.675237
Fe	108205	53474	52524.8	0.00032	211611.	2.677739
Co	53.2	12.1	41.2719	0.49959	75.3521	1.589336
Ni	23	4	0.00673	351975.	65.7017	19.88780

Mafic Partition Coefficients

(NA = "not available", ERR = "error")

Kds: Mineral	mafic Mode
oliv	0.0000
opx	0.0000
cpx	0.2000
plag	0.6300
amph	0.0500
	0.0000
	0.0000
garn	0.0000
	0.0000
	0.0000
	0.0000
mgnt	0.0800
ilmn	0.0400
zirc	0.0000
	0.0000
apat	0.0020
	0.0000
	0.0000
	0.0000
	0.0000
	0.0000
Total	1.0020

M. F. Liquid
F = 0.650

M. F. Xtals
(1-F)= 0.350

Temperature Dependent Kds

Kds: mafic

T(C) = 1020

Dated: 24nov87

Table 4b. HIGH-TI SPUD MOUNTAIN BASALTIC ANDESITE (PARENT) - SPUD MOUNTAIN ANDESITE (DAUGHTER)

Open-System RTF (O'Hara)
Comment: High Ti SMB - SMA And

	Co	Cl	Cl	Sqred Resid	Cl/Co	D
Na	19536	23162	232.490	9727.03	0.01190	30.2325
K	11454	17762	15174.8	0.02906	1.32484	0.3996
Rb	37	57	56.6186	0.00004	1.53023	0.14
Sr	256	181	218.724	0.02974	0.85439	1.396
Cs	1.45	2.99	2.34821	0.07469	1.61945	0.046
Ba	432	664	582.266	0.01970	1.34783	0.367
Th	2.55	4.31	4.12325	0.00205	1.61696	0.0485
U	1.26	2.17	1.99450	0.00774	1.58294	0.0833
La	22.3	28.9	33.6087	0.01962	1.50711	0.166
Ce	51.05	67.58	76.2019	0.01280	1.49269	0.1826
Nd	0	0	NA	NA	1.48122	0.196
Sm	6.58	8.9	9.26998	0.00159	1.40881	0.2852
Eu	2.14	2.17	2.71455	0.04024	1.26848	0.484
Tb	1.12	1.69	1.55998	0.00694	1.39284	0.306
Yb	4.38	6.46	6.32061	0.00048	1.44306	0.242
Lu	0.77	1.16	1.13728	0.00039	1.47699	0.201
P	1395	1003	1106.23	0.00870	0.79300	1.6
Sc	47.8	20.5	47.2204	0.32020	0.98787	1.02908
Ti	9780	4500	4208.08	0.00481	0.43027	3.714
Y	41.9	59.9	57.2953	0.00206	1.36742	0.34
Zr	135.8	198.7	173.136	0.02180	1.27493	0.474
Nb	10.4	9.5	13.6822	0.09343	1.31560	0.413
Hf	4	6	6.12367	0.00040	1.53091	0.13924
Ta	0.42	0.48	0.57617	0.02786	1.37185	0.334
V	446	23	326.059	0.86389	0.73107	1.835
Cu	0	0	NA	NA	1.40741	0.287
Zn	0	0	NA	NA	1.09667	0.7885
Pb	0	0	NA	NA	1.42069	0.27
Cr	11	1	0.96313	0.00146	0.08755	13.17147
Mg	24663	10311	10603.3	0.00076	0.42993	3.717321
Mn	0	0	NA	NA	1.30403	0.43
Fe	108205	53474	31351.8	0.49788	0.28974	5.536702
Co	53.2	12.1	26.9347	0.30334	0.50629	3.0706
Ni	23	4	11.6447	0.43098	0.50629	3.0706

Mafic Partition Coefficients

(NA = "not available", ERR = "error")

Kds: Mineral	mafic Mode
oliv	0.0000
opx	0.0000
cpx	0.0000
plag	0.6000
amph	0.3100
	0.0000
	0.0000
garn	0.0000
	0.0000
	0.0000
	0.0000
mgnt	0.0300
ilmn	0.0600
zirc	0.0000
	0.0000
apat	0.0020
	0.0000
	0.0000
	0.0000
	0.0000
	0.0000
Total	1.0020

M. F. Leakage
Y = 0.150

M. F. Xtals
X = 0.100

M. F. Injectn
Z = 0.250

Temperature Dependent Kds

Kds: mafic

T(C) = 1020

Number of Cycles

n =1.6E+01

Dated: 24nov87

Table 4c. SPUD MOUNTAIN ANDESITE (PARENT) - SPUD MOUNTAIN RHYOLITE (DAUGHTER)

Closed-System Fractional XL (given Co)
Comment: SMA - SMR

	Co	Cl	Cl	Sqred Resid	Cs	D
Na	23162	28342	22383.8	0.07085	24329.2	1.0669
K	17762	15272	25276.8	0.15666	6489.73	0.3093
Rb	57	26	85.6729	0.48514	13.9906	0.2023
Sr	181	87	101.435	0.02025	300.346	2.1336
Cs	3	0.6	4.61442	0.75685	0.57836	0.1571
Ba	664	710	739.303	0.00157	551.044	0.7897
Th	4.31	8.1	5.98799	0.12440	1.79300	0.3563
U	2.17	2.6	3.53682	0.07016	0.11976	0.0437
La	28.9	40.65	39.3072	0.00116	13.2890	0.3979
Ce	67.58	90.6	85.4153	0.00368	40.8270	0.5415
Nd	0	0	NA	NA	NA	0.7432
Sm	8.9	8.72	9.86439	0.01345	7.45341	0.7986
Eu	2.17	1.13	2.06615	0.20529	2.32577	1.096
Tb	1.69	1.76	1.78813	0.00024	1.54279	0.8895
Yb	6.46	7.08	6.93182	0.00045	5.75226	0.862
Lu	1.16	1.33	1.29532	0.00071	0.95701	0.784
P	1003	44			0	0
Sc	20.5	4.6	5.72821	0.03879	42.6576	3.496
Ti	4500	720	802.428	0.01055	10046.3	4.3753
Y	59.9	68.4	78.1047	0.01543	32.5929	0.4805
Zr	198.7	182.1	192.899	0.00313	207.401	1.058
Nb	9.5	14.4	10.3592	0.15215	8.21117	0.8305
Hf	6	7	6.52830	0.00522	5.20753	0.8348
Ta	0.48	0.92	0.52189	0.58189	0.41716	0.8362
V	23	0	0.84750	NA	56.2287	7.462
Cu	0	0	NA	NA	NA	0
Zn	0	0	NA	NA	NA	1.56
Pb	0	0	NA	NA	NA	0.455
Cr	1	0	0.00006	NA	2.49990	19.83136
Mg	10311	1869	5568.41	0.44137	17424.8	2.206088
Mn	0	0	NA	NA	NA	0.737990
Fe	53475	10415	10327.6	0.00007	118195.	4.219076
Co	12.1	1	8.16937	0.77016	17.9959	1.768976
Ni	4	0	0.07699	NA	9.88450	8.733137

Intermediate Partition Coefficients

(NA = "not available", ERR = "error")

Kds: Mineral	inter Mode
oliv	0.0000
opx	0.0000
cpx	0.0500
plag	0.7000
amph	0.0800
biot	0.0500
kspr	0.0000
garn	0.0000
qtz	0.0000
	0.0000
	0.0000
mgnt	0.0500
ilmn	0.0700
zirc	0.0010
alln	0.0001
apat	0.0030
sphn	0.0000
	0.0000
	0.0000
	0.0000
	0.0000
Total	1.0041

M. F. Liquid
F = 0.600

M. F. Xtals
(1-F)= 0.400

Temperature Dependent Kds

Kds: inter

T(C) = 995

Dated: 24nov87

Table 4d. IRON KING BASALT (PARENT) - SPUD MOUNTAIN ANDESITE CRYSTAL TUFF (DAUGHTER)

Closed-System Fractional XL (given Co)
Comment: IKA - SMCT

	Co	Cl	Cl	Sqred Resid	Cs	D
Na	22792	26418	8368.13	4.65254	152606.	10.51
K	3735	6640	3860.30	0.51850	2607.23	0.6868
Rb	9.9	14	10.8138	0.08681	1.67543	0.162
Sr	314	199	319.405	0.14210	265.350	0.838
Cs	0.36	0.31	0.39693	0.04796	0.02758	0.073
Ba	281	390	295.389	0.10258	151.492	0.526
Th	1.28	3.04	1.41430	1.32127	0.07127	0.053
U	0.85	1.59	0.93293	0.49604	0.10360	0.1164
La	9.56	11.21	10.3919	0.00619	2.07228	0.208
Ce	24.34	24.29	26.2283	0.00546	7.34440	0.2908
Nd	0	0	NA	NA	NA	0.36
Sm	3	2.65	3.13791	0.02417	1.75875	0.5734
Eu	0.94	0.65	0.97100	0.10928	0.66096	0.692
Tb	0.41	0.5	0.42665	0.02954	0.26007	0.622
Yb	1.86	1.96	1.96806	0.00001	0.88743	0.464
Lu	0.33	0.33	0.35220	0.00397	0.13018	0.382
P	567	349	379.930	0.00662	2250.62	4.8
Sc	33.9	21.4	31.5953	0.10412	54.6421	1.66824
Ti	4380	2220	2926.27	0.05825	17463.5	4.828
Y	17.1	20.7	17.6268	0.03039	12.3585	0.712
Zr	68.7	87.1	68.5120	0.07360	70.3914	1.026
Nb	6.6	5.5	6.78687	0.03595	4.91815	0.735
Hf	2.14	2.64	2.30702	0.02083	0.63680	0.28672
Ta	0.22	0.32	0.23187	0.14443	0.11311	0.501
V	260	134	202.334	0.11406	778.987	3.38
Cu	0	0	NA	NA	NA	0.51
Zn	0	0	NA	NA	NA	0.94
Pb	0	0	NA	NA	NA	0.09
Cr	25	42	2.20835	324.673	230.124	24.03166
Mg	23095	19598	11763.9	0.44347	125074.	7.402555
Mn	0	0	NA	NA	NA	0.83
Fe	82552	48231	31355.7	0.28964	543317.	10.18778
Co	28.9	17.5	17.3183	0.00010	133.134	5.8602
Ni	13	8	7.79027	0.00072	59.8875	5.8602

Mafic Partition Coefficients

(NA = "not available", ERR = "error")

Kds: Mineral	mafic Mode
oliv	0.0000
opx	0.0000
cpx	0.0000
plag	0.2000
amph	0.6800
	0.0000
	0.0000
garn	0.0000
	0.0000
	0.0000
	0.0000
mgnt	0.0400
ilmn	0.0700
zirc	0.0000
	0.0000
apat	0.0060
	0.0000
	0.0000
	0.0000
	0.0000
	0.0000
Total	0.9960

M. F. Liquid
F = 0.900

M. F. Xtals
(1-F)= 0.100

Temperature Dependent Kds

Kds: mafic

T(C) = 990

Dated: 24nov87

Table 4e. SPUD MOUNTAIN ANDESITE CRYSTAL TUFF (PARENT) - RHYODACITE QUARTZ PORPHYRY (DAUGHTER)

Closed-System Fractional XL (given Co)
Comment: smct-qp

	Co	Cl	Cl	Sqred Resid	Cs	D
Na	26418	11174	24319.8	0.29218	29565.2	1.162
K	6640	34777	10269.2	5.69548	1196.14	0.1464
Rb	14	57	22.8147	2.24515	0.77789	0.044
Sr	199	51	98.1328	0.23068	350.300	2.384
Cs	0.31	2	0.50621	8.70767	0.01567	0.04
Ba	390	1045	549.165	0.81520	151.251	0.33
Th	3.04	4	4.85881	0.03124	0.31177	0.082
U	1.6	1.6	2.65232	0.15741	0.02151	0.01056
La	11.21	17.75	17.7420	0.00000	1.41195	0.1012
Ce	24.29	44.1	35.9497	0.05139	6.80030	0.2325
Nd	0	0	NA	NA	NA	0.34964
Sm	2.65	3.71	3.58095	0.00129	1.25356	0.41062
Eu	0.65	0.73	0.68103	0.00516	0.60345	0.9087
Tb	0.5	0.68	0.62310	0.00833	0.31533	0.5691
Yb	1.96	2.55	2.52350	0.00011	1.11473	0.5053
Lu	0.33	0.55	0.45062	0.04862	0.14905	0.3901
P	349	44	581.666	0.85443	0	0
Sc	21.4	8.2	2.99736	3.01277	49.0039	4.848
Ti	2220	900	1098.10	0.03254	3902.83	2.378
Y	20.7	24.9	28.6739	0.01732	8.73906	0.3621
Zr	87.1	116	127.124	0.00765	27.0626	0.2598
Nb	5.5	9.1	7.79305	0.02812	2.06041	0.3178
Hf	2.64	3.9	3.93329	0.00007	0.70005	0.2195
Ta	0.32	0.55	0.42039	0.09503	0.16940	0.4658
V	134	6	150.890	0.92205	108.663	0.7676
Cu	0	0	NA	NA	NA	0
Zn	0	0	NA	NA	NA	0
Pb	0	0	NA	NA	NA	0.456
Cr	0	0	NA	NA	NA	NA
Mg	19500	2110	NA	NA	NA	NA
Mn	0	0	NA	NA	NA	NA
Fe	0	0	NA	NA	NA	NA
Co	0	0	NA	NA	NA	NA
Ni	0	0	NA	NA	NA	NA

Partition Coefficients (Intermediate)

(NA = "not available", ERR = "error")

Kds: Mineral	inter Mode
oliv	0.0000
opx	0.0000
cpx	0.2000
plag	0.7600
amph	0.0000
biot	0.0000
kspr	0.0000
garn	0.0000
	0.0000
	0.0000
	0.0000
mgnt	0.0000
ilmn	0.0450
zirc	0.0002
alln	0.0000
apat	0.0000
sphn	0.0000
	0.0000
	0.0000
	0.0000
	0.0000
Total	1.0052

M. F. Liquid
F = 0.600

M. F. Xtals
(1-F)= 0.400

Dated: 24nov87

REFERENCES

REFERENCES

Abbey, S., 1983, Studies in "standard samples" of silicate rocks and minerals, 1969-1982: Geol. Survey Canada, Paper 83-15.

Alibert, C., Michard, A., and Albarede, F., 1986, Isotope and trace element geochemistry of Colorado Plateau volcanics: Geochim. Cosmochim. Acta, v. 42, p. 743-770.

Allegre, C. J., Trenill, M., Minster, J. F., Minster, B., and Albarede, F., 1977, Systematic use of trace elements in igenous processes, Part 1: Fractional crystallization processes in volcanic suites: Contr. Mineral. Petrol., v. 60, p. 57-76.

Allegre, C. J., and Minster, J. F., 1978, Quantitative models of trace element behavior in magmatic processes: Earth and Planetary Science Letters, v. 38, p. 1-25.

Anderson, C. A., 1972, Precambrian rocks in the Cordes area, Yavapai County, Arizona: U. S. Geol. Survey Bull. 1345, 36 p.

Anderson, C. A., and Blacet, P. M., 1972, Geologic map of the Mayer Quadrangle; Yavapai County, Arizona: U. S. Geol. Survey Geol. Quad Map GQ-996.

Anderson, C. A., and Blacet, P. M., 1972, Geological map of the Mount Union Quadrangle: U. S. Geol. Survey Geol. Quad. Map GQ-997.

Anderson, C. A., and Blacet, P. M., 1972, Precambrian geology of the northern Bradshaw Mountains, Yavapai County, Arizona: U.S. Geol. Survey Bull. 1336, 82 p.

Anderson, C. A., Blacet, P. M., Silver, L. T., and Stern, T. W., 1971, Revision of the Precambrian stratigraphy in the Prescott-Jerome area, Yavapai County, Arizona: U. S. Geol. Survey Bull. 1324-C, 16 p.

Anderson, C. A., and Creasey, S. C., 1958, Geology and ore deposits of the Jerome area, Yavapai County, Arizona: U. S. Geol. Survey Prof. Paper 208, 185 p.

Anderson, C. A., and Nash, J. T., 1972, Geology of the massive sulfide deposits at Jerome, Arizona - a reinterpretation: Econ. Geol., v. 67, p. 845-863.

Anderson, C. A., Scholz, E. A., and Strobell, J. S., Jr., 1955, Geology and ore deposits of the Bagdad area, Yavapai County, Arizona: U. S. Geol. Survey Prof. Paper 278, 103 p.

Anderson, P., and Guilbert, J. M., 1979, The Precambrian massive sulfides of Arizona - a distinct metallogenic epoch and province: Nevada Bur. Mines Geology Rept. 33, p. 39-48.

Arculus, R. J., and Johnson, R. W., 1978, Criticism of generalized models for the magmatic evolution of arc-trench systems: Earth Planet. Sci. Letters, v. 39, p. 118-125.

Arculus, R. J., and Powell, R., 1986, Source component mixing in the regions of arc magma generation: Jour. Geophys. Res., v. 91, n. B6, p. 5913-5926.

Argenbright, D. N., and Karlstrom, K. E., 1986, Revised structural and stratigraphic interpretation of the Proterozoic Yavapai Supergroup, Crazy Basin, Arizona: Geol. Soc. America Abstracts with Programs, v. 18, p 338.

Armstrong, D. G., and Handverger, P., 1986, Recent geological investigations of the Jerome massive sulfide camp, Verde mining district, north central Arizona, a background review: Geol. Soc. Arizona Digest, v. 16, p. 326-329.

Arnorrsson, S., Gunnlaugsson, E., and Svavarsson, H., 1983, The chemistry of geothermal waters in Iceland. 2. Mineral equilibria and independent variables controlling water compositions: Geochim. et Cosmochim. Acta, v. 47, p. 547-566.

Atherton, M. P., 1984, The coastal batholith of Peru: in Harmon, R. S., and Barreiro, B. A., (eds) Andean Magmatism, Chemical and Isotopic Constraints, Shiva, Cheshire, U. K., p. 168-180.

Bailey, J. C., 1981, Geochemical criteria for a refined tectonic discrimination of orogenic andesites: Chem. Geology, v. 32, p. 139-154.

Bain, G. W., 1973, Geology of the massive sulfide deposits at Jerome, Arizona - a reinterpretation - a discussion: Econ. Geol., v. 68, p. 709-711.

Baker, A., and Clayton, R. L., 1968, Massive sulfide deposits of the Bagdad District, Yavapai County, Arizona, in Ridge, J.

D., (ed), Ore Deposits of the United States, 1933-1967, AIME, p. 1311-1327.

Barker, F., 1979, Trondhjemite: definition, environment and hypotheses of origin: in Barker, F., (ed), Trondhjemites, dacites and related rocks, Elsevier, Amsterdam, p. 1-11.

Basaltic volcanism on the terrestrial planets, 1981, Elmsford, New York, Pergamon Press, p. 108-211.

Berner, R. A., 1971, Principles of chemical sedimentology: New York, McGraw-Hill, 240 p.

Bischoff, J. L., and Dickson, F. W., 1975, Seawater-basalt interaction at 200 C and 500 bars: Implications for the origin of sea-floor heavy-metal deposits and regulation of seawater chemistry: Earth Planet. Sci. Letters, v. 25, p. 385-397.

Bischoff, J. L. , Rosenbauer, R. J., Aruscauage, P. J., Baedecker, P. A., and Crock, J. G., 1983, Sea-floor massive sulfide deposits from 20 N, East Pacific Rise: Juan de Fuca Ridge; and Galapagos rift: Bulk chemical composition and economic implications: Econ. Geol., v. 78, p. 1711-1720.

Blacet, P. M., 1966, Unconformity between gneissic granodiorite and overlying Yavapai Series, Central Arizona: U. S. Geol. Survey Paper 550-B, p. 1-5.

Blacet, P. M., 1985, Proterozoic geology of the Brady Butte area, Yavapai County, Arizona: U. S. Geol. Survey Bull. 1548, 55 p.

Bland, A. E., 1978, Trace element geochemistry of volcanic sequences of Maryland, Virginia, and North Carolina and its bearing on the tectonic evolution of the central Appalachians: Unpub. Ph.D. dissert., Lexington, Univ. Kentucky.

Bouma, A. H., 1962, Sedimentology of some flysch deposits; a graphic approach to facies interpretation: Elseview, Amsterdam, 168 p.

Bowring, S., Karlstrom, K. E., and Chamberlain, K., 1986, U-Pb zircon constraints on Proterozoic tectonic evolution in central Arizona: Geol. Soc. America Abstracts with Programs, v. 18, no. 5, p. 343.

Brown, G. C., Thorpe, R. S., and Webb, P. C., 1984, The geochemical characteristics of granitoids in contrasting arcs

and comments on magma sources: Jour. Geol. Soc. London, v.141, p. 413-426.

Brown, P. R. L., 1978, Hydrothermal alteration in active geothermal fields: Ann. Rev. Earth Planet. Sci., v. 6, p. 229-250.

Bryan, W. B., 1979, Low-K_2O dacite from the Tonga-Kermadec island arc: petrography, chemistry and petrogenesis: in Barker, F. (ed) Trondhjemites, dacites and related rocks, Elsevier, Amsterdam, p. 581-599.

Burke, K. and Kidd, W. S. F., 1980, Volcanism on Earth through time in Strangway, D.W. (ed) The Continental Crust and Its Mineral Deposits: Geol. Assoc. Canada Spec. Pap. No. 20, p. 503-522.

Campbell, I. H., Coad, P., Franklin, J. M., Gorton, M. P., Scott, S. D., Sowa, J., and Thurston, P. C., 1982, Rare earth elements in volcanic rocks associated with Cu-Zn massive sulfide mineralization, a preliminary report: Canadian Journal of Earth Sciences, v. 19, p. 619-623.

Campbell, I. H., Lesher, C. M., Coad, P., Franklin, J. M., Gorton, M. P., and Thurston, P. C., 1984, Rare-earth-element mobility in alteration pipes below massive Cu-Zn sulfide deposits: Chem. Geology, v. 45, p. 181-202.

Carey, S., and Sigurdsson, H., 1984, A model of volcanogenic sedimentation in marginal basins: in: Kokelaar, B. P., and Howells, M. F., (eds), Marginal Basin Geology, J. Wiley and Sons, London, p. 37-58.

Carmichael, I. S. E., Turner, F. J., and Verhoogen, J., 1974, Igneous Petrology, McGraw-Hill, San Francisco, 739 p.

Cas, R. A. F., and Wright, J. V., 1987, Volcanic successions, modern and ancient: Allen and Unwin, U. K., 528 p.

Cathles, L. M., 1983, An analysis of the hydrothermal system responsible for massive sulfide deposition in the Hokuroku basin of Japan: Econ. Geol. Mon. 5, p. 439-487.

Cathles, L. M., Guber, A. L., Lenagh, T. C., and Dudas, F. O., 1983, Kuroko-type massive sulfide deposits of Japan: Products of an aborted island-arc rift: Econ. Geol. Mon. 5, p. 96-115.

Cole, J. W., 1984, Taupo-Rotorua depression - an ensialic marginal basin of North Island, New Zealand, in Kokelaar, B. P., and

Howells, M. F., (eds), Marginal basin Geology: Geol. Soc. London Spec. Pub., 16, p. 109-120.

Colley, H., and Hindle, W. H., 1984, Volcano-tectonic evolution of Fiji and adjoining marginal basins: in, Kokelaar, B. P., and Howells, M. F., (eds), Marginal Basin Geology, p. 151-162.

Condie, K. C., 1986, Geochemistry and tectonic setting of Early Proterozoic supracrustal rocks in the southwestern United States: Jour. of Geology, v. 94, p. 845-864.

Condie, K. C., 1988, Geochemical changes in basalts and andesites across the Archean-Proterozoic boundary: Identification and significance: Lithos-preliminary draft.

Condie, K. C., Bowling, G. P., and Vance, R. K., 1985, Geochemistry and origin of early Proterozoic supracrustal rocks, Dos Cabezas Mountains, southeastern Arizona: Geol. Soc. America Bull., v. 96, p. 655-662.

Condie, K. C., and Knoper, M. W., 1986, Geology and origin of early Proterozoic rocks from the Gunnison area, central Colorado: Int. Field Conf., Proterozoic Geology and Geochemistry, Guidebook, p. 3-16.

Condie, K. C., and Nuter, J. A., 1981; Geochemistry of the Dubois Greenstone succession: An early Proterozoic bimodal volcanic association in west-central Colorado: Precambrian Research, v. 15, p. 131-155.

Condie, K. C., Viljoen, M. J., and Kable, E. J. D., 1977, Effects of alteration on element distributions in Archean tholeiites from the Barberton greenstone belt, South Africa: Contr. Mineralogy Petrology, v. 64, p. 75-89.

Conway, C. M., 1986, Field guide to early Proterozoic strata that host massive sulfide deposits at Bagdad, Arizona: Geol. Soc. America Rocky Mtn. Sec. Guidebook, Flagstaff, Arizona, p. 140-157.

Conway, C. M., and Silver, L. T., 1985, 1700-1600 Ma Proterozoic rocks in central to southeastern Arizona: Preliminary draft to Arizona Geol. Soc.

Corbett, K. D., 1981, Stratigraphy and mineralization in the Mt. Read Volcanics, western Tasmania: Econ. Geol., v. 76, p. 209-230.

Cox, K. G., 1983, The Karoo province of southern Africa: origin of trace element enrichment patterns: in Hawkesworth, C. J.,

and Norry, M. J. (eds), Continental Basalts and Mantle Xenoliths, Shiva Pub. Ltd., U.K., p. 139-158.

Crawford, A. J., Beccaluva, L. and Serri, G., 1981, Tectono-magmatic evolution of the West Phillipines - Mariana region and the origin of boninites: Earth Planet. Sci. Letters, v. 54, p. 346-356.

Crow, C., and Condie, K. C., 1988, Geochemistry and origin of late Archean volcanics from the Ventersdorp Supergroup, South Africa: Precambrian Research, v. 42, p. 19-37.

Dalziel, I. W. D., DeWit, M. J., and Palmer, K. F., 1974, Fossil marginal basin in the southern Andes: Nature, Lond., v. 150, p. 291-294.

Darrach, M. E., Karlstrom, K. E., and Argenbright, D. A., 1986, The Cleator Mylonite Zone: Sinistral strike slip adjacent to the Shylock Fault zone; central Arizona: Geol. Soc. America Abstracts with Programs, v. 18, no. 5, p 350.

Date, J., Watanabe, Y., and Saeki, Y., 1983, Zonal alteration around the Fukazawa Kuroko deposits, Akita Prefecture, northern Japan: Econ. Geol. Mon. 5, p. 365-386.

Davidson, J. P., 1986, Isotopic and trace element constraints on the petrogenesis of subduction-related lavas from Martinique, Lesser Antilles: Jour. Geophys. Res., v. 91, n. B6, p. 5943-5962.

Davidson, J. P., Dungan, M. A., Ferguson, K. M., Colucci, M. T., 1987, Crust-magma interactions and the evolution of arc magmas: The San Pedro-Pellado volcanic complex, southern Chilean Andes: Geology, v. 15, p. 443-446.

Davies, J. F., and Whitehead, R. E. S., 1980, Further immobile element data from altered volcanic rocks, Timmins Mining area, Ontario: Canadian Jour. Earth Sci., v. 17, p. 419-423.

DeBari, S., 1989, Examination of the deep levels of an island arc, evidence frm the Tonsina ultramafic-mafic assemblage, Tonsina, Alaska: EOS, Trans. Amer. Geophys. Union, v. 70, no. 9, p. 129.

DePaolo, D. J., and Wasserburg, G. J., 1976, Nd isotopic variations and petrogenetic models: Geophys. Res. Lett., v. 3, p. 248-252.

Dewey, J. F., and Bird, J. M., 1970, Mountain belts and the new global tectonics: Jour. Geophys. Res., v. 75, p. 2625-2647.

DeWitt, E., 1976, Precambrian geology and ore deposits of the Mayer-Crown King area, Yavapai County, Arizona: M.S. thesis, University of Arizona, Tucson, 150 p.

DeWitt, E., 1979, New data concerning Proterozoic volcanic stratigraphy and structure in central Arizona and its importance in massive sulfide exploration: Econ. Geol., v. 74, p. 1271-1382.

DeWitt, E., 1986, Distribution and grade of precious metals in the United Verde massive sulfide deposit, Jerome, Arizona: Geol. Soc. America Abstracts with Programs, v. 18, no. 5, p 351.

DeWitt, E., 1986, Geochemistry and tectonic polarity of 1700-1750 Ma plutons, north-central Arizona: G.S.A. Abst. with Programs, v. 18, n. 5, p. 351.

Dickson, F. W., Potter, J., Rytuba, J., and Radtke, A. S., 1978, Reaction of rhyolite with H_2O at 300° C and 500 bars [abs.]: Am. Geophys. Union, San Francisco, California, p. 1221.

Dickinson, W. R., 1982, Composition of sandstones in circum-Pacific subduction complexes and fore-arc basins: A.A.P.G. Bull., v. 66, n. 2, p. 121-137.

Dietz, R. S., 1972, Geosynclines, mountains and continent-building: in Wilson, J. T. (ed), Continents Adrift and Continents Aground, Scien. Amer. p. 104, 111.

Dudas, F. O., Campbell, I. H., and Gorton, M. P., 1983, Geochemistry of Igneous Rocks in the Hokuroku District, Northern Japan: Econ. Geol. Mon. 5, p. 115-134.

Duke, J. M., 1976, Distribution of the period four transition elements among olivine, calcic clinopyroxene and mafic silicate liquid: experimental results: Jour. Petrology, v. 17, no. 4, p 499-521.

Elders, W. A., Hoagland, J. R., and Williams, A. E., 1981, Distribution of hydrothermal mineral zones in the Cerro Prieto geothermal field of Baja California, Mexico: Geothermics, v. 10, no. 3/4, p. 245-253.

Elthon, D., 1983, Isomolar and isostructural pseudo-liquidus phase diagrams for oceanic basalts: Amer. Miner., v. 68, p. 506-511.

Elthon, D., and Scarfe, C. M., 1984, High-pressure phase equilibria of a high-magnesia basalt and the genesis of primary oceanic basalts: Amer. Miner., v. 69, p. 1-15.

Ernst, W. G., 1976, Petrologic Phase Equilibria, W. H. Freeman & Co., San Francisco, 333 p.

Ewart, A., 1982, The mineralogy and petrology of Tertiary - Recent orogenic volcanic rocks: with special reference to the andesitic-basaltic compositional range: in Thorpe, R. S., eds., Orogenic Andesites and Related Rocks, Chichester, Wiley, p 25-29.

Ewart, A., Chappel, B. W., and LeMaitre, R. W., 1985, Aspects of the mineralogy and chemistry of the intermediate-silicic Cainozoic volcanic rocks of eastern Australia. Part 1: introduction and geochemistry: Australian Jour. of Earth Sciences, v . 32, p. 359-382.

Ewart, A., and Hawkesworth, C. J., 1987, The Pleistocene-Recent Tonga-Kermadec Arc Lavas: Interpretation of isotopic and rare earth data in terms of a depleted mantle source model: Jour. of Petrology, v. 28, pt 3, p 495-530.

Fearing, J. L., and Benedict, P. C., 1925, Geology of the Verde Central mine: Eng. Mining Jour., v. 119, p. 609-611.

Finlow-Bates, T., and Stumpfl, E. F., 1981, The behavior of so-called immobile elements in hydrothermally altered rocks associated with volcanogenic submarine-exhalative ore deposits: Mineralium Deposita, v. 16, p. 319-328.

Franklin, J. M., Lydon, J. W., and Sangster, D. F., 1981, Volcanic-associated massive sulfide deposits: Econ. Geol. 75th Anniv. Vol., p. 485-627.

Garcia, M. O., 1978, Criteria for the identification of ancient volcanic arcs: Earth Sci. Rec., v. 14, p. 147-165.

Gelinas, L., Mellinger, M., and Trudel, P., 1982, Archean mafic metavolcanics from the Rouyn-Noranda district, Abitibi greenstone belt, Quebec. 1. Mobility of the major elements: Canadian Jour. Earth Sci., v. 19, p. 2258-2275.

Gibson, I. L., and Jagam, P., 1980, Instrumental neutron activation analysis of rocks and minerals: in G. K. Mueke, ed., Short Course in Neutron Activation in the Geosciences, Mineral. Assoc. Can., Ohawa, Ont., p. 109-131.

Gill, J. B., 1981, Orogenic andesites and plate tectonics, Springer-Verlag, Ny, 390 p.

Gill, J. B., 1987, Early geochemical evolution of an oceanic island arc and back arc: Fiji and the South Fiji Basin: Jour. of Geology, v. 95, p. 589-615.

Graf. J. L., Jr., 1977, Rare earth elements as hydrothermal tracers during the formation of massive sulfide deposits in volcanic rocks: Econ. Geol., v. 72, p. 527-548.

Gregory, R. T., and Taylor, H. P., Jr., 1981, An oxygen isotope profile in a section of Cretaceous oceanic crust, Samail Ophiolite, Oman: Evidence for ^{18}O buffering of the oceans by deep (> 5 km) seawater-hydrothermal circulation at mid-ocean ridges: Jour. Geophys. Res., v. 86, p. 2737-2755.

Guber, A. L., and Merrill, S., 1983, Paleobathymetric significance of foraminifera from the the Hokuroku District: Econ. Geol. Mon. 5, p. 55-71.

Gust, D. A., and Arculus, R. J., 1986, Petrogenesis of alkalic and calcalkalic volcanic rocks of Mormon Mountain Volcanic Field, Arizona: Contr. Miner. Petr., v. 94, p. 416-426.

Guston, M. S., 1986, A preliminary report on a petrological, geochemical and stable-isotope study of the orebody and associated alteration, United Verde volcanogenic massive sulfide deposit, Jerome, Arizona: Arizona Geol. Soc. Digest, v. 16, p. 339-342.

Handverger, P. A., 1975, Geology and alteration of the United Verde Extension Mine, Jerome, Arizona: AIME, Sept., 26 p.

Hart, S. R., and Davis, K. E., 1978, Nickel partitioning between olivine and silicate melt: Earth Planet. Sci. Letters, v. 40, p. 203-219.

Hashiguchi, H., Yamada, R., and Inoue, T., 1983, Practical application of low Na_2O anomalies in footwall acid lava for delimiting promising areas around the Kosaka Fukazawa Kuroko deposits, Akita Prefecture, Japan: Econ. Geol. Mon. 5, p. 387-394.

Haskin, L. A., and Paster, T. P., 1979, Geochemistry and mineralogy of the rare earths, in Gschneider, K. A., Jr., and Eyring, L., eds., Handbook on the physics and chemistry of rare earths: Amsterdam, North Holland, v. 3, chap. 21.

Henderson, P., 1984, General geochemical properties and abundances of the rare earth elements: in Henderson. P. (ed) Rare Earth Element Geochemistry, Elsevier, Amsterdam, p. 1-32.

Henley, R. W., and Ellis, A. J., 1983, Geothermal systems - ancient and modern: A geochemical review: Earth Sci. Rev., v. 19, p. 1-50.

Hickey, R. L., and Frey, F. A., 1982, Geochemical characteristics of boninite series volcanics: implications for their source: Geochim. Cosmochim. Acta, v. 46, p. 2099-2115.

Hickey, R. L., Frey, F. A., and Gerlach, D. C., 1986, Multiple sources for basaltic arc rock from the southern volcanic zone of the Andes: Subducted oceanic crust, mantle, and continental crust: Jour. Geophys. Res., v. 91, n. B6, p. 5963-5983.

Hildreth, W., 1979, The Bishop Tuff: evidence for compositional zonation in silic magma chambers: Geol. Soc. Amer. Spec. Pap. 180, p. 43-75.

Hildreth, W., and Moorbath, S., 1988, Crustal contributions to arc magmatism in the Andes of central Chile: Contrib. Miner. Petr., V. 98, p. 455-489.

Hirano, T., and Oki, Y., 1978, Importance of Mg and SiO2 (aq) reaction for pH control in sea water-rock interaction [abs.]: Am. Geophys. Union, San Francisco, California, p. 1220.

Hoffman, P. F., 1980, Wopmay Orogen: A Wilson Cycle of early Proterozoic age in the northwest of the Canadian Shield: Geol. Assoc. Canada Sp. Pap. No. 20, p. 523-549.

Hynes, A., 1980, Carbonatization and mobility of Ti, Y, and Zr in Ascot Formation metabasalts, SE Quebec: Contr. Mineralogy Petrology, v. 75, p. 79-87.

Iijima, A., 1974, Clay and zeolite alteration zones surrounding Kuroko deposits in the Hokuroko district, northern Akita, as submarine hydrothermal-diagenetic alteration products: Soc. Mining Geologists Japan Spec. Issue 6, p. 267-290.

Irvine, T. N., and Barager, W. R. A., 1971, A guide to the chemical classification of the common volcanic rocks, Canadian Jour. Earth Science, v. 8, p. 523-548.

Irving, A. J., 1978, A review of experimental studies of crystal/liquid trace element partitioning: Geochim. Cosmochim. Acta, v. 42, p. 743-770.

Ishikawa, Y., Sawaguchi, T., Iwaya, S., and Horiuchi, M., 1976, Delineation of prospecting targets for Kuroko deposits based

on modes of volcanism of underlying dacite and alteration haloes: Mining Geology, v. 26, p. 105-117.

Jakes, P., and White, A. J. R., 1972, Major and trace element abundances in volcanic rocks of orogenic areas: Geol. Soc. Amer. Bull., v. 83, p. 29-40.

Jensen, B. B., 1973, Patterns of trace elment partitioning: Geochim. Cosmochim. Acta, v. 37, p. 2227-2242.

Jenson, L. S., 1976, A new cation plot for classifying subalkalic volcanic rocks: Ontario Div. Mines Misc. Pap. 66, 22 p.

Johnson, N. A., 1986, Preliminary discussion of the geochemistry of some exhalites from the Copper Chief Mine, Jerome District, Arizona: Arizona Geol. Soc. Digest, v. 16, p. 350-354.

Johnson, R. W., Jaques, A. L., Hickey, R. L., McKee, C. O., and Chappell, B. W., 1985, Manam Island, Papua New Guniea: Petrology and geochemistry of a low-TiO2 basaltic island-arc volcano: Jour. Petrol., v. 26, pt. 2, p. 283-323.

Kalogeropoulus, S. I., and Scott, S. D., 1983, Mineralogy and geochemistry of tuffaceous exhalites (Tetsusekiei) of the Fukazawa Mine, Hokuroku: Econ. Geol. Man. 5, p. 412-433.

Karig, D. E., 1971, Origin and development of marginal basins in the western Pacific: Jour. Geophys. Res., v. 76, n. 11, p. 2542-2561.

Karlstrom, K. E., 1986, Thrusting and strike-slip faulting during Proterozoic accretion in central Arizona: Geol. Soc. America Abstracts with Programs, v. 18, no. 5, p. 365.

Karlstrom, K. E., and Bowring, S. A., 1988, Early Proterozoic assembly of tectonostratigraphic terranes in Southwestern North America: Jour. Geol. v. 96, p. 561-576.

Karlstrom, K. E., Bowring, S. A., and Conway, C. M., 1987, Tectonic significance of an Early Proterozoic two-province boundary in central Arizona: Geol. Soc. America, v. 99, p. 529-538.

Karlstrom, K. E., and Conway, C. M., 1986, Deformational styles and contrasting lithostratigraphic sequences within an Early Proterozoic orogenic belt, central Arizona, in Nations, J. D., Conway, C. M., and Swann, G. A., eds., Geology of nothern and central Arizona: Geol. Soc. of America Field Trip Guidebook: Flagstaff, Arizona, Northern Arizona University, p. 1-25.

Karlstrom, K. E., and O'Hara, P. F., 1984, Polyphase folding in Proterozoic rocks of central Arizona: Geol. Soc. of America, Abstracts with Programs, v. 16, p. 226.

Kay, S. M., Kay, R. W., and Citron, G. P., 1982, Tectonic controls on tholeiitic and calc-alkaline magmatism in the Aleutian arc: Jour. Geophys. Res., v. 87, p. 4051-4072.

Kimberly, M. M., 1978, Paleoenvironmental classification of iron formations: Econ. Geol., v. 73, p. 215-229.

Knoper, M. W., 1988, MODULUS: An igneous geochemical spreadsheet modeling program using LOTUS (manuscript in prep.).

Knoper, M. W., and Condie, K. C., 1988, Geochemistry and petrogenesis of Early Proterozoic amphibolites, west-central Colorado, U.S.A.: Chem. Geology, v. 67, p. 209-225.

Kokelaar, B. P., Bevins, R. E., and Roach, R. A., 1985, Submarine silicic volcanism and associated sedimentary and tectonic processes, Ramsey Island, SW Wales: J. Geol. Soc. London, V. 142, p. 591-613.

Kokelaar, B. P., Howells, M. F., Bevins, R. E., Roach, R. A., and Dunkley, P. N., 1984, The Ordovician marginal basin of Wales: in Kokelaar, B. P., and Howells, M. F. (eds) Marginal Basin Geology, p. 151-162.

Krieger, M. H., 1965, Geology of the Prescott and Paulden quadrangles, Arizona: U. S. Geol. Survey Prof. Paper 467, 127 p.

Krupp, R. E., and Seward, T. M., 1987, The Rotokawa geothermal system, New Zealand: An active epithermal gold-depositing environment: Econ. Geol., v. 82, p. 1109-1129.

Kusakabe, H., 1982, An interpretation of zeolitic zoning around Kuroko ore deposits on the basis of hydrothermal experiments: Mining Geology, v. 26, p. 105-117.

Lambert, I. B., and Sato, K., 1974, The Kuroko and associated ore deposits of Japan: A review of their features and metallogenesis: Econ. Geol., v. 69, p. 1215-1236.

Larson, P. B., 1984, Geochemistry of the alteration pipe at the Bruce Cu-Zn volcanogenic massive sulfide deposit, Arizona: Econ. Geol., v. 79, p. 1880-1896.

Lavery, N., G., 1985, The use of fluorine as a pathfinder for volcanic-hosted massive sulfide ore deposits: Jour. Geochem. Explor., v. 23, p. 35-60.

LeMaitre, R. W., 1976, The chemical variability of some common igneous rocks: Jour. Petrol., v. 17, p. 589-637.

Lindberg, P. A., 1985, A volcanogenic intepretation for massive sulfide origin, West Shasta District, California: Econ. Geol., v. 80, p. 2240-2254.

Lindberg, P. A., 1986, A brief geologic history and field guide to the Jerome district, Arizona: Geol. Soc. America Guidebook, Flagstaff, Arizona, p. 127-139.

Lindberg, P. A., 1986, Geology of the Copper Chief Mine, Jerome District, Arizona: Arizona Geol. Soc. Digest, v. 16, p. 343-349.

Lindberg, P. A., and Jacobson, H. S., 1974, Economic geology and field guide of the Jerome district, Arizona, in Geology of northern Arizona, Part 2, Area studies and field guides: Geol. Soc. America, Rocky Mtn. Sec. Mtg., Flagstaff, Arizona, p. 794-804.

Lindgren, W., 1926, Ore deposits of the Jerome and Bradshaw Mountains and quadrangles, Arizona: U. S. Geol. Survey Bull. 782, 192 p.

Lindstrom, D. J., 1976, Experimental study of the partitioning of the transition metals between clinopyroxene and coexisting silicate liquids: unpub. Ph.D. dissertation, Univ. of Oregon, 188 p.

Lindstrom, D. J. and Korotev, R. L., 1982, TEABAGS: computer programs for instrumental neutron activation analysis: Radioanalyt. Chem., v. 20, p. 439-458.

Liou, J. G., and Dickson, F. W., 1978, The interaction of NaCl solution and seawater with andesite, 200° C, 500-1000 bars [abs.]: Am. Geophys. Union, San Francisco, California, p. 1221.

Ludden, J., Gelinas, L., and Trudel, P., 1982, Archean metavolcanics from the Rouyn-Noranda district, Abitibi greenstone belt, Quebec. 2. Mobility of trace elements and petrogenetic constraints: Canadian Jour. Earth Sci., v. 19, p. 2276-2287.

Ludden, J., Hubert, C., and Gariepy, C., 1986, The tectonic evolution of the Abitibi greenstone belt of Canada: Geol. Mag., v. 123, p. 153-166.

MacDonald, G. A., and Katsura, T., 1964, Chemical composition of Hawaiian lavas: Jour. Petrology, v. 5, p. 82-133.

MacGeehan, P. J., and MacLean, W. H., 1980, An Archean subseafloor geothermal system, calc-alkali trends, and massive sulfide genesis: Nature, v. 286, p. 767-771.

Miyashiro, A., 1973, Metamorphism and Metamorphic Belts: John Wiley & Sons, New York, 492 p.

Miyashiro, A., 1974, Volcanic rock series in island arcs and active continental margins: Amer. Jour. Sci., v. 274, p. 321-355.

Mullen, E. D., 1983, $MnO/TiO_2/P_2O_5$: a minor element discriminant for basaltic rocks of oceanic environment and its implications for petrogenesis: Earth Planet. Sci. Lett., v. 62, p. 53-62.

Nelson, D. O., Nelson, K. L., Reeves, K. D., and Mattison, G. D., 1987, Geochemistry of Tertiary alkaline rocks of the eastern Trans-Pecos Magmatic Province, Texas: Contrib. Mineral. Petrol., v. 97, p. 72-92.

Norman, G. W. H., 1977, Proterozoic massive sulfide replacements in volcanic rocks at Jerome, Arizona: Econ. Geol., v. 72, p. 642-656.

Norrish, K. and Chappell, B. W., 1977, X-ray Fluorescence Spectrometry: in Zussman, J. (ed), Physical Methods in Determinative Mineralogy, Academic Press, London, p. 201-272.

Norrish, K., and Hutton, J. T., 1969, An accurate x-ray spectrographic method for the analysis of a wide range of geological samples: Geochem. Cosmochim. Acta, v. 33, p. 431-435.

O'Hara, M. J., 1977, Geochemical evolution during fractional crystallization of a periodically refilled magma chamber: Nature, v. 265, p. 503-507.

O'Hara, P. F., 1980, Metamorphic and structural geology of the northern Bradshaw Mountains, Yavapai County, Arizona: Ph.D. dissertation, Arizona State University, Tempe, 146 p.

O'Hara, P. F., 1986, Potential thrusts, nappes and the presence of allocthonous terrain in Proterozoic rocks in Arizona: Geol. Soc. America Abstracts with Programs, v. 18, no. 5, p. 400.

O'Hara, P. F., 1986, Previous geologic work in the Prescott-Mayer area, Arizona: Arizona Geol. Soc. Digest, v. 16, p. 355-357.

O'Hara, P. F., 1986, Stratigraphy and structural geology in the Prescott-Mayer area, Arizona: Arizona Geol. Soc. Digest, v. 16, p. 358-363.

O'Hara, P. F., and Higgins, R. E., 1986, Geochemical evaluation of fossil hydrothermal systems in submarine volcanic terrain and the origin of mineralization: Geol. Soc. America Abstracts with Programs, v. 18, no. 5, p. 400.

O'Hara, P. F., Krinsley, D. H., Burton, J. H., and Higgins, R. E., 1987, Fe-Mg exchange in alteration chlorites associated with Proterozoic rhyolite hosted stratabound mineralization during regional metamorphism - the Copper Queen Mine, Yavapai County, Arizona: Geol. Soc. America Abstracts with Programs, v. 19, no. 5, p. 325.

Ohmoto, H., 1983, Geologic history of the Green Tuff Region: Econ. Geol. Mon. 5, p. 9-24.

Ohmoto, H., and Skinner, B. J., 1983, The Kuroko and related volcangenic massive sulfide deposits: Introduction and summary of new findings: Econ. Geol. Mon. 5, p. 1-8.

Ohmoto, H., and Takahashi, T., 1983, Submarine calderas and Kuroko genesis: Econ. Geol. Mon. 5, p. 39-54.

Onuma, N., Higuchi, H., Wakita, H. and Nagasawa, H., 1968, Trace element partition between two pyroxenes and the host lava: Earth Planet. Sci. Lett., v. 5, p. 47-51.

Pearce, J. A., 1975, Basalt geochemistry used to investigate past tectonic environment on Cyprus: Tectonophysics, v. 25, p. 41-67.

Pearce, J. A., 1982, Trace element characteristics of lavas from destructive plate boundaries: in, Thorpe, R. S., (ed), Orogenic Andesites, Wiley, New York, p. 525, 548.

Pearce, J. A., 1983, Role of the sub-continental lithosphere in magma genesis at active continental margins: in Hawkesworth, C. J., and Norry, M. J., (eds), Continental Basalts and Mantle Xenoliths, Sliver Pub. Ltd., U. K., p. 230-250.

Pearce, J. A., 1985, Characteristics and tectonic significance of supra-subduction zone ophiolites: in Kokelaar, B. P., and Howells, M. F., (eds), Marginal Basin Geology, J. Wiley and Sons, London, p. 77-94.

Pearce, J. A., and Cann, J. R., 1973, Tectonic setting of basic volcanic rocks determined using trace element analysis: Earth Planet. Sci. Letters, v. 19, p. 290-300.

Pearce, J. A., and Norry, M. G., 1979, Petrogenetic implications of Ti, Zr, Y, and Nb variations in volcanic rocks: Contrib. Mineral. Petrol., v. 69, p. 33-47.

Peccerillo, A., and Taylor, S. R., 1976, Geochemistry of Eocene calc-alkaline volcanic rocks from the Kastamonu area, Northern Turkey: Contri. Mineral. Petrol., v. 58, p. 63-81.

Perry, F. V., Baldridge, W. S., DePaolo, D. J., 1987, Role of asthenosphere and lithosphere in the genesis of late Cenozoic basaltic rocks from the Rio Grande Rift and adjacent regions of the southwestern United States: Jour. Geophys. Res., v. 92, n. B9, p. 9193-9213.

Pharaoh, T. C., and Pearce, J. A., 1984, Geochemical evidence for the geotectonic setting of early Proterozoic metavolcanic sequences in Lapland: Precambrian Research, v. 25, p. 283-308.

Phillips, W. R., and Griffen, D. T., 1981, Optical mineralogy: W. H. Freeman and Co., San Francisco, 677 p.

Pisutha-Arnond, V., and Ohmoto, H., 1983, Thermal history and chemical and isotopic compositions of the ore-forming fluids responsible for the Kuroko massive sulfide deposits in the Hokuroku district of Japan: Econ. Geol. Mon. 5, p. 523-558.

Pitcher, W. S., 1978, The anatomy of a batholith, J. Geol. Soc. Lond., v. 135, p. 157-182.

Plimer, I. R., 1978, Proximal and distal stratabound ore deposits: Mineralium Deposita, v. 13, p. 345-353.

Rajamani, V., Shivkumar, K. Hanson, G. N., and Shirey, S. B., 1985, Geochemistry and petrogenesis of amphibolites from the Kolar Schist Belt, south India: evidence for ultramafic magma generation by low percent melting: Jour. of Petrology, v. 26, p. 92-123.

Ramsay, J. G., 1967, Folding and Fracturing of Rock, McGraw-Hill, NY, 568 p.

Ratcliffe, N. M., 1987, Basaltic rocks in the Rensselaer Plateau and Chatham slices of the Taconic allochthon: Chemistry and tectonic setting: Geol. Soc. America Bull., v. 99, p. 511-528.

Ratcliffe, N. M., 1987, High TiO_2 metadiabase dikes of the Hudson Highlands, New York and New Jersey: Possible Late proterozoic rift rocks in the New York recess: Amer. Jour. Science, v. 287, p. 817-850.

Reber, L. E., Jr., 1938, Jerome district: Arizona Bur. Mines Bull. 145, p. 41-65.

Reed, J. C., Bidefored, M. E., Premo, W. R., Aleinekoff, J. N., and Pallister, J. S., 1987, Evolution of the Early Proterozoic Colorado province: Constraints from U-Pb geochronology: Geology, v. 15, p. 861-865.

Ridler, R. H., 1971, Analysis of Archean volcanic basins of the Canadian Shield using the exhalite concept [abs.]: Canadian Mining Metall. Bull., v. 64, n. 714, p. 20.

Ripley, E. M., and Ohmoto, H., 1977, Mineralogic, sulfur isotope and fluid inclusion studies of the stratabound copper deposits of the Raul mine, Peru: Econ. Geol., v. 72, p. 1017-1041.

Riverin, G., and Hodgson, C. J., 1980, Wall-rock alteration at the Millenback Cu-Zn mine, Noranda, Quebec: Econ. Geol., v. 75, p. 424-444.

Robson, D., and Cann, J. R., 1982, A geochemical model of mid-ocean ridge magma chambers: Earth Planet. Sci. Lett., v. 60, p. 93-104.

Roobol, M. J., and Hackett, D., 1987, Paleovolcanic facies and exhalite geochemistry: Guides for selecting exploration areas in volcano-sedimentary complexes: Econ. Geol., v. 82, p. 691-705.

Rytuba, J. J., Potter, J. M., Dickson, F. W., and Radtke, A. S., 1978, Experimental alteration of rhyolite glass at 300° C: Implication for silicate mineral zonation in the McDermitt mercury deposit, Nevada [abs.]: Am. Geophys. Union, San Francisco, California, p. 1220.

Saunders, A. D., Stern, C. R., and Dalziel, I. W. D., 1979, Geochemistry of Mesozoic marginal basin floor igneous rocks from southern Chile: Geol. Soc. Amer. Bull., v. 90, p. 237-258.

Saunders, A. D., and Tarney, J., 1984, Geochemical characteristics of basaltic volcanism within back-arc basins, in Kokelaar, B. P., and Howells, M. F., (eds) Marginal Basin Geology, J. Wiley and Sons, London, p. 59-76.

Scott, S. D., 1980, Geology and structural control of Kuroko-type massive sulfide deposits: in Strangway, D. W. (ed), the Continental Crust and Its Mineral Deposits, Geol. Assoc. Canada Spec. Pap. No. 20, p. 705-722.

Scott, R. B., 1983, Magmatic evolution of island arcs in the Phillipine Sea: in Hilde, T. W. C., and Uyeda, S., Geodynamics of the Western Pacific-Indonesian Region, p. 173-187.

Seyfried, W., and Bischoff, J. L., 1977, Hydrothermal transport of heavy metals by seawater: The role of seawater/basalt ratio: Earth Planet Sci. Letters, v. 34, p. 71-77.

Shervais, J. W., 1982, Ti-V plots and the petrogenesis of modern and ophiolitic lavas: Earth Planet. Sci. Lett., v. 59, p. 101-118.

Shimizu, N., and Arculus, R. J., 1975, Rare earth concentrations in a suite of basanitoids and alkali olivine basalts from Grenada, Lesser Antilles: Contr. Mineral. Petrol., v. 50, p. 231-240.

Smith, R. L., and Bailey, R. A., 1966, The Bandolier Tuff: a study of ash-flow eruption cycles from zoned magma chambers: Bull. Volc., v. 29, p. 83-103.

Strong, D. F., 1984, Rare earth elements in volcanic rocks of the Buchans area, Newfoundland: Canadian Jour. of Earth Sciences, v. 21, p. 775-780.

Sun, S., and Nesbitt, R. W., 1977, Chemical heterogeneity of the Archean mantle, compsition of the earth and mantle evolution: Earth Planet. Sci. Lett., v. 35, p. 429-448.

Takahashi, E., 1978, Partitioning of Ni, Co, Mn and Mg between olivine and silicate melts: compositional dependence of partition coefficient: Geochim. Cosmochim. Acta, v. 42, p. 1829-1844.

Takahashi, E., 1986, Genesis of calc-alkali andesite magma in a hydrous mantle-crust boundary: Petrology of lherzolite xenoliths from the Ichinomegata Crater, Oga Peninsula, northeast Japan, Pt. 2: Jour. Volcan. Geotherm. Res., v. 29, p. 355-395.

Tanimura, S., Date, J., Takahashi, T., and Ohmoto, H., 1983, Stratigraphy and structure of the Hokuroku District: Econ. Geol. Mon. 5, p. 24-39.

Thirlwall, M. F., and Jones, N. W., Isotope geochemistry and contamination of Tertiary lavas from Skye, northwest Scotland: in Hawkesworth, C. J., andNorry, M. J. (eds), Continental Basalts and Mantle Xenoliths, Sliver Pub. Ltd., U. K., p. 186-209.

Thompson, R. N., and Tilley, C. E., 1969, Melting and crystallization relations of Kilauean basalts of Hawaii, The lavas of the 1959-60 Kilauea eruption: Earth Planet. Sci. Lett., v. 5, p. 469-477.

Thompson, R. N., Morrison, M. A., Dickin, A. P., and Hendry, G. L., 1983, Continental flood basalts ... arachnids rule OK?: in Hawkesworth, C. J., and Norry, M. J. (eds), Continental Basalts and Mantle Zenoliths, Shiva Pub. Ltd., U. K. p. 158-186.

Thornton, C. P., and Tuttle, O. F., 1960, Chemistry of igneous rocks: Differentiation Index: Amer. Jour. Sci., v. 258, p. 671-747.

Thorpe, R. S., 1982, Introduction, in Thorpe, R. S. (ed), Andesites: Orogenic andesites and related rocks, John Wiley and Sons, Chichester, p. 1-7.

Titley, S. R., 1987, The crustal heritage of silver and gold ratios in Arizona ores: Geol. Soc. Amer. Bull., v. 99, p. 814.

Tomblin, J. F., 1974, Lesser Antilles: in Spencer, A. M. (ed), Mesozoic-Cenozoic Orogenic Belts, Data for Orogenic Studies, Geol. Soc. London, Spec. Pub. No. 4, p. 663-670.

Tomblin, J. F., 1979, Dacite of the lesser Antilles, in Barker, F., (ed), Trondhjemites, dacites and related rocks, Elsevier, Amsterdam, p. 601-626.

Underwood, M. B., 1986, Sediment provenance within subduction complexes - an example from the Aleutian forearc: Sed. Geology, v. 51, p. 57-73.

Urabe, T., Scott, S. D., and Hattori, K., 1983, A comparison of footwall-rock alteration and geothermal systems beneath some Japanese and Canadian volcanogenic massive sulfide dpeosits: Econ. Geol. Mon. 5, p. 345-364.

Uto, K., 1986, Variation of Al_2O_3 content in late Cenozoic Japanese basalts: A re-examination of Kuno's High-Alumina Basalt: Jour. Volcan. Geotherm. Res., v. 29, p. 397-411.

Vance, R. K., and Condie, K. C., 1986, Geochemistry and tectonic setting of the early Proterozoic Ash Creek Group, Jerome, Arizona [abs.]: Geol. Soc. America Abstracts with Programs, v. 18, p. 419.

Vance, R. K., and Condie, K. C., 1987, Geochemistry of footwall alteration associate with the Early Proterozoic United Verde massive sulfide deposit, Jerome, Arizona, Econ. Geol., v. 82, p. 571-586.

Warden, A. J. and Mitchell, A. H. G., 1974, New Hebrides: in Spencer, A. M. (ed), Mesozoic-Cenozoic Orogenic Belts, Data for Orogenic Studies, Geol. Soc. London, Spec. Pub. No. 4, p. 433-444.

Weaver, S. D., Saunders, A. D., Pankhurst, R. J., and Tarney, J., 1979, A geochemical study of magmatism associated with the initial stages of back-arc spreading, Contrib. Mineral. Petrol., v. 68, p. 151-169.

White, D., 1986, Gold distribution at the United Verde Extension, A Massive base-metal sulfide deposit, Jerome, Arizona, Arizona Geol. Soc. Digest, v. 16, p. 330-338.

Williams, H., and McBirney, A. R., 1979, Volcanology, Freeman, Cooper and Co., San Francisco, 397 p.

Williams, H., Turner, F. J., and Gilbert, C. M., 1982, Petrography: W. H. Freeman & Co., San Francisco, 626 p.

Winchester, J. A., and Floyd, P. A., 1977, Geochemical discrimination of different magma series and their differentiation products using immobile elements: Chem. Geology, v. 20, p. 325-343.

Winkler, H. G. F., 1979, Petrogenesis of metamorphic rocks: New York, Springer-Verlag, 348 p.

Wood, B. J., and Fraser, D. G., 1976, Elementary thermodynamics for geologists: London, Oxford University Press.

Wood, D. A., 1979, A variably veined suboceanic upper mantle-Genetic significance for mid-ocean ridge basalts from geochemical evidence: Geology, v. 7, p. 499-503.

Wood, D. A., 1980, The application of a Th-Hf-Ta diagram to problems of tectonomagmatic classification and to establishing the nature of crustal contamination of basaltic lavas of the British Tertiary volcanic province: Earth Planet. Sci. Letters, v. 50, p. 11-30.

Yashida, T., Mukaiyama, H., and Izawa, E., 1981, Alteration in the Iwamii Kuroko mining district, Shimane Prefecture, Japan: Mining Geology, V. 31, p. 367-381.

Zen, E-an, 1986, Aluminum enrichment in silicate melts by fractional crystallization, some mineralogic and petrographic constraints, Jour. of Petrology, v. 27, pt. 5, p. 1095-1117.

Zielinski, R. A., 1975, Trace element evaluation of a suite of rocks form Reunion Island, Indian Ocean: Geochim. Cosmochim. Acta, v. 39, p. 713-734.